

LANCASTER UNIVERSITY

DOCTORAL THESIS

---

**Quantitative assessment of autism spectrum disorder: From underlying mechanisms to a novel diagnostic approach**

---

*Author:*

**Samuel J.K. Barnes**

*Supervisor:*

**Aneta Stefanovska**

*A thesis submitted in fulfillment of the requirements  
for the degree of Doctor of Philosophy*

*in the*

**Nonlinear Dynamics and Biomedical Physics Group  
Physics Department, Lancaster University**

**July 24, 2025**

# Declaration of Authorship

This thesis is my original work and has not been submitted, in whole or in part, for a degree at this or any other university. Nor does it contain, to the best of my knowledge and belief, any material published or written by another person, except as acknowledged in the text.

Samuel J.K. Barnes

July 24, 2025

## Publications

The following publications are part of this thesis:

- Barnes, S. J.K., Stefanovska, A. (2021). Physics of cellular energy metabolism. *Contemporary Physics*, 62(3), 125-143.
- Barnes, S. J. K., Bjerkan, J., Clemson, P. T., Newman, J., Stefanovska, A. (2024). Phase coherence—A time-localized approach to studying interactions. *Chaos: An Interdisciplinary Journal of Nonlinear Science*, 34(7).
- Barnes, S. J.K., Thomas, M., McClintock, P. V.E., Stefanovska, A. (2025). Theta and alpha connectivity in children with autism spectrum disorder. *Brain Communications*, 7(2), fcaf084.
- Barnes, S. J.K., Alanazi, M., Yamazaki, S., Stefanovska, A. (2025). Methamphetamine alters the circadian oscillator and its couplings on multiple scales in Per1/2/3 knockout mice. *PNAS Nexus*, 4, pgaf070.

## Conference, symposia and seminar contributions

1. Barnes SJK, Bjerkan J. (24 May 2023) Interacting systems of the human body [Public science talk]. Pint of science, Lancaster, United Kingdom.
2. Barnes SJK, Stefanovska A. (13 September 2023) Phase and traditional coherence in non-autonomous systems [Conference poster]. Time series analysis of noisy data conference, Lancaster, Lancaster, United Kingdom.
3. Barnes SJK, Bjerkan J. (13-15, September 2023) MODA: An introduction [Conference workshop]. Time series analysis of noisy data conference, Lancaster, United Kingdom.
4. Barnes SJK, Bjerkan J, Clemson PT, Newman J, Stefanovska A. (16 April 2023) Phase coherence: A robust approach to quantify interactions [Conference poster]. Celebration of Science meeting, Lancaster, United Kingdom.
5. Barnes SJK, Yamazaki S, Alanazi M, Stefanovska A. (29 November 2024) Methamphetamine alters the circadian oscillator and its couplings on multiple scales in *Per1/2/3* knockout mice [Conference poster]. Medical Physics Group Translation Meeting, Institute of Physics, London, United Kingdom.
6. Barnes SJK, Thomas M, McClintock PVE, Stefanovska A. (29 November 2024) Wavelet phase coherence: a time-localised, robust approach to evaluating functional connectivity in autism spectrum disorder [Conference presentation]. Medical Physics Group Translation Meeting, Institute of Physics, London, United Kingdom.



*“If you want to find the secrets of the universe, think in terms of energy, frequency and vibration.”*

Nikola Tesla

# Acknowledgements

This work would have been impossible without a plethora of incredible people gracing my life.

Firstly, I will forever be grateful to Professor Aneta Stefanovska for her constant guidance, patience and inspiration during this crazy period. You believed in me long before I had the self-confidence to believe in myself and saw a potential which I never realised existed. Your drive to make the world a better place has been a constant source of energy and inspiration.

Special thanks go to Christoph, Jose, Elena and the entire team at BrainHero for supporting me throughout the course of my PhD. Passionate people proving that private industry can change the world positively.

Special thanks go out to Elsie, my driving force, support system and motivation during sleepless nights and stressful times. Knowing this journey will end with you is the light that I needed during difficult days.

I can't possibly thank my parents enough for the personal sacrifice, constant encouragement and incredible role models they have been for me. My mum, Jan, for teaching me that having a backbone and standing up for oneself is nothing to be ashamed of; her implacable work ethic and kindness are attributes that I can only hope to emulate in my daily life. My Dad, Ken, for imbuing me with a curiosity for all things which lasts to this day, constant life lessons, and incredible quotes such as 'luck is where hard work meets opportunity' and the 6 Ps. Thank you both for teaching me there is beauty in struggle, and that the journey can be even more beautiful than the destination.

---

# Abstract

Autism spectrum disorder (ASD) is a complex neurodevelopmental condition characterised by persistent challenges in social communication and interaction, alongside restricted and repetitive behaviours. Despite almost a century of research, precise aetiologies and biomarkers are yet to be elucidated. While metabolic and circadian dysfunction has been linked to ASD, the exact connection remains elusive. Additionally, ASD diagnosis remains reliant on qualitative assessments, which are time-consuming, resource-intensive, and inherently subjective. ASD rates have increased eightfold in the last two decades, underscoring the need for faster, objective assessments. The absence of an accurate, quantitative diagnostic tool delays early identification, intervention, and support for children with ASD.

In this work we use time-localised, phase-based, multiscale analysis approaches to gain diagnostic and mechanistic insights into systems implicated in ASD. Electroencephalographic measurements are inherently susceptible to movement artefacts. We demonstrate that phase-based connectivity measures, such as wavelet phase coherence (WPC) and dynamical Bayesian inference (DBI), can detect interactions between brain regions despite these disturbances. By applying WPC and DBI, we reveal distinct connectivity patterns in the frontal cortex of young males with ASD, suggesting a potential biomarker. Circadian dysregulation is also prevalent in ASD, yet remains poorly understood; time-localised analysis such as wavelet transforms, ridge extraction and harmonic analysis allows us to establish the presence of behavioural modes and trace their changing frequency content over time. We reveal an irregular circadian rhythm that may contribute to disrupted sleep patterns in ASD. Given the established links between cellular energy metabolism and ASD, we also propose a simple phase oscillator-based model that simulates altered metabolic pathways with significantly fewer parameters than mass-based approaches.

Applying physics-based approaches to understand cellular dynamics, electrophysiology, and circadian regulation, contributes towards a cohesive framework to understand the multifactorial nature of ASD. Collectively, these findings provide

mechanistic insights while enhancing diagnostic capabilities through practical guidance on measurement and analysis. By explicitly considering key physical principles of biological systems, the framework presented can significantly advance the assessment of ASD and other neurological conditions, such as ADHD, depression and dementia.

# Contents

<b>Acknowledgements</b>	<b>v</b>
<b>Abstract</b>	<b>vi</b>
<b>1 Introduction</b>	<b>1</b>
1.1 The brain . . . . .	3
1.1.1 Electroencephalogram . . . . .	4
1.1.2 Frequency bands . . . . .	5
Low frequency (0.8 - 3.5 Hz) . . . . .	6
Medium frequency (3.5 - 12 Hz) . . . . .	6
High frequency (12 - 48 Hz) . . . . .	6
1.2 Autism spectrum disorder . . . . .	7
1.2.1 The heterogeneity of ASD . . . . .	8
1.2.2 EEG measures in ASD . . . . .	9
Power in ASD . . . . .	10
Connectivity in ASD . . . . .	10
1.3 Metabolism . . . . .	11
1.3.1 Altered metabolism in ASD . . . . .	11
WNT- $\beta$ catenin pathway . . . . .	12
1.4 Circadian regulation . . . . .	12
1.4.1 Chronobiology, sleep and ASD . . . . .	13
1.5 Physical characteristics of living systems . . . . .	14
1.5.1 Nonlinearities . . . . .	14
1.5.2 The rhythms of life . . . . .	15
Autonomous systems . . . . .	15
Non-autonomous systems . . . . .	16
Time as an explicit physical parameter . . . . .	17
Multiscale oscillations . . . . .	17
1.5.3 Non-equilibrium systems . . . . .	19
Self-sustained oscillations and limit cycles . . . . .	19
1.5.4 Chronotaxic systems . . . . .	20
1.6 Modelling living systems . . . . .	22
1.6.1 The Kuramoto model . . . . .	22
Interactions and emergent phenomena . . . . .	23
Synchronisation . . . . .	23
Time-dependent oscillations . . . . .	24
1.6.2 Extension to networks . . . . .	25
1.6.3 Intranetwork interactions . . . . .	25
Internetwork Interactions . . . . .	26
1.7 Analysis of living systems . . . . .	26
1.7.1 Time-domain . . . . .	27
Actograms . . . . .	27
Autocorrelation . . . . .	28

1.7.2	Frequency-domain . . . . .	28
	Fourier transform . . . . .	28
1.7.3	Time-frequency domain . . . . .	29
	Short-time Fourier transform . . . . .	30
	Wavelet transform . . . . .	30
1.7.4	Comparing approaches . . . . .	31
1.7.5	Phase extraction approaches . . . . .	32
	Hilbert transform . . . . .	32
	Ridge extraction . . . . .	32
1.7.6	Harmonic Analysis . . . . .	33
1.7.7	Interactions . . . . .	35
	Surrogates . . . . .	35
	Functional connectivity . . . . .	36
	Coherence . . . . .	36
1.7.8	Effective connectivity . . . . .	38
	Bispectral analysis . . . . .	38
	Dynamical Bayesian inference . . . . .	39
	Practical implementation . . . . .	40
1.8	Thesis outline . . . . .	41
<b>2</b>	<b>Physics of cellular energy metabolism</b>	<b>43</b>
<b>3</b>	<b>Phase coherence - a time-localised approach to studying interactions</b>	<b>64</b>
<b>4</b>	<b>Theta and alpha connectivity in children with autism spectrum disorder</b>	<b>87</b>
<b>5</b>	<b>Methamphetamine alters the circadian oscillator and its couplings on multiple scales in <i>Per1/2/3</i> knockout mice</b>	<b>105</b>
<b>6</b>	<b>Cellular energy metabolism in ASD</b>	<b>119</b>
6.1	Metabolism in the brain . . . . .	120
6.2	Metabolic coupled phase oscillators . . . . .	121
6.2.1	Single phase oscillator model . . . . .	121
6.2.2	Network based model . . . . .	122
6.2.3	Parameter selection . . . . .	124
	Network model parameters . . . . .	125
6.2.4	Metabolic mode . . . . .	125
6.3	The parameter space . . . . .	126
6.4	Neuronal cellular energy metabolism in ASD . . . . .	128
	The Warburg effect . . . . .	129
6.4.1	Upregulation of the glucose transporter proteins . . . . .	129
6.4.2	Upregulation of both lactate and glucose transporter proteins . . . . .	130
6.5	Conclusion and future work . . . . .	131
<b>7</b>	<b>Discussion and conclusion</b>	<b>133</b>
7.1	Summary . . . . .	133
7.2	Original contribution . . . . .	134
7.3	Future work . . . . .	134
<b>A</b>	<b>Supplementary information</b>	<b>136</b>

# List of Figures

1.1	Diagram of the brain at different scales . . . . .	4
1.2	The 10-20 EEG system and frequency bands of interest . . . . .	5
1.3	Multiscale deterministic oscillations . . . . .	18
1.4	Phase space of a Van der Pol oscillator . . . . .	20
1.5	Conventional and chronotaxic limit cycles . . . . .	21
1.6	Arnold tongue for conventional phase synchronisation and intermit- tent synchronisation . . . . .	24
1.7	Comparison between time series analysis approaches . . . . .	33
1.8	Exemplar simulated coupling functions . . . . .	39
6.1	Simplified model of the interacting components of cellular energy metabolism . . . . .	120
6.2	Possible synchronisation states in healthy cells . . . . .	127
6.3	State space for healthy model parameters . . . . .	128
6.4	State space following upregulation of glucose transporter proteins . . .	130
6.5	State space following upregulation of glucose and lactate transporter proteins . . . . .	131

# List of Tables

1.1	Model parameters across different modes for the time series in Fig. 1.3	18
6.1	Table of parameters for the single oscillator model . . . . .	124
6.2	Table of parameters for the network based model . . . . .	125
6.3	Synchronisation states and their corresponding metabolic mode . . . .	127



# List of Abbreviations

<b>ASD</b>	<b>Autism Spectrum Disorder</b>
<b>EEG</b>	<b>ElectroEncepheloGraphy</b>
<b>fNIRS</b>	<b>functional Near InfRared Spectroscopy</b>
<b>DBI</b>	<b>Dynamical Bayesian Inference</b>
<b>GABA</b>	<b>Gamma-AminoButyric Acid</b>
<b>ATP</b>	<b>Adenosine TriPhosphate</b>
<b>OXPHOS</b>	<b>OXidative PHOSphorylation</b>
<b>MO</b>	<b>Mitochondrial Oscillator</b>
<b>GO</b>	<b>Glycolytic Oscillator</b>
<b>MASCO</b>	<b>MethAmphetamine Sensitive Circadian Oscillator</b>
<b>Per</b>	<b>Period genes</b>
<b>WPC</b>	<b>Wavelet Phase Coherence</b>
<b>AWPC</b>	<b>Amplitude Weighted Phase Coherence</b>
<b>VPA</b>	<b>ValProic Acid</b>
<b>WNT</b>	<b>Wingless Integration Site</b>
<b>MCT</b>	<b>MonoCarboxylate Transporter</b>
<b>GLUT</b>	<b>GLUcose Transporter</b>
<b>SCN</b>	<b>SupraChiasmatic Nucleus</b>
<b>ML</b>	<b>Machine Learning</b>

Dedicated to my family...

## Chapter 1

# Introduction

Autism Spectrum Disorder (ASD) is a complex neurodevelopmental condition with heterogeneous aetiologies [1] and diverse clinical presentations [2]. It is characterised by social and communication deficits, as well as restricted and repetitive behaviours, which are not better explained by intellectual disability or global developmental delay [3]. While several genetic and environmental factors have been linked to ASD [4], and its prevalence has risen significantly in recent years [5], the precise mechanisms underlying the condition remain unclear. Investigating common comorbidities, such as altered cellular energy metabolism and circadian dysregulation, may reveal the putative mechanisms underlying ASD.

The brain is one of the most energetically demanding organs in the body [6] and, as such, requires highly efficient metabolic processes to sustain its function. In ASD, evidence suggests that upregulation of the WNT- $\beta$  catenin pathway may drive a metabolic shift known as the Warburg effect [7, 8]. This hypothesis is further supported by findings of elevated lactate levels and decreased pH in the brains of individuals with ASD [9, 10, 11, 12]. To better understand these metabolic alterations, phenomenological phase-oscillator models can be employed to simulate metabolic transitions. Applying such models provides mechanistic insights into how metabolic dysregulation influences brain states in ASD.

Circadian dysregulation is disproportionately prevalent in individuals with ASD [13, 14], with up to 80% experiencing sleep disturbances [15]. While the canonical circadian oscillator is well studied, alternative, understudied pacemakers may also contribute to circadian dysregulation in ASD [16]. To investigate the role of one such alternative pacemaker, behavioural rhythms in mice were examined across various

experimental conditions. Our study reveals a time-variable circadian oscillator, the irregularity of which may contribute to the disrupted sleep patterns frequently observed in ASD [17].

Understanding the metabolic and circadian alterations associated with ASD provides key mechanistic insight into the underlying biology. These changes have a direct impact upon neuronal excitability and synaptic function, and therefore affect the overall connectivity of the brain. While it is vital to understand how metabolic and circadian mechanisms contribute to, or are influenced by, the condition, they cannot provide a robust diagnostic framework alone. The changes to brain connectivity, however, represent a measurable characteristic that has been shown to differ between individuals with ASD and neurotypical controls [18, 19].

Despite decades of research aimed at identifying quantitative biomarkers, the diagnosis of ASD remains reliant on qualitative assessments conducted by qualified paediatricians using behavioural questionnaires. Attempts at finding an objective, quantitative measure of ASD have been obfuscated by a series of experimental results with conflicting findings. For example, studies have reported both hyperconnectivity [20, 21] and hypoconnectivity [22, 23, 24, 25] of brain networks in children with ASD.

The heterogeneity in the literature may be partially attributed to traditional approaches not considering time as an explicit physical parameter. Approaches which average over time can disregard interesting transient phenomena as stochastic [26]. Additionally, shorter measurement intervals will contain fewer cycles of oscillation, and so less data, to analyse, particularly in lower frequency bands where there are fewer oscillations in a given measurement interval [27]. Efforts to mitigate movement artifacts, such as segmenting recordings into shorter epochs, can further exacerbate this issue by reducing the length of analysable time series. Moreover, such segmentation risks discarding deterministic dynamics [26].

Rather than treating electroencephalography (EEG) data as intractable due to participant movement or risk removing hidden determinism via excessive preprocessing, we apply time-localised analysis approaches that are inherently robust against perturbations. To demonstrate its resilience, wavelet phase coherence is compared to its amplitude-weighted counterpart [28]. Applying this analytical framework to

EEG data from a cohort of young males with ASD and neurotypical controls reveals theta and alpha connectivity patterns as a promising marker for ASD.

The thesis is structured as follows: The next subsection briefly introduces the brain and explains how EEG can be used to measure neural activity. This is followed by an overview of autism spectrum disorder (ASD), including its historical context and known EEG patterns. The roles of metabolic and circadian systems in ASD are then explored. Next, the physical characteristics of living systems, which require special consideration in data analysis, are described. A discussion on modelling such systems follows, culminating in a summary of time series analysis techniques.

Chapter 2 compares phase oscillator and mass-based models of cellular energy metabolism. Chapter 3 introduces wavelet phase coherence and contrasts it with its amplitude-weighted counterpart. Chapter 4 analyses EEG connectivity patterns in young males with ASD compared to neurotypical controls. Chapter 5 examines behavioural rhythm data in mice, revealing an irregular, non-canonical circadian oscillation. Chapter 6 proposes a phenomenological phase oscillator model replicating altered metabolic states caused by WNT- $\beta$  catenin pathway upregulation in ASD. Finally, Chapter 7 summarises the findings and outlines future research directions.

## 1.1 The brain

The brain plays a central role in interpreting and responding to environmental stimuli. Neurons, which propagate information through electrical signals and chemical interactions at synapses, are key to this process [29]. However, they depend on a diverse network of glial cells, which are present in approximately equal numbers to neurons in the brain [30]. Glial cells do not directly participate in electrical signalling, instead providing metabolic support [31]. Despite comprising only about 2% of the body's mass, the brain consumes roughly 20% of circulating oxygen and calories, highlighting the importance of metabolic support in neural circuitry [6].

The brain is composed of specialised lobes (as indicated in Fig. 1.1) that require a highly interconnected network to function efficiently. Different regions of the cerebral cortex are associated with distinct neural processes. Historically, behavioural changes following brain injury provided evidence regarding the specific functions

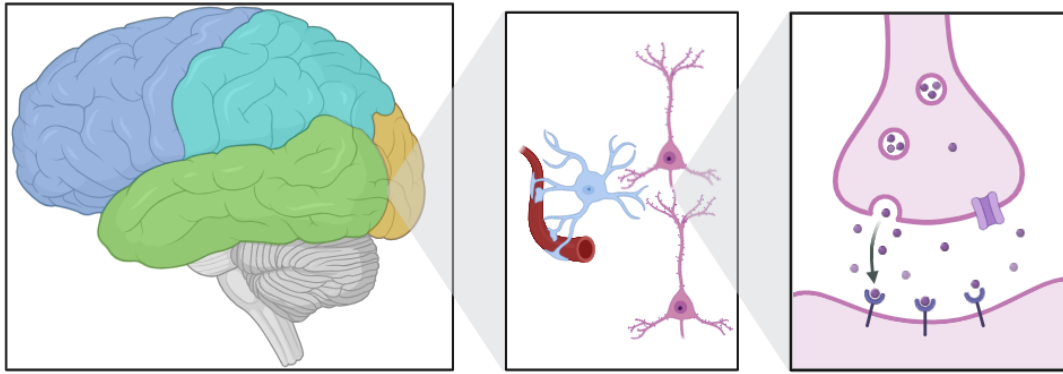


FIGURE 1.1: The brain at multiple scales. Left: different lobes of the cerebral cortex are labelled via colour, frontal lobe - dark blue, parietal lobe - light blue, occipital lobe - yellow, temporal lobe - green. Middle: red blood vessel carry nutrients which are transferred to the purple pyramidal cells via a light blue astrocyte. Right: synaptic cleft between neurons, circular vesicles carry neurotransmitters to the cleft, which diffuse across before binding to receptors on the opposite neuron. Created using BioRender.com

of lobes. For example, when a metal bar shot through the frontal lobe of Phineas Gage following a mining accident, he subsequently experienced a loss of executive function [32]. Similarly, damage to the occipital lobe can impair vision [33], while the temporal and parietal lobes have important functions in memory formation [34], and sensory information processing [35], respectively. Modern neuroscience has provided a more comprehensive understanding of these relationships, confirming the occipital lobe's role in visual processing and the frontal lobe's role in higher-order cognitive functions, thanks to the development of non-invasive devices capable of monitoring changes in neural state. Despite the brain's inherent complexity, certain patterns can be observed using non-invasive technologies to probe underlying neural activity patterns.

### 1.1.1 Electroencephalogram

To measure the electrical signals emanating from the cerebral cortex on a macroscopic scale, we use electroencephalography (EEG). These signals are generated by transmembrane ion currents in the pyramidal neurons of the cortex and propagate to scalp electrodes through the brain, skull, and scalp tissues [36].

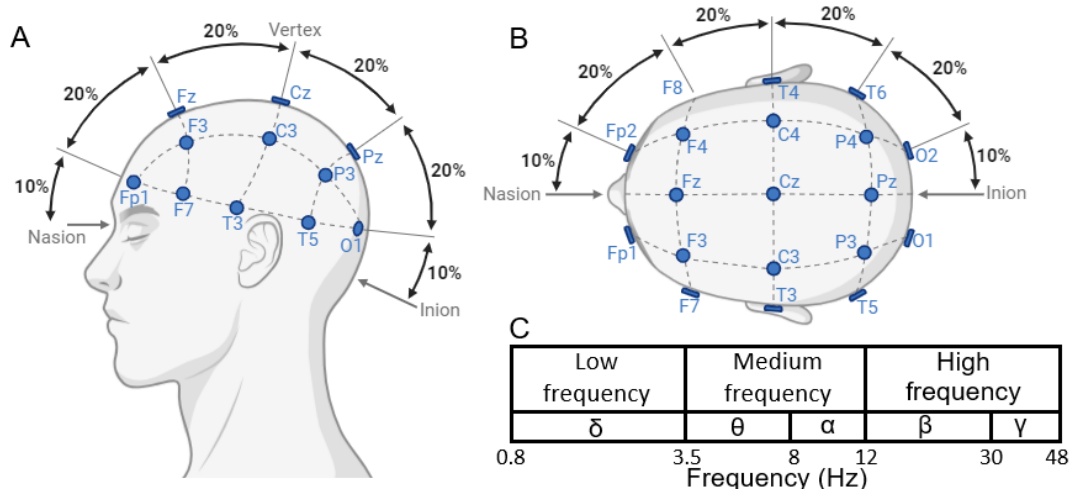


FIGURE 1.2: (A,B) Diagrams representing the 10-20 EEG system. Each probe position is labelled with reference to the inion and nasion in degrees. (A) EEG schematic side profile. (B) (A) EEG schematic top down. (C) The traditional frequency bands of interest, which are split into three different ranges with logarithmic frequency spacing. Created in BioRender.com

While EEG has limited spatial resolution [37], often suffering from volume conduction—where electrical signals propagate across the scalp and are detected by multiple probes [38]—it benefits from high temporal resolution. This makes EEG well-suited to time-localised analysis approaches. Additionally, EEG is cost-effective, portable, non-invasive and relatively comfortable making it an ideal tool for assessing neurological conditions. Comfort is a critical factor for EEG devices, especially for individuals with ASD, who may be predisposed to sensory hyper-responsiveness [39]. The electrical signal detected from the brain using EEG is relatively strong compared to external influences, unlike the magnetic field detected by magnetoencephalography, which requires a magnetically shielded room to avoid interference from the Earth’s magnetic field [40], thereby reducing portability and increasing the cost of application.

### 1.1.2 Frequency bands

Brain activity typically occurs at different frequencies depending on subject state during measurement. In the current work, the traditional five frequency bands have been consolidated into three, for the following reasons. First, the boundaries between the traditional bands (delta, theta, alpha, beta, and gamma) are not always

clearly distinguishable in the power spectra of EEG data, making it difficult to separate the alpha and theta bands consistently across subjects. Second, it is well-established that EEG power spectra evolve during childhood development as the brain matures, with alpha activity increasing from around 6 to 10 Hz during development [41]. Finally, prior studies on EEG activity in children with ASD have not adhered to strict frequency band limits, and no standardised frequency band definitions have been established to date.

### **Low frequency (0.8 - 3.5 Hz)**

Traditionally referred to as delta waves, low frequency oscillations are most prevalent during periods of deep sleep and rest [42]. Additionally, delta waves have been associated with inhibiting sensory interferences and modulating brain networks to support focused mental tasks such as working memory, semantic processing, and motor response inhibition [43]. It has also been proposed that reduced delta power in people with ADHD may be due to hypoactivity in the dopaminergic reward/reinforcement circuitry [44].

### **Medium frequency (3.5 - 12 Hz)**

The medium frequency range contains the traditional alpha and theta oscillations. These brain waves are present in wakeful states and are elevated during periods of relaxation, for example alpha-band amplitude increases when attention is unfocused or internally focused (e.g. when the eyes are closed) and decreases when attention is engaged on stimuli in the external environment (e.g. when the eyes are open, especially if attention is focused on a specific object) [45].

### **High frequency (12 - 48 Hz)**

Beta and gamma waves are higher frequency oscillations. While these waves can be emblematic of increased concentration and higher states of awareness, they are also present during bouts of anxiety or restlessness [46].



## 1.2 Autism spectrum disorder

Autism spectrum disorder (ASD) is a developmental condition characterised by persistent deficits in social interactions and/or restricted and repetitive behaviours [3]. Although some aspects of the ASD behavioural phenotype may be present during early development, they may not become fully manifest until social demands exceed limited capabilities, making early detection difficult [47].

It has been over 80 years since Leo Kanner first described what he termed 'infantile autism' - a condition characterised by a specific pattern of 'abnormal behaviour' [48]. Despite Kanner's description being used elsewhere in the literature, it took another 37 years for it to be entered into the American Psychiatric Association's Diagnostic and Statistical Manual, DSM III [49]. In the decades since, a wealth of research has been carried out to understand the multifaceted aetiologies and presentations of autism spectrum disorder [50]. ASD is now widely accepted as a complex, pervasive, heterogeneous condition with multiple aetiologies and developmental trajectories [2].

Several factors are thought to contribute to the development of ASD. These include, but are not limited to, environmental factors as diverse as prenatal medication exposure [51, 52], advanced parental age [53, 54] and nutritional deficiencies [55, 56]. Genetics are also a contributing factor in ASD, demonstrated by the high heritability (between 40 and 80 percent) of the condition [57], although known genes contributing to ASD can only account for less than a quarter of cases [57]. The aetiology of ASD is therefore multifactorial, with several potential environmental [58] and genetic links [59]. Despite decades of research, a theory linking the diverse aetiologies of ASD to a diagnosis is beyond reach.

Diagnosis of ASD still relies upon the qualitative observation of atypical behaviours using questionnaires. While valuable, these assessments are time-consuming, expensive (with a median cost of around £800 per child) and require assessment from a multidisciplinary team of healthcare professionals [60]. This process can also be uncomfortable for children with ASD, who may find interactions with unfamiliar adults or participation in structured social settings distressing. A quantitative assessment of ASD would decrease the cost and wait times for ASD diagnosis while

providing an objective evaluation.

### 1.2.1 The heterogeneity of ASD

While ASD is defined as a complex neurodevelopmental condition involving persistent challenges with social communication and/or restricted interests and repetitive behaviours [3], individuals with the condition exhibit remarkable phenotypic heterogeneity [61]. Presentations can vary widely, including differences in intellectual functioning (from profoundly low to exceptionally high IQ) [62], atypical sensory processing such as hyper- or hypo-responsiveness [63], and language impairments [64], among others. Some individuals with ASD display many of these characteristics, others few or none, and most present with a unique combination. This variability is why ASD is considered a spectrum—each individual may exhibit a distinct neurocognitive and behavioural profile [65]. Such diversity complicates the development of diagnostic tools, as each phenotype can be associated with different patterns of underlying neural activity. Future studies should aim to delineate behavioural subdomains and map them onto specific electrophysiological signatures, allowing for assessments that better reflect the complexity of the condition.

Adding further complexity, ASD frequently co-occurs with other neurodevelopmental and psychiatric conditions [66]. Most notably, over 50% of individuals with ASD also meet diagnostic criteria for ADHD [67]. Elevated rates of anxiety [68], depression [69], and epilepsy—especially in those with co-occurring intellectual disability [70]—have also been consistently reported. These comorbidities are important to consider when designing electrophysiological assessments for ASD, as each is known to independently influence EEG patterns [71, 72, 73]. Consequently, it is essential to control for the effects of these conditions when interpreting EEG data, to ensure that observed differences are truly reflective of ASD-specific neural characteristics.

Further challenges arise from the highly heterogeneous developmental trajectories observed in individuals with ASD [74]. Behavioural characteristics in people with ASD may shift substantially during development. Although neurotypical children also undergo developmental changes in brain function, these trajectories tend

to be more predictable and less variable than those seen in children with ASD. Moreover, our understanding of the mechanisms driving neurodevelopmental change remains incomplete [75]. These issues hinder efforts to track ASD over time or to evaluate the long-term effects of interventions. Longitudinal studies are therefore critical to disentangle age-related changes from ASD-specific developmental features and to understand how behaviour and neural activity co-evolve.

ASD is an umbrella term encompassing a diverse range of neurodevelopmental conditions that were previously diagnosed separately [3]. Recognising and embracing this complexity is essential to understanding both the heterogeneity of clinical features and the variability in underlying brain dynamics. Electrophysiological measures must therefore be interpreted in the context of individual behavioural profiles and their evolution over time. Explicit consideration of intra-group differences is vital for identifying reliable neural markers of ASD.

### 1.2.2 EEG measures in ASD

Over the past fifty years, several potential markers for ASD have been proposed [76]. However, conflicting findings have made it challenging to establish clear generalisations [77].

The heterogenous results can be partially attributed to a failure to consider age groups when comparing studies. EEG activity evolves with age [78], implying the differences between ASD and neurotypical evaluations of electrical activity are likely to evolve during development [79]. This is a particularly important consideration because ASD is a neurodevelopmental condition [80]. To control for developmental changes, study design should apply narrow age ranges.

Males and females can be reliably distinguished based on EEG data analysis alone, highlighting the confounding effect of sex [78]. In ASD this is further exacerbated as females present differently [81]. In particular, behaviours such as masking [82] are much more prevalent in females. ASD is currently diagnosed more frequently in males, at a rate between 3:1 and 4:1 [83] and EEG holds promise as an objective and qualitative tool that could aid in diagnosing the girls overlooked by traditional diagnostic methods [84]. To develop accurate diagnostic criteria the confounding effects of sex differences should be controlled.

The literature is also confounded by the vast array of different methods and measurement protocols applied to determine power and connectivity. Even within EEG measures, factors such as the duration of measurement [85], eyes open or eyes closed participant state [86], and rest vs active state of participants [87] can affect results. A wide range of analytical methods have been used to extract the power or connectivity from EEG time series [88]. These can produce different results, as we discuss in depth in Sect. 3. One should not expect the power and connectivity differences found by different protocols to be the same.

Despite these often contradictory findings, patterns have emerged capable of differentiating ASD from neurotypical signatures. Predominantly, the findings can be split into two types, those related to the connectivity between brain regions and the power of the EEG signals.

### **Power in ASD**

The literature reports both elevated [89, 90] and decreased [91] spectral power in ASD relative to controls, and these relationships are also confounded by changing patterns which depend on age [79, 92]. However the prevailing patterns generally represent ASD as having what is known as the 'u-shaped distribution', with elevated low and high frequency activity, while the medium frequencies are reduced relative to controls [92, 93].

### **Connectivity in ASD**

Several approaches have been attempted to assess the connectivity between brain regions using EEG. Similar to the power results, these are varied, however general trends exist, such as a prevailing tendency for reduced connectivity in ASD, especially at lower frequencies [19, 22, 94], although this picture is confounded by inconsistent findings [95].

The strength of long vs short-range connections is also regularly investigated, with short-range overconnectivity [96, 97] and long-range underconnectivity [98, 99] often reported; however, the situation is obfuscated by results which demonstrate conflicting findings [100, 101]. These discrepancies may stem from methodological inconsistencies regarding participant age [79], sex [91], analysis approach applied

and the experimental apparatus used [27, 77, 102]. Given the conflicting results in the literature, implementing time series analysis methods that are robust to movement artifacts and noise, along with standardised measurement protocols, may offer a reliable approach to characterising atypical connectivity patterns in ASD compared to neurotypical controls.

### 1.3 Metabolism

The body requires a continuous supply of ATP to sustain life, producing nearly its own weight in ATP daily [103]. ATP is predominantly generated through two main processes, with oxidative phosphorylation being the most efficient, yielding 28 molecules of ATP for every molecule of glucose oxidised. In contrast, glycolysis produces only two ATP molecules per glucose molecule [104]. However, glycolysis can quickly respond to increased energy demand, making it the preferred pathway in rapidly proliferating cells, such as those in cancer [105, 104]. Neuronal function would be impossible without the continuous energy production by glial cells such as astrocytes, which provide essential metabolic support to neurons [106].

The brain is remarkably metabolically demanding and accounts for over a fifth of the total bodies energy consumption at rest [107, 108]. Due to this extraordinary energy demand, it is perhaps unsurprising that a close relationship between metabolism and mental health exists [109, 110], and that altered metabolism is present in depression [111] and generalised anxiety disorder [112]. One of the earliest known altered metabolic states is the Warburg effect, first described by Otto Warburg in 1923 [113]. This effect details a shift from oxidative phosphorylation (OXPHOS) to an upregulation of glycolysis, a phenomenon now observed in several conditions such as cancer [114]. Metabolic shifts can produce altered levels of products such as lactate, which can change the PH of the brain [115].

#### 1.3.1 Altered metabolism in ASD

Decades of evidence suggest that ASD may be linked to altered energy metabolism in the brain [116, 117, 118, 119, 120]. In particular, the Warburg effect has been implicated as encouraging the progression of ASD [121]. Upregulated glycolysis in ASD

is indicated by elevated lactate levels [10, 11, 120], and mitochondrial dysfunction [122, 123, 124, 125]. Taken together, there exists strong evidence that metabolic dysfunction plays a significant role in ASD, yet the precise mechanism remains elusive [126].

### **WNT- $\beta$ catenin pathway**

One candidate for the mechanism linking metabolic dysfunction with ASD is the wingless and integration (WNT)  $\beta$ -catenin pathway [7]. The WNT pathway is a signalling cascade responsible for development, growth, and metabolism [127].

There is a large body of evidence linking WNT- $\beta$  catenin stimulation to the Warburg effect [128, 129]. Both the Warburg effect and disruptions to the the WNT-catenin pathway are implicated in the pathogenesis of several conditions including cancer [130]. Genetic evidence has also implicated dysregulated WNT pathways as being present in ASD [131, 132, 133]. Additionally, VPA exposure is known to stimulate the WNT- $\beta$  catenin pathway [134] and increases ASD risk [51]. Several rodent models have also demonstrated that disruptions to the WNT pathway proteins induces ASD-like behaviours [135]. Mice exposed to VPA upregulate proteins associated with ASD risk and demonstrate impaired social behaviours [136] following the activation of WNT pathways [137]. The metabolic reprogramming caused by this pathway may link the diverse aetiologies and phenotypic heterogeneity in ASD [138].

## **1.4 Circadian regulation**

To function optimally, human beings are constrained to live within a 24-hour cycle, dictated by the Earth's rotation [139]. This circadian rhythm governs many physiological processes via genetically encoded endogenous clocks which temporally regulate cellular systems [140]. Disregarding our intrinsic chronobiology leads to disease [141, 142]. For instance, shift workers have a marked increase in all-cause mortality [143]. Moreover, heart attack rates spike by 24% following the spring daylight-saving time adjustment [144], illustrating that even minor disruptions to circadian rhythms can have profound health consequences.

Despite consisting of only about 20,000 neurons, the suprachiasmatic nucleus (SCN) in the hypothalamus of the brain acts as our principle circadian clock [145]. Light is the primary zeitgeber (time giver) in this system allowing the SCN to synchronise with environmental stimuli [146]. Regulation of peripheral clocks via this central oscillator takes place via neural and humoral signals [147].

In addition to central circadian regulation in the SCN, mammals have two additional extra SCN clocks, the food entrainable oscillator and methamphetamine sensitive circadian oscillator (MASCO) which can drive physiological responses such as the sleep-wake cycle [148], autonomic nervous system responses and more [149]. Even though these SCN-independent oscillators have been demonstrated to coordinate the phases of peripheral clocks [149] their exact anatomical loci, biological mechanisms and influence over behaviour are unknown [16]. Studying the locomotor rhythms generated by these understudied circadian regulators may provide clarity regarding the dysfunctional sleep patterns often reported in people with neurological conditions [150, 151, 152].

### 1.4.1 Chronobiology, sleep and ASD

The ability to acquire sufficient sleep is essential for proper functioning in the brain [153]. Changes in circadian regulation disrupt proper sleep-wake cycles and so can exacerbate pre-existing mental conditions.

Over half of individuals with ASD also present with ADHD [67]. Individuals with ADHD are known to exhibit significant circadian disruption [154]. This irregular sleep-wake cycle is similar to that observed in rodents when driven by the methamphetamine sensitive circadian oscillator [155]. A growing body of evidence suggests circadian irregularities in individuals with ASD [156, 157]. Sleep disturbances are common in ASD [17], estimated at between 50 and 80 percent, compared to less than 30 percent in the general population [158]. Disruptions to circadian biomarkers such as melatonin [159, 160], cortisol [161, 162, 163] and serotonin [164, 165] have also been identified in ASD. Abnormal circadian regulation also dysregulates the WNT- $\beta$  catenin pathway [vallee2022wnt].

Non-canonical circadian oscillators have received little attention in the scientific community [16], and so their potential role in developmental disorders remains to be

elucidated. Identifying and describing the dynamics of these understudied oscillators may elucidate the cause of sleep disorders in several conditions. It is important to underline that the potential mechanistic factors we link here to ASD, from the cellular to the circadian level, are not specific to the condition. In fact, circadian abnormalities are present in almost all diseases [166]. Nevertheless, understanding the functional importance of the circadian clock in normal and aberrant neurodevelopmental processes may provide a novel perspective to understand ASD [167].

## 1.5 Physical characteristics of living systems

Living systems span a broad spectrum of temporal and spatial scales. Despite their apparent differences, all organisms share fundamental characteristics that can be understood within the framework of physics. Biological processes operate across diverse timescales, requiring multiscale representations to capture interactions spanning a wide range of frequencies. To sustain life, organisms must also exchange energy and matter with their environment through processes such as consumption and excretion. These interactions usually take place in a cyclic manner, resulting in most biochemical processes being oscillatory. Furthermore, biological systems are inherently time-dependent, continually evolving across the lifespan. Considering these factors is essential for accurately modelling and analysing living systems.

### 1.5.1 Nonlinearities

Biological processes are inherently nonlinear, meaning their output is not directly proportional to their input. Nonlinear dynamics is essential for accurately describing these systems, which typically consist of interconnected feedback loops that regulate homeostasis and enable adaptation to environmental changes.

For example, during exercise, chemoreceptors detect a drop in oxygen levels and signal the medulla oblongata to increase heart rate. Similarly, when blood pressure falls too low, baroreceptors trigger the medulla to adjust the autonomic nervous system, restoring heart rate and blood flow [168]. This dynamic feedback enables the cardiovascular system to adapt to varying physiological demands, such as exercise, stress, or rest, ensuring precise regulation and control [169].



Nonlinear responses also play a crucial role in nerve transmission, which relies on threshold-dependent activation. A small change in input can lead to a disproportionately large output. Specifically, an action potential—a rapid, all-or-nothing electrical signal—occurs only if the membrane potential reaches a critical threshold. Once triggered, the signal propagates along the neuron’s axon [170].

Emergent properties such as the synchronization of metabolic oscillations, cardiac rhythms, or neural oscillations also cannot be explained by the simple superposition principles of linear systems. These phenomena arise from the dynamic interactions of highly interconnected nodes within biological networks. Synchronization is a hallmark of nonlinear systems, reflecting collective behaviour that depends upon coupling mechanisms [171].

The presence of positive and negative feedback loops ensure biological parameters remain within a healthy range, while also giving rise to rhythmic behaviour.

### 1.5.2 The rhythms of life

Cycles are ubiquitous in nature, with levels of substrates and products fluctuating over time. These oscillations are often irregular and time-dependent, and their time-localised characteristics can reflect states of health or disease. For instance, heart rate variability, which monitors changes in the time between heartbeats, can measure fatigue and disease states [172]. However, many analytical frameworks erroneously treat these systems as isolated or closed, neglecting the crucial influence of their environment and external factors on their behaviour.

#### Autonomous systems

As the name suggests, autonomous systems are independent of interaction with their external environment [173]. From a thermodynamic perspective, they are isolated systems—exchanging neither matter nor energy with their surroundings. This framework has been used to describe a wide range of phenomena, from the swaying of footbridges under the influence of crowds [174] to the synchronisation of fireflies [175]. Autonomous systems can be described by differential equations of the form,

$$\frac{dx}{dt} = f(x(t)), \quad (1.1)$$

where  $x$  represents the state of the system and  $t$  denotes time. Crucially, the right-hand side does not depend explicitly on  $t$ ; the evolution of the system is determined solely by  $x(t)$ .

In the context of living systems, however, the notion of autonomy becomes problematic [173]. Biological processes are modulated by a range of external factors, including hormones, neurotransmitters, and their environment. Given that thermodynamic openness is a fundamental requirement for life, modelling living systems as autonomous is both biologically and physically inappropriate [176, 177]. Therefore, analytical frameworks must account for external influences to accurately reflect the dynamics of living organisms.

### Non-autonomous systems

Non-autonomous systems are influenced by their environment. Thermodynamic openness is essential for sustaining life, as organisms must constantly exchange matter and energy with their surroundings to survive [178]. These systems can be represented by equations of the form,

$$\frac{dx}{dt} = f(x(t), t), \quad (1.2)$$

where, unlike in the autonomous equation of Eq. 1.1, the law governing the state of the system does not depend solely upon  $x$ , but also upon time. This enables time-dependent couplings to influence the system, representative of external influences.

Far from being an obstacle to understanding these systems, this complexity enables further examination of their dynamical properties that can indicate pathogenic states. For example, the heart rate variability, a measure of the time between heartbeats, can fluctuate based on external factors such as physical activity, stress, or disease. The adaptive nature of non-autonomous systems, capable of continuously responding to internal and external stimuli, allows for dynamic regulation of systems in the face of a changing environment. Many traditional physics based approaches

treat systems as autonomous or isolated from their environment and so are often inadequate for describing the complexity of living systems. In this thesis, we present a fundamentally different approach.

### **Time as an explicit physical parameter**

Given that living systems are generally non-autonomous, averaging over transient phenomena using traditional analytical approaches risks neglecting valuable information. Behaviour such as couplings may come and go over time, and the information regarding the duration of events, which may be capable of betraying pathogenic states [179, 180, 181], will be lost. Averaging across time assumes stationarity, which may obscure the system's underlying state and mischaracterise deterministic behaviour as stochastic [26]. The presence of time-localised dynamics must therefore be considered explicitly during analysis.

By combining a multiscale approach with time localisation, one is able to track the presence and evolution of modes ranging across scales of different orders of magnitude and uncover previously hidden pockets of determinism. This topic is further explored, with methodological examples, in Sect. 1.7.

### **Multiscale oscillations**

Biomedical signals typically comprise multiple time-dependent, often self-sustained oscillations, each corresponding to a distinct biological process and conveying unique information. For instance, blood flow signals recorded using laser Doppler flowmetry reveal components related to cardiac, respiratory, myogenic, neurogenic, and endothelial activity, each operating at different characteristic frequencies within the same time series [182]. The superposition of such complex multiscale dynamics can give the false impression that the signal is purely noise-like, leading to a widespread tendency to filter these signals prior to analysis, discarding potentially deterministic information [183].

To illustrate how deterministic multiscale dynamics can easily be mistaken for randomness, consider three non-autonomous oscillatory modes, each defined by:

$$\omega(t) = \omega_i (1 + A_i \sin(\omega_{\text{mod}i} t)). \quad (1.3)$$

The parameters for each mode are provided in Table 1.1. The system was simulated using a fourth-order Runge-Kutta integration scheme over 400 seconds with a sampling frequency of 200 Hz.

TABLE 1.1: Model parameters across different modes for the time series in Fig. 1.3

	$\omega_i$	$\omega_{modi}$	$A_i$
Mode 1	6.1	0.015	15
Mode 2	1.25	0.005	2
Mode 3	0.2	0.0025	1

The sum of these three modes, combined with added pink noise to represent measurement noise, yields the time series shown in Fig. 1.3.

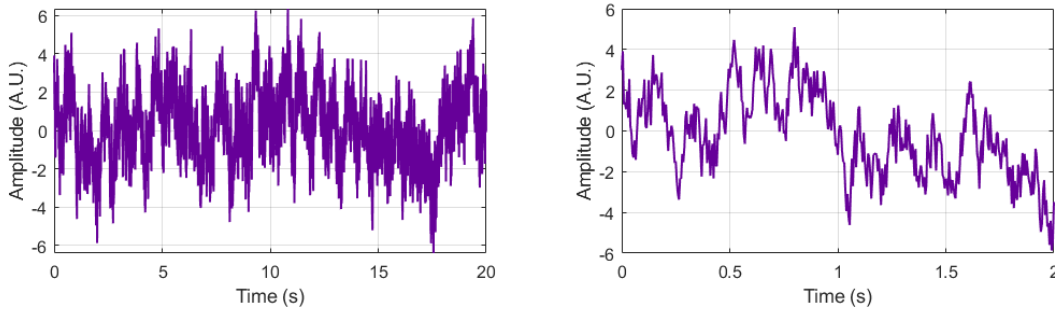


FIGURE 1.3: A simulated multiscale deterministic oscillation shown over 20 seconds (left) and 2 seconds (right).

Despite being composed of just three deterministic modes, the time series in Fig. 1.3 appear complex, and its structure is difficult to discern by visual inspection alone. In biological systems, the number of such oscillatory components is typically much greater, and signals are further obfuscated by movement artefacts and measurement difficulties [28]. Moreover, the characteristic timescales of different modes can vary by several orders of magnitude, requiring analytical tools capable of simultaneously resolving oscillations spanning from milliseconds to days.

Cross-frequency couplings also exist—for example, circadian rhythms are known to modulate cell cycle oscillations [184]. Rather than discarding this complexity through filtering, the methods presented in this thesis are designed to preserve and accommodate it. In doing so, this approach retains potentially valuable deterministic components that might otherwise be mistaken for noise [26]. A cornerstone of the approaches presented in this thesis is the maximal preservation of the underlying information.

### 1.5.3 Non-equilibrium systems

Life exists in a constant state of flux, with energy and matter continuously exchanged with the environment to expel waste and absorb nutrients. As discussed above, characterizing living systems as closed or isolated overlooks critical influences. Traditionally, many living systems have been described as autonomous (self-contained), while a more accurate description would be non-autonomous, as they are subject to external influences. Non-autonomous systems are more common in biology, however they are often inappropriately treated as autonomous.

#### Self-sustained oscillations and limit cycles

Self-sustained oscillators can oscillate without any external periodic input and are characterised by a stable limit cycle in their phase space. A limit cycle is a closed trajectory in phase space, where at least one neighbouring trajectory spirals toward it as time progresses toward positive or negative infinity [185]. By attracting nearby trajectories, limit cycles help maintain system stability, drawing the system back to its oscillatory characteristics after a perturbation. In living systems, stability is particularly important, as both the frequency and amplitude of biological oscillations must remain within a specific range to preserve health. To quantify and visualise this stability, we can plot the limit cycle of an oscillator. An example of one such system is the Van der Pol oscillator,

$$\frac{d^2x}{dt^2} - \mu (1 - x^2) \frac{dx}{dt} + x = 0. \quad (1.4)$$

Figure 1.4 illustrates the phase space of a Van der Pol oscillator, as the different initial conditions converge upon a closed trajectory over time.

Autonomous self-sustained oscillators can maintain amplitude stability; however, both frequency and phase must also remain stable in living systems. Therefore, to accurately describe biological processes a relatively new class of systems is required [186].

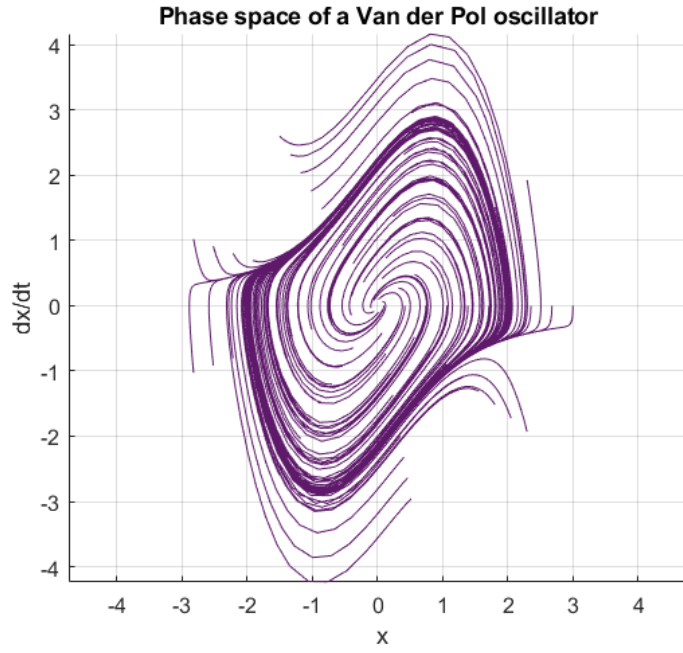


FIGURE 1.4: Phase space of a Van der Pol oscillator (Eq. 1.4). The  $x$  axis represents position, while  $y$  is the rate of change of  $x$  - the velocity.

#### 1.5.4 Chronotaxic systems

The etymology of chronotaxic, with *chronos* - time and *taxis* - order, demonstrates the defining property of this group of systems, the fact they can resist perturbations to time-varying parameters – specifically their frequencies – over time [186].

Descriptions of stable oscillatory dynamics are often performed using autonomous self-sustained limit cycles. While this approach provides stable amplitudes - returning to the limit cycle following perturbation, it is easy to disrupt the frequency of oscillation by weak external perturbation. In contrast, the amplitude and frequency of chronotaxic systems is brought back to that of a time-dependent point attractor following perturbation, inducing stability in the time-dependent frequencies of the system while allowing it to be open and dissipative. This subclass of nonautonomous systems are generated by a unidirectional coupling, known as a drive and response system [187],

$$\dot{\mathbf{p}} = \mathbf{f}(\mathbf{p}), \quad \dot{\mathbf{x}} = \mathbf{g}(\mathbf{x}, \mathbf{p}), \quad (1.5)$$

where the system  $\mathbf{x}$  can be considered as driven by the system  $\mathbf{p}$  over time. In both

Eq. 1.5 and autonomous systems, the amplitude dynamics are stable, as they converge upon a trajectory in the phase space,  $\Gamma_0$ , following perturbation. The position of an oscillator along this cycle - its phase - in autonomous systems does not exhibit the same stability - instead it is neutral. This means the frequency of the oscillation can be readily changed by perturbation. Chronotaxic systems can resist these changes while maintaining a time-varying frequency [188]. This is due to the presence of a time-dependent point attractor  $\mathbf{x}^A(t)$ . This unique steady state is a further defining property of chronotaxic systems. As time tends towards infinity, all points are brought towards the point attractor, satisfying the conditions of both forward and pullback attractors,

$$\begin{aligned} \lim_{t \rightarrow +\infty} \left| \mathbf{x}(t, t_0, \mathbf{x}_0) - \mathbf{x}^A(t) \right| &= 0, \\ \lim_{t_0 \rightarrow -\infty} \left| \mathbf{x}(t, t_0, \mathbf{x}_0) - \mathbf{x}^A(t) \right| &= 0, \end{aligned} \quad (1.6)$$

where  $\mathbf{x}_0$  is the initial condition of the system at time  $t_0$ . The phase stability induced by the time-dependent point attractor ensures that the frequency of oscillation can't be easily destabilised by continuous external perturbation. This is a key aspect of living systems as the frequency of oscillations such as the heart rate is required to return to resting state values following perturbation. This decay in perturbations to phase over time can't be explained by conventional limit cycle models of self-sustained oscillators. Thus, this non-autonomous and time-dependent system is able to describe the time-dependent, dissipative and stable oscillators seen throughout nature. Fig. 1.5 illustrates these differences graphically.

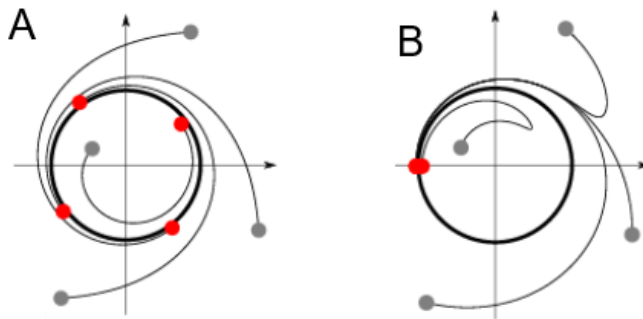


FIGURE 1.5: Starting from different initial conditions (gray balls) in (A) an autonomous systems the trajectories will end on the limit cycle but will never meet (red balls), while (B) in an non-autonomous system they will all end on the point attractor. [188].

Although Fig. 1.5A returns to the limit cycle from each of the initial points, their phases on the cycle remain different. In contrast, the chronotaxic limit cycle in Fig. 1.5B evolves such that the phases converge upon a point attractor over time.

The analysis and modelling approaches throughout this thesis are explicitly designed to accommodate nonlinear, multiscale, time-varying systems open to external influences from the environment. These physical considerations make them specifically tailored for interpreting data from living systems.

## 1.6 Modelling living systems

While the analysis methods applied in this thesis are model-free, it can be helpful to validate results obtained via experiment with computational models. Not only does this validate assumptions in the data analysis, but also helps to establish a ground truth with known parameters.

Self-sustained oscillations are ubiquitous throughout living systems [189]. Biological oscillators exhibit stability not only in their amplitude dynamics, but also the variable that parameterises movement along the limit cycle, the phase. In an isolated system, the instantaneous phase,  $\varphi$ , can be defined using the natural frequency  $\omega_0$ , of the associated oscillator,

$$\frac{d\varphi}{dt} = \omega_0. \quad (1.7)$$

The temporal evolution of phase can reveal insight into the driving forces of a system [190]. By modelling the interactions between several phase oscillators one may gain insights regarding if, how and why populations of oscillatory components interact.

### 1.6.1 The Kuramoto model

The Kuramoto model was first introduced in the 1970s and describes the collective dynamics of coupled oscillatory systems [191, 192], with a particular focus on synchronization phenomena. Synchronization can occur when a small periodic force is applied to a self-sustained oscillator. The interaction between an oscillator and



the external influence is characterised by a coupling function,  $Q$ , where the instantaneous phase of an oscillator is influenced such that,

$$\frac{d\varphi}{dt} = \omega_0 + Q(\varphi, \omega t). \quad (1.8)$$

Additionally, oscillators can interact bidirectionally to change the phases of one another.

$$\frac{d\varphi_1}{dt} = \omega_1 + Q_1(\varphi_1, \varphi_2), \quad \frac{d\varphi_2}{dt} = \omega_2 + Q_2(\varphi_2, \varphi_1). \quad (1.9)$$

If the couplings between oscillators are sufficiently large, this mutual adjustment of phases can lead to synchronisation.

### Interactions and emergent phenomena

Living systems are characterised by their structure and function. Structure refers to the morphology and organisation of system components, while function describes how these components operate dynamically over time. The human body exhibits a high degree of connectivity and interdependence between components, enabling complex and coordinated behaviours. This connectivity arises because the emergent properties of interconnected units often exceed the sum of their individual contributions. Understanding how these components function as nodes within an intricate networks requires examining the interactions between them. Synchronization facilitates these interactions, ensuring that processes such as signal transmission [193], metabolic regulation [194], and organ coordination [195] occur seamlessly, allowing macroscopic behaviours to emerge from microscopic dynamics.

### Synchronisation

Synchronization is the process by which oscillators mutually adjust their rhythms through weak interactions [171]. This interaction facilitates coordinated behaviours, giving rise to emergent phenomena such as glycolytic oscillations [196] or the steady heartbeat produced by cardiac pacemaker cells [197].

For systems to synchronise a coupling between them is required [171]. This coupling can take many forms including chemical [198], photic [199] and mechanical [200].

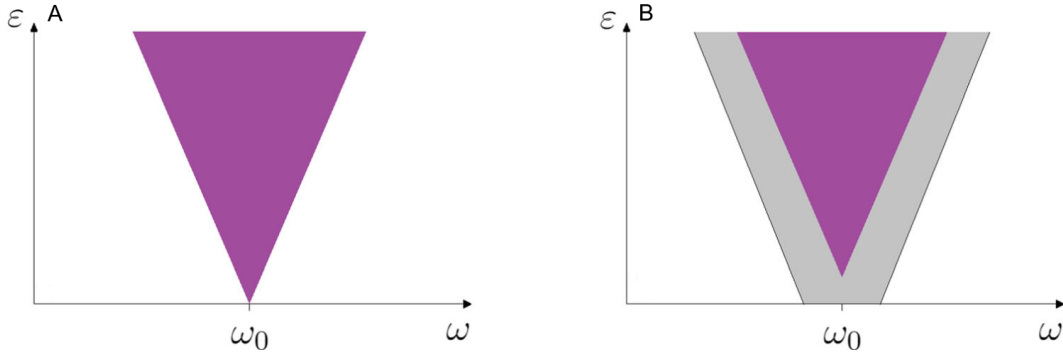


FIGURE 1.6: Arnold tongue demonstrating the parameter combinations whereby synchronisation is possible (purple region) (A) autonomous system (B) Non-autonomous oscillator with time varying frequencies which also exhibits intermittent synchronisation (grey)

The difference in natural frequency of the two systems ( $\Delta\omega = \omega_0 - \omega$ ) must also be relatively small compared to the coupling strength  $\epsilon$ . This leads to the emergence of the Arnold tongue (Fig. 1.6A), a parameter space where synchronisation is possible as the coupling strength is greater than the frequency mismatch  $\epsilon > |\Delta\omega| = |\omega_0 - \omega|$ . This universal concept is ubiquitous in nature, enabling mutual cooperation of many individual oscillating units to produce collective behaviour greater than the sum of its parts [201].

### Time-dependent oscillations

Living systems often exhibit frequencies that fluctuate around a central value [202], partly due to environmental perturbations. Explicitly modelling external influences on the system as non-autonomous, time-dependent phase oscillators reflect dynamics observed from measured data of living systems. Here, time-dependent frequencies are modulated such that,

$$\omega(t) = \omega (1 + A \sin(\omega_{\text{mod}} t)). \quad (1.10)$$

Where  $\omega_{\text{mod}}$  represents the modulation frequency, and  $A$  is the amplitude of modulation around the central value  $\omega$ . Somewhat counterintuitively, introducing a deterministic, non-autonomous frequency has been shown to expand regions of stability and enhance the system's robustness in the face of environmental changes [178]. The resulting time-varying frequency mismatch,

$$\begin{aligned}\Delta\omega(t) &= \omega_0 - \omega (1 + A \sin(\omega_{\text{mod}} t)) \\ &= \Delta\omega - A\omega \sin(\omega_{\text{mod}} t),\end{aligned}\tag{1.11}$$

means that the new synchronisation criteria becomes,

$$\epsilon > |\Delta\omega(t)| = |\Delta\omega - A\omega \sin(\omega_{\text{mod}} t)|.\tag{1.12}$$

As this criterion is time-dependent, a new, transient type of synchronization is introduced. This phenomenon is known as intermittent synchronization (grey region in the parameter space of Fig. 1.6B) [203].

### 1.6.2 Extension to networks

Modelling the system as above assumes two single oscillators. In the body, often there are many oscillators of the same type which operate in networks to produce a collective oscillation. each oscillator acts as a node of the overall network, and often a certain density of oscillators is required to produce the collective behaviour [194]. Considering the collective behaviour of oscillatory networks is therefore essential to categorise their dynamics.

### 1.6.3 Intranetwork interactions

The phase of each oscillator,  $\theta_i$ , is influenced by its natural frequency  $\omega_i$ , and its interactions with other oscillators and networks. Intranetwork interactions describe the adjustment of phases due to couplings between oscillators of the same type (here denoted as network X). The phase dynamics due to intranetwork interactions,

$$\dot{\theta}_{Xi} = \omega_i + \sum_{j=1}^N \frac{K_X}{N} \sin(\theta_{Xj} - \theta_{Xi}), \quad i = 1, \dots, N\tag{1.13}$$

depends upon  $N$ , the total number of oscillators in the network, and  $K_X$ , the intranetwork coupling strength [204].  $\theta_{Xj}(t)$  denotes the phase of the  $j$ -th oscillator. As the coupling strength  $K_X$  increases, the system undergoes a transition to collective synchronization, characterised by oscillators maintaining a constant phase difference

over time. The Kuramoto order parameter,  $r_X$ , evaluates the degree of synchronization achieved within the network,

$$r_X e^{i\Psi_X} = \frac{1}{N} \sum_{k=1}^N e^{i\theta_{Xk}}. \quad (1.14)$$

A completely ordered system with each oscillator synchronised to each other will therefore have an order parameter of  $r_X = 1$ , while a completely disordered one will have  $r_X = 0$ . The mean phase of the oscillator network,

$$\Psi_X = \frac{1}{N} \sum_{i=1}^N \theta_{Xi} \quad (1.15)$$

describes the time-dependent behaviour of this collective oscillation.

### Internetwork Interactions

The influence from the mean field of another network,  $\Psi_Y$ , can also affect the phase of an oscillator such that,

$$\dot{\theta}_{Y \rightarrow Xi} = F_{Y \rightarrow X} r_Y \sin(\Psi_Y - \theta_{Xi}). \quad (1.16)$$

Here,  $F_{Y \rightarrow X}$  represents the internetwork coupling strength from  $Y$  to  $X$ , and  $r_Y$  is the Kuramoto order parameter.

The phases of each oscillator are influenced by the natural frequency of the oscillator ( $\omega_{Xi}(t)$ ), the intranetwork couplings ( $\dot{\theta}_{Xi}$ ) and internetwork couplings ( $\dot{\theta}_{Y \rightarrow Xi}$ ), such that,

$$\dot{\theta}_{Xi} = \omega_{Xi}(t) + \dot{\theta}_{Xi} - \dot{\theta}_{Y \rightarrow Xi}. \quad (1.17)$$

In living systems there are often multiple internetwork couplings to consider.

## 1.7 Analysis of living systems

Before considering which analysis techniques are most appropriate for living systems, the data measurement procedure must be understood, as it imposes limitations on the analyses that can be performed. The first of these limitations is the

Nyquist frequency, which restricts the maximum observable frequency in a signal,  $F_{\max}$ , to half of the sampling frequency,  $F_s$ ,

$$F_{\max} = \frac{F_s}{2}. \quad (1.18)$$

Furthermore, the length of the recorded signal determines the minimum observable frequency. To reliably detect components within a time series, multiple cycles of oscillation must be measured. A minimum of six to ten cycles of the lowest frequency of interest is required to accurately resolve the power of an oscillation [177].

For coupling analyses, time series consisting of at least thirty cycles of the oscillation of interest are necessary to capture the mutual influences between systems [205]. Elongated time series are also necessary to capture transient phenomena [26].

Clinical trials can be labour-intensive and costly, often resulting in suboptimal recording durations. Certain measures may also be uncomfortable for participants, particularly those with ASD who may have sensory hyper-responsiveness [3]. However, insufficient recording time reduces the amount of useful information that can be extracted from a time series. Although there is no strict upper limit on recording duration, practical constraints necessitate a compromise when designing experiments.

Once the data has been collected, several approaches can be used to extract insights from the time-series.

### 1.7.1 Time-domain

As the name suggests, time-domain methods examine changing patterns in the data across time. These approaches assess the temporal structure of, and potential presence of interactions between, time series.

#### Actograms

Actograms plot activity patterns across time. Commonly used in chronobiology [206], actograms give a three dimensional representation of the amount of activity — such as locomotor movements, wheel running, or sensor-based motion detection — at a given time across many days. They can reveal unimodal prominent oscillations,

such as the circadian oscillation, from a time series due to the regularity of activity patterns. However, they can't resolve multiple oscillatory modes simultaneously or accurately assess changes in frequency over time.

### Autocorrelation

Another way to assess periodic activity in a time series is using autocorrelation. This statistical tool assesses periodicity in data by comparing a time series  $f_1(t)$  with a lagged version of itself  $f_1(t + \tau)$  [207]. This generates the autocorrelation function,

$$\phi_{11}(\tau) = \frac{1}{T_1} \int_{-T_1/2}^{T_1/2} f_1(t) f_1(t + \tau) dt, \quad (1.19)$$

where,  $\tau$  is the lag time. Plotting the function reveals periodicity in the data by the presence of peaks at certain time lags. Again however, as this approach assumes stationarity, it is inappropriate for capturing time varying frequencies.

### 1.7.2 Frequency-domain

An alternative set of approaches focus on observing the spectral content of a signal, averaged over time. These approaches demonstrate the frequencies present in a time series, however they often achieve this via the assumption of stationary dynamics, which is inappropriate in living systems.

#### Fourier transform

The Fourier transform reveals the spectral content of a signal by converting a time series into the frequency domain. It is derived from the Fourier series, which represents a periodic function as a sum of sine and cosine functions. The Fourier transform extends this concept by assuming the period of the signal,  $T$ , approaches infinity [207]. The frequency content is given by,

$$F(\omega) = \frac{1}{2\pi} \int_{-\infty}^{\infty} f(t) e^{-j\omega t} dt, \quad (1.20)$$

where  $F$  is a continuous function of the angular frequency  $\omega$  and  $j$  is the imaginary unit. Plotting this function reveals the amplitude of oscillations at different frequencies in the interval over which the time series was measured. While historically significant and helpful for quickly discovering peak frequencies, this approach has several drawbacks. In noisy signals, it is easy to disregard the dynamics as lacking determinism [26], Fig. 1.7 demonstrates that time-varying frequencies can easily be mistaken for noise given this approach. Additionally, by averaging over time, it is impossible to say if an oscillation was present transiently or for the entire time series at a lower power. To address these concerns, the time domain must also be resolved when analysing signals.

### 1.7.3 Time-frequency domain

Oscillatory behaviour is often non-stationary, requiring time-resolved methods to track the temporal evolution of oscillations. However, there are inherent mathematical constraints that limit the simultaneous resolution of time and frequency. According to the Heisenberg/Gabor uncertainty principle, it is fundamentally impossible to localise both time and frequency with arbitrary precision, as they are constrained by a trade-off [208],

$$\Delta t \Delta f \geq \frac{1}{2}. \quad (1.21)$$

This fundamental relationship, linking the uncertainty in frequency  $\Delta f$  to the uncertainty in time  $\Delta t$ , underpins modern communication systems and data analysis [208]. To understand its significance, consider that increasing the width of a time window improves frequency resolution by allowing the observation of more cycles. However, this comes at the cost of diminished time localisation, as the information is spread over a longer duration. Conversely, using smaller time windows enhances time localisation, enabling precise identification of when oscillations occur, but reduces frequency resolution due to the presence of fewer cycles. This compromise is fundamental to time-frequency analysis.

### Short-time Fourier transform

The Short-time Fourier transform (STFT) reveals the time-frequency domain by dividing a time series into overlapping windows and performing a Fourier transform on each segment. This approach provides the time-localised frequency content of a signal, allowing us to track how the frequency content of a signal evolves in time.

However, the STFT has a fixed frequency resolution, which is suboptimal for analysing signals with varying, multiscale frequency components. As a result, the choice of window size becomes crucial. A larger window improves frequency resolution by capturing more cycles of oscillation, but at the expense of time localisation. Conversely, a smaller window enhances time localisation but reduces frequency resolution, making it challenging to resolve fine frequency details.

Unlike alternative approaches, which perform multiple transforms at different scales, the STFT performs a single Fourier Transform for each time, maintaining uniform resolution throughout the analysis. While this simplicity can make the STFT computationally efficient and conceptually straightforward, it may not be ideal for signals with complex, multiscale characteristics. Fig. 1.7D demonstrates how the higher frequencies are poorly localised in time due to this non-adaptive frequency resolution.

### Wavelet transform

In the short-time Fourier transform, a single window is used to evaluate all frequencies at a given time. Improved multiscale resolution may be achieved by sliding wavelets of varying scales along the input signal and transforming the overlapping parts into the frequency domain. This adaptive resolution allows wavelets of optimal scale to detect each frequency. Lower frequencies exhibit fewer oscillations within a given time, necessitating a larger scale to capture the oscillatory activity effectively. Conversely, higher frequencies require less time to be captured, allowing the use of a smaller scale. This optimises the trade-off between time localisation and



frequency resolution, providing greater time-localisation at high frequencies and improved frequency resolution at low frequencies. Additionally, the frequency resolution can change logarithmically across scales, providing a more balanced distribution of information across frequency bands [209].

Essentially, the short time Fourier transform is a camera with only one focus, able to detect the presence of objects both large and small, but with poor resolution. In contrast, the wavelet transform is able to adjust its focus, stretching to obtain a sufficient number of oscillations for the observation of low frequency activity and contracting to better localise high frequency oscillations in time. The wavelet transform was therefore applied in the analyses throughout this thesis, and is defined by,

$$W_T(s, t) = \int_{-L/2}^{L/2} \Psi(s, u - t) f(u) d(u), \quad (1.22)$$

where the mother wavelet  $\Psi$  is squeezed and stretched to reveal the presence of oscillation at each frequency across time ( $t$ ),  $L$  is the signal length and  $s$  is the scale. Different types of wavelet may be applied, each suited to different types of analysis. For example, the Morlet wavelet,

$$\Psi(s, t) = \frac{1}{\sqrt[4]{\pi}} \left( e^{\frac{2\pi i \omega_c t}{s}} - e^{-\frac{2\pi \omega_c^2}{2}} \right) e^{-\frac{t^2}{2s^2}}, \quad (1.23)$$

is composed of a sinusoid within a Gaussian envelope. The frequency of the sinusoid allows the wavelet to be focused upon a certain scale, while the Gaussianity ensures a smoothly decaying amplitude, improving time-localisation.

#### 1.7.4 Comparing approaches

To highlight the differences between the above analysis approaches, consider a time series,

$$x(t) = \omega_1 (1 + A_1 \sin(\omega_{mod1} t)) + \omega_2 (1 + A_2 \sin(\omega_{mod2} t)) + \omega_3 (1 + A_3 \sin(\omega_{mod3} t)) + \eta(t), \quad (1.24)$$

consisting of three deterministic time-varying modes and pink noise ( $\eta(t)$ ). The parameters used to generate the time series and modelling approach are outlined in Tab. 1.3 Both the autocorrelation (Fig. 1.7B) and Fourier transform (Fig. 1.7C) suggest that there may be some oscillatory components, however the number of modes and their time-varying characteristics remain unclear. Evaluating the time domain using the STFT (Fig. 1.7D) reveals that the frequencies change over time, but with poor multiscale resolution. The multiscale, time-resolved (Morlet) wavelet transform is capable of elucidating the dynamic characteristics of this system (Fig 1.7F). By unlocking the temporal dimension, and applying multiscale adaptive resolution, a plethora of information is revealed.

### 1.7.5 Phase extraction approaches

Many of the methods applied in this thesis rely on the identification, isolation and analysis of phase behaviour in the time/frequency domain. These phases can be extracted from the time frequency domain by several approaches.

#### Hilbert transform

Prior to the emergence of the Hilbert transform (HT), the phase of a signal could only be assessed by interpreting the current point of a cycle in the time domain [210]. While this is possible in regular, relatively noiseless signals of a known construction, such as the heartbeat, it is not generally applicable. The HT creates a complex valued representation of the original, real signal. The phase information can then be extracted as the argument of this complex value. However, the HT is only effective if there is a single oscillatory mode in the frequency band of interest.

#### Ridge extraction

The underlying oscillatory modes may be harnessed to evaluate their changing power and phase over time [211]. The first step here is to find the ridge curve; a region in the time-frequency domain with a series of amplitude/power peaks and their corresponding phases. Tracing these modes in the time-frequency domain can reveal time-localised amplitudes and phases.

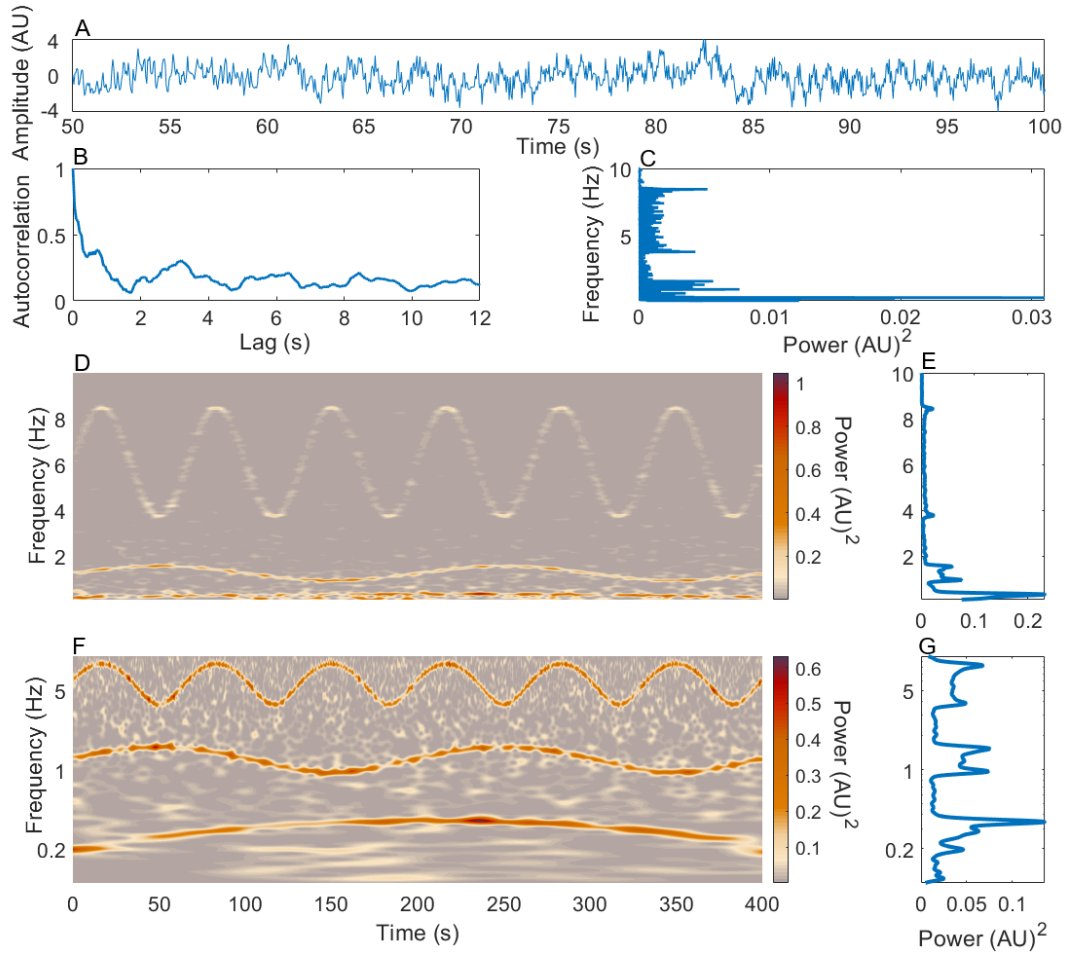


FIGURE 1.7: Analysis approaches applied to a simulated time series (Eq. 1.24). (A) A 50-second segment of the simulated time series. (B) Autocorrelation of the signal, normalised between 0 and 1, plotted for the first 12 seconds of lag. (C) Fourier transform of the time series, highlighting dominant frequency components. (D) Short-time Fourier transform reveals the power of the multiscale time-dependent modes. A linear frequency axis is used to reflect the linear nature of the windowing applied (E) Time-average of the STFT. (F) The time-resolved power of the oscillatory modes evaluated with a wavelet transform using logarithmic frequency resolution. A logarithmic frequency axis is used to reflect this. (G) The time averaged wavelet transform power.

### 1.7.6 Harmonic Analysis

Spectral peaks are obtained from a mathematical description of time series and are not necessarily linked to physical oscillatory systems or modes. In the case of nonlinearities, i.e. when the signal is not of sinusoidal shape, many high harmonic components can occur belonging to the activity of a single mode. When the rhythms are strictly periodic the detection of high harmonics is relatively straightforward because they appear at commensurate frequencies of the basic frequency. However, when the rhythms have variable, or non-stationary frequencies, the detection of high harmonics is more demanding. To determine whether the detected frequency

peaks correspond to independent modes, or the peaks are in harmonic relationship, we conduct harmonic analysis [212]. The method evaluates mutual information between time-localised phases across frequency bands. If sufficient shared phase information between a fundamental frequency and its harmonics exceeds a surrogate threshold, then the relationship can be considered as harmonic. For further details regarding surrogate data analysis, see Sect. 1.7.7 and [213].

To detect harmonics, we first extract the time-localised phases using the wavelet transform. This information is subsequently split into 24 equally spaced bins which are compared against each other using an information theoretic approach. First, the Shannon entropy [214] ( $H(\phi_1)$ ) of each phase distribution  $p(\phi_1)$  is found,

$$H(\Phi_1) = - \sum_{\phi_1=1}^{24} p(\phi_1) \log_2 p(\phi_1). \quad (1.25)$$

Following this, we obtain the mean entropy of the conditional distribution, given the phase distribution  $p(\phi_2)$  at a lower frequency evaluated at the same point in time,

$$H(\Phi_1|\Phi_2) = - \sum_{\phi_2=1}^{24} p(\phi_2) \sum_{\phi_1=1}^{24} p(\phi_1|\phi_2) \log_2 p(\phi_1|\phi_2). \quad (1.26)$$

The mutual information of the signals is calculated as the difference between Shannon and mean entropy,

$$M(\Phi_1, \Phi_2) = H(\Phi_1) - H(\Phi_1|\Phi_2). \quad (1.27)$$

Mutual information ( $M$ ) quantifies the mutual dependence between two variables by measuring the extent to which knowledge regarding the value of one variable reduces the uncertainty in predicting the other. If the probability distribution  $p(\phi_1)$  provides no information about  $p(\phi_2)$ , the phases are independent, and the mutual information is zero ( $M = 0$ ). Conversely, if  $p(\phi_2)$  completely determines  $p(\phi_1)$ , then  $M = 1$ . Harmonics exhibit the same phase behaviour as their fundamental frequency in both the time and frequency domains, resulting in high mutual information values. Surrogate testing is employed to distinguish genuine harmonic relationships from spurious patterns [213].

### 1.7.7 Interactions

Living systems must continually interact with their environment to sustain themselves. Coordination between time series suggests the presence of mutual interaction between oscillators; however, this does not necessarily imply they are coupled. As discussed in Sect. 1.6.1, an adjustment of rhythms between oscillators must be also present for synchronisation. To reduce the likelihood of detecting spurious interactions, surrogate testing is applied.

#### Surrogates

Methods that evaluate interactions are liable to detect a certain minimum level, even in entirely unconnected systems. In order to evaluate whether an interaction is actually present in a system, we must negate this zero error, this leaves the true - also known as effective - value of the measurement of interest.

To establish this threshold, we generate surrogate time series. Ideally, these incorporate as many features of the dynamical systems under investigation as possible, but without the aspect being measured. There are many types of surrogate, which can be generated from a variety of mathematical techniques [213], however intersubject surrogates are considered the gold standard as they retain as many statistical properties of the system as possible.

Intersubject surrogates are generated by assessing interactions between brain regions from different individuals. The connectivity between these regions is minimal, as they are functionally independent by virtue of originating from separate participants.

For example, consider investigating the connectivity between two brain regions corresponding to EEG probe sites, F3 and F4, in subject ( $S_1$ ). The first step is to calculate the raw connectivity between probes. Next, a threshold must be established to ensure the measured connectivity is not spurious. If the group contains 100 participants, the connectivity between  $S_1$  at F3 and the corresponding signals at F4 from the other 99 participants is calculated. Since no genuine connection exists between these measurements, this dataset is used to establish a baseline threshold, such as

the 50th percentile of the surrogate connectivity values. Finally, the effective connectivity is assessed as the difference between the raw connectivity and the established threshold value.

$$C_{effective} = C_{raw} - C_{Threshold} \quad (1.28)$$

Negative values reflect a lack of coherence and so are set to zero.

### Functional connectivity

Functional connectivity assesses the statistical dependence of one time series over another [215]. As previously addressed, this does not imply a coupling between them, but it can hint at the presence of interactions.

### Coherence

Coherence quantifies the phase relationship between a pair of time series measured concurrently. It has been used across various physics domains and has been responsible for breakthroughs such as Young's double slit experiment and the detection of gravitational waves at LIGO. With the advent of modern computational power, coherence has been applied to detect the putative presence of interactions between time series.

Traditionally, coherence was developed within the the field of optics, where it quantified the strength of interaction patterns from two sources of light. The visibility of each peak  $v$  can be determined by the intensity of the light at peaks  $I_{max}$  and troughs  $I_{min}$ , such that,

$$v = \frac{I_{max} - I_{min}}{I_{max} + I_{min}}. \quad (1.29)$$

Where  $v = 1$  indicates maximum interference and  $v = 0$  for no interference. While helpful for determining interference patterns of light, a modified expression is required to illustrate the interference of waves of arbitrary amplitude and phase more generally. The Fourier cross-spectrum can be calculated to assess the degree of interaction between two time series  $a$  and  $b$ , as

$$S_{ab}(f) = F_a(f) \times F_b^*(f), \quad (1.30)$$

where the asterisk denotes complex conjugation. However, this similarity measure remains influenced by the amplitude of the Fourier components. This implies that even if a dominant oscillation is present in one data series while only background fluctuations exist in the other, the cross-spectrum will still show a peak at the frequency of that oscillation, as long as some amplitude is present at that frequency in the second data series. To address this bias, we need to normalise the cross-spectrum. This is done by defining the Fourier coherence  $C(f)$  as:

$$C(f) = \frac{|\langle S_{ab}(f) \rangle|}{[\langle S_{aa}(f) \rangle \times \langle S_{bb}(f) \rangle]^{1/2}}, \quad (1.31)$$

where angular brackets indicate a time average of the Fourier autospectra  $S_{aa}, S_{bb}$  and the Fourier crossspectra  $S_{ab}$  while  $||$  denotes an absolute value. Similar to the initial introduction of visibility, this is defined on a scale from zero to one, where one is complete coherence and zero represents no coherence [216].

By applying wavelets, coherence can be extended to the time frequency domain, as popularised by Torrence and Webster [217] and then again by Lachaux et al. [218] who defined it as

$$C_W(f, t) = \frac{|SW_{ab}(f, t)|}{[SW_{aa}(f, t) \cdot SW_{bb}(f, t)]^{1/2}}, \quad (1.32)$$

Where  $SW_{ab}$  are the cross wavelet spectra and  $SW_{aa}, SW_{bb}$  are the auto spectra. One is able to determine the consistency in the phase difference across a window of size  $\delta$  using,

$$SW_{ab}(f, t) = \int_{t-\frac{\delta}{2}}^{t+\frac{\delta}{2}} W_a(f, \tau) \cdot W_b^*(f, \tau) d\tau, \quad (1.33)$$

where  $\delta = n_{cy}/f$  for a given number  $n_{cy}$  of cycles at a given frequency  $f$ . Using this approach, one is able to derive a time-localised, multiscale representation of interactions across time. Yet this method does not only compare the consistency in phases across time, but also similarity in amplitude. One can circumvent this amplitude dependence by explicitly focusing upon the phase dynamics of the two signals across

time and frequency by applying the approach developed independently by Lachaux et al. [218] and Bandrivsky et al. [219],

$$C_\theta(f, t) = \frac{1}{\delta} \left| \int_{t-\frac{\delta}{2}}^{t+\frac{\delta}{2}} e^{i(\theta_a(f, \tau) - \theta_b(f, \tau))} d\tau \right|. \quad (1.34)$$

This approach is completely independent of amplitude, and so is robust against amplitude perturbations such as movement artefacts.

### 1.7.8 Effective connectivity

Effective connectivity can establish the direction and presence of coupling, thus determining which oscillator is influencing the other. In contrast, functional connectivity methods identify statistical dependences between different brain regions, offering a descriptive measure of common behaviour between two-time series [215]. Functional connectivity methods can therefore reflect external influences rather than mutual couplings. Effective connectivity explicitly quantifies the influence oscillators over one another.

### Bispectral analysis

Wavelet bispectral analysis enables the detection of nonlinear couplings both between and within time series data [220]. Autobispectral analysis is applied to investigate the potential presence of coupling between modes within a single time series, while cross bispectral analysis can evaluate phase couplings between different time series [221]. The wavelet bispectrum,  $B_W$ , quantifies the phase coupling between modes at scales  $s_1$  and  $s_2$ , as follows:

$$B_W(s_1, s_2) = \int_T W_T(s_1, \tau) W_T(s_2, \tau) W_T^*(s, \tau) d\tau, \quad (1.35)$$

over a time interval,  $T$ , where:

$$\frac{1}{s_1} + \frac{1}{s_2} = \frac{1}{s}. \quad (1.36)$$

For a more detailed explanation, refer to [220].



## Dynamical Bayesian inference

Dynamical Bayesian inference (DBI) can also detect phase couplings between oscillators. DBI goes beyond traditional functional connectivity measures by reconstructing coupling functions, which describe the influence of one oscillator's phase on another. This information forms the coupling between systems, where the coupling function (CF) defines how information propagates from one oscillator to another [222]. In a unidirectionally coupled phase oscillator, the phase of oscillator X modulates the phase of oscillator P through a coupling function. This process can be simulated numerically, for example Fig. 1.8 and DBI successfully reconstruct the coupling functions across varying coupling strengths, indicating both the shape and strength of the couplings. Furthermore, DBI captures the directionality of interactions, as demonstrated in Fig. 1.8E, where no information flows from oscillator P to X in this simulated unidirectional phase oscillator (Eq. 1.37).

$$\begin{aligned}\dot{\phi}_X &= \omega_X + \eta(t) \\ \dot{\phi}_P &= \omega_P + q_P(\phi_X, \phi_P) = \omega_P + E \cos(\phi_X + \pi/2.5) + \eta(t).\end{aligned}\tag{1.37}$$

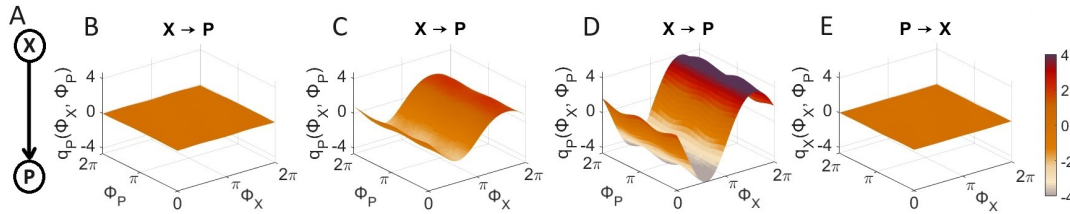


FIGURE 1.8: Coupling functions from the numerically generated example (Eq. 1.37). (A) The direction of coupling. (B-D) The coupling from X to P at different coupling strengths. (E) coupling from P to X, where there is no coupling present.

DBI is based on Bayes' theorem, incorporating both prior knowledge and current information to infer the time-evolving dynamics of couplings between signals. By using a sliding time window, DBI can track whether phase behaviour in one region influences another, capturing the dynamic evolution of couplings. This method avoids pitfalls of averaging, which could obscure transient phenomena. Instead, it uses windows to determine the coupling as it evolves in time. These windows must be at least the equivalent of ten cycles of oscillation at the minimum frequency of interest to faithfully recreate the dynamics [223].

**Practical implementation**

Applying dynamical Bayesian inference yields a series of phase coupling functions that represent the influence of one oscillator on another. For EEG data, phases extracted from the recorded time series serve as the input. To obtain these time-localised phases, ridge extraction is applied to each signal, as described in Section 1.7.5. This approach allows the phase dynamics to explicitly track the temporal evolution of each mode, while also providing a logarithmic frequency scaling that is particularly well suited to the analysis of living systems.

Once the phases have been extracted, they serve as input to dynamical Bayesian inference (DBI), which reconstructs a coupling function over a series of time windows. To introduce an additional temporal dimension, the percentage of time during which oscillators remain coupled can be assessed. In practice, this corresponds to the proportion of time for which the coupling strength exceeds a surrogate-derived threshold. By proxy, this allows us to estimate the duration over which the phase dynamics in one brain region influence those in another. The result is a directional, time-localised representation of how, when, and whether two regions exert influence over one another.

## 1.8 Thesis outline

Here we present a cohesive body of work, organised around four core papers that contribute to a broad understanding of diverse biological systems and how they relate to autism spectrum disorder. The analytical approaches applied adhere to the physical principles of living systems laid out in Sect. 1.5.

First, a comprehensive review of physics based approaches to modelling cellular energy metabolisms is presented. Coupled phase oscillators are capable of describing the dynamics of these systems with dramatically fewer parameters than mass-based models. This review presents an approach capable of representing pathological metabolic states, which we will later apply specifically to the case of autism spectrum disorder.

The next chapter delves into wavelet phase coherence, presenting a detailed comparison to amplitude-weighted methods. This highlights the advantages and limitations of current functional connectivity approaches. Wavelet phase coherence is demonstrated, via a series of simulated examples and experimental data, to be more resilient against amplitude perturbations. Robustness against movement artifacts is a particularly important property for analytical approaches that use data such as EEG in children which is prone to amplitude perturbation.

Subsequently, an investigation applying wavelet phase coherence and dynamical Bayesian inference to EEG data from young males with ASD is presented. This paper identifies unique neural patterns and offers a deeper understanding of the neural mechanisms involved in ASD. It is hoped that the reduced theta and alpha connectivity found in young males with ASD provides a promising marker for the condition.

The fourth paper presented focuses upon the circadian oscillations, which are severely disrupted in ASD [14, 17, 158, 159, 160]. A particularly understudied aspect of circadian regulation is the methamphetamine sensitive circadian oscillator [16]. The time-varying circadian oscillation highlighted by methamphetamine administration may be partially responsible for disrupted sleep in ASD.

Finally, a model of neuronal energy metabolism is presented. Simulations of healthy and altered states, induced by upregulation of the WNT- $\beta$  catenin pathway,

are compared to evaluate the hypothesis [7] that this pathway may contribute to the Warburg effect in ASD.

The thesis concludes with a summary of the work presented, highlighting contributions science and suggesting avenues for future research.

## Chapter 2

# Physics of cellular energy metabolism

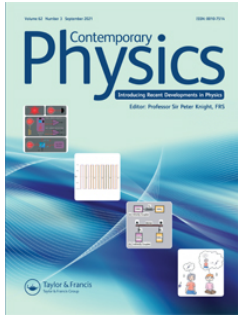
### **Student contribution:**

The student conducted a thorough literature review encompassing both cellular energy metabolism and the physics-based modelling approaches currently in use. They designed and implemented comparative analyses between real glycolytic oscillations and the outputs of two distinct modelling frameworks. In addition, the student performed all time-series analyses, curated the experimental and simulated data, developed the software used for analysis and figure generation, and wrote and edited the manuscript.

This research is published in Contemporary Physics.

Samuel JK Barnes and Aneta Stefanovska. “Physics of cellular energy metabolism”.

In: *Contemporary Physics* 62.3 (2021), pp. 125–143



## Physics of cellular energy metabolism

Samuel J. K. Barnes & Aneta Stefanovska

To cite this article: Samuel J. K. Barnes & Aneta Stefanovska (2021) Physics of cellular energy metabolism, Contemporary Physics, 62:3, 125-143, DOI: [10.1080/00107514.2022.2073046](https://doi.org/10.1080/00107514.2022.2073046)

To link to this article: <https://doi.org/10.1080/00107514.2022.2073046>



Published online: 26 May 2022.



Submit your article to this journal [↗](#)



Article views: 329



View related articles [↗](#)



View Crossmark data [↗](#)



Citing articles: 1 View citing articles [↗](#)



## Physics of cellular energy metabolism

Samuel J. K. Barnes and Aneta Stefanovska

Physics Department, Lancaster University, Lancaster, UK

### ABSTRACT

Contributions to the field of cellular energy metabolism have been dominated by biochemistry. Over the past decade, however, several physics-based approaches have been introduced. Oscillations are an intrinsic aspect of all living systems, from fluctuating substrate levels within cells to changes in electrical potential across membranes. Utilising physics-based approaches to analyse these time-dependent signals reveals pockets of predictable stability. By embracing the nonlinear, time-varying and open nature of cellular dynamics, new network-based approaches to modelling cells are emerging, capable of effectively replicating measured time-series data. These new approaches promise to bring greater comprehension of how various illnesses affect the cells, and indeed, to novel treatments or diagnostic methods.

### ARTICLE HISTORY

Received 24 March 2022  
Accepted 28 April 2022

### KEYWORDS

Synchronisation; nonlinear;  
non-autonomous; networks;  
metabolism

### 1. Introduction

Since the discovery of synchronisation by Christian Huygens in 1665, examples of this phenomenon in the physical, chemical, and biological sciences have been studied extensively [1]. Particular growth came in the early twentieth century, with one notable example being the work of Van der Pol which explicitly used relaxation oscillators to model heartbeat [2]. Following this, many other biological processes were reported as oscillatory, with the first observation of the glycolytic oscillator – representing the crucial start point of the central metabolic pathway – reported in 1957 [3]. Less than a decade later, Aldridge and Pye reported that glycolysis is dependent upon cell density [4], alluding to the importance of mutual interaction between oscillators. Many contemporary groups have introduced models and attempted to characterise the nature of these oscillations [5]. Both Yang et al. [6] and Ganitkevich et al. [7] recently demonstrated that under certain conditions, glycolytic oscillations drive those in the mitochondria and so dictate the entire metabolic rhythm. This amplified glycolytic influence is associated with pathophysiological states. Downregulation of glycolytic enzymes has consequentially emerged as a therapeutic strategy [8]. Understanding the transition from mitochondrial to glycolytic dominance over cellular energy metabolism may elucidate the role of oscillatory processes in pathogenesis. Sustained oscillatory behaviour has been demonstrated experimentally on both a population level [9] and in individual yeast

cells [10]. In the past few years, there has been further characterisation of glycolytic oscillation in cellular populations, highlighting both partial [11] and permanent synchronisation [12].

Under healthy conditions, the mitochondria are responsible for most ATP production in the cell. Mitochondrial oscillations were first demonstrated in 1966 when Chance and Yoshioka reported fluctuating ionic concentrations of potassium and hydrogen in pigeon heart cells [13]. Fluctuations in the mitochondrial membrane potential have been studied extensively since [14] a number of models have been introduced to describe the oscillatory behaviour of the organelle. Particular focus has been on network dynamics [15] and the spatial distribution of mitochondria [16]. Recently, computational models have also been used to demonstrate nonlinear behaviour in mitochondrial oscillations [17].

Cellular energy metabolism is predominantly controlled by several oscillating processes. Investigating the synchronisation states between these oscillators can indicate the dominant influences over the system. By observing time-series data from cells *in vitro*, and modelling metabolic processes, a greater understanding of the changes inflicted upon cells by numerous conditions – including COVID – could be gained [18]. Viral infections cause a transition between metabolic states within host cells following infection, and greater knowledge of these transitions may assist in developing effective antiviral treatments against such conditions.

Throughout this review, we highlight the issues – and potential solutions – of analysing and modelling metabolic processes. Synchronisation is introduced following a brief exploration of cellular energy metabolism and a kinetic model of glycolysis. Non-autonomous approaches describing both the mitochondrial and glycolytic branches of metabolism are also discussed before finally considering glycolytic oscillations within cellular populations.

## 2. Difficulties in modelling biological processes

A long-standing critique of the biological sciences is the lack of testable theories, unlike the highly successful equivalents of, for example, quantum theory in physics. Biological systems are inherently complex, and the openness of these systems often means a variety of factors can affect outcomes, making realistic modelling difficult. Intrinsic perturbations have formerly led to the incorrect assumption that many biological oscillators are purely stochastic processes [19]. To elucidate the potential role of physics-based approaches in modelling metabolic behaviour, one must first introduce the processes underlying cellular oscillations.

### 2.1. Cellular metabolism in healthy cells

Adenosine Triphosphate (ATP) is an organic compound used to provide energy for bodily processes, from the opening of specific ion channels in cell membranes to the contraction of muscles. Humans produce and utilise their body weight in this molecule daily [20], and therefore, its method of production is paramount.

Cellular ATP is predominantly generated by oxidative phosphorylation (OXPHOS) in the mitochondria and glycolysis in the cytoplasm of cells, with these processes consuming oxygen and glucose, respectively. In most healthy cells, the mitochondria should be responsible for the majority of ATP production, whilst cells relying on glycolysis for this are generally in an undesirable state. Fundamentally, within animal cells, this system can be simplified into four key processes [22]. Glycolysis is the first stage, converting glucose, ATP and ADP into nicotinamide adenine dinucleotide (NADH), pyruvate and ATP. Then, in the mitochondria, the metabolism of sugars is completed so efficiently that the synthesis of 28 molecules of ATP takes place per glucose molecule oxidised. By contrast, only two ATP molecules are produced for each glucose molecule by glycolysis alone. These mitochondrial processes occur via oxidative phosphorylation, which requires the NADH and pyruvate molecules produced in glycolysis and an external oxygen supply to synthesise the additional ATP. The supply of oxygen and

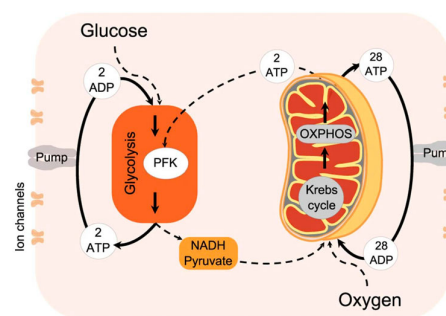


**Figure 1.** Metabolic pathways inside a cell during cellular energy metabolism. Arrows demonstrate the interaction of various chemicals. Phosphofructokinase (PFK) is an essential enzyme in glycolysis, while both the Krebs cycle and oxidative phosphorylation (OXPHOS) take place in the mitochondria, represented by the organelle on the right. In healthy conditions, mitochondrial processes produce 28 molecules of ATP per glucose molecule oxidised, compared to 2 ATP molecules generated by glycolysis. Reprinted with permission from [21].

glucose to the cells are the final key processes. Figure 1 illustrates the interplay between these interactions.

Oscillatory and non-autonomous behaviour is present in both glycolytic and mitochondrial pathways due to their explicit dependencies on time [23]. As indicated by dashed arrows within Figure 1, excitatory and inhibitory couplings also exist between these oscillators. In healthy states, most ATP production occurs during OXPHOS in the mitochondria. Glycolysis will therefore be suppressed to the low level necessary to provide substrates for mitochondrial reactions, and the mitochondria will drive overall metabolic oscillations. A further coupling between these oscillators exists in the form of an ATP/ADP sensing mechanism. If mitochondrial ATP production decreases, this ratio will also decrease. A sensing mechanism in the cell then reverses inhibition of the phosphofructokinase (PFK) enzyme used in glycolysis which leads to an increase in glycolytic ATP synthesis to meet cellular demand. This transition is a widespread occurrence in pathogenic cellular states [6, 7]. Understanding the nature of this transition may be a crucial starting point to uncover the nature of certain diseases.

### 2.2. Biological oscillators

Almost all biological processes include varying levels of products and substrates. The behaviour of these oscillating quantities can often be analysed to uncover an underlying order. Changes in these oscillations can indicate alterations in a cell's function or overall health. The processes under consideration in this review are microscopic, and their behaviour is analysed by considering substrates and products utilised in these interactions.



### 2.2.1. NADH oscillations

Monitoring levels of NADH enables one to observe alterations in the metabolic pathways of living cells. This molecule is produced during glycolytic oscillations and utilised in mitochondrial reactions, so its cellular abundance constantly fluctuates. The study of NADH fluctuations over time may indicate the cell's prevalence of different metabolic pathways. It was first shown in the 1960s that the nicotinamide group within NADH would absorb incident ultraviolet light of wavelength  $340 \pm 30\text{nm}$ , followed by the emission of a photon with wavelength  $460\text{ nm}$  [24]. Measuring variations in the intensity of the outputted light over time, using modern methods such as fluorescence lifetime imaging, enables the measurement of fluctuating cellular levels of NADH. Analytical techniques can then be applied to these time-series to extract information about underlying dynamics, such as how oscillation frequency changes over time.

### 2.2.2. Membrane potential oscillations

The study of the inner mitochondrial membrane potential can reveal another oscillating quantity. The distribution of ions across cell membranes can cause a potential difference between inner and outer cellular regions. A potential difference is induced in the mitochondria during OXPHOS [14] as an uneven distribution of protons exists in this region. This proton gradient is essential as the final stage of OXPHOS consists of protons flowing back into the mitochondrial matrix via an enzyme complex, driving the synthesis of ATP. Therefore throughout this process, the potential ( $\Delta\Psi_m$ ) remains in a state of flux, which can be measured using the fluorescent dye 3,30-diethyloxycarbocyanine iodide. Similar to the previously outlined method of measuring glycolysis by observing NADH levels, measuring variations in fluorescence may indicate changes in the mitochondrial membrane potential over time. Using time-series data generated by observation of NADH oscillations may help indicate novel findings about cellular dynamics and indeed help to model these systems.

## 3. Kinetic model of cellular energy metabolism

Due to the inherent complexity of biological systems, both modelling and analysing cellular data are fraught with difficulties. Despite this, several models have attempted to address the problem. Many of these models take an autonomous approach to modelling biological oscillators [25–28]. One such attempt is the kinetic model of Amemiya et al. [5]. This model attempts to describe the oscillatory glycolytic behaviour previously observed in HeLa cervical cancer cells [23]. As with all models, a large amount of simplification must occur, focusing

on the cell's fundamental glycolytic pathways and transport processes. This approach considers four enzymatic reactions and three transport processes.

### 3.1. Transport

To elucidate the interactions between metabolic processes in this model, it may be helpful to follow the path of substrates throughout glycolysis, beginning with the injection of glucose into the extracellular medium. The flux of this process,  $J_{in}$ , is given by

$$J_{in} = \begin{cases} \frac{G_i}{t_2 - t_1}, & t_1 \leq t \leq t_2, \\ 0 & \text{otherwise.} \end{cases} \quad (1)$$

Here,  $G_i$  is the concentration of glucose added to the extracellular solution and glucose transport takes place between times  $t_1$  and  $t_2$ . Transportation of glucose from the extracellular solution across the plasma membrane occurs with the aid of glucose transporter proteins (GLUT) [29]. Equation 2 describes the flux of glucose across the membrane [30]

$$J_{GLUT} = V_{max} \frac{G_{ex} - \frac{G}{K_{eq}}}{K_{out} \left(1 + \frac{G}{K_{in}}\right) + G_{ex}}. \quad (2)$$

Here,  $K_{in}$  and  $K_{out}$  are the affinity constants of the enzyme for both inter and extracellular glucose while  $K_{eq}$  is the equilibrium constant.  $V_{max}$  is the maximum velocity in the forward direction.  $G_{ex}$  is the extracellular glucose concentration while  $G$  is the concentration within the cell. Figure 2 further illustrates the interactions between variables and how they relate to cellular processes.

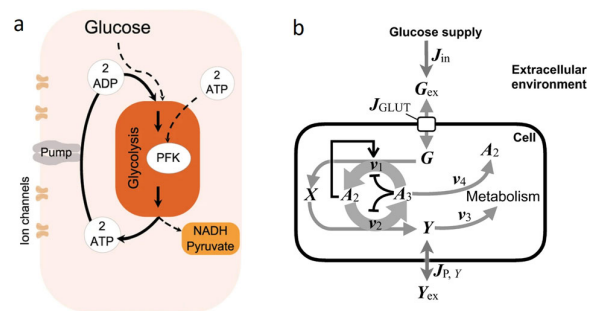


**Figure 2.** The glycolytic branch of cellular energy metabolism. (a) The cellular energy metabolism diagram of Figure 1 is reduced to show only the glycolytic pathway. Reproduced with permission from [21]. (b) Schematic diagram illustrating interactions between parameters in the Amemiya et al. model.  $X$  and  $Y$  are glycolytic intermediates,  $v_x$  represents the enzymatic processes within the cell, while  $J_x$  illustrates the respective transport processes.  $A_2$  and  $A_3$  represent ADP and ATP, respectively. Reprinted with permission from [5].

The final transport process to consider is the flux of the product,  $Y$ , leaving the cell. This flux,  $J_{P,Y}$ , is given by

$$J_{P,Y} = \kappa (Y - Y_{ex}), \quad (3)$$

and so is proportional to the concentration of  $Y$  inside and outside ( $Y_{ex}$ ) the cell and a coupling constant  $\kappa$ .  $\kappa$  is dependent upon both the surface area of the cell,  $S$ , cellular volume,  $V$ , and membrane permeability,  $P$ , such that  $\kappa = \frac{SP}{V}$  [31]. The intracellular concentrations of Equations 2 and 3 change thanks to several chemical reactions inside the cell.

### 3.2. Enzymatic processes

ATP is both utilised and produced at different stages of glycolysis. Initially, two molecules of ATP are consumed to instigate the reaction before four ATP molecules are generated at a later stage. This model simplifies the intermediate processes of glycolysis by capturing only the core glycolytic pathway. The first step to consider is the consumption of glucose and ATP in the phosphofructokinase (PFK) reaction. The rate of this reaction is given by  $v_1$  and represents the initial enzymatic processes in glycolysis. A Michaelis-Menten-type mechanism [32] is used to represent both this process and the second reaction. The reaction rate is expressed using the function  $f(G, A_3)$  such that

$$f(G, A_3) = \frac{A_2^m}{\left[1 + A_2^m \left(\frac{1}{K_1} + \frac{G}{K_1 K_3} + \frac{A_3}{K_1 K_4}\right) + \frac{A_3^m}{K_2}\right]},$$

$$v_1 = k_1 G A_3 f(G, A_3). \quad (4)$$

Here,  $m$  is the number of PFK enzymes present,  $G$  is the inter-cellular glucose concentration, and  $K_1$  and  $K_2$  are dissociation constants of PFK-ATP and PFK-ADP complexes, quantifying the propensity of the two objects to separate. Similarly,  $K_3$  and  $K_4$  are disassociation constants for other enzyme-substrate complexes involved at this stage. ADP is represented by  $A_2$  while  $A_3$  represents ATP and the sum of these molecules,  $A_2 + A_3 = A_0$ , was assumed to be constant. These reactions produce pools of intermediate compounds, labelled  $X$ , which are used as substrates in the second stage.

The pyruvate kinase (PK) reaction is substantially more straightforward, with only inhibition by ATP being considered, and so the formulation for  $v_2$  is more concise:

$$g(X, A_3) = \frac{1}{\left(1 + \frac{A_3^n}{K_5} + \frac{X}{K_6} + \frac{A_2}{K_7}\right)},$$

$$v_2 = k_2 X A_2 g(X, A_3). \quad (5)$$

In this case, the number of PK enzymes is given by  $n$ , and  $K_5$  is the disassociation constant between pyruvate kinase and ATP. As before,  $K_6$  and  $K_7$  are disassociation constants of subsequent enzyme-substrate complexes.

Finally,  $v_3$  represents the consumption of the product  $Y$  in other stages of metabolism, while  $v_4$  is the rate of consumption of ATP within the cell. These are given by

$$v_3 = k_3 Y,$$

$$v_4 = k_4 A_3. \quad (6)$$

Here,  $k_1, k_2, k_3$ , and  $k_4$  are all the respective rate constants. A series of six linear differential equations were used to simulate the changing levels of various substrates during these processes which are as follows:

$$\begin{aligned} \frac{dG}{dt} &= J_{GLUT} - v_1, \\ \frac{dX}{dt} &= v_1 - v_2, \\ \frac{dY}{dt} &= 2v_2 - v_3 - J_{P,Y}, \\ \frac{dA_3}{dt} &= -2v_1 + 4v_2 - v_4, \\ \frac{dG_{ex}}{dt} &= J_{in} - \frac{V}{V_{ex}} J_{GLUT}, \\ \frac{dY_{ex}}{dt} &= \frac{V}{V_{ex}} J_{P,Y}. \end{aligned} \quad (7)$$

The ratio of inter to extracellular volume is given by  $\frac{V}{V_{ex}}$ . Unlike the real glycolytic oscillator, the oscillations generated by this model are induced rather than self-sustained. This enables the system to reproduce certain experimental conditions; however, it may be ill-suited to represent the continuous oscillatory behaviour of cells *in vivo*. Comparing these induced glycolytic oscillations to experiment enables the model's validity to be assessed. To this end, a time-series of the substrate  $Y$  may be considered as, and directly compared to, observed NADH oscillations in real cells.

### 3.3. Experimental evidence

Any model must be compared to actual data to test its validity, so it is paramount to establish analytical methods to inspect biological signals. Amemiya et al. tested the validity of their model by measuring a group of HeLa cells [5]. Following incubation of the cells for 24 h without glucose, adding glucose to the chamber stimulated glycolytic oscillations. These oscillations continued until the supply of glucose was exhausted. Figure 3(a) illustrates these changes by measuring NADH fluorescence over a period of 800 s. These data are freely available at [33].

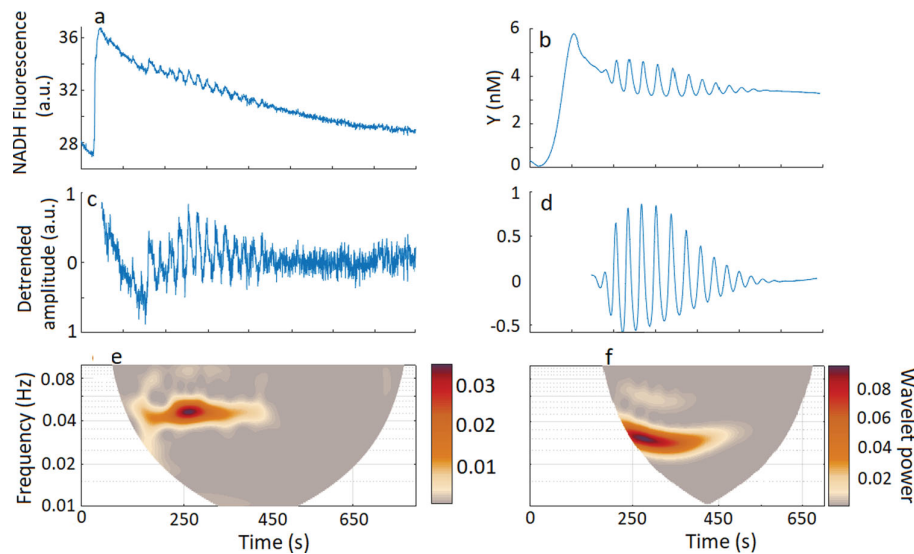


**Figure 3.** Experimental data (a, c, e) and data obtained from the kinetic model (b, d, f). The model derived data were obtained with parameters presented in [23]. (a) Fluctuations in NADH measured via fluorescence. From [23], with permission. (b) Simulated glycolytic oscillations from the kinetic Amemiya et al. model. Reprinted with permission from [5]. (c) The time-series data in (a) is detrended by subtraction of a best fit cubic polynomial following removal of the first 50s of data. (d) The time-series data in (b) detrended by subtraction of a best fit cubic polynomial after removing the first 150s of data. (e) Wavelet transform of the time-series data in (c). (f) Wavelet transform of the time-series data in (d). All wavelet transforms in this review were generated with a frequency resolution parameter  $f_0 = 1$ , between 0.01 and 0.1 Hz, and a lognorm wavelet was used. The freely available software package MODA (Multiscale Oscillatory Dynamics Analysis) was used to perform the transforms [34, 35].

To highlight the oscillatory behaviour of a time-series, one must represent the measured data in the time–frequency domain. To this end, the initial step due to the sudden availability of glucose in the first 50 s of measurements was removed. As such, Figure 3(c) represents the experimental data without this step and another crucial change, the time-series has also been detrended by subtraction of a best-fit cubic polynomial [34, 35]. In a similar manner, the initial step of the simulated data was also removed prior to detrending the signal. In this case, 150 s was removed as the initial spike is more elongated in time.

The time dependence of the oscillator is illustrated between 100 and 400 s in Figure 3(e) before vanishing as the injected glucose is wholly consumed. Following this, as can be seen in Figure 3(a) and 3(c), the time-series becomes noise-like, decreasing in NADH amplitude. The cells then die due to the lack of glucose present, hence the lack of sustained oscillations. This cessation would not be the case in actual cells as glucose is continually supplied, enabling the continuation of oscillatory behaviour. While this model can simulate a reduction in glycolytic activity over time, and indeed the cessation of glycolytic oscillations in this *in vitro* experiment, this is not necessarily the case *in vivo*. Glucose is continually supplied in the cell, enabling glycolysis to continue for extended periods. Induced oscillations cannot represent this sustained

oscillatory behaviour as their amplitude decreases over time. Modelling approaches that can recreate both these experimental conditions and sustained glycolytic oscillations would allow both *in vitro* and *in vivo* conditions to be replicated. The lack of non-autonomous terms in this modelling approach is highlighted by the smoothness of Figure 3(b, d, f) and illustrates how autonomous models can struggle to replicate the constant perturbations experienced in biological systems.

A wavelet transform (WT) has been performed upon the time-series to represent the glycolytic oscillations in time–frequency space. The windowed Fourier transform (WFT) may also be used to investigate the changing frequency over time. However, the WT has one particular key advantage when analysing signals of this type regarding frequency resolution. The WFT has a linear frequency resolution, while the WT's frequency resolution is logarithmic. This enables greater representation of low-frequency oscillations, and so, in general, low-frequency oscillations are better represented by the WT [36].

A total of 22 parameters and six autonomous, linear differential Equations (7) are required to yield the time-series represented in Figure 3(b). The implementation of time-independent equations means the model lacks the intrinsic time dependence present in many biological systems [37]. A nonlinear system in cellular energy

metabolism has also been replicated using only linear equations. Various metabolic masses, including the sum of ATP and ADP, are conserved throughout the system, and the focus of this investigation is mass. The cell is a thermodynamically open system, with matter and energy constantly being exchanged with the environment. Treating the system as such would remove the constraint of conservation of mass and provide a more accurate representation of the cell. While the focus here has been the work of Amemiya and colleagues, this is far from the only contribution to the field. Various other approaches, such as the work of Kembro et al., describe metabolic oscillations [17], as do a series of alternative models that also assume autonomous dynamics [25–28]. The Amemiya et al. model provides a point of comparison in this review as the experimentally derived results provide a valuable grounding to compare with theoretically generated figures.

Synchronisation between biological oscillators can provide a crucial source of stability in living systems, which cannot be replicated here as synchronisation is a purely nonlinear phenomenon. Alternative approaches to those outlined in this section have been proposed recently. By focusing upon temporal dynamics and phase relationships between biological oscillators, the above imposition of conservation of mass may become unnecessary. These new approaches may enable thermodynamically open, non-autonomous, nonlinear systems to be treated as such. Utilising this relatively new approach necessitates an explanation of several key concepts. One of the most important is synchronisation and the stability it can induce in dynamic systems.

## 4. Synchronisation

Synchronisation phenomena are abundant and varied in the world, from synchronous croaking in groups of frogs [38] to professional violin players in complex networks [39]. The etymology of synchronisation comes from the Greek words *syn* (same) and *chronos* (time), and as this would suggest, it describes two systems with similar relationships in time. Synchronisation in the sense of nonlinear dynamics must be differentiated from simple synchronous motion, however, as they are not equivalent. ‘Synchronous motion’ implies two or more oscillators moving coherently in time, that is to say, with a constant phase difference between them. A common influence, which may be between a pair of oscillators or an external driving force, must also be present for synchronisation.

As mentioned earlier, this phenomenon was discovered by Christian Huygens in 1665 when, lying in bed for several days due to illness, he noticed that two pendulum clocks on the opposite wall, which were attached

by a heavy wooden beam, eventually started to oscillate with the same amplitude and period in anti-phase to one another. He observed that this effect had taken place due to the hardly perceptible motion of the beam and was the first scientist to observe and record such synchronisation phenomena.

The two types of synchronisation phenomena which attract the most attention are phase synchronisation (PS) and general synchronisation (GS) [40]. Phase synchronisation is a purely temporal relation that describes a constant phase difference between coupled oscillators and may be present despite differences in the amplitudes of a pair of oscillators. Alternately, GS requires synchronisation in both phase and amplitude dynamics.

Phase synchronisation can be used to investigate mutual interaction between various oscillators and the self-organisation that may follow. Despite initial measurements of many biological systems being seemingly noise-like and unworkable, by considering synchronisation states, one may uncover previously hidden pockets of order and an underlying predictable stability. This may enable the analysis of complex interactions in a variety of oscillatory systems [41]. The self-organisation that arises in biological systems thanks to synchronisation provides a vital source of stability in the face of an ever-changing world [42–44].

Throughout this review, the term ‘synchronisation’ will refer to PS. This phenomenon relies on the concept of phase-locking, and so to appreciate PS, an understanding of phase is required. External influences on a system can modulate the phase and allow frequency locking to arise. Interacting periodic oscillators can also alter each other’s phases, leading to synchronisation. Larger network configurations may coordinate their oscillations via intra- and inter-network synchronisation. The synchronisation between non-autonomous systems, both permanent and intermittent, is also discussed. Combining these approaches illustrates how periodic driving forces, self-sustained oscillators and noise simultaneously influence phase dynamics.

### 4.1. Phase dynamics during oscillation

To understand the concept of synchronisation, one must first appreciate the variable that enables its emergence, the phase  $\varphi$ . Self-sustained oscillators exhibit periodic behaviour, and at each point in their respective cycles, they will have an associated value of phase. This variable may then be used to parameterise the motion along these cycles [41]. The instantaneous phase may also be defined using the natural frequency of the associated

oscillator ( $\omega_0$ )

$$\frac{d\varphi}{dt} = \omega_0. \quad (8)$$

The importance of phase concerning synchronisation is best outlined using an example. Consider a pair of pendulums. If both are equally displaced from equilibrium and travelling in the same direction, they can be considered ‘in phase’ ( $2\pi$  or  $0$  phase shift between them). Similarly, if the oscillations are at different points in their respective cycles, they can be described by the relative phase difference,  $\Delta\varphi$ , which takes a value  $0 \leq \Delta\varphi \leq 2\pi$ . This difference must be constant over time for synchronisation to occur. In an isolated, autonomous system, the phase exhibits neutral stability as perturbations encountered neither grow nor decay over time. This implies that a series of small perturbations such as an external periodic driving force or a coupling to another oscillator can cause significant changes in the phase to occur over time. Therefore, with a relatively weak driving force acting upon the oscillator, it is possible to adjust the phase of the system without influencing the amplitude. These changes are characteristics of phase synchronisation.

#### 4.2. Phase-locking and frequency entrainment

The easiest way to set up a synchronised system is to apply a periodic force to a self-sustained oscillator. Effects of such a small forcing will only be on the neutrally stable phase rather than the amplitude, and so it makes sense to describe it using a framework known as the ‘phase approximation’. Here, only the dynamics of the phase are considered [45] using an equation describing the perturbed phase dynamics

$$\frac{d\varphi}{dt} = \omega_0 + \varepsilon Q(\varphi, \omega t). \quad (9)$$

This describes the simple case of an oscillator driven by a periodic external influence with amplitude  $\varepsilon$ , and frequency  $\omega$ .  $Q$  represents the periodic coupling function

between the driving force and the oscillator. Expanding this  $Q$  function with a Fourier series enables its representation as slowly varying and quickly oscillating resonant terms. The former can be written as  $\mathbf{q}(\varphi - \omega t)$  whilst averaging is applied to the latter to obtain the Adler Equation (10), which is a fundamental equation for the dynamics of phase difference

$$\frac{d\Delta\varphi}{dt} = -(\omega - \omega_0) + \varepsilon \mathbf{q}(\Delta\varphi). \quad (10)$$

Here,  $\Delta\varphi = \varphi - \omega t$  is the difference between the phase of the oscillator and the forcing on the system. The function  $\mathbf{q}$  is periodic. Stable stationary solutions to Adler’s equation occur for certain values of  $\omega$  and  $\varepsilon$  when the phase change rate is zero. This corresponds to a specific area on the plane of parameters called the Arnold tongue, or synchronisation region, which is illustrated in Figure 4(a).

$\Delta\omega = \omega_0 - \omega$  is the frequency mismatch. This value, alongside the coupling strength  $\varepsilon$ , determines the system’s overall dynamics and stability. The purple region within Figure 4 meets the synchronisation criteria of  $\varepsilon > |\Delta\omega|$  and so synchronisation will occur within this region. Only within this Arnold tongue may phase-locking – the point at which the phase  $\varphi$  starts following the forcing phase – occur. Therefore, synchronisation will not be present within the surrounding white area, where this condition is not met. These criteria hold in this idealised, autonomous representation; however, as shown later in this review, slightly more consideration must be taken when considering non-autonomous systems.

#### 4.3. Interacting periodic oscillators

Just as external periodic forcing can cause synchronisation to occur in an oscillator, it may also transpire via couplings between two oscillators of phases  $\varphi_1$  and  $\varphi_2$ . To account for both oscillators interacting with one another, the following equation becomes necessary

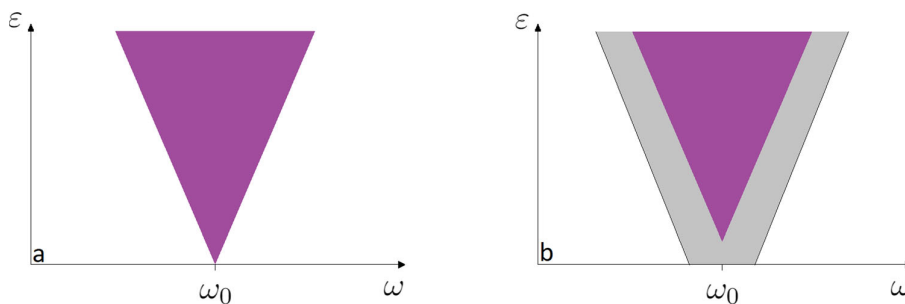


**Figure 4.** (a) The Arnold tongue (purple region) is plotted in the plane of parameters for an autonomous system. (b) The parameter space for a non-autonomous system. The purple region represents permanent synchronisation, while the grey region represents intermittent synchronisation [46], as discussed in Section 4.4.



$$\frac{d\varphi_1}{dt} = \omega_1 + \varepsilon Q_1(\varphi_1, \varphi_2), \quad \frac{d\varphi_2}{dt} = \omega_2 + \varepsilon Q_2(\varphi_2, \varphi_1). \quad (11)$$

In this case,  $\varepsilon$  represents the strength of the couplings between the systems [47]. Synchronisation implies that the two oscillators oscillate with a common frequency. This common value is typically between  $\omega_1$  and  $\omega_2$ . As before, phase-locking does not necessitate any restriction on the amplitude of either oscillator.

The above use of the Kuramoto model allows systems to be modelled as self-sustained oscillators. This type of oscillator is found in various living systems and is named after one of their key characteristics – the ability to continue oscillating even if isolated. Self-sustained oscillators provide an excellent way to model living systems, not just because of their ubiquity across a variety of life [41] but also thanks to their robustness against perturbation. These oscillators are often described in terms of their limit cycles. The limit cycle is the path in phase space upon which self-sustained oscillators converge over time. Limit cycles, therefore, act as an attractor, with any initial state of the system converging upon the cycle. This generates stability in an oscillator's amplitude; however, as mentioned previously, the phase exhibits neutral stability in isolated, autonomous systems, neither growing nor decaying once perturbed. This allows oscillators to easily influence each other's phases and become synchronised.

This approach contrasts with the type of oscillations generated by the model in Section 3. Here, oscillations are induced by the sudden influx of glucose into the model and continue for a short time before fading away. While this method can demonstrate oscillations, they are not self-sustained and may be unable to recreate some key characteristics of oscillating living systems, such as synchronisation. Induced oscillatory models would also be unable to recreate the long-term behaviour of cells *in vivo*, where cessation of oscillations does not occur as glucose supply to the system is continuous. Another area neglected by the kinetic approach is the intrinsic time dependence of living systems which can induce additional stability in their phase dynamics.

#### 4.4. Synchronisation in non-autonomous systems

While the mathematical framework outlined previously may be sufficient to describe synchronisation in closed systems shielded from external perturbations; a new approach must be taken to incorporate the constant disturbances experienced by living systems. Somewhat counter-intuitively, the inclusion of terms representing the perturbations experienced in time-dependent biological systems has been shown to enlarge regions of

stability and make the system itself more robust in the face of a changing environment. To demonstrate these changes, a new framework is introduced. A system similar to that of Equation 10 will be used, with the key difference being the introduction of non-autonicity by virtue of a time-dependent frequency term as follows:

$$\omega(t) = \omega(1 + A \sin(\omega_{mod}t)). \quad (12)$$

Here,  $\omega$  represents the same driving frequency as Equation 10 and  $\omega(t)$  is the new time-dependent driving frequency, modulated with amplitude  $A$  and at frequency  $\omega_{mod}$ . Implementing this new deterministic non-autonomous frequency means that the equation for the frequency mismatch,  $\Delta\omega$ , must be re-evaluated. Therefore, so must the criteria for synchronisation and indeed the Arnold tongue. This new, time-varying frequency mismatch is given by

$$\begin{aligned} \Delta\omega(t) &= \omega_0 - \omega(1 + A \sin(\omega_{mod}t)) \\ &= \Delta\omega - A\omega \sin(\omega_{mod}t). \end{aligned} \quad (13)$$

It is now possible for the synchronisation criteria ( $\epsilon > \Delta\omega(t)$ ) to only be satisfied at certain times due to the time-dependent nature of the new frequency mismatch [48]. This non-autonicity can lead to a new type of synchronisation and a new region on the parameter space. This is known as intermittent synchronisation and was recently introduced by Lucas et al. [46].

Figure 4(b) highlights the birth of this new region alongside a crucial implication of its introduction. Both the size of the white – no synchronisation – and purple – permanent synchronisation – regions have shrunk. Initially, this may seem inconsequential as both of the previous regions have diminished, seemingly cancelling each other out. However, this is not the case as the intermittent region can also induce stability in the system overall.

Introducing a relatively new class of non-autonomous oscillators, known as chronotaxic systems, and observing their properties may further elucidate the source of the increased stabilisation granted to a system by intermittent synchronisation. While intermittently synchronised non-autonomous oscillators are only attracted towards the moving point attractor at certain times, in chronotaxic systems, adjacent trajectories converge upon it at all times. Figure 5 demonstrates this behaviour with stability in both phase and amplitude.

The etymology of chronotaxic, with *chronos* meaning time and *taxis* meaning order, demonstrates the defining property of this group of systems. The fact they can resist perturbations to time-varying parameters – specifically their frequencies – over time [44]. These characteristics

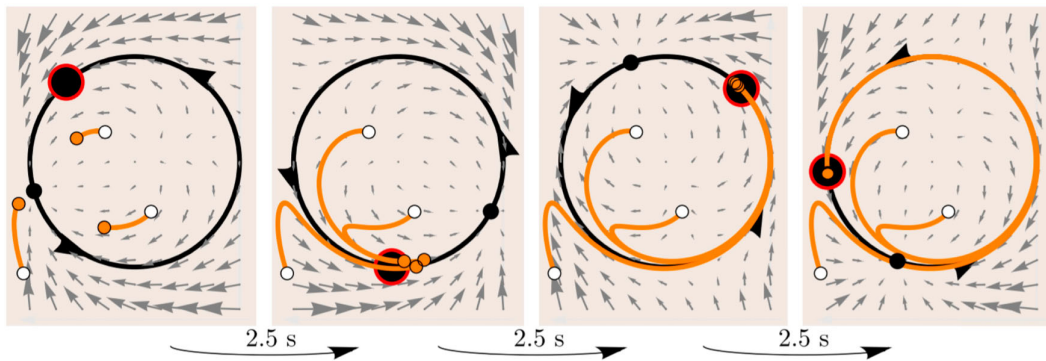


**Figure 5.** Time evolution of points around a chronotaxic limit cycle over time. The time-dependent point attractor is represented by the large black disc with red outline, arrows represent velocities and the white dots represent initial points, from which orange trajectories are followed as time evolves. From [44], with permission.

enable chronotaxic systems to represent thermodynamically open dissipative dynamical systems with an internal source of energy as they are robust in the face of external influences. Following perturbation, the phase will be drawn back to the point attractor moving along a stable trajectory. This point will be dependent on time, and all trajectories are drawn towards it. Figure 5 represents the behaviour of trajectories in the phase space of a chronotaxic system as time evolves. The large red circle represents the motion of the attractor through phase space while the orange lines track adjacent trajectories being drawn towards it. In a manner analogous to synchronisation inducing stability in autonomous systems, chronotaxicity may induce stability in time-dependent systems.

The introduction of the point attractor provides another approach to considering intermittent synchronisation. During periods when the synchronisation criterion is fulfilled,  $\epsilon > \Delta\omega(t)$ , the phase exhibits stability and is drawn towards the moving point attractor, similar to the orange trajectories in Figure 5. Meanwhile, when this criterion is not fulfilled and  $\epsilon < \Delta\omega(t)$ , the phase demonstrates neutral stability, neither converging upon nor diverging from the point attractor [49]. Over a long enough period, the lack of divergence and presence of convergence is enough to induce stability within the intermittently synchronised region.

The region of stability may now be considered as the sum of the permanently and intermittently synchronised regions. In this way, the new parameter space of the non-autonomous system has a larger stability region than the old, illustrating how non-autonomicity can induce stabilisation at parameter combinations that would formerly have been asynchronous. The very survival of living systems relies upon robust resistance in the face of environmental perturbation and intermittent synchronisation may provide a mechanism to increase this stability.

Non-autonomous systems are abundant in nature and the inherent self-organisation provided by chronotaxicity may be key in maintaining various biological systems and necessary to sustain life.

Thus far, only small collections of oscillators have been considered. However, this framework may also be extended to groups of oscillators that are more reminiscent of the large cellular ensembles seen in living systems.

#### 4.5. Networks

Synchronisation may occur between oscillators of the same or different types. Often, many of the same types of oscillators can coalesce in large network configurations. Each oscillator becomes a node of a much larger system in this arrangement. To describe this system, another parameter, known as the Kuramoto-order parameter  $r_X$ , is introduced, where

$$r_X e^{i\Psi} = \frac{1}{N} \sum_{k=1}^N e^{i\theta_{Xk}}. \quad (14)$$

When  $r_X = 1$ , a completely ordered system is represented, with each oscillator of the same type in a network oscillating with the same phase. When  $r_X = 0$  however, the oscillators are completely disordered [45]. Alongside the strengths of this approach in theoretical work and modelling, this order parameter may be used to express the degree of synchronisation between oscillators in an experiment. The review by Hauser illustrates this by using the order parameter to indicate the degree of synchronisation in a yeast cell population of intermediate cell density [12].

A pair of networks may be linked using the mean phase of the oscillators within a given network. This parameter,  $\Psi_X$ , is given for oscillators in a network of size

$N$ , as

$$\Psi_X = \frac{1}{N} \sum_{i=1}^N \theta_{Xi}. \quad (15)$$

Each oscillator has a phase  $\theta_{Xi}$ . This enables inter-network couplings to be represented [50]. Network-based approaches more accurately represent metabolic interactions, where both mitochondria and glycolytic enzymes synchronise their oscillations [16]. A further crucial consideration when investigating metabolic processes is that they exist in an open system. Indeed, all living systems exist in a state of dynamic equilibrium where both matter and energy must be utilised and excreted from the cell at different times to maintain life. This intrinsic thermodynamic openness requires these systems to be treated as non-autonomous and introduces several complex factors to consider.

## 5. Non-autonomous modelling of cellular energy metabolism

Several frameworks have been developed using the principles laid out in this review. The majority of these methods focus on either glycolytic [10] or mitochondrial [15] oscillators alone. However, an approach incorporating both mitochondrial and glycolytic oscillations has been established by Lancaster et al. [21]. This approach models cellular energy metabolism to demonstrate a transition from predominantly mitochondrial ATP production to glycolytic dominance. Modelling this switch requires simplification to the point that only the features required to detect chronotaxis are necessary. With this aim, glycolytic and mitochondrial oscillators were investigated, with simplified metabolic pathways and interactions between them to facilitate the detection of chronotaxis, which in itself will be able to describe subtle changes in dynamics arising due to alterations in cellular energy metabolism. Other attempts to model ATP synthesis have also been made, with a notable example being the linear, autonomous model developed by Amemiya et al. outlined earlier in this review [5] which will act as a comparison point between approaches.

### 5.1. Glycolytic and mitochondrial oscillators

Interactions between oscillations in both glycolytic and mitochondrial oscillators are ever-present in biological systems. From viruses hijacking cellular metabolism to favour their reproduction [51], to the ‘Warburg effect’ where increased glycolysis assists with cellular proliferation in cancer cells [52]. In general, when cells

become increasingly reliant on glycolysis for the production of ATP, this can be considered a sub-optimal, so-called altered state. Multiple studies have shown that the oscillations in glycolysis drive those in the mitochondria under these conditions [6, 7, 18, 52]. They have further shown that the production of ATP in the mitochondria can indirectly influence glycolysis via a sensing mechanism of the cellular ATP/ADP ratio [22]. The lower the relative proportion of ATP, the increased prevalence of glycolysis. This process occurs via reversal of PFK inhibition, an enzyme used in glycolysis. Healthy cellular states produce the majority of ATP via OXPHOS, a process in the mitochondria, and glycolysis will occur at a rate suitable to produce substrates such as pyruvate and NADH necessary for the mitochondrial oscillator to function. Through this, there will still be some influence from glycolysis on mitochondrial pathways, but the majority of ATP production in healthy cells will still occur during mitochondrial processes. These oscillations have a profound effect on each other; however, external influences such as the pulsatile supplies of glucose [53], and oxygen [54] must also be considered to model the system correctly.

### 5.2. External drivers

A driving influence over oscillators must be present to describe a system as chronotaxis. There are two main ways that these driving forces can emerge. The first is from interactions with external oscillators, where fluctuations in glucose or oxygen available to the cell may drive the glycolytic or mitochondrial oscillations. Chronotaxis may also arise due to variations in the duration of various metabolic pathways within the cell, implying a dependence upon the inner structure of the oscillator. The experiments by Gustavsson et al. illustrate this dependence as, despite constant glucose levels, oscillations were not synchronised, suggesting these dynamics must be due to internal mechanisms [10].

In the model demonstrated by Lancaster et al. [21], the supply of glucose and oxygen are considered as the drivers of the MO and GO, which define, either directly or indirectly, the chronotaxis of the system. This is independent of the exact mechanisms by which the chronotaxis arises. Sufficient information is acquired using this approach as alterations in the system chronotaxis reflect changes to the underlying metabolic state.

### 5.3. Phase dynamics

Several parameters are used in this model to demonstrate the strength of coupling between the various processes. Continuous interactions between the MO and



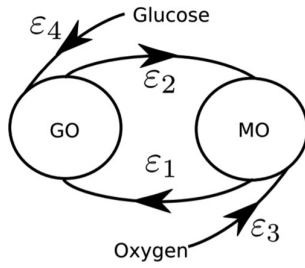


**Figure 6.** Couplings relevant to the model,  $\epsilon_1$  and  $\epsilon_2$  represent repulsive and attractive couplings between oscillators, respectively, whilst  $\epsilon_3$  and  $\epsilon_4$  represent external drivers. From [21], with permission.

GO require that they are represented by bidirectionally coupled oscillators of strength  $\epsilon_1$  and  $\epsilon_2$  both of which interact differently. As the effect of mitochondrial ATP production on glycolysis is inhibitory,  $\epsilon_1$  is a repulsive coupling and so preceded with a positive sign. In contrast, the excitatory nature of glycolysis on ATP production in the mitochondria necessitates the negative sign preceding  $\epsilon_2$ . In different metabolic states, the values of these couplings can vary. The influence of oxygen and glucose on the system is represented by unidirectionally coupled drivers  $\epsilon_3$  and  $\epsilon_4$ . Figure 6 demonstrates the influence of respective couplings over this model.

Only consideration of phase dynamics is necessary to describe chronotaxis in a system, and so any amplitude dynamics, regardless of their complexity, can be neglected. Therefore, the following coupled phase oscillators are sufficient to model a chronotactic system

$$\begin{aligned}\dot{\varphi}_{GO} &= \omega_{GO} + \epsilon_1 \sin(\varphi_{GO} - \varphi_{MO}) \\ &\quad - \epsilon_4 \sin(\varphi_{GO} - \omega_G t) + \sigma \eta(t), \\ \dot{\varphi}_{MO} &= \omega_{MO} - \epsilon_2 \sin(\varphi_{MO} - \varphi_{GO}) \\ &\quad - \epsilon_3 \sin(\varphi_{MO} - \omega_O t) + \sigma \eta(t).\end{aligned}\quad (16)$$

Here,  $\varphi_{GO}$  and  $\varphi_{MO}$  represent the instantaneous phases of the glycolytic and mitochondrial oscillator, respectively,  $\omega_{GO}$  and  $\omega_{MO}$  are their natural frequencies, whilst  $\omega_G$  and  $\omega_O$  are the frequencies of the glucose and oxygen drivers. The  $\eta(t)$  term represents white Gaussian noise in the system, representing natural perturbations in such an open system while also introducing non-autonomicity.

### 5.3.1. Possible changes due to infection

As previously discussed, the strengths of the couplings in the system can be variable, and this variability leads to different possible outcomes for the system as different drivers take prevalence. Figure 7 shows the effects of varying the coupling strengths between the oscillators and the different behaviour it produces in the system. Here, both  $\epsilon_3$  and  $\epsilon_4$  (which represent the driving influences of oxygen and glucose respectively) have been kept

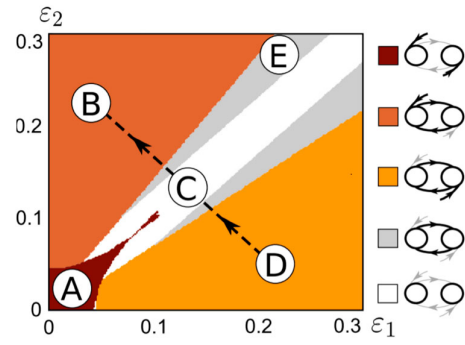


**Figure 7.** Numerical simulation varying coupling strengths between the mitochondrial and glycolytic oscillators, the colour key indicates the dominant driving influences in each part of the figure, referencing Figure 6.  $\epsilon_3 = \epsilon_4 = 0.025$  whilst  $\epsilon_1$  and  $\epsilon_2$  vary. From [21], with permission.

constant at 0.025 whilst the couplings between oscillators were varied to simulate different metabolic states.

The path indicated in Figure 7 from the D to B zone describes the cell transitioning between states. Initially, chronotactic dynamics are present as the oxygen driver dominates the metabolism at D. The system then transitions to a non-chronotactic region at C, where no oscillators are synchronised. Finally, the system moves onto the chronotactic region B, where glucose oscillations drive the system. A growing body of evidence suggests a similar transition takes place in coronavirus infected cells [18]. While this transition occurs, the observed cellular dynamics go from chronotactic to non-chronotactic before returning to a chronotactic state. This pathway indicates the transition from healthy to infected cells and could be observed by monitoring the chronotacticity of experimental data or used to model pathogenesis within cells.

When applying the model, the strength of the coupling constants in cells affected by disease must also be considered. Values of  $\epsilon$  may well change as various conditions alter the body's ability to provide the correct amounts of oxygen and glucose to cells by attacking the pulmonary, circulatory and endocrine systems, altering the values of the associated coupling. Coupling strengths between the mitochondrial and glycolytic oscillators may also be affected by various metabolic conditions [18] and must be considered before modelling specific disease impact upon the cell.

### 5.4. Network-based approaches

While the model outlined above successfully illustrates the changes during infection, it lacks several key properties. Within animal cells, there are on the order

of thousands of mitochondria and glycolytic sites distributed throughout the cytoplasm [55] and so only by considering larger network ensembles can the scope of interaction truly be appreciated and replicated. Several existing models utilise network-based approaches to replicate the complex dynamic behaviour exhibited by mitochondrial oscillations [15, 17, 28] however, to the author's knowledge, only the following approach can simultaneously replicate both branches of metabolism using a non-autonomous network-based approach.

As an extension to the framework presented in the previous subsection, Rowland Adams and Stefanovska [56] developed a network-based approach to account for this difference while applying some other essential alterations which are outlined in this section. The stochastic noise term  $\eta(t)$  previously provided a time dependence, whereas this has been replaced by deterministic frequency variation. The spatial distribution of oscillators, as is seen in real cells, could also not be considered formerly due to the restriction of only having a single oscillator of each type.

#### 5.4.1. Spatial distribution of oscillators

One area neglected in the Lancaster et al. approach is the distribution of oscillators throughout the cell. Mitochondria are distributed along the cytoskeleton [57] while glycolysis takes place at various sites in the cytoplasm of cells [55]. Due to this, there are different distances between any pair of oscillators. Mitochondria, for example, show intra-network couplings that are dependent upon the distances between organelles [58]. The spatial arrangement of organelles intrinsically affects the amplitude of the inter-network coupling as a pair of mitochondrial oscillators that are close together will have a more significant influence over each other than a more greatly displaced pair. To simulate this effect, an all-to-all network configuration is used while each organelle is considered a node on the perimeter of a ring. Adjacent oscillators then will have a maximum weighting in terms of influence over one another, while oppositely positioned mitochondria will have a minimal influence.

Figure 8 illustrates these distances with the length of the lines between respective nodes. Mathematically, each oscillator is assigned a number ( $i$ ), where  $i, i+1$  and  $i-1$  are all neighbours. The final,  $N$ th, oscillator is also adjacent to the first to create the ring structure of Figure 8. Using this configuration, each weighting is determined by the difference in the index of each node, with the distance separating oscillators being inversely proportional to the weighting between them. In the case of  $i$  being less than or equal to  $\frac{N}{2}$ , this is accounted for by the following

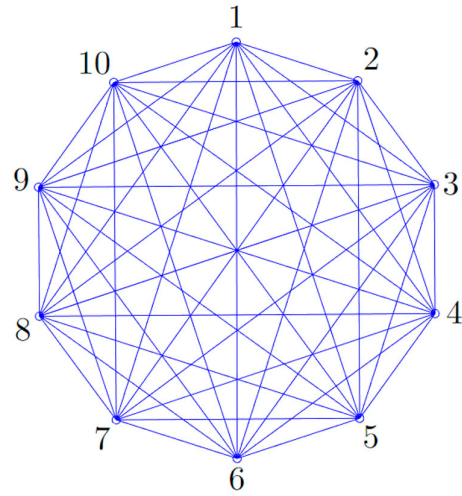


**Figure 8.** Visual representation of the distance between oscillators in the model. The distance between nodes 1 and 6 is the maximum while adjacent nodes are minimally displaced from one another. Network of size  $N = 10$  is represented; however, this parameter may be varied.

equation:

$$W_{ij} = \begin{cases} \frac{W}{|i-j|}, & \text{for } j \in \left[1, i + \frac{N}{2} - 1\right], \\ \frac{W}{|j-N-i|}, & \text{for } j \in \left[i + \frac{N}{2}, N\right]. \end{cases} \quad (17)$$

Here,  $W_{ij}$  is a constant. In the case of  $N \geq i \geq \frac{N}{2}$ , we have

$$W_{ij} = \begin{cases} \frac{W}{|i-j|}, & \text{for } j \in \left[i - \frac{N}{2} + 1, N\right], \\ \frac{W}{|j+N-i|}, & \text{for } j \in \left[1, i - \frac{N}{2}\right]. \end{cases} \quad (18)$$

Including this weighting factor enables oscillators closer together in space to interact more strongly and synchronise more readily than their more greatly displaced counterparts. The inclusion of parameters defining the weighting of couplings is crucial in mitochondrial networks as mitochondria in close clusters oscillate with the same frequency [16] and in glycolytic networks as the degree of synchronisation has been shown to depend upon density [11].

#### 5.4.2. Non-autonicity

The implementation of a time dependence is also slightly different. Formerly, a term representing time-dependent randomness ( $\eta(t)$ ) was added to the end of phase dynamics equations (16). Here, however, deterministic frequency variation is used to implement non-autonicity.

For example, the natural frequency of the glycolytic oscillator is varied in time according to

$$\omega_{GOi}(t) = \omega_{GO} + A_{GO} \sin(\omega_{GOM}t + t_i). \quad (19)$$

Here,  $\omega_{GOi}(t)$  is the natural frequency of each oscillator, which varies over time about a mean frequency  $\omega_{GO}$ . The amplitude of this variation is  $A_{GO}$ ,  $\omega_{GOM}$  is the frequency of the perturbation while  $t_i$  takes a random value between zero and  $\frac{1}{\omega_{GOM}}$  seconds. Implementing time variation in this way ensures each oscillator has a distribution of frequencies while still maintaining the same mean frequency for oscillators of the same type ( $\omega_{GO}$  in this case). The same approach is taken to generate non-autonomous frequencies for the mitochondrial oscillator ( $\omega_{MOi}(t)$ ) and two supply oscillation frequencies ( $\omega_{Oi}(t)$  and  $\omega_{Gi}(t)$ ).

#### 5.4.3. Network configuration

Like the Lancaster et al. model, a supply of oxygen and glucose is necessary to sustain glycolytic and mitochondrial oscillations. A key difference, however, is the number of these processes. Multiple oscillators of each type are used here to more accurately replicate cellular network dynamics. The interactions between these oscillators and networks are given in Figure 9.

This picture is significantly more complicated than the former model, so several alterations to the phase dynamics equations were necessary. While before, only the natural frequency of the substrate supplies and coupling strengths were considered, other factors must be implemented when employing a network-based approach, one of which is the spatial distribution of the oscillators within the cell. As discussed, inter-network synchronisation between the metabolic oscillators will partially be influenced by a weighting function  $W_{ij}$  and they will

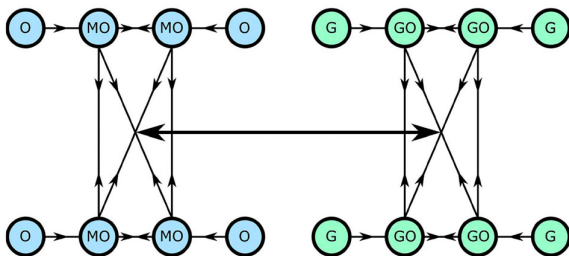


**Figure 9.** Visual representation of the network-based configuration behind the phase-based model. Arrows indicate the direction of the couplings while a network of size  $N = 4$  is represented. From [56], with permission.

influence each other such that

$$\begin{aligned} \dot{\varphi}_{GOi} &= \frac{K_{GO}}{N} \sum_{j=1}^N W_{ij} \sin(\varphi_{GOj} - \varphi_{GOi}), \\ \dot{\varphi}_{MOi} &= \frac{K_{MO}}{M} \sum_{j=1}^M W_{ij} \sin(\varphi_{MOj} - \varphi_{MOi}). \end{aligned} \quad (20)$$

Here,  $N$  and  $M$  are the numbers of glycolytic and mitochondrial oscillators, respectively, while  $K_X$  represents network coupling strength. Intra-network couplings are not the only influences present, as glycolytic oscillations can influence mitochondrial and vice versa. As such, the following inter-network equations must also be considered,

$$\begin{aligned} \dot{\varphi}_{GOMOi} &= F_{GORMO} \sin(\Psi_{MO} - \varphi_{GOi}), \\ \dot{\varphi}_{MOGOi} &= F_{MOrgo} \sin(\Psi_{GO} - \varphi_{MOi}), \end{aligned} \quad (21)$$

Here,  $F_X$  is the network coupling strength, and  $r_X$  is the Kuramoto order parameter described in Section 3. The networks are linked using the average phase  $\Psi_X$ . The final influence on the system is the driving force due to the supplies of oxygen and glucose

$$\begin{aligned} \dot{\varphi}_{GOGi} &= \epsilon_G \sin(\varphi_{GOi} - \varphi_{Gi}), \\ \dot{\varphi}_{MOOi} &= \epsilon_O \sin(\varphi_{MOi} - \varphi_{Oi}). \end{aligned} \quad (22)$$

Combining all of these influences gives the set of equations defining the phase of the oscillators

$$\begin{aligned} \dot{\varphi}_{Gi} &= \omega_{Gi}(t), \\ \dot{\varphi}_{Oi} &= \omega_{Oi}(t), \\ \dot{\varphi}_{GOi} &= \omega_{GOi}(t) + \dot{\varphi}_{GOi} - \dot{\varphi}_{GOGi} + \dot{\varphi}_{GOMOi}, \\ \dot{\varphi}_{MOi} &= \omega_{MOi}(t) + \dot{\varphi}_{MOi} - \dot{\varphi}_{MOOi} - \dot{\varphi}_{MOGOi}. \end{aligned} \quad (23)$$

As before, a negative sign represents an excitatory coupling, while a positive sign implies an inhibitory effect. Also, as in the Lancaster model, synchronisation states can be investigated to probe parameter combinations and investigate both healthy and altered states.

While the focus of this section has been on models based on phase dynamics, several other attempts to model cellular glycolysis have been made, including that of Amemiya et al. [5]. As previously outlined, a more classical approach focusing on conservation of mass has been taken here, in contrast to the Rowland Adams and Stefanovska model, which instead considers phase dynamics. The next significant difference is that the mass-based model utilises six autonomous, linear equations. In contrast, a fundamental aspect of the phase-based model [56] is that nonlinear systems are best understood by nonlinear methods and so only require the four nonlinear, non-autonomous equations (23).

The kinetic approach also requires 22 parameters to model only the glycolytic branch. In contrast, the nonlinear approach can represent both glycolysis and OXPHOS with only 21 parameters. This demonstrates a vital strength of the network oscillatory approach, the ability to cope with complexity, in this case by representing more processes using fewer differential equations and parameters.

#### 5.4.4. Comparing to experimental observations

Figure 10(D) uses a modified version of the Kuramoto order parameter outlined in Equation (14), which measures both glycolysis and OXPHOS networks, enabling a comparison between approaches

$$se^{i\Psi_{GOMO}} = \frac{1}{(N+M)} \left( \sum_{i=1}^N e^{i\theta_{GOi}} + \sum_{j=1}^M e^{i\theta_{MOj}} \right). \quad (24)$$

This order parameter,  $s$ , may be compared to the NADH fluorescence of Figure 10(c) as NADH production in the cell is maximised when glycolytic, and oxidative networks act coherently. This parameter may then be investigated to discover the dynamics of the system. The overall trend in NADH fluorescence is not initially replicated by Figure 10(d) as the focus of this approach is the phase,

rather than amplitude, dynamics. To enable comparison between modelling approaches, amplitude modulation was applied to this order parameter to obtain the time-series of Figure 10(b).

To replicate the experimental conditions, where injection of glucose followed a period of starvation, the parameter  $\epsilon_G$ , representing the amplitude of the glucose supply, was kept at zero for the first 50 s. Following this,  $\epsilon_G = 0.25e^{-\frac{t}{10000}}$ , with the exponential decay imitating glucose consumption and causing  $\epsilon_G$  to decrease over time. These parameters differ slightly from those used in [56] as the focus here is replicating the time-frequency domain rather than the amplitude dynamics. The mean frequency of the glycolytic oscillator and glucose supply used here is  $\omega_{GO} = 0.09\pi$  Hz while the mitochondrial frequency and oxygen supply had a frequency of  $0.2\pi$  Hz. The modulation frequencies are the inverse of each of these respective values. The code used to generate Figure 10(d) is publicly available in [59]. This model also uses non-autonomous frequencies to replicate the natural perturbations experienced by living systems, with the mean frequency values based upon experimental observation. Data from the experiment carried out by Amemiya et al. [23], as shown in Figure 10(a), enables the validity of this model to be assessed.

Figure 10(b, d, e), generated by the model introduced in [56], shares many general features with the

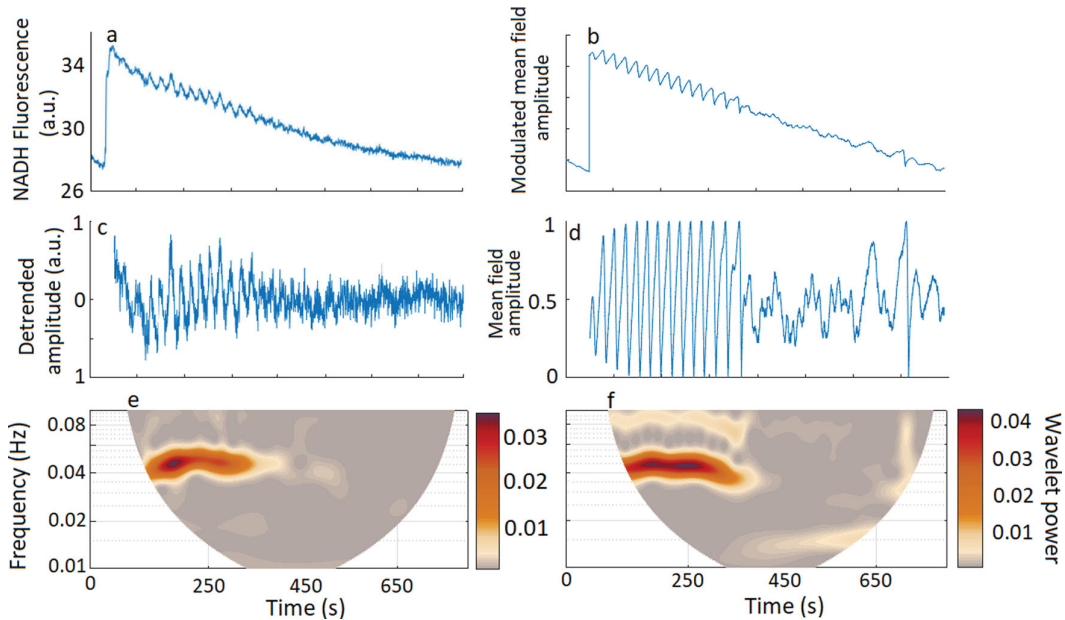


**Figure 10.** Comparison between experimentally derived data (a, c, e) and the phase dynamics model [56] (b, d, f). (a) NADH fluorescence in a single HeLa cell against time reproduced with permission from the Amemiya et al. experiment [23]. (b) Mean-field amplitude generated using the nonlinear approach, following amplitude modulation. (c) The detrended amplitude for experimental data. (d) The order parameter,  $s$  over time generated with the phase-based model [56]. (e) and (f) represent the experimental and model generated wavelet transforms, respectively.



experimental data. The initial glycolytic activity and subsequent cessation of oscillations are replicated in this simulation. It is worth noting, however, that this model is non-autonomous and so may differ slightly between simulations, in much the same way that the time-series of the experimental data differs slightly between cells, while the general trends remain the same. Figure 3(a) and Figure 10(a) illustrate these slight differences in the experimental data. As mentioned previously, the experimental data used to generate 3(a) and 10(a) are available at [33].

Comparing the wavelet transforms of both the experimentally derived and model-based data reveals some interesting similarities. As before, the frequency resolution parameter  $f_0 = 1$  and a lognorm wavelet was used to investigate frequencies between 0.01 and 0.1 Hz. The intrinsic non-autonicity of the nonlinear model used here is highlighted by the oscillatory frequency varying slightly over time, behaviour also seen in the experimental data. The peak of the power distribution in this model occurs around 0.04 Hz, again, in agreement with the experimental observations. The above similarities demonstrate that this method is capable of simulating *in vitro* experiments. The nonlinear approach can also replicate *in vivo* conditions. One may recreate sustained glycolytic behaviour by implementing the supply of glucose as pulsatile rather than decaying over time. Therefore, these GOs would continue in the same way as *in vivo* glycolytic oscillations. The nonlinear model uses fewer parameters and allows the system to be modelled as open and dissipative while also accurately reflecting the oscillating mitochondrial and glycolytic process over time.

## 6. Synchronisation in cellular populations

While the phase-based model uses a network-based configuration to model the many glycolytic sites and mitochondria within a cell, many other approaches have been developed that consider oscillations in cell populations. This section will mainly focus on the work describing glycolytic oscillations in populations of cells and the coupling that has been shown experimentally to emerge in these ensembles, giving rise to synchronisation [11]. Kinetic models that have been extended to describe macroscopic dynamics in collections of cells [12] will also be discussed.

In general, two main areas need to be focused upon when considering either the experimental evidence or attempting to model glycolytic oscillations within a population of cells. The first involves glycolysis in individual cells, while the second describes the concentration of a messenger molecule in the extracellular medium. This messenger, called acetaldehyde [60],

enables inter-cellular communication and, in turn, glycolytic oscillations to become synchronised. Similar to spatial differences between cells considered in [56] for a single cell, one must consider the distance between cells. Spatial distribution raises a series of questions regarding the density of cells required to cause synchronisation and the nature of these oscillations. The intrinsic time dependence of these systems is also highlighted with results from an investigation into the partial synchronisation of yeast.

### 6.1. Modelling cellular populations

A general form of the network-based approach to modelling oscillating populations of cells is given in a recent review by Hauser [12]. An outline of how to describe the kinetics of glycolysis in individual cells and a more extensive network configuration is given. On the level of a single cell,  $i$ , this is illustrated by

$$\frac{\partial \mathbf{x}_i}{\partial t} = F(\mathbf{x}_i, \mathbf{p}_i) - k(x_i - X), \quad (25)$$

where  $X$  is the concentration of acetaldehyde in the extracellular medium, while  $x_i$  describes the concentration in a given cell, and  $k$  is the exchange rate of acetaldehyde through the cell membrane. The vector  $\mathbf{x}_i$  describes the concentration of various substrates and products within the cell while  $\mathbf{p}_i$  represents the reaction rates. Using this approach may then provide a natural extension to the model introduced in [5]. This yields a bridge between single-cell mass-based models and cellular populations, enabling investigation into large ensembles of cells and their collective dynamics. The concentration of acetaldehyde in the extracellular medium,  $X$ , changes over time according to

$$\frac{\partial X}{\partial t} = N\alpha \left( \sum_i^N k(x_i - X) \right) - JX, \quad (26)$$

where  $\alpha$  is the ratio between cellular and extracellular volume,  $J$  is the rate constant of acetaldehyde decay/consumption and  $N$  is the number of cells. The total number of differential equations needed to model a population of cells oscillating in this way depends on the number of differential equations that describe the intracellular glycolytic reactions,  $q$ . The total number of equations required is given by  $qN + r$ , where  $r$  is the number of equations describing the extracellular compounds, like acetaldehyde. Modelling larger populations can, therefore, be computationally intensive due to this scaling.

While Equation (26) describes the available concentration of acetaldehyde in the extracellular medium, it

lacks a term describing the diffusion of this messenger. Therefore, this approach assumes homogeneity of the acetaldehyde in space. This model is only suitable to represent stirred solutions or dense populations of cells where the diffusion of acetaldehyde may be ignored.

To counter the above shortcomings, some models have been built upon the same principles while also incorporating terms representing the diffusion of acetaldehyde in the extracellular medium. Fick's law of diffusion is used to represent the movement of acetaldehyde in the work by Iyaniwura and Ward [61]. Here to describe a population of cells that are randomly distributed in space, equations analogous to Equation (26) are used alongside a partial differential equation that describes the diffusion of the messenger molecule. In this model, the bulk diffusivity is not taken to be infinite, as this can only be assumed in well-stirred solutions where the acetaldehyde concentration is constant. By assessing the bulk diffusivity as finite, this approach attempts to replicate the effect of spatial diffusion on the cells using a PDE-ODE model and remove the need for the previous assumption. However, this model does, in the same way as the general approach, assume that the concentration

of glycolytic metabolites is homogeneous across the cell and so only partially acknowledges spatial heterogeneity. Models of this type also neglect to include the time-dependent nature of the oscillation frequencies shown in multiple experiments [11, 23].

## 6.2. Partial synchronisation in groups of yeast cells

Analysing the state of a large number of cells simultaneously to observe changes can be difficult due to the large numbers of oscillating units. Observing synchronisation may enable this highly complex system comprising several different oscillations to be probed and crucial transition points to be monitored. A significant level of mutual interaction exists between cells in the body, so considering cells on a population level enables an investigation closer to the conditions *in vivo*. Recent work by Webber et al. displays how the frequency of the oscillations produced by these cellular populations changes over time [11]. Figure 11 illustrates this time dependence using an experiment where a collection of yeast cells were immobilised, and their synchronisation was measured via the autofluorescence of NADH. Simultaneously measuring

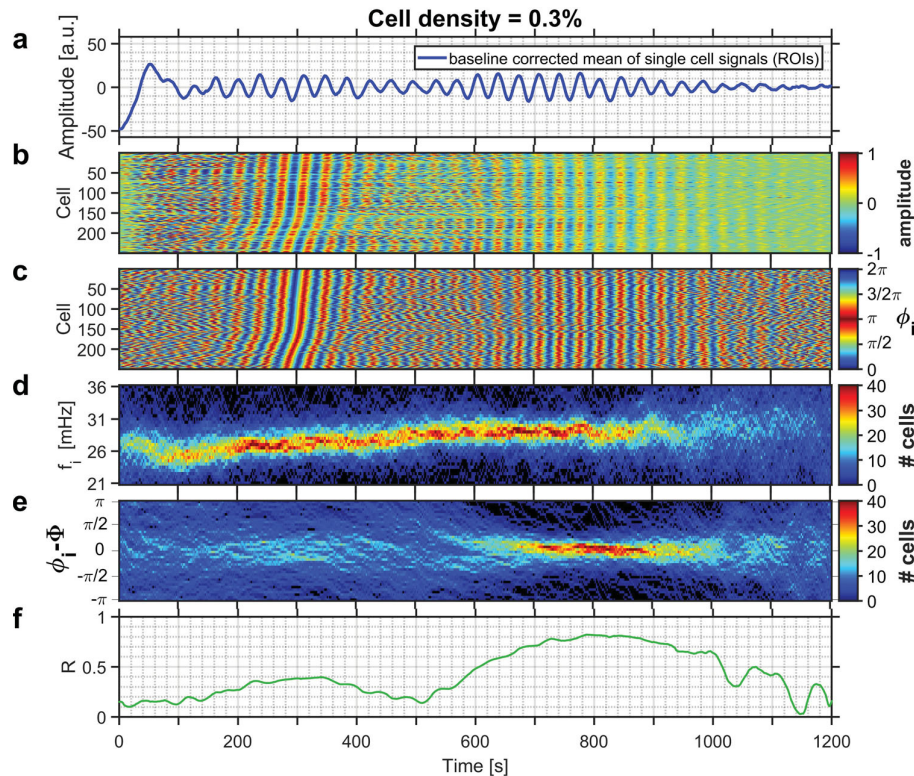


**Figure 11.** Synchronisation of several glycolytic oscillators in a cellular population. (a) Time-series of the mean amplitude of a number of cells at a density of 0.3%. (b) Relative amplitude of each cell as it evolved over time. (c) Evolution of each cell phase. (d) Number of cells at a given instantaneous frequency. (e) Cells at a given phase difference  $\phi_i - \Phi$  from the mean phase  $\Phi$ . (f) Kuramoto order parameter, as defined in Section 4, describes the presence and time dependence of synchronisation. Reprinted with permission from [11].

the time-series of fluorescence amplitude for each cell enabled continuous monitoring of their frequencies and phases. This allowed the time at which partial synchronisation was achieved to be recorded at different cellular densities.

This study is carried out at a cell density of 0.3% as, above this point, cells became utterly, rather than partially, synchronised. Partial synchronisation describes a state where some of the cells oscillate with a common phase difference while others do not and is dependent upon the density of the cells. In this study, the Kuramoto order parameter  $R$  was used to indicate synchronisation when it had a value between 0.4 and 0.85. The time dependence of the Kuramoto order parameter is represented in Figure 11(d). The time dependence of the frequencies in a majority of cells in the population is shown in Figure 11(f).

The experimental results presented in Figure 11 highlight the importance of considering time as a crucial variable in analysing and modelling such systems. A time-averaging approach would have neglected the collective macroscopic dynamics of the system. Time is especially significant when replicating cells *in vivo* as the system is significantly open, with matter and energy constantly being exchanged with the environment to provide a constant source of perturbation and intrinsic time dependence to the system's dynamics.

The temporal changes mean that the assumptions of homogeneity and nonautonicity in the model described in the previous section may ultimately be unrealistic. Considering the spatial distribution and time dependence of models as intrinsic and crucial aspects of the cellular dynamics that cannot be ignored may assist in bridging the gap between describing controlled *in vitro* experiments and real *in vivo* measurements.

## 7. Summary and outlook

In this review, non-autonomous and network-based models are highlighted that can replicate self-sustained glycolytic oscillations. These approaches were compared with experimental data and autonomous approaches to modelling the same system.

Synchronisation is a ubiquitous phenomenon in nature, and this purely nonlinear effect is a means by which organisms may induce stability between interactions. While synchronisation is commonplace in biology, it may only occur in simulated systems when the coupling strength and frequency mismatch meet specific criteria. When these parameters are suitable, however, various cellular states may be recreated.

We emphasised that while the linear models used so widely in the field can induce glycolytic oscillations, they cannot represent synchronisation in self-sustained oscillators. Non-autonomous, nonlinear models, on the other hand, are able to replicate the synchronisation states, which are a defining characteristic of metabolic interactions. The introduction of time-varying frequencies to the system may, somewhat counter-intuitively, increase the size of the stabilisation region. This stabilisation mechanism may prove to be a source of the inherent stability that helps biological systems maintain life in the face of an ever-changing environment.

Extending single oscillator models to include larger network ensembles may be a vital step in replicating cellular dynamics. As demonstrated by Rowland Adams and Stefanovska, models may be built upon the principles of nonlinear network dynamics and non-autonicity that replicate glycolytic oscillations. By modelling large-scale mitochondrial and glycolytic networks capable of inter and intra-network couplings, interactions between oscillators may be reproduced and subsequently investigated. This oscillatory approach has been shown to demonstrate the complexity of living systems using fewer parameters and differential equations than previous autonomous models. Selecting appropriate parameters based on experimental evidence to represent the oscillator's coupling strengths and natural frequencies enables time-dependent cellular dynamics to be probed. The logical next step of this analysis would be to consider inter-cellular communication in larger network populations as this may also have significant repercussions for pathogenesis.

Further expansion of current models to consider the oscillatory supplies of oxygen and glucose as nodes of another network may further expand modern approaches, and represent the fluctuating supply of oxygen and glucose across the cell membrane. Pathogenesis is a complex process comprising multiple simultaneous, interacting parts. However, applying appropriate parameters derived from experimental observation to model the cell in both healthy and altered states may help elucidate the transition from oxidative to glycolytic metabolism that often precedes disease. A number of neurological conditions have also been associated with altered metabolic states. A model of cellular energy metabolism capable of replicating *in vivo* dynamics could prove to be an important tool in understanding these conditions.

Living systems are complex, thermodynamically open, time-dependent and constantly undergoing perturbation. Embracing this inherent complexity rather than

treating it as unworkable and stochastic may reveal a new frontier in biomedical physics.

## Acknowledgments

The authors would like to thank Marcus J. B. Hauser for permission to reprint Figure 11. We are also grateful to Takashi Amemiya for sharing the experimental data used to generate Figure 10(a), Figure 3(a) and the data derived from their model used to generate Figure 3(b). The authors are particularly grateful to Joe Rowland Adams for many useful discussions.

## Disclosure statement

No potential conflict of interest was reported by the author(s).

## Funding

This work was funded by the EPSRC grant EP/T518037/1 Quantitative Assessment of Autistic Spectrum Disorder.

## Notes on contributors

**Sam Barnes** obtained his MPhys degree from Lancaster University in 2021 and he is currently pursuing research for a PhD in Biomedical Physics and Non-linear Dynamics at the same institution. His current research interests include the application of time-resolved methods to identify differences in the brains of individuals with autistic spectrum disorder. He is also working on models of cellular energy metabolism.

**Aneta Stefanovska** is Professor of Biomedical Physics at Lancaster University. Her longstanding interests in the physical principles of life brought her to the idea that interacting non-autonomous oscillators operating far from equilibrium are basic characteristics of life. She is especially interested in processes related to energy and information within the human body, and is focusing on cell energy metabolism, and cardiovascular and brain dynamics. With collaborators, she has created a set of novel algorithms that can time-resolve the behaviour of interacting systems acting on multiple time scales.

## References

- [1] Huygens C. *Horologium oscillatorium*. Parisiis: Apud E. Muguet; 1673.
- [2] Van der Pol B, Van der mark J. Lxxii. The heartbeat considered as a relaxation oscillation, and an electrical model of the heart. *Philos Mag*. 1928;6:763–775.
- [3] Duysens L, Ames J. Fluorescence spectrophotometry of reduced phosphopyridine nucleotide in intact cells in the near-ultraviolet and visible region. *Biochim Biophys Acta*. 1957;24:19–26.
- [4] Aldridge J, Pye EK. Cell density dependence of oscillatory metabolism. *Nature*. 1976;259(5545):670–671.
- [5] Amemiya T, Shibata K, Du Y, et al. Modeling studies of heterogeneities in glycolytic oscillations in HeLa cervical cancer cells. *Chaos*. 2019;29(3):033132.
- [6] Yang JH, Yang L, Qu Z, et al. Glycolytic oscillations in isolated rabbit ventricular myocytes. *J Biol Chem*. 2008;283(52):36321–36327.
- [7] Ganitkevich V, Mattea V, Benndorf K. Glycolytic oscillations in single ischemic cardiomyocytes at near anoxia. *J Gen Physiol*. 2010;135(4):307–319.
- [8] Susan WSL, Shi Y. The glycolytic process in endothelial cells and its implications. *Acta Pharmacol Sin*. 2021;43:251–259.
- [9] Danø S, Sørensen PG, Hynne F. Sustained oscillations in living cells. *Nature*. 1999;402(6759):320–322.
- [10] Gustavsson AK, van Niekerk DD, Adiels CB. Sustained glycolytic oscillations in individual isolated yeast cells. *FEBS J*. 2012;279(16):2837–2847.
- [11] Weber A, Zuschratter W, Hauser MJ. Partial synchronisation of glycolytic oscillations in yeast cell populations. *Sci Rep*. 2020;10(1):1–15.
- [12] Hauser MJ. Synchronisation of glycolytic activity in yeast cells. *Curr Genet*. 2022;68:69–81.
- [13] Chance B, Yoshioka T. Sustained oscillations of ionic constituents of mitochondria. *Arch Biochem Biophys*. 1966;117(2):451–465.
- [14] Aon MA, Cortassa S, O'Rourke B. Mitochondrial oscillations in physiology and pathophysiology. *Adv Exp Med Biol*. 2008;641:98–117.
- [15] Kurz FT, Derungs T, Aon MA, et al. Mitochondrial networks in cardiac myocytes reveal dynamic coupling behavior. *Biophys J*. 2015;108(8):1922–1933.
- [16] Kurz FT, Aon MA, O'Rourke B, et al. Spatio-temporal oscillations of individual mitochondria in cardiac myocytes reveal modulation of synchronized mitochondrial clusters. *Proc Natl Acad Sci USA*. 2010;107(32):14315–14320.
- [17] Kembro JM, Cortassa S, Lloyd D, et al. Mitochondrial chaotic dynamics: Redox-energetic behavior at the edge of stability. *Sci Rep*. 2018;8(1):1–11.
- [18] Codo AC, Davanzo GG, Monteiro LB. Elevated glucose levels favor SARS-CoV-2 infection and monocyte response through a HIF-1 $\alpha$ /glycolysis dependent axis. *Cell Metab*. 2020;32(3):437–446.
- [19] Kiviet DJ, Nghe P, Walker N. Stochasticity of metabolism and growth at the single-cell level. *Nature*. 2014;514(7522):376–379.
- [20] Törnroth-Horsefield S, Neutze R. Opening and closing the metabolite gate. *Proc Natl Acad Sci USA*. 2008;105(50):19565–19566.
- [21] Lancaster G, Suprunenko YF, Jenkins K, et al. Modelling chronotoxicity of cellular energy metabolism to facilitate the identification of altered metabolic states. *Sci Rep*. 2016;6:29584.
- [22] Shrestha B. *Single cell metabolism: methods and protocols*. New York (NY): Humana Press; 2020. (Methods in molecular biology; vol. 2064).
- [23] Amemiya T, Shibata K, Itoh Y. Primordial oscillations in life: direct observation of glycolytic oscillations in individual HeLa cervical cancer cells. *Chaos*. 2017;27(10):104602.
- [24] Chance B, Schoener B, Oshino R, et al. Oxidation-reduction ratio studies of mitochondria in freeze-trapped samples, NADH and flavoprotein fluorescence signals. *J Biol Chem*. 1979;254(11):4764–4771.
- [25] Cortassa S, Aon MA, Marbán E, et al. An integrated model of cardiac mitochondrial energy metabolism and calcium dynamics. *Biophys J*. 2003;84(4):2734–2755.



- [26] Bertram R, Pedersen MG, Luciani DS, et al. A simplified model for mitochondrial ATP production. *J Theor Biol.* **2006**;243(4):575–586.
- [27] Jacobsen EW, Cedersund G. Structural robustness of biochemical network models – with application to the oscillatory metabolism of activated neutrophils. *IET Syst Biol.* **2008**;2(1):39–47.
- [28] Kurz FT, Kembro JM, Flesia AG. Network dynamics: quantitative analysis of complex behavior in metabolism, organelles, and cells, from experiments to models and back. *Wiley Interdiscip Rev Syst Biol Med.* **2017**;9(1):e1352.
- [29] Gudas W. How glucose gets into cells. *Nutr Rev.* **1990**;48:357–358.
- [30] Marín-Hernández A, Gallardo-Pérez JC, Rodríguez-Enriquez S, et al. Modeling cancer glycolysis. *Biochim Biophys Acta Bioenerg.* **2011**;1807(6):755–767.
- [31] Wolf J, Heinrich R. Effect of cellular interaction on glycolytic oscillations in yeast: a theoretical investigation. *Biochem J.* **2000**;345(2):321–334.
- [32] Michaelis L, Menten ML. Die kinetik der invertinwirkung. *Biochem Z.* **1913**;49:333–369.
- [33] Amemiya T, Shibata K, Du Y. Glycolytic oscillations in cervical cancer hela cells; 2019 [cited 2021 Mar 11]. Available from: <https://www.research.lancs.ac.uk/portal/en/datasets/>.
- [34] Iatsenko D, Lancaster G, McCormack S. MODA (Multiscale Oscillatory Dynamics Analysis); 2019. DOI:10.5281/zenodo.3470856.
- [35] Newman J, Lancaster G, Stefanovska A. Multiscale Oscillatory Dynamics Analysis. v1.01. User Manual; 2018.
- [36] Clemson P, Lancaster G, Stefanovska A. Reconstructing time-dependent dynamics. *Proc IEEE.* **2016**;104(2):223–241.
- [37] Kloeden PE, Pötzsche C. Nonautonomous dynamical systems in the life sciences. In: Kloeden PE, Pötzsche C, editors. *Nonautonomous dynamical systems in the life sciences*. Cham: Springer; 2013. p. 3–39.
- [38] Ott E, Antonsen Jr TM. Frequency and phase synchronization in large groups: low dimensional description of synchronized clapping, firefly flashing, and cricket chirping. *Chaos.* **2017**;27(5):051101.
- [39] Shahal S, Wurzburg A, Sibony I, et al. Synchronization of complex human networks. *Nat Commun.* **2020**;11(1):1–10.
- [40] Stankovski T, McClintock PVE, Stefanovska A. Dynamical inference: where phase synchronization and generalized synchronization meet. *Phys Rev E.* **2014**;89(6):062909.
- [41] Pikovsky A, Kurths J, Rosenblum M. Synchronization: a universal concept in nonlinear sciences. Cambridge: Cambridge University Press; **2003**.
- [42] Goldbeter A. Dissipative structures in biological systems: bistability, oscillations, spatial patterns and waves. *Philos Trans R Soc A: Math Phys Eng Sci.* **2018**;376(2124):20170376.
- [43] Haken H. Synergetics: an introduction: nonequilibrium phase transitions and self-organization in physics, chemistry, and biology. Berlin: Springer; **1978**.
- [44] Suprunenko YF, Clemson PT, Stefanovska A. Chronotactic systems: A new class of self-sustained nonautonomous oscillators. *Phys Rev Lett.* **2013**;111:024101.
- [45] Kuramoto Y. Chemical oscillations, waves, and turbulence. Berlin: Springer; **1984**.
- [46] Lucas M, Newman J, Stefanovska A. Stabilization of dynamics of oscillatory systems by nonautonomous perturbation. *Phys Rev E.* **2018**;97:042209.
- [47] Strogatz S. Sync: the emerging science of spontaneous order. London: Penguin; **2004**.
- [48] Lucas M, Newman J, Stefanovska A. Synchronisation and non-autonicity. In: Stefanovska A, McClintock PVE, editors. *Physics of biological oscillators new insights into non-equilibrium and non-autonomous systems*. Cham: Springer; 2006. p. 85–111.
- [49] Newman J, Lucas M, Stefanovska A. Stabilization of cyclic processes by slowly varying forcing. *Chaos.* **2021**;31(12):123129.
- [50] Petkoski S, Iatsenko D, Basnarkov L, et al. Mean-field and mean-ensemble frequencies of a system of coupled oscillators. *Phys Rev E.* **2013**;87(3):032908.
- [51] Thaker SK, Ch'ng J, Christofk HR. Viral hijacking of cellular metabolism. *BMC Biol.* **2019**;17(1):59.
- [52] Passalacqua KD, Lu J, Goodfellow I. Glycolysis is an intrinsic factor for optimal replication of a norovirus. *mBio.* **2019**;10(2):e0052119 e00519 e0052119–19.
- [53] Satin LS, Butler PC, Ha J, et al. Pulsatile insulin secretion, impaired glucose tolerance and type 2 diabetes. *Mol Aspects Med.* **2015**;42:61–77.
- [54] Formenti F, Bommakanti N, Chen R, et al. Respiratory oscillations in alveolar oxygen tension measured in arterial blood. *Sci Rep.* **2017**;7(1):1–10.
- [55] Cole LW. The evolution of per-cell organelle number. *Front Cell Dev Biol.* **2016**;4:85–92.
- [56] Rowland Adams J, Stefanovska A. Modelling cell energy metabolism as weighted networks of nonautonomous oscillators. *Front Physiol.* **2021**;11:1845–1857.
- [57] Mirzapoiazova T, Li H, Nathan A, et al. Monitoring and determining mitochondrial network parameters in live lung cancer cells. *J Clin Med.* **2019**;8(10):1723.
- [58] Aon MA, Cortassa S, Marbán E, et al. Synchronized whole cell oscillations in mitochondrial metabolism triggered by a local release of reactive oxygen species in cardiac myocytes. *J Biol Chem.* **2003**;278(45):44735–44744.
- [59] Rowland Adams J, Stefanovska A. Metabolism weighted networks code – frontiers; 2021 [cited 2022 Mar 11]. Available from: <https://www.research.lancs.ac.uk/portal/en/datasets/>.
- [60] Weber A, Prokazov Y, Zuschratter W, et al. Desynchronisation of glycolytic oscillations in yeast cell populations. *PLoS ONE.* **2012**;7(9):e43276.
- [61] Iyaniwura SA, Ward MJ. Synchrony and oscillatory dynamics for a 2-D PDE-ODE model of diffusion-mediated communication between small signaling compartments. *SIAM J Appl Dyn Syst.* **2021**;20(1):438–499.

## Chapter 3

# Phase coherence - a time-localised approach to studying interactions

### **Student contribution:**

The student contributed to the conceptualisation of the study and curated portions of both the experimental and model-derived data. They performed formal analysis and investigation, comparing two analytical methods to evaluate their respective advantages and limitations. The student also wrote sections of the manuscript, edited the overall text, and generated most of the figures presented throughout the paper.

This research is published in *Chaos: An Interdisciplinary Journal of Nonlinear Science*.




Samuel JK Barnes, J Bjerkan, Philip T Clemson, Julian Newman, and Aneta Stefanovska. "Phase coherence—A time-localized approach to studying interactions".

In: *Chaos: An Interdisciplinary Journal of Nonlinear Science* 34.7 (2024)

RESEARCH ARTICLE | JULY 25 2024

# Phase coherence—A time-localized approach to studying interactions

Special Collection: [Data-Driven Models and Analysis of Complex Systems](#)


S. J. K. Barnes  ; J. Bjerkan  ; P. T. Clemson  ; J. Newman  ; A. Stefanovska  



*Chaos* 34, 073155 (2024)

<https://doi.org/10.1063/5.0202865>






## Chaos

Special Topic:  
Anomalous Diffusion and Fluctuations  
in Complex Systems and Networks

**Submit Today**

 AIP  
Publishing

# Phase coherence—A time-localized approach to studying interactions

Cite as: Chaos **34**, 073155 (2024); doi: 10.1063/5.0202865

Submitted: 7 February 2024 · Accepted: 13 June 2024 ·

Published Online: 25 July 2024



View Online



Export Citation



CrossMark

S. J. K. Barnes,<sup>1</sup> J. Bjerkan,<sup>1</sup> P. T. Clemson,<sup>1</sup> J. Newman,<sup>2</sup> and A. Stefanovska<sup>1,a)</sup>

## AFFILIATIONS

<sup>1</sup> Physics Department, Lancaster University, Lancaster LA1 4YB, United Kingdom

<sup>2</sup> Department of Mathematics and Statistics, University of Exeter, Exeter, United Kingdom

**Note:** This paper is part of the Focus Issue: Data-Driven Models and Analysis of Complex Systems.

<sup>a)</sup> Author to whom correspondence should be addressed: [aneta@lancaster.ac.uk](mailto:aneta@lancaster.ac.uk)

## ABSTRACT

Coherence measures the similarity of progression of phases between oscillations or waves. When applied to multi-scale, nonstationary dynamics with time-varying amplitudes and frequencies, high values of coherence provide a useful indication of interactions, which might otherwise go unnoticed. However, the choice of analyzing coherence based on phases and amplitudes (amplitude-weighted phase coherence) vs only phases (phase coherence) has long been seen as arbitrary. Here, we review the concept of coherence and focus on time-localized methods of analysis, considering both phase coherence and amplitude-weighted phase coherence. We discuss the importance of using time-localized analysis and illustrate the methods and their practicalities on both numerically modeled and real time-series. The results show that phase coherence is more robust than amplitude-weighted phase coherence to both noise perturbations and movement artifacts. The results also have wider implications for the analysis of real data and the interpretation of physical systems.

© 2024 Author(s). All article content, except where otherwise noted, is licensed under a Creative Commons Attribution-NonCommercial-NoDerivs 4.0 International (CC BY-NC-ND) license (<https://creativecommons.org/licenses/by-nc-nd/4.0/>). <https://doi.org/10.1063/5.0202865>

**Coherence is a universal principle of interactions between oscillations and waves. We explain how coherence has been introduced in physics and review procedures to measure coherence numerically. We expand the current knowledge by establishing the universal importance of measuring coherence not only as a static property but as a property evaluated locally in time. We also compare coherence defined to involve amplitude (the peak-to-peak height) vs purely the phase (the position in the cycle) by applying these different approaches to numerically modeled data. We argue that phase coherence is more robust and less susceptible to noise, particularly in cases where measurements are influenced by movement relative to the sensors. We provide an in-depth guide to the application of methods to measure coherence in data and demonstrate these points using real-world examples, including the interaction between the heart and lungs, noisy measurements of the brain, and the movement of electrons on the surface of liquid helium.**

## I. INTRODUCTION

Oscillations and waves are ubiquitous in nature. They occur in mechanical and dynamical systems in virtually all areas of science:

many physiological processes are oscillatory, such as the beating of the heart, breathing, or neuronal oscillations in the brain; the ecology abounds with seasonal cycles; most dynamical phenomena in astrophysics and space science are oscillatory, as are geological and hydrodynamics phenomena, such as ocean waves or earthquakes; there are business cycles in economy; strings in musical instruments produce vibrations, as do many man-made devices. Most electronic devices, the Internet, TV signals, communication systems, and medical imaging, use electromagnetic waves. The study of oscillations and waves is, therefore, essential for understanding the universe, as stated by Tesla in the quote: “If you want to find the hidden secrets of the universe, you must think in terms of energy, frequency, and vibration.”

While the underlying dynamical system may be very different in distinct cases, oscillatory processes share two key time-dependent features: *amplitude* (associated with the energy of the oscillation) and *phase* (associated with the time evolution of the oscillation). To identify interactions between different parts of a system, we can calculate the similarity of these features using the physical property known as *coherence*.

In this paper, we provide a review of coherence, beginning in its conceptualization in physics and subsequently evaluating

relevant numerical methods used to measure coherence. In particular, we improve current understanding by both establishing the fundamental importance of taking a time-localized approach to coherence and comparing a method based on amplitude and phase to one only using phase information.

In Sec. II, we provide an overview of the development of coherence in physics and its adoption in time-series analysis. We also provide a definition of coherence based on the Fourier transform and explain the differences between coherence and the related concept of synchronization.

In Sec. III, we provide a model for a dynamical system, which is used to numerically illustrate the differences between the phase-only and amplitude-weighted methods of measuring coherence when the system is perturbed by different forms of noise.

In Sec. IV, we introduce wavelet-based coherence and explain the consequences of moving to the time–frequency domain that arise from the uncertainty principle. In this section, we also specify the alternate definitions of coherence in amplitude and phase and, based on results found using the illustrative model, argue that phase coherence is more resistant to the effects of noise and particularly movement artifacts.

In Sec. V, we provide an in-depth guide to the application of coherence in time-series analysis, including how to identify significant coherence.

In Sec. VI, we apply this knowledge and evaluate the two methods considered by considering four real-world problems, including the cardio-respiratory interaction, noisy electroencephalography (EEG) and functional near infrared spectroscopy (fNIRS) data, and electron dynamics on the surface of liquid helium.

We conclude in Sec. VII with a discussion of the time-localized approach to coherence and the impact of using methods based on only phase to those that rely also on amplitude information.

## II. BACKGROUND

### A. Physics of coherence

The theory of waves was initially developed by Young, Huygens, and Fresnel.<sup>1</sup> Along with providing explanations for phenomena, such as diffraction and refraction, they also studied wave interference. In this latter case, multiple waves combine to produce a characteristic pattern of spatially and time-localized maxima and minima. However, this effect is only seen clearly when the change in the phase of the waves is the same. It is this property of the waves that we term coherence.

The study of interference and wave coherence has already led to many well-known discoveries. These include the Michelson–Morley experiment, which disproved the existence of the luminiferous ether.<sup>2</sup> Variations of Young's double-slit experiment have also played an important role in the understanding of wave–particle duality.<sup>3–5</sup> In addition, the drive to develop a coherent source of light led to the invention of the laser.<sup>6</sup> Subsequent to the development of lasers, larger-scale interference experiments have been possible, which resulted in the discovery of gravitational waves.<sup>7</sup> Coherence is now studied across a broad spectrum of domains. This includes solid state and quantum physics,<sup>8–11</sup> remote sensing,<sup>12</sup> electrophysiology,<sup>13–15</sup> communications,<sup>16</sup> and space science.<sup>17</sup>

### B. Coherence in time-series analysis

With the advent of computers, the study of coherence is no longer restricted to physical experiments. Numerical methods allow for the analysis of oscillations in recorded data. Using this recorded data, coherence can be investigated.<sup>18</sup> Coherence between different parts of a dynamical system can result from either synchronization or from modulation by a common process. While one can separately analyze two variables and qualitatively assess the common features present in each, interactions are often nonlinear in nature and, hence, difficult to discern. Coherence, therefore, provides a useful quantitative measure to identify these interactions.

An important aspect of coherence is that it is a time-localized phenomenon. This makes it particularly useful for analyzing dynamics comprised of oscillations with time-dependent quantitative characteristics. Such dynamics has been modeled using chaotic, stochastic, and non-autonomous systems.<sup>19,20</sup> Time-series analysis methods that give a non-time-dependent representation of a time-series, such as its histogram or Fourier transform, may yield some insight into the amplitudes of oscillations present. However, these methods will generally provide little understanding of phase dynamics if the quantitative characteristics of the oscillations, or of their interactions with each other, are being modulated over time. In contrast to this, the time evolution of phases carries a great wealth of information about the underlying system when such time modulation exists.<sup>21</sup>

Time-evolving time-localized analysis is typically performed in the time–frequency domain. This type of analysis was originally developed in quantum mechanics, with the distribution proposed by Wigner providing the highest possible frequency resolution that is mathematically possible within the limitations of the uncertainty principle.<sup>22</sup> Ville later applied this function in the context of time–frequency analysis more generally.<sup>23</sup> At the same time, the windowed Fourier transform was also developed,<sup>24</sup> and the field has since been advanced with the introduction of the continuous wavelet transform.<sup>25,26</sup> Time–frequency analysis has been applied most commonly to deal with simple forms of nonstationary data, with applications in communications, radar, sonar, and acoustics.<sup>27</sup> Recently, it has also been invaluable in the analysis problems, such as turbulence,<sup>28</sup> brain signals,<sup>29</sup> blood flow,<sup>30</sup> and excited electron oscillations on liquid helium.<sup>31</sup> These systems involve multiple potentially mutually interacting oscillatory processes that take place simultaneously across a range of timescales; we refer to such systems as *multi-scale* systems.

One specific advantage of the time–frequency methods is that they, to various degrees, allow for the time-localized extraction of instantaneous phases over time (see, e.g., Ref. 32). These phases can be studied further to give insight into the system. This can be seen in phase synchronization methods, which have been applied to the cardiorespiratory system.<sup>33</sup> Phase differences can also be observed and point to delays in coupled networks of oscillators, such as those seen in biology.<sup>34</sup> Beyond this, we can estimate coupling functions and infer the directionality of coupling (see Ref. 35 and the references therein). In the case of weakly coupled oscillator networks, connectivity can be inferred directly from the phases.<sup>36</sup> There are also phase stability methods, which have been used to find stable oscillations in the heart rate variability.<sup>37</sup>



In the case of coherence represented in the time–frequency domain, the initial development of the methods was motivated by applications to biomedical data. Specifically, it has been of great importance to the mapping of functional connectivity and study of synchronization in the brain.<sup>38–45</sup> At the same time, the development of time–frequency coherence has spearheaded investigations into microvasculature dynamics.<sup>46–51</sup> It has since been used in other biomedical studies and found use as a marker for ageing of the cardiorespiratory system,<sup>52</sup> as well as revealing the relation between the width of the subarachnoid space and blood pressure.<sup>53</sup> Moreover, the generality of time–frequency coherence means that it has found applicability elsewhere. In particular, these methods have also been used extensively in the analysis of solar, geophysical, and meteorological time-series to determine the Earth–Sun dynamical relationship.<sup>54–57</sup> Coherence has also found use in the analysis of economic time-series, where it has been used to identify instability and risk in specific markets as well as the relation between the monetary policy and the macroeconomic activity.<sup>58–62</sup> It has also been applied in the case of cyclo-nonstationarity, where it has been used to analyze mechanical systems, such as engines and wind turbines.<sup>63</sup> Further examples include the evaluation of electron dynamics,<sup>31</sup> behavioral rhythms in mice,<sup>64</sup> and social networks.<sup>65</sup>

### C. Definition of coherence

The original formulation of coherence was within the field of optics, where it is used to quantify the degree to which two sources of light can interfere. It was developed from a similar measure of the intensity of the interference pattern, or *visibility*,

$$v = \frac{I_{\max} - I_{\min}}{I_{\max} + I_{\min}}, \quad (1)$$

where  $I_{\max}$  is the intensity of the light at the peaks and  $I_{\min}$  is the intensity at the troughs. The value of  $v$  is 1 when the interference is maximized and 0 is the case of no interference (i.e., the intensity curve of the light is smooth). While this definition is useful from an empirical standpoint, it is more difficult to use for the mathematical analysis of waves of arbitrary phase and amplitude. Coherence was, therefore, developed as a similar measure of the degree of interference, but using the phase and amplitude of the interfering waves as parameters.<sup>66</sup>

It is worth noting that while interference was originally investigated in optics, the phenomenon prevails throughout all types of waves. As such, coherence can also be defined for any type of wave. A general analytic framework for the study of waves is provided by the Fourier transform. In this context, we can find a measure of the similarity between the waves in two data series by computing the Fourier cross spectrum,

$$S_{ab}(f) = F_a(f) \times \overline{F_b(f)}, \quad (2)$$

where  $F_a$  and  $F_b$  are the corresponding Fourier transforms of the two series and  $\overline{\phantom{x}}$  denotes the complex conjugate. However, this similarity measure is still proportional to the amplitude of the Fourier components. This means that if a dominant oscillation appears in one data series but only background fluctuations are present in the other, then the cross spectrum will still have a peak at the frequency of that oscillation as long as there is *some* amplitude at that frequency

in the other data series. With this in mind, it is clear that we need to normalize the cross spectrum so that it is not biased by this effect. The way this is achieved is by defining *Fourier coherence* as

$$C(f) = \frac{|(S_{ab}(f))|}{[\langle S_{aa}(f) \rangle \times \langle S_{bb}(f) \rangle]^{1/2}}, \quad (3)$$

where the angle brackets  $\langle \phantom{x} \rangle$  denote taking an average value of the Fourier spectra  $S_{ab}(f)$ ,  $S_{aa}(f)$ ,  $S_{bb}(f)$  computed for different time-segments of the time-series.<sup>66</sup> This defines coherence on a scale between 0 and 1, making it directly comparable with the interference visibility shown in (1).

### D. Coherence and synchronization

It is worth noting that coherence should not be confused with synchronization. In terms of dimensionality, synchronization is defined specifically in the time dimension and, therefore, applies to the dynamics of oscillations in time. In contrast, coherence refers to a more general phenomenon, which extends to waves that are defined across space as well as time.

There are also important differences in the context of time-series generated by dynamical systems. While many types of synchronization exist, they all result from an interaction between two or more oscillations.<sup>33,67</sup> As such, synchronization refers to a process of adjustment of rhythms caused by interactions. In contrast, coherence implies that two oscillations are observed to have the same frequency and frequency modulation, but this does not necessarily imply that they are coupled.

As examples, consider two linear oscillators with the same frequencies or two autonomous nonlinear oscillators with the same parameters and initial conditions. In both of these cases, the oscillations produced by the two systems will be coherent. However, since the state of one oscillator does not depend on the state of the other, they are not coupled.

Despite this difference, there is still a strong connection between coherence and specific types of synchronization. The states of complete 1:1 synchronization or 1:1 phase synchronization are more or less the same as coherence as the strength of the interaction reduces to a small value when two oscillators are completely synchronized. One can also consider indirect synchronization, such as two non-autonomous oscillators becoming synchronized via the same time-dependent modulation. In each of these cases, the effect can be measured directly using coherence.<sup>39</sup>

## III. ILLUSTRATIVE MODEL

### A. Poincaré oscillators

In order to illustrate the factors affecting the measurement of coherence, we consider a pair of time-series, which contain common oscillations generated by non-autonomous systems with independent perturbations. To ensure that we are not biased toward perturbations in amplitude or phase, we consider a system with a separable amplitude and phase dynamics.

The Poincaré oscillator is a two-dimensional limit cycle oscillator, which can be defined in polar coordinates as

$$\frac{dr}{dt} = -\alpha r(r - a), \quad \frac{d\theta}{dt} = \omega, \quad (4)$$

where  $r$  is the amplitude and  $\theta$  is the phase of the oscillator. A stable limit cycle is defined in state space with radius  $r = a$ , with  $\alpha$  parameterizing the rate at which the trajectory converges to this amplitude. The phase is neutrally stable and changes with a rate defined by the frequency  $\omega$ . A time-series  $x(t)$  of the oscillation can be generated by transforming from polar coordinates by using  $x(t) = r(t) \cos(\theta(t))$ .

The important feature of this system is that  $r$  and  $\theta$  vary independently. This means that the amplitude of the oscillator can be perturbed without affecting the phase and vice versa. However, comparing the effect of amplitude and phase perturbations this way using the current system would not be a fair comparison since  $r$  has a stable point attractor while  $\theta$  does not. This leads to the perturbations to  $r$  being suppressed over time, while perturbations to  $\theta$  are integrated over time.<sup>37</sup>

To resolve this issue, we modify the Poincaré oscillator so that the form of stability is the same in both amplitude and phase. Unfortunately, we cannot simply copy the function used for  $\frac{dr}{dt}$  to  $\frac{d\theta}{dt}$  since  $\theta$  will converge to  $a$ . For persistent oscillations,  $\theta$  needs to change on average monotonically, which is provided by the parameter  $\omega$  in the current form. However, we cannot use  $\frac{d\theta}{dt} = \omega - \alpha\theta(\theta - a)$  either as  $\theta$  is unbounded and  $\lim_{t \rightarrow \infty} [\omega - \alpha\theta(\theta - a)] = -\alpha\theta^2$ , which results in an unstable trajectory. Instead, we use the following modification:

$$\begin{aligned} \frac{dr}{dt} &= -\alpha(r - a)^3 + \xi_r \eta_r, \\ \frac{d\theta}{dt} &= \omega - \alpha(\theta - \phi)^3 + \xi_\theta \eta_\theta, \\ \frac{d\phi}{dt} &= \omega, \end{aligned} \quad (5)$$

where  $\phi$  is an auxiliary dimension, which is left unperturbed and provides a stable point in phase moving at the same rate  $\omega$ . The cubic function was chosen because it gives similar scaling of the strength of attraction to the stable point relative to the distance, but is symmetric around the stable point. The terms  $\xi_i \eta_i$  are white Gaussian noise with a standard deviation specified by  $\xi_i$ .

To generate each time-series, the amplitudes  $\{r_1, r_2\}$  and phases  $\{\theta_1, \theta_2\}$  of two modified Poincaré oscillators were numerically modeled and summed together in a time-series  $X(t) = r_1(t) \cos(\theta_1(t)) + r_2(t) \cos(\theta_2(t))$ . However, even with perturbations, this time-series would appear as two noisy sinusoids with approximately stationary dynamics. To simulate more realistic nonstationary time-series, the system was made non-autonomous by modulating the oscillator frequencies with  $\omega(t) = 2\pi\omega_0 + A \sin(2\pi\omega_m t)$ . To investigate the effect of phase differences, the phase offset of the oscillations was also adjusted by changing the initial value of  $\phi$ .

In the numerically modeled examples used in Sec. IV, we considered a high-frequency mode with  $\omega_0 = 1$ ,  $\omega_m = 0.008$ ,  $A = 0.8$  and a low-frequency mode with  $\omega_0 = 0.5$ ,  $\omega_m = 0.0055$ ,  $A = 0.2$ . For the other oscillator parameters, we used  $a = 1$  and  $\alpha = 5$  in each case.

## B. Noise

Noise plays a significant role in the evaluation of coherence. Consider two time-series with a single, identical sinusoidal oscillation with frequency  $f_{\text{sin}}$ . By analyzing Eq. (3), we can see that  $S_{ab}(f_{\text{sin}}) \equiv S_{aa}(f_{\text{sin}})$  and  $S_{aa}(f_{\text{sin}}) \equiv S_{bb}(f_{\text{sin}})$ , which results in the expected value  $C(f_{\text{sin}}) = 1$ . However, since the time-series contain no other oscillations, this relation holds true not just for  $f_{\text{sin}}$  but for *all* values of  $f$ . This means that we might mistakenly believe that coherent oscillations exist at all frequencies.

Similar behavior is apparent whenever dominant oscillations are present in both time-series. Without independent fluctuations at adjacent frequencies, significant coherence will be observed at values far from the frequencies of the corresponding oscillations.

In most real data, this is not an issue as they are usually influenced by both system noise and measurement noise. We must, therefore, take care to approximate real-world examples in our analysis by including noise in the numerical model.

To investigate the effect of both amplitude and phase perturbations, two cases were considered. In the first case, each of the modes was perturbed only by amplitude noise with  $\xi_r = 0.5$ ,  $\xi_\theta = 0$ , while in the second case, they were perturbed only by phase noise with  $\xi_r = 0$ ,  $\xi_\theta = 0.5$ . We also considered a case with additive noise to simulate measurement noise and common artifacts in the time-series. These were generated by adding the same dichotomous noise, with random abrupt transitions between two states, to both time-series. This was defined using the time-dependent transition probabilities,

$$\begin{aligned} p_{0 \rightarrow d}(t) &= \frac{\lambda_1}{\Lambda} - \frac{\lambda_1}{\Lambda} e^{-\Lambda t}, \\ p_{d \rightarrow 0}(t) &= \frac{\lambda_2}{\Lambda} - \frac{\lambda_2}{\Lambda} e^{-\Lambda t}, \end{aligned} \quad (6)$$

where  $t$  is the time since the last transition from one state to another and  $\Lambda = \lambda_1 + \lambda_2$ . The transition rates were chosen as  $\lambda_1 = 0.00001$  Hz and  $\lambda_2 = 0.00019$  Hz, causing a series of spike-like features with rare  $0 \rightarrow d$  transitions followed by quicker  $d \rightarrow 0$  transitions. The amplitude of the spikes was chosen as  $d = 10$ . In addition to these spikes, independent  $1/f$  noise series were added to each time-series to simulate background fluctuations.

## IV. WAVELET COHERENCE

### A. Time-frequency analysis

For the analysis of coherence of phases of oscillations in time-series, the Fourier-based definition of coherence is perfectly valid when the time-series are stationary. However, for multi-scale, non-stationary time-series, the dynamics cannot be approximated by assuming a constant time-averaged phase and amplitude, as is assumed in the Fourier transform. As discussed in Rowland Adams *et al.*,<sup>21</sup> such time-series must not be analyzed from the infinite-time, non-time-evolving framework of analysis that is designed for stationary time-series—which is precisely the framework within which Fourier coherence exists—but rather, such time-series need to be analyzed from within the framework of time-evolving time-localized analysis of oscillatory characteristics.

Accordingly, it is natural to seek a way to compute coherence from time–frequency representations of the data. As already mentioned, we can compute a time–frequency representation using an ordinary Fourier transform with a moving window, which is also known as a short-time Fourier transform. However, as soon as we do this, we must ask what size of window? A large window gives us excellent frequency resolution, but then it is more difficult to determine the time at which oscillation frequencies change. Similarly, while a small window enables us to track the change in frequency more precisely, the frequency resolution is lower and makes it difficult to determine the exact frequencies of oscillations. These characteristics of the measurement of waves are well known in quantum mechanics and famously summarized in the Heisenberg uncertainty principle.

The main limiting factor in the choice of window size is the lowest-frequency oscillation that we wish to observe. It is necessary to choose a window that contains enough cycles of this oscillation to determine its frequency to reasonable precision. However, this window size is larger than the window needed to have the same frequency resolution for higher-frequency oscillations. For higher-frequency oscillations, this window size will represent a slower timescale than the timescale of these oscillations, making the analysis effectively equivalent to the kind of long-time-averaging associated with the classical non-time-evolving, long-time-asymptotic-statistics framework designed for stationary time-series described above.

Therefore, to achieve a time-localized analysis of multi-scale time-series, we would need to use an adaptive window size to increase the time resolution at high frequencies while maintaining an optimal frequency resolution overall.

The difference between this time-localized approach and the slow-timescale averaging that takes place in the fixed-window-size approach is illustrated in Fig. 1. Here, time–frequency analysis is performed on a time-series from the illustrative Poincaré oscillator model. In this case, the oscillators were not perturbed with phase noise, and only minimal amplitude noise,  $\xi_r = 0.005$ , was introduced. In addition, background fluctuations were numerically modeled by adding independent  $1/f$  noise to each time-series. In Fig. 1(a), depicting the fixed-window approach, the idea is to characterize all aspects of the dynamics at a given time using the data in a given window. This means that all of the analysis for every frequency is performed within the same window (note that this window is shown as rectangular for illustrative purposes only—a Gaussian window was used in the short-time Fourier transform to enable a fairer comparison of the two approaches).

By contrast, as depicted in Fig. 1(b), the time-localized approach uses a variable-sized window depending on which frequency is being analyzed. For the former approach, where at each time a full-frequency-spectrum Fourier transform is performed inside a pre-specified window, the result is that the time–frequency analysis can be optimized around one frequency only. However, in the time-localized approach, the analysis is centered around each frequency under analysis, much like adjusting an optical focus. This means that the time–frequency plots for this latter approach provide much greater detail across time at high frequencies, as well as much greater detail across frequency at low frequencies. An alternative version, with a Fourier transform presented with a logarithmic

scale, is provided in Fig. 1 of the [supplementary material](#). When comparing the two figures, it is obvious that a logarithmic scale is disadvantageous for the Fourier transform, which is calculated with linear frequency resolution.

The time-localized, adaptive window approach is realized by the *continuous wavelet transform*<sup>26</sup> (which we shall sometimes just call the wavelet transform, abbreviated WT). This is defined by

$$W(s, t) = \frac{1}{s} \int_0^T \overline{\Psi\left(\frac{u-t}{s}\right)} x(u) du, \quad (7)$$

where  $x(t)$  is a time-series of length  $T$ ; the variable  $s > 0$ , called the “scale,” controls the width of the windowing function, enabling it to be adapted to the frequency under investigation (as described shortly); and  $\Psi$  is a complex-valued function called the *mother wavelet*. Using the convolution theorem (or, equivalently, Fourier isometry), the wavelet transform can be computed in the Fourier domain by

$$W(s, t) = \frac{1}{2\pi} \int_{-\infty}^{\infty} \overline{\hat{\Psi}(s\omega)} \hat{x}(\omega) e^{i\omega t} d\omega,$$

where

$$\begin{aligned} \hat{\Psi}(\omega) &= \int_{-\infty}^{\infty} \Psi(\tau) e^{-i\omega\tau} d\tau, \\ \hat{x}(\omega) &= \int_0^T x(t) e^{-i\omega t} dt. \end{aligned}$$

An example of a mother wavelet is the Morlet wavelet, which is approximately a complex exponential function multiplied by a Gaussian envelope, such that the resulting wavelet transform is approximately the adaptive-window-width version of the Gaussian-windowed Fourier transform. Specifically, the Morlet wavelet is given by

$$\Psi(\tau) = \frac{1}{\sqrt{2\pi}} \left( e^{2\pi i f_0 \tau} - e^{-\frac{(2\pi f_0)^2}{2}} \right) e^{-\frac{\tau^2}{2}}, \quad (8)$$

where  $f_0$  is a free parameter called the *frequency resolution*: it can be changed to adjust the resolution toward greater frequency precision (higher  $f_0$ ) or time precision (lower  $f_0$ ). The Fourier-domain representation of the Morlet wavelet  $\Psi$  is given by

$$\hat{\Psi}(\omega) = e^{-\frac{(\omega - 2\pi f_0)^2}{2}} (1 - e^{-2\pi f_0 \omega}).$$

Note that  $\hat{\Psi}$  is a real-valued function; i.e., the Morlet wavelet  $\Psi$  is a Hermitian function.

In the wavelet transform, one can adapt the scale  $s$  to the frequency  $f$  under investigation in such a manner as to give logarithmic frequency resolution by taking  $s$  to be inversely proportional to  $f$ . Specifically, when working with the Morlet wavelet, we take

$$s = \frac{\omega_{\max}}{2\pi f},$$

where  $\omega_{\max}$  is the value at which the real-valued function  $\hat{\Psi}$  is maximized. Provided  $f_0$  is not too small (larger than about 0.5),  $\omega_{\max}$  is almost exactly equal to  $2\pi f_0$ , i.e.,  $s \approx \frac{f_0}{f}$ .



It is worth noting an issue that arises from the fact that the integral in Eq. (7) is bounded between 0 and  $T$ . This means that when  $t$  is close to one end of  $x(t)$ , a significant part of the amplitude of the wavelet function extends beyond the bounds of the integral. This bounded integral is also equivalent to an unbounded integral where the ends of  $x(t)$  are padded with infinite zeros. This problem is common among methods using a moving window and other strategies include using reflected data or predicted data equal to half the length of the window. However, each of these methods causes boundary effects that result in errors in the time–frequency representation.<sup>68</sup> The other alternative is to not include these regions in the plot. This results in a *cone of influence*, which is larger in size at lower

frequencies due to the larger-sized wavelets reaching the ends sooner than smaller wavelets.

From the wavelet transform, one can extract an instantaneous amplitude and phase associated to each frequency  $f$  at each time  $t$  by expressing  $W(s, t) = |W(s, t)|e^{i\theta(s, t)}$  and taking  $|W(s, t)|$  as the amplitude and  $\theta(s, t)$  as the phase.

## B. Definition of wavelet coherence

With an optimal time–frequency representation of the time-series, we can proceed to define the coherence between them. Following from the original definition in Eq. (3), time–frequency

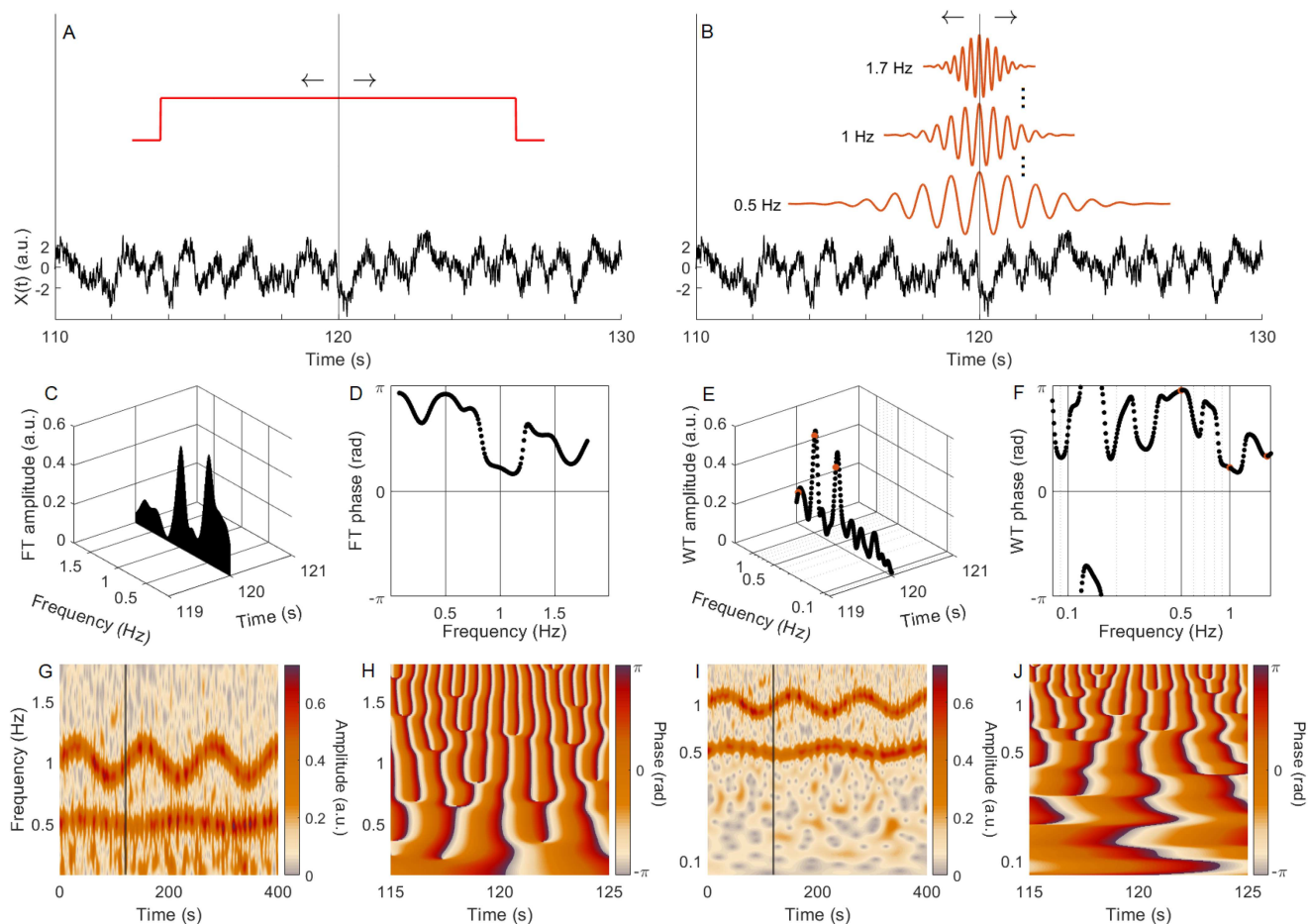


**FIG. 1.** Time–frequency analysis illustrated for time-localized vs fixed-window approaches. (a) Generated time-series of Poincaré oscillators as defined by Eq. (5), with additive  $1/f$  noise and  $\xi_r = 0.005$ . A window of size 12.6s centered at 120s is drawn above the time-series. The arrows above the window illustrate that the window slides across the time-series when the short-time Fourier transform (STFT) is applied. (b) The same time-series as in (a), with three wavelets with frequency resolution  $f_0 = 2$  at different frequencies (0.5, 1, and 1.7 Hz) drawn above the time-series. The wavelets slide across the time-series when the WT is applied. The dots between the wavelets illustrate that there is one wavelet for each frequency, in our case 288 wavelets. (c) The STFT amplitude found at 120s. (d) The STFT phase found at 120s projected onto the frequency–phase plane. (e) The WT amplitude found at 120s. The orange dots correspond to the frequencies of the three wavelets in (b). Note the logarithmic frequency resolution of the WT. (f) The WT phase found at 120s projected onto the frequency–phase plane. (g) The STFT amplitude for the whole 400s time-series. A line is drawn at 120s. (h) The STFT phase for 10s of the time-series. (i) The WT amplitude for the whole 400s time-series. (j) The WT phase for 10s of the time-series.

domain coherence between two time-series  $x(t)$  and  $y(t)$  was originally popularized by Torrence and Webster<sup>69</sup> and then again by Lachaux *et al.*<sup>38</sup> where it was defined as

$$C_W(f, t) = \frac{|SW_{ab}(f, t)|}{[SW_{aa}(f, t) \cdot SW_{bb}(f, t)]^{1/2}}, \quad (9)$$

where  $SW_{ab}$  are the wavelet cross spectra as defined by

$$SW_{ab}(f, t) = \int_{t-\frac{\delta}{2}}^{t+\frac{\delta}{2}} W_a(f, \tau) \cdot W_b^*(f, \tau) d\tau. \quad (10)$$

Here and in the rest of the text  $*$  denotes complex conjugate.  $\delta$  defines the length of a moving window in the time domain over which the cross spectra are averaged. Like wavelets,  $\delta$  is chosen to be adaptive in order to maintain an optimal resolution over frequency such that  $\delta = n_{cy}/f$ , where  $n_{cy}$  is the number of cycles at any given frequency. Values between 6 and 10 for  $n_{cy}$  were originally recommended in the context of data recorded by brain electrodes.<sup>38</sup> However, in other applications of time–frequency analysis,  $n_{cy} = 5$  has been used.<sup>70</sup>

The application of a wavelet-based approach vs a Fourier-based approach has a significant effect on the information provided by coherence analysis. This can be seen by comparing the studies of Karavaev *et al.*<sup>71</sup> and Mizeva *et al.*,<sup>72</sup> both of which consider cardiovascular time-series recorded over similar timescales (15 and 20 min, respectively). In the former study, the macroscopic autonomic control is characterized by dividing the Fourier coherence into a “high-frequency” (0.15–0.4 Hz) and “low-frequency” (0.05–0.15 Hz) band. In the latter study, the wavelet coherence is divided into five separate frequency bands with ranges 0.6–2, 0.145–0.6, 0.052–0.145, 0.021–0.052, and 0.0095–0.021 Hz, which allows for the characterization of both the macroscopic and microscopic dynamics. The logarithmic scale provided by the wavelet coherence, therefore, acts much like a telescope or microscope, allowing us to zoom in and out of all frequencies of interest at every moment in time.

### C. Phase coherence

If we use a complex wavelet, such as the Morlet wavelet defined in Eq. (8), then the cross spectrum in the numerator of Eq. (9) can be separated into phase and amplitude, with

$$SW_{ab}(f, t) = \int_{t-\frac{\delta}{2}}^{t+\frac{\delta}{2}} |W_a(f, \tau)| \cdot |W_b(f, \tau)| e^{i(\theta_a(f, \tau) - \theta_b(f, \tau))} d\tau. \quad (11)$$

Doing the same for the denominator terms, we find

$$\begin{aligned} SW_{aa}(f, t) &= \int_{t-\frac{\delta}{2}}^{t+\frac{\delta}{2}} |W_a(f, \tau)| \cdot |W_a(f, \tau)| e^{i(\theta_a(f, \tau) - \theta_a(f, \tau))} d\tau \\ &= \int_{t-\frac{\delta}{2}}^{t+\frac{\delta}{2}} |W_a(f, \tau)|^2 d\tau. \end{aligned} \quad (12)$$

Written this way, the coherence defined in Eq. (9) is expressed as a phasor of the phase difference,  $e^{i(\theta_a(f, \tau) - \theta_b(f, \tau))}$ , multiplied by the normalized amplitudes. We, therefore, term this definition as amplitude-weighted phase coherence (AWPC).

However, we can actually remove the influence of the wavelet amplitude altogether. We can define *phase coherence* (PC) as

$$C_\theta(f, t) = \frac{1}{\delta} \left| \int_{t-\frac{\delta}{2}}^{t+\frac{\delta}{2}} e^{i(\theta_a(f, \tau) - \theta_b(f, \tau))} d\tau \right|. \quad (13)$$

This definition of coherence was developed independently by Lachaux *et al.*<sup>38</sup> (where it was termed single-trial phase coherence) and Bandrivskyy *et al.*<sup>46</sup> While Eq. (13) defines PC for a pair of time-series, it has since been extended to groups of three or more time-series.<sup>73,74</sup>

Like Fourier coherence, both PC and AWPC take values between 0 and 1. Note, however, that for oscillations with time-dependent characteristics, strong coherence will not typically manifest as a coherence value of 1, but often as distinctly less than 1.

In the examples shown in this paper, PC was calculated using MODA—an interactive MATLAB toolbox.<sup>75</sup> We also encourage readers to consult the MODA user guide, which contains practical information for performing PC and other time–frequency analyses.<sup>76</sup>

The differences between PC and AWPC are shown in Figs. 2–4 using the previously defined illustrative Poincaré model. In each case, the two time-series, their corresponding WT, and the PC and AWPC plots are shown. The methods were applied using three different time–frequency resolutions by changing the central frequency  $f_0$  of the Morlet wavelet. The effect of adjusting  $f_0$  can be seen in the WT, where the frequency width of the bands corresponding to the oscillatory modes is decreased with increasing  $f_0$ . This effect is also seen for the coherence plots. Here, the darker bands of coherence reveal the common frequency modulation of the two modes, which becomes more localized in frequency as  $f_0$  is increased.

An additional effect seen when increasing the frequency resolution is that the background coherence between the modes also increases. The reason for this effect is due to the fact that larger wavelets average over more cycles, leading to extracted wavelet components that are more stationary in frequency. These components, therefore, appear coherent, but only because the rate of change in frequency converges to the same value (i.e., 0) for all oscillations as  $f_0$  is increased.

Figure 2 shows the effect of amplitude perturbations on the modes following the two coherence measures. The coherence bands associated with the modes are lighter and less well-defined in the case of AWPC, with the effect being greatest for the lowest frequency resolution. The explanation for this can be found in the independent fluctuations seen in the amplitude of the WT. As highlighted in Eq. (11), AWPC is dependent on the wavelet amplitude, which means that the amplitude perturbations result in lower coherence. In contrast, PC is not dependent on the wavelet amplitude and is, therefore, resistant to such perturbations.

As one might expect, the effect is similar for both approaches when the perturbations are instead applied to the phase of oscillations. Figure 3 illustrates the effect of phase perturbations, where PC and AWPC are affected similarly by the noise due to both methods being dependent on the phase of the wavelet components.

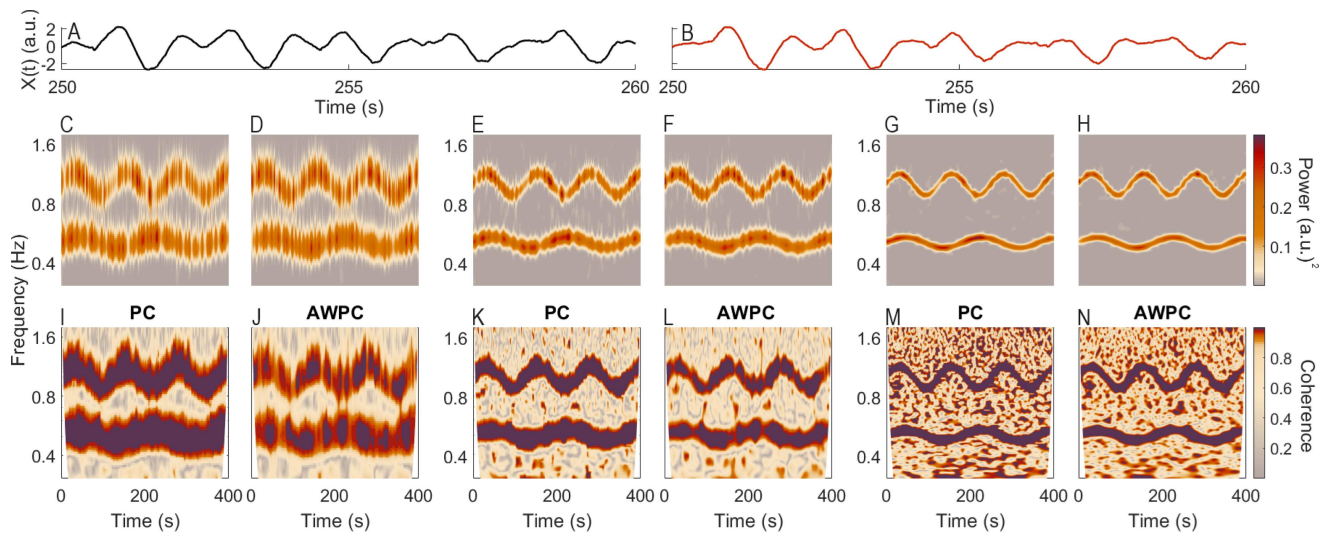


**FIG. 2.** Comparison between PC and AWPC applied using wavelets of different frequency resolution to modes generated by amplitude-perturbed Poincaré oscillators as defined by Eq. (5). (a) and (b) Ten-second segments of the two time-series containing modes with independent perturbations. The second row (c)–(h) presents the WT plots of the two time-series at different frequency resolutions:  $f_0 = 1$  (c) and (d),  $f_0 = 2$  (e) and (f), and  $f_0 = 5$  (g) and (h). The time-series in (a) was the input for the transforms (c), (e), and (g), while (b) provided the input for (d), (f), and (h). The final row (i)–(n) indicates the time-localized coherence for the PC and AWPC methods using the transforms shown in (c)–(h). For example, (i) and (j) were both generated using the WT plots indicated by (c) and (d).

A significant difference between PC and AWPC can be seen in the additive noise case shown in Fig. 4. Here, the common dichotomous noise results in time-localized spikes in the time domain. These can be seen as large cones of amplitude permeating into the

lower frequencies in the WT. In the coherence plots, this effect has the most significant impact on the low frequencies, as larger wavelets have a lower time resolution and span across a greater period. Furthermore, it can be seen that the case for  $f_0 = 5$  is most

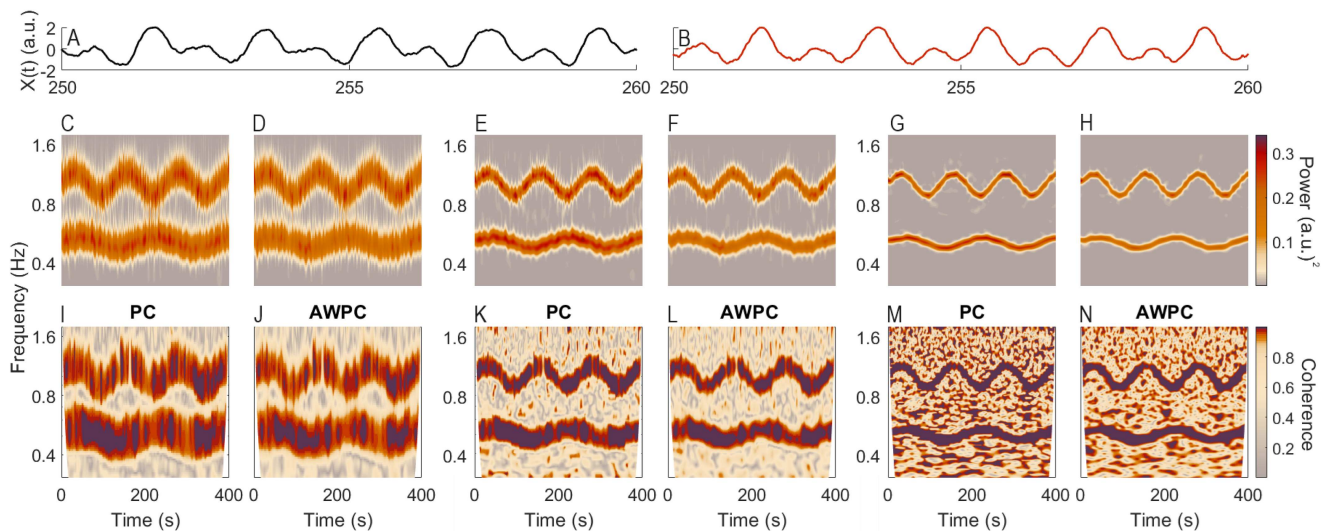


**FIG. 3.** Comparison between PC and AWPC applied using wavelets of different frequency resolution to modes generated by phase-perturbed Poincaré oscillators as defined by Eq. (5). (a) and (b) Ten-second segments of the two time-series containing modes with independent perturbations. The second row (c)–(h) presents the WT plots of the two time-series at different frequency resolutions:  $f_0 = 1$  (c) and (d),  $f_0 = 2$  (e) and (f), and  $f_0 = 5$  (g) and (h). The time-series in A was the input for the transforms (c), (e) and (g), while (b) provided the input for (d), (f) and (h). The final row (i)–(n) indicates the time-localized coherence for the PC and AWPC approaches using the transforms shown in (c)–(h). For example, (i) and (j) were both generated using the WT plots indicated by (c) and (d).



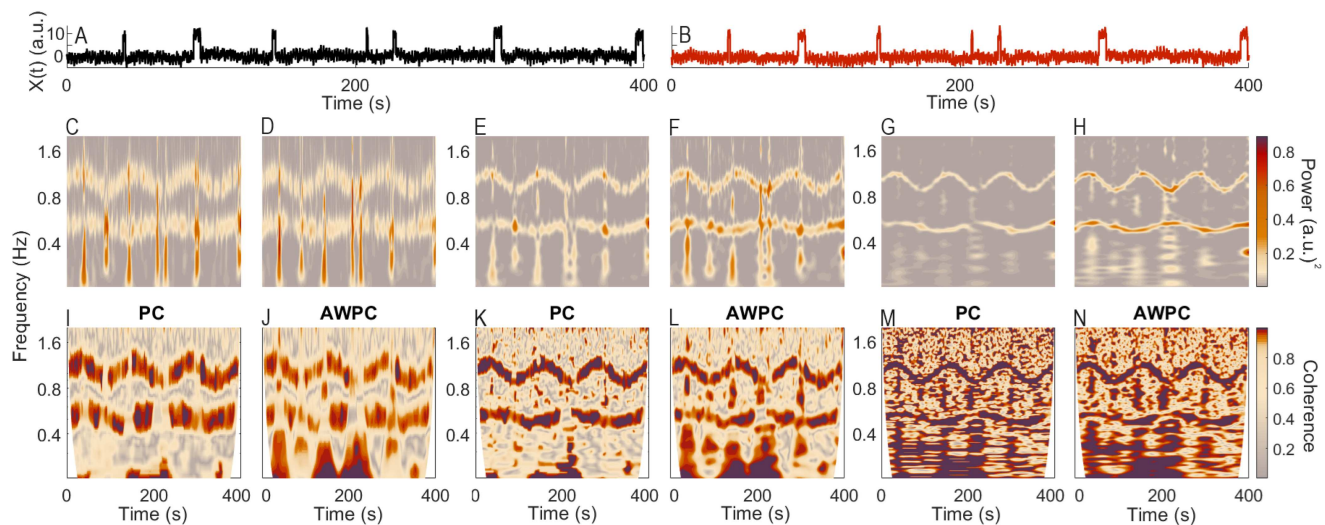


**FIG. 4.** Comparison between PC and AWPC applied using wavelets of different frequency resolution to modes generated by phase-perturbed Poincaré oscillators as defined by Eq. (5), with the same dichotomous noise and independent realizations of  $1/f$  noise added to both time-series. (a) and (b) The independently generated time-series. The second row (c)–(h) presents the WT plots of the two time-series at different frequency resolutions:  $f_0 = 1$  (c) and (d),  $f_0 = 2$  (e) and (f), and  $f_0 = 5$  (g) and (h). The time-series in (a) was the input for the transforms (c), (e), and (g), while (b) provided the input for (d), (f), and (h). The final row (i)–(n) indicates the time-localized coherence for the PC and AWPC approaches using the transforms shown in (c)–(h). For example, (i) and (j) were both generated using the WT plots indicated by (c) and (d).

affected by the amplitude perturbations due to the increased temporal width of the wavelets. Generally speaking, therefore, smaller values of  $f_0$  should be used in cases where extremely time-localized noise features are present, such as movement artifacts in biomedical measurements.

Also worth noting in the additive noise example is that even though the added dichotomous and  $1/f$  noise affect both the phase and amplitude of the wavelet components, the coherence bands of the modes are more strongly defined in the PC plots and the low-frequency coherence is reduced. This is caused by the time-localized properties of the dichotomous noise, which only affect a relatively small number of cycles at each wavelet scale. Since the window used to calculate the coherence averages the phase difference over a relatively large number of cycles, the effect on PC is reduced. In contrast, as shown in Eq. (11), the phase difference in AWPC is weighted by the amplitude. This means that even though the noise spikes last only a small number of cycles, the relative weight to the calculation of the coherence is increased due to the large associated amplitude.

#### D. Phase difference

Beyond coherence, it is often useful to extract the instantaneous wavelet phase difference ( $\theta_a(f, t) - \theta_b(f, t)$ ) and analyze this directly. This has been done in many studies to investigate deterministic phase differences in oscillations from two time-series.<sup>77–80</sup> While phase is technically a time-independent measure, the direction and magnitude of the phase difference are still a valuable measure that can be used to determine time lags, which provide weight to statements of causality.

In the studies cited above, analysis of the phase difference involves extracting individual pairs of instantaneous phases and examining the change in the phase difference over time. However, in time-series containing many modes, it is often useful to analyze the phase differences in the frequency domain. Doing this reveals the phase relationships present across different timescales of the dynamics.

To define the time-averaged phase difference, we use

$$\psi(f) = \arg \left[ \int_0^T e^{i(\theta_a(f,t) - \theta_b(f,t))} dt \right]. \quad (14)$$

To be able to take the integral in Eq. (14) over the whole duration  $[0, T]$  of the signal, it would be necessary to add padding to the signal before time 0 and after time  $T$  before computing the WT. If, instead, one just computes the WT within the cone of influence, then the time-interval over which the integral in Eq. (14) is taken is the  $f$ -section of the cone of influence—that is, the set of times  $t$  over which  $W(f, t)$  has been computed; this is a subinterval of  $[0, T]$  that depends on  $f$ : as  $f$  decreases, this subinterval becomes narrower.

Note that while this definition of the time-averaged phase difference correctly identifies the phase differences of the coherent modes, it does not necessarily provide a meaningful value for areas of zero coherence. This is because the result will be the argument of the sum of random phasors. While the amplitude of this sum correctly gives a value of the time-averaged PC at the background level, the argument will be a random angle between 0 and  $2\pi$ . It is, therefore, important to assess such a measure of the phase difference in conjunction with the actual coherence and only to evaluate its values where the coherence is significant.

In analogy to the difference between PC and AWPC, it is also possible to define an overall phase difference using not the *time-averaged* phase difference as in (14), but rather the *energy-averaged* phase difference,

$$\begin{aligned}\psi_E(f) &= \arg \left[ \int_0^T W_a(f, t) \cdot W_b^*(f, t) dt \right] \\ &= \arg \left[ \int_0^T |W_a(f, t)| \cdot |W_b(f, t)| e^{i(\theta_a(f, t) - \theta_b(f, t))} dt \right].\end{aligned}$$

In this paper, we use the time-averaged phase difference.

### E. Time-averaged coherence

We have defined PC and AWPC as functions of time and frequency since they represent information about the time-localized frequency content of the pair of signals. When we want an overall measure of the coherence at each frequency-value, taken over the whole duration of the signal, there are two approaches that one can take:

One is simply to take the time-average of the time-localized PC or AWPC as already defined in Secs. IV B and IV C.

The other is to compute PC or AWPC not over small time-windows  $(t - \frac{\delta}{2}, t + \frac{\delta}{2})$  as in Eqs. (10)–(13), but rather over the whole duration of the signal.

Under the former approach, we have a time-averaged PC given by

$$C_\theta^{\text{average}}(f) = \frac{1}{T - \delta} \int_{\frac{\delta}{2}}^{T - \frac{\delta}{2}} C_\theta(f, t) dt \quad (15)$$

and a time-averaged AWPC given by

$$C_W^{\text{average}}(f) = \frac{1}{T - \delta} \int_{\frac{\delta}{2}}^{T - \frac{\delta}{2}} C_W(f, t) dt. \quad (16)$$

Let us recall here that  $\delta$  itself depends on  $f$ , as described in Sec. IV B. Under the latter approach, we have an over-all-time PC given by

$$C_\theta^{\text{overall}}(f) = \frac{1}{T} \left| \int_0^T e^{i(\theta_a(f, \tau) - \theta_b(f, \tau))} d\tau \right|$$

and an over-all-time AWPC given by

$$C_W^{\text{overall}}(f) = \frac{|SW_{ab}^{\text{total}}(f)|}{[SW_{aa}^{\text{total}}(f) \cdot SW_{bb}^{\text{total}}(f)]^{1/2}},$$

where  $SW_{ab}^{\text{total}}$  are the over-all-time wavelet cross spectra as defined by

$$\begin{aligned}SW_{ab}^{\text{total}}(f) &= \int_0^T W_a(f, t) \cdot W_b^*(f, t) dt \\ &= \int_0^T |W_a(f, t)| \cdot |W_b(f, t)| e^{i(\theta_a(f, t) - \theta_b(f, t))} dt.\end{aligned}$$

In all four cases, we have given formulas according to the assumption that the WT is defined over the whole of  $[0, T]$ . Once again, this requires that padding has been added to the signal before

time 0 and after time  $T$ ; if, instead, the WT has been computed only over the cone of influence, then the integrals  $\int_0^T$  or averages  $\frac{1}{T} \int_0^T$  taken over the time-interval  $[0, T]$  in the above formulas need to be taken instead over the  $f$ -section of the cone of influence.

In this paper, we work with the former of the two approaches, namely, Eqs. (15) and (16).

### V. PRACTICAL ASPECTS

Coherence analysis is restricted by the properties of the measured data. Each dataset is likely to contain idiosyncrasies that require specific attention to avoid false representation of the results. By unlocking the temporal dimension with time-resolved analysis methods, one may properly view and assess the type of data under investigation, and once this step is completed, choose and perform the appropriate analysis. The multi-scale nature of the present analysis also enables simultaneous observation of the behavior across a number of frequencies, which in many cases are representative of various independent behaviors in the system. A review of the statistical properties of wavelet coherence is provided in Cohen and Walden.<sup>81</sup> However, here, we focus on the practical implementation and application of these methods.

To demonstrate the nuance required when selecting parameters for analysis, we consider two sets of time-series containing two common modes. As before, the modes are generated using the modified Poincaré system and have independent perturbations. The key difference is that the first set of time-series has modes with frequencies  $\omega_0 = 1$  and  $\omega_0 = 0.2$  that are stationary in time, with  $\omega_m = 0$  (the leftmost set of Fig. 5). In contrast, in the second set of time-series, the frequency of the modes varies with  $\omega_m = 0.016\pi$  for the high-frequency mode and  $\omega_m = 0.010\pi$  for the low-frequency mode (the rightmost set of Fig. 5).

Importantly, when considering coherence between simultaneously measured time-series, one may use two sets of apparatus with varying sampling frequencies,  $f_s$ . For the calculation of coherence, a common  $f_s$  must be established. While it is theoretically possible to up-sample the data series with the smaller sampling frequency, this is not recommended as it will not recover information regarding higher-frequency oscillations. Instead, the solution is to downsample the larger time-series so that a common  $f_s$  is established.

The value of  $f_s$  determines the maximum observable frequency,  $f_{\text{max}}$ , because we need at least two points in each cycle to capture an oscillation. Consequently, the upper-frequency limit, or the Nyquist frequency, is defined as  $f_N = f_s/2$ . A low value of  $f_{\text{max}}$  can introduce problems when assessing data, as seen in Fig. 5(j). In this case, the system was simulated with  $f_s = 4$  Hz, which means that  $f_{\text{max}} = 2$  Hz is selected. The coherent mode seemingly passes above  $f_{\text{max}}$ , illustrating the need for a higher  $f_s$ .

The lowest attainable frequency,  $f_{\text{min}}$ , is determined by the length of the time-series. In the examples demonstrated in this work, AWPC and PC are evaluated across ten cycles of oscillation at a given frequency. It follows that the length of the time-series restricts  $f_{\text{min}}$  and that the length must be at least ten times the length of the minimum frequency of interest. If the interaction is time-varying, then more cycles are needed to account for the modulation present, dependent upon the frequency of the modulation. The time-varying

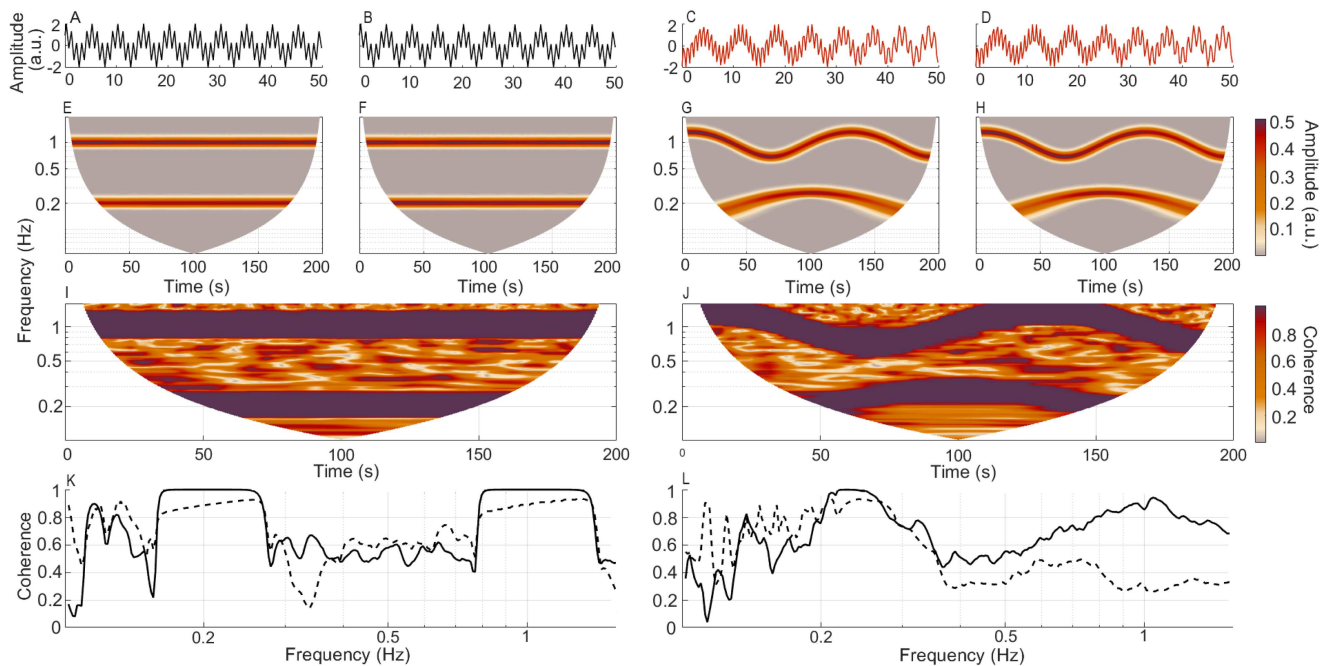


**FIG. 5.** Practical aspects to consider when applying phase coherence. Time-series generated from a pair of Poincaré oscillators, as defined by Eq. (5). The time-series were obtained numerically with  $f_0 = 4$  Hz and minimal amplitude modulation ( $\xi_r = 0.005$ ,  $\xi_\theta = 0$ ). The frequencies of these modes are unchanging in time for (a) and (b) and time-varying in (c) and (d). Their corresponding WT (e)–(h) demonstrate these differences. The time-localized phase coherence plots (i) and (j) are generated from the wavelet transforms (e)–(h). (k) and (l) Time-average values are shown as solid black lines and mismatch surrogate thresholds as dashed lines.

example shown in Figs. 5(c), 5(d), 5(g), 5(h), 5(j), and 5(l) demonstrates a situation where the simulated mode may be interpreted as being centered upon a greater frequency (0.25 Hz) than it really is. Specifically, the mode should be centered upon 0.2 Hz. Due to the shortness of the recording, the cone of influence contains only the upper half of the modulation cycle, resulting in an apparently higher value. In the non-time-varying frequency case, there is no issue, and the peak coherence is centered around 0.2 Hz.

The presence of oscillatory dynamics can be confirmed by first considering the time–frequency representation of the data. In addition, this step will provide information on the frequency range of interest if this is not known beforehand. Limiting the coherence analysis to this range will reduce the burden on computational capacity and save time. The WT will guide the choice of the resolution parameter. However, one must consider that this is always a trade-off, as discussed in Sec. IV C and seen in Figs. 2–4.

### A. Testing for significance

The considerations outlined above will help to reduce false conclusions regarding the data. However, to further reduce the chance of falsely representing spurious coherence as significant, a further step must be performed.

Even with the existence of independent fluctuations in both time-series, the interpretation of coherence is not straightforward, as illustrated by Holm.<sup>82</sup> This is because even two completely

independent noise time-series will contain fluctuations that appear at the same time and frequency, resulting in a non-zero value of coherence.

We must, therefore, determine whether observed coherence is *significant*. This is necessary both for being able to make physical inferences from the observation of coherence values and for being able to make physical inferences from phase-shift values  $\psi(f)$  associated with high coherence. Consideration of significance of coherence values can be divided into two aspects: First, the coherence values themselves need to be statistically significant in terms of exceeding some critical threshold, i.e., some baseline coherence value. Second, when one computes the time-averaged phase difference  $\psi(f)$  as a function of  $f$ , where there is significant coherence, one should observe a plateau—i.e., an approximately constant phase difference—over the frequency range in which the phase-coherent oscillations manifest in the time–frequency representation. One should only regard coherence as significant if it is found to satisfy both of these aspects of testing for significance.

In regard to the first aspect, defining the baseline coherence value for significance is not trivial, as it is dependent on the nature of the background dynamics generated by the system under investigation. For example, in the system described above, the independent fluctuations generated from perturbations to the phase and amplitude will result in a different level of background coherence to the case of independent  $1/f$  additive noise. Furthermore, in real systems, the deterministic dynamics cannot be separated from the

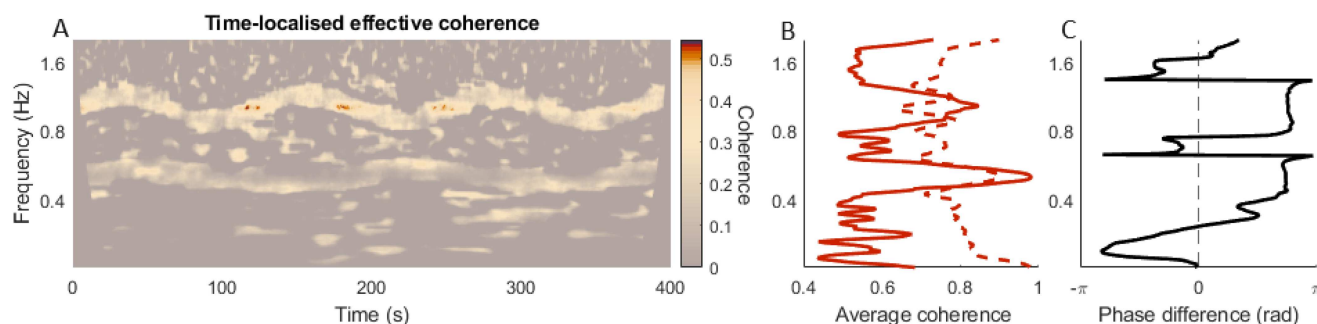


**FIG. 6.** (a) Time-localized effective phase coherence generated using the Poincaré oscillator example with amplitude noise and a frequency resolution parameter of  $f_0 = 2$ . The 75th percentile of 99 mismatch surrogates was considered as a zero threshold and was subtracted from the original time-localized coherence. Resulting negative values were set to zero. (b) The time-average of the raw coherence (solid line) and the surrogate threshold (dashed line). (c) The average phase difference across frequency.

noise perturbations, which increases the difficulty of defining a coherence baseline.

A more formulaic approach is to use a hypothesis test. Specifically, we would like to test a null hypothesis that two time-series are not coherent at a specific frequency. Such a hypothesis can be tested through the use of surrogate data.<sup>83</sup> Surrogate data are numerically modeled time-series that are designed to preserve all features of the measured time-series apart from the feature under investigation. In this method, a set of surrogate time-series is first randomly generated. The same analysis that is performed on the real time-series is then performed on the surrogates, with the end result being the discriminating statistic corresponding to the factor of interest. This results in a distribution of values for these statistics, which can then be used to define a specific confidence interval (i.e., the value of a percentile) for discerning significance and rejection of the null hypothesis.

The optimal percentile to use in the test varies from case to case. This can be due to a number of factors. For example, a high intensity of the difference between the noises affecting the two time-series will decrease the coherence between the two time-series to a greater extent than it would decrease the coherence between surrogates, making a lower percentile for the surrogate threshold more appropriate. In this paper, we will adopt a 95th percentile threshold for most cases. However, in some cases, due to factors like the one we have just mentioned, we will use a lower threshold.

One of the most common uses of surrogate data is to test for nonlinearity, where it is possible to apply methods, such as amplitude-adjusted Fourier transform surrogates, that preserve only the linear statistical properties of the time-series (see Ref. 84 for a review of surrogate data methods). However, in testing for significant coherence, we must also preserve the effects of nonlinearity in the surrogate data. Otherwise, even if the surrogates preserve the linear statistical properties, such as the amplitude probability distribution and the frequency spectrum, the null hypothesis may still be spuriously rejected due to increased coherence resulting from nonlinearity.

Mismatched surrogates, also known as intersubject surrogates in the context of biomedical data, are one of the simplest ways to

preserve potential nonlinearity in the surrogate data. With this method, pairs of real measurements of the same system (such as the human body, measured across different subjects) are separated and then re-paired with the corresponding time-series from an independent measurement (i.e., another subject). This has the advantage of preserving all properties of the time-series apart from the time-specific information. However, coherence is not preserved as the oscillations are no longer ordered in time.

While mismatched surrogates usually apply only to measured data from real systems, it is still possible to generate time-series approximating mismatched surrogates with the illustrative model defined in Sec. III. In this case, we can simply modify the frequency modulation of the two modes,  $\omega(t) = 2\pi\omega_0 + A \sin(2\pi\omega_m t + \psi)$ , where  $\psi$  is a phase offset of the modulation. Each pair of surrogate time-series is then generated using different values of  $\psi$  for each mode, which are uniformly sampled on the interval  $[0, 2\pi]$ .

It is also worth noting that surrogate testing is not the only method for determining significance thresholds for coherence values. The method proposed by Sheppard *et al.*<sup>85</sup> provide analytically derived significance thresholds based on higher-order statistics, which was shown to give better performance than amplitude-adjusted Fourier transform surrogates.

The effect of time-averaged surrogates is illustrated in Figs. 5(k) and 5(l), which show the 95th percentile of 99 mismatch surrogates. These surrogate thresholds give a much clearer indication of the coherence values that are present in the system vs the spurious coherence. One may also choose to illustrate the time-localized effective coherence. This is demonstrated in Fig. 6, with parameters identical to those in Figs. 2(e), 2(f), 2(k), and 2(l). The threshold here was chosen as the 75th percentile of 99 mismatch surrogates. One can now discriminate the coherence due to the modes vs the background fluctuations in the time-averaged coherence. However, many areas of significant coherence still remain in the time-localized plot distributed away from the modes. This illustrates the fact that it is easier for spurious significant coherence to occur in the time-frequency domain, where the testing area is essentially squared.

The other effect of surrogates can be seen on the effective coherence of the low-frequency mode, which is much reduced



compared to the high-frequency mode. This is due to the fact that spurious coherence between random fluctuations is more likely to be found since the average coherence is calculated over fewer cycles. This essentially reduces the observable frequency range, adding to the effects already caused by the size of the wavelets (parameterized by  $f_0$ ) and the window size used for the coherence calculation (parameterized by  $n_{cy}$ ). Taking into account these cumulative effects, we generally recommend that effective coherence can only be assessed if a minimum of 30 cycles can be observed, giving the lowest observable frequency of  $30/T$ .

Now, to illustrate the second aspect of considering significance of coherence: In the two frequency bands where Fig. 6(b) shows coherence values exceeding the surrogate threshold, Fig. 6(c) shows the phase difference plateauing at about  $0.75\pi$ . These plateaus in conjunction with the statistical significance of the coherence values suggest that the coherence in these two frequency bands is significant. Moreover, as a consequence, we can conclude that the value  $0.75\pi$  around which the phase difference plateaus is the amount by which the first time-series leads the second, consistent with the numerically modeled input values.

Therefore, we have seen that the surrogate threshold and the phase difference are invaluable tools when interpreting coherence; this will be demonstrated in Sec. VI via a series of examples.

## VI. APPLICATIONS

### A. Cardio-respiratory coherence

The heart rate is modulated through several processes, with respiration being an important factor. During inhalation, the heart tends to beat quicker, and during exhalation, it tends to slow down. This interaction is known as respiratory sinus arrhythmia.<sup>86</sup> Cardio-respiratory interactions are perhaps one of the most widely studied interactions. Several methods have been employed,<sup>87,88</sup> including coherence analysis based on the Fourier and wavelet transforms.<sup>89,90</sup> Utilizing PC to study cardio-respiratory interactions has also proven valuable,<sup>50</sup> for example, in the context of ageing,<sup>52</sup> malaria,<sup>91</sup> and hypoxia.<sup>92</sup>

In this example, we evaluate cardio-respiratory interactions based on the simultaneously recorded respiratory effort and the electric activity of the heart. The 1400 s recordings are taken from a 28-year healthy male participating in the study of ageing,<sup>93</sup> where the sensor/electrode placements are described. A time-insert of respiration is shown in Fig. 7(a) and the ECG in Fig. 7(b). The instantaneous frequencies of respiration [IRR, Fig. 7(c)] and beating of the heart [IHR, Fig. 7(d)] are extracted by ridge extraction<sup>32</sup> after the WT has been obtained. Two types of interactions are investigated: (a) between the original respiratory time-series and the IHR and (b) between both instantaneous rates, IRR and IHR. The PC and AWPC for both cases are shown in Figs. 7(e), 7(f), 7(i), and 7(j). The surrogate threshold was set to the 95th percentage of 140 intersubject surrogates, as used in the original study.<sup>93</sup> The time-averaged values of PC and AWPC from the entire 1400 s recordings are shown in Figs. 7(g) and 7(k) for the cases (a) and (b), respectively. The phase differences, as a function of frequency, obtained for case (a) and (b), are shown in Figs. 7(h) and 7(l).

It is clear that both PC and AWPC are much higher for the respiration-IHR case, compared to IRR-IHR case, and that the highest values of coherence are at the frequency of respiration (around 0.2–0.3 Hz), consistent with earlier studies. This indicates that, in the resting state, the heart rate is strongly modulated by the amplitude of respiration and to a much lesser extent by the frequency of respiration. In Fig. 7(g), one can see that the PC and AWPC are similar. The phase difference at the respiration frequency is around 0 rad.

### B. Phase coherence and movement artifacts

Coherence analysis is often applied to find common oscillatory behavior between brain signals from different locations. This can elucidate the functional connectivity of the brain, which is known to change in various conditions.<sup>94,95</sup> Spontaneous activity in the brain can be measured noninvasively at a relatively low cost using EEG or fNIRS with minimal discomfort to the subjects. However, both methods are susceptible to movement artifacts.<sup>96</sup> Several approaches exist to remove these artifacts from the data, although they often compromise the quality of the data and may additionally remove information of interest.<sup>97,98</sup> As seen in Secs. IV, phase-based approaches may be more resilient against movement artifacts and noise and, as such, can circumvent some of the more draconian preprocessing requirements. In this section, we investigate two examples of movement artifacts, one using EEG and the second using fNIRS.

#### 1. Autism spectrum disorder

Non-invasive brain activity measurements in children are fraught with artifacts due to difficulties in keeping younger subjects still for extended periods. Analysis of signals derived from younger cohorts, therefore, necessitates methods that are robust to movement artifacts. In addition, when considering the presence of interactions between time-series, it can be important to assess how the nature of these interactions changes over time. Time-localized methods can reveal temporal dependencies in this mutual behavior. In a wide array of neurological conditions, it is not only the intensity of interaction between brain regions but the duration of interaction that is altered.<sup>99,100</sup> By observing the time-localized coherence, one may deduce the regularity and strength of time-varying interactions.

We consider a resting-state measurement with eyes open of two simultaneously recorded EEG time-series. These data were measured in a cohort of male children aged 3–5 years old with a diagnosis of autism spectrum disorder (ASD). The time-series were captured using a Nicolet cEEG instrument (Viasys Healthcare, USA) at a sampling rate of 256 Hz. A 20-min recording period was used to collect the data, and a 180-second interval was analyzed, with the central 60 s illustrated in Fig. 8 as it contained a clear artifact. Measurement sites corresponding to F3 and F4 in the international 10–20 system were chosen, as the initial objective of the investigation was to assess reports of reduced frontal connectivity in children with ASD.<sup>101–104</sup>

The effect of the movement artifact is clearly seen in both the time domain, Figs. 8(a) and 8(b), and the WT, Figs. 8(c) and 8(d), where at the instance of the movement, all frequencies are present (around 93 s) in the spectrum. The effect on the coherence is much stronger and can be seen in Figs. 8(e)–8(g) for the AWPC compared



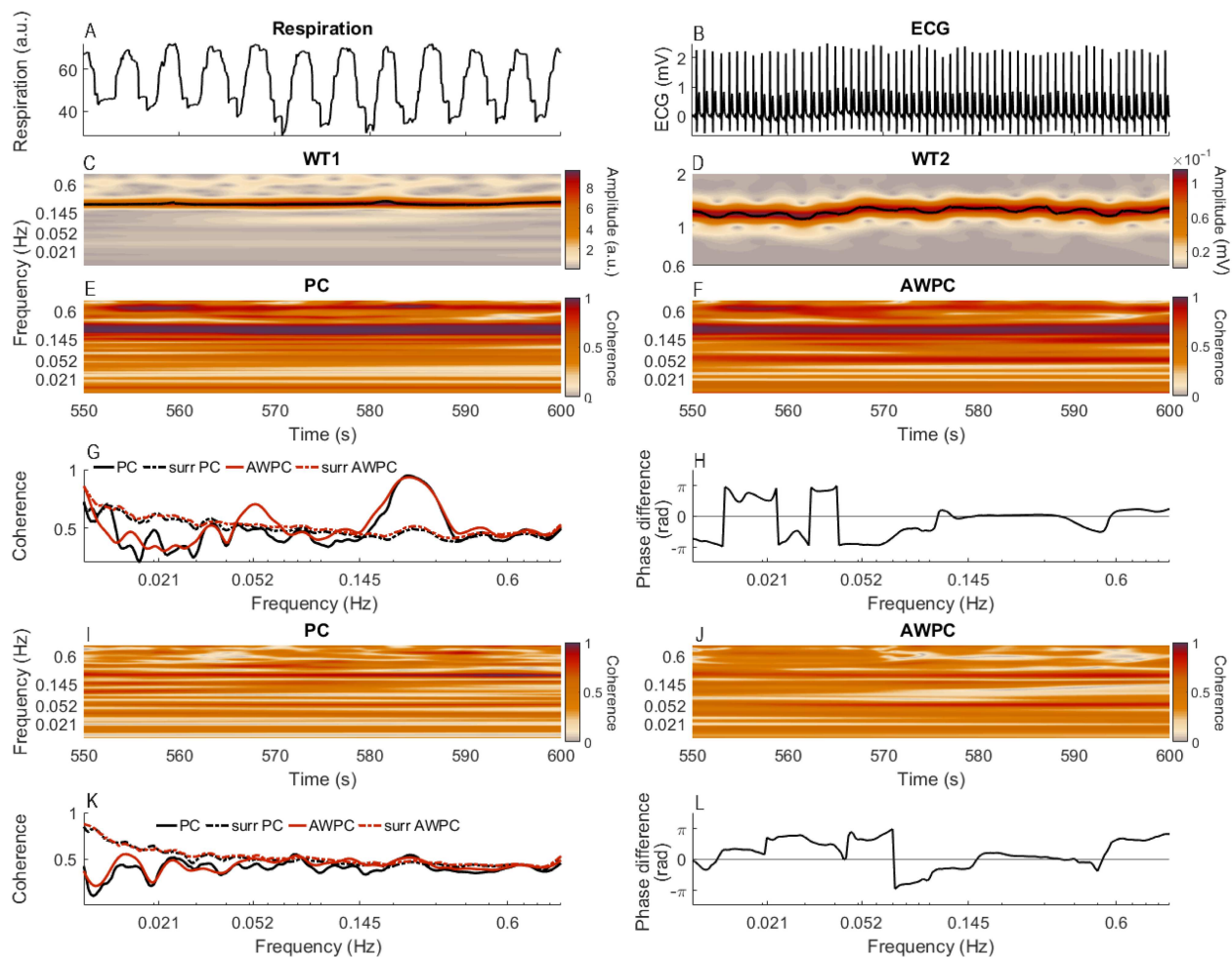


**FIG. 7.** (a) and (b) Time-series of respiration and ECG from a 28-year-old healthy man, shown for 50 out of the 1400 s of recordings. (c) The WT of the time-series in (a). The solid line is the extracted ridge, giving the instantaneous respiration rate (IRR). (d) The WT of the time-series in (b). The solid line is the extracted ridge, giving the instantaneous heart rate (IHR). (e) The PC between the respiration and IHR. (f) The AWPC between the respiration and IHR. (g) The time-averaged PC (solid black line) and AWPC (solid orange line), with the corresponding surrogate thresholds (dashed lines). (h) The time-averaged phase difference at each frequency. A positive value means that the time-series in (a) is leading. (i) The PC between IHR and IRR. (j) The AWPC between IHR and IRR. (k) The time-averaged PC (solid black line) and AWPC (solid orange line), with the corresponding surrogate thresholds (dashed lines) for IHR and IRR. (l) The time-averaged phase difference at each frequency. A positive value means that the IRR is leading. The time-averaged coherence and the phase difference in (g), (h), (k), and (l) is calculated using the whole time-series (1400 s).

to the PC. A threshold of the 75th percentile of 156 intersubject surrogates was used, leaving only the significant coherence. The time-localized coherence [Fig. 8(e)] shows that the magnitude and presence of the interactions vary over time. Both the time-localized, Figs. 8(e) and 8(f), and the time-average, Fig. 8(g), coherence are elevated for the AWPC compared to the PC.

## 2. Chorea in Huntington's disease

Now, we consider two time-series recorded from the temporal brain areas, in a study that investigated coherence between neuronal and vascular function.<sup>105</sup> These locations often have

artifacts due to movement of the jaw. The data are from a participant with a positive genetic test for Huntington's disease (HD), who has not yet developed the movement disorder known as chorea. Still, as chorea is a hallmark of the disease, HD research would benefit from methods that are resistant to movement artifacts.

We compared PC and AWPC of two resting-state oxygenated hemoglobin (oxyHb) time-series measured using a fNIRS device (NIRScout, NIRx, Germany) with a sampling frequency of 31.25 Hz over 20 min (for further details on measurements, see Ref. 93). The measurement sites correspond to T7 and T8 in the international 10–20 system (left and right temporal locations). The resolution

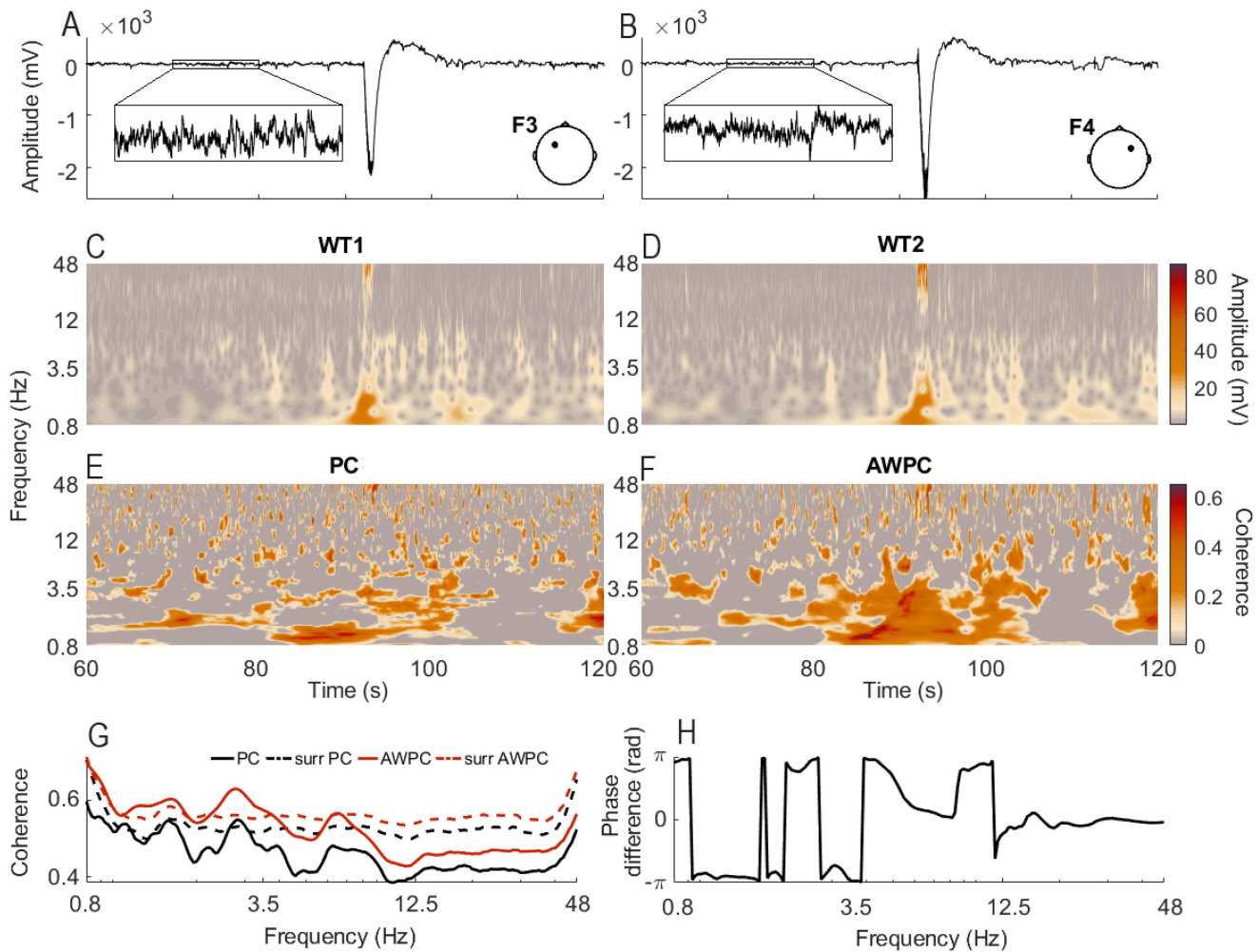


**FIG. 8.** Movement artifact represented as a downward spike in the time-series recorded simultaneously at two probes: F3 (a) and F4 (b). Their corresponding WTs [(c) and (d), respectively], indicate the amplitude perturbation at around 93 s. The effective phase coherence (e) is resilient against this perturbation, while the amplitude-weighted phase coherence (f) exhibits spurious coherence. In both cases, the surrogate threshold is taken as the 75th percentile of 156 intersubject surrogates. (g) The time-averaged PC (solid black line) and AWPC (solid orange line), with the corresponding surrogate thresholds (dashed lines). (h) The time-averaged phase difference across frequency.

parameter  $f_0$ , Eq. (8), was set to 1, as to minimize the spread of an artifact.

The results are shown in Fig. 9. The time-series contain two movement artifacts, which appear as high-amplitude cones in the WT and have the greatest impact at low frequencies. The artifacts have a very significant impact on the AWPC plot and affect an even wider area of time and frequency than is visible in the WT plots. This is a consequence of the moving window used to calculate wavelet coherence. In the plot of PC, the effect of the artifacts is not obvious. This illustrates how any simultaneous increase in amplitude, even if not phase coherent, results in AWPC appearing significant over large areas of the time–frequency domain. This can also be seen in the time-averaged coherence plot, where the AWPC (orange line) is

much higher than the PC (black line). The two dashed lines show the 95th percentile of the 136 intersubject surrogates.

This example illustrates that PC is relatively resistant to artifacts, which is beneficial when analyzing time-series from various non-invasive measurement techniques.

### C. Electron dynamics on the surface of liquid helium

Time–frequency and coherence analysis can provide valuable information about the dynamics of a system. In addition, the phase difference between oscillations can give information about the direction of influence. We consider the movement of electrons on the surface of liquid helium at very low temperatures, as discussed in Siddiq

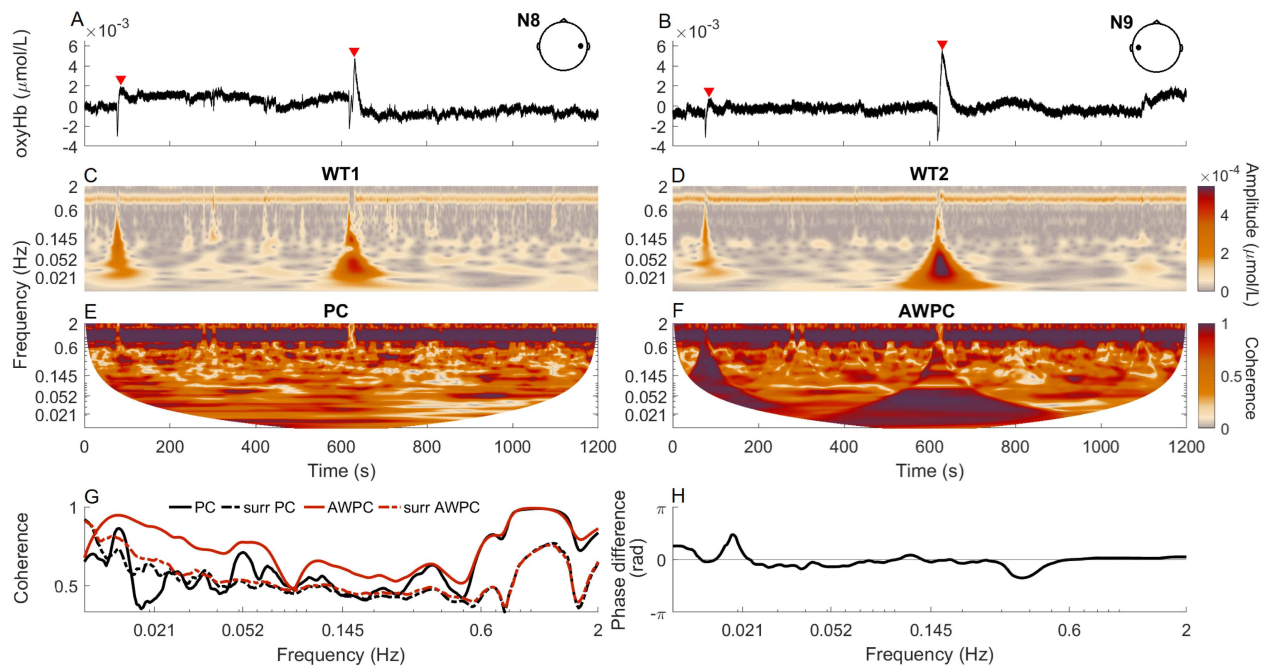


**FIG. 9.** (a) and (b) Two fNIRS time-series measured from a participant with Huntington's disease. The locations of two artifacts are marked on the time-series using red triangles. (c) The WT of the time-series in (a). (d) The WT of the time-series in (b). (e) The PC of the two time-series. (f) The AWPC plots of the two time-series. (g) The time-averaged PC (solid black line) and AWPC (solid orange line), with the corresponding surrogate thresholds (dashed lines). (h) The time-averaged phase difference at each frequency. A positive value means that the time-series in (a) is leading.

*et al.*<sup>31</sup> At very low temperatures, the helium will be a superfluid. Since such a system can be used for constructing the qubits that are needed for quantum computers, increasing the understanding of its dynamics is important.

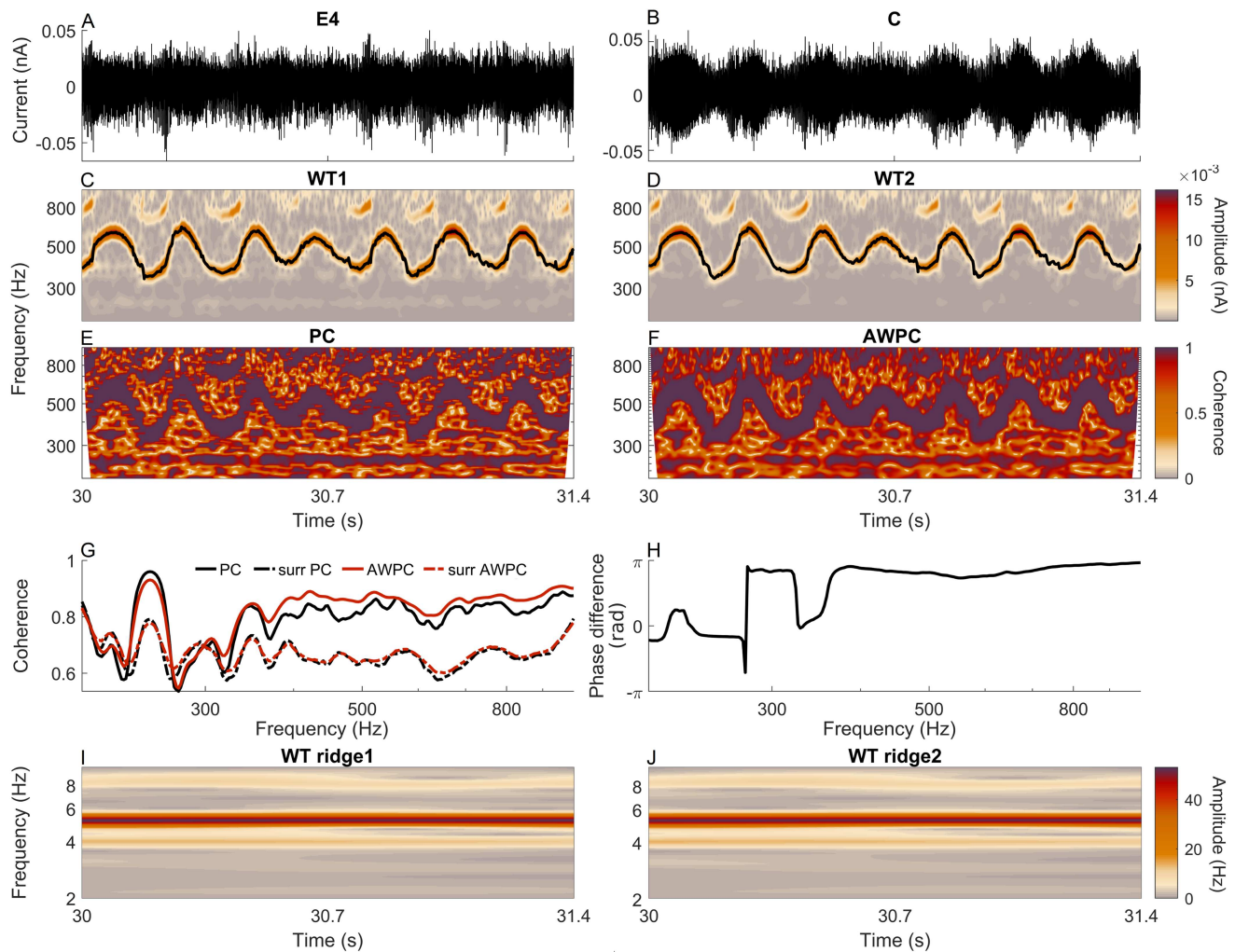
In the experiments, the electrons were just above the liquid helium, trapped between the helium and a vacuum. They were in a perpendicular magnetic field and subjected to microwave radiation and varying pressing voltage. Current oscillations were recorded from five electrodes for 60 s at 100 kHz. The full experimental setup is described in Ref. 31. We chose an example with low electron density and 4.18 V pressing voltage. Currents measured from electrodes E4 and C in the time-interval 30–31.4 s were selected for analysis, and high coherence was obtained as in the original paper.<sup>31</sup>

Figure 10 shows the PC and AWPC between current oscillations at the two electrodes. The current signals were first down-sampled to 20 kHz, as in this example, we will focus on oscillations around 0.5 kHz. The resolution parameter was set to 3, in line with the original paper.<sup>31</sup> 100 iterated amplitude-adjusted Fourier transform (IAAFT) surrogates were used to calculate the surrogate thresholds.<sup>84</sup>

Both PC and AWPC methods pick up a time-varying coherence following the dominant mode in the WT plots, which resembles a non-autonomous influence on the system. The time-averaged PC (black line) and AWPC (orange lines) are similar, with

the AWPC having a slightly higher value at the higher frequencies. This could indicate that there is some amplitude covariance. The surrogate thresholds are very similar for both methods. The time-averaged phase difference is positive, meaning that the oscillation at E4 is preceding that at C.

The existence of coherence indicates that the electrons are moving, and the phase difference suggests that they are moving toward the C electrode from the E4 electrode. This is consistent with the microwave radiation being applied closer to E4. Furthermore, by studying the time–frequency representations, we see a clear mode with a time-varying frequency. Using ridge extraction,<sup>32</sup> which essentially tracks the maximum amplitude within a frequency range, we can extract a time-series of the instantaneous frequency. The WT of this time-series shows a clear amplitude peak at around 5.2 Hz, indicating modulation of the electron movement at this frequency. This was shown to be caused by slow gravity waves on the liquid helium.<sup>31</sup> It is important to note that in the WT of the original current data, there is also a peak at around 5.2 Hz. However, this peak is relatively weak compared to the rest of the spectrum, and, in particular, compared with the dominant oscillatory component, making it challenging to observe and identify directly from the frequency spectrum. This illustrates that time-localized, time-frequency methods can uncover a great deal of physically meaningful information.



**FIG. 10.** (a) and (b) Time-series of current oscillations caused by the movement of electrons on the surface of liquid helium. The two electrodes are labeled E4 and C. (c) and (d) The WT of the time-series in (a) and (b), respectively, with the extracted ridge shown by the solid black line. (e) The PC of the two time-series. (f) The AWPC of the two time-series. (g) The time-averaged PC (solid black line) and AWPC (solid orange line), with the corresponding surrogate thresholds (dashed lines). (h) The time-averaged phase difference at each frequency. A positive value means that the time-series in (a) is leading. (i) The WT of the ridge time-series plotted in (c). (j) The WT of the ridge time-series plotted in (d).

## VII. DISCUSSION AND SUMMARY

The study of coherence has its foundations in physics, where methods were first developed to measure the coherence between the phases of waves. It has then been extended to considering coherence between the phases of more general oscillatory processes occurring in a wide variety of scientific disciplines; for this, one of the most fundamental issues is the quantification of such coherence from measured data. Accordingly, it is a subject particularly treated by harmonic analysis in mathematics and by signal-processing theory. We have approached this same question again from a physics perspective, but still with this greater generality than the kinds of setup

that initiated the study of coherence—namely, from the perspective of multi-scale time-dependent oscillatory dynamics.

We have seen that for time-series data recorded from systems involving interacting oscillations, key information about the interactions is contained in the time evolution of the phases of the oscillations. Moreover, we have seen that for the analysis of systems involving oscillations with temporally modulated quantitative characteristics, such as frequency and amplitude, time-series analysis methods that are fundamentally designed for time-series with stationary statistics are inappropriate. For example, the measure of coherence of phases intended to be revealed by Fourier



coherence will have little meaning for systems with frequency-modulated oscillations. Rather, tools designed to extract time-evolving, time-localized information about systems exhibiting time-dependent far-from-equilibrium dynamics are needed. In particular, phase information needs to be extracted in a suitably time-localized manner.

Such time-localization inherently needs to be understood relative to the timescale of the dynamical process under investigation, and therefore, for multi-scale time-series involving oscillations of a range of frequencies, this time-localization needs to be adaptive to the range of timescales involved. This has been illustrated in Fig. 1.

In the setting of time–frequency analysis, where the Heisenberg uncertainty principle requires a trade-off between precision in measurements of frequency and precision in location in time, this multi-scale adaptivity corresponds to a logarithmic frequency resolution. This is achieved by the continuous wavelet transform, where the scale variable is taken as inversely proportional to the frequency under investigation. Accordingly, we have seen that the wavelet transform is the appropriate tool for extracting phase information from multi-scale nonstationary time-series, and in particular, WT-based coherence analysis is the appropriate approach to investigating coherence of phases manifesting in such time-series.

In this paper, we have provided an introduction to wavelet-based coherence analysis and evaluated several related issues—some already established and others that had not previously been addressed.

Existing discussions of different approaches to quantifying coherence, and more generally of different approaches to time–frequency analysis, have mainly treated the different approaches as if on essentially equal footing, and practical choices, such as the use of WT over STFT, or of PC over AWPC, are often treated merely as a matter of quantitative optimization, without theoretically reasoned or experimentally explored consideration of the qualitative impact of such choices on the resulting analysis.

To address this issue, we have provided a systematic explanation of the practicalities and pitfalls of how to carry out wavelet coherence analysis in practice. In particular, we have provided a detailed review of the methodology for reliably testing for and detecting significant phase coherence from measured data.

Since the wavelet transform provides extractable phases and amplitudes, one can calculate<sup>38,46</sup> a measure of coherence independent of changes in the amplitude, namely, PC, as well as a measure of coherence that is weighted in time by amplitude, namely, AWPC. Prior to this work, an in-depth comparison between AWPC and PC had not been performed. Perhaps counterintuitively, we found a consistent difference in the performance of the two definitions of coherence when applied to noisy time-series. PC is, in general, more robust to noise and particularly to time-localized perturbations, meaning that it is affected to a much lesser degree by phenomena, such as movement artifacts.

Along with the definition of PC, one can also analyze phase differences in the oscillations present in the pair of time-series under investigation. This is first needed as one of the aspects of determining significance of coherence, along with statistical significance of the coherence values themselves: the time-averaged phase difference as a function of frequency needs to have a plateau in the frequency band where coherent oscillations manifest in

time–frequency representation. Second, where there is significant coherence, the phase difference can provide indications of which oscillation is leading.<sup>106</sup> However, it is important to note that causality (i.e., which process is the origin of the common oscillations) is not always possible to infer from the phase shift. This can be because the phase shift is wrapped on the interval  $[-\pi, \pi]$  or because of the existence of higher degree interactions, such as node triples.<sup>107</sup>

This investigation of coherence has revealed the wealth of information provided by the phase. Part of the utility of phase over amplitude comes from the fact that phase dynamics is constrained by the frequency interval within which an oscillation lies. For example, each wavelet has a defined frequency response, which limits the rate at which the phase can change. However, in contrast to the phase, the amplitude is not bounded to frequency in such a manner, making the separation of amplitude dynamics from noise harder to satisfactorily achieve. This is analogous to the advantages of frequency modulation over amplitude modulation in radio communications.<sup>108</sup>

The practical implications of the main points highlighted by our work are effectively illustrated in our analyses of real data in Sec. VI. In the examples shown in Sec. VI B, the presence of movement artifacts has a significant effect on the results of any analysis. Such artifacts usually need to be removed prior to analysis, which often requires subjective identification. The techniques used to remove identified artifacts may also introduce artificial manipulations in the data.<sup>109</sup> The resistance of amplitude-independent phase-based methods to these sorts of artifacts allows for the analysis of noisy data without the need for preprocessing or constraints on the measurement setup, leading to better research into conditions, such as HD and ASD.

In the example of electron dynamics on the surface of liquid helium, using phase coherence analysis, we identified the existence of gravity waves. Without the time-localized approach, these waves might not have been detected. This illustrates how the application of coherence methods and time–frequency analysis can be used to identify specific properties of a physical system. Thus, we see the importance of using a time-localized approach instead of an asymptotic approach, i.e., infinite-time, non-time-evolving approach. The wider adoption of explicitly finite-time and time-localized methods should, therefore, lead to similar discoveries in systems characterized by non-autonomous dynamics involving nonstationary amplitudes and frequencies.

## VIII. CONCLUSION

We review the current understanding of coherence, a universal phenomenon that can appear between oscillations or waves, irrespective of their origin. We start from its definition in physics and review numerical methods for analyzing coherence from modeled or real data. We focus particularly on coherence between non-autonomous oscillatory processes whose oscillations have deterministically time-varying frequencies. For this reason, we apply wavelet-based, time-resolved coherence analysis. We discuss differences between amplitude-weighted phase coherence and phase coherence. In the former case, time-resolved information includes both the amplitude and the phase; in the latter case, only the information about phase is considered. We illustrate that the amplitudes

are more readily perturbed than phases by noise or movement artifacts, and consequently, that phase coherence provides more robust information about interacting oscillatory systems. We illustrate this in relation to several real-world examples.

## SUPPLEMENTARY MATERIAL

An alternative to Fig. 1 in the main paper is presented in the [supplementary material](#). It shows the Fourier transform in a logarithmic scale. By comparing Figs. 1(c), 1(d), 1(g), and 1(h) in the main text and supplementary Figs. 1(c), 1(d), 1(g), and 1(h), it is clear that the logarithmic scale is disadvantageous to the short-time Fourier transform, which is obtained with linear frequency resolution.

## ACKNOWLEDGMENTS

We are grateful to Peter McClintock and Kostya Nasyedkin for useful comments on the paper. The work of P.T.C. and A.S. is funded through the Sony Research Award Program. A.S. is also funded by the Engineering and Physical Sciences Research Council, UK (Grant No. EP/X004597/1). J.B. is supported by the Sir John Fisher Foundation. S.J.K.B. is jointly supported by the EPSRC, UK and the MyMind GmbH—Brain Hero, Vienna, Austria (Grant No. EP/T518037/1). The High End Computing facility at Lancaster University was used for some of the computations. The experimental part of the ASD study was supported by the Action Medical Research (UK) MASDA Project (GN1963) and partly by the Slovenian Research Agency (Program No. P20232). The HD and ageing studies were funded by the Engineering and Physical Sciences Research Council, UK (Grant No. EP/M006298/1) and the Slovenian Research Agency (ARRS) (Program No. P20232). The experimental data used for the example on electron dynamics on the surface of liquid helium were obtained by Kostyantyn Nasyedkin in the Quantum Condensed Phases Research Team, RIKEN CEMS, Japan, headed by Kimitoshi Kono. The development of the MODA toolbox used for analyses has been supported by the Engineering and Physical Sciences Research Council, UK (Grant Nos. EP/100999X1 and EP/M006298/1), the EU projects BRACCIA (517133) and COSMOS (642563), the Action Medical Research (UK) MASDA Project (GN1963), and the Slovene Research Agency (Program No. P20232).

## AUTHOR DECLARATIONS

### Conflict of Interest

The authors have no conflicts to disclose.

### Author Contributions

The authors have been listed alphabetically due to their approximately equal contributions.

**S. J. K. Barnes:** Conceptualization (supporting); Data curation (equal); Formal analysis (equal); Investigation (equal); Software (equal); Validation (equal); Visualization (equal); Writing – review & editing (equal). **J. Bjerkkan:** Conceptualization (equal); Data curation (equal); Formal analysis (equal); Investigation (equal); Software (equal); Validation (equal); Visualization (equal); Writing – review & editing (equal). **P. T. Clemson:** Conceptualization (equal);

Data curation (equal); Formal analysis (equal); Investigation (equal); Methodology (equal); Software (equal); Supervision (equal); Validation (equal); Visualization (equal); Writing – original draft (equal); Writing – review & editing (equal). **J. Newman:** Conceptualization (supporting); Data curation (supporting); Formal analysis (supporting); Funding acquisition (supporting); Investigation (equal); Methodology (supporting); Validation (supporting); Visualization (supporting); Writing – review & editing (equal). **A. Stefanovska:** Conceptualization (equal); Data curation (equal); Formal analysis (equal); Funding acquisition (equal); Investigation (equal); Methodology (equal); Project administration (equal); Resources (equal); Supervision (equal); Validation (equal); Visualization (equal); Writing – review & editing (equal).

## DATA AVAILABILITY

The data used in this work are available in the Publications and Research (Pure) portal on Lancaster University's research information management system. The data used in the cardio-respiratory example can be found at [doi.org/10.17635/lancaster/researchdata/630](https://doi.org/10.17635/lancaster/researchdata/630). The data used in the ASD example can be found at [doi.org/10.17635/lancaster/researchdata/604](https://doi.org/10.17635/lancaster/researchdata/604). The data used in the HD example can be found at [doi.org/10.17635/lancaster/researchdata/631](https://doi.org/10.17635/lancaster/researchdata/631). The data used for the electron dynamics on the surface of a liquid helium example can be found at [doi.org/10.17635/lancaster/researchdata/655](https://doi.org/10.17635/lancaster/researchdata/655).

## REFERENCES

- <sup>1</sup>H. Crewe, C. Huygens, T. Young, A. J. Fresnel, and F. Arago, *The Wave Theory of Light; Memoirs of Huygens, Young and Fresnel* (Cincinnati American Book Company, New York, 1900).
- <sup>2</sup>A. Michelson and E. W. Morley, *Am. J. Sci.* **s3–34**, 333 (1887).
- <sup>3</sup>C. Jönsson, *Z. Phys.* **161**, 454 (1961).
- <sup>4</sup>P. G. Merli, G. F. Missiroli, and G. Pozzi, *Am. J. Phys.* **44**, 306 (1976).
- <sup>5</sup>A. Ananthaswamy, *Through Two Doors at Once: The Elegant Experiment That Captures the Enigma of Our Quantum Reality* (Penguin Publishing Group, 2018).
- <sup>6</sup>T. H. Maiman, *Nature* **187**, 493 (1960).
- <sup>7</sup>B. P. Abbot *et al.*, (LIGO Scientific Collaboration and Virgo Collaboration), *Phys. Rev. Lett.* **116**, 061102 (2016).
- <sup>8</sup>P. Ilzhöfer, M. Sohmen, G. Durastante, C. Politi, A. Trautmann, G. Natale, G. Morpurgo, T. Giamarchi, L. Chomaz, M. J. Mark, and F. Ferlaino, *Nat. Phys.* **17**, 356 (2021).
- <sup>9</sup>D. Huang and Y. Yang, *Phys. Rev. B* **104**, L081115 (2021).
- <sup>10</sup>S. Ye, C. Zou, H. Yan, Y. Ji, M. Xu, Z. Dong, Y. Chen, X. Zhou, and Y. Wang, *Nat. Phys.* **19**, 1301 (2023).
- <sup>11</sup>A. E. Miroshnichenko, S. Flach, and Y. S. Kivshar, *Rev. Mod. Phys.* **82**, 2257 (2010).
- <sup>12</sup>J. R. Kim, C. W. Lin, and S. Y. Lin, *Remote Sens.* **13**, 2240 (2021).
- <sup>13</sup>A. Delorme and S. Makeig, *J. Neurosci. Methods* **134**, 9 (2004).
- <sup>14</sup>M. Jensen, R. Hyder, B. U. Westner, A. Højlund, and Y. Shtyrov, *Neuropsychologia* **188**, 108602 (2023).
- <sup>15</sup>A. Sauer, T. Grent-t-Jong, M. Zeev-Wolf, W. Singer, A. Goldstein, and P. J. Uhlhaas, *Schizophr. Res.* **261**, 60 (2023).
- <sup>16</sup>T. Gänsler, M. Hansson, C.-J. Ivarsson, and G. Salomonsson, *IEEE Trans. Commun.* **44**, 1421 (1996).
- <sup>17</sup>T. Hada, D. Koga, and E. Yamamoto, *Space Sci. Rev.* **107**, 463 (2003).
- <sup>18</sup>P. C. Liu, in *Wavelets in Geophysics*, edited by P. Kumar and E. Foufoula-Georgiou (Elsevier, 1994), Vol. 4, pp. 151–166.
- <sup>19</sup>J. P. Eckmann and D. Ruelle, *Rev. Mod. Phys.* **57**, 617 (1983).
- <sup>20</sup>P. T. Clemson and A. Stefanovska, *Phys. Rep.* **542**, 297 (2014).

- <sup>21</sup> J. Rowland Adams, J. Newman, and A. Stefanovska, *Eur. Phys. J. Spec. Top.* **232**, 3435–3457 (2023).
- <sup>22</sup> E. P. Wigner, *Phys. Rev.* **40**, 749 (1932).
- <sup>23</sup> J. Ville, *Cables Transm.* **2A**, 61 (1948).
- <sup>24</sup> D. Gabor, *J. IEEE* **93**, 429 (1946).
- <sup>25</sup> J. Morlet, in *Issues on Acoustic Signal/Image Processing and Recognition*, Vol. I, NATO ASI series, edited by C. H. Chen (Springer, Berlin, 1983).
- <sup>26</sup> G. Kaiser, *A Friendly Guide to Wavelets* (Birkhäuser, Boston, MA, 1994).
- <sup>27</sup> B. Boashash, *Time Frequency Signal Analysis and Processing: A Comprehensive Reference* (Academic Press, Boston, MA, 2016).
- <sup>28</sup> M. Farge, *Annu. Rev. Fluid Mech.* **24**, 395 (1992).
- <sup>29</sup> S. L. Bressler, R. Coppola, and R. Nakamura, *Nature* **366**, 153 (1993).
- <sup>30</sup> M. Bračič and A. Stefanovska, *Bull. Math. Biol.* **60**, 919 (1998).
- <sup>31</sup> H. Siddiq, K. Nasyedkin, K. Kono, D. E. Zmeev, P. V. E. McClintock, Y. A. Pashkin, and A. Stefanovska, *Phys. Rev. B* **107**, 104501 (2023).
- <sup>32</sup> D. Iatsenko, P. V. E. McClintock, and A. Stefanovska, *Signal Process.* **125**, 290 (2016).
- <sup>33</sup> C. Schäfer, M. G. Rosenblum, H. H. Abel, and J. Kurths, *Phys. Rev. E* **60**, 857 (1999).
- <sup>34</sup> P. Kvandal, L. Sheppard, S. A. Landsverk, A. Stefanovska, and K. A. Kirkeboen, *J. Clin. Monit. Comput.* **27**, 375 (2013).
- <sup>35</sup> T. Stankovski, T. Pereira, P. V. E. McClintock, and A. Stefanovska, *Rev. Mod. Phys.* **89**, 045001 (2017).
- <sup>36</sup> M. Rosenblum and A. Pikovsky, *Front. Netw. Physiol.* **3**, 1298228 (2023).
- <sup>37</sup> P. T. Clemson, Y. F. Suprunenko, and A. Stefanovska, *Phys. Rev. E* **89**, 032904 (2014).
- <sup>38</sup> J.-P. Lachaux, E. Rodriguez, M. Le Van Quyen, A. Lutz, J. Martinerie, and F. J. Varela, *Int. J. Bifurcat. Chaos* **10**, 2429 (2000).
- <sup>39</sup> F. Mormann, K. Lehnertz, P. David, and C. E. Elger, *Physica D* **144**, 358 (2000).
- <sup>40</sup> B. J. Roach and D. H. Mathalon, *Schizophr. Bull.* **34**, 907 (2008).
- <sup>41</sup> C. Chang and G. H. Glover, *NeuroImage* **50**, 81 (2010).
- <sup>42</sup> C. M. Sweeney-Reed, P. M. Riddell, J. A. Ellis, J. E. Freeman, and S. J. Nasuto, *PLoS One* **7**, e48357 (2012).
- <sup>43</sup> E. Angelopoulos, E. Koutsoukos, A. Maillis, G. N. Papadimitriou, and C. Stefanis, *Schizophr. Res.* **153**, 109 (2014).
- <sup>44</sup> L. Bu, C. Huo, G. Xu, Y. Liu, Z. Li, Y. Fan, and J. Li, *Front. Physiol.* **9**, 669 (2018).
- <sup>45</sup> L. Xu, B. Wang, G. Xu, W. Wang, Z. Liu, and Z. Li, *Neurosci. Lett.* **640**, 21 (2017).
- <sup>46</sup> A. Bandrivskyy, A. Bernjak, P. V. E. McClintock, and A. Stefanovska, *Cardiovasc. Eng.* **4**, 89 (2004).
- <sup>47</sup> L. W. Sheppard, V. Vuksanović, P. V. E. McClintock, and A. Stefanovska, *Phys. Med. Biol.* **56**, 3583 (2011).
- <sup>48</sup> V. Ticcinielli, T. Stankovski, D. Iatsenko, A. Bernjak, A. E. Bradbury, A. R. Gallagher, P. B. M. Clarkson, P. V. E. McClintock, and A. Stefanovska, *Front. Comput. Physiol.* **8**, 749 (2017).
- <sup>49</sup> S. Smirni, A. D. McNeilly, M. P. MacDonald, R. J. McCrimmon, and F. Khan, *Sci. Rep.* **9**, 186 (2019).
- <sup>50</sup> I. V. Tikhonova, A. A. Grinevich, and A. V. Tankanag, *Biomed. Signal Process. Control* **71**, 103091 (2022).
- <sup>51</sup> I. V. Tikhonova, A. V. Tankanag, I. E. Guseva, and A. A. Grinevich, *Biomed. Signal Process. Control* **79**, 104222 (2023).
- <sup>52</sup> D. Iatsenko, A. Bernjak, T. Stankovski, Y. Shioyai, P. J. Owen-Lynch, P. B. Clarkson, A. Stefanovska, and P. V. E. McClintock, *Phil. Trans. R. Soc. Lond. A* **371**, 20110622 (2013).
- <sup>53</sup> M. Gruszecki, G. Lancaster, A. Stefanovska, J. P. Neary, R. T. Dech, W. Guminski, A. F. Frydrychowski, J. Kot, and P. J. Winkowski, *Sci. Rep.* **8**, 3057 (2018).
- <sup>54</sup> A. Grinsted, J. C. Moore, and S. Jevrejeva, *Nonlin. Process. Geophys.* **11**, 561 (2004).
- <sup>55</sup> D. S. Bloomfield, R. T. J. McAteer, B. W. Lites, P. G. Judge, M. Mathioudakis, and F. P. Keenan, *Astrophys. J.* **617**, 623 (2004).
- <sup>56</sup> R. Donner and M. Thiel, *Astron. Astrophys.* **475**, L33 (2007).
- <sup>57</sup> A. Volvach, G. Kurbasova, and L. Volvach, *Heliyon* **10**, e23237 (2024).
- <sup>58</sup> L. Aguiar-Conraria, N. Azevedo, and M. J. Soares, *Physica A* **387**, 2863 (2008).
- <sup>59</sup> L. Aguiar-Conraria and M. J. Soares, *Empir. Econ.* **40**, 645 (2011).
- <sup>60</sup> L. Vacha and J. Barunik, *Energy Econ.* **34**, 241 (2012).
- <sup>61</sup> C. Aloui and B. Hkiri, *Econ. Model.* **36**, 421 (2014).
- <sup>62</sup> J. C. Reboredo, M. A. Rivera-Castro, and A. Ugolini, *Energy Econ.* **61**, 241 (2017).
- <sup>63</sup> D. Abboud, S. Baudin, J. Antoni, D. Rémond, M. Eltabach, and O. Sauvage, *Mech. Syst. Signal Process.* **75**, 280 (2016).
- <sup>64</sup> M. Morris, S. Yamazaki, and A. Stefanovska, *J. Biol. Rhythms* **37**, 310 (2022).
- <sup>65</sup> A. Monterde, A. Calleja-López, M. Aguilera, X. E. Barandiaran, and J. Postill, *Inf. Commun. Soc.* **18**, 930 (2015).
- <sup>66</sup> F. Zernike, *Physica* **5**, 785 (1938).
- <sup>67</sup> A. Pikovsky, M. Rosenblum, and J. Kurths, *Synchronization—A Universal Concept in Nonlinear Sciences* (Cambridge University Press, Cambridge, 2001).
- <sup>68</sup> D. Iatsenko, P. V. E. McClintock, and A. Stefanovska, *Digit. Signal Process.* **42**, 1 (2015).
- <sup>69</sup> C. Torrence and P. J. Webster, *J. Clim.* **12**, 2679 (1999).
- <sup>70</sup> L. Keselbrener and S. Akselrod, *IEEE Trans. Biomed. Eng.* **43**, 789 (1996).
- <sup>71</sup> A. S. Karavaev, A. S. Borovik, E. I. Borovkova, E. A. Orlova, M. A. Simonyan, V. I. Ponomarenko, V. V. Skazkina, V. I. Gridnev, B. P. Bezruchko, M. D. Prokhorov, and A. R. Kiselev, *Biophys. J.* **120**, 2657 (2021).
- <sup>72</sup> I. Mizeva, C. D. Maria, P. Frick, S. Podtaev, and J. Allen, *J. Biomed. Opt.* **20**, 037007 (2015).
- <sup>73</sup> L. W. Sheppard, J. R. Bell, R. Harrington, and D. C. Reuman, *Nat. Clim. Change* **6**, 610 (2016).
- <sup>74</sup> J. Rowland-Adams and A. Stefanovska, *Front. Physiol.* **11**, 613183 (2021).
- <sup>75</sup> D. Iatsenko, G. Lancaster, S. McCormack, J. Newman, G. V. Policharla, V. Ticcinielli, T. Stankovski, and A. Stefanovska, Lancaster University; see <https://doi.org/10.5281/zenodo.3470856> (2019).
- <sup>76</sup> J. Newman, G. Lancaster, and A. Stefanovska, Lancaster University; see <https://doi.org/10.5281/zenodo.3470856> (2018).
- <sup>77</sup> R. W. Thatcher, D. M. North, and C. J. Biver, *NeuroImage* **42**, 1639 (2008).
- <sup>78</sup> D. J. DeShazer, R. Breban, E. Ott, and R. Roy, *Phys. Rev. Lett.* **87**, 044101 (2001).
- <sup>79</sup> O. V. Sosnovtseva, A. N. Pavlov, E. Mosekilde, K. Yip, N. Holstein-Rathlou, and D. J. Marsh, *Am. J. Physiol. Renal Physiol.* **293**, F1545–F1555 (2007).
- <sup>80</sup> G. Carl, D. Doktor, D. Koslowsky, and I. Kühn, *Stoch. Environ. Res. Risk Assess.* **27**, 1221–1230 (2013).
- <sup>81</sup> E. A. K. Cohen and A. T. Walden, *IEEE Trans. Signal Process.* **58**, 2964 (2010).
- <sup>82</sup> S. Holm, *Astrophys. Space Sci.* **357**, 106 (2015).
- <sup>83</sup> T. Schreiber and A. Schmitz, *Physica D* **142**, 346 (2000).
- <sup>84</sup> G. Lancaster, D. Iatsenko, A. Pidde, V. Ticcinielli, and A. Stefanovska, *Phys. Rep.* **748**, 1 (2018).
- <sup>85</sup> L. W. Sheppard, A. Stefanovska, and P. V. E. McClintock, *Phys. Rev. E* **85**, 046205 (2012).
- <sup>86</sup> F. Yasuma and J. Hayano, *Chest* **125**, 683 (2004).
- <sup>87</sup> M. Bračič Lotrič and A. Stefanovska, *Physica A* **283**, 451 (2000).
- <sup>88</sup> Y. Shioyai, A. Stefanovska, and P. V. E. McClintock, *Phys. Rep.* **488**, 51 (2010).
- <sup>89</sup> G. Stanley, D. Verotta, N. Craft, R. A. Siegel, and J. B. Schwartz, *Am. J. Physiol. Heart Circ. Physiol.* **270**, H1833 (1996).
- <sup>90</sup> K. Keissar, L. R. Davrath, and S. Akselrod, *Phil. Trans. R. Soc. A* **367**, 1393 (2009).
- <sup>91</sup> Y. A. Abdulhameed, A. G. Habib, P. V. E. McClintock, and A. Stefanovska, “Phase coherence between cardiovascular oscillations in malaria: The basis for a possible diagnostic test,” in *Physics of Biological Oscillators: New Insights into Non-Equilibrium and Non-Autonomous Systems*, edited by A. Stefanovska and P. V. E. McClintock (Springer International Publishing, Cham, 2021), pp. 401–419.
- <sup>92</sup> G. Lancaster, T. Debevec, G. P. Millet, M. Poussel, S. J. Willis, M. Mramor, K. Goričar, D. Osredkar, V. Dolžan, and A. Stefanovska, *J. Physiol.* **598**, 2001–2019 (2020).
- <sup>93</sup> J. Bjerkan, G. Lancaster, B. Meglič, J. Kobal, T. J. Crawford, P. V. E. McClintock, and A. Stefanovska, *Brain Res. Bull.* **201**, 110704 (2023).
- <sup>94</sup> P. Van Mierlo, M. Papadopoulou, E. Carrette, P. Boon, S. Vandenberghe, K. Vonck, and D. Marinazzo, *Prog. Neurobiol.* **121**, 19 (2014).
- <sup>95</sup> A. J. Mackintosh, R. de Bock, Z. Lim, V.-N. Trulley, A. Schmidt, S. Borgwardt, and C. Andreou, *Neurosci. Biobehav. Rev.* **120**, 354 (2021).
- <sup>96</sup> T. D. Satterthwaite, R. Ciric, D. R. Roalf, C. Davatzikos, D. S. Bassett, and D. H. Wolf, *Hum. Brain Mapp.* **40**, 2033 (2019).

- <sup>97</sup>A. Delorme, *Sci. Rep.* **13**, 2372 (2023).
- <sup>98</sup>E. Arad, R. P. Bartsch, J. W. Kantelhardt, and M. Plotnik, *PLoS One* **13**, e0197153 (2018).
- <sup>99</sup>E. T. Rolls, W. Cheng, and J. Feng, *Transl. Psychiatry* **11**, 70 (2021).
- <sup>100</sup>S. Petkoski, P. Ritter, and V. K. Jirsa, *Cereb. Cortex* **33**, 6241 (2023).
- <sup>101</sup>D. Liloia, J. Manuella, T. Costa, R. Keller, A. Nani, and F. Cauda, *Eur. Arch. Psychiatry Clin. Neurosci.* **274**, 3 (2023).
- <sup>102</sup>R. Coben, A. R. Clarke, W. Hudspeth, and R. J. Barry, *Clin. Neurophysiol.* **119**, 1002 (2008).
- <sup>103</sup>A. Dickinson, M. Daniel, A. Marin, B. Gaonkar, M. Dapretto, N. M. McDonald, and S. Jeste, *Biol. Psychiatry Cogn. Neurosci. Neuroimaging* **6**, 59 (2021).
- <sup>104</sup>M. M. Chan, M.-C. Chan, O. L.-H. Lai, K. Krishnamurthy, and Y. M. Han, *Biomedicines* **10**, 1132 (2022).
- <sup>105</sup>J. Bjerkan, J. Kobal, G. Lancaster, S. Šešok, B. Meglič, P. V. E. McClintock, K. Budohoski, P. Kirkpatrick, and A. Stefanovska, *Brain Commun.* **6** (2024).
- <sup>106</sup>A. Arinyo-i-Prats, V. J. López-Madróna, and M. Paluš, *NeuroImage* **292**, 120610 (2024).
- <sup>107</sup>M. Günther, J. W. Kantelhardt, and R. P. Bartsch, *Front. Netw. Physiol.* **2**, 893743 (2022).
- <sup>108</sup>M. G. Crosby, *Proc. IRE* **25**, 472 (1937).
- <sup>109</sup>W. Mumtaz, S. Rasheed, and A. Irfan, *Biomed. Signal Process. Control* **68**, 102741 (2021).



## Chapter 4

# Theta and alpha connectivity in children with autism spectrum disorder

### **Student contribution:**

The student curated the data and acquired an additional validation dataset from external sources. They performed formal analysis and investigation on both datasets and created a software environment based on existing methods for this analysis. The student also classified the results, wrote and edited the manuscript, and generated the figures included in the paper.

This research is published in Brain Communications.

Samuel JK Barnes, Megan Thomas, Peter VE McClintock, and Aneta Stefanovska.

“Theta and alpha connectivity in children with autism spectrum disorder”. In: *Brain Communications* (2025), fcac084

# BRAIN COMMUNICATIONS

## Theta and alpha connectivity in children with autism spectrum disorder

 Samuel J. K. Barnes,<sup>1</sup>  Megan Thomas,<sup>2,3</sup> Peter V. E. McClintock<sup>1</sup> and  Aneta Stefanovska<sup>1</sup>

Spontaneous electroencephalography (EEG) measurements have demonstrated putative variations in the neural connectivity of subjects with autism spectrum disorder, as compared to neurotypical individuals. However, the exact nature of these connectivity differences has remained unknown, a question that we now address. Resting-state, eyes-open EEG data were recorded over 20 min from a cohort of 13 males aged 3–5 years with autism spectrum disorder, and nine neurotypical individuals as a control group. We use time-localized, phase-based methods of data analysis, including wavelet phase coherence and dynamical Bayesian inference. Several 3 min signal segments were analysed to evaluate the reproducibility of the proposed measures. In the autism spectrum disorder cohort, we demonstrate a significant ( $P < 0.05$ ) reduction in functional connectivity strength across all frontal probe pairs. In addition, the percentage of time during which frontal regions were coupled was significantly reduced in the autism spectrum disorder group compared to the control group. These changes remained consistent across repeated measurements. To further validate the findings, an additional resting-state EEG dataset (eyes open and closed) from 67 individuals with autism spectrum disorder and 66 control group individuals (male, 5–15 years) was assessed. The functional connectivity results demonstrated a reduction in theta and alpha connectivity on a local, but not global, level. No association was found with age. The connectivity differences observed suggest the potential of theta and alpha connectivity as biomarkers for autism spectrum disorder. Additionally, the robustness to amplitude perturbations of the methods proposed here makes them particularly suitable for the clinical assessment of autism spectrum disorder and of the efficacy of therapeutic interventions.

1 Department of Physics, Lancaster University, Lancaster LA1 4YB, UK

2 Department of Paediatrics, Blackpool Teaching Hospitals NHS Foundation Trust, Blackpool FY3 8NR, UK

3 Department of Pediatrics, Faculty of Medicine, Dalhousie University, Halifax, Nova Scotia, Canada NS B3H 4R2

Correspondence to: Aneta Stefanovska

Department of Physics, Lancaster University

Bailrigg, Lancaster LA1 4YB, UK

E-mail: [aneta@lancaster.ac.uk](mailto:aneta@lancaster.ac.uk)

**Keywords:** electroencephalogram; neural connectivity; phase coherence; wavelet; coupling

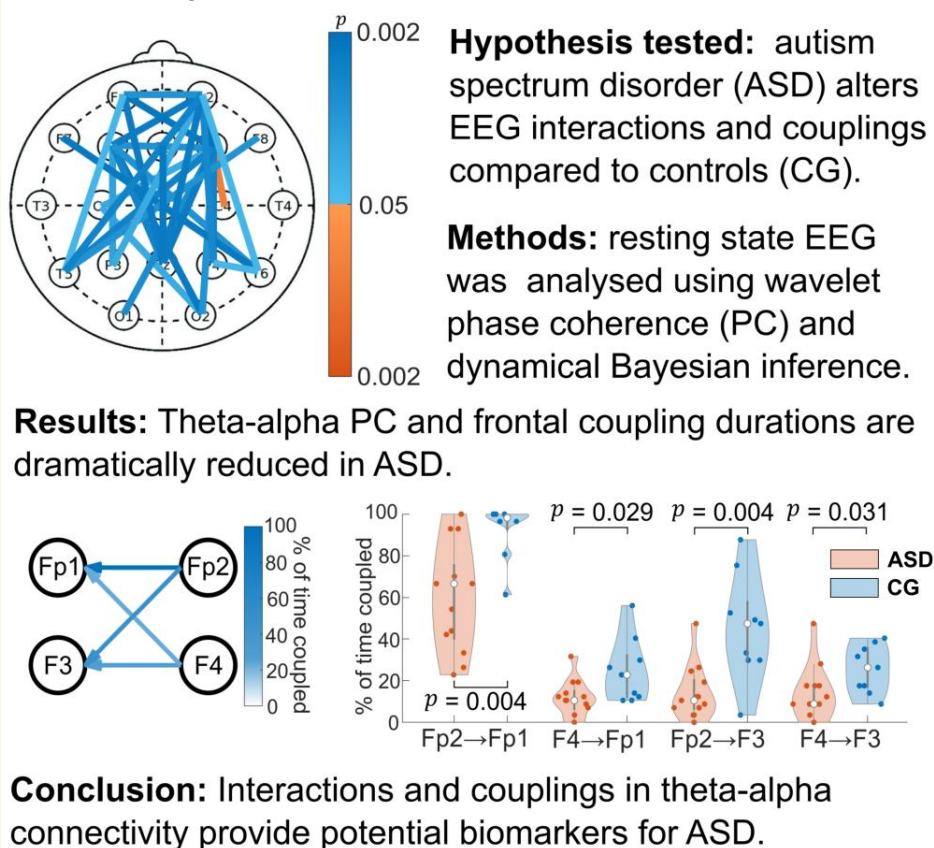
Received September 09, 2024. Revised January 10, 2025. Accepted February 18, 2025. Advance access publication February 19, 2025

© The Author(s) 2025. Published by Oxford University Press on behalf of the Guarantors of Brain.

This is an Open Access article distributed under the terms of the Creative Commons Attribution License (<https://creativecommons.org/licenses/by/4.0/>), which permits unrestricted reuse, distribution, and reproduction in any medium, provided the original work is properly cited.

## Graphical Abstract

## Theta and alpha connectivity is reduced in autism spectrum disorder



## Introduction

Altered neural connectivity is a hallmark of autism spectrum disorder (ASD).<sup>1-7</sup> In general, a prevailing pattern of hypo-connectivity in the low- and medium-frequency bands, alongside over-connectivity in the high-frequency intervals, has been observed.<sup>8</sup> Concurrently, the role of temporal regulation in maintaining couplings between brain regions has become apparent in a wide range of neurological conditions including ASD.<sup>9-11</sup> Despite this, previous results exhibit considerable variability.<sup>12</sup> Particular inconsistencies pertain to the balance between long- and short-range connections in ASD,<sup>8,13-16</sup> and the relative hyperconnectivity<sup>17,18</sup> or hypoconnectivity<sup>16,19-21</sup> of frontal regions. These discrepancies can be attributed partially to the heterogeneity of ASD populations,<sup>22</sup> variations in measurement approaches<sup>23,24</sup> and alternative data analysis methodologies.<sup>25</sup> Additionally, the duration of observation may have been insufficient to reveal

couplings. Detecting coupled oscillatory behaviour requires the observation of at least thirty cycles, and is therefore dependent on the frequency of interest. This requirement is particularly relevant for EEG data, which is often highly nonlinear, non-autonomous, and non-stationary, leading to fluctuations in frequency content over time.<sup>26</sup>

When measuring brain activity in children, movement artefacts are inevitable and should be anticipated and accounted for. Artefact-resilient approaches are therefore necessary for findings to be reliable and appropriate for clinical application. The methods employed in this study focus on phase, rather than amplitude, dynamics. By also focusing on finite-time dynamics, our approach acknowledges the non-autonomous nature of underlying oscillatory modes and reduces the effects of amplitude perturbations on measured connectivity. Additionally, our method detects non-linear interactions, overlooked by linear, statistical approaches.<sup>27,28</sup> The wavelet transform enables an optimal trade-off between the time-localization and frequency

resolution, avoiding the bias in Fourier based approaches.<sup>29</sup> Furthermore, our approach<sup>26,30</sup> enables the simultaneous detection of phase differences across multiple modes within a frequency band, in contrast to methods that reduce the phase to a single value.<sup>31-33</sup> Taken together, these features enable the present approach to provide an interpretable way of uncovering deterministic oscillations within multi-scale, nonlinear and time-varying data.

In recent years, there has been a growing emphasis on adopting effective connectivity methods for assessing brain network dynamics.<sup>1,34</sup> Effective connectivity approaches can capture the directionality of couplings within the brain whilst also enabling the inference of causal relationships between different regions. In contrast, functional connectivity methods may mistake a common external factor for mutual interaction.<sup>35</sup> Novel approaches that incorporate directionality and infer causality may offer a more comprehensive view of the complex interactions occurring within the brain. Living systems are inherently non-autonomous. Therefore, when evaluating time series of biological origin, time should be treated as an explicit physical parameter.<sup>36</sup> To account for underlying temporal variability, here effective connectivity is calculated over a sequence of data windows. The duration of couplings may then be calculated to assess their presence over a larger time interval. The non-autonomous nature of neural couplings, which time-asymptotic approaches would disregard,<sup>30,37</sup> may thereby be captured.

Individuals with ASD often exhibit deficits in executive function (EF), manifesting as several core challenges.<sup>21,38-40</sup> Previous research has associated frontal areas of the brain with EF,<sup>41-43</sup> and ASD individuals exhibit structural differences in these regions, such as minicolumnar abnormalities<sup>44</sup> and brain overgrowth.<sup>45,46</sup> Additionally, an imbalance of GABA and glutamate has been identified, prompting pharmacological interventions that have enhanced prefrontal connectivity in ASD individuals.<sup>47</sup> Multiple studies have also reported decreased inter-hemispheric connectivity in ASD<sup>48-51</sup> particularly in homotopic regions.<sup>52</sup>

We hypothesize that, using our novel approach to data analysis, we can quantify the deficits in frontal inter-hemispheric connectivity and characterize their time-variations. Our results demonstrate a significant reduction in alpha and theta functional connectivity in children with ASD. It is hoped that this approach will provide a valuable tool in the quest for quantitative biomarkers characterizing ASD.

## Materials and methods

Fourteen males aged 3–5 years with diagnoses of ASD were identified through Blackpool Teaching Hospitals NHS Foundation Trust's Child Development Centre. Ethical approval was obtained from the NRES Committee North West — Lancaster REC, reference number: 13/NW/0509. Participants' parents provided informed consent, and the clinical study was registered as UKCRN ID14936. Ten age-matched neurotypical controls were recruited through

advertisements at Health and University sites and nurseries. One individual in each group was unable to complete the full recording. Inclusion criteria were either a clear diagnosis of an ASD, confirmed by an Autism Diagnostic Observation Schedule (ADOS) assessment; or no concerns about development or features of ASD, confirmed by a developmental history and ADOS assessment. Exclusion criteria were epilepsy or undiagnosed seizure episodes; medications known to affect brain function; structural brain abnormalities; chromosome abnormalities; and, for the control group only, a first-degree relative with ASD diagnosis. Initially, the study aimed to recruit a similar number of female participants. However, due to the lower incidence of diagnosed ASD in females, it was not possible to recruit enough girls with an ASD diagnosis within the study's time frame. A small age range was selected to control for developmental changes. Based upon the sizes of the ASD and CG groups, sensitivity analysis was performed using G\*Power. Due to the sample sizes used in this study, effect sizes of 1.387 were able to be reliably detected. A full summary, including further details of the sensitivity analysis, is given in the [Supplementary material](#). The age, ADOS score and hand preference of each participant are provided in [Table 1](#).

## Data recording

EEG signals were recorded using a Nicolet cEEG instrument (Viasys Healthcare, USA) at a sampling rate of 256 Hz, with 19 probes and one reference electrode placed on the child's scalp using the standard 10–20 configuration. EEG was recorded for 20 min while the child was in an eyes-open resting condition and sitting on a chair, their stroller, or their parent's lap. When necessary to maintain a relaxed state, participants were presented with soap bubbles or smartphone videos. Details for individual participants are provided in [Table 1](#). A 3 min segment was selected from the data, based on a video of the child recorded during the data collection. It was chosen as being the interval where the child appeared to move the least. Henceforth, this shall be referred to as the 'video' segment. As this segment was expected to have minimal movement artefacts, it provided a reliable starting point for the initial investigation. A retest procedure was employed to assess the robustness of the findings and account for the real-world conditions encountered in clinical settings. Five additional segments, each lasting 3 min, were chosen by visual inspection of the data, aiming to avoid segments with the largest spikes in the time series. Details regarding the pre-processing of the data are given in the [Supplementary material](#).

## Additional dataset

An additional dataset was acquired to further validate the results. The Healthy Brain Network (HBN) biobank contains multimodal brain imaging datasets complemented by a wide range of phenotypic data.<sup>53</sup> The recruitment procedure utilized a community-referred model, in which

**Table 1** Participant details

Subjects	Age (months)	ADOS score	Hand R: 53.8% L: 7.7% ND: 38.5%	Setting		Activity			State		
				Lap	Chr	Rest	Screen	BBles	Slp	Qt	SM
<b>ASD</b>	<b>Mean: 50 ± 6</b>	<b>Mean: 17.6 ± 3.5</b>									
1	42	19	ND	X		X			X		
2	45	19	ND	X				X			X
3	50	19	R	X			X			X	
4	56	11	ND	X		X				X	
5	50	22	ND	X		X				X	
6	50	20	ND	X		X				X	
7	52	20	R		X		X			X	
8	47	21	ND		X	X				X	
9	56	13	L		X	X				X	
10	43	19	ND	X			X			X	
11	58	16	R	X			X			X	
12	56	18	R	X			X			X	
13	58	12	R	X		X				X	
<b>CG</b>	<b>Mean: 46 ± 7</b>	<b>Mean: 1 ± 1</b>	<b>R: 55.6% L: 0% ND: 44.4%</b>								
1	55	0	R	X			X		X		
2	45	2	R		X	X				X	
3	53	0	R		X		X			X	
4	55	0	ND	X		X				X	
5	44	2	ND	X		X					X
6	44	0	R	X		X				X	
7	47	1	R	X		X				X	
8	36	2	ND	X		X					X
9	36	2	ND	X		X				X	

The state of each participant during the measurements for each group. The first four columns give summary data: ASD (autism spectrum disorder) or CG (control group) subject number; age in months; ADOS (autism diagnostic observation schedule) score; and right (R) or left (L) or not-defined (ND) handedness. The next two columns show whether the participant was sitting on their parents' lap (Lap) or on a chair (Chr). The next three columns show what the participant was doing during the recording, either at rest (Rest), or watching a screen (Screen), or watching bubbles (BBles). The final three columns indicate their level of activity during the recording, whether sleepy (Slp), quiet (Qt), or exhibiting some small movements (SM). All participants were male. Details regarding effect size are given in the [Supplementary material](#).

**Table 2** Median values and significances between groups in the HBN data

Groups	ASD (n = 67)			CG (n = 66)			Group comparison
	Median	SD	Range	Median	SD	Range	
Age (years)	8.73	2.58	9.61	8.99	2.76	9.95	0.721
IQ	100	17.3	84.0	104	11.8	68.0	0.0517
Handedness	68.4	58.3	198	86.7	51.8	196	0.0529
SRS	85	30.9	114	26	15.8	81	$4.07 \times 10^{-19}$

The median, standard deviation (SD) and range of age, IQ, handedness and social responsiveness score (SRS) in the ASD and CG groups. All participants were male. The Wilcoxon rank-sum test was used to evaluate the differences in potentially confounding factors between groups; none of which were significant apart from the SRS. Handedness was evaluated using the Edinburgh Handedness Questionnaire, with 100 being right hand dominant, 0 ambidextrous and -100 implying left-hand dominance.

advertisements invited concerned parents and caregivers to seek diagnosis and support for their children if needed. From this neurodiverse cohort, several children were diagnosed with ASD, while a group of individuals were given no diagnosis and acted as a control group. Age, gender, IQ and handedness were matched between the groups compared. Statistical descriptions of each group's composition are given in [Table 2](#).

The HBN data had been recorded using a 128-channel EEG Geodesic Hydrocel System by Electrical Geodesics

Inc. (EGI) sampled at 500 Hz with a bandpass of 0.1–100 Hz. The resting state measurement procedure entailed viewing a fixation cross on a computer screen, with eyes sequentially opened and closed in 20/40 s repeats.<sup>53</sup> The recordings lasted 5 min, and the central 3 min were selected for analysis. Except where stated otherwise, the same procedures and analysis were applied to both datasets. The results and discussion presented in this paper generally describe the Blackpool data, with the HBN dataset being treated as a validation dataset.

### Frequency bands

For three reasons, we chose to merge the theta–alpha range into a single frequency interval (3.5–12 Hz). First, the limits of the five traditional frequency bands (delta, theta, alpha, beta and gamma) were not clearly distinguishable in the power spectra of the EEG data. Thus, it was not possible to draw clear boundaries between the alpha and theta bands for any given subject without crossing peaks in the spectra of other subjects. Secondly, it has been found that EEG power spectra evolve during developmental years as children's brains undergo maturation of cellular substrates.<sup>54,55</sup> Specifically, alpha activity has been found to occur at lower frequencies (~8 Hz instead of ~10 Hz) in younger children.<sup>54,56</sup> Finally, previous studies of EEG activity in children with ASD do not use strict limits for their frequency bands, and no standard has been established to date.

### Data analysis

Rate processes are ubiquitous in nature. From celestial motion to cellular metabolism, oscillatory behaviour is pervasive across all spatial and temporal scales of existence. The brain is no different, with electrical activity that propagates information between regions, often taking certain characteristic frequencies dependent on the information it conveys.<sup>57</sup> The exceedingly high connectivity between neurons gives rise to networks of oscillators. EEG signals are generated by transmembrane ion currents in the pyramidal neurons of the cortex and are transmitted to electrodes on the scalp via volume conduction.<sup>58</sup> The nature of these signals is inherently oscillatory. To elucidate their underlying behaviour, we focus on time-resolved oscillatory modes present in the recorded EEG signals.

### Time-frequency representation

The first step in identifying these modes is to explore their presence in the time-frequency domain. The wavelet transform can reveal potential non-autonicity within oscillations.<sup>59</sup> Additionally, the logarithmic frequency resolution offered by this method provides a more balanced distribution of information across frequency bands. The time-frequency representation is generated by sliding wavelets of varying scales along the input signal and transforming the overlapping parts into the frequency domain. Lower frequencies exhibit fewer oscillations within a given time, necessitating a larger scale to capture the oscillatory activity effectively. Conversely, higher frequencies require less time to be captured, allowing the use of a smaller scale. This optimizes the trade-off between time-localization and frequency resolution, providing greater time-localization at high frequencies and improved frequency resolution at low frequencies. The wavelet transform was therefore chosen for the initial analysis of these signals. It is defined by

$$W_T(s, t) = \int_{-L/2}^{L/2} \Psi(s, u - t) f(u) du, \quad (1)$$

where the mother wavelet,  $\Psi(s, t)$ , is the object contracted and dilated to reveal oscillatory behaviour at various times and scales. For the present study, the Morlet mother wavelet was used,

$$\Psi(s, t) = \frac{1}{\sqrt{\pi}} \left( e^{\frac{2\pi i \omega_c t}{s}} - e^{-\frac{2\pi \omega_c^2}{2}} \right) e^{-\frac{t^2}{2s^2}}, \quad (2)$$

which is composed of a sinusoidal wave within a Gaussian envelope.<sup>60</sup> The frequency of the sinusoid allows one to focus upon a given scale, while the Gaussianity ensures a smoothly decaying amplitude and, therefore, greater time-localization. The enhanced temporal resolution, and its common use in neuroscience,<sup>61</sup> motivated the selection of this wavelet.

In contrast, linear approaches, such as those based on the Fourier transform, often use a fixed window size when evaluating the time-frequency domain. This fixed window length leads to suboptimal multiscale analysis. Furthermore, linear methods often reduce the amount of information captured by averaging over time, or filtering out potentially deterministic oscillations that are falsely categorized as noise.<sup>30</sup> A cornerstone of the present approach is the maximal preservation of the underlying information.

The wavelet transform generates a complex matrix containing both phase and amplitude information, facilitating a comprehensive multiscale analysis across time. This dual representation captures the magnitude of specific frequencies while also elucidating the temporal evolution of oscillatory modes, enabling a more nuanced understanding of the underlying dynamics. A simulated example signal (Fig. 1A and B) containing two oscillatory modes at different frequencies is analysed in Fig. 1C and D. It is evident that the wavelet approach readily elucidates that there are two modes with time-varying frequencies representative of alpha and theta oscillations. The time-localization and logarithmic frequency resolution reveal the non-autonomous nature of the oscillatory modes.

When considering non-autonomous dynamics, time-averaged approaches may not always faithfully represent the number of oscillatory modes present in the signal. For example, Fig. 1D in isolation may naively give the impression that additional oscillatory modes are present. The time-frequency domain, as illustrated in Fig. 1C, reveals, however, that this is not the case. The false identification of modes is a common mischaracterization<sup>30</sup> resulting from a failure to consider the time domain. Once the oscillatory modes have been identified, functional connectivity methods may then be applied to ascertain dependences between the respective oscillators.

### Wavelet phase coherence

The wavelet transform assigns phase values to each point in the time-frequency domain for the underlying oscillatory modes. Following this, wavelet phase coherence (WPC) is calculated to determine the interaction between a pair of signals and how it develops over time.<sup>62–65</sup> The consistency of



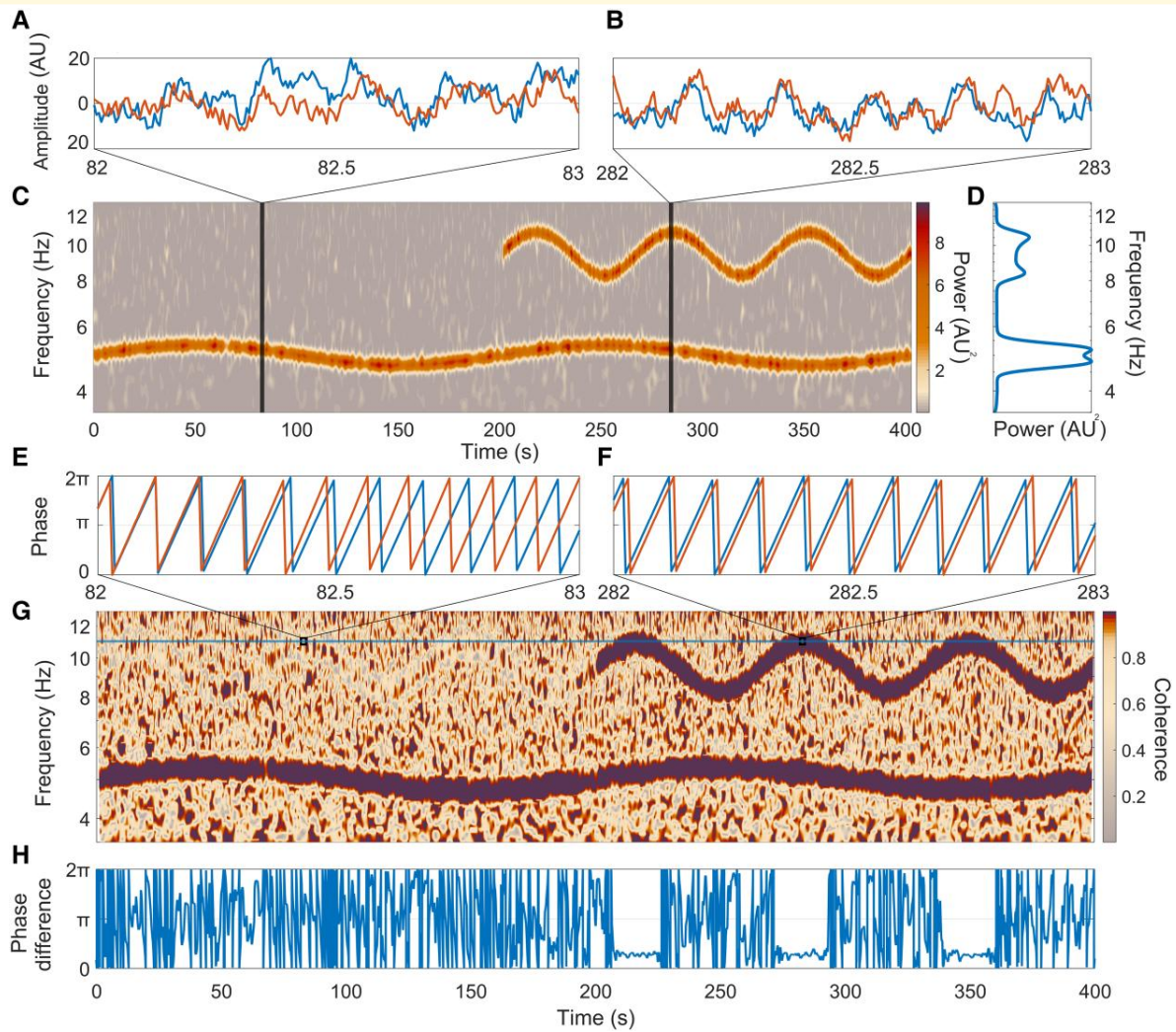


**Figure 1 Demonstration of wavelet phase coherence using a pair of simulated time series.** (A). A 1s-long window taken from the first half of the simulated time series. Further details of the modelling procedure and parameters are given in the [Supplementary material](#). (B) A 1s-long window taken from the second half of the simulated time series. (C) Time-frequency representation of the warmer coloured (orange) time series' power calculated using the wavelet transform (Morlet wavelet, frequency resolution = 4). (D) Time-averaged power of the warm coloured (orange) series. The frequency axes of (C) and (D) are logarithmic. (E–H) A step-by-step evaluation of wavelet phase coherence. (E, F) The phases of the time series, calculated at 11 Hz, for intervals corresponding to those in A and B. (G) Time-localized phase coherence between the warm (orange) and cooler coloured (blue) time series. The horizontal line at 11 Hz indicates where the phases (E, F) and phase difference (H) were evaluated. (H) The phase difference at 11 Hz is almost flat across times that correspond to high time-localized coherence values.

the phase difference between the signals at each point in the time-frequency domain is evaluated across several (in the present case 10) complete oscillations at a given frequency,  $f$ ,

$$\text{WPCt}, f = \frac{f}{10} \left| \int_{t-\frac{f}{10}}^{t+\frac{f}{10}} e^{i(\phi_{s,f}^1 - \phi_{s,f}^2)} ds \right|. \quad (3)$$

Subsequently, a value is allocated between zero (complete lack of coherence) and unity (perfect coherence—where the difference in the phases ( $\phi_{s,f}^1 - \phi_{s,f}^2$ ) at each point in the time-frequency domain remains constant over the time interval).

The WPC is completely independent of amplitude dynamics and depends purely on the phase of the oscillations. By only considering phase dynamics, this approach is more resilient to movement artefacts and noise than its amplitude-weighted counterpart.<sup>26</sup>

An illustrative example demonstrating time-localized WPC is depicted in [Fig. 1A–H](#). Two model time series are represented by the blue and orange lines respectively in [Fig. 1A and B](#). Specific details of the modelling procedure used to generate these time series are outlined in the [Supplementary material](#). To summarize, the orange line lacks the high-frequency (HF) mode for the first 200 s (see

Fig. 1C for the time-frequency representation of the orange line), the blue line is modelled similarly, but with the HF mode lasting the entire 400 s. Independent realizations of white Gaussian noise were applied to both of the simulated signals. Consequently, there is no shared high frequency oscillatory component between these signals for the first 200 s, resulting in a continuously changing phase difference (Fig. 1E). This variability in phase difference is further depicted in the time-localized phase coherence in Fig. 1G.

To contrast this inconsistency between the phases of the HF mode in the first half of the signal, coherent signals were generated in the subsequent half; establishing shared behaviour between the time series during this interval. WPC detects this shared oscillatory component by examining the phase difference between the oscillations. The phase difference at 11 Hz (Fig. 1H) is constant during intervals of high time-localized coherence (Fig. 1G).

### Global coherence

The wavelet mean field was used to evaluate global coherence across the brain. For  $N$  time series evaluated simultaneously at different probe locations, we have,

$$r_\sigma(t) = (1/N) \sum_{n=1}^N w_{n,\sigma}(t), \quad (4)$$

where,

$$w_{n,\sigma}(t) = W_{n,\sigma}(t) / \sqrt{(1/NT) \sum_{n=1}^N \sum_{t=1}^T W_{n,\sigma}(t) \overline{W_{n,\sigma}(t)}}. \quad (5)$$

The corresponding wavelet transforms across time and scale are represented as  $W_{n,\sigma}(t)$ , with the overbar denoting complex conjugation. When the time series exhibit similar phases at a given time and frequency, the average  $\sum_{n=1}^N w_{n,\sigma}(t)$  will yield a large complex number due to the reinforcement of synchronized oscillations. Conversely, when the probe signals are unsynchronized, the phasors will point in random directions in the complex plane and cancel. The degree of interaction across the brain is calculated with the mean-squared magnitude of the wavelet mean field,  $(1/T) \sum_{t=1}^T |r_\sigma(t)|^2$ . This takes a value between zero and unity, where 1 represents complete synchrony across the brain and 0 is perfect desynchronization.<sup>66</sup>

### Dynamical Bayesian inference

Functional connectivity methods, such as those outlined above, identify statistical dependences between different brain regions.<sup>35</sup> While this is helpful in highlighting differences between groups, it is essentially a descriptive measure of the common behaviour between a pair of time series. Further, although high values of functional connectivity may reflect underlying neural connections, they may also arise due to a common external influence. Effective connectivity goes beyond this by explicitly describing the influence

that one neural region exerts over another. In this way, the strength and direction of influence between regions can be described and quantified. This information comprises the coupling between systems, and the coupling function (CF) describes the way in which information is propagated from one oscillator to another.<sup>67</sup> Dynamical Bayesian inference<sup>68</sup> (DBI) was chosen to detect phase couplings between the probes. To appreciate the utility of CFs, consider a pair of unidirectionally coupled phase oscillators,

$$\begin{aligned} \phi_X &= \omega_X, \\ \phi_P &= \omega_P + q_P(\phi_X, \phi_P) = \omega_P + E \cos(\phi_X + \pi/2.5), \end{aligned} \quad (6)$$

where the phase of oscillator  $X$  ( $\phi_X$ ) modulates the phase of  $P$  ( $\phi_P$ ) according to the behaviour of a CF  $q_P(\phi_X, \phi_P)$ . As an illustration, this system (Fig. 2A) was simulated numerically, and DBI was applied to reconstruct the coupling functions over a range of coupling strengths. The couplings are represented in Fig. 2B–E, with varying amplitudes, demonstrating that in addition to reconstructing the shape of CFs, DBI can also infer the coupling strength. Directionality may also be captured using this approach. In Fig. 2E, the coupling function is almost zero as there is no information flow from  $P$  to  $X$ ; thus, via the inference of and comparison between CFs, one can also deduce the direction of an interaction. Real data are also used to demonstrate the bidirectional nature of the couplings under investigation (Fig. 2G–J).

By use of a sliding time window, DBI can evaluate the presence and time evolution of couplings between signals, and so can detect whether the phase behaviour at one location is influencing that at another. DBI is based on Bayes' theorem and so uses prior knowledge of the parameters of a system to evaluate its current state. Time-evolving dynamics can then be inferred as the information is propagated between windows. Mathematical details of this approach were given earlier.<sup>68–70</sup> Importantly, as the coupling is assessed over a sequence of windows, its dynamical evolution may be investigated. Even at rest, the influence of brain regions over one another changes with time, so that asymptotic approaches may inadvertently average out interesting transient phenomena. Furthermore, quantifying the coupling strength between probes may lead to false conclusions when averaging over time. A high coupling strength averaged across the entire interval might lead to the incorrect conclusion that the coupling remained consistent throughout. In reality, it could be attributed to one isolated, exceptionally high value in a single window. To avoid this problem, we instead measure the percentage of time during which probes remain coupled. The dynamical nature of this coupling is indicated by Fig. 2L. Here, the dashed lines represent the respective intersubject surrogates, while the solid lines represent the coupling strengths of randomly chosen CG and ASD individuals. In this way, the amount of time spent in a coupled/decoupled state is calculated. In the present study, a window size of 3 s was selected, as it contained at least 10 cycles of the slowest oscillation of interest ( $10/3.5 = 2.8$ ). The propagation constant was set at 0.2 to



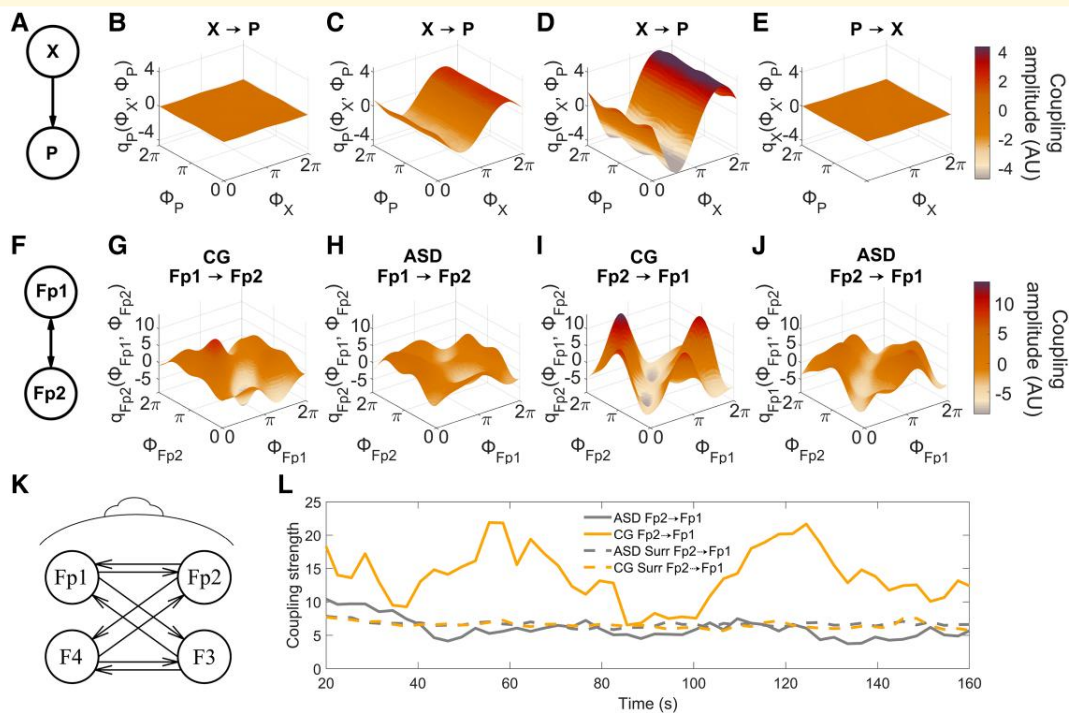


**Figure 2 Dynamical Bayesian inference applied to a model and measured data.** (A) A model of the unidirectional coupling  $X \rightarrow P$ , where the coupling functions ( $q$ ) depend upon the phases ( $\phi$ ) of each oscillator. Further details of the modelling procedure and parameters are given in the [Supplementary material](#). (B–D) Coupling functions at different strengths ( $E = 0, 5$  and  $10$ , respectively). (E) Coupling in the opposite direction ( $P \rightarrow X$ ) simulated with  $E = 10$ , illustrating the unidirectional nature of the coupling. (F) Bidirectional neural coupling measured between two probes, Fp1 and Fp2. (G–J) Time-averaged coupling functions in an individual with autism spectrum disorder (ASD—H, J) and a control group individual (CG—G, I). (K) The frontal network couplings evaluated in the present study. (L) An example of the coupling strength from Fp2 to Fp1 in a randomly selected individual with ASD (cool colour, grey) and a CG participant (warm colour, gold). Surrogate values are indicated by the dashed lines (95th percentile, intersubject surrogates).

control the information transferred between windows, and the overlap parameter was set to unity (no overlap).

## Statistical analysis

### Testing for significance using surrogate data

Surrogate analysis was used to assess the significance of results. The underlying goal is to generate a surrogate time series with similar statistical properties to the original time series, but with randomized phase evolution. Any coherence found to be significantly lower than that produced between uncorrelated time series is treated as non-significant. A significance threshold is set, based on the surrogate values. Different types of surrogate data have been discussed.<sup>71</sup>

For any pair of probes, the time-averaged (mean) coherence was calculated between the respective time series of all subjects in each group. For example, in the ASD group, for probe pair F3–F4, coherence was calculated between the F3 time series of 13 subjects and the F4 time series of the same 13 subjects. This results in a set of  $13 \times 13$  overall coherence values. The 13 diagonal values were the actual coherence values for a given person between the probe pair F3–F4, while the remaining 156 were the ‘apparent’ coherence

between different subjects’ signals (whereas, in reality, there could not have been any coherence). First, the mean of the 156 surrogate coherence values was calculated for each frequency within the frequency band of interest. This was treated as a threshold and subtracted from the actual coherence to give the net, or effective, coherence. Any values below the surrogate threshold following this subtraction were set to zero. The mean coherence was then calculated as a single value for each participant and each probe combination. For the DBI analysis, the 95th percentile served as a surrogate threshold because the results were systematically higher for coupling time.

### Statistical tests

Following the application of surrogate testing, statistical tests were applied. Given that the data did not follow a normal distribution, non-parametric tests were selected; further details of these tests and the rationale for using a non-parametric approach are provided in the [Supplementary material](#). For groupwise comparisons, the Wilcoxon rank-sum test was applied, with a significance threshold set to 0.05.

Friedman's test for repeated measures was used to investigate the consistency of results for the same subject across different time intervals. This was done for two reasons: first, to establish whether the suggested measures were consistent over time, and thus validate their potential as biomarkers; and secondly, to assess whether the results can be treated as repeated measures. In all groups across both the WPC and DBI, the  $P$ -value was above 0.05, suggesting that this treatment is appropriate. Further details and assessments of the repeated measures are presented alongside [Supplementary Tables 13–16](#).

In addition, the Kruskal–Wallis test was used to further assess the consistency of results across repeats on an individual subject level. Only a single CG individual provided inconsistent results across repeats for the DBI measure, while all were consistent for WPC.

### Repeated measurements

Alongside the video segments, five sequential measurements of 3 min were compared. To ensure that the timing within the overall 20 min recording was not a confounding factor, the segments were also shuffled. A randomly selected segment from each subject was chosen, and a rank-sum test was used to assess group differences. This process was repeated 1000 times, and the percentage of tests yielding significant outcomes ( $P < 0.05$ ) was calculated.

### Effect size

Cohen's  $d$  was used to evaluate the effect sizes when comparing the groups.<sup>72</sup> Further detail is provided in the [Supplementary material](#) and [Supplementary Tables 1–4](#). In general, an effect size of  $d = 0.5$  is considered medium, while  $d = 0.8$  is considered large.

## Classification

Following the calculation of coherence and couplings, classification analysis was performed. A J48 tree classifier machine-learning algorithm was used in WEKA.<sup>73</sup> Leave-one-out cross validation was performed. Details of the classification analysis are presented in the [Supplementary material](#).

## Results

The Blackpool and HBN data were analysed separately due to procedural differences during data collection. In the Blackpool data, no significant differences were found in the power between groups in the frontal region, over the medium-frequency band (3.5–12 Hz), across any of the time-segments analysed ([Supplementary material](#) Sect. 5.1). However, both the amount of time during which regions remained coupled, and the functional connectivity, were reduced in the ASD group. First, we will focus on the wavelet phase coherence results.

## Coherence

Initially considering the video segments in the Blackpool data, functional connectivity is significantly ( $P < 0.05$ ) decreased across all frontal probe pairs in the ASD group. [Figure 3A and B](#) shows the group median coherence for the video acquired data in the ASD and CG cases, respectively. [Figure 3C](#) illustrates the distribution of the data. Probe pair Fp1–F4 showed the greatest difference between groups ( $P = 0.005$ ).

To assess repeatability in data more prone to movement artefacts, the analysis was performed again in five chronologically selected intervals, each of length 3 min. [Figure 3D and E](#) shows the median coherence for each subject across the six segments analysed. The differences between groups in each of these additional segments proved to be significant. In addition, the F3–Fp2 connection was significant at the Bonferroni adjusted  $P$ -value of 0.0125 for all six intervals initially analysed. The F3–Fp2 connection also had the largest effect size (1.55) of the video segments. Further details regarding the analysis of each segment, including group median values, their corresponding violin plots and all effect sizes are given in the [Supplementary material](#). The level of significance between groups at each frontal probe combination and across all segments is illustrated by the  $P$ -values in [Table 3](#).

To ensure that the time at which the recording was taken was not a confounding factor, shuffled repeats were assessed. All connections for which over half the repeats demonstrate significance are plotted in [Fig. 4B](#). The most consistent differences between groups were found in the frontal network, with 100% of shuffled repeats significantly greater for F3–Fp2, Fp1–F4 and F3–F4 and 92% for Fp1–Fp2.

For the video acquired segment, functional connectivity across the entire head (3.5–12 Hz) was also evaluated, 28 connections showed significantly increased coherence in the controls relative to the ASD group ([Fig. 4A](#)). WPC was also assessed in the HBN data ([Fig. 4C](#)): 28 significant connections were found, with the majority being more posteriorly located than in the Blackpool cohort.

Global synchrony demonstrated no significant differences in the 3–5 (Blackpool) or the 5–15-year-old (HBN) age ranges between the ASD and CG groups ([Fig. 4D](#)). Regression found no significant association with age in the 5–15 range for either the ASD or CG groups.

## Couplings

Effective connectivity is reduced in the ASD group. [Figure 5](#) illustrates these differences, separated into connections from the left to right hemisphere ([Fig. 5A–C](#)) and right to left ([Fig. 5D–F](#)) for frontal areas. Each of the probe combinations demonstrated a significantly reduced ( $P < 0.05$ ) coupling time in the video acquired segment, except for F3 → F4. The violin plots of [Fig. 5C and F](#) present the distribution of these values, alongside the  $P$ -value for each bidirectional coupling.

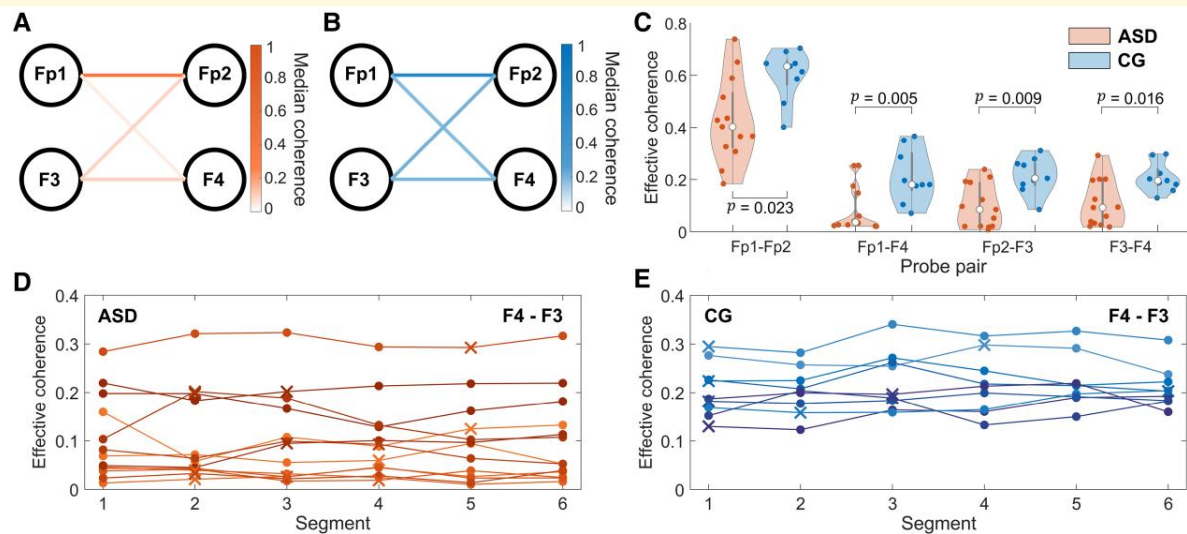


**Figure 3 Coherence results across segments.** (A) Heatmap showing the group median coherence in the autism spectrum disorder group (ASD,  $N = 13$ , male), averaged across theta and alpha bands between probes during the video segment. (B) Equivalent heatmap for the control group (CG,  $N = 9$ , male). (C) Median effective coherence in the frontal network evaluated across the medium-frequency band (3.5–12 Hz) for the video segment. Cool coloured (blue) violins represent CG while warm colours (orange) indicates ASD. The median of each distribution is indicated by the central circle, and the box indicates the interquartile range. Each filled datapoint represents the mean coherence across the theta and alpha bands for each participant. The Wilcoxon rank-sum test was used to evaluate group differences ( $N = 13$  ASD,  $N = 9$  CG). (D, E) The effective coherence results between F3 and F4 for the sequential, and video segments, in the ASD and CG groups, respectively. Filled circles indicate that the segment was chosen sequentially, while a cross represents a video acquired segment. Each line represents a different participant across repeats ( $N = 13$  ASD,  $N = 9$  CG for each segment).

**Table 3 Reported  $P$ -values in the video segments for the WPC (top) and DBI (bottom)**

	P-values					Video	Shuffled repeats (%)
	1	2	3	4	5		
WPC							
Fp1–Fp2	0.038	0.027	0.004	0.027	0.016	0.023	92
F3–Fp2	0.009	0.002	0.006	0.004	0.004	0.009	100
Fp1–F4	0.009	0.011	0.007	0.003	0.009	0.005	100
F3–F4	0.001	0.004	0.003	0.004	0.005	0.016	100
DBI							
Fp1 → Fp2	0.081	0.020	0.027	0.026	0.017	0.010	72
Fp1 ← Fp2	0.047	0.003	0.031	0.006	0.014	0.004	84
Fp1 → F4	0.108	0.001	0.030	0.094	0.032	0.003	72
Fp1 ← F4	0.045	0.004	0.032	0.013	0.004	0.028	92
F3 → F4	0.041	0.013	0.123	0.095	0.017	0.344	64
F3 ← F4	0.070	0.003	0.021	0.032	0.131	0.031	60
F3 → Fp2	0.014	0.004	0.065	0.011	0.048	0.007	76
F3 ← Fp2	0.071	0.001	0.008	0.003	0.003	0.004	96

Bold numbers indicate statistical significance ( $P < 0.05$ ,  $N = 13$  ASD,  $N = 9$  CG) obtained using the Wilcoxon rank-sum test. A hyphen between probes indicates WPC was used, while an arrow indicates DBI, with the direction specified. In the WPC group, 24 out of a potential 24 group comparisons proved to be significant. In DBI, 39 out of a possible 48 were significant. The final row indicates the percentage of total temporally shuffled datasets that were significant, for 1000 shuffles of the five sequential segments.

The analysis was repeated across a series of chronologically derived segments. The violin plots representing the distribution of coupling times found for these intervals are illustrated in [Supplementary Figs 11–15](#). Only the couplings  $Fp2 \rightarrow Fp1$  and  $F4 \rightarrow Fp1$  were significantly reduced across all six of the intervals under consideration. The  $P$ -values for each bidirectional probe combination and across all segments are illustrated in [Table 3](#), and [Fig. 5A, B, D, and E](#)

shows the median time coupled in the video segment for the ASD and CG groups, respectively. Although still relatively high, the percentage of shuffled repeats that were significant when applying DBI was lower than in the WPC case ([Table 3](#)). Interestingly, the most repeatable difference between groups in terms of coupling was  $Fp2 \rightarrow Fp3$ , with 96% of shuffled repeats demonstrating significance, consistent with the WPC analysis for  $Fp2 \rightarrow Fp3$ . The percentage of

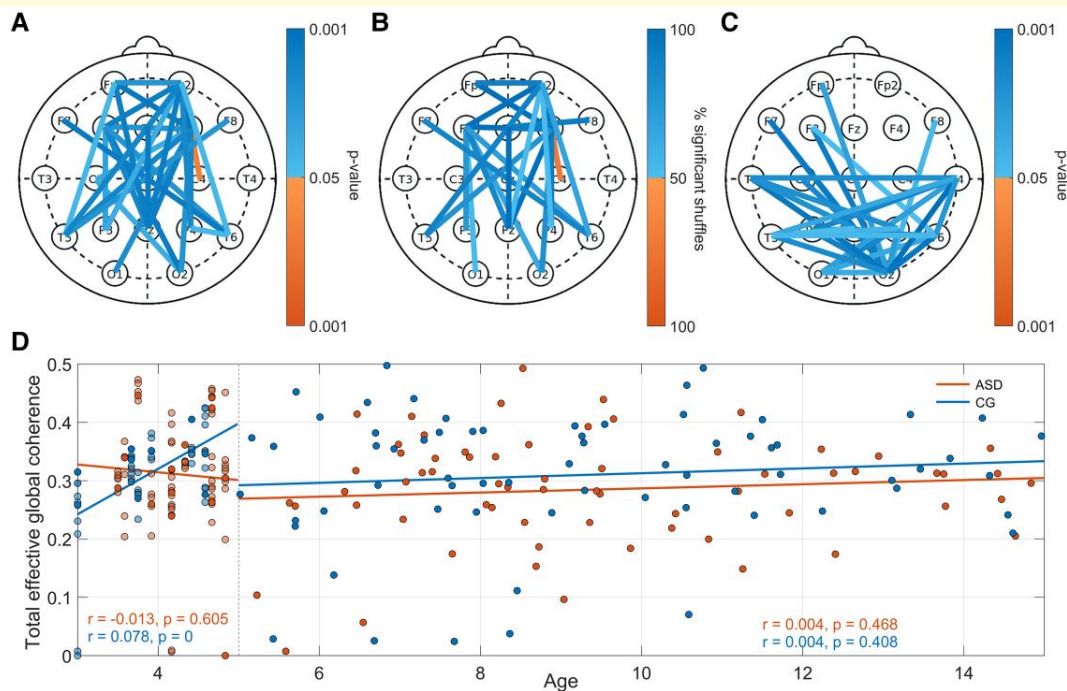


**Figure 4** Coherence differences between autism spectrum disorder (ASD) and control (CG) groups. **(A)** Coherence differences between probes (3–5-year-old, male, ASD:  $N = 13$ , CG:  $N = 9$ ). Probe pairs with significant differences ( $P < 0.05$ , Wilcoxon rank-sum test) are plotted: cool coloured (blue) lines indicate higher coherence in the CG, and warmer coloured (orange) lines indicate higher coherence in the ASD group **(B)** Headmap of significant ( $P < 0.05$ , Wilcoxon rank-sum test) coherence differences from 1000 randomly shuffled repeats for the 3–5-year-old male group. The headmap shows the percentage of the 1000 tests yielding significant differences. **(C)** Coherence differences for 5–15-year-old males (ASD:  $N = 67$ , CG:  $N = 66$ ), using the same method as in **(A)**. **(D)** Total global effective coherence in the 3.5–12 Hz frequency band for males with and without ASD in both the Blackpool ( $N = 65$  ASD,  $N = 45$  CG) and Healthy Brain Network ( $N = 67$  ASD,  $N = 66$  CG) datasets. Each coloured datapoint represents the global effective coherence across the theta and alpha bands for each participant. Regression analysis was performed separately for the two datasets. In the Blackpool data for the ASD group,  $r = -0.013$ ,  $P = 0.605$  and for the CG group  $r = 0.078$ ,  $P < 0.000$ . In the HBN data for the ASD group,  $r = 0.004$ ,  $P = 0.468$  and for the CG group  $r = 0.004$ ,  $P = 0.408$ . The data were also pooled together. In this case, for the ASD group,  $r = -0.003$ ,  $P = 0.355$  and for the CG group  $r = 0.003$ ,  $P = 0.305$ .

time coupled also exhibited more variability across repeats than WPC, as demonstrated by comparing Figs 3D and E and 5G–J. The Kruskal–Wallis test also revealed that one of the CG participants yielded DBI results that were not consistent across time.

## Classification

Using the J48 decision tree algorithm in WEKA, 86% accuracy was achieved when discriminating between ASD and CG in the Blackpool video segment (3–5 years,  $N = 13$  ASD,  $N = 9$  CG), and 80% was achieved in the older group of the HBN dataset (9–15 years,  $N = 31$  ASD,  $N = 33$  CG). Further details, including the parameters used as attributes, are provided in the [Supplementary material](#).

## Discussion

The results confirm our hypothesis of reduced connectivity in the alpha and theta bands for young males with ASD,

possibly due to the couplings between these areas being more transient.

The time-resolved analysis methods used here are based on the theory of chronotaxic,<sup>74</sup> finite-time dynamics<sup>75</sup> and the definition of instantaneous phases.<sup>76</sup> This approach enables the simultaneous detection of multiple deterministic, non-linear, multiscale and time-varying interactions that may be neglected by traditional analysis approaches<sup>25,28,29,31–33,77</sup> or treated as stochastic.<sup>30</sup>

## Functional connectivity

The functional connectivity was assessed using phase coherence. The ASD group was shown to have significantly reduced MF connectivity. This result was replicated across each of the sequential time intervals and also in the HBN data. The largest difference between groups in the Blackpool data was F3–Fp2, which proved to be significant at the Bonferroni adjusted  $P$ -value of 0.0125 for all six intervals, and 100% of the shuffled repeats. In the HBN data, posteriorly located probe combinations demonstrated more significant connectivity



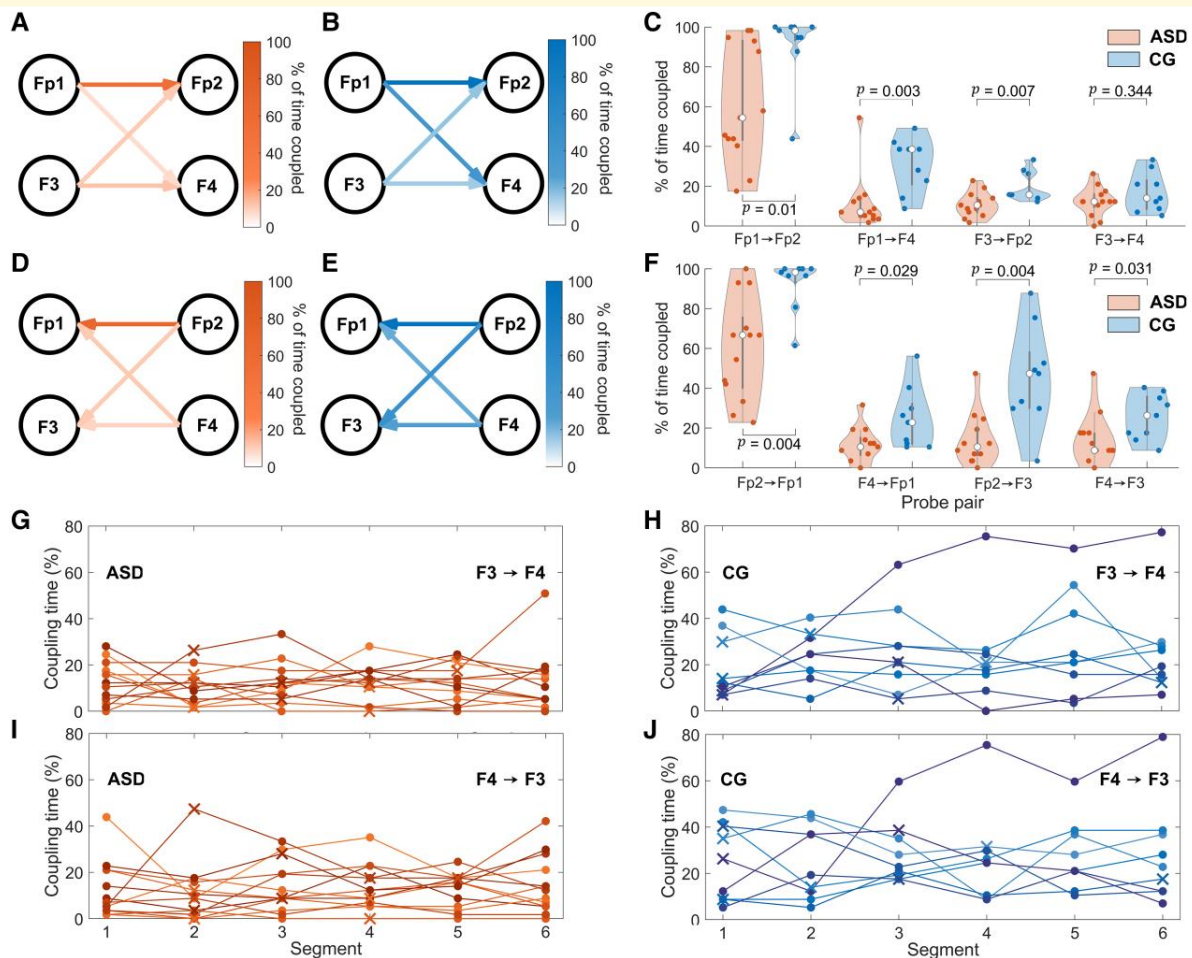


**Figure 5 Coupling time results across segments.** (A, B, D, E) Headmaps representing the group median percentage coupling time between probes for the video segment in the autism spectrum disorder group (ASD,  $N = 13$ , male, warm colours - orange) and the control group (CG,  $N = 9$ , male, cool colours - blue). (C, F) Percentage time coupled between the measured EEG signal locations evaluated across the medium-frequency band (3.5–12 Hz) in the video segments, from the left to the right (C), and right to left (F) hemisphere. The Wilcoxon rank-sum test was used to assess group differences ( $N = 13$  ASD,  $N = 9$  CG). Cool coloured (blue) violins represent the CG while warm colours (orange) indicates the ASD group. The Wilcoxon rank-sum test was used to assess group differences. (G–J) The coupling time for each of the sequential, and video, segments. Each line represents a different participant across repeats ( $N = 13$  ASD,  $N = 9$  CG for each segment). Filled circles indicate that the segment was chosen sequentially, while crosses represent video acquired segments. In this case, the bidirectional coupling between F3 and F4 is illustrated, for the ASD (G, I) and (H, J) cases.

differences between groups. This is likely due to eyes-closed being used predominantly as the HBN protocol, which is known to generate greater occipital alpha band activity.<sup>78</sup> In addition, the action of opening and closing the eyes periodically may have induced movement artefacts that confounded the connectivity results between frontal probes.

Reduced frontal connectivity in ASD, as found in the Blackpool cohort, confirms the results of some earlier studies,<sup>16,19,21,47,49</sup> and may predict subsequent outcomes in children as young as three months old.<sup>20</sup> The consistency of this measure over time probably depends on using a sufficiently large measurement window to capture the underlying oscillatory dynamics. Longer windows ensure the capture of time-varying behaviour across many cycles of the oscillation of interest.

Global coherence demonstrated no significant relationship with age in either the 5–15-year-old (HBN) group or the 3–5-year-old (Blackpool) group. Local coherence differences were much more significant and are promising as a potential determinant. For both groups, the local functional connectivity, evaluated with phase coherence, indicated a consistent trend towards reduced functional connectivity in ASD.

Despite the strength of this result, it is not possible to infer whether it is due to mutual interaction between oscillators, rather than to a shared common influence.

## Effective connectivity

To assess effective connectivity, the couplings were calculated using DBI, which was applied to the Blackpool data.

By considering the time over which couplings are significant, another temporal dimension is introduced. Using this framework, it was found that the frontal couplings were present for shorter times in the ASD group than in the neurotypical controls. This reduction in coupling time for ASD individuals may be symptomatic of a reduction in executive function.<sup>21,38-40</sup> In each frontal probe combination, a greater proportion of the shuffled repeats were significant for WPC than for DBI, indicating that DBI, although able to reveal more information about the dynamics, may be less repeatable than WPC. ASD has been associated with longer dwell times in a disconnected state, and our results support this conclusion for the frontal region.<sup>3</sup> DBI was not assessed in the HBN data as the changing measurement condition made it inappropriate for evaluation with the Bayesian framework.

Recent publications have emphasized the need to shift the research focus in ASD from functional connectivity analyses to directional, effective connectivity.<sup>1</sup> Notably, temporal dysregulation has also been identified as a significant factor in ASD.<sup>3,4</sup> We have presented a method for evaluating the duration of coupling between various brain regions. While we specifically demonstrate the application of this approach in individuals with ASD and within the frontal network, it also holds potential for broader implementation across different cohorts, frequency bands and brain regions.

## Resilience of the phase-based approach

Coherence was reduced in the ASD group for all time intervals investigated across the frontal region. A high level of consistency was found with both methods and for both datasets, despite the increased presence of movement artefacts across the sequentially obtained segments, compared to the video segments. WPC was more reproducible than DBI. Effective clinical implementations of EEG analysis, particularly in paediatric cases, require methods capable of detecting interactions, even in the presence of amplitude perturbations. Evidence regarding connectivity differences in the literature remains inconsistent, with both hyperconnectivity<sup>16,19,21,47,49</sup> and hypoconnectivity<sup>16,19-21</sup> being reported in individuals with ASD. These inconsistencies may be due in part to amplitude-weighted measures affecting the reliability of the results.<sup>26</sup> It is hoped that phase-based approaches will ameliorate this situation.

## Assessing connectivity evaluation methods

Direct comparison between the different methods of calculating connectivity from EEG data is challenging due to the variety of measurement protocols used. Factors such as participant age, sex and state during recording have been shown to influence EEG connectivity.<sup>79-81</sup> For example, reduced frontal theta/alpha connectivity has been reported<sup>82</sup> in ASD; however, this finding was based on data collected

under eyes-closed conditions, using 2s epochs. The Blackpool data in the present study consisted of 3 min, eyes open EEG recordings, and so one would not necessarily expect identical results. A future methodological project to benchmark connectivity methods against one another, using the 'same' dataset in each case, would provide clearer insights into their respective strengths and weaknesses. We emphasize, however, that the methods used in the present study amount to much more than just another alternative approach to EEG analysis. As discussed in the Introduction, they are the first to be applied that are able to take fully into account the inherent non-autonomicity of biological oscillators. The advantages and, in many cases, necessity of using such an approach are explored and described in detail in the papers cited.<sup>30,36,83</sup> It is thus to be expected that the approach used here should yield more insightful results than any of the alternatives.

## Feasibility of biomarkers

Given the lack of consensus in the literature, novel analytical approaches may play a crucial role in elucidating the underlying connectivity differences present in ASD. The brain is an incredibly complex organ, and despite a multitude of research into biomarkers for ASD assessment, a single diagnostic test is still beyond reach. Here, by explicit consideration of time as a physical parameter during data analysis and consideration of finite-time dynamics, we have paved a way for novel biomarkers.

Due to the demand for fast throughput in clinical settings, 20 min EEG recordings may not always be achievable. Additionally, when measuring brain activity in children, movement artefacts are inevitable and should be anticipated and accounted for. It is therefore crucial to use methods that yield reproducible findings despite the presence of movement artefacts.

Like other dynamical analyses of physiological data, EEG investigations are complicated by the thermodynamically open nature of biological systems and their inherent fluctuations. The underlying oscillatory processes are consequently non-autonomous, exhibiting characteristic frequencies that vary in time. This feature must be considered in the data analysis<sup>36,83</sup> for the results to be reliable. Explicit consideration of recording length is paramount when assessing oscillatory neural activity, especially when considering interactions.

The vast heterogeneity of ASD means that individuals with the condition are highly unlikely to share identical EEG signatures. A range of biomarkers, each with their own behavioural correlate, may enable a more stringent evaluation. Further research considering the putative relationship between frontal connectivity and restricted and repetitive behaviours in ASD across various age ranges, using larger cohorts and comparing with behavioural measures may elucidate the potential behavioural correlates suggested by this investigation. Using a very simple classification method, a classification accuracy of 86% was obtained.

In our current approach, we employ the same frequency band for both probes in the DBI calculation. However, alternative cross-frequency approaches can also be explored. For example, one could investigate the influence of delta activity in one region on alpha activity in another region.<sup>84</sup> Cross-frequency coupling functions have demonstrated aberrations in various neurological conditions<sup>85</sup> and may offer an additional avenue for assessing ASD.

In isolation, the functional connectivity results may indicate that there is simply a lower, constant, coherence across time. The coupling results supplement the WPC by showing that the amount of time over which coupling is present is also reduced in ASD. By unlocking the temporal dimension in this way, additional information about the dynamical nature of the couplings is revealed. In combination, both the connectivity strength, and the time over which the regions are coupled, are shown to be significantly different in ASD, and may provide the basis for a potential biomarker.

## Limitations and strengths

Although we report the potential of frontal network connectivity as a biomarker for ASD, more research based on larger groups and different age bands would be required to ascertain if this outcome can be realized. Additional analyses with the same age range and measurement procedure are needed to validate the findings.

It is crucial to acknowledge that a comprehensive diagnostic tool would necessitate multiple markers, each capturing distinct aspects of the ASD experience. One may argue that the observed decrease in frontal connectivity in the Blackpool data may be associated with the characteristic restricted and repetitive behaviours exhibited by some individuals with ASD.<sup>38,45,86</sup> However, using the HBN data, we show that phase coherence is also a useful marker when the measurements are conducted in a different brain state. Further investigations could elucidate the origins of other behavioural correlates, such as social and communication difficulties.

The size of the Blackpool data is relatively small. Several arguments indicate, however, that the conclusions are reliable. First, as shown in the results section and the [Supplementary material](#), the effect size is large. Secondly, the Blackpool recordings were sufficiently long to allow for six different 3 min segments to be analysed, and thus for the reproducibility of the results to be evaluated. The results ensured that the inferred interactions were not spurious. The additional HBN dataset, coming from a larger cohort with a wider age range, provided a further reassuring validation of our conclusions.

Only boys were recruited in the present study as the neural signatures of ASD are known to vary between the sexes<sup>52,80</sup> and a sufficient number of females could not be recruited within the time frame of the study to warrant an additional investigation.

The effect of volume conduction may have influenced the effect sizes of the phase coherence and couplings analyses. In

the absence of reliable models to take volume conduction into account, we have mitigated this problem in several ways. It is known that the spatial separation minimizes the impact of volume conduction.<sup>87</sup> The probe density in both datasets is relatively small, hence even the nearest probes can be expected to be weakly affected. Next, the probe pair F3–Fp2, which are widely separated within the frontal network, exhibited the most pronounced differences in coherence between groups. Furthermore, as our primary aim is to compare coherence and coupling values between ASD and neurotypical control groups, it is reasonable to assume that volume conduction would likely affect both groups similarly.

The use of phase coherence and coupling functions allow an investigation of neural dynamics with reduced influence from the movement artefacts and noise that can bedevil amplitude-based methods. The robustness to amplitude effects enables the analysis of relatively long segments that contain more information than the shorter epochs often investigated in EEG studies.<sup>15,18,19,79,88</sup>

## Concluding remarks

Despite the condition having been recognized for over a century, ASD diagnoses still depend on behavioural tests and interviews. As well as being time-consuming, these assessments require certain characteristic features to be apparent, meaning that most children do not receive a diagnosis until age 3/4 or even later.<sup>89</sup> A diagnostic tool that revealed the presence of ASD before its behavioural emergence could be useful, quite apart from its utility in assessing the response to intervention. Our investigation of electrophysiological signatures in ASD and neurotypical children provides a promising step towards putative biomarkers for identifying and categorizing the condition.

## Supplementary material

[Supplementary material](#) is available at *Brain Communications* online.

## Acknowledgements

We are grateful to the children and families who participated in the study and gave valuable feedback. We also thank Jackie Bradley, Paediatric Research Nurse, and the Northwest Coast CRN for their support. We acknowledge the expertise of the Clinical Physiologists, Priscilla Springett, Jane Grenfell and Jennifer Campbell who ensured that all children, with only one exception in each of the groups, were able to complete fully the EEG recordings. We also thank Benediktas Valys and Valentina Ticcinielli for their contributions and Jose Guzman for useful discussions.

## Funding

The experimental part of the study was supported by Action Medical Research (UK) Project [GN1963] and partly by the Slovenian Research Agency (program no. P20232). S.J.K.B. is jointly supported by the Engineering and Physical Sciences Research Council and MyMind GmbH—Brain Hero, Vienna, Austria (grant EP/T518037/1, ‘Quantitative Assessment of Autistic Spectrum Disorder’). The development of the MODA toolbox used for analyses has been supported by the Engineering and Physical Sciences Research Council (UK) [grants no. EP/100999X1 and no. EP/M006298/1], the European Union projects BRACCIA (Brain, Respiration and Cardiac Causalities in Anaesthesia) [517133] and COSMOS (Complex Oscillatory Systems: Modeling and Analysis) [642563], the Action Medical Research (United Kingdom) Project [GN1963] and the Slovenian Research Agency (program no. P20232).

## Competing interests

The authors report no competing interests.

## Data availability

The EEG data recorded in Blackpool, codes used in the work and some additional figures in .mat format are publicly available on Lancaster University’s Pure database, DOI: 10.17635/lancaster/researchdata/694. The phenotypic data from the HBN may be accessed upon request from the bio-bank and following the acceptance of a data usage agreement. The majority of the analyses were done using the MODA (Multiscale Oscillatory Dynamics Analysis) software toolbox, which is publicly available at <https://github.com/luphysics/MODA>, and the background of the methods is provided in its handbook.<sup>90</sup>

## References

- Mohammad-Rezazadeh I, Frohlich J, Loo SK, Jeste SS. Brain connectivity in autism spectrum disorder. *Curr Opin Neurol*. 2016; 29(2):137-147.
- Yahata N, Morimoto J, Hashimoto R, *et al*. A small number of abnormal brain connections predicts adult autism spectrum disorder. *Nat Commun*. 2016;7(1):11254.
- Rashid B, Blanken LME, Muetzel RL, *et al*. Connectivity dynamics in typical development and its relationship to autistic traits and autism spectrum disorder. *Hum Brain Mapp*. 2018;39(8):3127-3142.
- Mash LE, Linke AC, Olson LA, Fishman I, Liu TT, Müller RA. Transient states of network connectivity are atypical in autism: A dynamic functional connectivity study. *Hum Brain Mapp*. 2019; 40(8):2377-2389.
- Haendel AD, Barrington A, Magnus B, *et al*. Changes in electroencephalogram coherence in adolescents with autism spectrum disorder after a social skills intervention. *Autism Res*. 2021;14(4): 787-803.
- Garcés P, Baumeister S, Mason L, *et al*. Resting state EEG power spectrum and functional connectivity in autism: A cross-sectional analysis. *Mol Autism*. 2022;13(1):22.
- Wantzen P, Clochon P, Doidy F, *et al*. EEG resting-state functional connectivity: Evidence for an imbalance of external/internal information integration in autism. *J Neurodev Disord*. 2022; 14(1):47.
- O’Reilly C, Lewis JD, Elsabbagh M. Is functional brain connectivity atypical in autism? A systematic review of EEG and MEG studies. *PLoS One*. 2017;12(5):e0175870.
- Rolls ET, Cheng W, Feng J. Brain dynamics: The temporal variability of connectivity, and differences in schizophrenia and ADHD. *Transl Psychiatry*. 2021;11(1):70.
- Petkoski S, Ritter P, Jirsa VK. White-matter degradation and dynamical compensation support age-related functional alterations in human brain. *Cereb Cortex*. 2023;33(10):6241-6256.
- Malaia EA, Ahn S, Rubchinsky LL. Dysregulation of temporal dynamics of synchronous neural activity in adolescents on autism spectrum. *Autism Res*. 2020;13(1):24-31.
- Hull JV, Dokovna LB, Jacokes ZJ, Torgerson CM, Irimia A, Van Horn JD. Resting-state functional connectivity in autism spectrum disorders: A review. *Front Psychiatry*. 2017;7:205.
- Vissers ME, Cohen MX, Geurts HM. Brain connectivity and high functioning autism: A promising path of research that needs refined models, methodological convergence, and stronger behavioral links. *Neurosci Biobehav Rev*. 2012;36(1):604-625.
- Long Z, Duan X, Mantini D, Chen H. Alteration of functional connectivity in autism spectrum disorder: Effect of age and anatomical distance. *Sci Rep*. 2016;6(1):26527.
- Wang J, Wang X, Wang X, *et al*. Increased EEG coherence in long-distance and short-distance connectivity in children with autism spectrum disorders. *Brain Behav*. 2020;10(10):e01796.
- Liloia D, Manuella J, Costa T, Keller R, Nani A, Cauda F. Atypical local brain connectivity in pediatric autism spectrum disorder? A coordinate-based meta-analysis of regional homogeneity studies. *Eur Arch Psychiatry Clin Neurosci*. 2024;274(1):3-18.
- Courchesne E, Pierce K. Why the frontal cortex in autism might be talking only to itself: Local over-connectivity but long-distance disconnection. *Curr Opin Neurobiol*. 2005;15(2):225-230.
- Orekhova EV, Elsabbagh M, Jones EJ, *et al*. EEG hyper-connectivity in high-risk infants is associated with later autism. *J Neurodev Disord*. 2014;6(1):40.
- Coben R, Clarke AR, Hudspeth W, Barry RJ. EEG power and coherence in autistic spectrum disorder. *Clin Neurophysiol*. 2008; 119(5):1002-1009.
- Dickinson A, Daniel M, Marin A, *et al*. Multivariate neural connectivity patterns in early infancy predict later autism symptoms. *Biol Psychiatry Cogn Neurosci Neuroimaging*. 2021;6(1):59-69.
- Chan MMY, Chan MC, Lai OLH, Krishnamurthy K, Han YMY. Abnormal prefrontal functional connectivity is associated with inflexible information processing in patients with autism spectrum disorder (ASD): An fNIRS study. *Biomedicine*. 2022;10(5):1132.
- Masi A, DeMayo MM, Glozier N, Guastella AJ. An overview of autism spectrum disorder, heterogeneity and treatment options. *Neurosci Bull*. 2017;33(2):183-193.
- Mathewson KJ, Jetha MK, Drmic IE, Bryson SE, Goldberg JO, Schmidt LA. Regional EEG alpha power, coherence, and behavioral symptomatology in autism spectrum disorder. *Clin Neurophysiol*. 2012;123(9):1798-1809.
- Wang J, Barstein J, Ethridge LE, Mosconi MW, Takarae Y, Sweeney JA. Resting state EEG abnormalities in autism spectrum disorders. *J Neurodev Disord*. 2013;5(1):24.
- Bastos AM, Schoffelen JM. A tutorial review of functional connectivity analysis methods and their interpretational pitfalls. *Front Syst Neurosci*. 2016;9:175.
- Barnes SJK, Bjerkan J, Clemson PT, Newman J, Stefanovska A. Phase coherence—A time-localized approach to studying interactions. *Chaos*. 2024;34(7):073155.



27. Barnett L, Seth AK. The MVGC multivariate Granger causality toolbox: A new approach to Granger-causal inference. *J Neurosci Methods*. 2014;223:50-68.
28. Kamiński M, Ding M, Truccolo WA, Bressler SL. Evaluating causal relations in neural systems: Granger causality, directed transfer function and statistical assessment of significance. *Biol Cybern*. 2001;85(2):145-157.
29. Nolte G, Bai O, Wheaton L, Mari Z, Vorbach S, Hallett M. Identifying true brain interaction from EEG data using the imaginary part of coherency. *Clin Neurophysiol*. 2004;115(10):2292-2307.
30. Rowland Adams J, Newman J, Stefanovska A. Distinguishing between deterministic oscillations and noise. *Eur Phys J Spec Top*. 2023;232(20):3435-3457.
31. Stam CJ, Nolte G, Daffertshofer A. Phase lag index: Assessment of functional connectivity from multi channel EEG and MEG with diminished bias from common sources. *Hum Brain Mapp*. 2007;28(11):1178-1193.
32. Bruña R, Maestú F, Pereda E. Phase locking value revisited: Teaching new tricks to an old dog. *J Neural Eng*. 2018;15(5):056011.
33. Lachaux JP, Rodriguez E, Martinerie J, Varela FJ. Measuring phase synchrony in brain signals. *Hum Brain Mapp*. 1999;8(4):194-208.
34. Rolls ET, Zhou Y, Cheng W, Gilson M, Deco G, Feng J. Effective connectivity in autism. *Autism Res*. 2020;13(1):32-44.
35. Friston KJ. Functional and effective connectivity: A review. *Brain Connect*. 2011;1(1):13-36.
36. Clemson PT, Stefanovska A. Discerning non-autonomous dynamics. *Phys Rep*. 2014;542(4):297-368.
37. Lucas M, Newman J, Stefanovska A. Stabilization of dynamics of oscillatory systems by nonautonomous perturbation. *Phys Rev E*. 2018;97(4):042209.
38. Lopez BR, Lincoln AJ, Ozonoff S, Lai Z. Examining the relationship between executive functions and restricted, repetitive symptoms of autistic disorder. *J Autism Dev Disord*. 2005;35(4):445-460.
39. Yuk V, Dunkley BT, Anagnostou E, Taylor MJ. Alpha connectivity and inhibitory control in adults with autism spectrum disorder. *Mol Autism*. 2020;11(1):95.
40. Leisman G, Melillo R, Melillo T. Prefrontal functional connectivities in autism spectrum disorders: A connectopathic disorder affecting movement, interoception, and cognition. *Brain Res Bull*. 2023;198:65-76.
41. Jones DT, Graff-Radford J. Executive dysfunction and the prefrontal cortex. *Contin Minneap Minn*. 2021;27(6):1586-1601.
42. Schmitt LM, Li J, Liu R, et al. Altered frontal connectivity as a mechanism for executive function deficits in fragile X syndrome. *Mol Autism*. 2022;13(1):47.
43. Friedman NP, Robbins TW. The role of prefrontal cortex in cognitive control and executive function. *Neuropsychopharmacology*. 2022;47(1):72-89.
44. Casanova MF, Buxhoeveden DP, Switala AE, Roy E. Minicolumnar pathology in autism. *Neurology*. 2002;58(3):428-432.
45. Rojas DC, Peterson E, Winterrowd E, Reite ML, Rogers SJ, Tregellas JR. Regional gray matter volumetric changes in autism associated with social and repetitive behavior symptoms. *BMC Psychiatry*. 2006;6(1):56.
46. Courchesne E, Mouton PR, Calhoun ME, et al. Neuron number and size in prefrontal cortex of children with autism. *JAMA*. 2011;306(18):2001-2010.
47. Ajram LA, Horder J, Mendez MA, et al. Shifting brain inhibitory balance and connectivity of the prefrontal cortex of adults with autism spectrum disorder. *Transl Psychiatry*. 2017;7(5):e1137.
48. Anderson JS, Druzgal TJ, Froehlich A, et al. Decreased interhemispheric functional connectivity in autism. *Cereb Cortex*. 2011;21(5):1134-1146.
49. Dickinson A, DiStefano C, Lin YY, Scheffler AW, Senturk D, Jeste SS. Interhemispheric alpha-band hypoconnectivity in children with autism spectrum disorder. *Behav Brain Res*. 2018;348:227-234.
50. Yao S, Becker B, Kendrick KM. Reduced inter-hemispheric resting state functional connectivity and its association with social deficits in autism. *Front Psychiatry*. 2021;12:629870.
51. Wegiel J, Kaczmarek W, Flory M, et al. Deficit of corpus callosum axons, reduced axon diameter and decreased area are markers of abnormal development of interhemispheric connections in autistic subjects. *Acta Neuropathol Commun*. 2018;6(1):143.
52. Kozhemiako N, Vakorin V, Nunes AS, Iarocci G, Ribary U, Doesburg SM. Extreme male developmental trajectories of homotopic brain connectivity in autism. *Hum Brain Mapp*. 2019;40(3):987-1000.
53. Alexander LM, Escalera J, Ai L, et al. An open resource for transdiagnostic research in pediatric mental health and learning disorders. *Sci Data*. 2017;4(1):170181.
54. Marshall PJ, Bar-Haim Y, Fox NA. Development of the EEG from 5 months to 4 years of age. *Clin Neurophysiol*. 2002;113(8):1199-1208.
55. Edgar JC, Dipiero M, McBride E, et al. Abnormal maturation of the resting-state peak alpha frequency in children with autism spectrum disorder. *Hum Brain Mapp*. 2019;40(11):3288-3298.
56. Boersma M, Smit DJA, de Bie HMA, et al. Network analysis of resting state EEG in the developing young brain: Structure comes with maturation. *Hum Brain Mapp*. 2011;32(3):413-425.
57. Cebolla AM, Cheron G. Understanding neural oscillations in the human brain: From movement to consciousness and vice versa. *Front Psychol*. 2019;10:1930.
58. Beniczky S, Schomer DL. Electroencephalography: Basic biophysical and technological aspects important for clinical applications. *Epileptic Disord*. 2020;22(6):697-715.
59. Kaiser G. *A friendly guide to wavelets. Reprint of the 1994 original*. Birkhäuser; 2011.
60. Addison PS. *The illustrated wavelet transform handbook: Introductory theory and applications in science, engineering, medicine and finance*. Routledge; 2020.
61. Hramov AE, Koronovskii AA, Makarov VA, Maksimenko VA, Pavlov AN, Sitnikova E. *Wavelets in neuroscience*. Springer International Publishing; 2021.
62. Lachaux JP, Rodriguez E, Le Van Quyen M, Lutz A, Martinerie J, Varela F. Studying single-trials of phase synchronous activity in the brain. *Int J Bifurc Chaos*. 2000;10:2429-2439.
63. Lachaux JP, Lutz A, Rudrauf D, et al. Estimating the time-course of coherence between single-trial brain signals: An introduction to wavelet coherence. *Neurophysiol Clin Clin Neurophysiol*. 2002;32(3):157-174.
64. Bandrivskyy A, Bernjak A, McClintock PVE, Stefanovska A. Wavelet phase coherence analysis: Application to skin temperature and blood flow. *Cardiovascular Engineering*. 2004;4(1):89-93.
65. Sheppard LW, Stefanovska A, McClintock PVE. Testing for time-localized coherence in bivariate data. *Phys Rev E*. 2012;85(4 Pt 2):046205.
66. Sheppard LW, Bell JR, Harrington R, Reuman DC. Changes in large-scale climate alter spatial synchrony of aphid pests. *Nat Clim Change*. 2016;6(6):610-613.
67. Stankovski T, Pereira T, McClintock PVE, Stefanovska A. Coupling functions: Universal insights into dynamical interaction mechanisms. *Rev Mod Phys*. 2017;89(4):045001.
68. Stankovski T, Duggento A, McClintock PVE, Stefanovska A. Inference of time-evolving coupled dynamical systems in the presence of noise. *Phys Rev Lett*. 2012;109(2):024101.
69. Smelyanskiy VN, Luchinsky DG, Stefanovska A, McClintock PVE. Inference of a nonlinear stochastic model of the cardiorespiratory interaction. *Phys Rev Lett*. 2005;94(9):098101.
70. Stankovski T, Duggento A, McClintock PVE, Stefanovska A. A tutorial on time-evolving dynamical Bayesian inference. *Eur Phys J Spec Top*. 2014;223(13):2685-2703.

71. Lancaster G, Iatsenko D, Pidde A, Ticcinelli V, Stefanovska A. Surrogate data for hypothesis testing of physical systems. *Phys Rep.* 2018;748:1-60.
72. Cohen J. *Statistical power analysis for the behavioral sciences*. 2nd ed. Routledge; 1988.
73. The WEKA workbench—Eibe Frank, Mark A. Hall, Ian H. Witten—Google Books. Accessed 26 November 2024. [https://books.google.co.uk/books/about/The\\_WEKA\\_Workbench.html?id=4-FZuwEACAAJ&redir\\_esc=y](https://books.google.co.uk/books/about/The_WEKA_Workbench.html?id=4-FZuwEACAAJ&redir_esc=y)
74. Suprunenko YF, Clemson PT, Stefanovska A. Chronotaxic systems: A new class of self-sustained nonautonomous oscillators. *Phys Rev Lett.* 2013;111(2):024101.
75. Stefanovska A, McClintock PVE, editors. *Physics of biological oscillators: New insights into non-equilibrium and non-autonomous systems*. Springer; 2021.
76. Newman J, Scott JP, Rowland Adams J, Stefanovska A. Intermittent phase dynamics of non-autonomous oscillators through time-varying phase. *Phys Nonlinear Phenom.* 2024;461:134108.
77. Kaminski MJ, Blinowska KJ. A new method of the description of the information flow in the brain structures. *Biol Cybern.* 1991;65(3): 203-210.
78. Hohaia W, Saurels BW, Johnston A, Yarrow K, Arnold DH. Occipital alpha-band brain waves when the eyes are closed are shaped by ongoing visual processes. *Sci Rep.* 2022;12(1):1194.
79. Gabard-Durnam LJ, Wilkinson C, Kapur K, Tager-Flusberg H, Levin AR, Nelson CA. Longitudinal EEG power in the first post-natal year differentiates autism outcomes. *Nat Commun.* 2019; 10(1):4188.
80. Neuhaus E, Lowry SJ, Santhosh M, *et al.* Resting state EEG in youth with ASD: Age, sex, and relation to phenotype. *J Neurodev Disord.* 2021;13(1):33.
81. Barry RJ, Clarke AR, Johnstone SJ, Magee CA, Rushby JA. EEG differences between eyes-closed and eyes-open resting conditions. *Clin Neurophysiol.* 2007;118(12):2765-2773.
82. Rogala J, Zygierewicz J, Malinowska U, *et al.* Enhancing autism spectrum disorder classification in children through the integration of traditional statistics and classical machine learning techniques in EEG analysis. *Sci Rep.* 2023;13(1):21748.
83. Clemson PT, Lancaster G, Stefanovska A. Reconstructing time-dependent dynamics. *Proc IEEE.* 2016;104(2):223-241.
84. Manasova D, Stankovski T. Neural cross-frequency coupling functions in sleep. *Neuroscience.* 2023;523:20-30.
85. Yakubov B, Das S, Zomorodi R, *et al.* Cross-frequency coupling in psychiatric disorders: A systematic review. *Neurosci Biobehav Rev.* 2022;138:104690.
86. Sadeghi S, Pouretmad HR. Executive functions predict restricted and repetitive behaviors in toddlers under 36 months old with autism spectrum disorder. *Infant Behav Dev.* 2022;67:101721.
87. Holsheimer J, Feenstra BW. Volume conduction and EEG measurements within the brain: A quantitative approach to the influence of electrical spread on the linear relationship of activity measured at different locations. *Electroencephalogr Clin Neurophysiol.* 1977; 43(1):52-58.
88. O'Reilly C, Huberty S, van Noordt S, *et al.* EEG functional connectivity in infants at elevated familial likelihood for autism spectrum disorder. *Mol Autism.* 2023;14(1):37.
89. Steiner AM, Goldsmith TR, Snow AV, Chawarska K. Practitioner's guide to assessment of autism spectrum disorders in infants and toddlers. *J Autism Dev Disord.* 2012;42(6):1183-1196.
90. Iatsenko D, Lancaster G, McCormack S, *et al.* Multiscale oscillatory dynamics analysis (MODA) toolbox, Lancaster University, <https://github.com/luphysics/MODA>.

## Chapter 5

# Methamphetamine alters the circadian oscillator and its couplings on multiple scales in *Per1/2/3* knockout mice

### Student contribution:

The student conducted formal analysis and investigation, implemented the software used in the study, and contributed to validation of the results. They also wrote and edited the manuscript and prepared all accompanying figures.

This research is published in PNAS nexus.

Samuel JK Barnes, Mansour Alanazi, Shin Yamazaki, and Aneta Stefanovska. "Methamphetamine alters the circadian oscillator and its couplings on multiple scales in *Per1/2/3* knockout mice". In: *Proceedings of the National Academy of Sciences Nexus* 4 (2025)

# Methamphetamine alters the circadian oscillator and its couplings on multiple scales in *Per1/2/3* knockout mice

Samuel J.K. Barnes <sup>a</sup>, Mansour Alanazi <sup>a,b</sup>, Shin Yamazaki <sup>c</sup> and Aneta Stefanovska <sup>a,\*</sup>

<sup>a</sup>Physics Department, Lancaster University, Lancaster LA1 4YB, United Kingdom

<sup>b</sup>Department of Physics, Northern Border University, Arar 73311, Kingdom of Saudi Arabia

<sup>c</sup>Department of Neuroscience and Peter O'Donnell Jr. Brain Institute, UT Southwestern Medical Center, Dallas, TX 75390-9111, USA

\*To whom correspondence should be addressed: Email: [aneta@lancaster.ac.uk](mailto:aneta@lancaster.ac.uk)

Edited By Daniel Aeschbach

## Abstract

Disruptions to circadian rhythms in mammals are associated with alterations in their physiological and mental states. Circadian rhythms are currently analyzed in the time domain using approaches such as actograms, thus failing to appreciate their time-localized characteristics, time-varying nature and multiscale dynamics. In this study, we apply time-resolved analysis to investigate behavioral rhythms in *Per1/2/3* knockout (KO) mice and their changes following methamphetamine administration, focusing on circadian (around 24 h), low-frequency ultradian (around 7 h), high-frequency ultradian (around 30 min), and circadian (around 48 h) oscillations. In the absence of methamphetamine, *Per1/2/3* KO mice in constant darkness exhibited a dominant, ~7 h oscillation. We demonstrate that methamphetamine exposure restores the circadian rhythm, although the frequency of the methamphetamine sensitive circadian oscillator varied considerably compared to the highly regular wild-type circadian rhythm. Additionally, methamphetamine increased multiscale activity and induced a circadian oscillation in the *Per1/2/3* KO mice. The information transfer between oscillatory modes, with frequencies around circadian, low-frequency ultradian and high-frequency ultradian activity, due to their mutual couplings, was also investigated. For *Per1/2/3* KO mice in constant darkness, the most prevalent coupling was between low and high-frequency ultradian activity. Following methamphetamine administration, the coupling between the circadian and high-frequency ultradian activity became dominant. In each case, the direction of information transfer was between the corresponding phases from the slower to faster oscillations. The time-varying nature of the circadian rhythm exhibited in the absence of *Per1/2/3* genes and following methamphetamine administration may have profound implications for health and disease.

**Keywords:** circadian rhythms, biological oscillators, time-resolved analysis, multiscale analysis, nonlinear dynamics

## Significance Statement

Disrupted circadian rhythms are implicated in several pathologies. This study reveals the time-varying multiscale dynamics underlying such rhythms in mice. By analyzing the wheel running activity of mice lacking canonical circadian clocks (*Per1/2/3* KO) exposed to methamphetamine, which stimulates dopamine signaling, we demonstrate the dynamical characteristics of the methamphetamine sensitive circadian oscillator (MASCO). Although the MASCO period coincides with the canonical circadian rhythm, its frequency varies significantly in time. Methamphetamine administration also increased multiscale activity, induced a circadian oscillation, and altered couplings between behavioral modes. The time-varying MASCO may explain the sleep-wake cycle disturbances reported in individuals treated with stimulants, especially those with attention-deficit/hyperactivity disorder (ADHD). This research highlights the importance of time-resolved analysis in revealing previously unexplored aspects of circadian biology.

## Introduction

Periodic activity manifests across all temporal and spatial scales throughout nature. One of the most widely recognized cycles is the circadian rhythm, which is closely associated with numerous pathologies (1–3). In mammals, the circadian rhythm is primarily regulated by the suprachiasmatic nucleus (SCN) (4, 5), which serves as a central pacemaker entrained to the light/dark cycle (6). Additionally, peripheral oscillators are affected by nonphotic cues such as restricted feeding (7, 8) and methamphetamine

administration (9, 10). However, the relationship between canonical circadian oscillators and those influenced by dietary or pharmacological interventions remains unclear.

Mammalian circadian rhythms are governed by transcriptional–translational feedback loops within cells (5, 11, 12). *Period* (*Per*) genes are known to regulate circadian behaviors (13). The removal of these genes disrupts the 24-h timekeeping system, thereby eliminating the circadian rhythm (14). Consequently, *Per1/2/3* knockout (KO) mice offer a model to explore alternative

**Competing Interest:** The authors declare no competing interests.

**Received:** October 4, 2024. **Accepted:** February 10, 2025

© The Author(s) 2025. Published by Oxford University Press on behalf of National Academy of Sciences. This is an Open Access article distributed under the terms of the Creative Commons Attribution-NonCommercial License (<https://creativecommons.org/licenses/by-nc/4.0/>), which permits non-commercial re-use, distribution, and reproduction in any medium, provided the original work is properly cited. For commercial re-use, please contact [reprints@oup.com](mailto:reprints@oup.com) for reprints and translation rights for reprints. All other permissions can be obtained through our RightsLink service via the Permissions link on the article page on our site—for further information please contact [journals.permissions@oup.com](mailto:journals.permissions@oup.com).

OXFORD  
UNIVERSITY PRESS

pacemakers such as the methamphetamine sensitive circadian oscillator (MASCO), which operates independently of canonical clock genes (15). This approach avoids the interference from endogenous canonical circadian oscillations that would otherwise confound the results.

In addition to circadian oscillations (~24 h) (16–21), ultradian (<24 h) (22) and infradian (>24 h) (23) rhythms coexist, resulting from several biological mechanisms. These range from cellular dynamics occurring over minutes (24) to elongated multiday periods (25). Current methods largely analyze behavioral rhythms in the time domain using techniques such as actograms (26). Recently introduced multiscale analysis methods (27–34), able to detect the presence of oscillations and their mutual interactions on wide time-scales, promise to advance the study of behavioral rhythms. Additionally, they explicitly consider time as a physical parameter (35, 36), enabling time-localization. Hence, they are not based on time-asymptotic assumptions and therefore enable the temporal variability of these oscillations to be explored. In contrast, traditional, time-asymptotic analysis approaches may inappropriately categorize deterministic oscillations acting on multiple scales with time-varying frequency as noise (33).

Although ultradian rhythms are ubiquitous in biological systems and are found in all organisms from single cells to complex multicellular animals, their origin is still unclear (22, 37, 38). There is no known environmental signal that synchronizes with ultradian rhythms (38). However, it has been shown that ultradian rhythms interact with the circadian rhythm and the daily light/dark cycle (39) and that ultradian rhythmicity can persist in the absence of functional molecular circadian clocks at both behavioral and cellular levels (40, 41). Recent study suggests that the balance between circadian and ultradian rhythmicity is determined by energy balance (42). It is also known that there are multiple ultradian rhythms of physiological or behavioral origin, and that they can be synchronized with each other. However, no central ultradian pacemaker has been identified so far (43). Yet, it has been shown that among the coupled ultradian rhythms, the hippocampal theta wave is phase leading, suggesting a central control of some of the ultradian rhythms (43). It has also been shown that striatal dopamine exhibits an ultradian rhythm and that its signaling manipulation alters ultradian periodicity (44). This suggests that dopamine is involved in mediating ultradian rhythms. Furthermore, the ultradian feeding rhythm in the common vole is known to synchronize between individuals, suggesting that some of the ultradian rhythms have functional significance (39).

To investigate the circadian and ultradian rhythms and their couplings, the running wheel activity of wild-type mice, heterozygous PER2::LUC knockin mice, and *Per1/2/3* KO mice was measured in several conditions. First, the behavior of a control group containing seven heterozygous PER2::LUC knockin Mice and a wild-type littermate in constant darkness was established. Then, the behavior of *Per1/2/3* KO mice in constant darkness with and without methamphetamine was evaluated. Lastly, the behavior of *Per1/2/3* KO mice was measured with and without methamphetamine in constant darkness and in constant light, as well as in conditions of 12 h darkness and 12 h light alternating for several days.

Data were analyzed using novel methods for tracing instantaneous frequencies (30) and mutual couplings (32, 45) in time, based on the theory for discerning time-resolved oscillatory dynamics (35, 36, 46). Characteristic frequencies of relevant oscillations on time-scales between days and minutes were calculated over time using the wavelet transform and ridge extraction (28, 30). The frequency content was additionally checked using harmonic analysis (47) to establish the presence of modes and distinguish them from

high harmonic components. Once modes were established, wavelet bispectral analysis (32) and dynamic Bayesian inference (DBI) (27, 31) were used to infer directions of coupling between modes under various experimental conditions, as outlined above.

Our results demonstrate that the circadian rhythm is highly stable in wild-type and PER2::LUC knockin mice. Knocking out *Per1/2/3* genes reduces the power of the circadian rhythm and introduces irregularity. Methamphetamine reinstates an irregular, nonstationary, circadian rhythm in the absence of canonical clock genes. When evaluated using a time-localized approach, there exists clear evidence of birhythmicity (48–50) in *Per1/2/3* KO mice following methamphetamine administration. Additionally, for the first time, we demonstrate changes in the coupling between modes following methamphetamine exposure. The dynamic, time-varying, characteristics of the MASCO may have implications regarding sleep disorders following stimulant exposure (51–54), particularly in individuals with attention deficit/hyperactivity disorder (ADHD) (55–57), and in several other conditions including schizophrenia, Alzheimer's disease, and autism spectrum disorder (58–63). A clearer understanding of the mechanisms behind the irregular nature of the MASCO may elucidate dynamic aspects of circadian regulation.

## Results

### Highly regular circadian oscillations in wild-type and PER2::LUC knockin mice

To determine the behavior of the canonical circadian rhythm, wheel running activity of a control group containing heterogeneous PER2::LUCIFERASE knockin mice, and one wild-type littermate, was assessed in constant darkness ( $n = 8$ ). The wavelet transform in Fig. 1B demonstrates highly regular nature of the circadian rhythm in this control group. Furthermore, the time-averaged power in Fig. 1C demonstrates a sharp peak centered ~24 h. The average frequency of this oscillation in the control group was  $23.9 \pm 0.1$  h. Two cohorts of wild-type mice ( $n = 5$ ,  $n = 6$ ) were also measured in constant darkness, over a shorter recording interval (20 and 21 days, respectively). The circadian oscillation was confirmed as being highly regular in these mice. Their group median circadian frequencies were  $23.4 \pm 0.2$  h and  $23.6 \pm 0.2$  h, respectively. Full details, including the frequency of each mode for each mouse and their time-localized powers, are given in the [Supplementary material](#). The presence of ultradian and high-frequency modes were also detected in the heterozygous PER2::LUC knockin and wild-type mice, but at a much lower power relative to the circadian rhythm.

### Ultradian oscillations are prevalent in *Per1/2/3* knockout mice

Wheel running activity in a cohort of *Per1/2/3* knockout mice in constant darkness ( $n = 6$ , *Per1/2/3* KO DD hereafter) demonstrated significant changes to the circadian oscillation observed in wild-type and heterozygous PER2::LUC knockin mice. Instead of a single, nontime-varying mode, an intermittent quasi-circadian rhythm appeared around every 22 days, as previously reported (41). The average frequency of the most prominent oscillatory mode in the *Per1/2/3* KO DD group was  $7.2 \pm 0.9$  h, with both the large standard deviation (SD), and Fig. 1E highlighting the time variability of this mode.

### Methamphetamine exposure induces a time-varying circadian rhythm

Analysis of wheel running activity in a cohort of *Per1/2/3* knockout mice in constant darkness with methamphetamine exposure



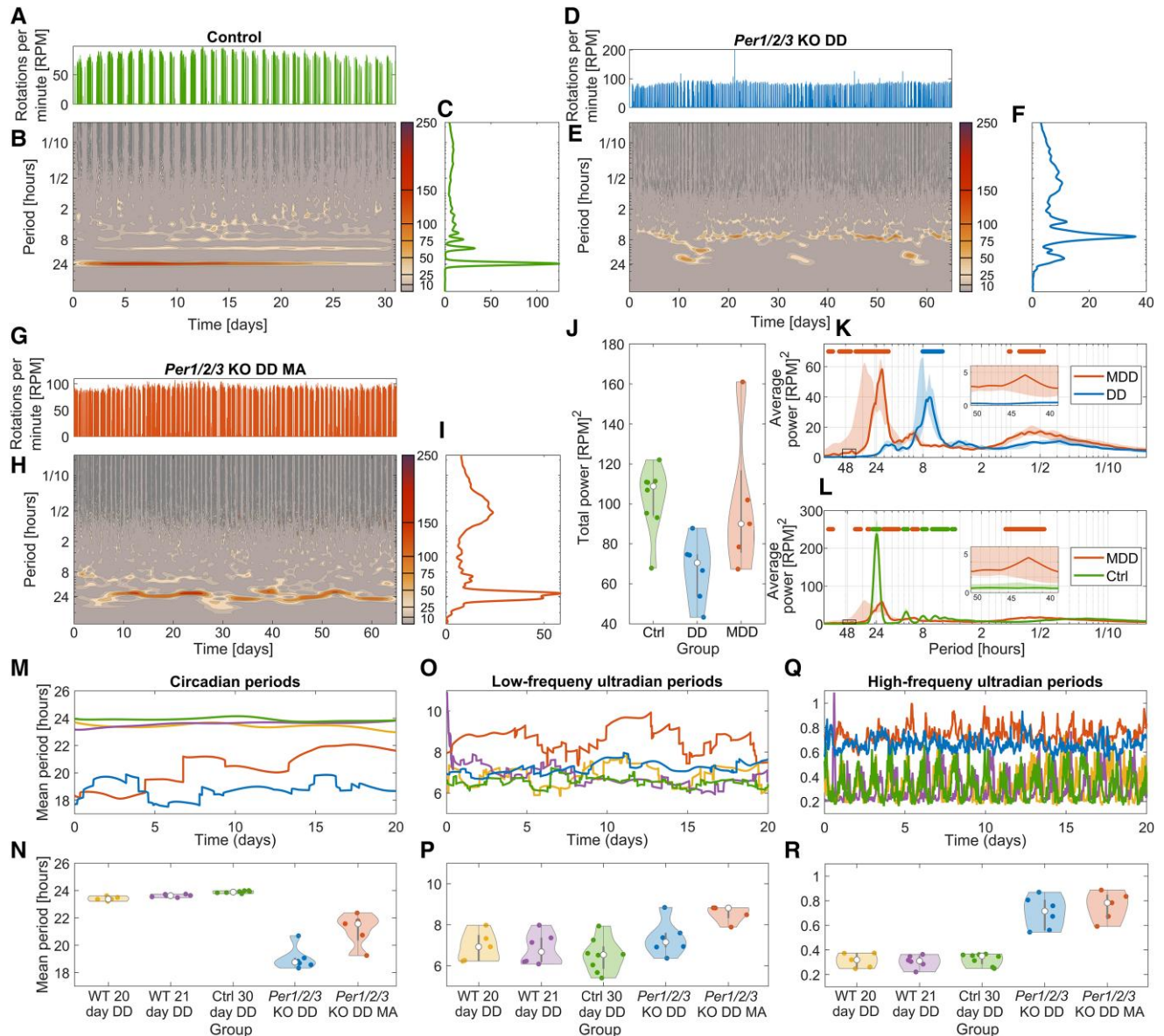


**Fig. 1.** Multiscale oscillatory activity in heterozygous *PER2::LUC* knockin, wild-type and *Per1/2/3* KO mice with and without methamphetamine administration. For all plots, yellow is used for data related to wild-type mice from the group measured for 20 days, purple is used for the wild-type group measured for 21 days, green is used for the control group measured for 30 days, blue is used for the *Per1/2/3* KO mice measured for 65 days, and red is used for the *Per1/2/3* KO mice exposed to methamphetamine for 65 days. All mice were in constant darkness. A, D, G) Time-series of wheel rotations per minute in the control group, *Per1/2/3* KO (DD), *Per1/2/3* KO DD MA mice. B, E, H) Time-frequency representations of the control group, *Per1/2/3* KO DD and *Per1/2/3* KO DD MA data. C, F, I) Time-averaged power for each group, respectively. J) Total power evaluated between periods of 84 h and 4 min in each condition. The total power between the control group (Ctrl) and *Per1/2/3* KO mice is statistically significant ( $P = 0.0047$  Wilcoxon rank sum, effect size = 2.2, Cohens D. K, L) Group median time-averaged power plot (K) compares the *Per1/2/3* KO mice with and without methamphetamine, while (L) compares the methamphetamine *Per1/2/3* KO mice and the control group. The shading represents the 25th and 75th percentile while the circles indicate frequencies where there were significant differences between groups, with the color of the circle indicating the group with the greater power (Wilcoxon rank-sum test  $P < 0.01$ ). M, O, Q) Group median instantaneous frequencies for the circadian and ultradian modes evaluated over time. N, P, R) Time average instantaneous frequencies for the circadian and ultradian modes for each mouse. The instantaneous frequency of each mode was obtained using ridge extraction (30).

( $N = 5$ , *Per1/2/3* KO DD MA) reveals the restoration of the circadian rhythm compared to the *Per1/2/3* KO DD mice. The wavelet transform in Fig. 1H, and the width of the time averaged power peak in Fig. 1I illustrate circadian behavior with significant time-variability compared to the wild-type and heterozygous *PER2::LUC* knockin mice. The average frequency of the circadian activity was  $21.6 \pm 2.5$  h. Closer inspection of the time-localized power in Fig. 1H reveals that the MASCO seems to exhibit birhythmicity, seemingly switching between periods greater than and less than 24 h over time.

To further evaluate the differences following methamphetamine exposure, group median power values were compared. Figure 1K illustrates these differences, with the colored circles representing the group with a significantly higher power at a given frequency (Wilcoxon rank sum test,  $p < 0.01$ ) while the shaded area represents the 25/75th percentile. Circadian and high-frequency ultradian power are elevated following methamphetamine administration. Additionally, methamphetamine administration introduced a significant circadian rhythm with period of around 2 days. A low-frequency ultradian mode was also

present in the *Per1/2/3* KO DD MA mice, albeit at a slightly elongated average period of  $8.8 \pm 1.3$  h and reduced power compared to the *Per1/2/3* KO DD group, as Fig. 1K demonstrates.

### Methamphetamine exposure induces a time-varying circadian rhythm

The frequencies of the circadian and ultradian modes were analyzed in two wild-type groups ( $n = 5$  WT, 20-day DD;  $n = 6$  WT, 21-day DD) to ensure that the luciferase knock-in (30-day control group) did not affect the stability of rhythms. Figure 1 demonstrates the group average (M, O, Q) and time average (N, P, R) frequencies for each mode. All wild-type mice exhibited consistent average frequency values across groups. In contrast, *Per1/2/3* KO mice displayed slightly faster circadian activity and slightly slower high-frequency ultradian activity. The frequencies of each individual mouse for the three modes are provided in the [Supplementary material](#).

### The behavioral dynamics of *Per1/2/3* KO mice in multiple conditions

The wheel running activity of *Per1/2/3* KO mice ( $N = 8$ ) was assessed across a series of conditions. The behavioral rhythms generally exhibited time-varying frequencies, with the dominant oscillation changing dependent upon the experimental condition,

illustrated in Fig. 2B. Initially, the mice were exposed to light/dark cycles (LD, 12 h light and 12 h dark), and they exhibited a stable daily rhythm with a period of 24 h. Subsequently, the light periods were removed, leaving the mice in constant darkness (DD). In the absence of light and with *Period* genes knocked out, the dominant oscillatory mode was at around 7 h. Following administration of methamphetamine during constant darkness (MDD), the dominant rhythm is within the circadian range. When exposed to methamphetamine in constant light (MLL), a similar behavior was observed, but at a slightly higher frequency. After methamphetamine was removed, the mice remained in constant light (LL), where the dominant period was around 4 h. When constant darkness was restored (FDD), both a 7 h and circadian mode were present. The additional circadian mode, reminiscent of the MDD condition, may suggest an enduring effect from methamphetamine in the system. The results of *Per1/2/3* KO mice both with and without methamphetamine were consistent with our previous findings. The wavelet transforms for each mouse under investigation are provided in the [Supplementary material](#).

### Methamphetamine increases total power

Comparing control group, *Per1/2/3* KO DD and *Per1/2/3* KO DD MA mice revealed that the total power was significantly different (Wilcoxon rank-sum,  $P = 0.0047$ , effect size = 2.2, Cohen's  $D$ )

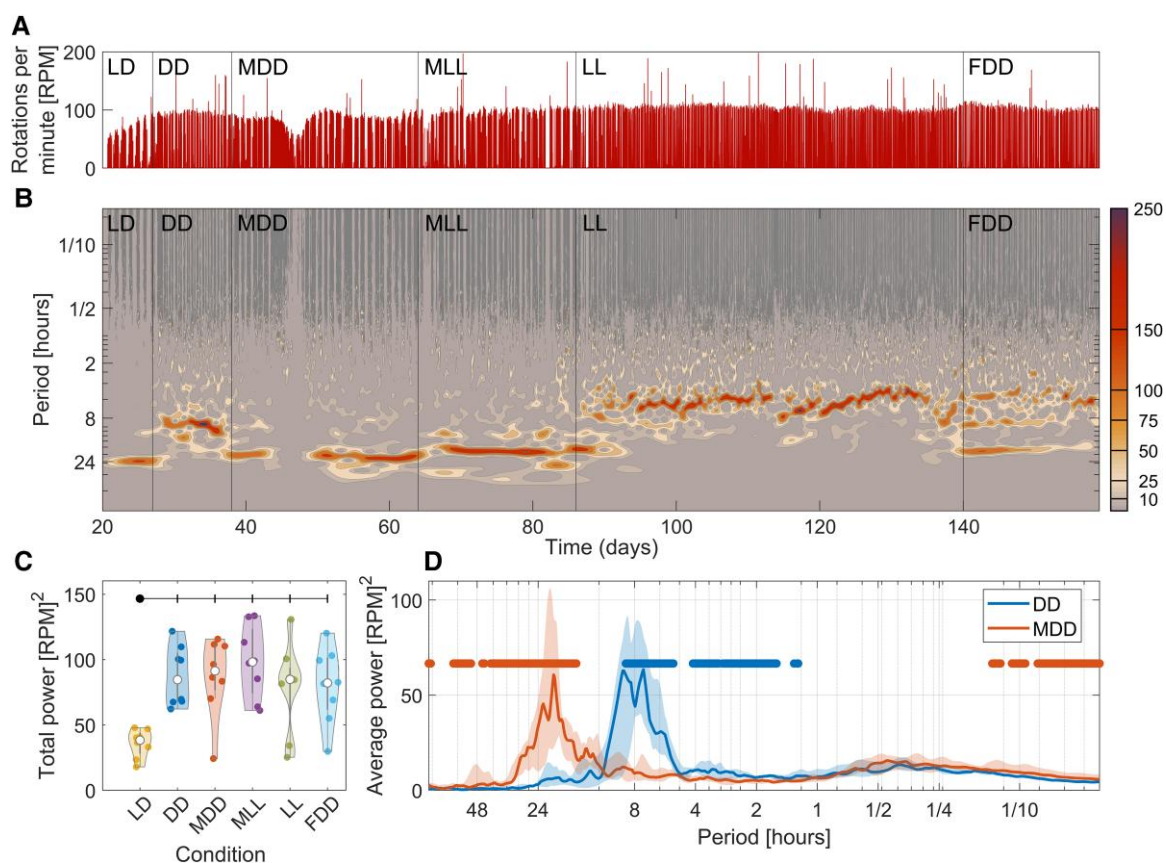


**Fig. 2.** The effect of different environmental and pharmacological modalities on the locomotor rhythms of *Per1/2/3* KO mice. A) time-series recorded for 139 days under varying conditions. The separate experimental conditions are denoted as follows: LD, light/dark cycles of period 24 h; DD, constant darkness; MDD, constant darkness with methamphetamine administration; MLL, constant light with methamphetamine administration; LL, constant light; FDD, final condition of constant darkness. B) Time-frequency representation across all conditions. C) The total power evaluated in a central 7 day window of each measurement modality across scales with periods between 84 h and 4 min. Circles and dashes on top of the plot denote significant differences between conditions ( $P < 0.05$ ). D) Time-averaged power in the DD (blue) and MDD (orange) modalities. shading denotes the 25th to 75th percentiles, the bold line represents the median value across frequency and blue/orange dots represent a significant difference between groups at a given frequency ( $P < 0.05$ ) evaluated using the Wilcoxon rank sum test.



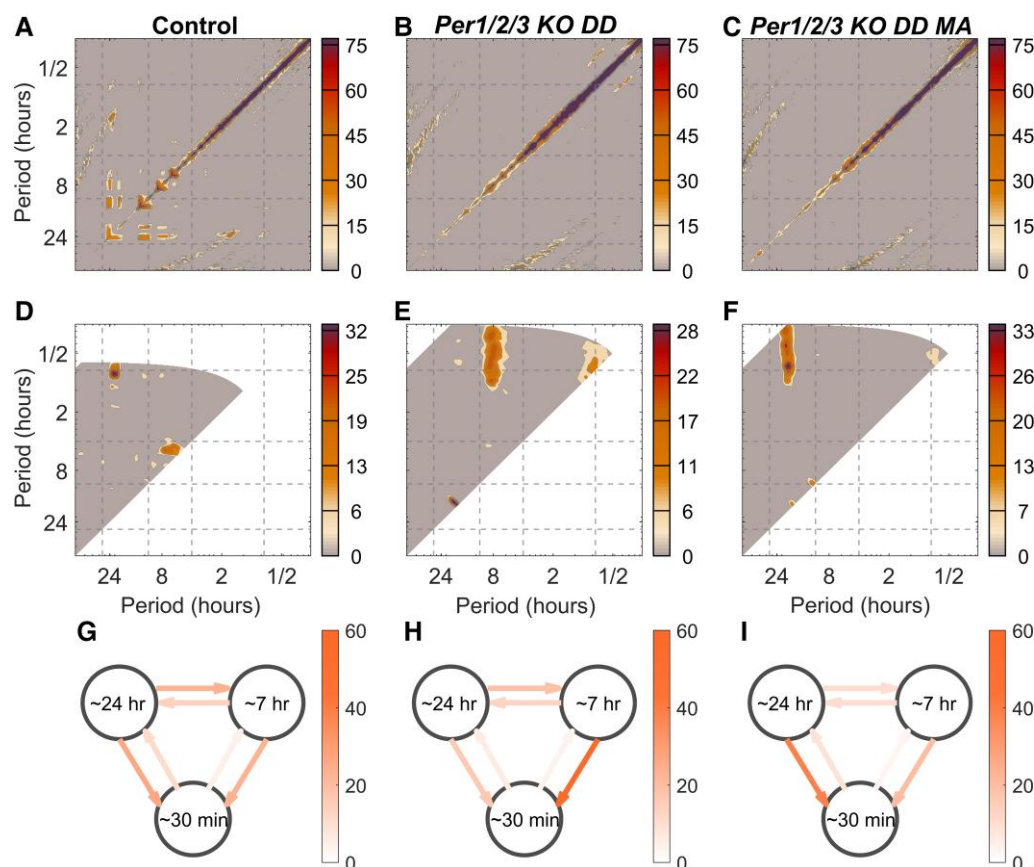


**Fig. 3.** Harmonic and coupling analysis between the control group (first column), *Per1/2/3* KO DD mice (second column), and *Per1/2/3* KO DD MA mice (third column). Harmonic analysis (A–C) demonstrates pronounced harmonics in the control group, arising from circadian oscillations. The colorful peaks indicate the detection of these harmonics. The diagonal line, representing the comparison of the same oscillation to itself, shows high mutual information, while off-diagonal peaks signify the presence of harmonics, such as those observed between 24 and 12 h in (A). Bispectral analysis (D–F) highlights couplings between oscillatory modes at different frequencies. Similar to harmonics, contoured peaks indicate regions of significant coupling between these modes. DBI (G–I) shows the percentage of time during which the oscillatory modes (circadian  $\approx 24$  h, low-frequency ultradian  $\approx 7$  h, high-frequency ultradian  $\approx 30$  min) remained coupled throughout the time series. Increased color intensity corresponds to a longer duration of coupling between specific modes.

between the control group and *Per1/2/3* KO DD group, but not *Per1/2/3* KO DD MA and *Per1/2/3* KO DD mice. This was despite a tendency for increased total power in *Per1/2/3* KO DD MA mice. This is likely due to the reduced statistical strength owing to small sample sizes ( $N_{\text{Ctrl}} = 8$ ,  $N_{\text{DD}} = 6$ ,  $N_{\text{MDD}} = 5$ ).

Total power results were also calculated in the *Per1/2/3* KO mice across the different experimental conditions. Only the LD condition total power differed significantly from the other conditions (Wilcoxon rank-sum,  $P < 0.05$ , Fig. 2C).

### Harmonic detection

Before considering the presence of mutual coupling between modes, the independence of activity in the time-frequency domain must be ascertained. Harmonic analysis in Fig. 3A–C demonstrates the control group, *Per1/2/3* KO DD and *Per1/2/3* KO DD MA data, respectively. The control group mouse has significant evidence for harmonics of the circadian oscillation, indicating that the peaks at around 12, 8, and 4 h in the power plots of Fig. 1B and C are not independent modes. There was no evidence for harmonics in the *Per1/2/3* KO mice exposed to methamphetamine. Notably, the circadian oscillations present in *Per1/2/3* KO DD MA mice are independent modes, and not the result of harmonics. In contrast, *Per1/2/3* KO DD mice demonstrated evidence of a harmonic in about half of the mice between 7 and 3.5 h. Harmonic

analysis for each of the mice is presented in the [Supplementary material](#).

### Couplings change following methamphetamine administration

The presence of mutual coupling between modes was evaluated using bispectral analysis. Figure 3D–F indicate phase couplings between behavioral modes for the control group, *Per1/2/3* KO DD mice and *Per1/2/3* KO DD MA mice, respectively. The control group mice were measured for 30 days, hence insufficient data were present to consider the couplings to the high-frequency activity. Although a number of bands demonstrated traces of significant couplings in the control mice, these patterns were not consistent across the group (Fig. 3G and [Supplementary material](#)). Both *Per1/2/3* KO DD, Fig. 3E, and *Per1/2/3* KO DD MA, Fig. 3F, reveal the presence of couplings within the high-frequency ultradian band. In the *Per1/2/3* KO DD mice, the predominant coupling was between the  $\sim 7$  h oscillation and higher frequencies. Following methamphetamine exposure the coupling between the circadian rhythm and high-frequency ultradian activity became dominant.

DBI was employed to further confirm the presence of these couplings and detect the direction of the information flow between modes. This metric was evaluated as the percentage time over which certain directional couplings were present (Fig. 3G–I). In

*Per1/2/3* KO DD mice, the 7 h mode drove high-frequency activity, while in *Per1/2/3* KO DD MA mice circadian rhythms became the dominant driver (Fig. 3I).

## Discussion

Circadian rhythms are a fundamental characteristic of mammalian life. To function optimally, humans are constrained to operate within a 24 h cycle. Neglecting our implicit chronobiology may lead to mental illness and disease (55–59, 61–64). While many recent discoveries have shed light upon the canonical circadian clock, less is known about alternative pacemakers which may impact these processes (15, 65). A more comprehensive understanding of these noncanonical oscillators, such as the MASCO may elucidate the mechanisms behind, for example, human sleep disorders (10) and addiction to psychostimulants (15).

### Time-localized, multiscale analysis approach

Here, we apply time-localized multiscale analysis approaches to investigate behavioral dynamics following methamphetamine administration in *Per1/2/3* KO mice (33, 46, 66). The approach exploits wavelet analysis to evolve the power and frequency of the rhythms over time and allow for studying their nonstationary time-variable nature. Wavelets are usually considered as a linear method (67). Because of the time evolution they provide, they allow for studying the signatures of nonlinearities such as the occurrence of high harmonics (47), and their time-variable frequencies (68). The time-variable frequencies can then be extracted using ridge extraction (30) and in this way, frequency and phase relationships can be evaluated under different conditions. In particular, couplings between instantaneous frequencies and phases can be studied (32, 45). Couplings have been demonstrated to provide a wealth of information about the state of a system in various applications (31, 69). Here, we demonstrate how couplings change with *Per1/2/3* genes knocked out and in the presence of methamphetamine. In this way, we add an additional approach to studying periodic behavior on multiple scales to the existing methods (67, 70, 71).

### Behavioral rhythms in *PER2::LUC* knockin and wild-type mice

To understand the effect of methamphetamine on circadian oscillations, a series of experiments were conducted. Initially, the behavioral rhythms of a control group containing heterozygous *PER2::LUC* knockin mice and a wild-type littermate in constant darkness were established. A circadian rhythm with a strong and distinct peak was present at  $23.9 \pm 0.1$  h. Similarly stable circadian oscillations were found in two additional cohorts of wild-type mice, with periods of  $23.4 \pm 0.2$  h and  $23.6 \pm 0.2$  h respectively. The strength of this peak arises for two reasons: first, it is dominant compared to the low (5.4–8.0 h) and high (0.22–0.37 h) frequency ultradian activity, but more importantly, the frequency is highly regular and almost constant over time (Fig. 1B).

### The effect of *Per1/2/3* KO on behavioral rhythms

Wheel running activity in *Per1/2/3* KO mice in constant darkness was analyzed to elucidate what happens to behavioral rhythms when genes responsible for the canonical circadian rhythm are removed. The results revealed that knocking out the *Period* genes significantly altered the circadian rhythm. *Per1/2/3* KO DD mice exhibited an intermittent quasicircadian oscillation which

seemed to appear around every 22 days, supporting previous results from this type of murine sample (41). Due to the intermittent and relatively weak nature of the circadian activity, the low-frequency ultradian oscillation, which occurred at a frequency of  $7.2 \pm 0.9$  h, was dominant, as demonstrated in Fig. 1E.

### The impact of methamphetamine exposure upon circadian and ultradian dynamics

The effect of methamphetamine upon *Per1/2/3* KO mice in constant darkness was established. A peak in power around the circadian frequencies was detected. However, while methamphetamine is able to reinstate a circadian oscillation, we found several characteristic features of the data are altered. The average period of circadian activity in the *Per1/2/3* KO DD MA group occurred at  $21.6 \pm 2.5$  h, compared to  $23.9 \pm 0.1$  h in the control group. The reduced SD in the control group indicates a lack of time variability. In contrast, the peak MASCO frequency in the *Per1/2/3* KO DD MA mice varied significantly over time (Fig. 1H) and was much less regular. Closer inspection revealed birhythmicity between modes at periods slightly longer and shorter than 24 h, in agreement with previous findings (9, 49, 72). The ultradian mode present in the *Per1/2/3* KO DD mice persisted following methamphetamine administration, though with reduced intensity, and an elongated period of  $8.8 \pm 1.3$  h. Total power indicated that methamphetamine administration restored activity levels similar to those observed in the control group. Methamphetamine administration also significantly elevated high-frequency ultradian activity compared to both the control group and *Per1/2/3* KO DD mice, suggesting erratic, quick bouts of activity, likely associated with methamphetamine-induced hyperactivity in mice (73–75). Moreover, methamphetamine exposure induced a circadian oscillation, a documented behavior in rodents (23, 76).

### Couplings between circadian and ultradian rhythms

Elongated recordings for the *Per1/2/3* KO DD mice enabled harmonic and coupling analyses between modes. Harmonic analysis confirmed that the circadian, low-frequency ultradian and high-frequency ultradian modes observed were independent. Importantly, the circadian oscillation induced by methamphetamine was also confirmed as an independent mode. Bispectral analysis revealed that a significant coupling existed between the low- and high-frequency ultradian activity in the *Per1/2/3* KO mice without methamphetamine, supporting previous findings (41). When *Per1/2/3* KO mice were exposed to methamphetamine, the significant coupling was instead detected between the circadian and high-frequency activity. DBI was subsequently employed to confirm the results of the bispectral analysis and determine the direction of information flow between the behavioral modes. DBI confirmed the presence of couplings. The direction of information flow was from the slower to the quicker oscillation in each case. These results highlight that not only the presence of modes but also the interactions between them are altered following methamphetamine administration.

### Influence of methamphetamine and light on *Per1/2/3* KO mice.

Finally, *Per1/2/3* KO mice were exposed to a series of different light and pharmacological conditions. Following methamphetamine exposure in both constant darkness and constant light, an ~24 h periodicity was restored, supporting the findings in *Per1/2/3* KO DD MA mice reported above. The results also demonstrated that

methamphetamine may have long-term effects upon the system as the constant darkness condition following drug exposure still contained significant evidence of sustained 24 and 7 h oscillations (Fig. 2B). It has been previously reported that LL exposure rescued the circadian behavioral rhythm in *Cry1/2* double knockout mice (77, 78). Therefore it is possible that the behavioral circadian rhythm we observed in DD is due to LL exposure. While these oscillations are known to be present (65, 79), further clarification of their duration and intensity may have important implications for future experimental designs.

## Phenomenological model

A simple phenomenological model was utilized to further validate the observed behaviors against a ground truth. Simulating the time series as several interacting phase oscillators yielded power results strikingly similar to those from the analyzed experimental data. Furthermore, altering the coupling strength between oscillators yields the same outputs as the experimentally derived coupling results, as demonstrated in Fig. 4 and the [Supplementary material](#). The similarity between experimental and phenomenological model derived results validates the nonautonomous phase network dynamics framework used in the analysis (33, 46), while also verifying our interpretation of the results using a ground truth.

## MASCO and internal dissociation

Previous studies on humans isolated from social and natural environments have demonstrated a phenomenon called internal dissociation, where the sleep-wake cycle shifts to either a longer (30-h) or shorter (20-h) rhythm, despite the body's core temperature maintaining an ~24-h cycle (80). Although our study was conducted in mice, the behavioral rhythms observed following methamphetamine administration closely resemble those during internal dissociation in the human sleep-wake cycle. This similarity suggests that the MASCO may play a crucial role in regulating the human sleep-wake cycle (81). The involvement of the MASCO may partially explain the sleep disorders frequently reported in individuals treated with stimulants, such as those with ADHD (55–57).

## Conclusion and future work

Our results suggest that two main factors are crucial for period determination in wheel running activity: the use of time-localized analysis approaches, which do not average over transient dynamics, and the use of extended recording intervals, sufficient to capture the inherent time-variability of the MASCO. The instability of the MASCO may suggest that *Period* genes play a crucial role in regulating the time-variability of the circadian rhythm, or alternately that the MASCO itself is inherently time-variable. Additionally, the multiscale nature of the investigation enabled circadian, circadian and ultradian oscillations to be considered simultaneously, whilst also being a sufficient length for coupling analysis.

The presence of an additional low-frequency (~3.5 h) ultradian rhythm has been previously reported in *Per1/2/3* KO DD mice (41). However, in the present study, there was insufficient evidence to classify this period as a distinct mode. Future investigations involving mice under varied experimental conditions and extended measurement intervals are necessary to confirm or contradict its existence.

Future investigations may utilize this approach to evaluate dynamical characteristics in different experimental conditions and animal populations. For instance, analysis of alternative

noncanonical oscillators, such as the food-entrainable oscillator, and comparison to the MASCO may provide evidence regarding a proposed common dopaminergic basis (82). Additionally, investigating the number of cycles which behavioral patterns persist for in the absence of the stimuli that induced them may inform future experimental design.

Time-resolved analysis methods offer a wealth of additional information and insight into the mechanisms of complex behavior, unlike detrended fluctuation analysis which provides information about the balance between randomness and regularity (70, 71). By considering behaviors throughout time, one can observe temporal variability that may betray underlying biological implications (83). Circadian rhythms are intimately linked to several pathologies, both mental and physical (84–86). By applying novel time-series analysis approaches one may reveal an abundance of information, previously disregarded as stochastic, and move towards a more complete description of circadian regulation.

## Materials and methods

### Animals

All mouse experiments were approved by the Institutional Animal Care and Use Committee at UT Southwestern Medical Center (Protocol #2013-0035 and #2016-10376-G).

*Bmal1* KO mice are commonly used for studying the functional significance of the circadian rhythm because this single gene knockout can disrupt molecular circadian oscillations entirely. However, *Bmal1* KO mice have a significantly reduced life span and experience premature ageing (87). Therefore, they are inappropriate for studies which require long-term behavioral recordings. Although *Per1/2/3* KO mice have disrupted molecular circadian rhythms, no notable health issues have been reported (48), hence their use in this study.

In the initial investigation,  $N = 8$  *Per1/2/3* KO mice (Yamazaki Lab Experiment #74; 4 males, 4 females; 5–8 months old; C57BL/6J or C57BL/6J and C57BL/6N mixed backgrounds (41, 50)) were measured in a variety of conditions. Mice were first exposed to 12 h light, 12 h dark cycles for 7 days (LD, light intensity ~450 lux at cage level) and then kept in constant darkness for 11 days (DD). Subsequently, methamphetamine was administered through drinking water for 26 days while they remained in constant darkness (MDD). The mice were then exposed to constant light for 22 days while methamphetamine administration continued (MLL, light intensity ~170 lux at cage level). Subsequently, methamphetamine was removed while still in constant light for 54 days (LL, light intensity ~170 lux at cage level). The final 24 days of the experiment were conducted in constant darkness for 24 days (FDD). This group is referred to as “*Per1/2/3* KO DD multiple conditions” throughout the text.

To better understand the multiscale behavioral changes following exposure to methamphetamine across elongated measurement intervals, five additional cohorts of mice were investigated. A cohort of heterozygous *PER2:luciferase* knockin mice ( $n = 7$ ) and one wild-type littermate ( $n = 1$ ), were used as a comparison point (Yamazaki Lab Experiment #17; 5 males, 3 females; 1.3–9.5 months old; C57BL/6J background (88, 89)). These mice were kept in constant darkness for 95 days without methamphetamine. General cage activity was recorded with an infrared motion detector in the cage without a running wheel for the first 10 days, then in a cage containing a locked running wheel for 11 days. After that, the running wheel was unlocked and both general activity and wheel running activity were recorded for 20



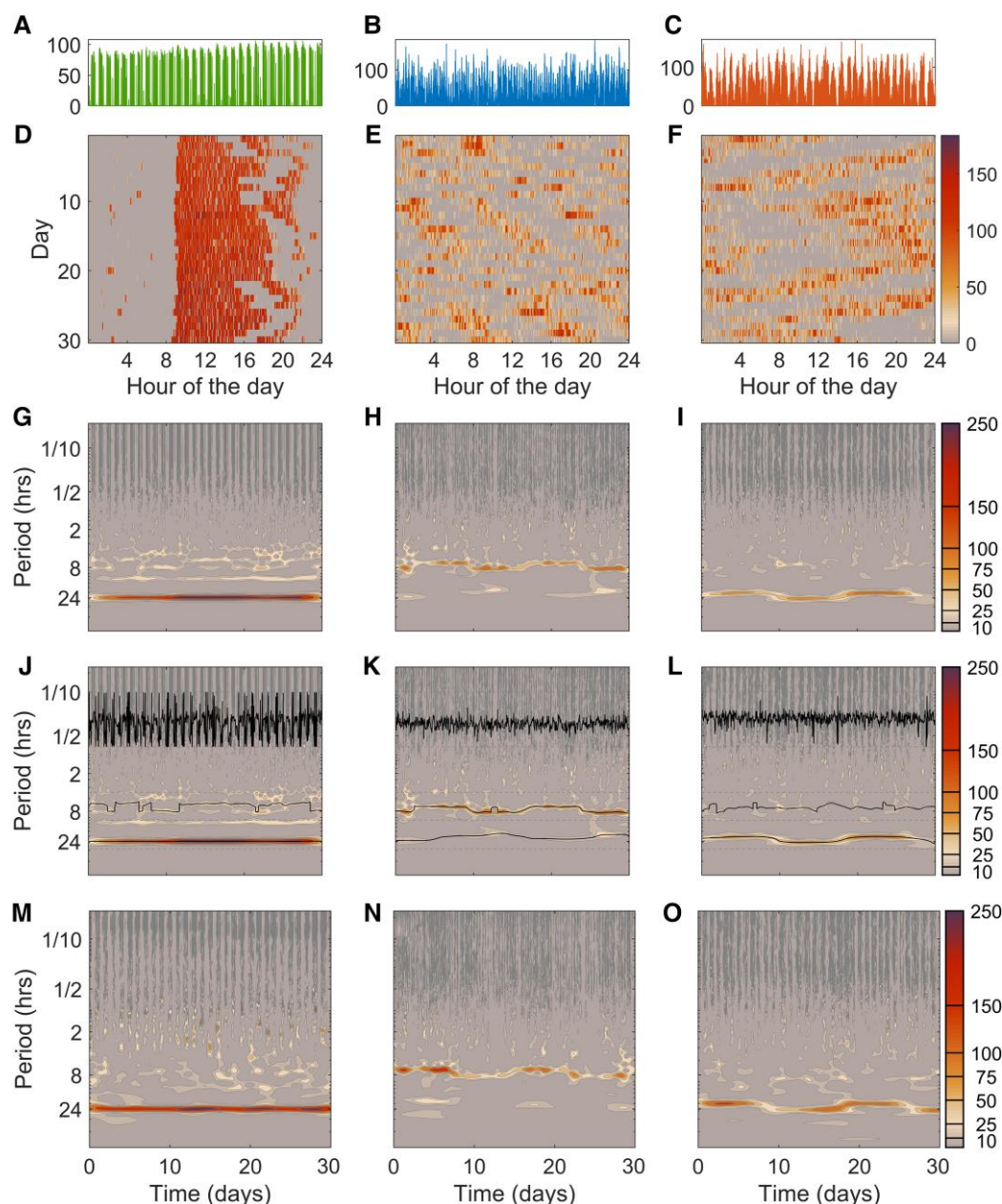


**Fig. 4.** Comparison between the time and time-frequency domains for evaluating characteristic features of underlying dynamics. Each mouse condition is represented by a column; the control group (first column), *Per1/2/3* KO DD mice (second column), and *Per1/2/3* KO DD mice with methamphetamine (third column). A–C) Thirty days of the recorded wheel running activity per minute. D–F) Actograms representing the amount of wheel turns for each minute of activity. G–I) Time-frequency representation of each condition. J–L) Extracted ridges for each of the time-frequency representations. In each frequency band, the ridges follow a high amplitude peak through time. The phases at each of these points are used in the coupling analysis. M–O) Data generated by the phenomenological model which was used to validate conclusions.

days. The wheel was then locked once again for a further 21 days, before being unlocked for the final 30 days. Here, we analyzed the last 30 days of running wheel activity. This group is referred to as “the control group” throughout the text.

Heterozygous *PER2:luciferase* knockin mice were used as the control group due to their elongated recordings in constant darkness, which enabled coupling analysis. To confirm that the power results observed in these knockin mice are consistent with those in pure wild-type cohorts, two groups of wild-type mice recorded over shorter intervals were analyzed.

In one of these experiments,  $n=5$  wild-type male mice (Yamazaki Lab experiment #17B; 5 weeks old at the beginning of the experiment; strain C57BL/6N), were included. Mice were first

exposed to 12 h light, 12 h dark cycles for 7 days. Subsequently, they were kept in constant darkness for the duration of the recordings analyzed in the present study. On the 22nd day, the mice were moved into cages containing a locked wheel, while remaining under DD. On day 33, the running wheels were unlocked and the running wheel activity could be measured for the subsequent 20 days, until they were once again locked. This procedure resulted in a 20 day recording of running wheel activity in wild-type mice in DD. The time-localized powers of these mice are summarized in the [Supplementary material](#). This group is referred to as “wild-type 20 days.”

Additionally,  $n=6$  males (Yamazaki lab experiment #20;) were analyzed; all mice were between 7 and 8 weeks old at the

beginning of the experiment; strain: C57BL/6J. The mice were exposed to light/dark 12 h repeats for 7 days. A constant darkness protocol was then initiated. After 21 days, the mice were switched to a cage with a wheel to measure movement. They remained in this cage for another 21 days in constant darkness, and the wheel allowed their movement to be tracked during this interval. The time-localized power for each of the six mice measured under these conditions is shown in the [Supplementary material](#). This group is referred to as “wild-type 21 days.”

A cohort of *Per1/2/3* KO mice (Yamazaki Lab Experiment #86; three males, four females; 3.5–8.5 months old; C57BL/6J background with *cfos-shGFP* transgene (90)) were initially exposed to constant light (~220 lux at cage level) for 26 days then kept in constant darkness for 65 days without methamphetamine exposure. A male mouse (#2 in the [Supplementary material](#)) was excluded as the entire recording length was not completed. The 65 days of running wheel activity in constant darkness were analyzed in this manuscript. This group is referred to as “*Per1/2/3* KO DD.”

Another cohort of *Per1/2/3* KO mice (Yamazaki Lab Experiment #54; one male, four females; 4.5–5.5 months old; C57BL/6J or C57BL/6J and C57BL/6N mixed background) were kept in DD for 27 days without methamphetamine, before being exposed to methamphetamine for the subsequent 101 days. The first 65 days of activity during methamphetamine administration was analyzed and is referred to as “*Per1/2/3* KO DD MA.”

Each mouse was housed individually in a plastic cage (length × width × height: 29.5 × 11.5 × 12.0 cm) containing running wheels of diameter 11 cm. Wheel revolutions were continuously recorded every minute by the ClockLab system (Actimetrics, Wilmette, IL, USA). As described above, general cage activity was monitored with a passive infrared sensor (product ID 189, Adafruit, New York City, NY, USA) placed above the cages without a running wheel or with locked running wheels, however those data were not analyzed in the current study. The cages were placed in light-tight ventilated cabinets and the temperature, humidity, and light intensity inside the cabinet were recorded every 5 min by Chamber Controller software (Actimetrics, Wilmette, IL, USA). The white LEDs inside the cabinet were controlled by the Chamber Controller software. Cages and water bottles were changed once every 3 weeks. An infrared viewer (FIND-R-SCOPE Infrared Viewer; FJW Optical Systems, Inc., Palatine, IL, USA) was used to perform maintenance in the dark without exposing mice to visible light. For methamphetamine administration, water bottles were replaced with drinking (tap) water containing 0.005% methamphetamine (Sigma-Aldrich, St. Louis, MO, USA). Water bottles containing methamphetamine were changed once every 3 weeks. During the experiment mice had *ad liberum* access to food and regular or methamphetamine water.

## Time-series length

Elongated time-series are required to reduce the measurement uncertainty for the following reasons. Firstly, time-varying modes require many cycles to accurately determine the frequency. In addition, it enabled the avoidance of transitory periods when switching between measurement conditions. Thirdly, couplings between modes require a minimum number of cycles to be detected. Asymptotic approaches treat data as stationary by measuring only a minimal number of cycles and averaging across time. In contrast, the approaches presented here harness the maximal amount of information by explicit consideration of time-localized behavior.

## Time-resolved analysis

Evaluating multiscale oscillatory behavior requires methods that can effectively extract information across wide-ranging scales and time periods (68). Without explicitly considering the time-localized, multiscale dynamics, time-series that contain multiple deterministic modes might be incorrectly interpreted as noise (33). The wavelet transform enables such a representation of the data,

$$W_T(s, t) = \int_{-L/2}^{L/2} \Psi(s, u - t) f(u) du, \quad (1)$$

where the mother wavelet,  $\Psi(s, t)$ , is expanded and contracted to optimize the trade off between time-localization and frequency resolution at a given scale, akin to changing the focus on a camera to increase image sharpness. In contrast, Fourier-based approaches use a single window to obtain information across all frequencies, leading to sub-optimal resolution. Here, the lognormal wavelet was used due its superior logarithmic frequency resolution (28). In the frequency domain, it is defined as

$$\hat{\psi}(\omega) = e^{-(\omega_0 \log \omega)^2 / 2}, \quad \text{where } \omega > 0, \quad (2)$$

where  $\omega_0 = 2\pi f_0$  is the frequency resolution parameter of the wavelet. As  $\log \omega$  is the argument of this wavelet, it is particularly well suited to the logarithmic frequency resolution of the transform.

The wavelet transform facilitates multiscale evaluation of time-series (29). This enables the simultaneous evaluation of oscillatory activity taking place over days, hours, minutes, and seconds. In contrast, actograms demonstrate information regarding only the most prominent oscillation. As demonstrated in Fig. 4, this is helpful for illustrating the highly regular, circadian behavior of the wild-type or heterozygous *PER2::LUC* knockin mice; however, this approach is inappropriate when multiple time-varying modes are present simultaneously. As such, the time-frequency representation unlocks a wealth of information compared to purely time domain methods. It also allows for time-localized features in the behavior to be identified and evaluated.

## Total power

Total power can be thought of as the total energy ( $\mathcal{E}$ ) content in the signal (91). In the present investigation, this is defined as

$$\mathcal{E} = \frac{1}{T} \int_0^T \int_{1/2\pi f_{\min}}^{1/2\pi f_{\max}} \frac{1}{s} |W_T(s, t)|^2 ds dt, \quad (3)$$

where  $T$  is the total time, and  $f_{\min}$ ,  $f_{\max}$  represent the minimum and maximum frequencies used when calculating the wavelet transform. The logarithmic frequency distribution resulting from the wavelet transform was explicitly considered when performing the integral. When analyzing multiple conditions in the same experiment, total power was evaluated across the central 7 days to reduce edge effects.

## Harmonic analysis

Spectral peaks are obtained from a mathematical description of time series and are not necessarily linked to physical oscillatory systems or modes. In the case of nonlinearities, i.e. when the signal is not of sinusoidal shape, many high harmonic components can occur belonging to the activity of a single mode. When the rhythms are strictly periodic the detection of high harmonics is relatively straightforward because they appear at commensurate frequencies of the basic frequency. However, when the rhythms have variable, or nonstationary frequencies, the detection of

high harmonics is a demanding task. To determine whether the detected frequency peaks correspond to independent modes, or the peaks are in harmonic relationship, we conduct harmonic analysis (47). This method evaluates mutual information between time-localized phases across frequency bands. If sufficient shared phase information between a fundamental frequency and its harmonics exceeds a surrogate threshold, then the relationship can be considered as harmonic. For details of the method for surrogate data analysis, see below and Ref. (92).

## Ridge extraction

The underlying oscillatory modes may be harnessed to evaluate their changing power and phase over time (30). The first step here is to find the ridge curve; a region in the time-frequency domain with a series of amplitude/power peaks and their corresponding phases. Tracing these modes in the time-frequency domain can reveal time-localized amplitudes and phases.

## Coupling

Once the independent modes are identified, the presence and direction of their mutual couplings and interactions can be investigated (31). The coupling analyses presented here focuses on phase relationships, independent of amplitude dynamics. The presence of couplings may be detected by bispectral analysis (32), while the direction and duration of coupling can be deduced using DBI (31).

## Bispectral analysis

Wavelet bispectral analysis facilitates the detection of couplings between and/or within time-series (32). Here, we apply autobispectral analysis to ascertain the putative presence of coupling between modes within a single time series; that derived from the wheel running activity of mice. The wavelet bispectrum  $B_W$  measures the amount of phase coupling between modes at scales  $s_1$  and  $s_2$  as,

$$B_W(s_1, s_2) = \int_T W_T(s_1, \tau) W_T(s_2, \tau) W_T^*(s, \tau) d\tau, \quad (4)$$

during a time interval,  $T$  (93) where,

$$\frac{1}{s_1} + \frac{1}{s_2} = \frac{1}{s}. \quad (5)$$

For further details see (32). Surrogate analysis is also applied to verify results.

## Dynamical Bayesian inference

To ascertain the direction of phase information flow between oscillators, we apply DBI (45). This approach infers the coupling function between oscillators by applying Bayes theorem and using both prior and current information via a windowed approach across the time series (27). From the coupling functions, we derive coupling strength over several sequential windows. The number of windows over which the coupling strength exceeds a predefined surrogate threshold defines the coupling time; a metric representing the duration over which a coupling is present.

## Statistical analysis

Due to the non-Gaussian distribution of the data, Wilcoxon rank-sum test was used to compare groups. A P-value of 0.05 was used as a significance threshold when comparing groups evaluated over 6 days, while 0.01 was used as a threshold for the longer recordings as the additional amount of information enabled a reduced threshold.

Once the instantaneous frequencies over time were obtained using ridge extraction, their mean and SD were calculated. In this way, average frequencies and their SD of the individual modes for each mouse were obtained. Group averages were obtained as medians of the average instantaneous frequencies and as medians of the SD.

## Surrogates

To assess whether obtained coupling results are genuine or spurious, we employ surrogate data (92). Connectivity analyses always detect a baseline level of interaction, even between independent time-series, especially when the data are short relative to the frequencies of interest. Surrogates help establish a threshold to minimize the impact of these spurious measurements. The goal when generating surrogates is to maintain the same statistical properties to measured data, with the exception of the specific characteristic being investigated (92, 94).

The same analysis performed between experimental data is applied to the generated surrogate data. This establishes a baseline of measurement outcomes in the absence of true coupling. The process is repeated many times, and a percentile of these surrogate outputs is used to set a threshold value. Results exceeding this threshold are then considered statistically significant (92).

For DBI, 19 cyclic phase permutation surrogates were generated to randomize the phase behavior, while for bispectral analysis 19 iterative amplitude adjusted Fourier transform surrogates were used. In both cases, a 95th percentile threshold was implemented.

## Acknowledgments

The authors thank Crystal N. Bettilyon and Alexandra J. Brown for assistance with generating experimental mice and for animal care during behavior recording.

## Supplementary Material

[Supplementary material](#) is available at PNAS Nexus online.

## Funding

S.J.K.B. is jointly supported by the Engineering and Physical Sciences Research Council (EPSRC), UK and the MyMind GmbH – Brainhero, Vienna, Austria (grant no. EP/T518037/1). MA extends his appreciation to the Deanship of Scientific Research at Northern Border University, Arar, 73311, KSA for funding the research work through the project number “NBU-FFR-2025-0000-01”. The work of S.Y. is supported by National Science Foundation grants IOS-1419477, IOS-1931115, National Institutes of Health grants R21 NS099809, R01NS114527. The work of A.S. is funded through the Sony Research Award Program and the Engineering and Physical Sciences Research Council, UK (grant no. EP/X004597/1). The development of the MODA toolbox used for analyses has been supported by the Engineering and Physical Sciences Research Council (UK) [grant nos EP/100999X1 and EP/M006298/1], the European Union projects BRACCIA (Brain, Respiration and Cardiac Causalities in Anaesthesia) [517133] and COSMOS (Complex Oscillatory Systems: Modeling and Analysis) [642563], the Action Medical Research (United Kingdom) Project [GN1963], and the Slovenian Research Agency (program no. P20232). The High End Computing facility at Lancaster University was used for some of the computations.



## Author Contributions

S.J.K.B.: data curation, software, formal analysis, investigation, methodology, writing-original draft, writing-review and editing investigation; M.A.: formal analysis, investigation, methodology, software; S.Y.: conceptualization, resources, data curation, supervision, project administration, writing-review and editing; A.S.: conceptualization, supervision, funding acquisition, investigation, visualization, methodology, project administration, writing-review and editing.

## Data Availability

The data analyzed in this investigation are available at <https://doi.org/10.17635/lanaster/researchdata/683>. The majority of the analyses were done using the MODA (Multiscale Oscillatory Dynamics Analysis) software toolbox, which is publicly available at <https://github.com/luphysics/MODA> (95).

## References

- Barger LK, Lockley SW, Rajaratnam SMW, Landrigan CP. 2009. Neurobehavioral, health, and safety consequences associated with shift work in safety-sensitive professions. *Curr Neurol Neurosci Rep.* 9(2):155–164.
- Fagiani F, et al. 2022. Molecular regulations of circadian rhythm and implications for physiology and diseases. *Signal Transduct Target Ther.* 7(1):41.
- Chen K, et al. 2024. Biological clock regulation by the PER gene family: a new perspective on tumor development. *Front Cell Dev Biol.* 12:1332506.
- Ralph MR, Foster RG, Davis FC, Menaker M. 1990. Transplanted suprachiasmatic nucleus determines circadian period. *Science.* 247(4945):975–978.
- Inagaki N, Honma S, Ono D, Tanahashi Y, Honma K-I. 2007. Separate oscillating cell groups in mouse suprachiasmatic nucleus couple photoperiodically to the onset and end of daily activity. *Proc Natl Acad Sci U S A.* 104(18):7664–7669.
- Weaver DR. 1998. The suprachiasmatic nucleus: a 25-year retrospective. *J Biol Rhythms.* 13(2):100–112.
- Pendergast JS, Yamazaki S. 2018. The mysterious food-entrainable oscillator: insights from mutant and engineered mouse models. *J Biol Rhythms.* 33(5):458–474.
- Brown AJ, Pendergast JS, Yamazaki S. 2019. Focus: clocks and cycles: peripheral circadian oscillators. *Yale J Biol Med.* 92(2):327.
- Honma K-I, Honma S. 2009. The SCN-independent clocks, methamphetamine and food restriction. *Eur J Neurosci.* 30(9):1707–1717.
- Taufique SK, Ehichioya D, Pendergast J, Yamazaki S. 10 2022. Genetics and functional significance of the understudied methamphetamine sensitive circadian oscillator (MASCO). *F1000Res.* 11:1018.
- Bell-Pedersen D, et al. 2005. Circadian rhythms from multiple oscillators: lessons from diverse organisms. *Nat Rev Genet.* 6(7):544–556.
- Nakamura TJ, et al. 2023. Long days restore regular estrous cyclicity in mice lacking circadian rhythms. *Heliyon.* 9(6):e16970.
- Cox KH, Takahashi JS. 2019. Circadian clock genes and the transcriptional architecture of the clock mechanism. *J Mol Endocrinol.* 63(4):R93–R102.
- Bae K, Weaver DR. 2007. Transient, light-induced rhythmicity in mPer-deficient mice. *J Biol Rhythms.* 22(1):85–88.
- Mohawk JA, Baer ML, Menaker M. 2009. The methamphetamine-sensitive circadian oscillator does not employ canonical clock genes. *Proc Natl Acad Sci U S A.* 106(9):3519–3524.
- Colwell CS, et al. 2003. Disrupted circadian rhythms in VIP-and PHI-deficient mice. *Am J Physiol.* 285(5):R939–R949.
- Brown TM, Hughes AT, Piggins HD. 2005. Gastrin-releasing peptide promotes suprachiasmatic nuclei cellular rhythmicity in the absence of vasoactive intestinal polypeptide-VPAC2 receptor signaling. *J Neurosci.* 25(48):11155–11164.
- Aton SJ, Colwell CS, Hattar AJ, Waschek J, Herzog ED. 2005. Vasoactive intestinal polypeptide mediates circadian rhythmicity and synchrony in mammalian clock neurons. *Nat Neurosci.* 8(4):476–483.
- Hughes ATL, Piggins HD. 2008. Behavioral responses of *Vipr2*–mice to light. *J Biol Rhythms.* 23(3):211–219.
- Power A, Hughes ATL, Samuels RE, Piggins HD. 2010. Rhythm-promoting actions of exercise in mice with deficient neuropeptide signaling. *J Biol Rhythms.* 25(4):235–246.
- Hughes ATL, et al. 2021. Timed daily exercise remodels circadian rhythms in mice. *Commun Biol.* 4(1):761.
- van der Veen DR, Gerkema MP. 2024. Re-scoping ultradian rhythms in the context of metabolism. *Front Psychol.* 15:1504879.
- Markam PS, et al. 2025. Mesolimbic dopamine neurons drive infradian rhythms in sleep-wake and heightened activity state. *Sci Adv.* 11(1):eado9965.
- Barnes SJK, Stefanovska A. 2021. Physics of cellular energy metabolism. *Contemp Phys.* 62(3):125–143.
- Goldbeter A. 2008. Biological rhythms: clocks for all times. *Curr Biol.* 18(17):R751–R753.
- Reid KJ. 2019. Assessment of circadian rhythms. *Neurol Clin.* 37(3):505–526.
- Stankovski T, Duggento A, McClintock PVE, Stefanovska A. 2014. A tutorial on time-evolving dynamical Bayesian inference. *Eur Phys J.* 223:2685–2703.
- Iatsenko D, McClintock PVE, Stefanovska A. 2015. Linear and synchrosqueezed time–frequency representations revisited: overview, standards of use, resolution, reconstruction, concentration, and algorithms. *Digit Signal Process.* 42(2):1–26.
- Iatsenko D. *Nonlinear mode decomposition: theory and applications* Springer, 2015.
- Iatsenko D, McClintock PVE, Stefanovska A. 2016. Extraction of instantaneous frequencies from ridges in time–frequency representations of signals. *Signal Process.* 125(8):290–303.
- Stankovski T, Pereira T, McClintock PVE, Stefanovska A. 2017. Coupling functions: universal insights into dynamical interaction mechanisms. *Rev Mod Phys.* 89(4):045001.
- Newman J, Pidde A, Stefanovska A. 2021. Defining the wavelet bispectrum. *Appl Comput Harmon Anal.* 51(18):171–224.
- Adams JR, Newman J, Stefanovska A. 2023. Distinguishing between deterministic oscillations and noise. *Eur Phys J.* 232(20):3435–3457.
- Barnes SJK, Bjerkan J, Clemson PT, Newman J, Stefanovska A. 2024. Phase coherence—a time-localized approach to studying interactions. *Chaos.* 34(7):073155.
- Newman J, Lucas M, Stefanovska A. 2021. Stabilization of cyclic processes by slowly varying forcing. *Chaos.* 31(12):123129.
- Newman J, Scott JP, Rowland Adams J, Stefanovska A. 2024. Intermittent phase dynamics of non-autonomous oscillators through time-varying phase. *Phys D Nonlinear Phenom.* 461(4010):134108.
- Pendergast BJ, Zucker I. 2016. Ultradian rhythms in mammalian physiology and behavior. *Curr Neurobiol.* 40:150–154.

- 38 Goh GH, Maloney SK, Mark PJ, Blache D. 2019. Episodic ultradian events—ultradian rhythms. *Biology (Basel)*. 8(1):15.
- 39 Gerkema MP, Daan S, Wilbrink M, Hop MW, van der Leest F. 1993. Phase control of ultradian feeding rhythms in the common vole (*Microtus arvalis*): the roles of light and the circadian system. *J Biol Rhythms*. 8(2):151–171.
- 40 Yang S, et al. 2022. Coupling-dependent metabolic ultradian rhythms in confluent cells. *Proc Natl Acad Sci U S A*. 119(45): e2211142119.
- 41 Morris M, Yamazaki S, Stefanovska A. 2022. Multiscale time-resolved analysis reveals remaining behavioral rhythms in mice without canonical circadian clocks. *J Biol Rhythms*. 37(3): 310–328.
- 42 van Rosmalen L, Hut RA. 2021. Negative energy balance enhances ultradian rhythmicity in spring-programmed voles. *J Biol Rhythms*. 36(4):359–368.
- 43 Ootsuka Y, et al. 2009. Brown adipose tissue thermogenesis heats brain and body as part of the brain-coordinated ultradian basic rest-activity cycle. *Neuroscience*. 164(2):849–861.
- 44 Blum ID, et al. 2014. A highly tunable dopaminergic oscillator generates ultradian rhythms of behavioral arousal. *Elife*. 3: e05105.
- 45 Stankovski T, Duggento A, McClintock PVE, Stefanovska A. 2012. Inference of time-evolving coupled dynamical systems in the presence of noise. *Phys Rev Lett*. 109(2):024101.
- 46 Lucas M, Newman J, Stefanovska A. Synchronisation and non-autonomicity. In: McClintock PVE, Stefanovska A, editors. *Physics of biological oscillators: new insights into non-equilibrium and non-autonomous systems*. Springer, 2021. p. 85–110.
- 47 Sheppard LW, Stefanovska A, McClintock PVE. 2011. Detecting the harmonics of oscillations with time-variable frequencies. *Phys Rev E*. 83(1):016206.
- 48 Pendergast JS, Oda GA, Niswender KD, Yamazaki S. 2012. Period determination in the food-entrainable and methamphetamine-sensitive circadian oscillator (s). *Proc Natl Acad Sci U S A*. 109(35):14218–14223.
- 49 Pendergast JS, Niswender KD, Yamazaki S. 2013. The complex relationship between the light-entrainable and methamphetamine-sensitive circadian oscillators: evidence from behavioral studies of period-mutant mice. *Eur J Neurosci*. 38(7):3044–3053.
- 50 Flôres DEFL, Bettilyon CN, Yamazaki S. 2016. Period-independent novel circadian oscillators revealed by timed exercise and palatable meals. *Sci Rep*. 6(1):21945.
- 51 Ironside S, Davidson F, Corkum P. 2010. Circadian motor activity affected by stimulant medication in children with attention-deficit/hyperactivity disorder. *J Sleep Res*. 19(4):546–551.
- 52 Hasler BP, Smith LJ, Cousins JC, Bootzin RR. 2012. Circadian rhythms, sleep, and substance abuse. *Sleep Med Rev*. 16(1):67–81.
- 53 Antle MC, et al. 2012. Methylphenidate modifies the motion of the circadian clock. *Neuropsychopharmacology*. 37(11):2446–2455.
- 54 Ramasamy T, Doke M, McLaughlin JP, Samikkannu T. 2023. Circadian disruption and psychostimulants dysregulates plasma acute-phase proteins and circulating cell-free mitochondrial DNA. *Brain Behav Immun*. 31:100659.
- 55 Stein MA, Weiss M, Hlavaty L. 2012. ADHD treatments, sleep, and sleep problems: complex associations. *Neurotherapeutics*. 9(3): 509–517.
- 56 Becker SP. 2020. ADHD and sleep: recent advances and future directions. *Curr Opin Psychol*. 34:50–56.
- 57 Surman CBH, Walsh DM. 2022. Understanding the impact of stimulants on sleep in ADHD: evidence from systematic assessment of sleep in adults. *CNS Drugs*. 36(3):253–260.
- 58 Musiek ES, Xiong DD, Holtzman DM. 2015. Sleep, circadian rhythms, and the pathogenesis of Alzheimer disease. *Exp Mol Med*. 47(3):e148–e148.
- 59 Snitselaar MA, Smits MG, van der Heijden KB, Spijker J. 2017. Sleep and circadian rhythmicity in adult ADHD and the effect of stimulants: a review of the current literature. *J Atten Disord*. 21(1):14–26.
- 60 Vallée A, Lecarpentier Y, Guillevin R, Vallée J-N. 2020. The influence of circadian rhythms and aerobic glycolysis in autism spectrum disorder. *Transl Psychiatry*. 10(1):400.
- 61 Walker WH, Walton JC, DeVries AC, Nelson RJ. 2020. Circadian rhythm disruption and mental health. *Transl Psychiatry*. 10(1):1–13.
- 62 Lorsung E, Karthikeyan R, Cao R. 2021. Biological timing and neurodevelopmental disorders: a role for circadian dysfunction in autism spectrum disorders. *Front Neurosci*. 15:642745.
- 63 Martinez-Cayuelas E, et al. 2024. Sleep problems, circadian rhythms, and their relation to behavioral difficulties in children and adolescents with autism spectrum disorder. *J Autism Dev Disord*. 54(5):1712–1726.
- 64 Foster RG. 2020. Sleep, circadian rhythms and health. *Interface Focus*. 10(3):20190098.
- 65 Tataroglu Ö, Davidson AJ, Benvenuto LJ, Menaker M. 2006. The methamphetamine-sensitive circadian oscillator (MASCO) in mice. *J Biol Rhythms*. 21(3):185–194.
- 66 Clemson PT, Stefanovska A. 2014. Discerning non-autonomous dynamics. *Phys Rep*. 542(4):297–368.
- 67 Gao C, et al. 2023. Approaches for assessing circadian rest-activity patterns using actigraphy in cohort and population-based studies. *Curr Sleep Med Rep*. 9(4):247–256.
- 68 Clemson P, Lancaster G, Stefanovska A. 2016. Reconstructing time-dependent dynamics. *Proc IEEE*. 104(2):223–241.
- 69 Stankovski T, Pereira T, McClintock PVE, Stefanovska A. 2019. Coupling functions: dynamical interaction mechanisms in the physical, biological and social sciences.
- 70 Guzmán DA, et al. 2017. The fractal organization of ultradian rhythms in avian behavior. *Sci Rep*. 7(1):684.
- 71 Minaeva O, et al. 2024. Fractal motor activity during wakefulness and sleep: a window into depression recency and symptom recurrence. *Psychol Med*. 54:1–9.
- 72 Honma S, Yasuda T, Yasui A, Van Der Horst GTJ, Honma K-I. 2008. Circadian behavioral rhythms in Cry1/Cry2 double-deficient mice induced by methamphetamine. *J Biol Rhythms*. 23(1):91–94.
- 73 Honma K-I, Honma S, Hiroshige T. 1987. Activity rhythms in the circadian domain appear in suprachiasmatic nuclei lesioned rats given methamphetamine. *Physiol Behav*. 40(6):767–774.
- 74 Fujii H, et al. 2007. Methamphetamine-induced hyperactivity and behavioral sensitization in PACAP deficient mice. *Peptides*. 28(9): 1674–1679.
- 75 Salahpour A, et al. 2008. Increased amphetamine-induced hyperactivity and reward in mice overexpressing the dopamine transporter. *Proc Natl Acad Sci U S A*. 105(11):4405–4410.
- 76 Honma S, Kanematsu N, Honma K-I. 1992. Entrainment of methamphetamine-induced locomotor activity rhythm to feeding cycles in SCN-lesioned rats. *Physiol Behav*. 52(5):843–850.
- 77 Ono D, Honma S, Honma K-I. 2013. Postnatal constant light compensates Cryptochrome1 and 2 double deficiency for disruption of circadian behavioral rhythms in mice under constant dark. *PLoS One*. 8(11):e80615.
- 78 Putker M, et al. 2021. CRYPTOCHROMES confer robustness, not rhythmicity, to circadian timekeeping. *EMBO J*. 40(7):e106745.
- 79 Masubuchi S, Honma S, Abe H, Namihira M, Honma K-I. 2007. Methamphetamine induces circadian oscillation in the brain

- outside the suprachiasmatic nucleus in rats. *Sleep Biol Rhythms*. 5(2):132–140.
- 80 Wever RA. *The circadian system of man: results of experiments under temporal isolation* Springer Science & Business Media, 1979.
  - 81 Honma K, Hashimoto S, Natsubori A, Masubuchi S, Honma S. 2013. Sleep-wake cycles in humans. *Indian J Sleep Med*. 8(2):51–57.
  - 82 Tang Q, Assali DR, Güler AD, Steele AD. 2022. Dopamine systems and biological rhythms: let's get a move on. *Front Integr Neurosci*. 16:957193.
  - 83 Shaffer F, Ginsberg JP. 2017. An overview of heart rate variability metrics and norms. *Front Public Health*. 5:258.
  - 84 Gehrman P, et al. 2005. The relationship between dementia severity and rest/activity circadian rhythms. *Neuropsychiatr Dis Treat*. 1(2):155–163.
  - 85 Wang XS, Armstrong MEG, Cairns BJ, Key TJ, Travis RC. 2011. Shift work and chronic disease: the epidemiological evidence. *Occup Med*. 61(2):78–89.
  - 86 Ashton A, Jagannath A. 2020. Disrupted sleep and circadian rhythms in schizophrenia and their interaction with dopamine signaling. *Front Neurosci*. 14:636.
  - 87 Kondratov RV, Kondratova AA, Gorbacheva VY, Vykhovanets OV, Antoch MP. 2006. Early aging and age-related pathologies in mice deficient in BMAL1, the core component of the circadian clock. *Genes Dev*. 20(14):1868–1873.
  - 88 Yoo S-H, et al. 2004. PERIOD2::LUCIFERASE real-time reporting of circadian dynamics reveals persistent circadian oscillations in mouse peripheral tissues. *Proc Natl Acad Sci U S A*. 101(15):5339–5346.
  - 89 Pendergast JS, et al. 2013. High-fat diet acutely affects circadian organisation and eating behavior. *Eur J Neurosci*. 37(8):1350–1356.
  - 90 Ehichioya DE, Taufique SKT, Farah S, Yamazaki S. 2023. A time memory engram embedded in a light-entrainable circadian clock. *Curr Biol*. 33(23):5233–5239.
  - 91 Bračič M, Stefanovska A. 1998. Wavelet-based analysis of human blood-flow dynamics. *Bull Math Biol*. 60(5):919–935.
  - 92 Lancaster G, Iatsenko D, Pidde A, Ticcinelli V, Stefanovska A. 2018. Surrogate data for hypothesis testing of physical systems. *Phys Rep*. 748(4):1–60.
  - 93 Jamšek J, Stefanovska A, McClintock PVE. 2007. Wavelet bispectral analysis for the study of interactions among oscillators whose basic frequencies are significantly time variable. *Phys Rev E*. 76(4):046221.
  - 94 Paluš M, Vejmelka M. 2007. Directionality of coupling from bi-variate time series: how to avoid false causalities and missed connections. *Phys Rev E*. 75(5):056211.
  - 95 Iatsenko D, et al. Multiscale Oscillatory Dynamics Analysis (MODA) Toolbox. [accessed 2025 Feb 25] <https://github.com/luphysics/MODA>.

## Chapter 6

# Cellular energy metabolism in ASD

## 6.1 Metabolism in the brain

The brain is one of the most metabolically active organs in the body, accounting for approximately 20% of total energy consumption at rest. Therefore, employing appropriate pathways to synthesize ATP, the body's primary energy currency, is paramount.

In mammals, cellular energy metabolism can be summarized into four key processes. The first stage, glycolysis, occurs in the cytoplasm, where glucose is converted into pyruvate. This process produces two molecules of adenosine triphosphate (ATP) and reduces nicotinamide adenine dinucleotide ( $\text{NAD}^+$ ) to NADH. Next, in the mitochondria, oxidative phosphorylation (OXPHOS) completes metabolism so efficiently that 28 molecules of ATP are synthesised per glucose molecule. OXPHOS utilises NADH and pyruvate from glycolysis, and oxygen, which diffuses across cell membranes. Glucose is delivered to the cytoplasm for glycolysis via glucose transporter proteins (GLUTs), which facilitate membrane diffusion [226].

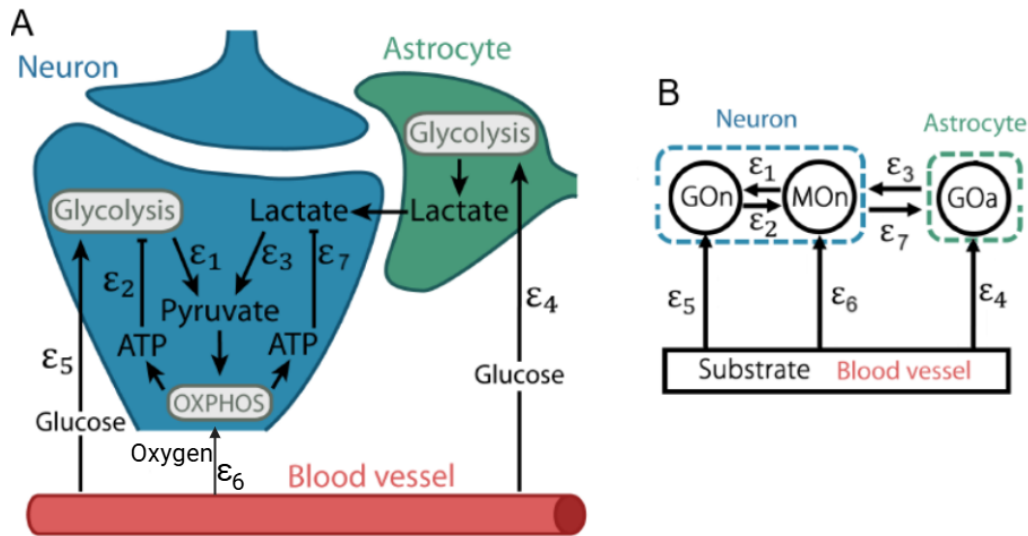


FIGURE 6.1: Simplified model of the interacting components of cellular energy metabolism. (A) Interactions between the blood vessel (red), neuron (blue) and astrocyte (green). (B) Schematic representation of the couplings  $\epsilon$  in the cellular energy metabolism model between the mitochondrial oscillator ( $\text{MO}_n$ ) and glycolytic oscillator in the neuron ( $\text{GO}_n$ ) and the astrocyte ( $\text{GO}_a$ ).

In the brain, glycolysis can also take place in glial cells called astrocytes. This process generates lactate, which is shuttled into the neuron to provide an alternative

fuel source for the mitochondria [227]. Lactate transporter proteins called monocarboxylate transporters (MCTs) shuttle this metabolite from the astrocyte to the neuron, supporting oxidative metabolism. The interplay between these processes is illustrated in Fig. 6.1.

## 6.2 Metabolic coupled phase oscillators

Metabolic processes are inherently oscillatory. Mitochondrial function is dictated by oscillations between an oxidative and reductive environment [228, 229]. These oscillations can be measured by the fluorescence of NADH [230] or the mitochondrial membrane potential [231]. Furthermore, glycolysis exhibits oscillatory characteristics regulated by several protein complexes [232]. Concentrations of glycolytic intermediates oscillate with a period of a few minutes [189] and produce NADH which is measured using fluorescence [233]. When operating optimally, the glycolytic and mitochondrial oscillators synchronise. This enables glycolysis to provide oxphos with sufficient molecular substrates to enable optimal energy metabolism. Additionally, the supply of oxygen to the brain is characterised by a baseline level around which oscillations occur [234]. These dynamics are influenced by changes in the vascular tone of arterioles and vary with age [235]. The oscillatory nature of cellular energy metabolism necessitates an approach that explicitly treats each component as such.

### 6.2.1 Single phase oscillator model

Cellular energy metabolism consists of multiple interacting periodic processes. Simulating these processes with coupled phase oscillators enables the replication of their dynamics. Due to the open nature of the system, the frequency of each oscillator was allowed to vary in time. Additionally, the initial phase,  $\varphi_0$ , of each oscillator was randomised, while maintaining the same average frequency  $\omega_{mX}$  [183]. The time-dependent frequency of each oscillator,  $\omega_X(t)$ , was modulated such that,

$$\omega_X(t) = \omega_{mX} + A_X \sin(\omega_{modX}t + \varphi_0). \quad (6.1)$$



The amplitude of frequency modulation,  $A_X$ , was set to one-third of the mean frequency, while the frequency of modulation,  $\omega_{\text{mod}X}$ , was assigned a value equal to one-tenth of the mean frequency (Hz). The rates of change of phase of each oscillator in the model are given by,

$$\begin{aligned}
 \dot{\phi}_{Ox} &= \omega_{Ox} + \sigma\eta(t) \\
 \dot{\phi}_{Glu} &= \omega_{Glu} + \sigma\eta(t) \\
 \dot{\phi}_{GOa} &= \omega_{GOa} + \varepsilon_{MOGOa} \sin(\phi_{GOa} - \phi_{MO}) - \varepsilon_{GluGOa} \sin(\phi_{GOa} - \phi_{Glu}) + \sigma\eta(t) \\
 \dot{\phi}_{GO} &= \omega_{GO} + \varepsilon_{MOGO} \sin(\phi_{GO} - \phi_{MO}) - \varepsilon_{GluGO} \sin(\phi_{GO} - \phi_{Glu}) + \sigma\eta(t) \\
 \dot{\phi}_{MO} &= \omega_{MO} - \varepsilon_{GOMO} \sin(\phi_{MO} - \phi_{GO}) - \varepsilon_{GOaMO} \sin(\phi_{MO} - \phi_{GOa}) \\
 &\quad - \varepsilon_{OxMO} \sin(\phi_{MO} - \phi_{Ox}) + \sigma\eta(t).
 \end{aligned} \tag{6.2}$$

Where  $\sigma\eta(t)$  represents white additive noise. The sign preceding each coupling term in Eqs. 6.2 indicates the type of coupling: a positive sign denotes repulsive coupling, while a negative sign represents attractive coupling. For example,

$+\varepsilon_{MOGO} \sin(\phi_{GO} - \phi_{MO})$  models the inhibitory influence of the mitochondrial oscillator on the glycolytic oscillator. This is due to a sensing mechanism that detects the ATP/ADP ratio. When this ratio decreases below a certain threshold, the PFK enzyme is inhibited, causing glycolysis to compensate by increasing its activity. However, under normal conditions, this ratio remains high as the mitochondria fulfil cellular energy demands [236, 237].

The Runge-Kutta fourth-order integration scheme was used to compute the phase values of each oscillator over time. A step size of 0.1 seconds was employed for a total duration of 2000 seconds. The resulting phase values were subsequently analysed to determine the presence of synchronization between oscillators.

### 6.2.2 Network based model

While modelling individual cellular units and their interactions is valuable, it's important to recognize that these cells do not exist in isolation in real biological systems. Networks of oscillators are particularly relevant when modelling cellular energy metabolism. For example, glycolytic oscillations in yeast have been shown to

represent a collective phenomenon: isolated yeast cells do not oscillate on their own, but once a certain cell density is reached, the cells synchronize and oscillate in phase with one another [238, 239]. To accurately capture the interactions between numerous neurons and astrocytes, it is essential to extend the model to a network-based framework; The defining equations of which are as follows,

$$\begin{aligned}
 \dot{\phi}_{Gloi} &= \omega_{Gloi}(t) + \dot{\phi}_{Gloni}, \\
 \dot{\phi}_{Oxyi} &= \omega_{Oxyi}(t) + \dot{\phi}_{Oxyni}, \\
 \dot{\phi}_{GOi} &= \omega_{GOi}(t) + \dot{\phi}_{GOni} - \dot{\phi}_{GluGOi} + \dot{\phi}_{MOGOi}, \\
 \dot{\phi}_{GOai} &= \omega_{GOai}(t) + \dot{\phi}_{GOani} - \dot{\phi}_{GluGOai} + \dot{\phi}_{MOGOai}, \\
 \dot{\phi}_{MOi} &= \omega_{MOi}(t) + \dot{\phi}_{MONi} - \dot{\phi}_{OxyMOi} - \dot{\phi}_{GOMOi} - \dot{\phi}_{GOaMOi}.
 \end{aligned} \tag{6.3}$$

Where  $\dot{\phi}_{Xi}$  represents the time derivative of the phase of each individual oscillator ( $i$ ) of type  $X$  in the network, which is influenced by three factors. Firstly, the time-varying natural frequency of the oscillator,  $\omega_{Xi}$ , as outlined in Eq. 6.1. Secondly, the intranetwork couplings between itself and other oscillators ( $j$ ),

$$\dot{\phi}_{Xni} = \frac{K_X}{N} \sum_{j=1}^N \sin(\phi_{Xj} - \phi_{Xi}), \tag{6.4}$$

where  $K$  is the intranetwork coupling strength and  $N$  is the number of oscillators in the network. Finally, the influence from other oscillator networks, ( $Y$ ), over the oscillator  $X$ ,

$$\dot{\phi}_{YXi} = F_{YX} r_Y \sin(\Psi_Y - \phi_{Xi}), \tag{6.5}$$

where  $F_{YX}$  is the inter-network coupling strength and  $\Psi_Y$  is the average phase of network  $Y$  and  $r$  represents the Kuramoto order parameter [192].

The Runge-Kutta fourth-order integration scheme was used to compute the phase values of each oscillator over time. A step size of 0.1 seconds was employed for a total duration of 5000 seconds. The resulting mean phase values of each network were subsequently analysed to determine the presence of synchronization between oscillators.

### 6.2.3 Parameter selection

As little literature exists regarding the exact frequency of metabolic processes in the brain, the parameter values have been estimated based on known oscillatory frequencies in other cell types. Glycolysis usually takes place on the scale of a few minutes [240, 241, 189] while oxidative phosphorylation is slightly quicker, with a period around 100s [242, 229]. Given the lack of literature on the frequency of glycolysis in the astrocytes and neurons, they were set to the same value.

Biological correlate	Parameter	Value (Hz)	References
Oxygen supply freq	$\omega_{ox}$	$\frac{2\pi}{100}$	[234]
Glucose supply freq	$\omega_{Glu}$	$\frac{2\pi}{200}$	[236]
Glycolysis natural freq (neuron)	$\omega_{GO}$	$\frac{2\pi}{200}$	[240, 241, 189]
Glycolysis natural freq (astrocyte)	$\omega_{GOa}$	$\frac{2\pi}{200}$	[240, 241, 189]
OxPhos natural freq neuron	$\omega_{MO}$	$\frac{2\pi}{100}$	[243, 229]
Oxygen $\rightarrow$ neuron	$\epsilon_{Ox \rightarrow MO}$	0.1	[235]
Glucose $\rightarrow$ neuron	$\epsilon_{Glu \rightarrow GO}$	0.1	[244]
Glucose $\rightarrow$ astrocyte	$\epsilon_{Glu \rightarrow GOa}$	0.05	[245]
Lactate $\rightarrow$ neuron	$\epsilon_{GOa \rightarrow MO}$	0.025	[246, 247]
Glycolysis neuron $\rightarrow$ oxphos	$\epsilon_{GO \rightarrow MO}$	range	[248]
Glycolysis neuron $\leftarrow$ oxphos	$\epsilon_{MO \rightarrow GO}$	range	[248]

TABLE 6.1: Table of parameters for the single oscillator model. The arrows indicate the direction of coupling.

The coupling strengths between oscillators were selected based upon their known interactions. Both neuronal glycolysis and oxidative phosphorylation require a constant source of glucose and oxygen to function [235, 244], as such this coupling was relatively high. In contrast, astrocytes have do not need a constant supply, as they have supplies of glycogen which can be used during periods of high energy demand [245]. Furthermore, astrocytic glycolysis plays only a supporting role to overall metabolism [246, 247], hence the coupling from the astrocyte to the neuron is relatively lower. There is evidence to suggest a wide dynamic range in the brains energy demands from moment to moment [248]. As such, it is likely that the amount of energy required and so the coupling strength between mitochondrial and glycolytic oscillators fluctuate over time. Here, the coupling strengths are simulated across a range of values to demonstrate the dynamic range of interaction.

### Network model parameters

The network based approach requires additional parameters to represent the inter and intra network coupling strengths.

Biological correlate	Parameter	Value	References
Oxygen $\rightarrow$ neuron	$F_{Ox \rightarrow MO}$	0.2	[235]
Glucose $\rightarrow$ neuron	$F_{Glu \rightarrow GO}$	0.2	[244]
Glucose $\rightarrow$ astrocyte	$F_{Glu \rightarrow GOa}$	0.1	[245]
Lactate $\rightarrow$ neuron	$F_{GOa \rightarrow MO}$	0.05	[246, 247]
Glycolysis neuron $\rightarrow$ oxphos	$F_{GO \rightarrow MO}$	0-0.3	[248]
Glycolysis neuron $\leftarrow$ oxphos	$F_{MO \rightarrow GO}$	0-0.3	[248]
Intranetwork couplings	$K_X$	0.05	[248]
Network size	$N$	4	

TABLE 6.2: Table of parameters for the network based model. The angular frequency values  $\omega$  are the same as in Table. 6.1

The internetwork coupling strengths are proportional to those implemented in the single oscillator model. At the current stage of investigation, each of the intranetwork coupling have been set to 0.05 for simplicity. Conditions such as dementia may have unsynchronised metabolic networks due to damage to the vasculature causing metabolic oscillators to desynchronise. Future models describing neurodegenerative diseases should take this explicitly into account. There is little evidence of desynchronised intranetwork couplings in ASD however, and so this was deemed an unnecessary level of complexity for the current work. The network size,  $N$ , was set to 4 as the computational load dramatically increases as a function of network size. In reality, there are thousands of mitochondria in mammalian cells [249].

#### 6.2.4 Metabolic mode

In a healthy, resting brain, oxidative phosphorylation (OXPHOS) is the primary pathway for energy metabolism in neurons, offering high efficiency with the production of 28 ATP molecules for every glucose molecule oxidized. Under aerobic conditions, glycolysis is reduced to a level that provides just enough substrates for OXPHOS to proceed. While glycolysis can temporarily become the dominant ATP-producing pathway during periods of high energy demand, relying on glycolysis for energy is considered sub-optimal, as it produces byproducts like lactate, which can

shift the brain's pH [248]. Therefore, under standard conditions, the optimal form of energy production is primarily via OXPHOS, this is known as the aerobic state.

During periods of heightened neuronal stimulation, however, glycolysis increases to meet energy demand. Positron emission tomography (PET) studies have shown that following brain activation, blood flow to a given region increases by about 50%, with a corresponding rise in glucose consumption. Oxygen uptake, however, only increases by about 5%, indicating that during periods of high demand, glucose becomes the primary energy substrate [250]. Furthermore, a net increase in lactate levels following stimulation suggests that both neuronal and astrocytic glycolysis are upregulated to meet increased energy demands [251, 252, 253]. Much like in the case of a sprinter, this adaptation is appropriate for providing increased ATP over a short period of time, but it is not suitable or sustainable in the long term, and extended periods in this state may lead to pathogenesis.

A transition takes place between these states, where the synchronisation state is optimised for neither type of metabolism. This state would be transient as it is incapable of producing sufficient ATP when the mitochondrial and glycolytic oscillators are not synchronised. By considering the synchronisation states between oscillators we can deduce whether glycolytic or aerobic processes are more prevalent in the system for a range of coupling strengths.

### 6.3 The parameter space

Mapping the specific states of synchronization between oscillators across different parameter combinations produces the parameter space. By assigning a unique colour to each distinct regime, these states can be quickly visualised and interpreted. As we run several simulations across a range of parameter values, a wide variety of synchronisation states are possible. To illustrate the breadth of possible states, we begin with the single-oscillator example. Simulating the model using the healthy parameter values listed in Table 6.1 gives the phases of each oscillator over time. By analysing the phase differences between oscillators, we can determine the synchronization state associated with each parameter combination. As mentioned in Sect. 1, understanding the synchronisation states of the system enables us to determine

which factors are influencing it, and so determine whether healthy or altered states are present. This is visualized in Fig. 6.2, which depicts the parameter space, while Table 6.3 defines the synchronization state represented by each colour.

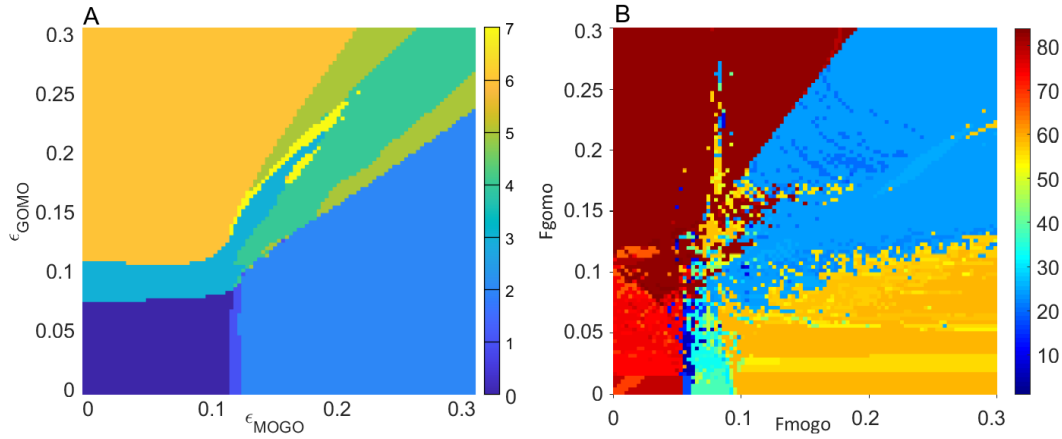


FIGURE 6.2: Synchronisation regimes in a neurotypical single oscillator model of neuronal cellular metabolism. (A) The different synchronisation regimes are all associated with a colour. The colour bar relates each of these colours to a number. Table 6.3 contains a reference for which oscillators are synchronised in each of these regimes. (B) The dramatically greater number of regimes in the network model.

Number	Glu - GO	GO - MO	Oxy - MO	GOa - MO	Glu - GOa	State
0	X		X		X	Transition
1			X		X	Transition
2		X	X		X	Aerobic
3	X				X	Transition
4					X	Transition
5		X			X	Transition
6	X	X		X	X	Glycolytic
7				X	X	Glycolytic

TABLE 6.3: Synchronisation states corresponding to Fig. 6.2A. An X in the box corresponds to synchronisation between the two oscillators. The final column indicates the metabolic mode for that synchronisation regime.

The synchronisation regimes in Fig. 6.2B are difficult to interpret owing to the large number of regimes. Accounting for intermittent synchronisation [173] and intra-network synchronisation upon the introduction of the network approach, as in the case of Fig. 6.2B increases the number of states to an intractable quantity. Some of this information is also redundant, as it represents the same overall affect on the system, which can ultimately fall into one of three types of metabolic mode.

The aerobic state is the standard, healthy configuration of the cell, with the efficient oxidative phosphorylation responsible for most energy production. Here,



oxygen supply dominates the system.

Glycolytic states are unfavourable altered metabolic states. They are categorised as having the glucose supply driving neuronal metabolism.

Finally, there are several transitional states in which neither glucose nor oxygen predominantly drives the metabolic coupling in the neuron. These states are inherently unsustainable, as the lack of coordinated operation between the key oscillatory units compromises the cell's ability to maintain function. Such transitional states may occur as metabolism shifts between aerobic and glycolytic pathways or vice versa.

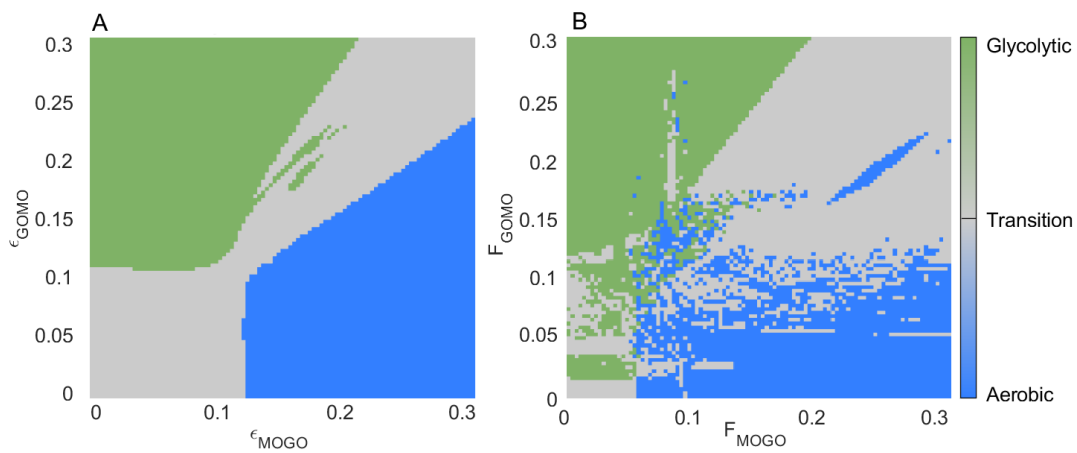


FIGURE 6.3: each of the synchronisation regimes are categorised into either glycolytic (green) transition (grey) or aerobic (blue) metabolic modes (A) The single oscillator model. (B) The same categories applied for the network based model.

By considering the biological relevance of different synchronisation states we can re-allocate parameter space into one of these three categories. If the supply of oxygen is driving the metabolic coupling between the mitochondrial and glycolytic oscillators, then the regime is categorised as aerobic (blue). If glucose is driving the coupling, the regime is glycolytic (green). If neither oxygen or glucose are driving the system, then it is a transitional (grey) state. Fig. 6.3 indicates the metabolic mode for each parameter combination.

## 6.4 Neuronal cellular energy metabolism in ASD

While there is no known, precise etiology in ASD [254] there are a myriad of factors linked to increasing the likelihood of ASD which also affect cellular energy

metabolism [14, 126, 255, 256, 257]. One of the most commonly reported metabolic abnormalities is mitochondrial dysfunction [124]. Mitochondria are particularly sensitive to environmental factors [256], especially those known to increase ASD risk [258, 259, 260, 261, 262]. Additionally, abnormal metabolite concentrations have been reported in ASD [263], including increased lactate [10, 11]. Pharmacological risk factors, such as prenatal exposure to valproic acid (VPA), significantly increase ASD risk [51]. VPA stimulates the WNT pathway [134, 261] which is also upregulated in mouse models of ASD [136]. Upregulation of this pathway increases the level of glucose transporter and lactate shuttle proteins [264, 8]. This evidence has led to the hypothesis that disruptions to the WNT/ $\beta$ -catenin pathway may induce altered metabolism in ASD [265, 7].

### The Warburg effect

The Warburg effect is defined as a metabolic shift towards glucose uptake and lactate production, despite the presence of oxygen [114]. Upregulation of glycolysis is present in many pathologies, such as cardiovascular disease [266], diabetes [267] and cancer [114]. Increasingly, the Warburg effect has been implicated as a potential contributing factor towards ASD development [7, 121]. Here, we apply the phenomenological model defined formerly to assess the hypothesis that upregulation of GLUT and MCT proteins via the WNT/ $\beta$ -catenin pathway triggers the Warburg effect in ASD [7].

#### 6.4.1 Upregulation of the glucose transporter proteins

Stimulation of the WNT/ $\beta$ -catenin pathway upregulates glucose transporter proteins, which facilitate the diffusion of glucose into the neuron and astrocyte. To understand what effect this has on possible metabolic states, the coupling parameters corresponding to the link between glucose and the neuron/astrocyte have been doubled, while the other parameters in Tables 6.1, 6.2 remain the same. The shift in the size of the relevant synchronisation states are illustrated in Fig. 6.4A for the single oscillator model, and Fig. 6.4B for the network based model.

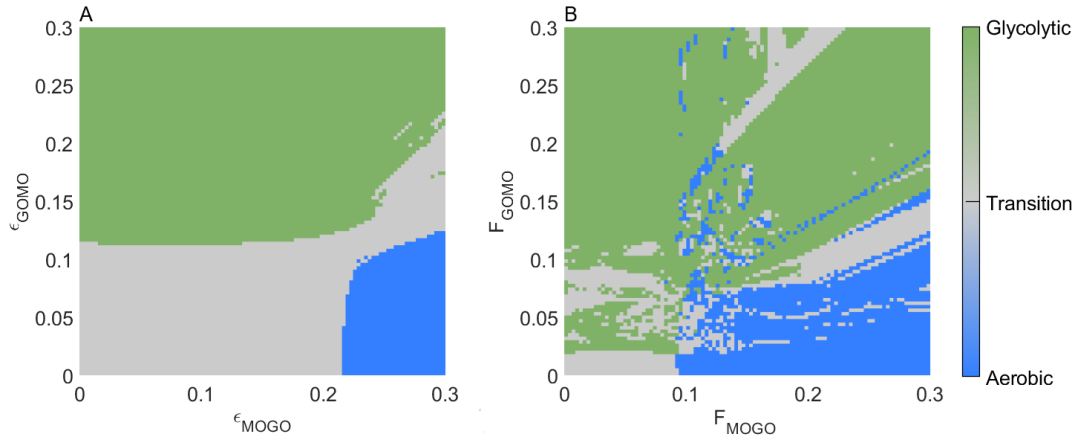


FIGURE 6.4: The parameter space when the couplings associated with glucose transport proteins is increased. (A) The single oscillator parameter space. (B) The network based parameter space.

Increasing the couplings associated with the glucose transporter proteins dramatically changes the phase space. The area associated where glycolysis is the predominant metabolic mode (green) is increased in both the single oscillator (Fig. 6.4A) and network (Fig. 6.4B) approach, symptomatic of the Warburg effect.

#### 6.4.2 Upregulation of both lactate and glucose transporter proteins

Following stimulation of the WNT/ $\beta$ -catenin pathway, the production of lactate transporter proteins are upregulated. These proteins shuttle lactate generated by glycolysis in the astrocyte to the neuron to support metabolism. As such, their upregulation is associated to an increase in the coupling from the astrocyte to the mitochondrial oscillators in our model. Fig. 6.5 demonstrates the effect of both GLUT and MCT upregulation simultaneously.

Again, a clear switch to the Warburg effect is present, revealed by a substantial increase in the size of the glycolytic parameter space. Interestingly, the change is similar to when only the glucose transporter proteins are upregulated. This may indicate that increased glucose diffusion, and so glycolysis in the neuron, causes the shift towards glycolysis, while the increase in astrocytes glycolysis plays a supporting role, corroborating experimental findings [268].

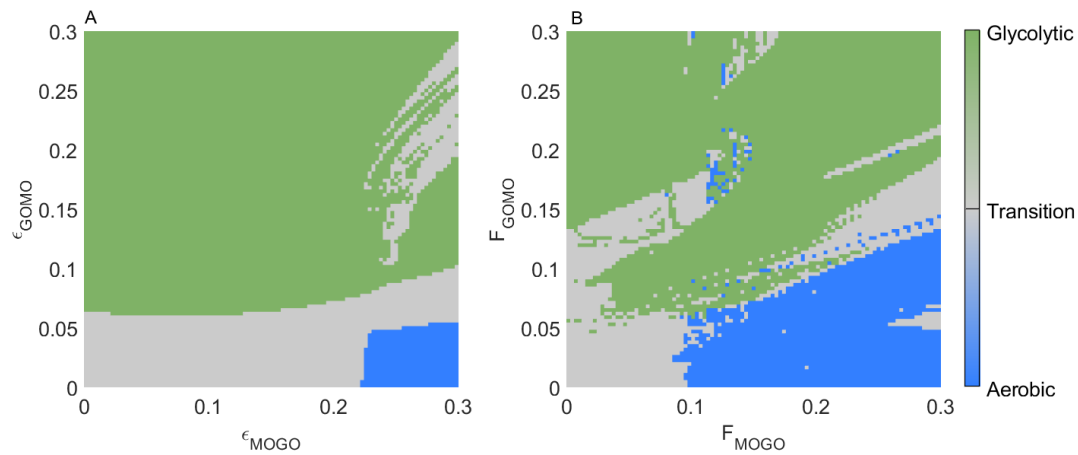


FIGURE 6.5: The parameter space when accounting for upregulated glucose and lactate transport proteins. (A) Single oscillator approach. (B) Network based model.

## 6.5 Conclusion and future work

Autism Spectrum Disorder (ASD) is a complex neurodevelopmental condition influenced by a combination of genetic and environmental factors that increase susceptibility. Historically, these diverse factors have been considered unconnected. More recently, efforts to uncover potential links through shared cellular pathways have emerged. As one of the most metabolically active organs in the body, the brain relies heavily on efficient ATP production, making cellular energy metabolism a promising avenue to unify the diverse etiological factors and clinical presentations of ASD. Notably, the WNT- $\beta$ -catenin pathway is upregulated in ASD [134, 136, 261]. This upregulation is associated with increased expression of glucose and lactate transporters, highlighting a potential metabolic mechanism underlying the condition.

Circadian disruption has been implicated in the dysregulation of the WNT/ $\beta$ -catenin pathway [269], which, in turn, impacts cellular energy metabolism [14]. Moreover, circadian disruption has been associated with ASD [270], with 50–80% of children with ASD reported to experience disturbed sleep patterns [271]. Additional factors such as exposure to valproic acid [51, 137, 272], genetic influences [273] and elevated lactate levels [115, 122] are also all implicated both in upregulation of the WNT/ $\beta$ -catenin pathway and ASD development. Understanding the connections between cellular energy metabolism and the diverse factors contributing to ASD risk may help guide the development of future therapeutic strategies or early interventions.

In this work, phenomenological phase oscillator models are introduced to represent various cellular states. By adjusting the parameters of these models, the impact of specific changes on cellular behaviour can be considered. These models enable the exploration of the hypothesis that upregulation of the WNT- $\beta$ -catenin pathway induces the Warburg effect in ASD. Specifically, increasing the associated coupling of glucose and lactate transporter proteins shifts ATP production towards glycolytic states, where glycolysis becomes the dominant mode of ATP synthesis.

It has been suggested that the upregulation of neuronal glucose supply, rather than lactate transport, plays a dominant role in the increased metabolism following neuronal stimulation. The similar results from Fig. 6.4 and Fig. 6.5 suggest that this is likely to be true, with the astrocytic shuttle playing a supporting role [268] and not greatly increasing the glycolytic parameter space.

Little literature exists about the exact frequencies of the metabolic oscillations in the brain. Here we have used metabolic frequencies corresponding to cell types from around the body. Further experiments are required to elucidate these parameter values and allow us to apply more specific values for each parameter in the model.

In future, the network based approach may be extended to include networks of oxygen and glucose supply. This may make the neurovascular unit in conditions like dementia easier to model, where supply of oxygen and glucose is a key attribute in disease progression [274].

A network size of  $N = 4$  is applied in the network model, as increasing  $N$  dramatically increases the computational load. In reality there are thousands of mitochondria in mammalian cells [275]. The relatively low network size here may have impacted the synchronisation states. By introducing parallel processing this can be dramatically sped up, enabling network sizes more representative of metabolic networks.

This model is capable of elucidating which changes to parameters cause shifts to different metabolic modes in cells. By applying parameters relevant to different conditions, it is hoped this approach can elucidate the changes they impart upon the metabolic mode, which can have wide ranging overall consequences to health.

## Chapter 7

# Discussion and conclusion

### 7.1 Summary

Living systems are inherently open to the environment and time-dependent. Neglecting these key aspects of life leads us to reject key deterministic dynamics capable of revealing states of health and disease. By applying physics-based approaches that acknowledge and accommodate the complexities of living systems, rather than treating them as stochastic or intractable, we can gain more accurate and profound insights. This thesis presents a holistic approach to understanding the underpinning of ASD, from cellular dynamics to circadian disruption, alongside practical application of these methods to real data.

Methodological approaches to the analysis of EEG data may be hampering efforts to categorise the condition. By comparing phase and amplitude based methods for measuring interactions, we have shown that amplitude effects can confound evaluation of connectivity, especially in the case of EEG which is particularly susceptible to movement artefacts. Additionally, the neural dynamics measured by EEG are inherently time-varying and so extended recording intervals are better suited to capturing their interactions.

It is the hope of the author that by applying a truly multiscale approach - not just to our analysis but also our overall understanding of ASD - that we can progress towards a more nuanced understanding of the condition.



## 7.2 Original contribution

- Demonstrated that the application of time-varying phase dynamics enables accurate representation of living systems and their dynamic interactions, while using fewer parameters and requiring less computational capacity than alternative approaches.
- Performed a comparison of amplitude-weighted coherence and a purely phase-based counterpart using both simulated and experimentally derived time-series. Phase coherence is more robust against perturbations than its amplitude weighted counterpart, and thus more appropriate for the analysis of noisy data containing movement artefacts, like EEG.
- Showed that the phase coherence and dynamical Bayesian inference indicate a reduction in theta and alpha connectivity in children with ASD. Hopefully this measure will provide the basis of a future quantitative assessment of ASD.
- Showed that the irregularity of the methamphetamine induced circadian oscillator was described using time localised analysis. The birhythmic behaviour of this oscillator may explain disturbances in the sleep of neurodiverse individuals.
- Introduced a phenomenological network-based phase oscillator model capable of describing neuronal energy dynamics, and applied it to demonstrate the Warbug effect in ASD.

## 7.3 Future work

Machine learning (ML) may expedite the process of identifying differences in electrophysiology between ASD and neurotypical individuals. However it is unable to determine *why* specific differences are present. This is not to say ML will not play a role in identifying biomarkers in the future, on the contrary, it may serve to greatly speed up discoveries. This being said, artificial intelligence will only take us so far. A large number of different potential causes have been identified which may lead to ASD, and although ML may be able to identify differences between groups, it will

likely fall short of being able to theorise *why* these differences exist. For that, natural intelligence, and methods like those used in this thesis, will be key.

Neuronal energy dynamics is impacted by many of the environmental and genetic correlates of ASD. By modelling the balance between oxidative phosphorylation and glycolysis in the brain, a picture linking many disparate factors emerges. Given the importance of energy metabolism in the brain, measurement approaches that link oxygen supply to electrical activity may be crucial for identifying metabolic anomalies. The fusion of fNIRS and EEG could play a key role in unveiling additional markers.

Given the heterogeneity of ASD, it is highly unlikely that a single EEG based biomarker will suffice for accurate diagnosis. Instead, a spectrum of markers, each linked to different ASD phenotypes, may provide a more comprehensive assessment. Future studies will require data from large cohorts of individuals with minimal confounding factors such as other comorbidities. By recruiting individuals that have specific aspects, such as low social communication scores, and matching these to the underlying electrophysiology, further markers of the condition may be elucidated. By integrating these electroencephalographic signatures, including the one demonstrated in this paper, with additional measures like fNIRS, the goal of a robust quantitative assessment of ASD may one day be realised.

Despite a century of research into ASD, the field is still obfuscated by conflicting results. The application of methods that explicitly account for and accommodate the physical characteristics of living systems may clarify these inconsistencies and lead to an accurate quantitative assessment of the condition.

## Appendix A

# Supplementary information

# SUPPLEMENTARY MATERIAL

## Phase coherence – A time-localised approach to studying interactions

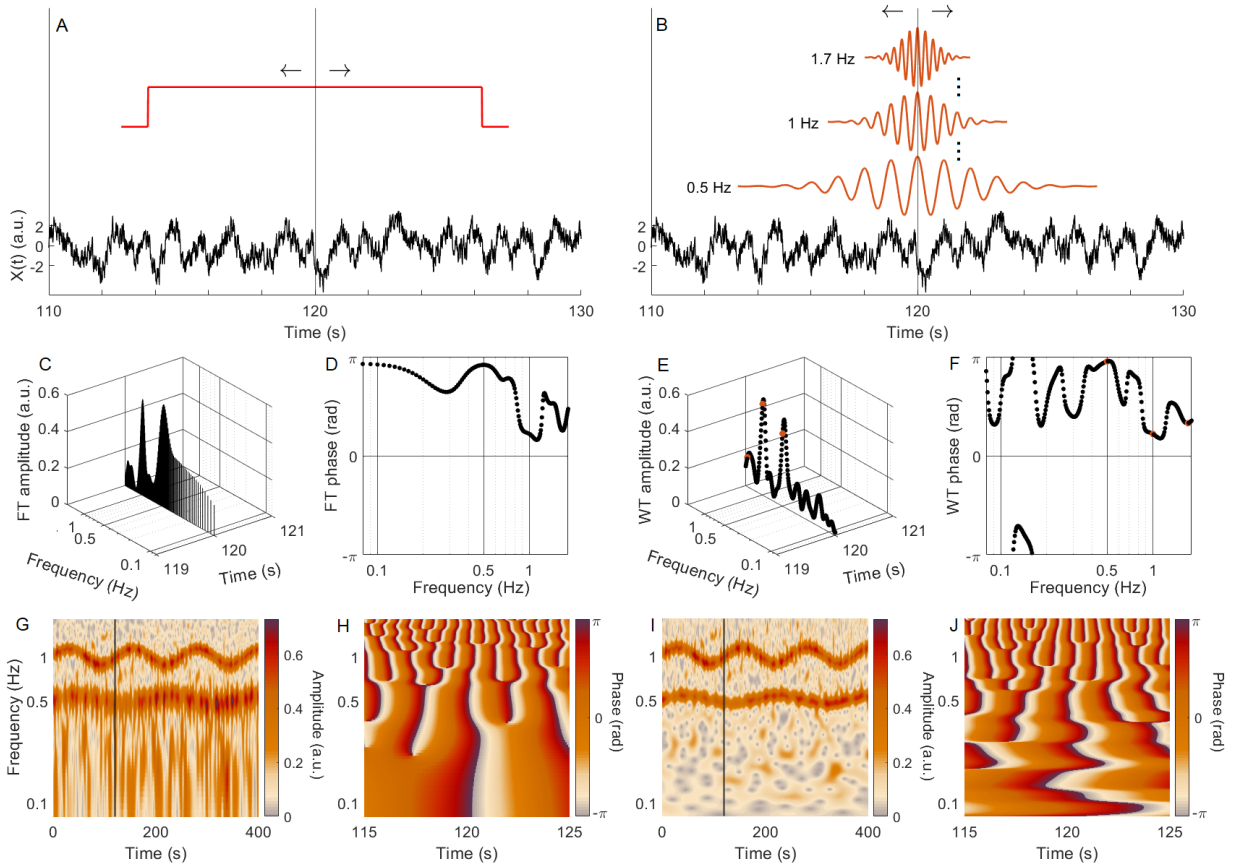
S. J. K. Barnes<sup>1</sup> J. Bjerkan<sup>1</sup> P. T. Clemson<sup>1</sup> J. Newman<sup>2</sup> A. Stefanovska<sup>1\*</sup>

<sup>1</sup>Lancaster University Physics Department, Lancaster, LA1 4YB, England

<sup>2</sup>Department of Mathematics and Statistics, University of Exeter, Exeter, UK

\*Corresponding author: aneta@lancaster.ac.uk

Here we present an alternative to figure 1 in the main manuscript. Namely, to facilitate the comparison of both representations, the Fourier transform is now shown in logarithmic scale in figures 1C,D,G,H. By comparing figure 1 in the main text and supplementary figure 1, it is clear that the logarithmic scale is disadvantageous to the short-time Fourier transform, which is obtained with linear frequency resolution.



Supplementary Figure 1: Time-frequency analysis illustrated for time-localised versus fixed-window approaches. (A) Generated time-series of Poincaré oscillators as defined by Eq. (5) in the main manuscript, with additive  $1/f$  noise and  $\xi_r = 0.005$ . A window of size 12.6 s centred at 120 s is drawn above the time-series. The arrows above the window illustrate that the window slides across the time-series when the short-time Fourier transform (STFT) is applied. (B) The same time-series as in A, with three wavelets with frequency resolution  $f_0 = 2$  at different frequencies (0.5 Hz, 1 Hz and 1.7 Hz) drawn above the time-series. The wavelets slide across the time-series when the WT is applied. The dots between the wavelets illustrates that there is one wavelet for each frequency, in our case 288 wavelets. (C) The STFT amplitude found at 120 s. Note the logarithmic frequency scale. (D) The STFT phase found at 120s projected onto the frequency-phase plane. (E) The WT amplitude found at 120s. The orange dots correspond to the frequencies of the three wavelets in B. Note the logarithmic frequency resolution of the WT. (F) The WT phase found at 120s projected onto the frequency-phase plane. (G) The STFT amplitude for the whole 400s time-series. A line is drawn at 120s. Note the logarithmic frequency scale. (H) The STFT phase for 10s of the time-series. (I) the WT amplitude for the whole 400s time-series. (J) The WT phase for 10s of the time-series.

# SUPPLEMENTARY MATERIAL

for

## Theta and alpha connectivity in children with autism spectrum disorder

Samuel J.K. Barnes<sup>1</sup>

Megan Thomas<sup>2,3</sup>

Peter V.E. McClintock<sup>1</sup>

Aneta Stefanovska<sup>1\*</sup>

<sup>1</sup>Lancaster University Physics Department, Lancaster, LA1 4YB, England

<sup>2</sup>Department of Pædiatrics, Blackpool Teaching Hospitals NHS Foundation Trust,  
Blackpool, United Kingdom

<sup>3</sup>Now at Department of Pediatrics, Faculty of Medicine, Dalhousie University, Halifax,  
Nova Scotia, Canada

\*Corresponding author: aneta@lancaster.ac.uk

### Contents

<b>1</b>	<b>Introduction</b>	<b>2</b>
<b>2</b>	<b>Model procedure and parameters</b>	<b>2</b>
2.1	Wavelet phase coherence (WPC) model . . . . .	2
2.2	Dynamical Bayesian inference (DBI) Model . . . . .	2
<b>3</b>	<b>Signal preprocessing</b>	<b>3</b>
<b>4</b>	<b>Movement artefacts and amplitude weighting</b>	<b>3</b>
<b>5</b>	<b>Statistical tests</b>	<b>4</b>
5.1	Wilcoxon rank-sum test . . . . .	4
5.2	Friedman's test for repeated measures . . . . .	5
<b>6</b>	<b>Effect sizes</b>	<b>5</b>
6.1	Study sensitivity . . . . .	5
6.2	Wavelet phase coherence effect size . . . . .	5
6.3	Dynamical Bayesian inference effect size . . . . .	7
<b>7</b>	<b>Controlling for relaxation aids in resting state measurements</b>	<b>7</b>
<b>8</b>	<b>Classification</b>	<b>11</b>
<b>9</b>	<b>Additional results</b>	<b>11</b>
9.1	Power . . . . .	11
9.2	Wavelet phase coherence . . . . .	12
9.3	Dynamical Bayesian inference . . . . .	15
<b>10</b>	<b>Healthy Brain Network</b>	<b>21</b>
10.1	Inclusion criteria . . . . .	21
10.2	Splitting the age groups . . . . .	22

# 1 Introduction

This document provides supplementary material for “Frontal connectivity in children with autism spectrum disorder”. The procedures and parameters used to generate illustrative models in the paper are given in section 2. Section 3 describes the preprocessing that was performed on the measured EEG signals. An example using real data to illustrate why phase, rather than amplitude-weighted, measures were chosen for the investigation is provided in section 4. In section 5, the statistical methods used, and the reasoning behind their application, are described. This includes the group medians and Friedman’s test results, which confirm that there is consistency across the repeats for each person. Additional details pertaining to the effect sizes are given in section 6. Section 7 demonstrates the results when controlling for relaxation aids in the resting state. The classification analyses performed are described in section 8. Following this, section 9 provides violin plots for each of the repeats to highlight the distribution of the data across all of the segments in the Blackpool results. Finally, section 10. gives further analysis of the validation dataset.

## 2 Model procedure and parameters

Two models were employed to demonstrate the methods used in the paper; they relate to Figs. 1. and 2. of the main text.

### 2.1 Wavelet phase coherence (WPC) model

Wavelet phase coherence assesses the degree to which a pair of oscillatory processes share a common phase evolution. To demonstrate cases which display both high and low coherence, a pair of time series were numerically generated.

The first series,  $x_1(t)$  contains two time-varying oscillatory modes centred at frequencies  $\omega_1 = 5\text{Hz}$  and  $\omega_2 = 9.5\text{Hz}$ . The modulation frequency of these modes is  $\omega_{m1} = 0.005\text{Hz}$  and  $\omega_{m2} = 0.015\text{Hz}$ , while the amplitudes of modulation are  $A_1 = 2$ ,  $A_2 = 8$ . The following differential equation for the phases of the system is solved using the fourth-order Runge-Kutta approach (RK4). A total time of 400 seconds was iterated over, with a time step of 0.005s for each oscillatory mode to determine the phases,  $\alpha_i$ , present in the system at each time.

$$\dot{\alpha}_i = \omega_{0i}(t) = \omega_i + A_i \sin(\omega_{mi}t) \quad (1)$$

These derived phases are then used to generate the signal with two independent modes, such that,

$$x(t) = 5 \cos(\alpha_1 t) + 5 \cos(\alpha_2 t) + \eta(t), \quad (2)$$

where  $\eta$  is an additive pink ( $\frac{1}{f}$ ) noise term. The noise was obtained using the Matlab built-in *pinknoise* function, with the output being multiplied by a factor of 150.

The above enables the user to generate a signal with two oscillatory modes. To enable the juxtaposition of coherence both with and without a constant phase difference, a further time series is needed. As such, an additional time series was generated, which lacked the high frequency oscillatory mode for the first 200s. This initial series was subsequently concatenated with another 200s time series, simulated with both modes. This concatenated time series is represented by the orange lines in Fig.1A, B of the main text. and is also represented in the time/frequency domain (Fig.1C main text), while its time-averaged power is given in Fig.1D (main text). The phases of this signal are also represented over a short interval in the orange lines of Figs. 1E, F in the main text.

To evaluate the time/frequency representation of Fig. 1C, a Morlet wavelet was used with a frequency resolution parameter of  $F_0 = 4$ . The wavelet transforms of both the aforementioned signals served as inputs to the coherence calculation.

### 2.2 Dynamical Bayesian inference (DBI) Model

While the WPC model as outlined above only needed to demonstrate the presence of oscillatory modes, the DBI model needed to illustrate a coupling between time series. A total period of 1000 seconds were simulated across with a time step of 0.03s using RK4 to find the phases of a pair of unidirectionally coupled phase oscillators. The frequencies of these modes do not vary in time and  $\omega_1 = 6\text{Hz}$ ,  $\omega_2 = 9\text{Hz}$ ,



$$\begin{aligned}\dot{\phi}_1 &= \omega_1 + \eta(t), \\ \dot{\phi}_2 &= \omega_2 + q_2(\phi_1, \phi_2) = \omega_2 + E \cos(\phi_1 + \pi/2.5) + \eta(t).\end{aligned}\tag{3}$$

Where the noise  $\eta$ , in this case, is white Gaussian and applied to the instantaneous frequency, implemented using the built-in *wgn* Matlab function. In the above example,  $E$ , is the coupling strength between the oscillators and can be varied to increase or decrease the amount of information transfer between the systems. This is shown in Fig. 2 of the main text.

Once this ground truth had been established, the couplings were verified using dynamical Bayesian inference. The parameters applied for the DBI are as follows: window size = 100s, propagation constant = 0.2 and the overlap parameter = 1 (no overlap between windows).

### 3 Signal preprocessing

During the collection of the Blackpool data, two different reference electrode positions were used. To account for the resultant bias in recording, the data were re-referenced to the common average. This involved subtracting the average sum of all 19 electrodes from each individual probe's time series. The equations describing this procedure are:

$$V_{CA} = \frac{1}{N} \sum_i^N V_i,\tag{4}$$

$$V'_i = V_i - V_{CA},\tag{5}$$

where  $V_{CA}$  is the common average,  $V_i$  is the time series for the individual probes,  $V'_i$  is the rereferenced time series, and  $N$  is the total number of electrodes ( $N = 19$ ). After the time series were rereferenced, they were bandpassed with a Butterworth filter of order proportional to the frequency band of interest, and then detrended by subtracting the 3rd order polynomial. This was done using the MATLAB functions *bandpass* and *detrend* respectively.

### 4 Movement artefacts and amplitude weighting

The methods used throughout this investigation are independent of amplitude and instead, focus solely on phase dynamics. Alternative measures that also incorporate amplitude information are frequently employed to evaluate functional connectivity. Among these measures, one of the most extensively utilised is amplitude-weighted phase coherence (AWPC) [6, 7]. This method considers both the amplitude and phase at each point in the time/frequency domain to calculate coherence. For a pair of time series AWPC is defined as the normalised wavelet cross-spectrum at each point in time and frequency [6],

$$AWPC(t, f) = \frac{|W_{12}(t, f)|}{[W_{11}(t, f) \cdot W_{22}(t, f)]^{1/2}}.\tag{6}$$

Where  $W_{12}$  is the wavelet cross-spectrum, and  $W_{11}$ ,  $W_{22}$  are the auto-spectra. As before, a value of 1 is found for perfect coherence, while 0 represents a complete lack of coherence. The key distinction between these approaches is that a simultaneous amplitude change for a pair of time series will cause an increase in the AWPC, but not in the WPC [1, 5]. This makes WPC more resistant to sudden amplitude perturbations – such as those arising from movement artefacts – than AWPC [1].

Data containing a clear movement artefact were analysed to illustrate the differences between these methods. These time series were selected by visual inspection of the large amplitude spike, which was concurrently present across all probes. This spike is likely unrelated to the underlying neural dynamics, and so obfuscates approaches that incorporate amplitude information.

Despite the pervasive effect of the movement artefact on the data, Fig. 1. illustrates that WPC remains resilient as a representation of shared phase information between the signals. In contrast, the amplitude dependence of AWPC suffers a significant susceptibility to simultaneous amplitude changes, exhibiting a peak at around 90 seconds that coincides with the mutual spike. In addition, EEG data are particularly affected by noise and amplitude effects due to, for example, differential signal attenuation

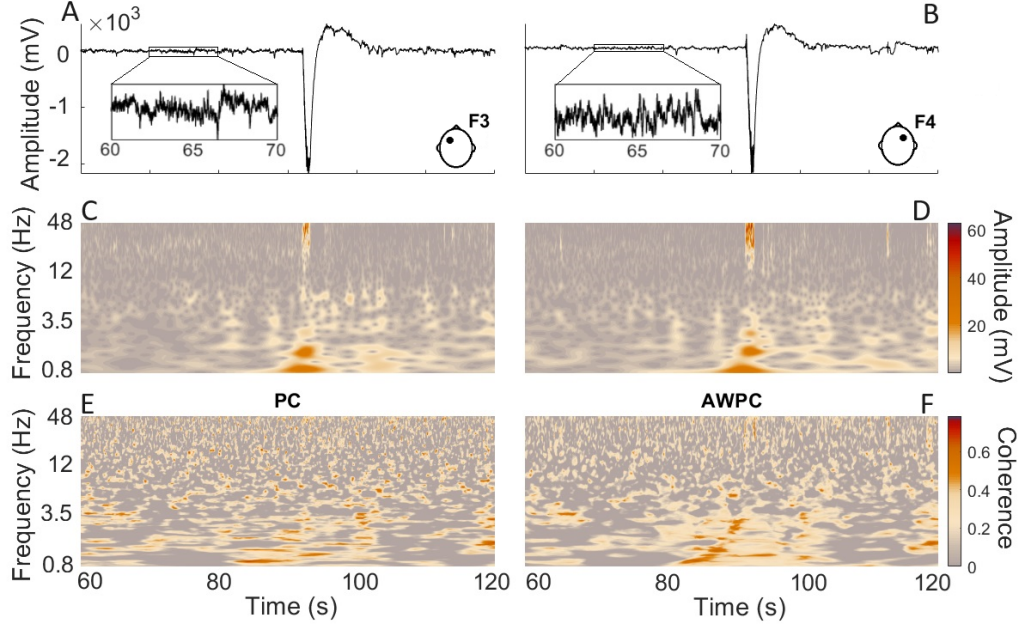


Figure 1: Movement artefact present the ASD time series (subject 4, segment 3). A pair of EEG time series from probes F3 (A) and F4 (B), each containing a large artefact. Their respective wavelet transforms (C, D) further indicate a multiscale spike in power. Both wavelet transforms (C, D) serve as inputs for the respective coherence calculations (E, F). The time-localised phase coherence (E) is fairly resilient against this perturbation when compared to its amplitude-weighted counterpart (F). The time-localised coherence was calculated by subtracting the 50th percentile of intersubject surrogates (72 for the control group and 156 for the ASD group). Any coherence values that fell below this threshold were set to zero.

arising from the varying separations of EEG electrodes from the cortical surface. The relative resilience of WPC to amplitude effects suggests that it may provide a more appropriate approach for the investigation of functional connectivity.

A Morlet wavelet with a frequency resolution parameter of  $F_0 = 2$  was used. The mean value of 156 intersubject surrogates at each point in the time/frequency domain was used to reduce the amount of spurious time-localised coherence that was detected. Despite this, a larger degree of seemingly coherent behaviour is present in the AWPC compared to the PC, due to the amplitude weighting, which detects a simultaneous spike in both data. Phase coherence is robust against this perturbation.

## 5 Statistical tests

An assumption of normally distributed data is needed when using parametric approaches; however, the results were generally not normally distributed. Given this lack of Gaussianity, non-parametric tests were applied to compare differences between and within groups.

### 5.1 Wilcoxon rank-sum test

To assess differences between the groups while acknowledging the non-normal distribution of the data, the Wilcoxon rank-sum test was used. The null hypothesis was that there was no difference in connectivity between the CG and ASD groups.

All of the results from the ASD and CG groups were first ranked. The summation of all the ranks for each group was then calculated. The difference between these sums was then used to assess the statistical significance of any difference between groups. A  $p$ -value could then be calculated, and if this fell below 0.05, then we were able to reject the null hypothesis.

## 5.2 Friedman’s test for repeated measures

Friedman’s test serves as a non-parametric alternative to the repeated measures ANOVA, aiming to uncover variations among the same subjects over multiple time points. Here, we utilise this test to assess the consistency of results for all subjects across different time intervals, ensuring that results are consistent across repeats. This consistency is vital for two reasons. First, in the context of diagnostic tests, biomarkers must be stable regardless of when a measurement is taken; our analysis seeks to assess this required consistency. Secondly, this approach allows us to see if we can treat the results as repeated measures.

As with the Wilcoxon test outlined above, the data are ranked. In this case, however, they were ranked across the repeats at a given probe pair for each subject. The sum of each column, corresponding to the rank-sum of each repeat, is then taken. These rank-sums are then compared to assess whether there are significant differences at different measurement times.

## 6 Effect sizes

A post hoc analysis was conducted to determine the effect size using Cohen’s  $d$  [2]. This metric relies on the means of the two groups being compared, denoted as  $m_1$  and  $m_2$ , along with the pooled standard deviation  $sd$  which is calculated as

$$sd = \sqrt{\frac{(n_1 - 1)SD_1^2 + (n_2 - 1)SD_2^2}{n_1 + n_2 - 2}}, \quad (7)$$

where  $n_1$  and  $n_2$  represent the sample sizes of the two groups, and  $SD_1$  and  $SD_2$  denote their respective standard deviations. Cohen’s  $d$  is then computed from the formula:

$$d = \frac{m_1 - m_2}{sd}. \quad (8)$$

In general, an effect size of  $d = 0.5$  is considered medium, while  $d = 0.8$  is considered large.

### 6.1 Study sensitivity

The study’s sensitivity was assessed using G\*Power [3], with a screenshot of the test being presented in Fig. 2. The analysis incorporated a power of 0.5, a significance level of 0.05, and the sample sizes (13 ASD and 9 CG) utilized in the investigation as input parameters.

As depicted in Fig. 2, the exploratory nature of this study resulted in a large effect size of 1.387, due to the modest sample sizes. However, as demonstrated later, many of the repeats surpassed this threshold.

### 6.2 Wavelet phase coherence effect size

Effect sizes for WPC were initially calculated using the Blackpool dataset. Specifically, the analysis focused on four probe pairs that demonstrated the most significant differences between groups. These probe pairs were evaluated across the six data segments, yielding Cohen’s  $d$  values ranging from 1.051 to 1.884, with a mean of 1.393. All observed effect sizes in the frontal network exceeded 1 and are shown in Tab. 1.

Table 1: Effect sizes for all segments in the inter-hemispheric frontal network evaluated across the medium frequency band (3.5-12 Hz) between groups. The numbered sections 1-5 were found chronologically, while the video segment reflects data intervals selected for their relative lack of movement artefacts.

From/To	Effect sizes					
	1	2	3	4	5	Video
<b>Fp1 - Fp2</b>	1.051	1.295	1.133	1.182	1.191	1.232
<b>F3 - Fp2</b>	1.376	1.884	1.476	1.587	1.502	1.554
<b>Fp1 - F4</b>	1.273	1.227	1.232	1.630	1.239	1.266
<b>F3 - F4</b>	1.357	1.534	1.526	1.883	1.492	1.311

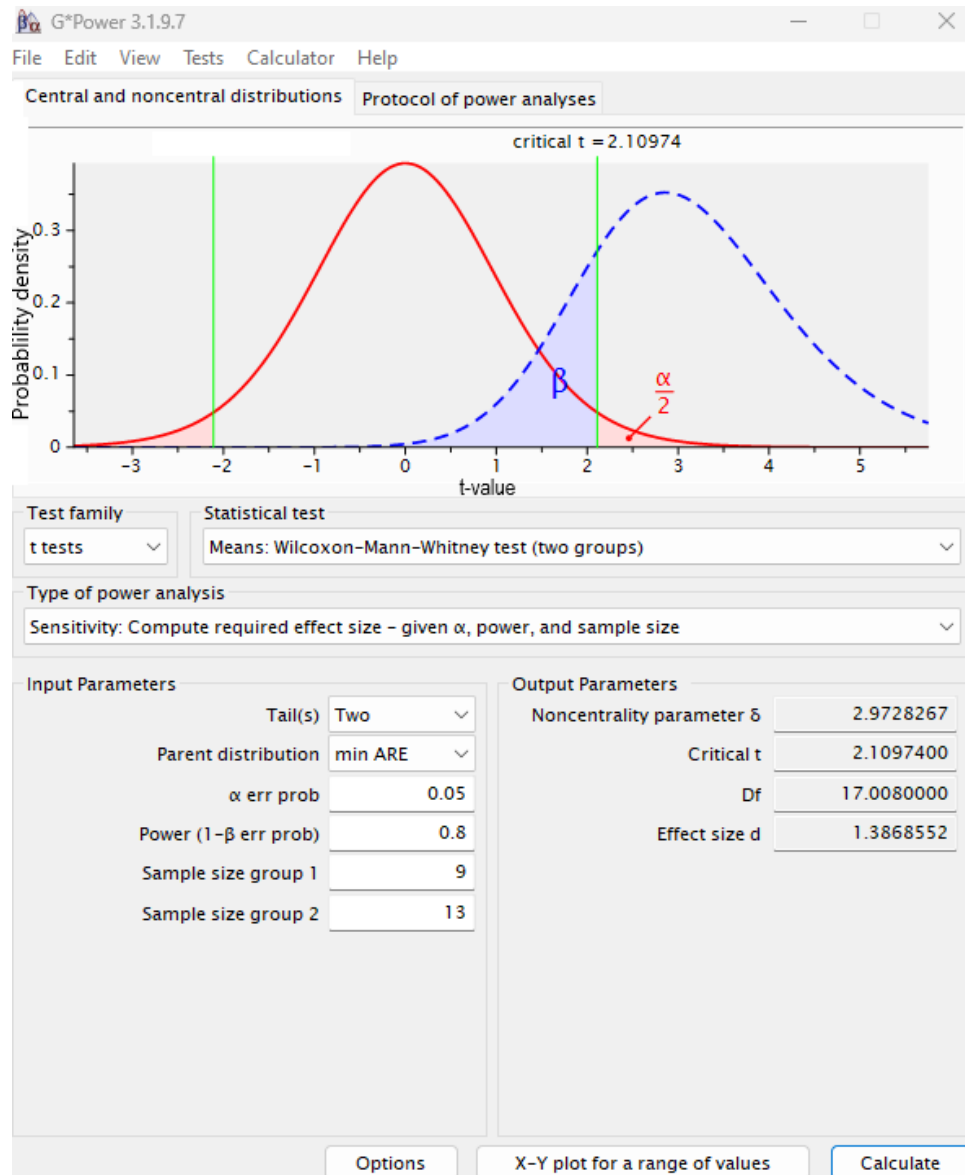


Figure 2: Screenshot of the G\*power software demonstrating the input and output parameters used. Given an input of 9 control group individuals and 13 participants with autism spectrum disorder and a two tailed distribution. The parent distribution is set to min ARE (minimum asymptotic relative efficiency) to optimise the analysis. The alpha error probability ( $\alpha$  err prob) was set to 0.05; this is the significance level of the test. The power, 1-beta error probability ( $1 - \beta$  err prob) is the probability of not detecting a true effect and was set to 0.8 (meaning there is an 80 % chance of detecting a true event if one exists). For our purposes, the important output is the effect size,  $d$ , which indicates the value that effect sizes must be larger than given the sample sizes and significance level.

Effect sizes from the HBN network data were also calculated. For reasons explained in section 10.2, the entire age group (5-15) and older age group (9-15) were considered separately. Tab 2 presents the effect sizes for each probe pair that exceeded a significance threshold of 0.01 in the older group when applying the Wilcoxon rank-sum test.

Table 2: Effect sizes for all segments in the Healthy Brain Network evaluated across the medium frequency band (3.5-12 Hz) for the older (9-15 years-old) group. The probe pairs indicated here all had a  $p$ -value less than 0.01 from a Wilcoxon rank-sum test.

<b>C3-PZ</b>	<b>F3-O1</b>	<b>F3-O2</b>	<b>F3-T3</b>	<b>F3-T6</b>	<b>O1-P4</b>	<b>O2-P3</b>
0.63	0.70	0.86	0.69	0.79	0.70	0.65

<b>O2-T3</b>	<b>O2-T4</b>	<b>P3-P4</b>	<b>P-3PZ</b>	<b>P3-T4</b>	<b>P3-T6</b>	<b>T3-T4</b>
0.78	0.86	0.69	0.65	0.80	0.71	0.75

As elaborated upon in section 10.2, there was more significance in the older group, likely due to their increased ability to tolerate a more demanding measurement protocol. Coherence between probe pair O2-T4 demonstrated the largest effect size (0.86 in the older group). Interestingly however, significance was retained when considering the 5-15 years-old group. Tab. 3 demonstrates the effect sizes in this case.

Table 3: Effect sizes for all segments in the Healthy Brain Network evaluated across the medium frequency band (3.5-12 Hz) for the older (5-15 years-old) group. The probe pairs indicated here all had a  $p$ -value less than 0.01 from a Wilcoxon rank-sum test.

<b>F3-O2</b>	<b>F7-O2</b>	<b>F7-Pz</b>	<b>O2-T3</b>	<b>O2-T4</b>	<b>O2-T6</b>
0.48	0.44	0.49	0.46	0.62	0.27

### 6.3 Dynamical Bayesian inference effect size

For the DBI, eight directional probe pairs in the frontal network were evaluated across six time segments. The range of Cohen’s  $d$ -values spanned from a minimum of 0.554 to a maximum of 2.18, with a mean value of 1.17. These are presented in Tab. 4

Table 4: Effect sizes across retests for frontal networks evaluated across the medium frequency band (3.5-12 Hz) between groups. The numbered sections, 1-5, were found chronologically, while the video segment reflects data intervals selected for their relative lack of movement artefacts.

<b>From/To</b>	<b>Effect sizes</b>					
	<b>1</b>	<b>2</b>	<b>3</b>	<b>4</b>	<b>5</b>	<b>Video</b>
<b>Fp1 → Fp2</b>	0.834	1.318	1.312	1.027	1.126	1.165
<b>Fp1 ← Fp2</b>	0.690	1.273	1.187	1.344	1.450	1.519
<b>Fp1 → F4</b>	0.772	1.664	1.178	0.783	1.081	1.473
<b>Fp1 ← F4</b>	1.025	1.507	1.081	1.175	1.326	1.118
<b>F3 → F4</b>	1.115	1.170	0.750	0.966	0.852	0.554
<b>F3 ← F4</b>	0.817	1.481	1.023	1.068	0.766	0.958
<b>F3 → Fp2</b>	1.119	1.654	0.993	1.262	1.033	1.333
<b>F3 ← Fp2</b>	0.848	2.178	1.377	1.614	1.542	1.664

Despite the relatively modest sample sizes employed in this study, the observed differences, as indicated by Cohen’s  $d$ , were fairly large. This also motivates further exploration of the suggested electroencephalographic measures with larger sample sizes to enhance the validity of findings.

## 7 Controlling for relaxation aids in resting state measurements

In this study, a resting-state paradigm was employed. Some participants occasionally found it difficult to maintain an eyes-open, restful state during measurements. To help them remain relaxed, either bubbles

or a smartphone were used as a focus, with these aids used slightly more often in the ASD group than in the control group (46% in ASD vs. 22% in CG). To ensure these interventions did not bias the results, the analysis was repeated after controlling for this factor. Specifically, ASD participants 12, 11, and 10 (who used the screen) and participant 2 (who used bubbles) were excluded from the analysis. This adjustment resulted in 9 participants per group, with no bubbles used in either group and both groups having 22% of participants using the screen in the resting state. The same analysis was performed as in the main manuscript.

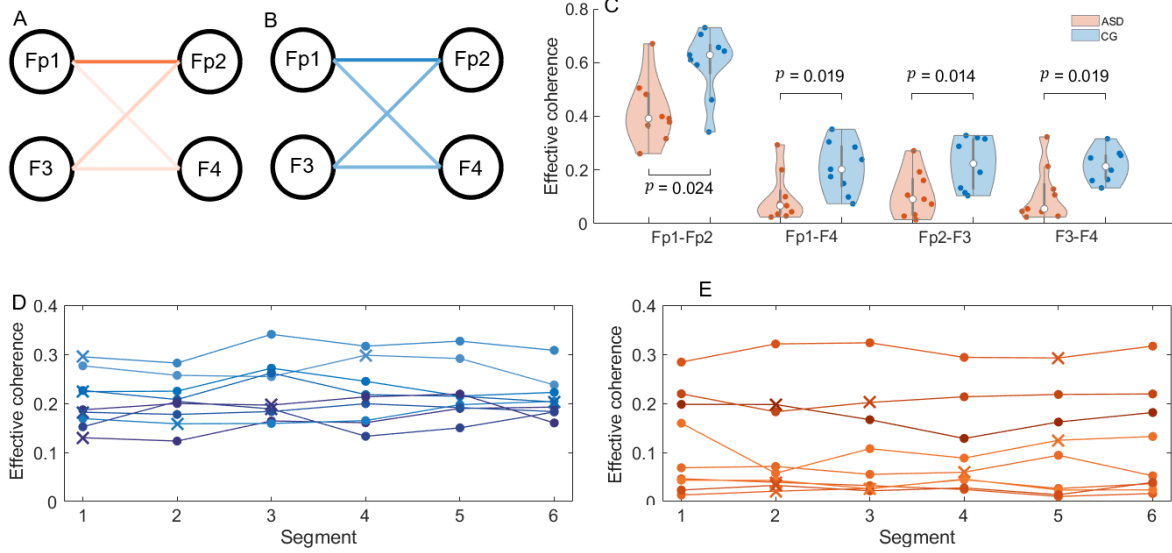


Figure 3: Coherence results across all segments when controlling for resting state relaxation aids (A) Headmap representing the group median coherence averaged across the theta and alpha bands following the subtraction of intersubject surrogates between probes for the video segment in the autism spectrum disorder (ASD,  $N = 9$ , male) group (B) and the control group (CG,  $N = 9$ , male). (C) Median effective coherence between the measured EEG signal locations evaluated across the medium frequency band (3.5-12 Hz) in the video segment. Blue violins represent CG while red indicates ASD. The median of each distribution is indicated by the white circle and the box indicates the interquartile range. Each coloured datapoint represents the mean coherence across the theta and alpha bands for each participant. The Wilcoxon rank-sum test was used to evaluate the  $p$ -values ( $N = 9$  ASD,  $N = 9$  CG). (D) The effective coherence results for each of the sequential, and video, segments. Filled circles indicate that the segment was chosen sequentially, while a cross represents video acquired segments. Each line represents a different participant across repeats ( $N = 9$  ASD,  $N = 9$  CG for each segment). In this case, the probe pair F3-F4 is illustrated, for the ASD (D) and CG (E) cases.

The same pattern was observed in the coherence results as had been obtained when using relaxation aids as described in the main manuscript; and the same was true for the dynamical Bayesian inference results (Figs. 3 and 4 respectively). To ensure the results were consistent across the segments investigated, this analysis was repeated.

The same pattern, with significance regardless of the time measurements were conducted, were found when the relaxation states were matched. The slightly lower  $p$ -values (Tab. 5 for coherence and Tab. 6 for Bayesian) are likely due to the reduced statistical power as we have decreased the size of the ASD group.

Bayesian results followed the same trend. With slightly lower significance likely due to the reduced sample size, but the same patterns identified. Effect sizes were subsequently checked for both analysis approaches and across the segments (Tab. 7 and 8).

Generally, our results were very similar, indicating that the resting state paradigm made little difference. The small changes to  $p$ -values can be explained as the smaller groups hold less statistical strength.



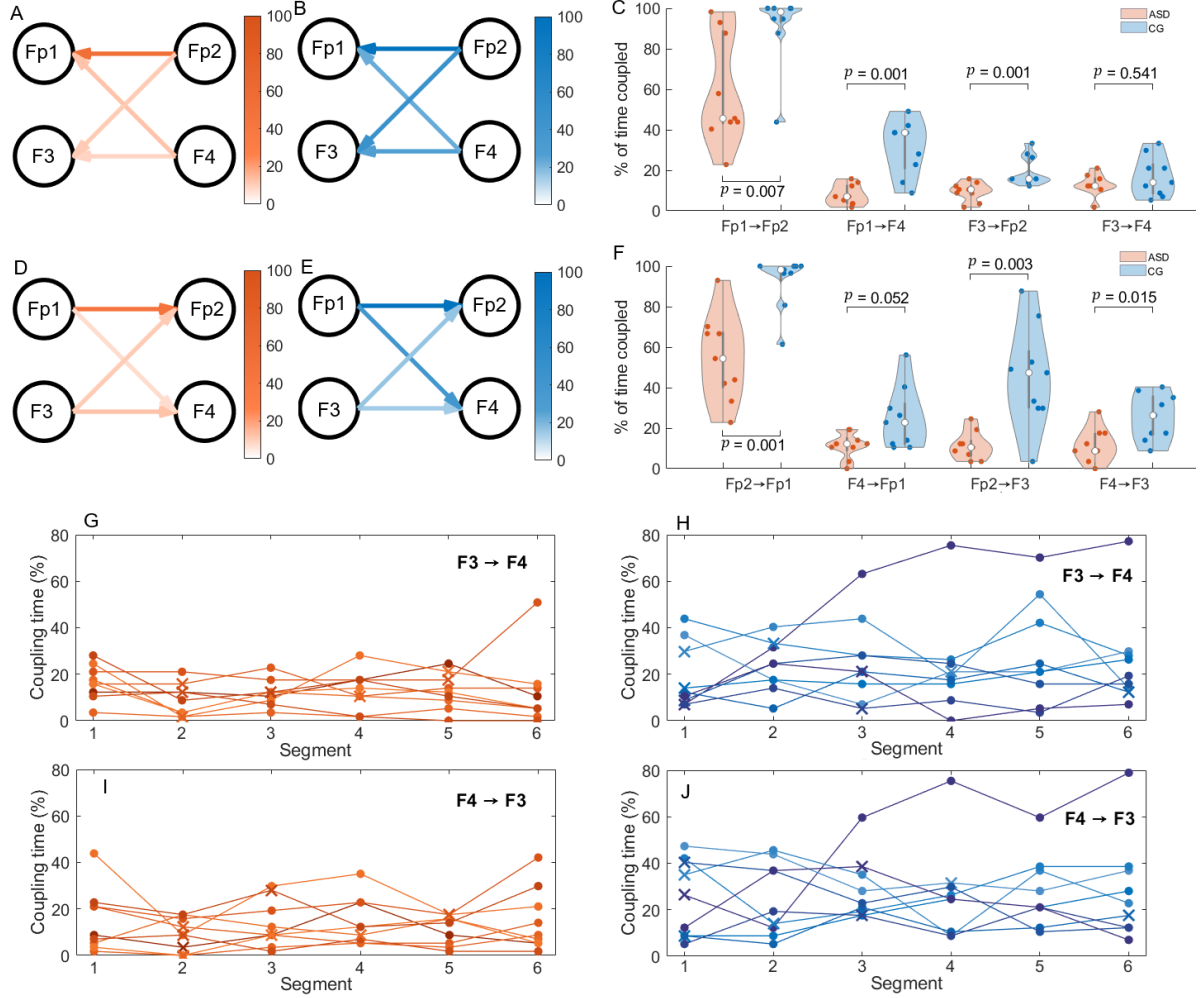


Figure 4: Absolute and  $p$ -values for the dynamical Bayesian inference coupling time in the groups controlling for resting state. (A, B, D, E) Headmaps representing the group median percentage coupling time between probes for the video segment in the autism spectrum disorder (ASD,  $N = 9$ , male participants) group (orange) and the control group (CG,  $N = 9$ , male participants) (blue). The 95th percentile of intersubject surrogates was applied to remove the effect of spurious interactions. (C, F) Percentage time coupled between the measured EEG signal locations evaluated across the medium frequency band (3.5-12 Hz) in the video segments, from the left to right (C), and right to left (F) hemisphere. The Wilcoxon rank-sum test was used to assess group differences ( $N = 9$  ASD,  $N = 9$  CG). Blue violins represent CG while red indicates ASD. The Wilcoxon rank-sum test was used to evaluate the  $p$ -values. (G-J) The coupling time for each of the sequential, and video, segments. Each line represents a different participant across repeats ( $N = 9$  ASD,  $N = 9$  CG for each segment). Filled circles indicate that the segment was chosen sequentially, while crosses represent video acquired segments. In this case, the bidirectional coupling between F3 and F4 is illustrated, for the ASD (G, I) and (H, J) cases.

Table 5:  $p$  values for all segments in the inter-hemispheric frontal network evaluated across the medium frequency band (3.5-12 Hz) between groups when the resting state relaxation aids are matched. The numbered sections 1-5 were found chronologically, while the video segment reflects data intervals selected for their relative lack of movement artefacts.

From/To	$p$ -values					
	1	2	3	4	5	Video
<b>Fp1 - Fp2</b>	<b>0.024</b>	<b>0.014</b>	<b>0.024</b>	<b>0.014</b>	<b>0.006</b>	<b>0.008</b>
<b>Fp1 - F4</b>	<b>0.014</b>	<b>0.024</b>	<b>0.019</b>	<b>0.008</b>	<b>0.024</b>	<b>0.006</b>
<b>F3 - Fp2</b>	0.050	<b>0.011</b>	<b>0.014</b>	<b>0.011</b>	<b>0.008</b>	<b>0.024</b>
<b>F3 - F4</b>	0.094	<b>0.011</b>	<b>0.019</b>	<b>0.024</b>	<b>0.031</b>	<b>0.04</b>

Table 6:  $p$ -values across retests for frontal networks evaluated across the medium frequency band (3.5-12 Hz) between groups when the resting states are matched. The numbered sections, 1-5, were found chronologically, while the video segment reflects data intervals selected for their relative lack of movement artefacts.

From/To	$p$ -values					
	1	2	3	4	5	Video
<b>Fp1 <math>\rightarrow</math> Fp2</b>	0.052	<b>0.012</b>	<b>0.008</b>	<b>0.012</b>	<b>0.011</b>	<b>0.007</b>
<b>Fp1 <math>\leftarrow</math> Fp2</b>	0.057	<b>0.001</b>	<b>0.020</b>	<b>0.006</b>	<b>0.013</b>	<b>0.001</b>
<b>Fp1 <math>\rightarrow</math> F4</b>	0.098	<b>0.0002</b>	<b>0.029</b>	<b>0.037</b>	<b>0.023</b>	<b>0.001</b>
<b>Fp1 <math>\leftarrow</math> F4</b>	0.072	<b>0.001</b>	0.065	<b>0.009</b>	<b>0.013</b>	0.052
<b>F3 <math>\rightarrow</math> Fp2</b>	0.095	<b>0.004</b>	0.141	<b>0.042</b>	0.141	<b>0.001</b>
<b>F3 <math>\leftarrow</math> Fp2</b>	0.098	<b>0.0004</b>	<b>0.020</b>	<b>0.004</b>	<b>0.005</b>	<b>0.003</b>
<b>F3 <math>\rightarrow</math> F4</b>	0.248	<b>0.007</b>	0.197	0.183	<b>0.013</b>	0.541
<b>F3 <math>\leftarrow</math> F4</b>	0.0.197	<b>0.001</b>	0.052	<b>0.037</b>	0.141	<b>0.015</b>

Table 7: Median effect sizes for all segments in the inter-hemispheric frontal network evaluated across the medium frequency band (3.5-12 Hz) between groups when the resting states are matched. The numbered sections 1-5 were found chronologically, while the video segment reflects data intervals selected for their relative lack of movement artefacts.

From/To	Effect sizes					
	1	2	3	4	5	Video
<b>Fp1 - Fp2</b>	1.283	1.643	1.430	1.505	1.539	1.679
<b>F3 - Fp2</b>	1.116	1.624	1.335	1.440	1.392	1.490
<b>Fp1 - F4</b>	1.198	1.147	1.132	1.405	1.069	1.287
<b>F3 - F4</b>	1.096	1.408	1.366	1.651	1.249	1.254

Table 8: Dynamical Bayesian inference effect sizes across retests for frontal networks evaluated across the medium frequency band (3.5-12 Hz) between groups when the resting states are matched. The numbered sections, 1-5, were found chronologically, while the video segment reflects data intervals selected for their relative lack of movement artefacts.

From/To	Effect sizes					
	1	2	3	4	5	Video
<b>Fp1 <math>\rightarrow</math> Fp2</b>	0.998	1.523	1.462	1.219	1.343	1.382
<b>Fp1 <math>\leftarrow</math> Fp2</b>	0.775	1.430	1.477	1.578	1.601	2.110
<b>Fp1 <math>\rightarrow</math> F4</b>	0.850	2.281	1.226	1.312	1.355	2.279
<b>Fp1 <math>\leftarrow</math> F4</b>	0.992	1.863	0.924	1.249	1.091	1.131
<b>F3 <math>\rightarrow</math> F4</b>	0.756	1.294	0.668	0.835	0.821	0.511
<b>F3 <math>\leftarrow</math> F4</b>	0.587	1.564	0.893	1.039	0.686	1.373
<b>F3 <math>\rightarrow</math> Fp2</b>	0.774	1.688	0.822	1.030	0.781	1.635
<b>F3 <math>\leftarrow</math> Fp2</b>	0.782	3.349	1.212	1.544	1.370	1.834

## 8 Classification

To assess the strength of this approach to discriminate between groups, a simple classification was performed using the J48 decision tree algorithm in the Waikato Environment for Knowledge Analysis (WEKA) software [4].

In the Blackpool data video segment a classification accuracy of 86% was achieved using only F3-F4 coherence and the coupling  $Fp2 \rightarrow F3$  as attributes and leave one out cross validation. Table 9 indicates the confusion matrix for this case.

Table 9: Confusion matrix for for Blackpool video segment (ASD=13, CG=9). The columns indicate what the rows were classified as, for example, 8 CG participants were correctly classified as CG, while one was incorrectly classified as ASD via this approach.

	CG	ASD
CG	8	1
ASD	2	11

The same attributes were used in the other segments to yield confusion matrices for each of the segments investigated (Tab. 10).

Table 10: Confusion matrix for Blackpool sequential segments (ASD = 13, CG = 9). The columns indicate what the rows were classified as.

	Seg 1		Seg 2		Seg 3		Seg 4		Seg 5	
	CG	ASD	CG	ASD	CG	ASD	CG	ASD	CG	ASD
CG	9	0	8	1	9	0	8	1	8	1
ASD	5	8	2	11	3	10	6	7	6	7

In the Healthy brain network case the data was split into a younger (5-9) and older (9-15) year-old age range groups, for reasons explained in Section 10.2. Classification analysis was subsequently performed on the older age group, with an accuracy of 80% achieved using only coherence between F3-O2, T3-T4 and T3-F3 as attributes. Table 11 indicates the confusion matrix for this case.

Table 11: Confusion matrix for for Blackpool video segment (ASD = 31, CG = 33). The columns indicate what the rows were classified as, for example, 29 CG participants were correctly classified as CG, while four were incorrectly classified as ASD.

	CG	ASD
CG	29	4
ASD	9	22

## 9 Additional results

While the main results pertaining to the  $p$ -values are given in the main paper, the associated violin plots and group medians are given below to indicate the distributions of the data for each of the sequential time intervals. Additionally, the results of the power analysis are presented.

### 9.1 Power

While the focus of this investigation was on the connectivity of the frontal region, a preliminary analysis was also performed to assess the differences in power between groups using the wavelet transform, as outlined in the main body. The differences between groups are presented via the  $p$ -values generated with the Wilcoxon rank-sum test, analogous to Tab. 3 in the main manuscript.

As demonstrated in Tab. 12, none of the power analyses yielded significant differences, this is in contrast to the consistent variations in connectivity found across the frontal region. The movement

Table 12: Reported  $p$ -values for power differences between groups across all segments in the frontal electrodes evaluated across the medium frequency band (3.5-12 Hz). The numbered sections 1-5 were found chronologically, while the video segment reflects data intervals selected for their relative lack of movement artefacts. Bold values indicate a  $p$ -value  $< 0.05$ .

Probe	Power $p$ -values					
	1	2	3	4	5	Video
<b>F3</b>	0.893	0.593	0.593	0.317	0.285	0.640
<b>F4</b>	0.841	0.285	0.689	0.125	0.256	0.385
<b>Fp1</b>	0.423	0.947	0.548	0.548	0.689	0.463
<b>Fp2</b>	0.463	0.504	0.548	0.463	0.640	1.000

artefacts that often bedevil EEG measurements may be responsible for this, as they have a substantially greater affect on amplitude than phase-based measures.

The power measurements also demonstrated far less consistency across repeats, as demonstrated in Fig. 5.

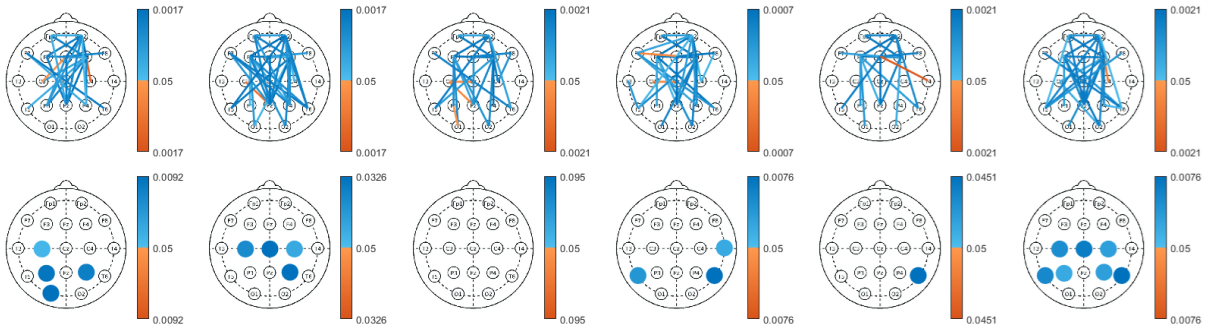


Figure 5: The significant ( $p < 0.05$ , Wilcoxon rank-sum test) coherence (top row) and power (bottom row) differences between groups (ASD = 13, CG = 9) across the sequential and video segments. The columns are in order, so that the first column corresponds to the first segment etc, until the sixth column, which represents the video segment.

In each of the repeats, the frontal network demonstrated greater coherence in the video group. In contrast, although the control group generally expressed greater power than the ASD group, the locations of the probes that were significantly different between groups were not consistent across repeats.

## 9.2 Wavelet phase coherence

Before presenting the violin plots of each segment, the median effective coherence values and associated Friedman test  $p$ -value for given probe pairs are indicated. The control group data are given in Tab. 13 and, for comparison, those for the ASD group are given in Tab. 14.

Table 13: Median effective coherence values for all segments in the inter-hemispheric frontal network evaluated across the medium frequency band (3.5-12 Hz) for the CG. The numbered sections 1-5 were found chronologically, while the video segments reflect data intervals selected for their relative lack of movement artefacts. The final column gives the Friedman test results.

From/To	Median effective coherence						Friedman test $p$ -value
	1	2	3	4	5	Video	
<b>Fp1 - Fp2</b>	0.608	0.630	0.628	0.626	0.642	0.635	0.763
<b>F3 - Fp2</b>	0.210	0.245	0.224	0.215	0.270	0.205	0.570
<b>Fp1 - F4</b>	0.186	0.178	0.202	0.188	0.196	0.181	0.968
<b>F3 - F4</b>	0.187	0.204	0.213	0.215	0.204	0.196	0.490

At no point did the  $p$ -value from the Friedman test fall below the threshold of 0.05, ensuring that, subject-wise, these measures were consistent across the sequential measurements.

Table 14: Median effective coherence values for all segments in the inter-hemispheric frontal network evaluated across the medium frequency band (3.5-12 Hz) for the ASD group. The numbered sections 1-5 were found chronologically, while the video segment reflects data intervals selected for their relative lack of movement artefacts. The final column gives the Friedman test results.

From/To	Median effective coherence						Friedman test $p$ -value
	1	2	3	4	5	Video	
<b>Fp1 - Fp2</b>	0.449	0.406	0.399	0.414	0.383	0.403	0.899
<b>F3 - Fp2</b>	0.050	0.078	0.073	0.057	0.054	0.086	0.967
<b>Fp1 - F4</b>	0.034	0.040	0.044	0.047	0.042	0.037	0.791
<b>F3 - F4</b>	0.069	0.058	0.099	0.089	0.053	0.099	0.370

The distributions of the data for each of the sequential segments are given in Figs. 6 - 10.

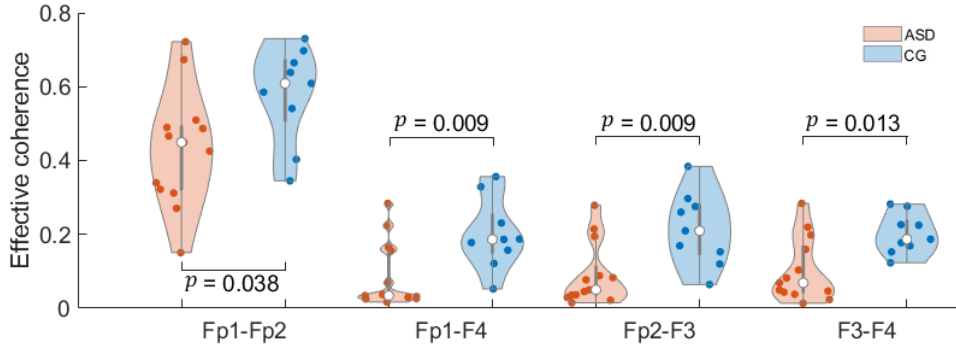


Figure 6: Effective coherence values between the measured EEG signal locations for the first sequential segment. The Wilcoxon rank-sum test was used to assess coherence differences between groups ( $N = 13$  ASD,  $N = 9$  CG). Orange violins represent the ASD group, while blue indicates CG. The white circles illustrate group median values, while the coloured dots represent the effective coherence for each participant in the theta and alpha band between the indicated probe pair.

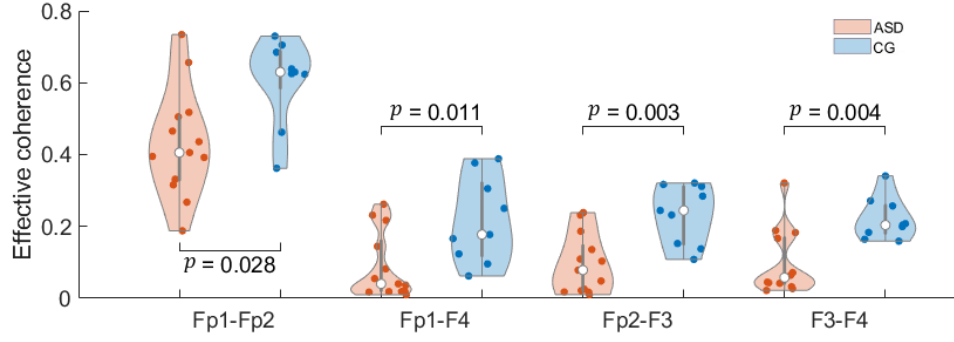


Figure 7: Effective coherence values between the measured EEG signal locations for the second sequential segment. Wilcoxon rank-sum test was used to assess coherence differences between groups ( $N = 13$  ASD,  $N = 9$  CG). Orange violins represent the ASD group, while blue indicates CG. The white circles illustrate group median values, while the coloured dots represent the effective coherence for each participant in the theta and alpha band between the indicated probe pair.

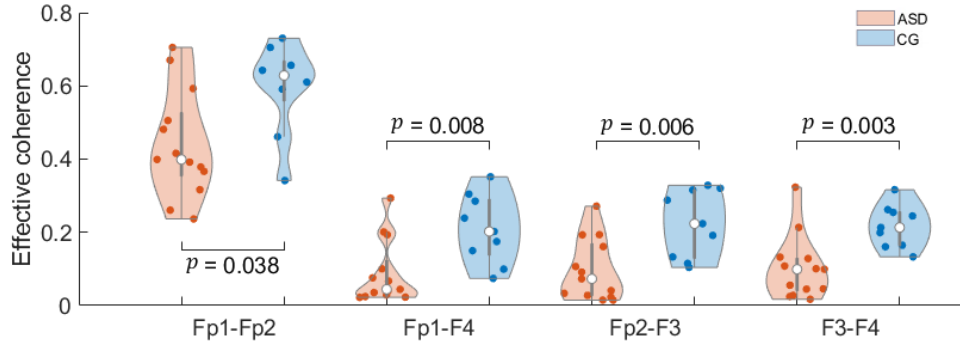


Figure 8: Effective coherence values between the measured EEG signal locations for the third sequential segment. Wilcoxon rank-sum test was used to assess coherence differences between groups ( $N = 13$  ASD,  $N = 9$  CG). Orange violins represent the ASD group, while blue indicates CG. The white circles illustrate group median values, while the coloured dots represent the effective coherence for each participant in the theta and alpha band between the indicated probe pair.

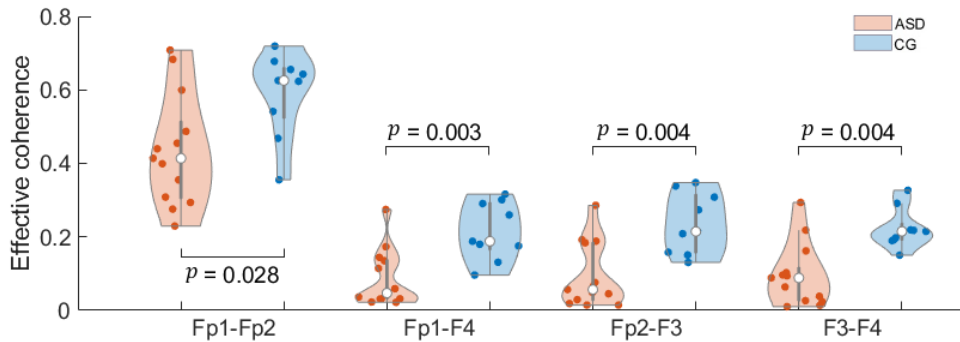


Figure 9: Effective coherence values between the measured EEG signal locations for the fourth sequential segment. Wilcoxon rank-sum test was used to assess coherence differences between groups ( $N = 13$  ASD,  $N = 9$  CG). Orange violins represent the ASD group, while blue indicates CG. The white circles illustrate group median values, while the coloured dots represent the effective coherence for each participant in the theta and alpha band between the indicated probe pair.



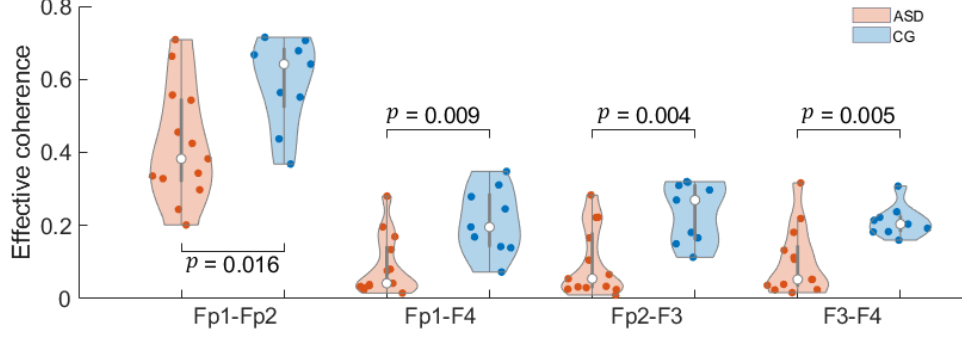


Figure 10: Effective coherence values between the measured EEG signal locations for the fifth sequential segment. Wilcoxon rank-sum test was used to assess coherence differences between groups ( $N = 13$  ASD,  $N = 9$  CG). Orange violins represent the ASD group, while blue indicates CG. The white circles illustrate group median values, while the coloured dots represent the effective coherence for each participant in the theta and alpha band between the indicated probe pair.

### 9.3 Dynamical Bayesian inference

As with the WPC, we also illustrate the median values of the coupling time between probes. First we consider the control group (Tab. 15) and then the ASD group (Tab. 16).

Table 15: Median coupling duration across retests for frontal networks evaluated across the medium frequency band (3.5-12 Hz) for the control group. The numbered sections 1-5 were found chronologically, while the video segment reflects data intervals selected for their relative lack of movement artefacts. The final column indicates the Friedman test  $p$ -values, none of which were significant

From/To	Coupling duration (%)						Friedman test $p$ -value
	1	2	3	4	5	Video	
<b>Fp1 <math>\rightarrow</math> Fp2</b>	98.2	98.2	98.2	98.2	96.5	98.2	0.782
<b>Fp1 <math>\leftarrow</math> Fp2</b>	98.2	96.5	98.2	100	96.5	98.2	0.478
<b>Fp1 <math>\rightarrow</math> F4</b>	22.8	33.3	33.3	33.3	31.6	38.6	0.896
<b>Fp1 <math>\leftarrow</math> F4</b>	29.8	28.1	22.8	29.8	22.8	22.8	0.800
<b>F3 <math>\rightarrow</math> F4</b>	24.6	24.6	19.3	21.1	24.6	14.0	0.360
<b>F3 <math>\leftarrow</math> F4</b>	12.3	22.8	24.6	21.1	22.8	26.3	0.999
<b>F3 <math>\rightarrow</math> Fp2</b>	22.8	29.8	14.0	26.3	28.1	15.8	0.793
<b>F3 <math>\leftarrow</math> Fp2</b>	29.9	43.9	33.3	35.1	35.1	47.4	0.732

At no point did the  $p$ -value from the Friedman test fall below the threshold of 0.05, ensuring that, subject-wise, these measures were consistent across the sequential measurements.

The average time coupled between frontal probes in the ASD group was consistently reduced in each sequential segment. As such, the rank-sum test was employed to assess if the difference was statistically significant across the couplings investigated. Figs. 11 - 15 give this  $p$ -value for each segment. A table containing all  $p$ -values is given in the main text. The violin plots also demonstrate the distributions of the data.

Table 16: Median coupling duration across retests for frontal networks evaluated across the medium frequency band (3.5-12 Hz) for the ASD group. The numbered sections 1-5 were found chronologically, while the video segment reflects data intervals selected for their relative lack of movement artefacts. The final column indicates the Friedman test  $p$ -values, none of which were significant

From/To	Coupling duration (%)						Friedman test $p$ -value
	1	2	3	4	5	Video	
<b>Fp1 <math>\rightarrow</math> Fp2</b>	57.9	50.9	61.4	70.2	59.6	54.4	0.332
<b>Fp1 <math>\leftarrow</math> Fp2</b>	71.9	70.2	63.2	66.7	61.4	66.7	0.612
<b>Fp1 <math>\rightarrow</math> F4</b>	8.77	5.26	12.3	8.77	5.26	7.02	0.622
<b>Fp1 <math>\leftarrow</math> F4</b>	12.3	7.02	8.77	7.02	8.77	10.5	0.811
<b>F3 <math>\rightarrow</math> F4</b>	12.3	8.77	14.0	12.3	10.5	12.3	0.835
<b>F3 <math>\leftarrow</math> F4</b>	7.02	8.77	12.3	15.8	12.3	8.77	0.834
<b>F3 <math>\rightarrow</math> Fp2</b>	14.0	10.5	8.77	12.3	12.3	10.5	0.795
<b>F3 <math>\leftarrow</math> Fp2</b>	14.0	8.77	8.77	8.77	8.77	10.5	0.520

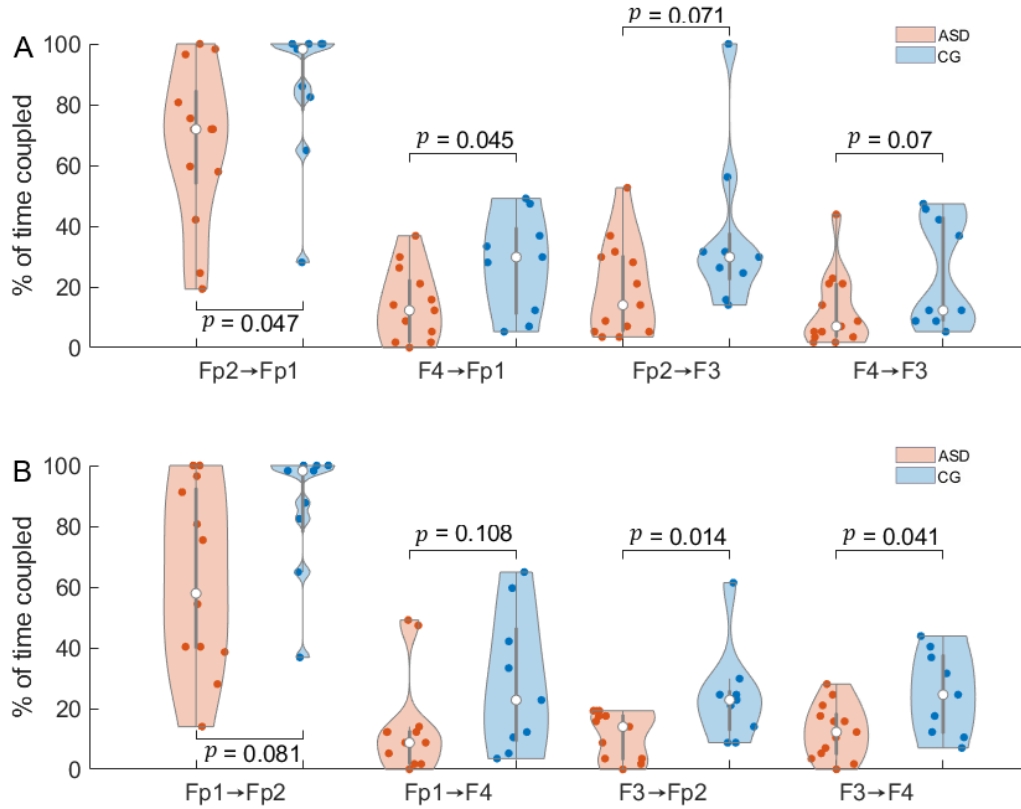


Figure 11: Percentage time coupled between EEG probes in the first sequential segment. Wilcoxon rank-sum test was used to assess coupling time differences between groups ( $N = 13$  ASD,  $N = 9$  CG). A) Signals from the left to the right hemisphere. B) Signals from the right to the left hemisphere.  $p$ -values indicating differences between the groups are indicated in the figures. Blue violins represent CG while orange indicates ASD. The white circles illustrate group median values, while the coloured dots represent the coupling time for each participant in the theta and alpha band between the indicated probe pair.

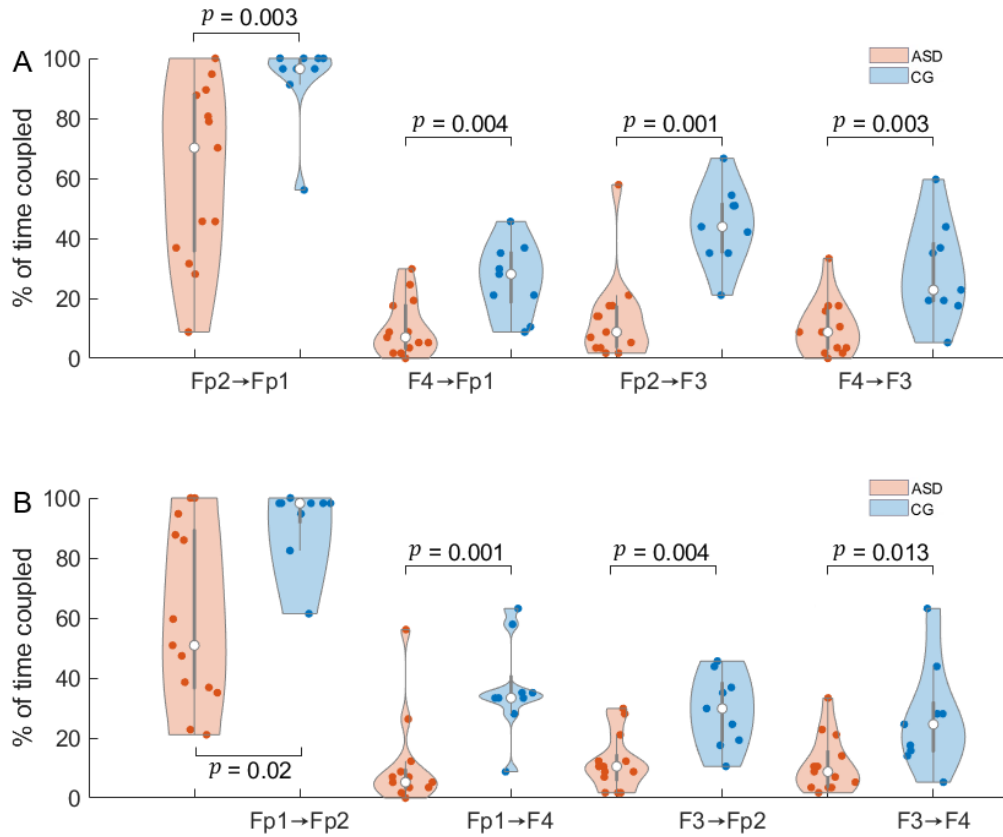


Figure 12: Percentage time coupled between EEG probes in the second sequential segment. Wilcoxon rank-sum test was used to assess coupling time differences between groups ( $N = 13$  ASD,  $N = 9$  CG). A) Signals from the left to the right hemisphere. B) Signals from the right to the left hemisphere.  $p$ -values indicating differences between the groups are indicated in the figures. Blue violins represent CG while orange indicates ASD. The white circles illustrate group median values, while the coloured dots represent the coupling time for each participant in the theta and alpha band between the indicated probe pair.

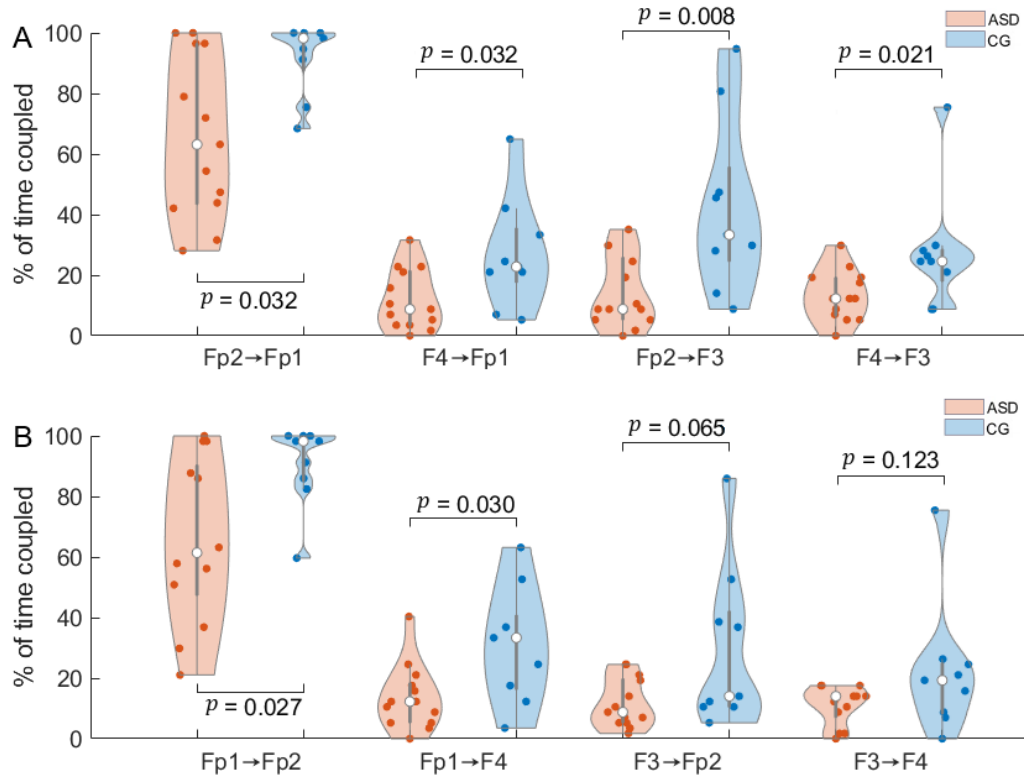


Figure 13: Percentage time coupled between EEG probes in the third sequential segment. Wilcoxon rank-sum test was used to assess coupling time differences between groups ( $N = 13$  ASD,  $N = 9$  CG). A) Signals from the left to the right hemisphere. B) Signals from the right to the left hemisphere.  $p$ -values indicating differences between the groups are indicated in the figures. Blue violins represent CG while orange indicates ASD. The white circles illustrate group median values, while the coloured dots represent the coupling time for each participant in the theta and alpha band between the indicated probe pair.

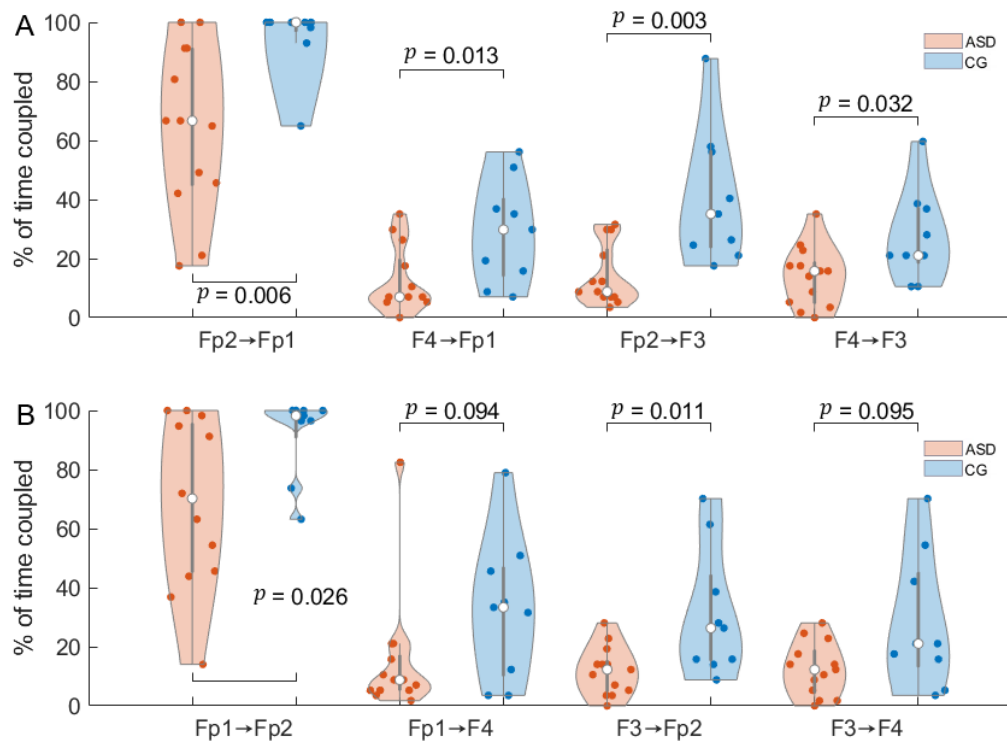


Figure 14: Percentage time coupled between EEG probes in the fourth sequential segment. Wilcoxon rank-sum test was used to assess coupling time differences between groups ( $N = 13$  ASD,  $N = 9$  CG). A) Signals from the left to the right hemisphere. B) Signals from the right to the left hemisphere.  $p$ -values indicating differences between the groups are indicated in the figures. Blue violins represent CG while orange indicates ASD. The white circles illustrate group median values, while the coloured dots represent the coupling time for each participant in the theta and alpha band between the indicated probe pair.

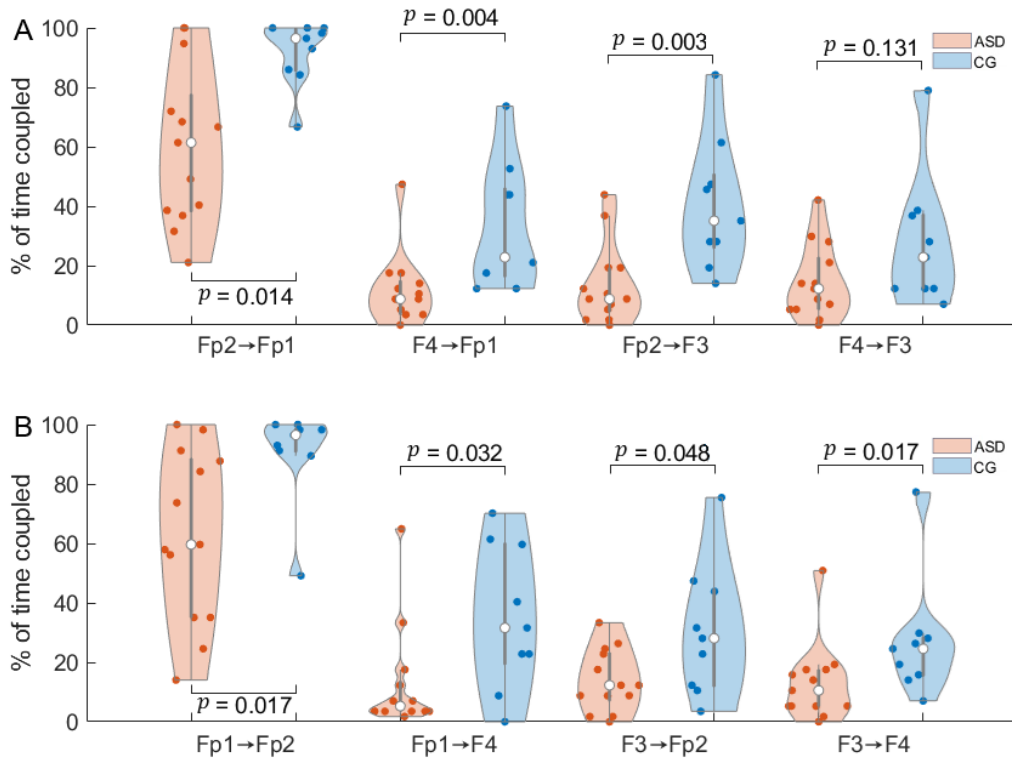


Figure 15: Percentage time coupled between EEG probes in the fifth sequential segment. A Wilcoxon rank-sum test was used to assess coupling time differences between groups ( $N = 13$  ASD,  $N = 9$  CG). A) Signals from the left to the right hemisphere. B) Signals from the right to the left hemisphere.  $p$ -values indicating differences between the groups are indicated in the figures. Blue violins represent CG while orange indicate ASD. The white circles illustrate group median values, while the coloured dots represent the coupling time for each participant in the theta and alpha band between the indicated probe pair.



## 10 Healthy Brain Network

Additional analysis performed on the Healthy Brain Network (HBN) dataset is provided here, including regression and further comparisons across narrow age ranges. Details of the measurements, including inclusion criteria are also outlined. The statistical breakdown of age, IQ and handedness in the ASD and control groups are given in Tab. 2 of the main text.

### 10.1 Inclusion criteria

As the data were derived from an external source, a number of checks were necessary prior to analysis to ensure they were of sufficient quality. First, the wavelet transforms of each time series recorded, from each probe of interest, were calculated for each individual. This step identified measurement errors that had occurred during data collection. The subsequent corrupted datasets were disregarded.

An example of a clearly nonphysical measurement is illustrated in Fig. 16. The average power was orders of magnitude greater when measurement errors had taken place, and so this was selected as the primary exclusion criterion.

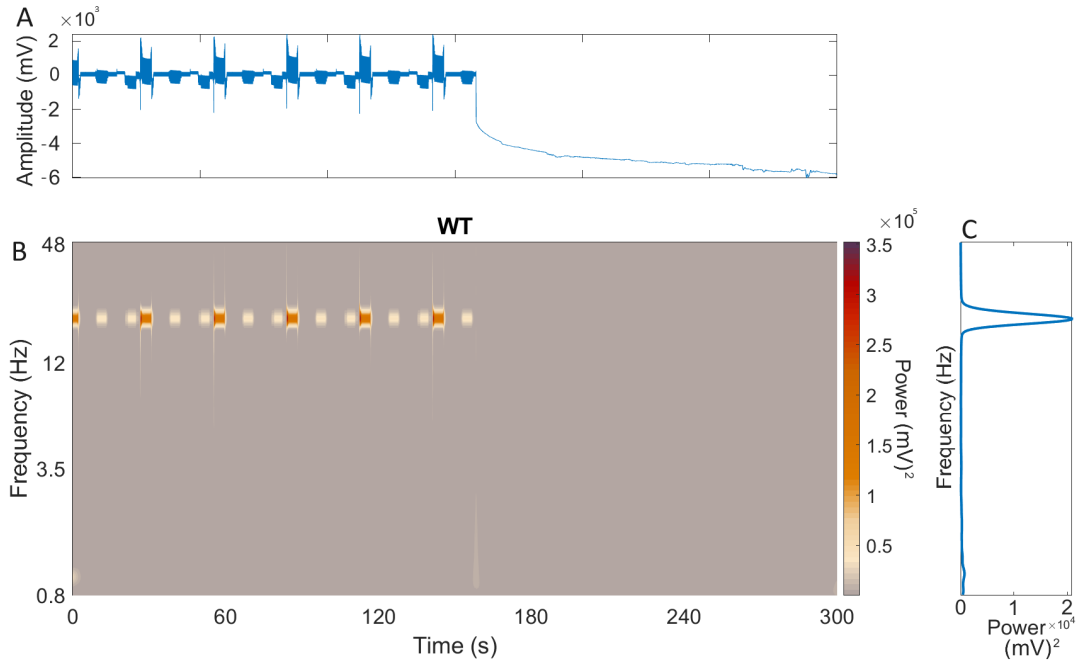


Figure 16: EEG data where measurement errors had taken place. A) Time series of the data recorded over 5 minutes. B) Time frequency representation of an EEG signal from the measured data. C) Time-averaged power.

Finally, the groups were selected to ensure IQ, age and handedness were matched so that there were no significant differences ( $p < 0.05$ ) between groups following the application of a Wilcoxon rank-sum test. A statistical breakdown of the phenotypic data within the HBN groups is given in Tab. 2 of the main text.

## 10.2 Splitting the age groups

The size of the HBN dataset enabled further analysis between two cohorts; one younger (5-9 years) and one older (9-15 years). Here, we compare both the global and local coherence across various age ranges. For comparison, additional analysis of the 5-15 group is also presented.

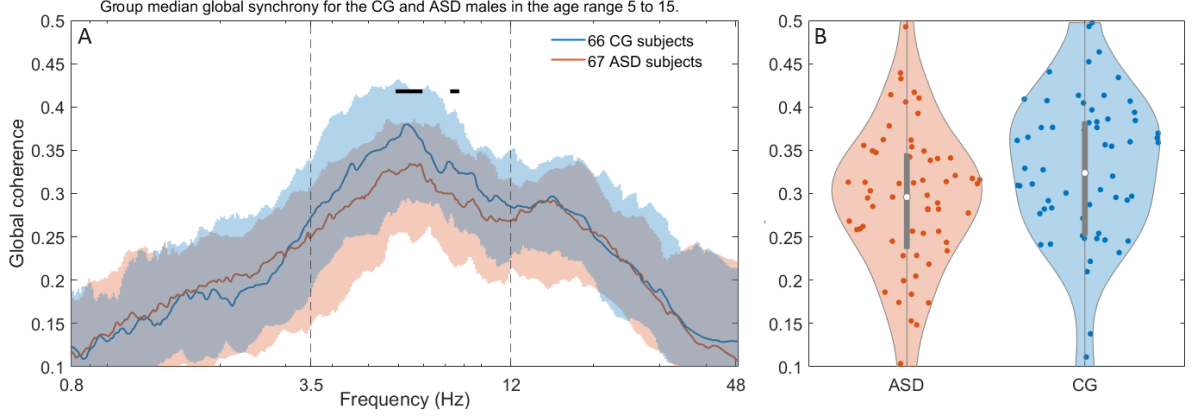


Figure 17: Total global coherence for the 5-15 age range. (A) Median total global coherence for the ASD (orange) and CG (blue) individuals. Shaded areas represent the 25th and 75th percentiles, while the solid lines indicate group medians. The Wilcoxon rank-sum test was applied between the groups at each frequency ( $N = 67$  ASD,  $N = 66$  CG). Black lines plotted above the medians indicate a  $p$ -value less than 0.05. In this case, there were no significant differences at any frequency. (B) Violin plot of the mean global coherence across the medium frequency (3.5-12 Hz) region. The median is given by the white circle while the grey box illustrates the interquartile range. Wilcoxon rank-sum test found no significant difference between groups, with  $p = 0.0641$

Despite the CG group coherence being higher on average in the MF region, and significantly so at certain frequencies as depicted in Fig. 17A, a rank-sum test across the entire MF band failed to exceed the significance threshold ( $p = 0.0641$ ). The global coherence was also not significantly different ( $p = 0.601$ ) for the 5-9-year-old group (Fig. 18).

There is, however, a significantly greater global coherence in the medium frequency region for the 9-15-year-old age group ( $p = 0.029$ , Fig. 19).

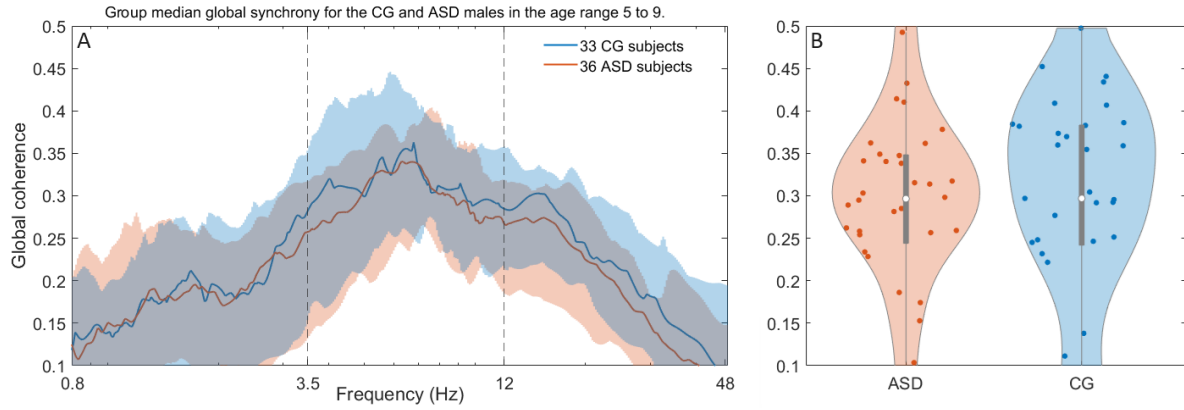


Figure 18: Total global coherence for the 5-9 age range. (A) Median total global coherence for the ASD (orange) and CG (blue) individuals. the shaded areas represent the 25th and 75th percentiles while the lines indicate group medians. groups were assessed at each frequency bin using the Wilcoxon rank-sum test ( $N = 37$  ASD,  $N = 33$  CG). Black lines plotted above the medians indicate a  $p$ -value less than 0.05. (B) Violin plot of the average value across the medium frequency (3.5-12Hz) region. the median is given by the white circle and the box illustrates the interquartile range. A Wilcoxon rank-sum test found no significant difference between groups, with  $p = 0.601$

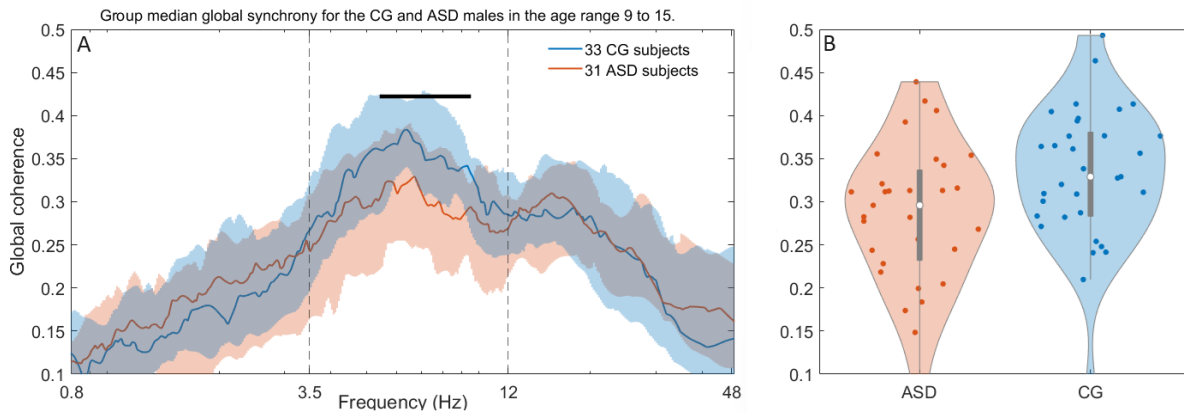


Figure 19: Total global coherence for the 9-15 age range. (A) Median total global coherence for the ASD (orange) and CG (blue) individuals. the shaded areas represent the 25th and 75th percentiles while the lines indicate group medians. groups were assessed at each frequency bin using the Wilcoxon rank-sum test ( $N = 31$  ASD,  $N = 33$  CG). Black lines plotted above the medians indicate a  $p$ -value less than 0.05. (B) Violin plot of the average value across the medium frequency (3.5-12Hz) region. the median is given by the white circle and the box illustrates the interquartile range. A Wilcoxon rank-sum test found a significant difference between the groups, with  $p = 0.029$

Considering the above results there seems to be a dependence upon age regarding the level of global coherence. As this data was collected externally, it is possible that the younger children were less able to tolerate the battery of tests. As participants must remain still and follow experimental instructions, it is possible that the older group were better able to tolerate the procedure. This may be responsible for the differences in the groups. The 9-15 group comparison supports the conclusion of decreased global connectivity across the entire brain for the medium frequency region.

In the 5-9 group there are also very few local connectivity differences (Fig. 20A). In contrast, both the 5-15 (Fig. 20B) and 9-15 (Fig. 20C) age ranges have many significant differences, with more in the latter (18 and 25 percent of possible connections, respectively). This may be further evidence that the data in the 5-9 age group are obfuscated by a reduced ability to tolerate the measurement procedure.

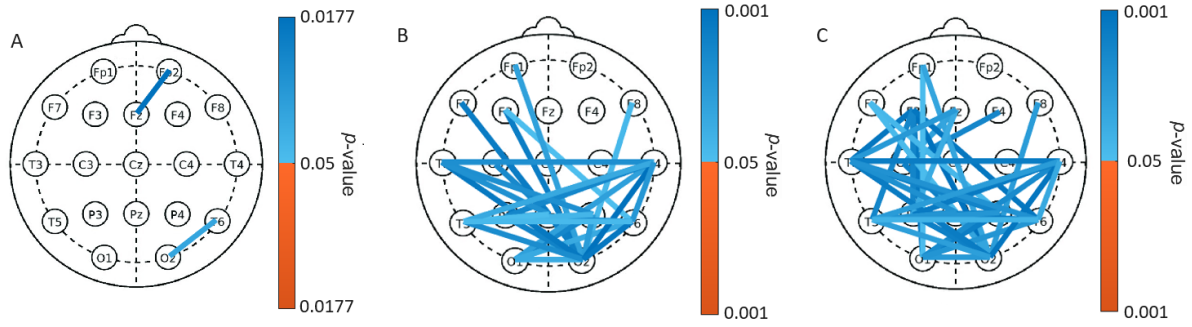


Figure 20: Local coherence differences between ASD and CG groups in various age ranges. A Wilcoxon rank-sum test was performed to compare coherence between groups  $p$ -values are plotted when the threshold of 0.05 is exceeded. Orange indicates ASD > CG while blue indicates CG > ASD. (A) The 5-9 age range ( $N = 37$  ASD,  $N = 33$  CG), only 2 connections were significantly different, meaning 1.3 % of possible probe pairs. (B) The 5-15 age range ( $N = 67$  ASD,  $N = 66$  CG), 28 connections were significant, 18 percent of the possible combinations. (C) The 9-15 age range ( $N = 31$  ASD,  $N = 33$  CG), 38 connections were significant, 25 percent of the possible combinations.

## References

- [1] SJK Barnes, J Bjerkan, PT Clemson, J Newman, and A Stefanovska. Phase coherence — A time-localized approach to studying interactions. *Chaos: An Interdisciplinary Journal of Nonlinear Science*, 34(7), 2024.
- [2] Jacob Cohen. *Statistical Power Analysis for the Behavioral Sciences*. Academic Press, 2013.
- [3] Franz Faul, Edgar Erdfelder, Albert-Georg Lang, and Axel Buchner. G\* power 3: A flexible statistical power analysis program for the social, behavioral, and biomedical sciences. *Behavior Research Methods*, 39(2):175–191, 2007.
- [4] Eibe Frank, Mark A Hall, and Ian H Witten. *The WEKA workbench*. Morgan Kaufmann, 2016.
- [5] Jean-Philippe Lachaux, Eugenio Rodriguez, Michel Le Van Quyen, Antoine Lutz, Jacques Martinerie, and Francisco J Varela. Studying single-trials of phase synchronous activity in the brain. *International Journal of Bifurcation and Chaos*, 10(10):2429–2439, 2000.
- [6] Jean-Philippe Lachaux, Antoine Lutz, David Rudrauf, Diego Cosmelli, Michel Le Van Quyen, Jacques Martinerie, and Francisco Varela. Estimating the time-course of coherence between single-trial brain signals: an introduction to wavelet coherence. *Neurophysiologie Clinique/Clinical Neurophysiology*, 32(3):157–174, 2002.
- [7] Christopher Torrence and Peter J Webster. Interdecadal changes in the enso–monsoon system. *Journal of climate*, 12(8):2679–2690, 1999.



1

## 2 **Supporting Information for**

3 **Methamphetamine alters the circadian oscillator and its couplings on multiple scales in**  
4 ***Per1/2/3* knockout mice**

5 **Samuel J.K. Barnes, Mansour Alanazi, Shin Yamazaki and Aneta Stefanovska**

6 **Aneta Stefanovska**

7 **E-mail: [aneta@lancaster.ac.uk](mailto:aneta@lancaster.ac.uk)**

8 **This PDF file includes:**

9 Figs. S1 to S84

10 Tables S1 to S6

## Contents

12	<b>1 Introduction</b>	<b>3</b>
13	<b>2 Actograms</b>	<b>4</b>
14	A Heterozygous PER2::LUC knockin and wild-type littermate 30 day . . . . .	4
15	A.1 Full length IR actogram examples . . . . .	6
16	B <i>Per1/2/3</i> KO DD . . . . .	7
17	C <i>Per1/2/3</i> KO DD MA . . . . .	9
18	D Multiple conditions . . . . .	10
19	E Wild-type 20 day . . . . .	14
20	F Wild-type 21 day . . . . .	16
21	<b>3 Wavelet transforms</b>	<b>18</b>
22	A Heterozygous PER2::LUC knockin and wild-type littermate 30 day . . . . .	18
23	B <i>Per1/2/3</i> KO DD . . . . .	22
24	C <i>Per1/2/3</i> KO DD MA . . . . .	25
25	D Multiple conditions . . . . .	28
26	E Wild-type 20 day . . . . .	32
27	F Wild-type 21 day . . . . .	34
28	<b>4 Ridge extraction</b>	<b>37</b>
29	A Heterozygous PER2::LUC knockin and wild-type littermate group, 30 day . . . . .	37
30	B <i>Per1/2/3</i> KO DD . . . . .	37
31	C <i>Per1/2/3</i> KO DD MA . . . . .	38
32	D Wild-type 20 day . . . . .	38
33	E Wild-type 21 day . . . . .	38
34	<b>5 Harmonic analysis</b>	<b>39</b>
35	A Heterozygous PER2::LUC knockin and wild-type littermate group, 30 day . . . . .	39
36	B <i>Per1/2/3</i> KO DD . . . . .	41
37	C <i>Per1/2/3</i> KO DD MA . . . . .	43
38	<b>6 Bispectral analysis</b>	<b>44</b>
39	A Heterozygous PER2::LUC knockin and wild-type littermate 30 day group, 30 day . . . . .	44
40	B <i>Per1/2/3</i> KO DD . . . . .	47
41	C <i>Per1/2/3</i> KO DD MA . . . . .	48
42	<b>7 The model</b>	<b>50</b>
43	A <i>Per1/2/3</i> KO mice . . . . .	50
44	B Wild-type mice . . . . .	50
45	C Recreating Fig.1 . . . . .	52
46	D Recreating Fig.3 . . . . .	53



# 1. Introduction

This document provides the supporting information for ‘Methamphetamine alters the circadian oscillator and its couplings on multiple scales in *Per1/2/3* knockout mice’. Six different cohorts of mice were analysed during the experiments. Details of each group are given in Tab. S1.

Group	Strain	Analysis length	Methamphetamine	Age	Sex
Heterozygous PER2::LUC KI and wild-type littermate	C57BL/6J, <i>N</i> = 7 <i>Per2</i> ::luciferase knockin, <i>N</i> = 1 wild-type litter-mate	30 days	No	1.3-9.5 months	5 male, 3 female
<i>Per1/2/3</i> KO DD	C57BL/6J background with cfos-shGFP transgene	65 days	No	3.5-8.5 months	3 male, 4 female
<i>Per1/2/3</i> KO DD MA	C57BL/6J or C57BL/6J and C57BL/6N mixed	65 days	Yes	4.5-5.5 months	1 male, 4 female
<i>Per1/2/3</i> KO multiple conditions	C57BL/6J or C57BL/6J and C57BL/6N mixed	139 days	Yes - in part	5-8 months	4 male, 4 female
WT 20 day	C57BL/6N	20 days	No	1.25 months	5 male
WT 21 day	C57BL/6J	21 days	No	2 months	6 male

**Table S1. Details pertaining to each group of mice analysed in the present study. WT = wild-type, KO = knockout, KI = knockin MA implies methamphetamine administration and *Per1/2/3* KO refers to the knocked out *Period* genes.**

Thorough descriptions of each experiment are given in the materials and methods section of the main manuscript. With the exception of the ‘multiple conditions’ group, all results presented were measured in constant darkness. Coupling analyses were not performed upon the multiple conditions group or the 20, 21 day wild-type groups due to insufficient duration of recording. In section 2, actograms representing wheel running activity in all groups are illustrated. Time/frequency representations of the same data are illustrated in section 3, revealing multiscale and time-localised behaviour. Section 4 contains the time-averaged frequencies of each of the modes observed in all measured mice, detected via ridge extraction. In section 5, the results of harmonic analysis are presented for the 30 day heterozygous PER2::LUC knockin and wild-type littermate control group and 65 day *Per1/2/3* KO mice. Section 6 provides the results of bispectral analyses. Finally, the procedures and parameters used to generate the phenomenological model used in this paper are given in section 7.

## 2. Actograms

Actograms of all mice analysed in this study are presented in this section.

**A. Heterozygous PER2::LUC knockin and wild-type littermate 30 day.** Here we present the actograms for the heterozygous PER2::LUC knockin and wild-type littermate mice in constant darkness for 30 days.

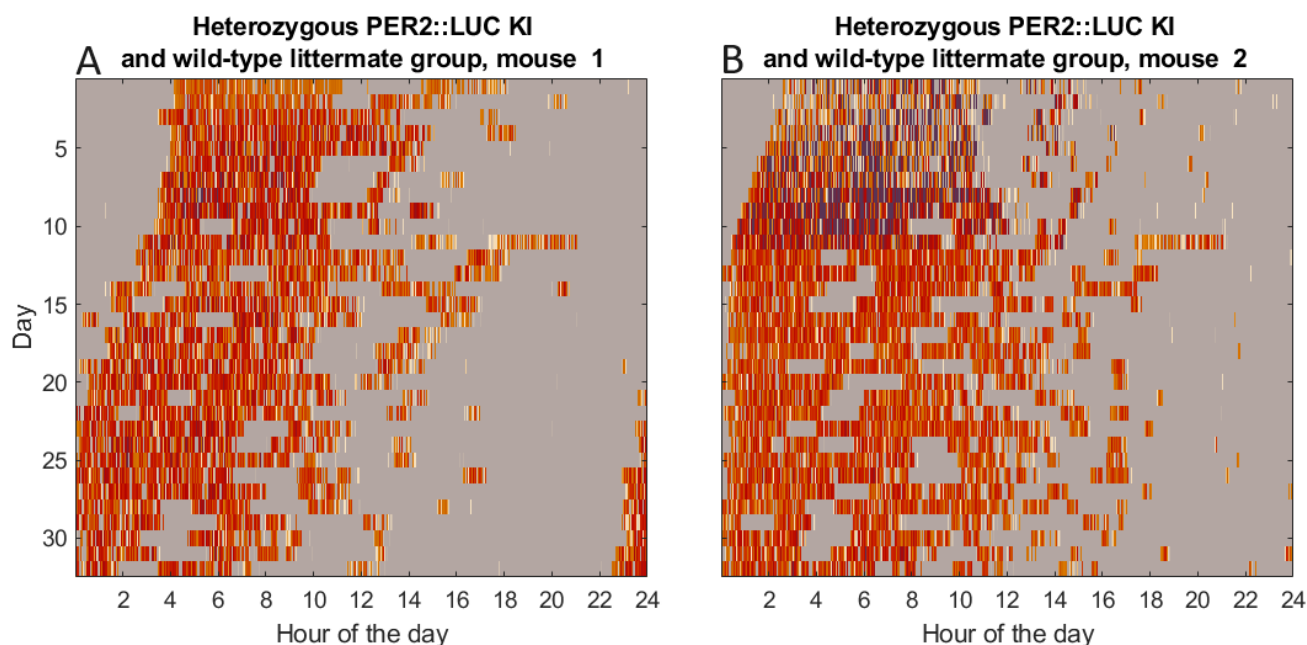


**Fig. S1.** Actograms for mouse 1 (A) and mouse 2 (B) in the heterozygous PER2::LUC knockin and wild-type littermate 30 day group.

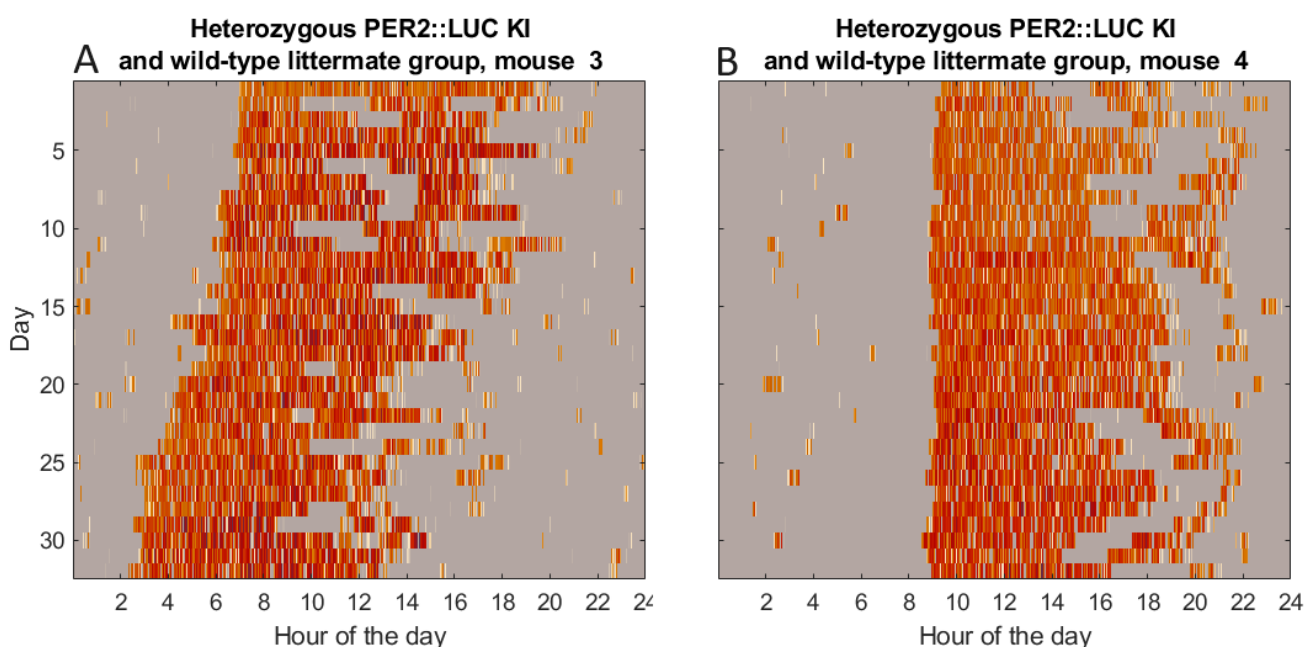


**Fig. S2.** Actograms for mouse 3 (A) and mouse 4 (the wild-type littermate (B) in the heterozygous PER2::LUC knockin and wild-type littermate 30 day group.

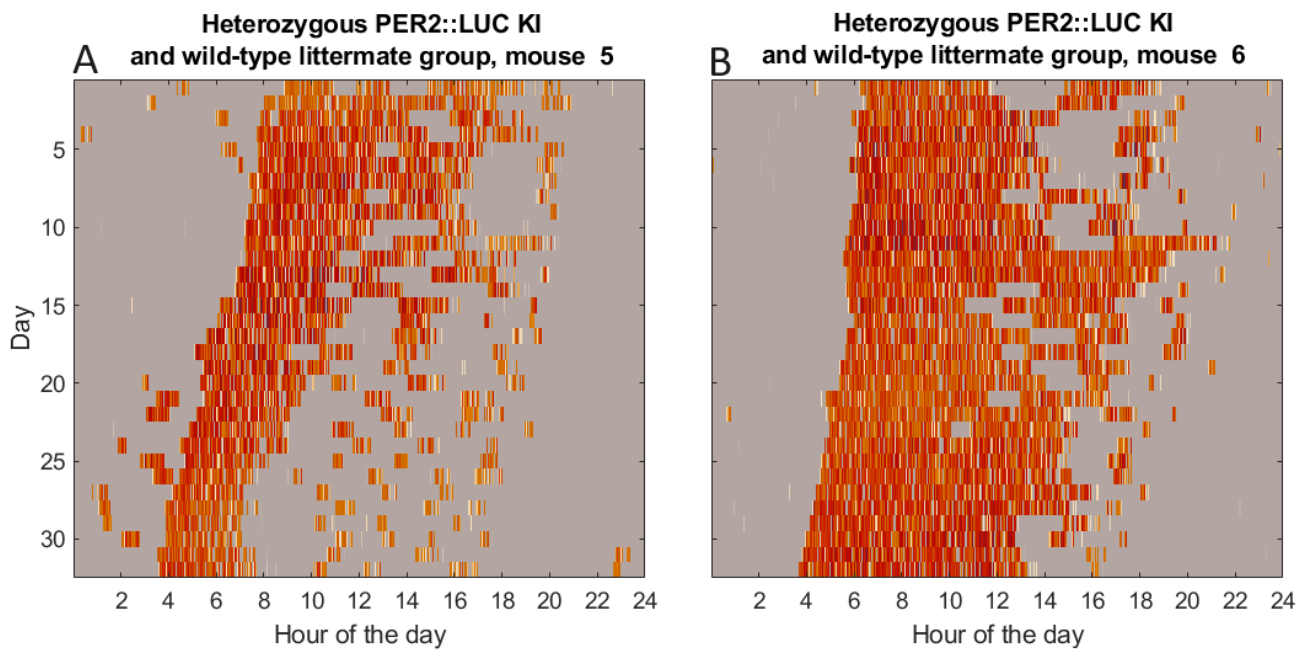


**Fig. S3.** Actograms for mouse 5 (A) and mouse 6 (B) in the heterozygous PER2::LUC knockin and wild-type littermate 30 day group.

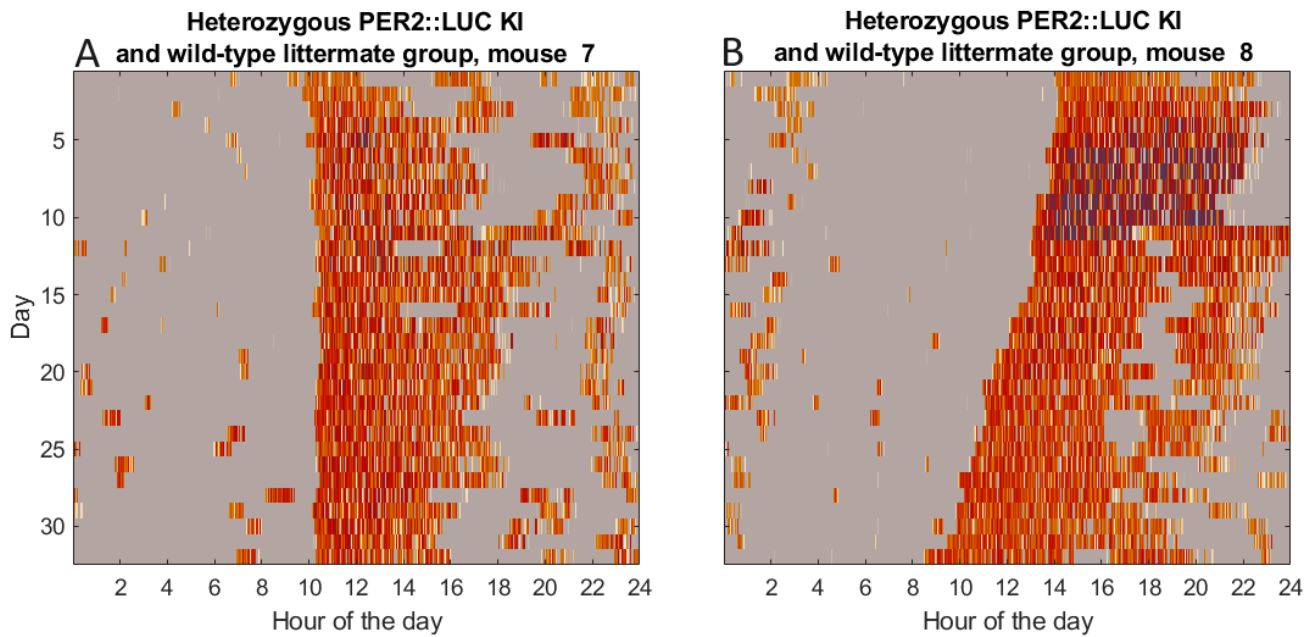


**Fig. S4.** Actograms for mouse 7 (A) and mouse 8 (B) in the heterozygous PER2::LUC knockin and wild-type littermate 30 day group.

64 **A.1. Full length IR actogram examples.** The endogenous circadian rhythm reported for the WT 30 day mice ( $23.9 \pm 0.1$  hrs) is  
 65 slightly longer than those typically reported in laboratory mice. This is likely due to the extend amount of time over which  
 66 the mice were exposed to constant darkness. As indicated in the materials and methods section, this group was in constant  
 67 darkness for 65 days before the wheel was released for a final 30 day recording. Infrared motion detectors recorded activity  
 68 throughout, as the actograms of Fig. S5 demonstrate.

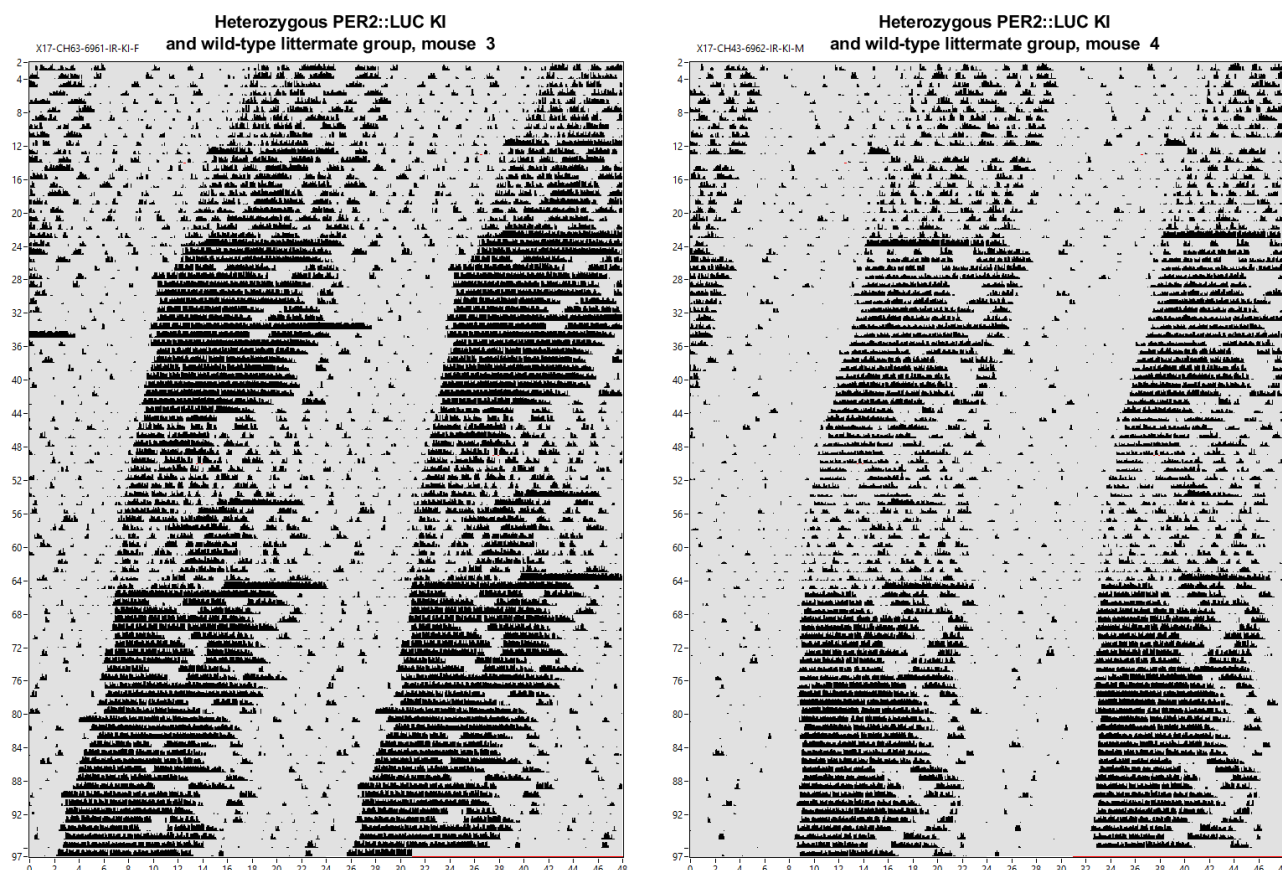
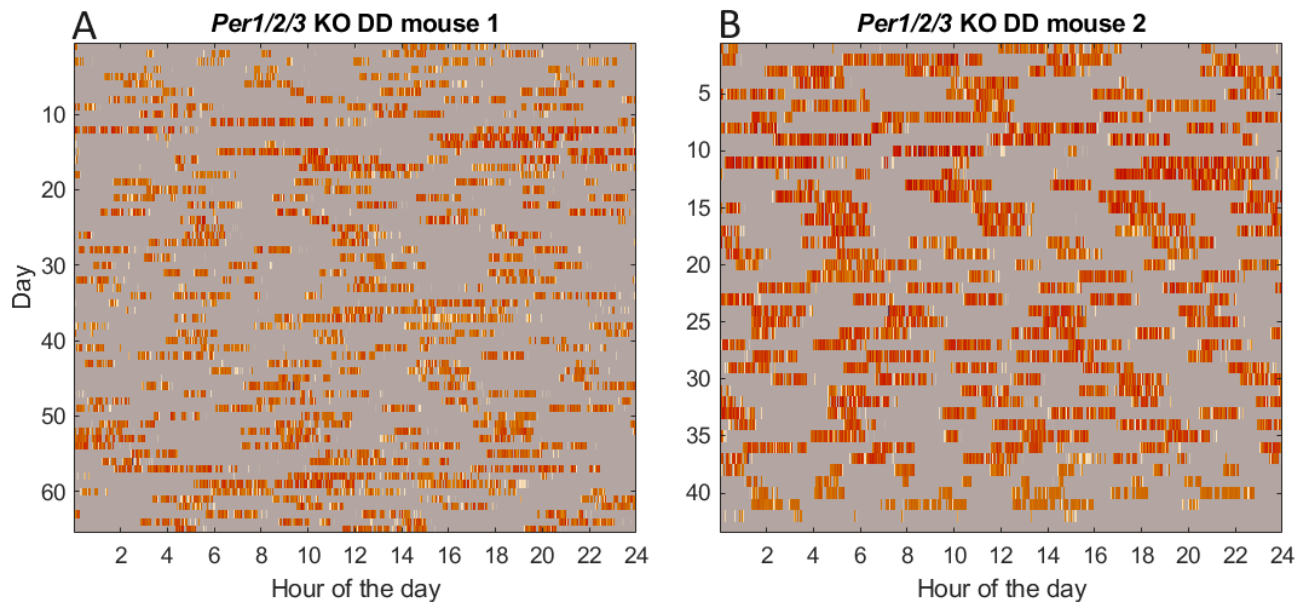


Fig. S5. Actograms from infrared recordings for mouse 3 (A) and mouse 4 (B) in the heterozygous PER2::LUC knockin and wild-type littermate 30 day group.

69 The initial free-running period of PER2::LUC heterozygous knock-in mice was approximately 23.7 hours, which is consistent  
 70 with typical values observed in C57BL/6 mice. However, in constant darkness, the circadian period of some mice lengthened to  
 71 around 24 hours during the final 30 days. For instance, mouse 3, as shown in Fig. S5, exhibited a modest elongation from an  
 72 initial period of approximately 23.7 hours to  $23.8 \pm 0.1$  hours. Other mice in this group, such as mouse 4 (Fig. S5), displayed a  
 73 more considerable elongation in circadian period to  $24.0 \pm 0.1$  hours.

74 **B. *Per1/2/3* KO DD.** Here we present the actograms for the *Per1/2/3* KO DD mice in constant darkness for 65 days.



**Fig. S6.** Actograms for mouse 1 (A) and mouse 2 (B) in the *Per1/2/3* KO DD group.

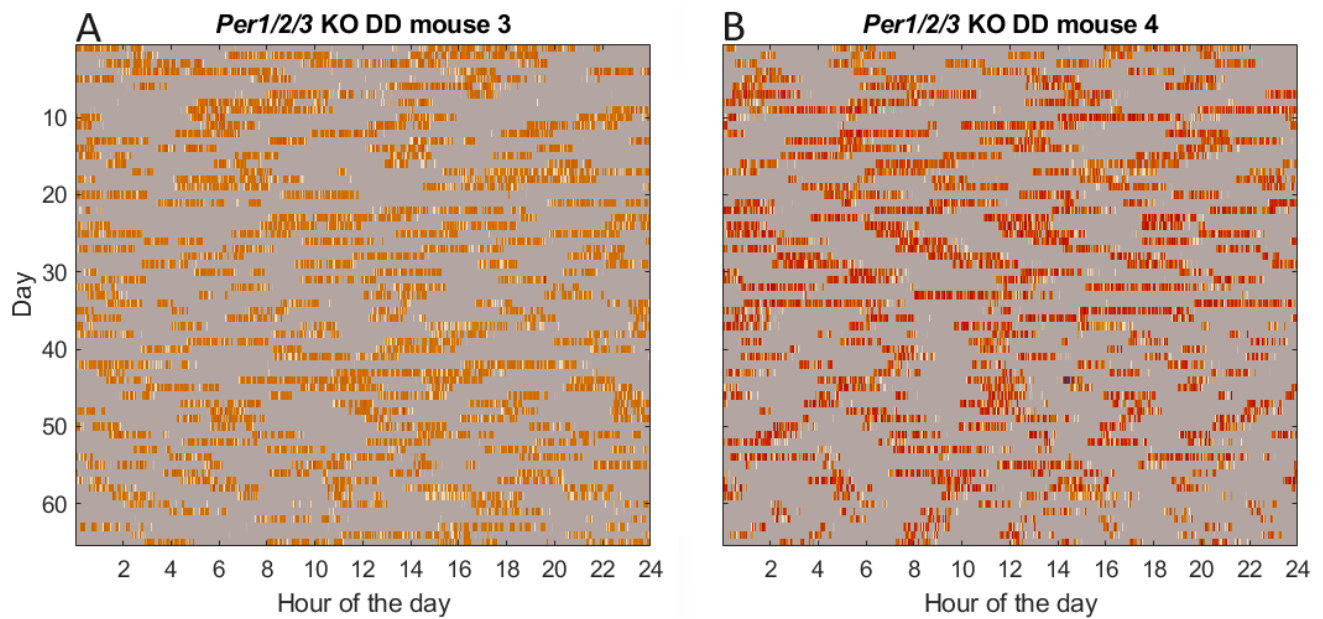


**Fig. S7.** Actograms for mouse 3 (A) and mouse 4 (B) in the *Per1/2/3* KO DD group.

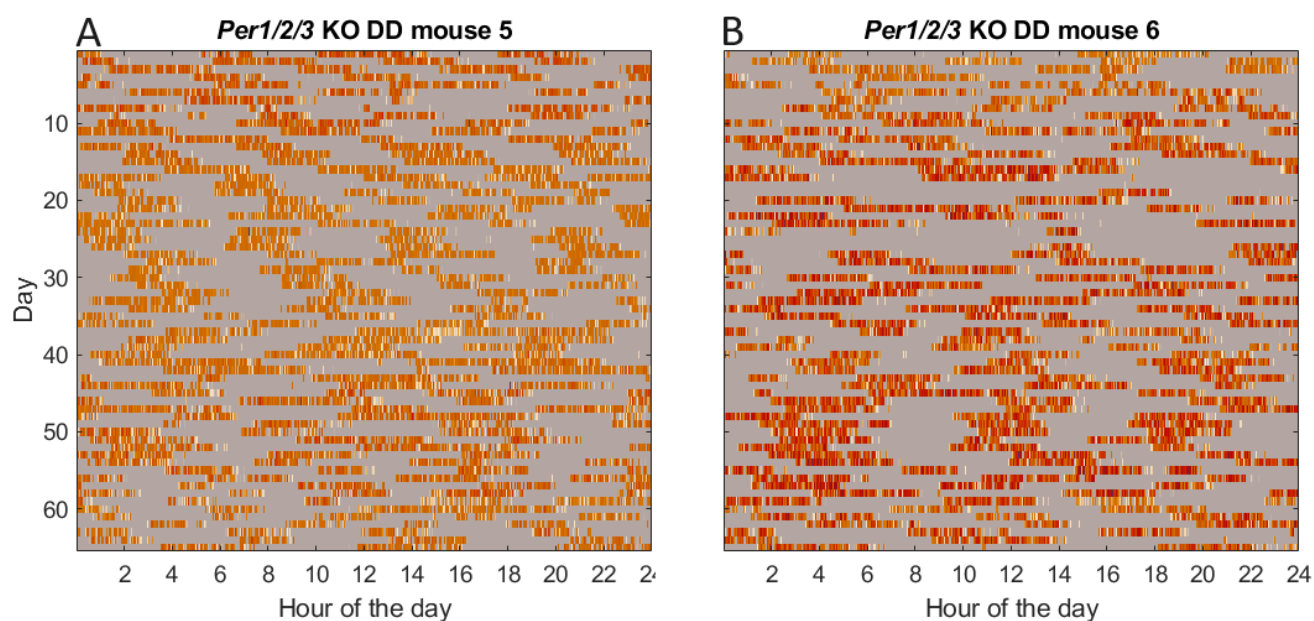


**Fig. S8.** Actograms for mouse 5 (A) and mouse 6 (B) in the *Per1/2/3* KO DD group

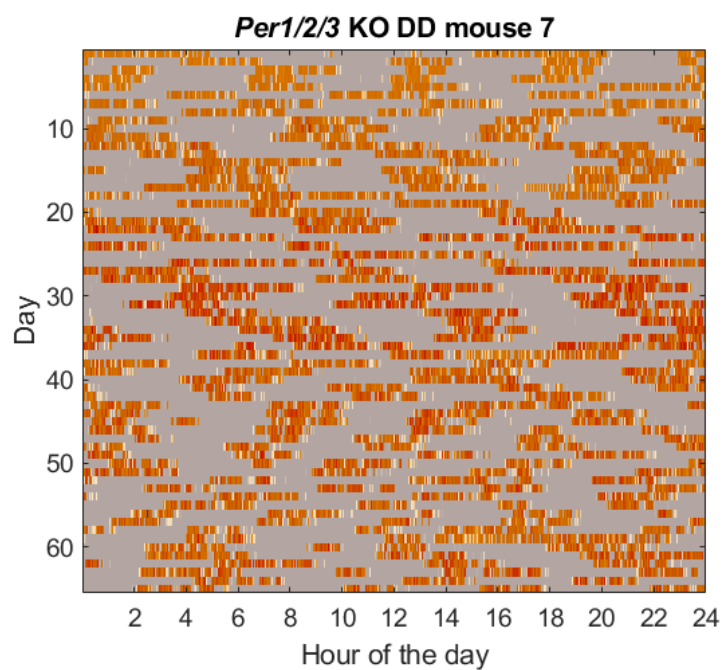


**Fig. S9.** Actogram for mouse 7 in the *Per1/2/3* KO DD group



75 **C. *Per1/2/3* KO DD MA.** Here we present the wavelet transforms for the *Per1/2/3* KO DD MA mice in constant darkness for 65  
76 days.

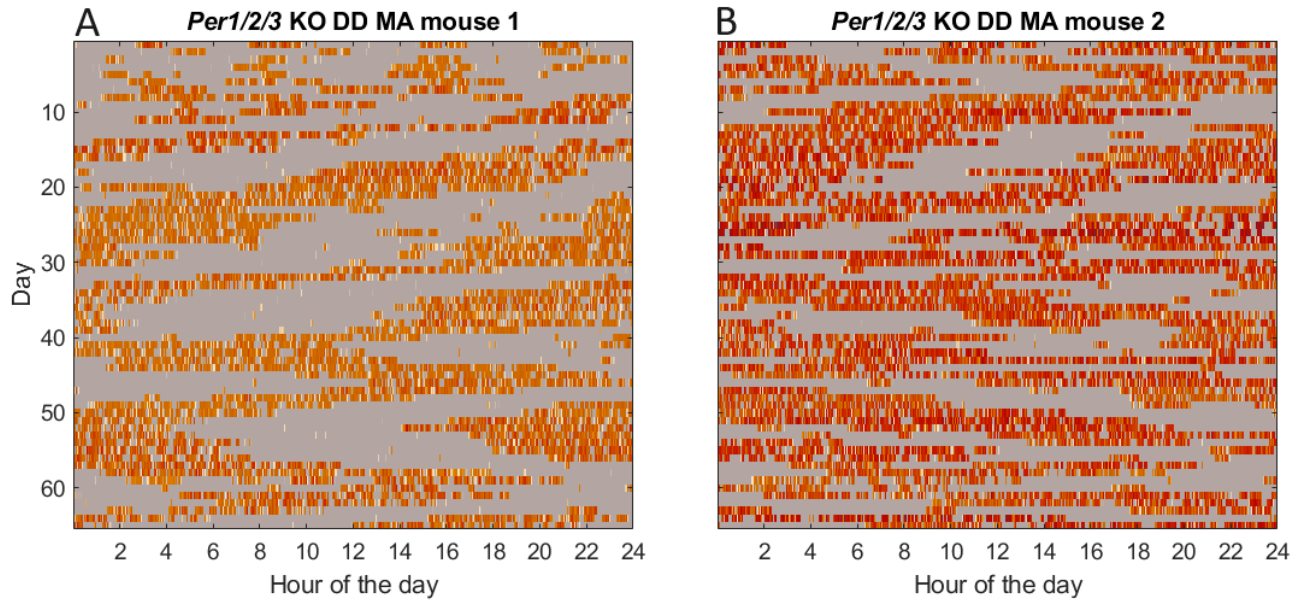


**Fig. S10.** Actograms for mouse 1 (A) and mouse 2 (B) in the *Per1/2/3* KO DD MA group.

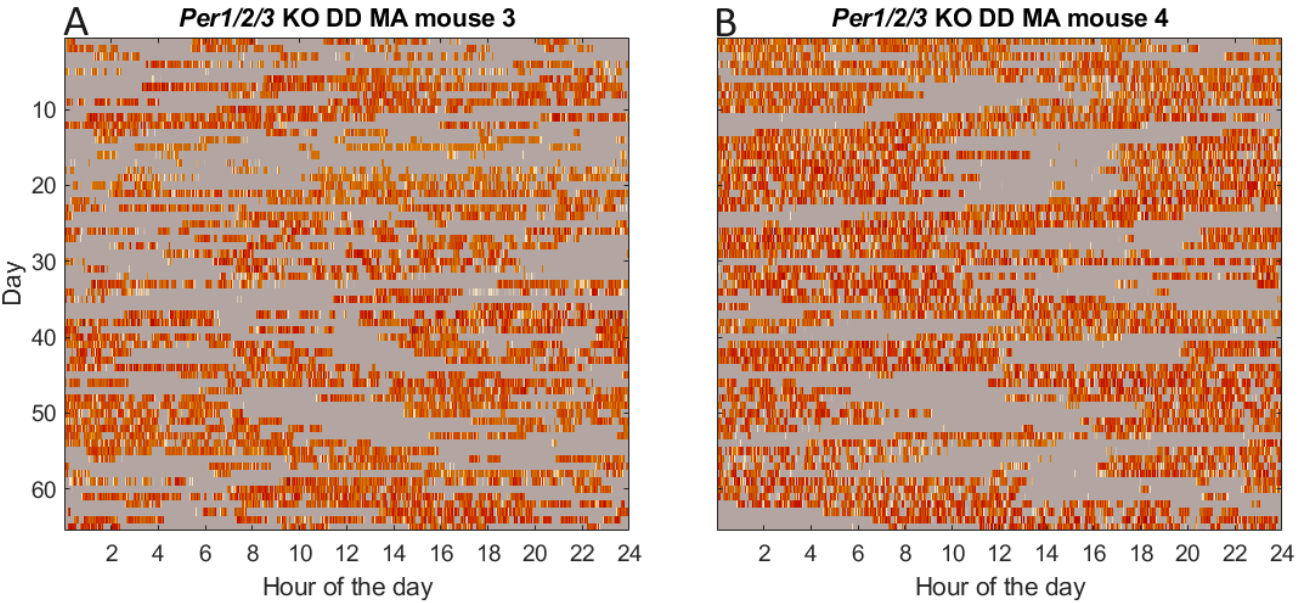


**Fig. S11.** Actograms for mouse 3 (A) and mouse 4 (B) in the *Per1/2/3* KO DD MA group.

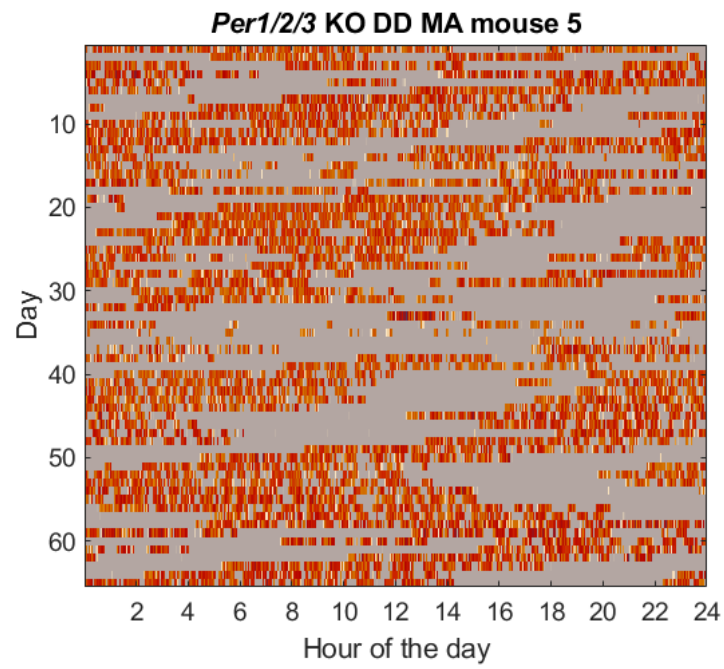


**Fig. S12.** Actogram for mouse 5 in the *Per1/2/3* KO DD MA group.

<sup>77</sup> **D. Multiple conditions.** The actograms from *Per1/2/3* KO mice in multiple conditions are presented here.

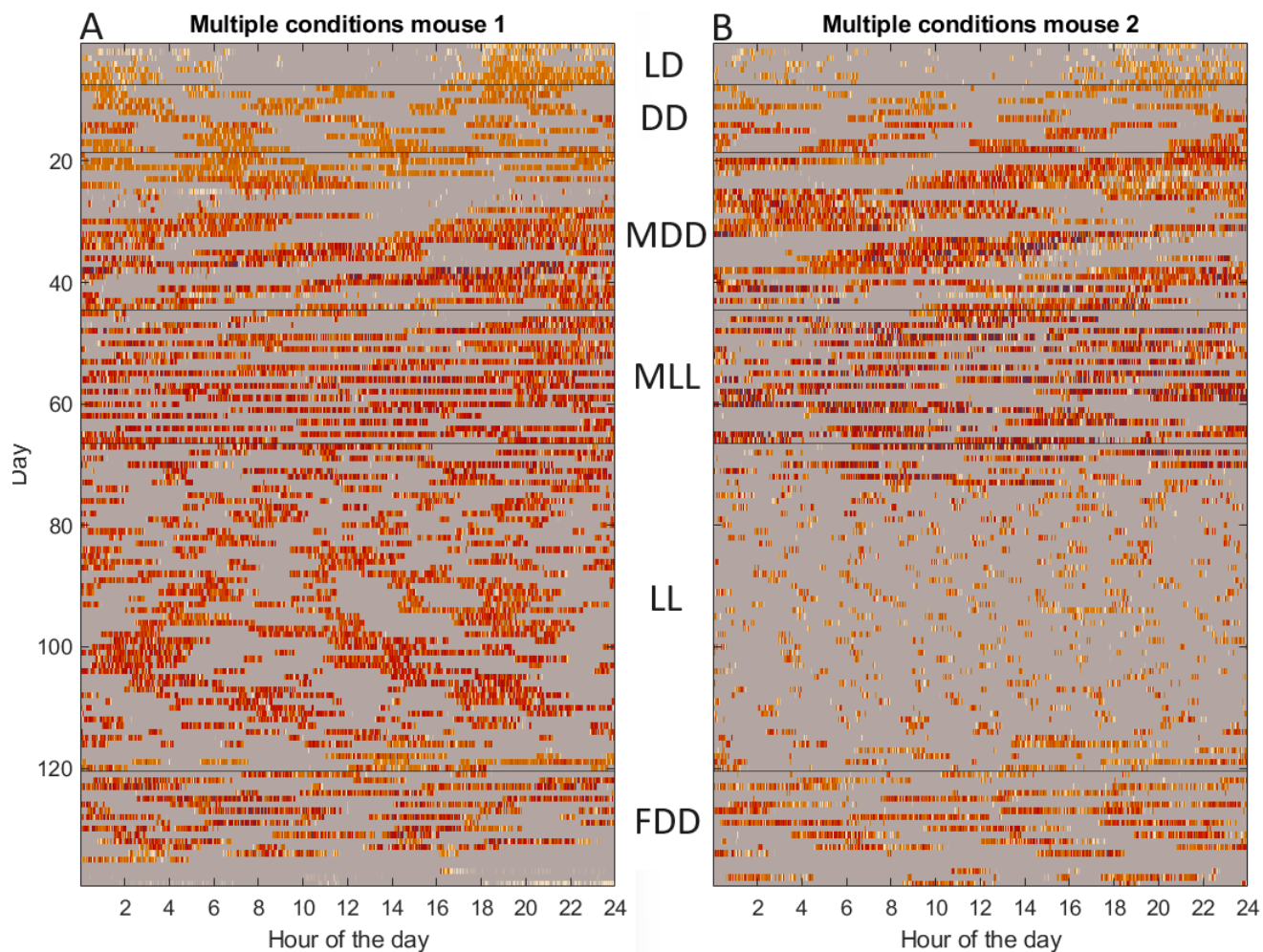


**Fig. S13.** Actograms for mouse 1 (A) and mouse 2 (B) in the multiple conditions group. The separate modalities are denoted as follows: LD = light/dark cycles of period 24 hours, DD = constant darkness, MDD = constant darkness with methamphetamine administration, MLL = constant light with methamphetamine administration, LL = constant light, FDD = final condition of constant darkness.

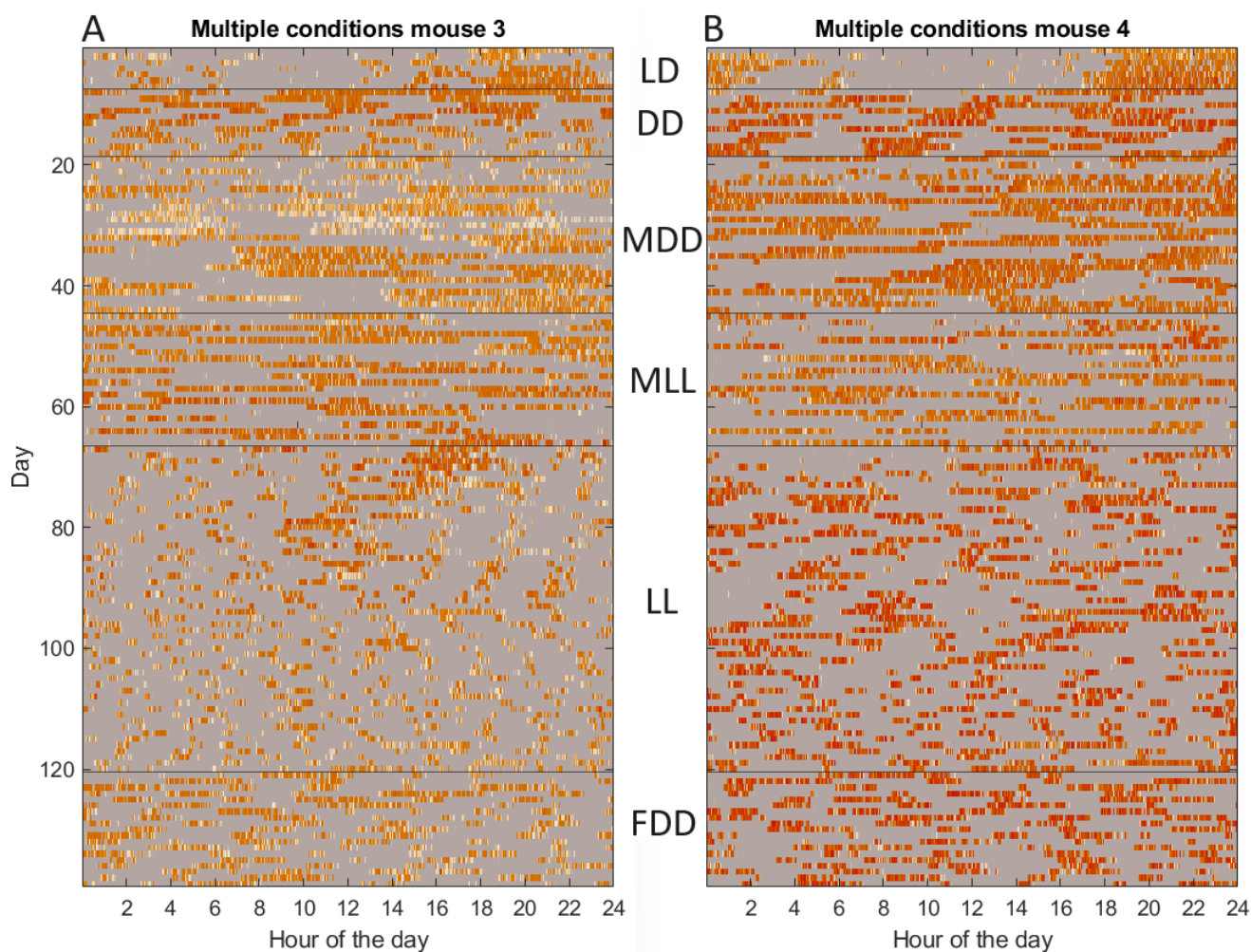


**Fig. S14.** Actograms for mouse 3 (A) and mouse 4 (B) in the multiple conditions group exposed to methamphetamine. The separate modalities are denoted as follows: LD = light/dark cycles of period 24 hours, DD = constant darkness, MDD = constant darkness with methamphetamine administration, MLL = constant light with methamphetamine administration, LL = constant light, FDD = final condition of constant darkness.

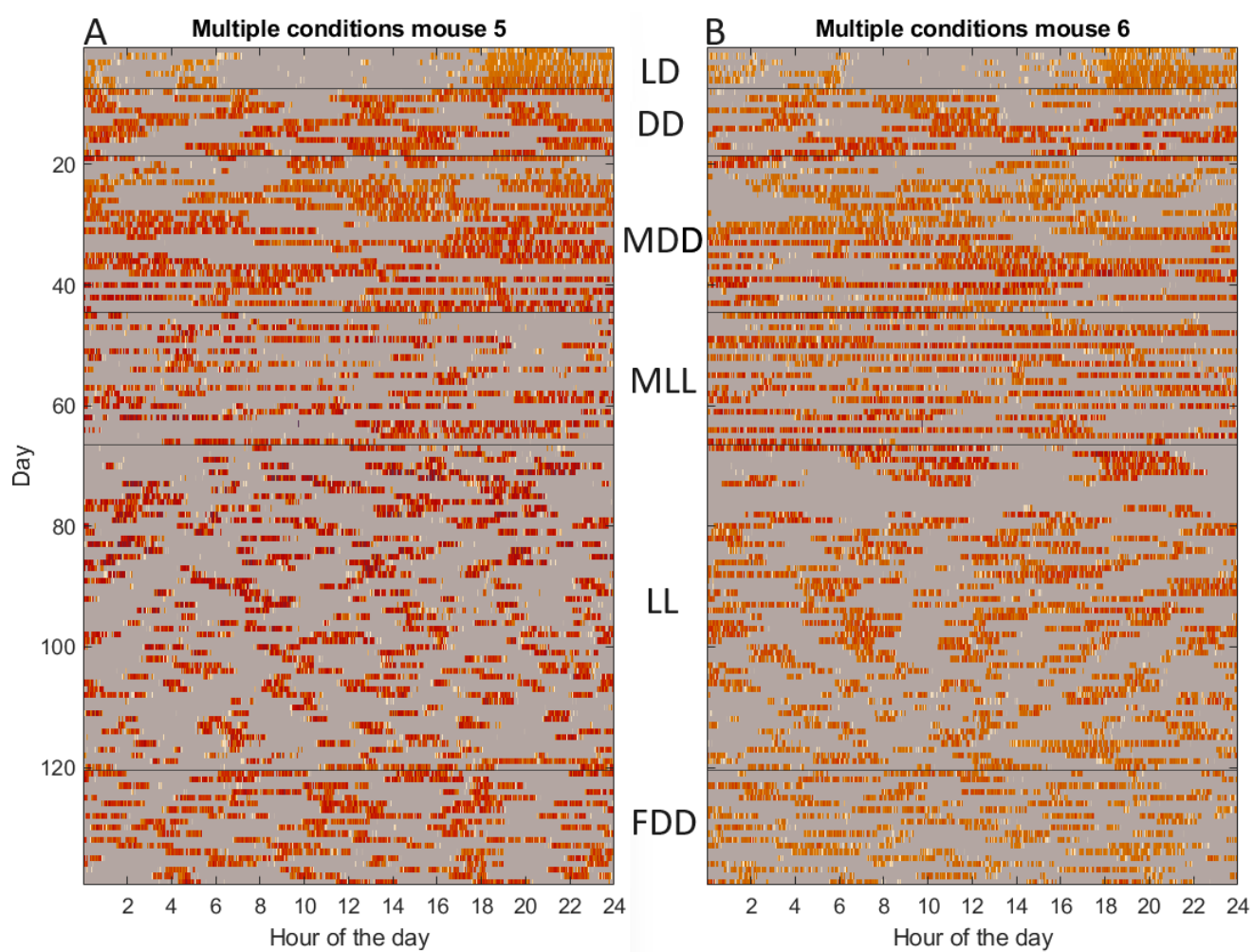


**Fig. S15.** Actograms for mouse 5 (A) and mouse 6 (B) in the multiple conditions group. The separate modalities are denoted as follows: LD = light/dark cycles of period 24 hours, DD = constant darkness, MDD = constant darkness with methamphetamine administration, MLL = constant light with methamphetamine administration, LL = constant light, FDD = final condition of constant darkness.

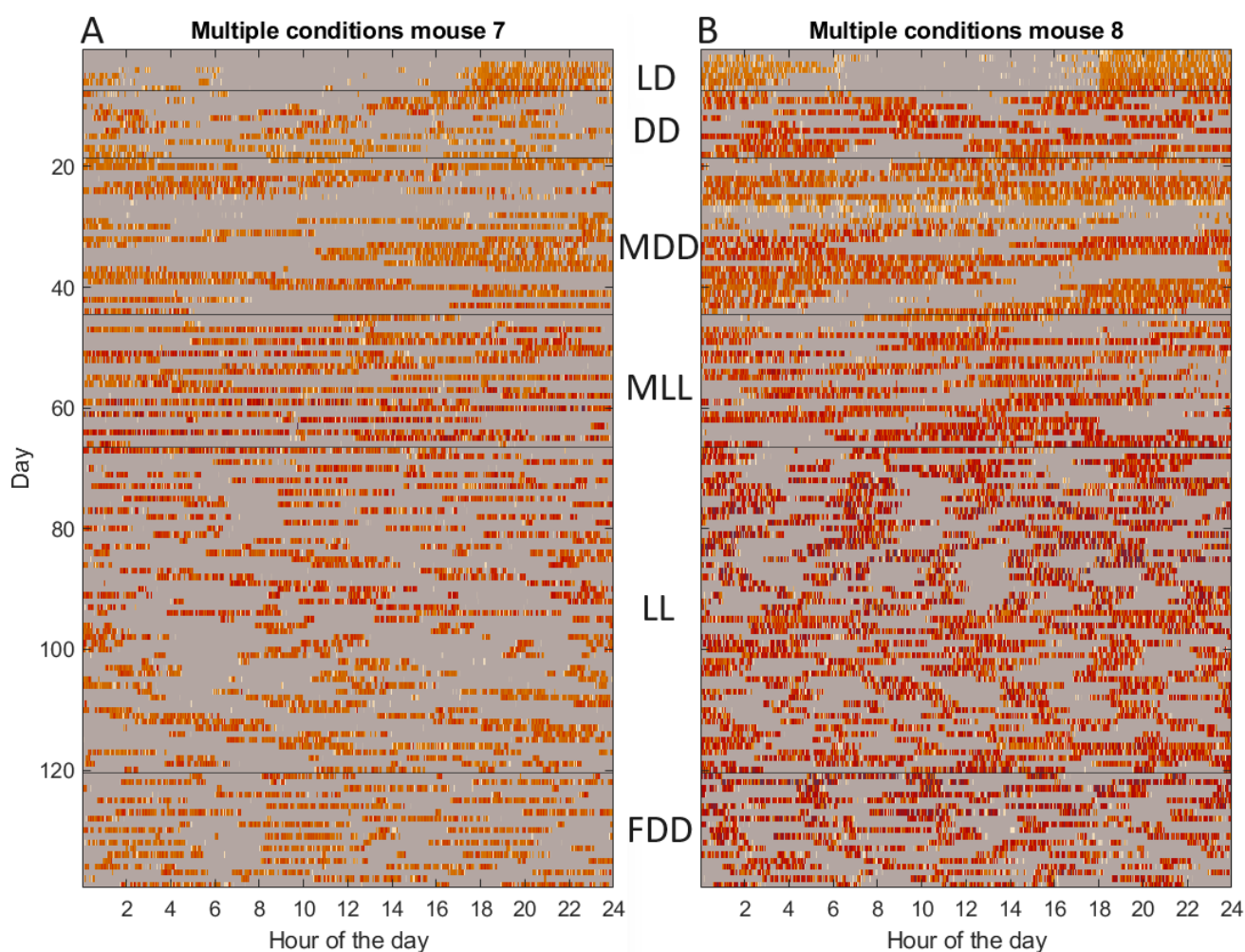


**Fig. S16.** Actograms for mouse 7 (A) and mouse (8) in the multiple conditions group. The separate modalities are denoted as follows: LD = light/dark cycles of period 24 hours, DD = constant darkness, MDD = constant darkness with methamphetamine administration, MLL = constant light with methamphetamine administration, LL = constant light, FDD = final condition of constant darkness.

78 **E. Wild-type 20 day.** Here we present the actograms for the wild-type mice in constant darkness for 20 days.

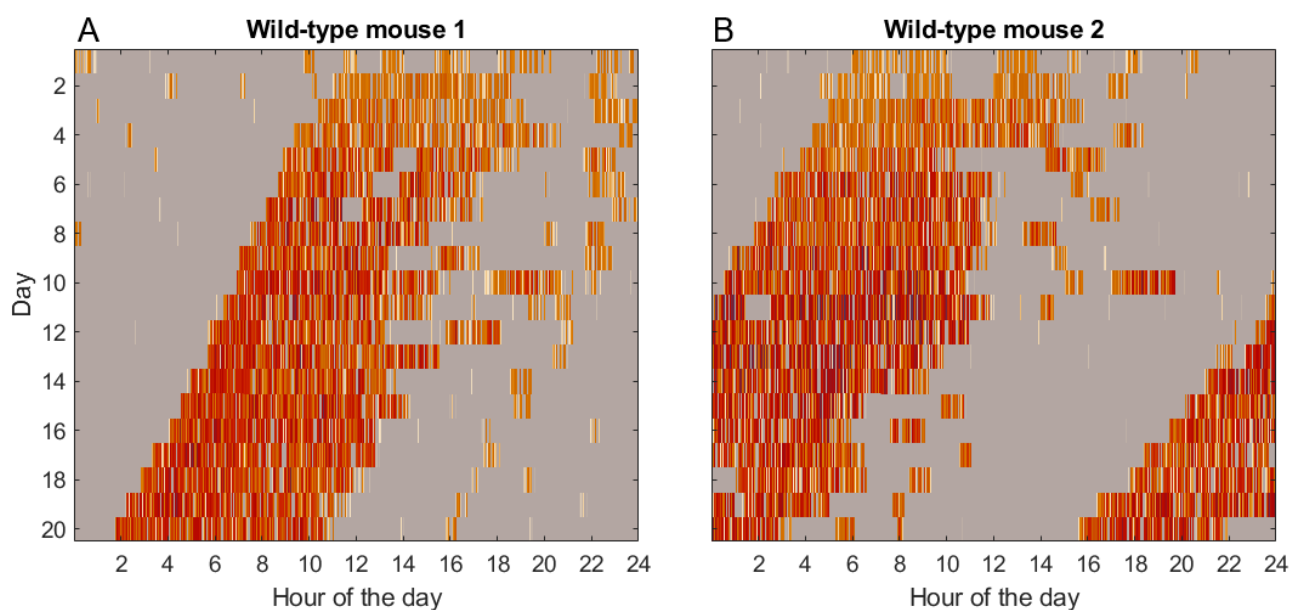


**Fig. S17.** Actograms for mouse 1 (A) and mouse 2 (B) in the wild-type 20 day group.

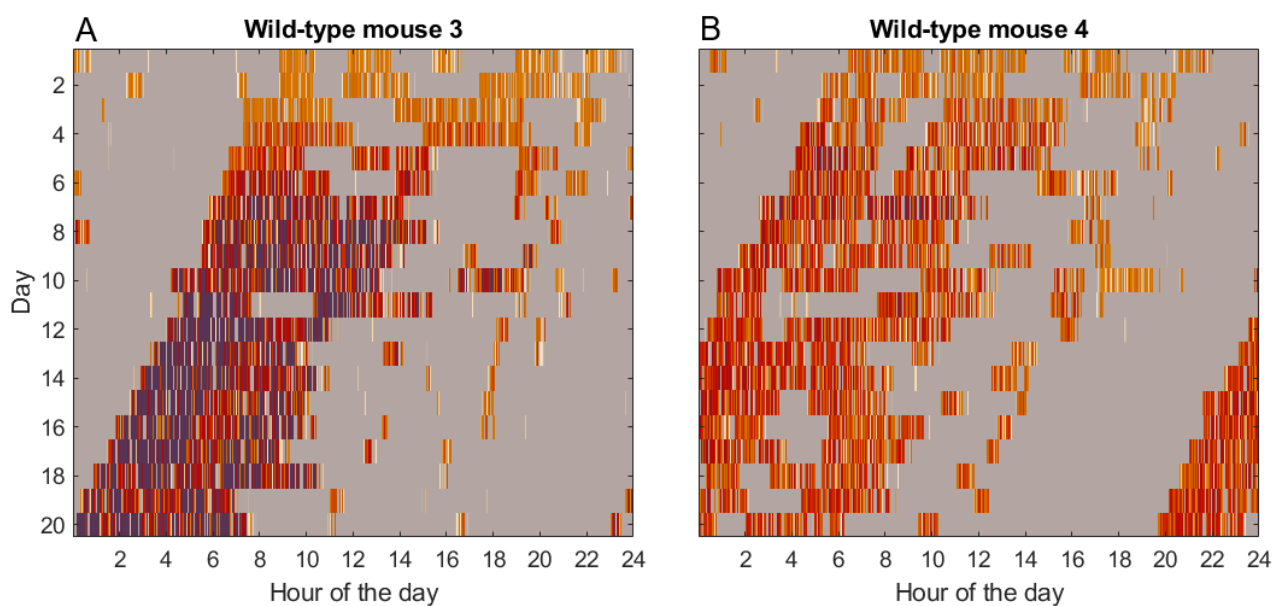


**Fig. S18.** Actograms for mouse 3 (A) and mouse 4 (B) in the wild-type 20 day group.



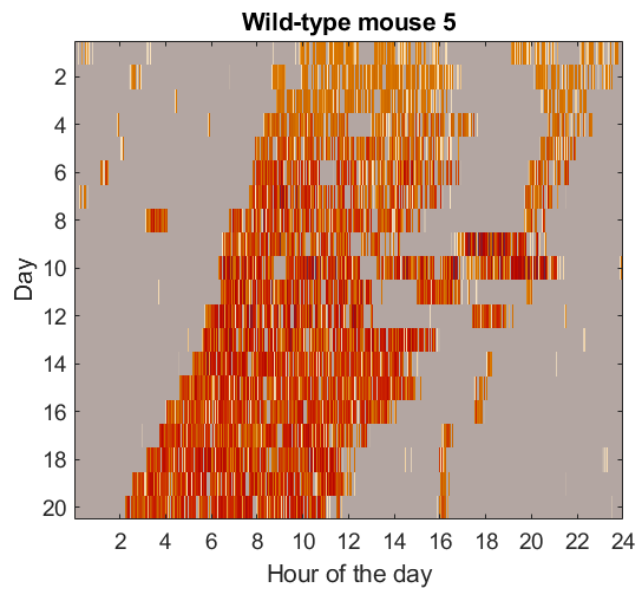


**Fig. S19.** Actogram for mouse 5 in the wild-type 20 day group

**F. Wild-type 21 day.** Here we present the actograms for the wild-type mice in constant darkness for 21 days.

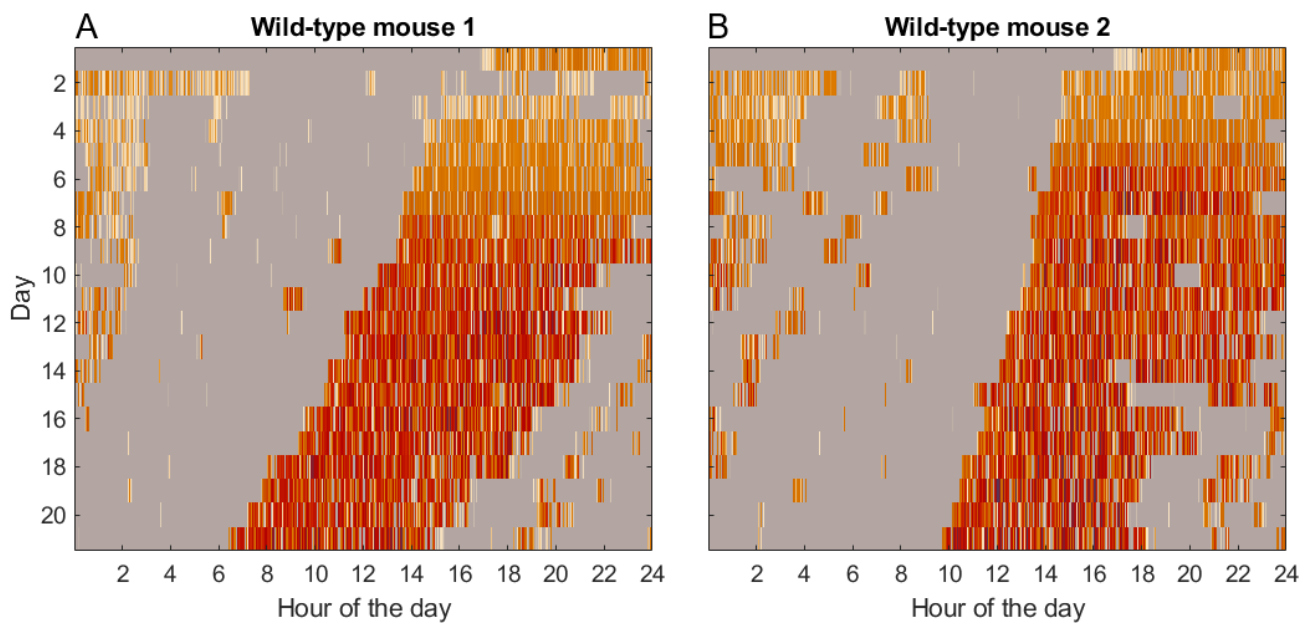


**Fig. S20.** Actograms for mouse 1 (A) and mouse 2 (B) in the wild-type 21 day group.

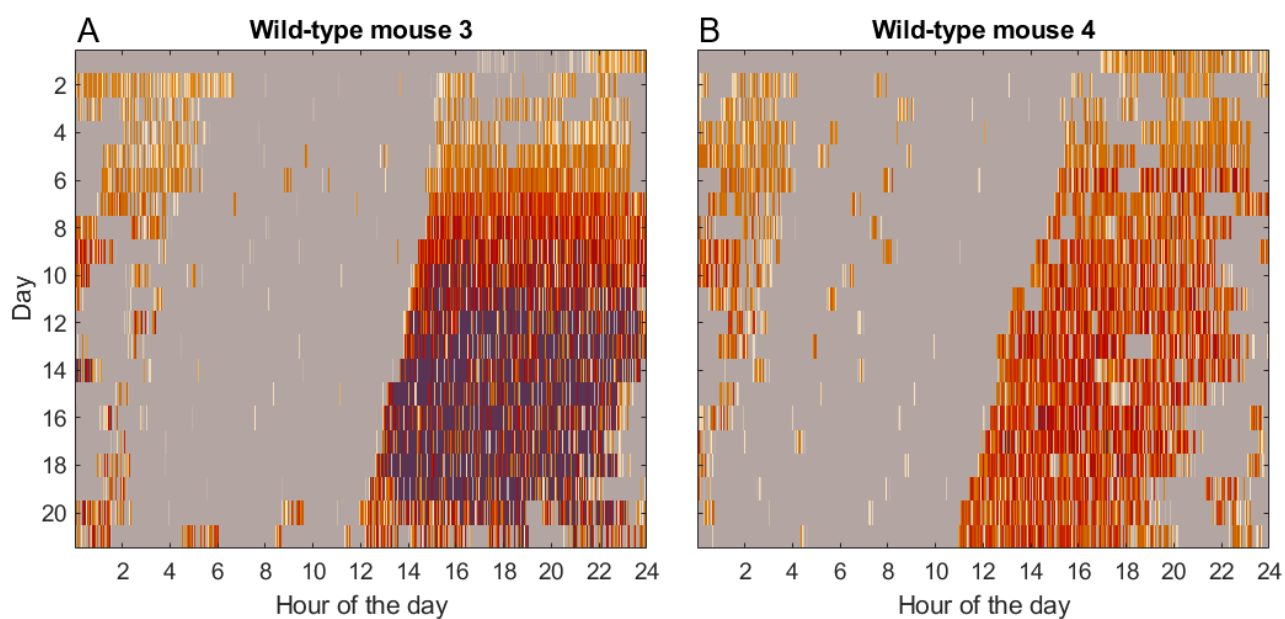


**Fig. S21.** Actograms for mouse 3 (A) and mouse 4 (B) in the wild-type 21 day group.

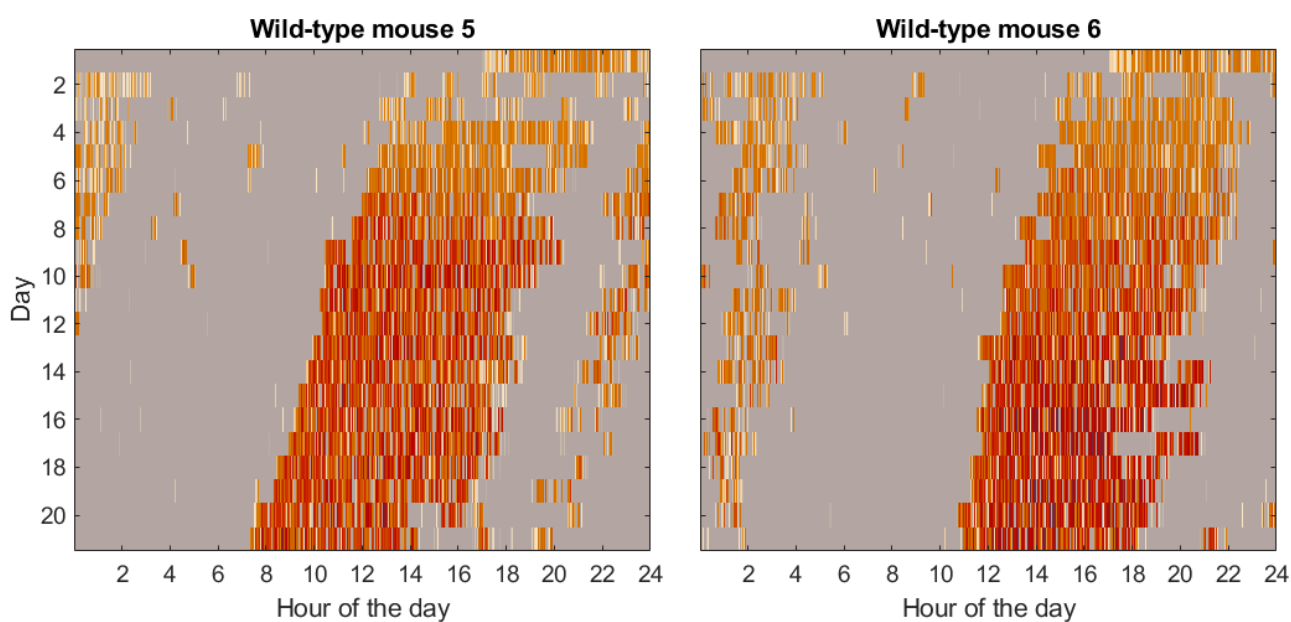


**Fig. S22.** Actograms for mouse 5 (A) and mouse 6 (B) in the wild-type 21 day group.

### 3. Wavelet transforms

In the main text, specific wavelet transforms (WTs) are illustrated to convey the message. As there is not sufficient space to include all WTs, the remainder of them are presented here.

**A. Heterozygous PER2::LUC knockin and wild-type littermate 30 day.** Here we present the wavelet transforms for the heterozygous PER2::LUC knockin and wild-type littermate mice in constant darkness for 30 days.

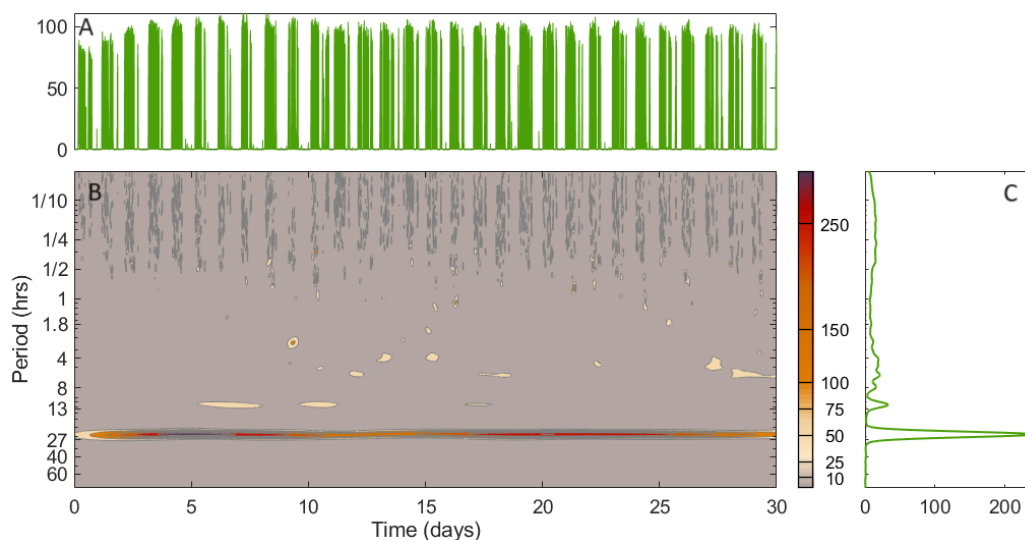


**Fig. S23.** Multiscale oscillatory activity in the heterozygous PER2::LUC knockin and wild-type littermate group, mouse 1. (A) Time-series of wheel rotations per minute (B) Wavelet transform of the data in (A). (C) Time-averaged power from the wavelet transform.

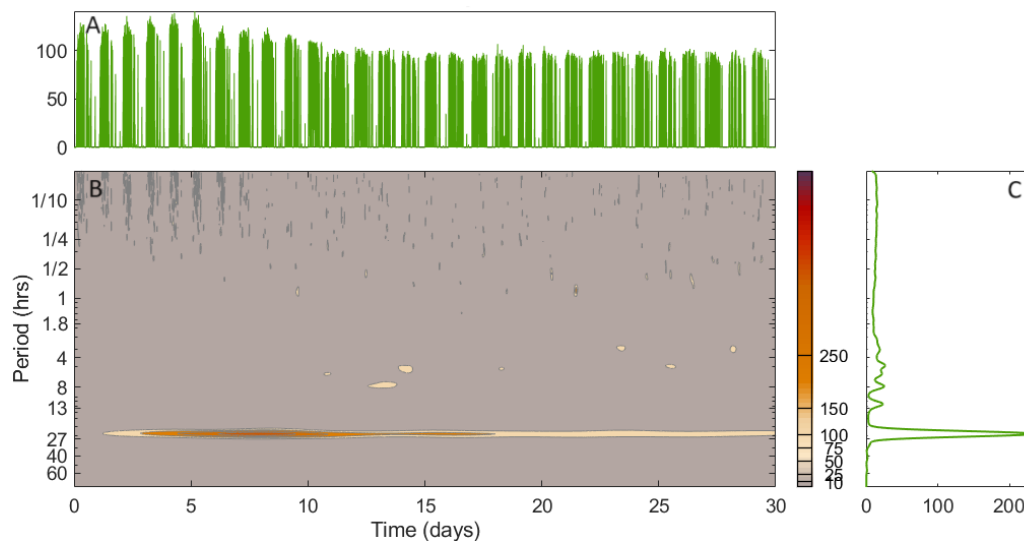


**Fig. S24.** Multiscale oscillatory activity in the heterozygous PER2::LUC knockin and wild-type littermate group, mouse 2. (A) Time-series of wheel rotations per minute (B) Wavelet transform of the data in (A). (C) Time-averaged power from the wavelet transform.

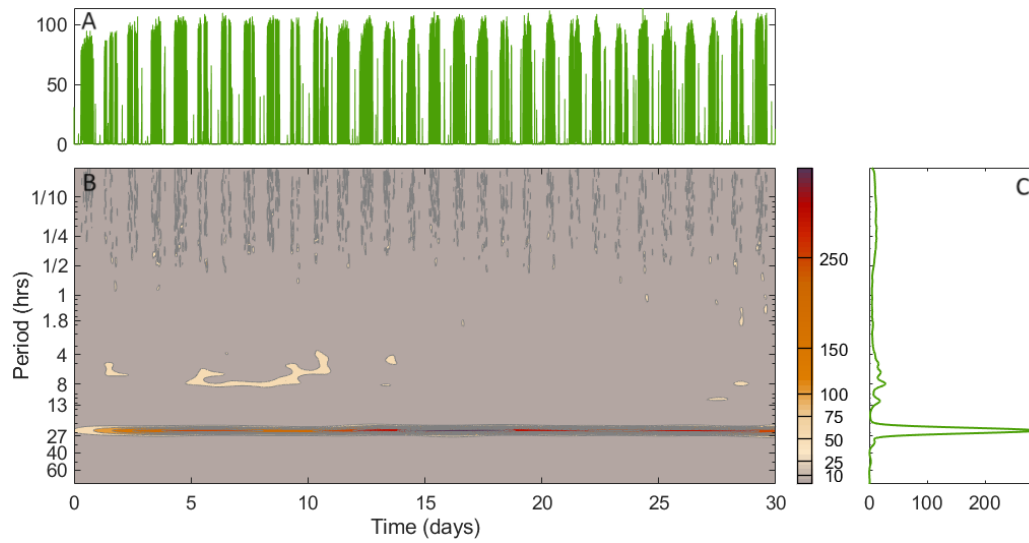


**Fig. S25.** Multiscale oscillatory activity in the heterozygous PER2::LUC knockin and wild-type littermate group, mouse 3. (A) Time-series of wheel rotations per minute (B) Wavelet transform of the data in (A). (C) Time-averaged power from the wavelet transform.

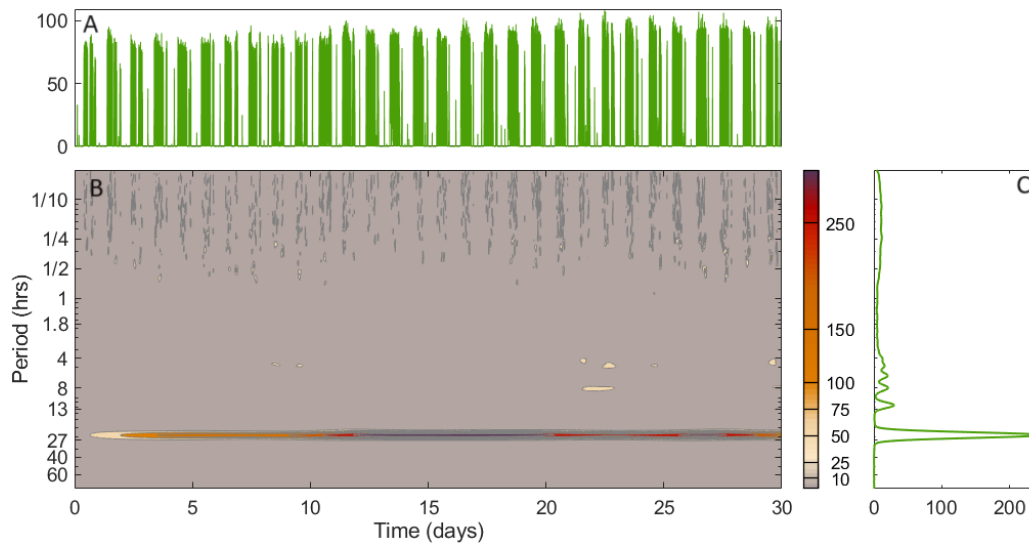


**Fig. S26.** Multiscale oscillatory activity in the heterozygous PER2::LUC knockin and wild-type littermate group, mouse 4. (A) Time-series of wheel rotations per minute (B) Wavelet transform of the data in (A). (C) Time-averaged power from the wavelet transform.

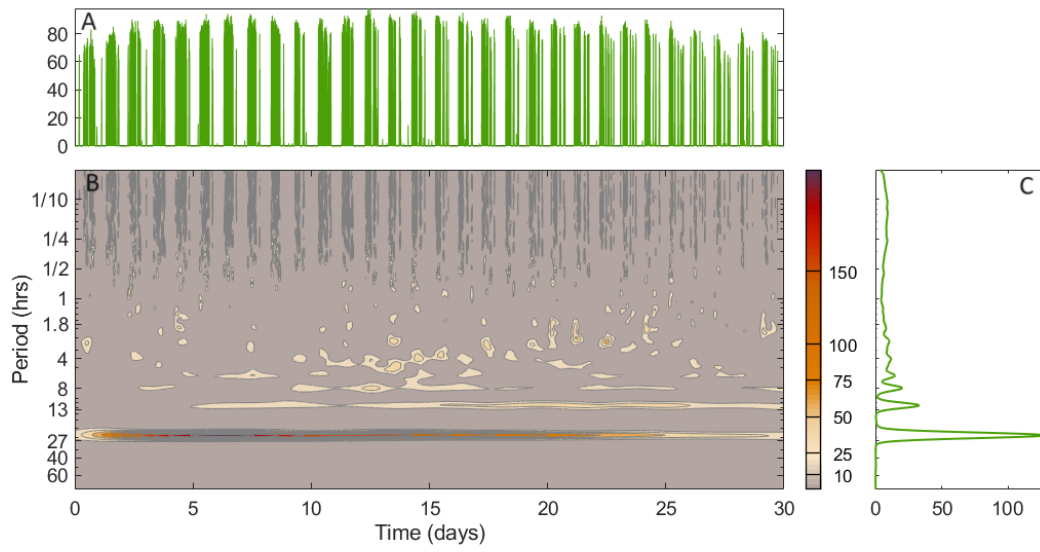


**Fig. S27.** Multiscale oscillatory activity in the heterozygous PER2::LUC knockin and wild-type littermate group, mouse 5. (A) Time-series of wheel rotations per minute (B) Wavelet transform of the data in (A). (C) Time-averaged power from the wavelet transform.

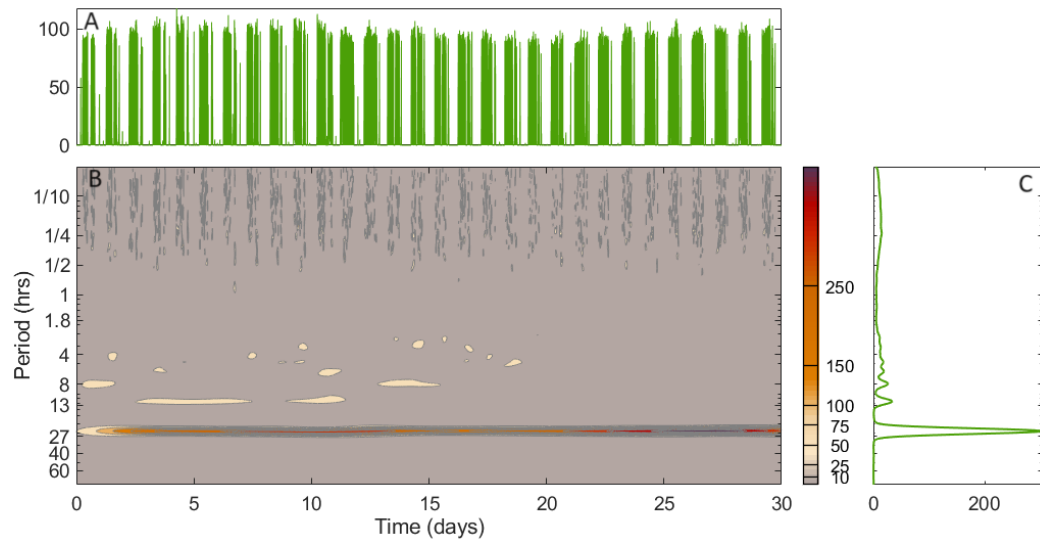


**Fig. S28.** Multiscale oscillatory activity in the heterozygous PER2::LUC knockin and wild-type littermate group, mouse 6. (A) Time-series of wheel rotations per minute (B) Wavelet transform of the data in (A). (C) Time-averaged power from the wavelet transform.

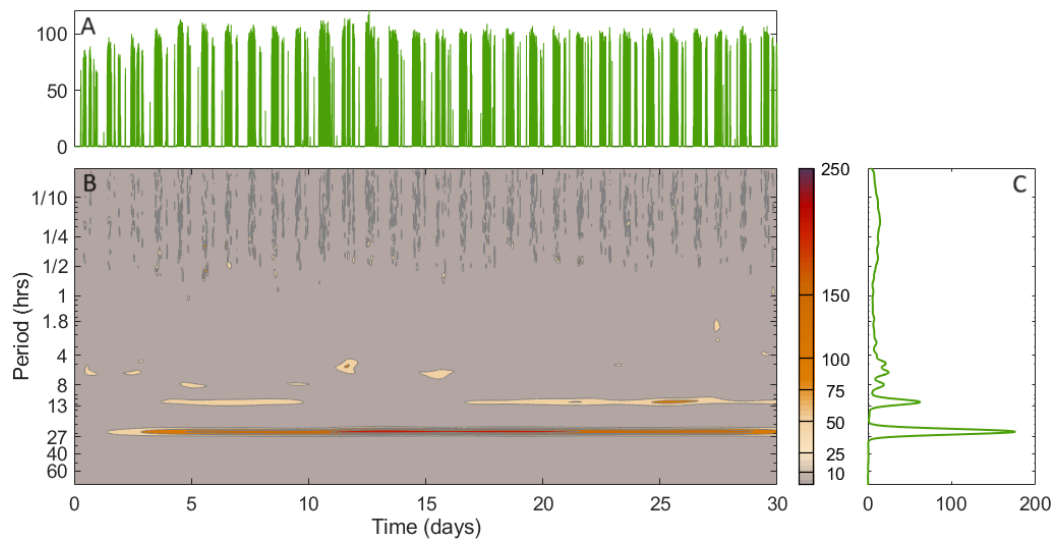


**Fig. S29.** Multiscale oscillatory activity in the heterozygous PER2::LUC knockin and wild-type littermate group, mouse 7. (A) Time-series of wheel rotations per minute (B) Wavelet transform of the data in (A). (C) Time-averaged power from the wavelet transform.

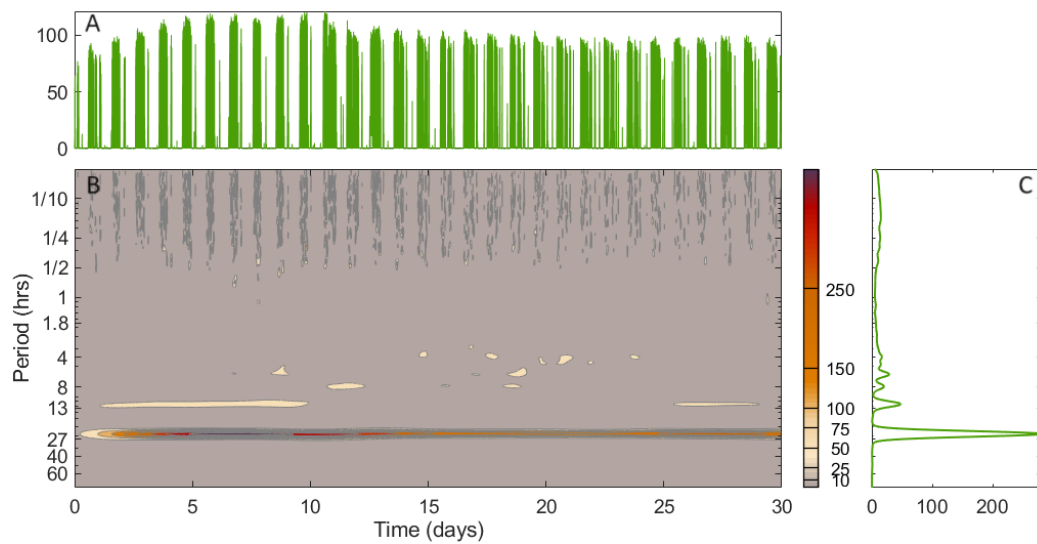


**Fig. S30.** Multiscale oscillatory activity in the heterozygous PER2::LUC knockin and wild-type littermate group, mouse 8. (A) Time-series of wheel rotations per minute (B) Wavelet transform of the data in (A). (C) Time-averaged power from the wavelet transform.

85 **B. *Per1/2/3* KO DD.** Here we present the wavelet transforms for the *Per1/2/3* KO DD mice in constant darkness for 65 days.

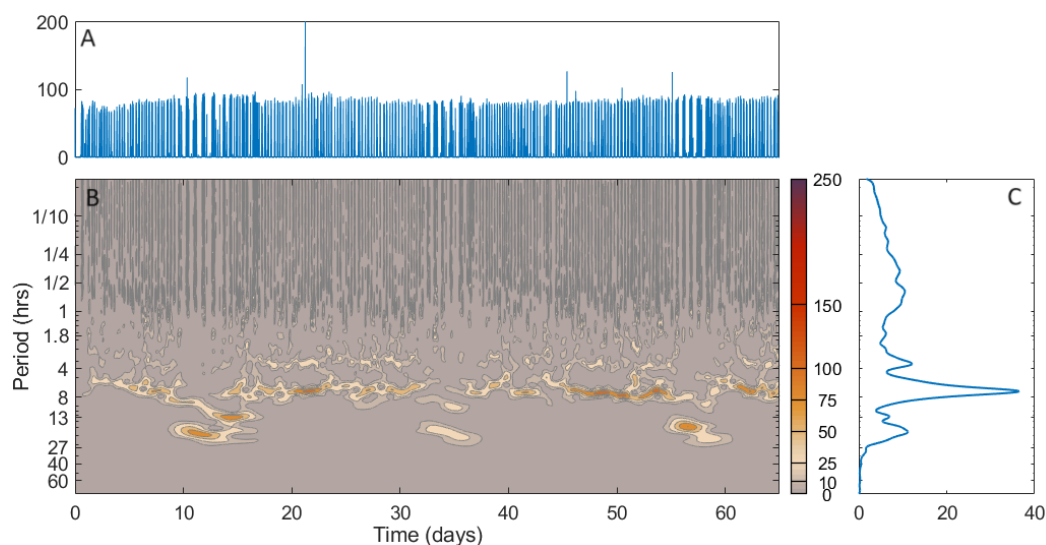


**Fig. S31.** Multiscale oscillatory activity in *Per1/2/3* KO DD mouse 1. (A) Time-series of wheel rotations per minute (B) Wavelet transform of the data in (A). (C) Time-averaged power from the wavelet transform.

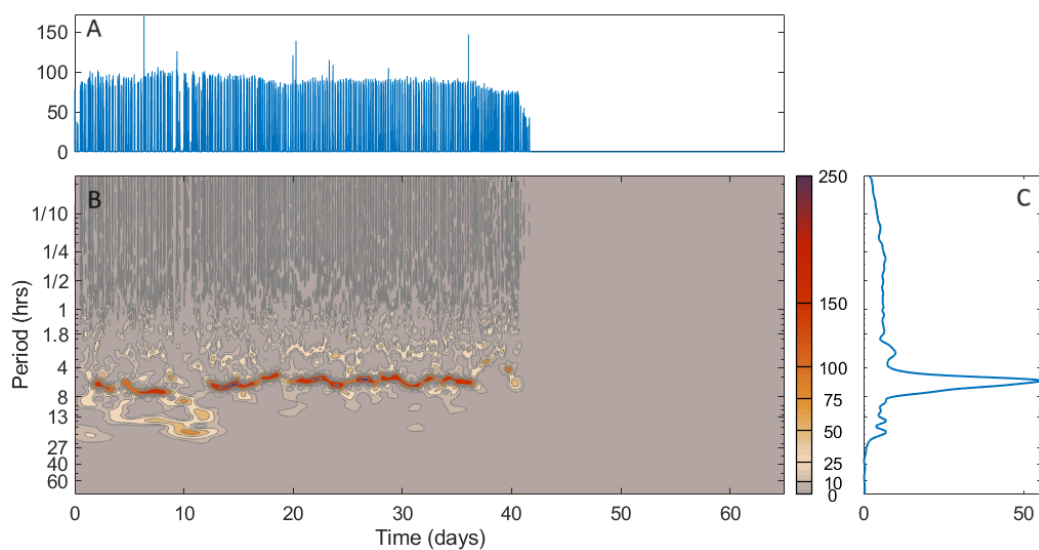


**Fig. S32.** Multiscale oscillatory activity in *Per1/2/3* KO DD mouse 2. (A) Time-series of wheel rotations per minute (B) Wavelet transform of the data in (A). (C) Time-averaged power from the wavelet transform. This mouse was not included in the group average calculations as the full 65 day duration of recording was not completed. Nevertheless, it is included here for completeness and to demonstrate that the same pattern was followed for the duration which was recorded.



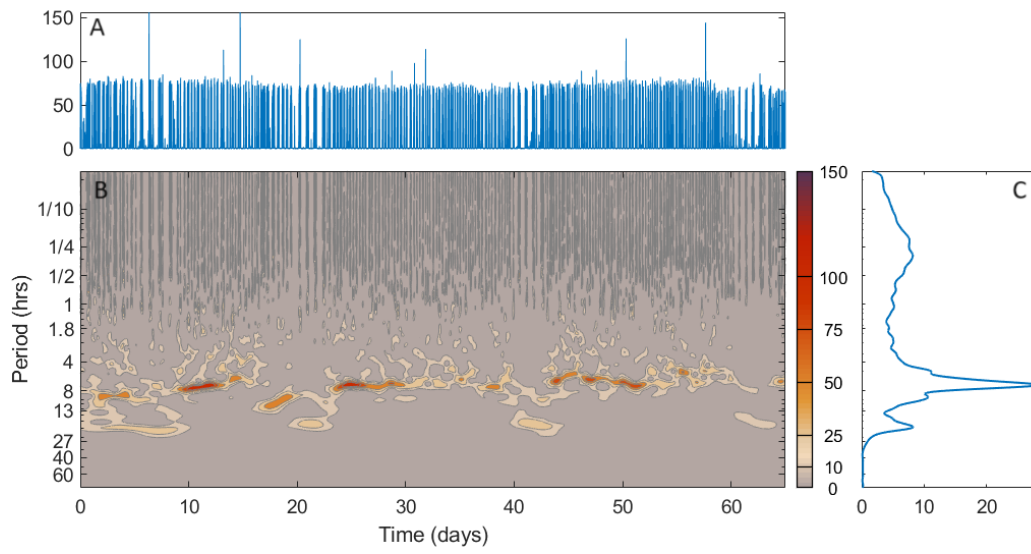


**Fig. S33.** Multiscale oscillatory activity in *Per1/2/3* KO DD mouse 3. (A) Time-series of wheel rotations per minute (B) Wavelet transform of the data in (A). (C) Time-averaged power from the wavelet transform.

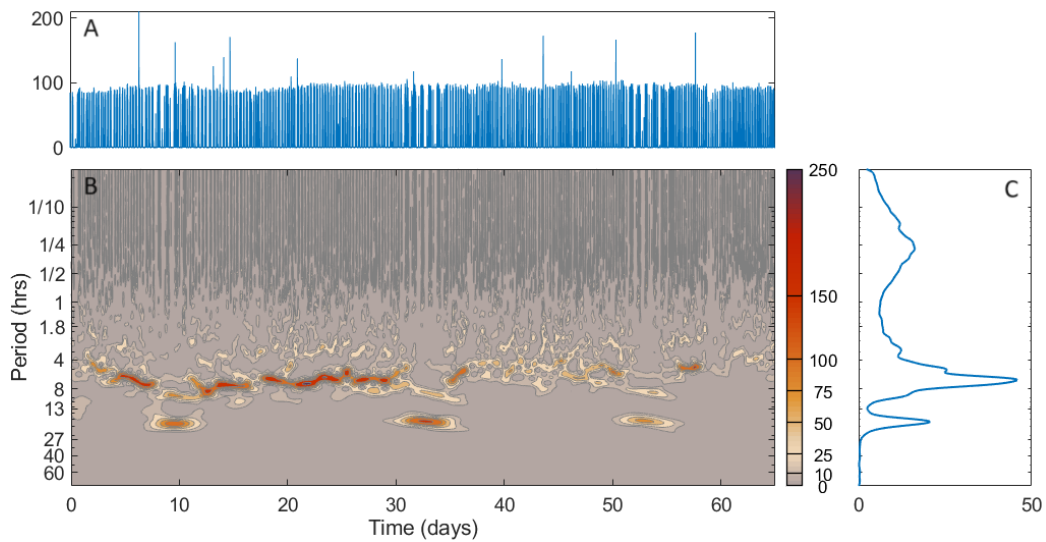


**Fig. S34.** Multiscale oscillatory activity in *Per1/2/3* KO DD mouse 4. (A) Time-series of wheel rotations per minute (B) Wavelet transform of the data in (A). (C) Time-averaged power from the wavelet transform.

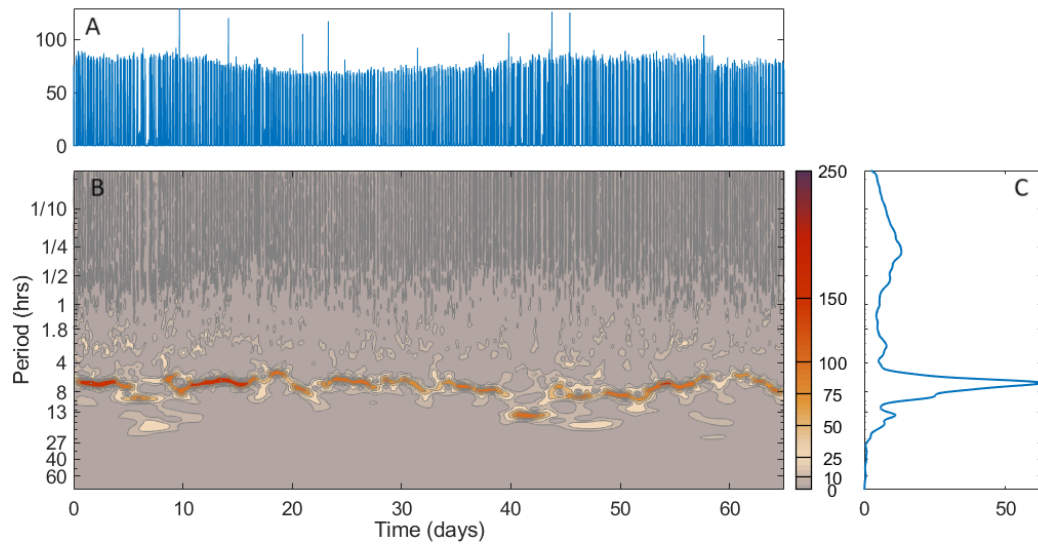


**Fig. S35.** Multiscale oscillatory activity in *Per1/2/3* KO DD mouse 5. (A) Time-series of wheel rotations per minute (B) Wavelet transform of the data in (A). (C) Time-averaged power from the wavelet transform.

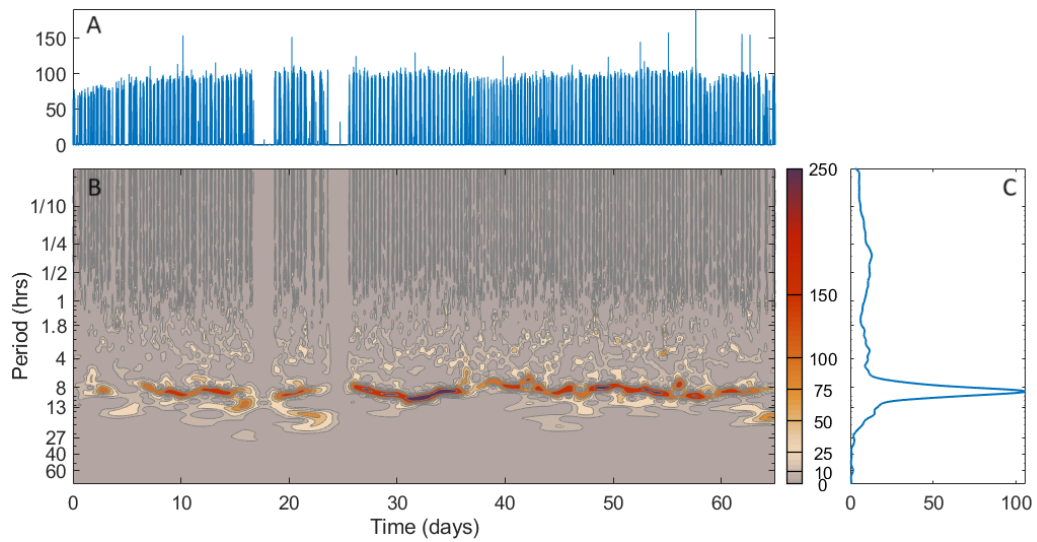


**Fig. S36.** Multiscale oscillatory activity in *Per1/2/3* KO DD mouse 6. (A) Time-series of wheel rotations per minute (B) Wavelet transform of the data in (A). (C) Time-averaged power from the wavelet transform.

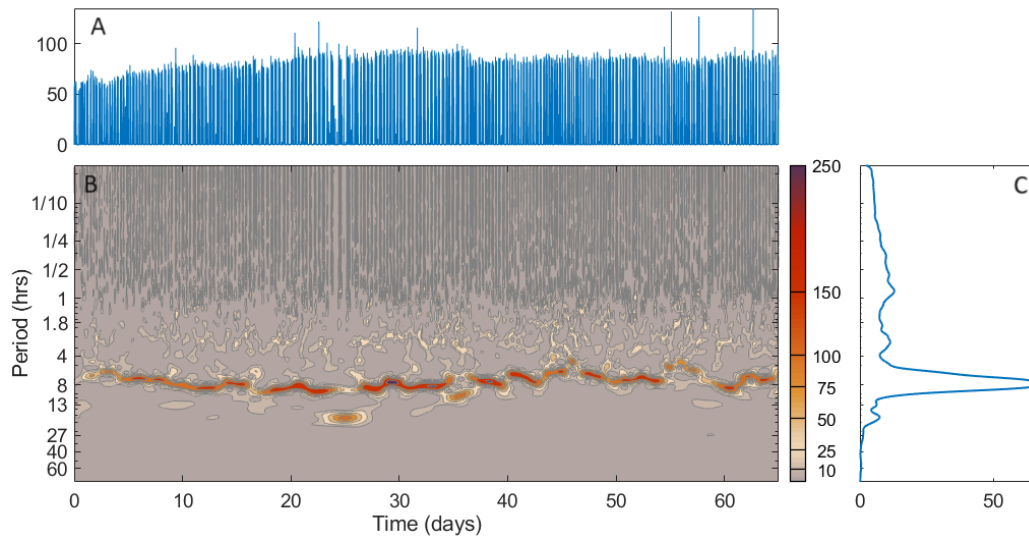


**Fig. S37.** Multiscale oscillatory activity in *Per1/2/3* KO DD mouse 7. (A) Time-series of wheel rotations per minute (B) Wavelet transform of the data in (A). (C) Time-averaged power from the wavelet transform.

86 **C. *Per1/2/3* KO DD MA.** Here we present the wavelet transforms for the *Per1/2/3* KO DD MA mice in constant darkness for 65  
87 days.

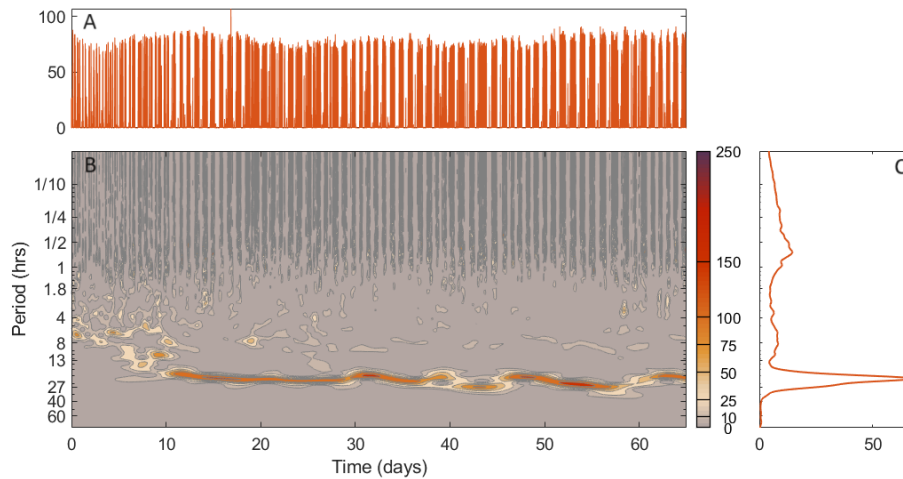


**Fig. S38.** Multiscale oscillatory activity in *Per1/2/3* KO DD MA mouse 1. (A) Time-series of wheel rotations per minute (B) Wavelet transform of the data in (A). (C) Time-averaged power from the wavelet transform.

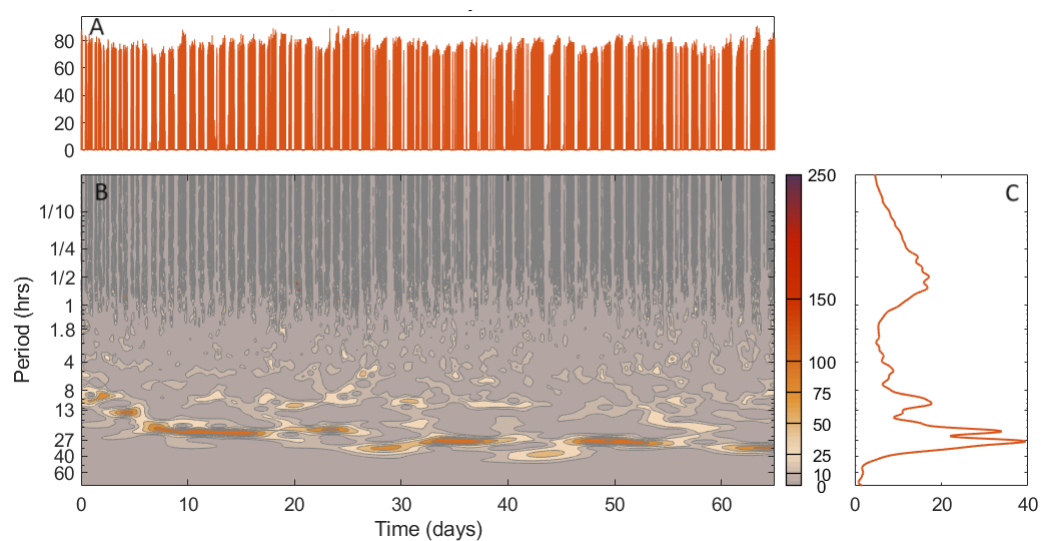


**Fig. S39.** Multiscale oscillatory activity in *Per1/2/3* KO DD MA mouse 2. (A) Time-series of wheel rotations per minute (B) Wavelet transform of the data in (A). (C) Time-averaged power from the wavelet transform.

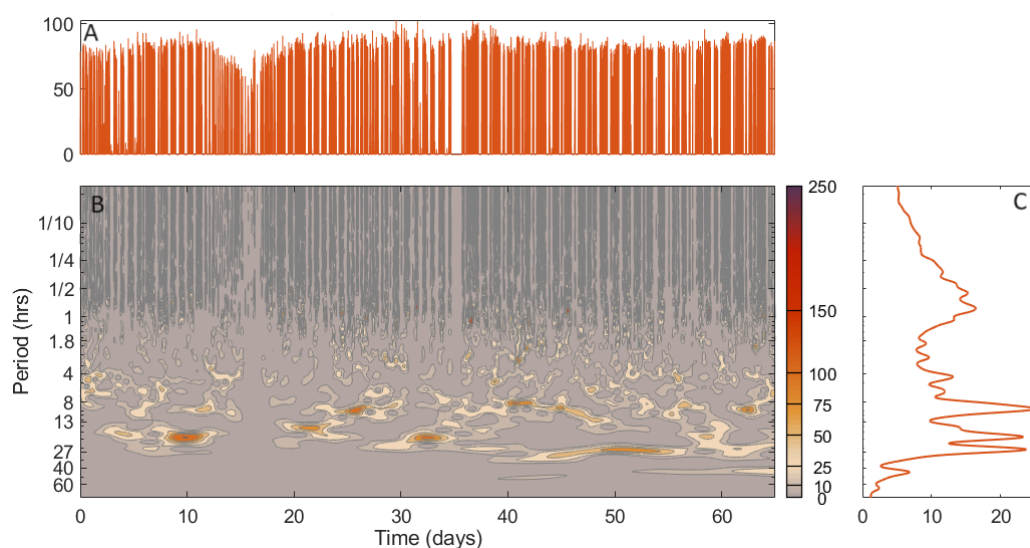


**Fig. S40.** Multiscale oscillatory activity in *Per1/2/3* KO DD MA mouse 3. (A) Time-series of wheel rotations per minute (B) Wavelet transform of the data in (A). (C) Time-averaged power from the wavelet transform.

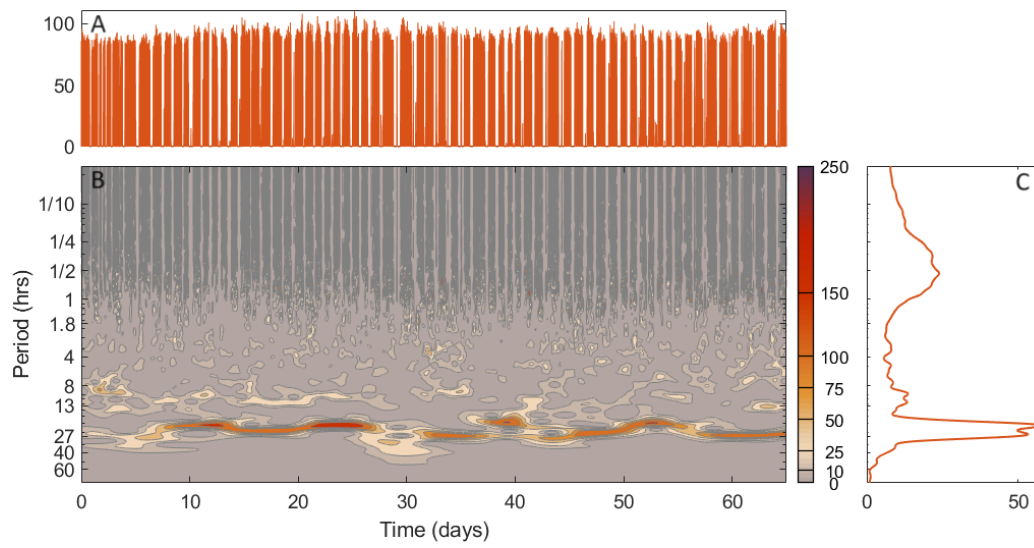


**Fig. S41.** Multiscale oscillatory activity in *Per1/2/3* KO DD MA mouse 4. (A) Time-series of wheel rotations per minute (B) Wavelet transform of the data in (A). (C) Time-averaged power from the wavelet transform.

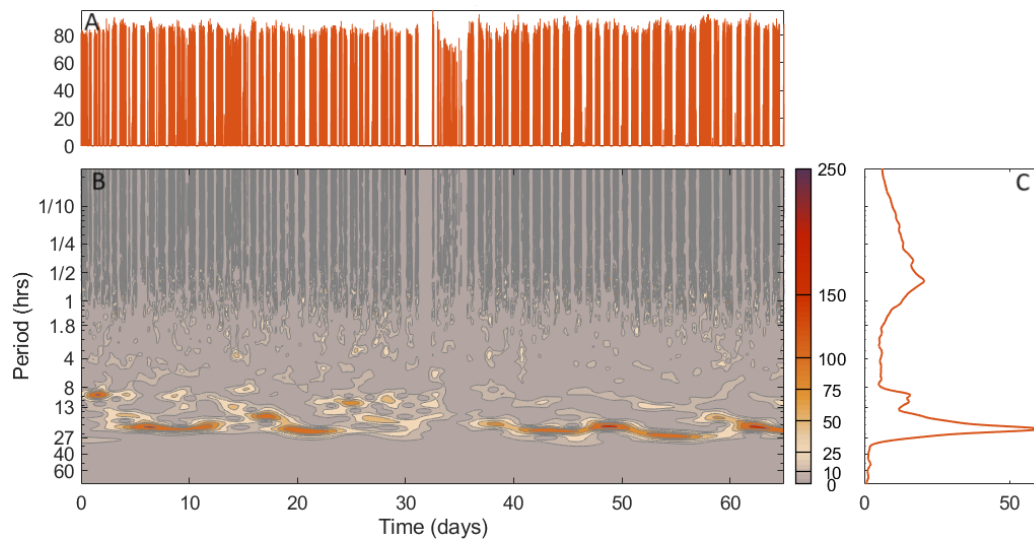


**Fig. S42.** Multiscale oscillatory activity in *Per1/2/3* KO DD MA mouse 5 exposed to methamphetamine. (A) Time-series of wheel rotations per minute (B) Wavelet transform of the data in (A). (C) Time-averaged power from the wavelet transform.

88 **D. Multiple conditions.** Here we present the WTs for the *Per1/2/3* knockout (KO) mice recorded for 139 days across varying  
89 conditions.

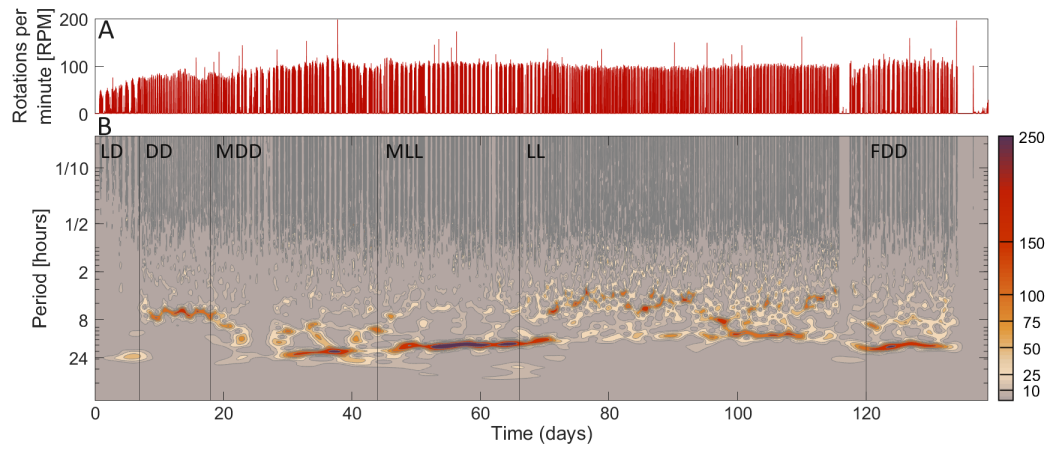


**Fig. S43.** The effect of different environmental and pharmacological modalities on the locomotor rhythms of *Per1/2/3* KO mice (mouse 1). (A) Time-series recorded for 139 days under varying conditions. (B) Time/frequency representation across all conditions. The separate modalities are denoted as follows: LD = Light/Dark cycles of period 24 hours, DD = constant darkness, MDD = constant darkness with methamphetamine administration, MLL = constant light with methamphetamine administration, LL = constant light, FDD = final condition of constant darkness.

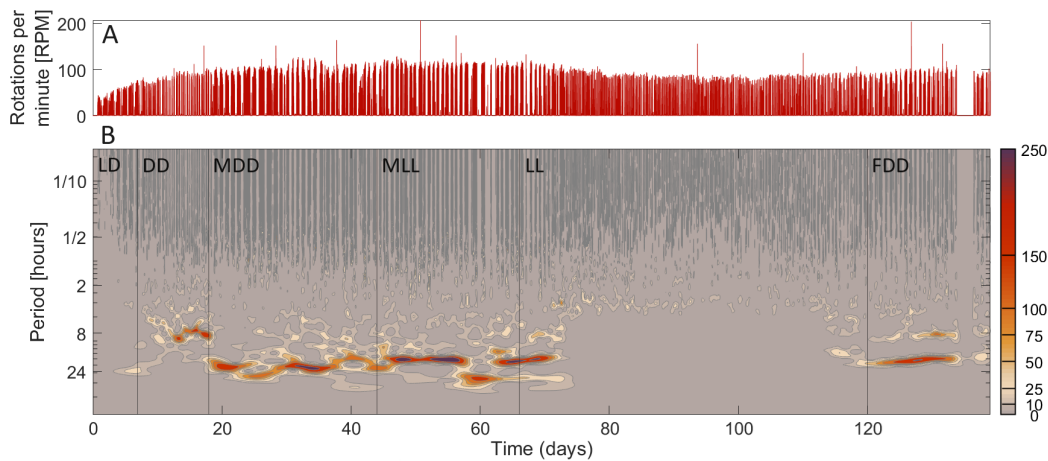


**Fig. S44.** The effect of different environmental and pharmacological modalities on the locomotor rhythms of *Per1/2/3* KO mice (mouse 2). (A) Time-series recorded for 139 days under varying conditions. (B) Time/frequency representation across all conditions. The separate modalities are denoted as follows: LD = Light/Dark cycles of period 24 hours, DD = constant darkness, MDD = constant darkness with methamphetamine administration, MLL = constant light with methamphetamine administration, LL = constant light, FDD = final condition of constant darkness.



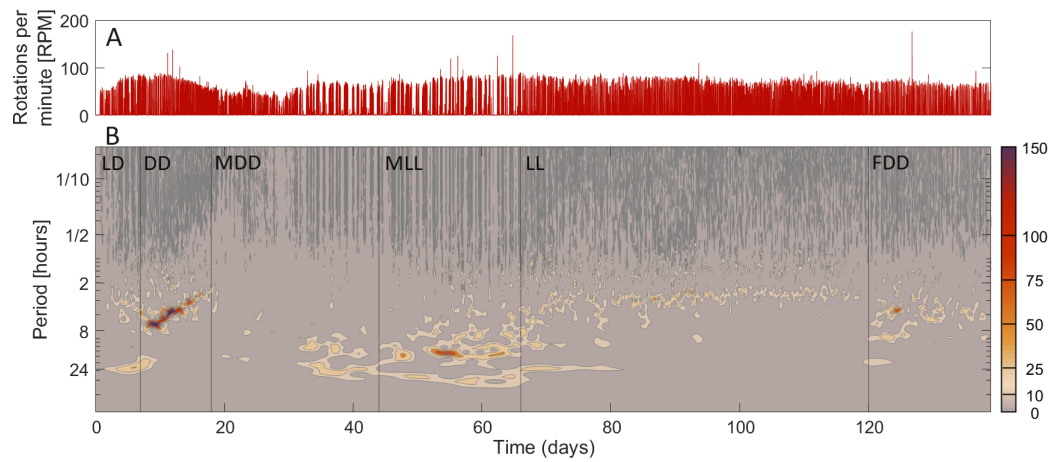


**Fig. S45.** The effect of different environmental and pharmacological modalities on the locomotor rhythms of *Per1/2/3* KO mice (mouse 3). (B) Time/frequency representation across all conditions. The separate modalities are denoted as follows: LD = Light/Dark cycles of period 24 hours, DD = constant darkness, MDD = constant darkness with methamphetamine administration, MLL = constant light with methamphetamine administration, LL = constant light, FDD = final condition of constant darkness.

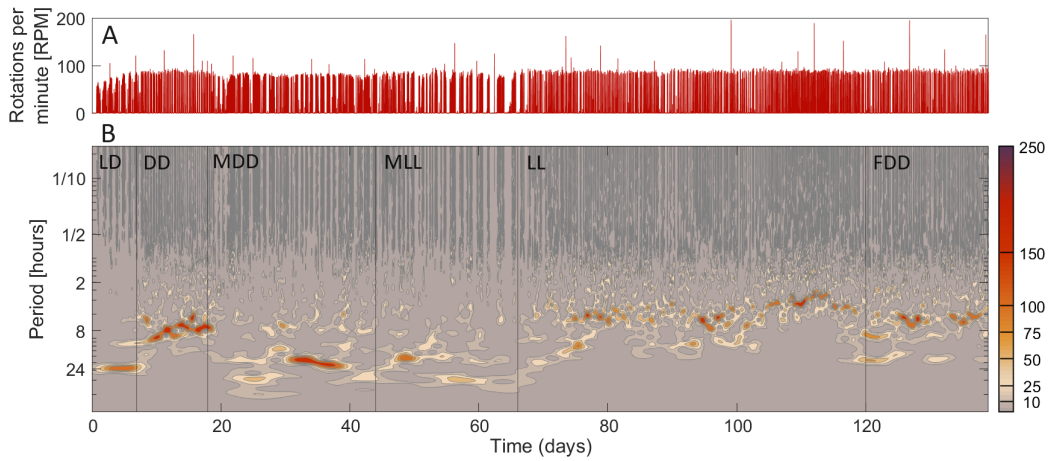


**Fig. S46.** The effect of different environmental and pharmacological modalities on the locomotor rhythms of *Per1/2/3* KO mice (mouse 4). (A) Time-series recorded for 139 days under varying conditions. (B) Time/frequency representation across all conditions. The separate modalities are denoted as follows: LD = Light/Dark cycles of period 24 hours, DD = constant darkness, MDD = constant darkness with methamphetamine administration, MLL = constant light with methamphetamine administration, LL = constant light, FDD = final condition of constant darkness.



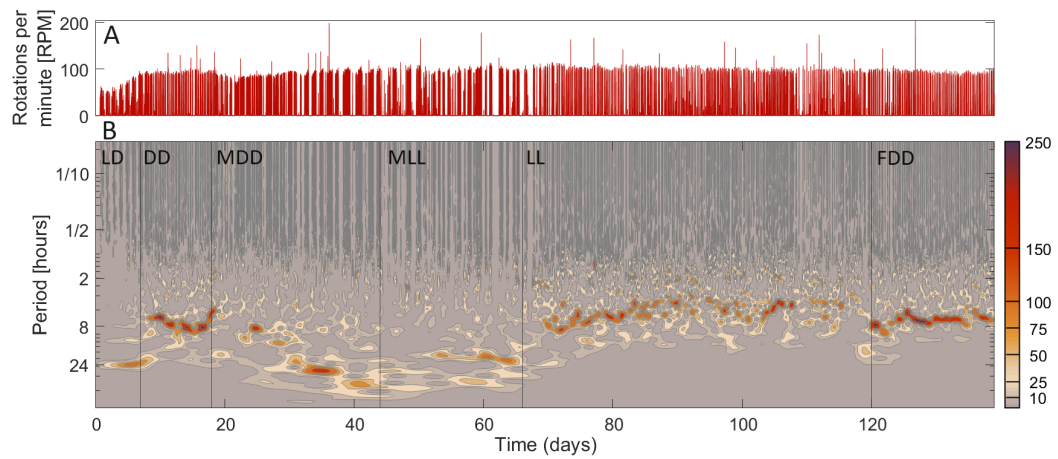


**Fig. S47.** The effect of different environmental and pharmacological modalities on on the locomotor rhythms of *Per1/2/3* KO mice (mouse 5). (A) Time-series recorded for 139 days under varying conditions. (B) Time/frequency representation across all conditions. The separate modalities are denoted as follows: LD = Light/Dark cycles of period 24 hours, DD = constant darkness, MDD = constant darkness with methamphetamine administration, MLL = constant light with methamphetamine administration, LL = constant light, FDD = final condition of constant darkness.

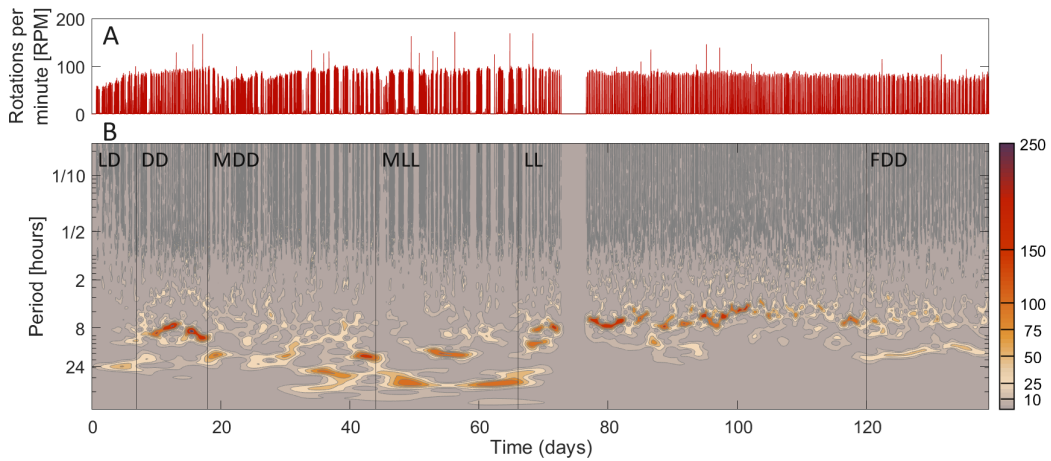


**Fig. S48.** The effect of different environmental and pharmacological modalities on on the locomotor rhythms of *Per1/2/3* KO mice (mouse 6). (A) Time-series recorded for 139 days under varying conditions. (B) Time/frequency representation across all conditions. The separate modalities are denoted as follows: LD = Light/Dark cycles of period 24 hours, DD = constant darkness, MDD = constant darkness with methamphetamine administration, MLL = constant light with methamphetamine administration, LL = constant light, FDD = final condition of constant darkness.

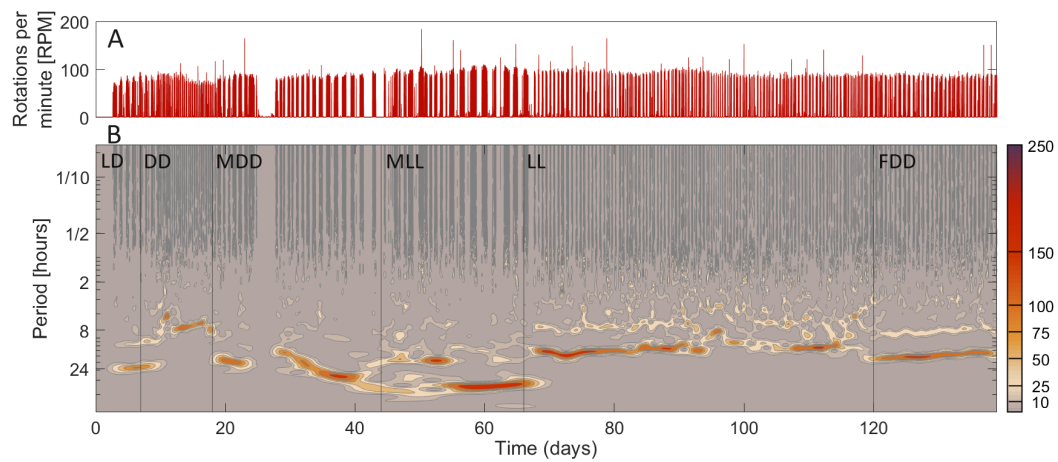


**Fig. S49.** The effect of different environmental and pharmacological modalities on the locomotor rhythms of *Per1/2/3* KO mice (mouse 7). (A) Time-series recorded for 139 days under varying conditions. (B) Time/frequency representation across all conditions. The separate modalities are denoted as follows: LD = Light/Dark cycles of period 24 hours, DD = constant darkness, MDD = constant darkness with methamphetamine administration, MLL = constant light with methamphetamine administration, LL = constant light, FDD = final condition of constant darkness.

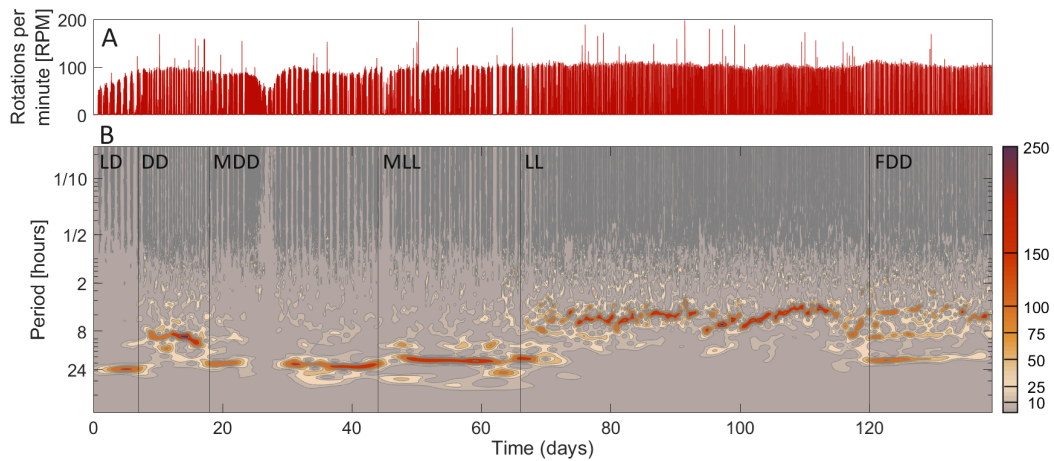


**Fig. S50.** The effect of different environmental and pharmacological modalities on the locomotor rhythms of *Per1/2/3* KO mice (mouse 8). (A) Time-series recorded for 139 days under varying conditions. (B) Time/frequency representation across all conditions. The separate modalities are denoted as follows: LD = Light/Dark cycles of period 24 hours, DD = constant darkness, MDD = constant darkness with methamphetamine administration, MLL = constant light with methamphetamine administration, LL = constant light, FDD = final condition of constant darkness.

90 **E. Wild-type 20 day.** Here we present the wavelet transforms for the wild-type mice in constant darkness for 20 days.

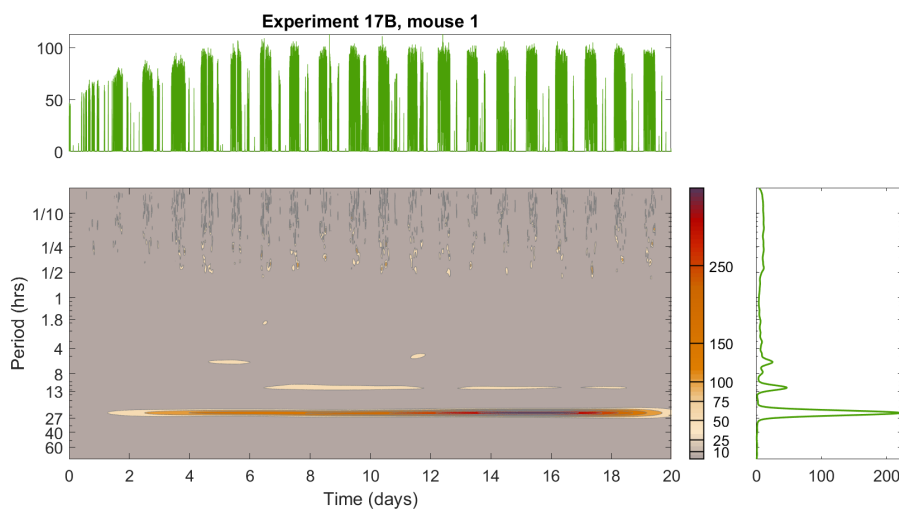


**Fig. S51.** Multiscale oscillatory activity in wild-type (20 day) mouse 1. (A) Time-series of wheel rotations per minute (B) Wavelet transform of the data in (A). (C) Time-averaged power from the wavelet transform.

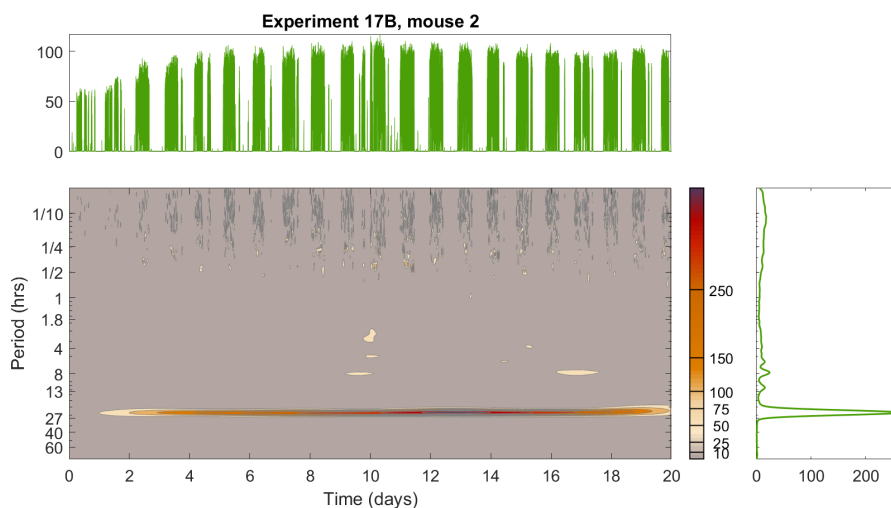


**Fig. S52.** Multiscale oscillatory activity in wild-type (20 day) mouse 2 from experiment 17B. (A) Time-series of wheel rotations per minute (B) Wavelet transform of the data in (A). (C) Time-averaged power from the wavelet transform.

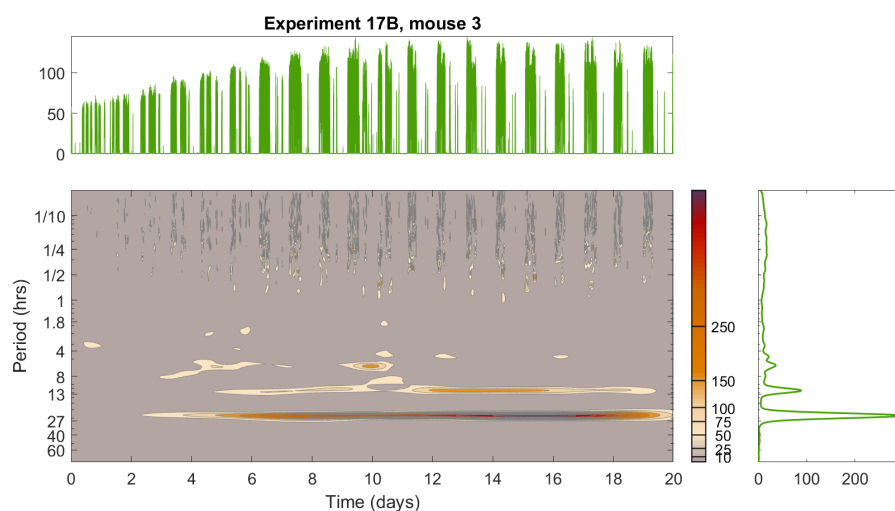


**Fig. S53.** Multiscale oscillatory activity in wild-type (20 day) mouse 3 from experiment 17B. (A) Time-series of wheel rotations per minute (B) Wavelet transform of the data in (A). (C) Time-averaged power from the wavelet transform.

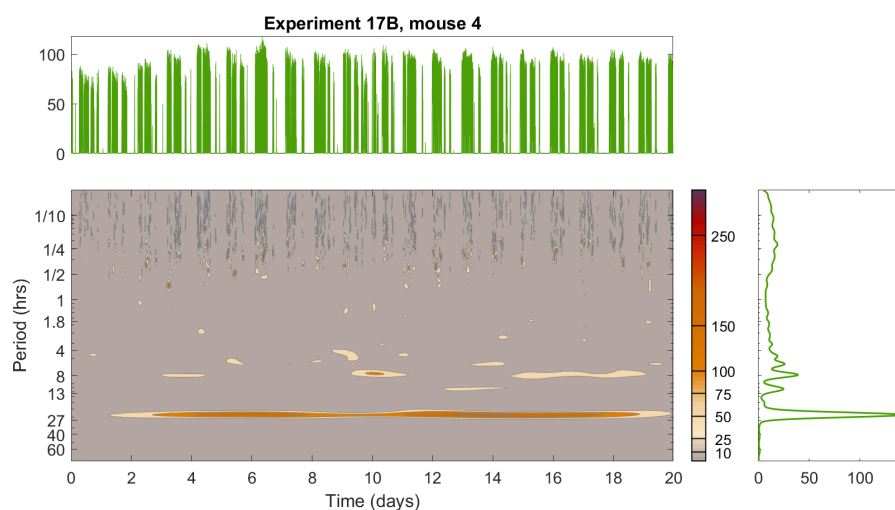


**Fig. S54.** Multiscale oscillatory activity in wild-type (20 day) mouse 4 from experiment 17B. (A) Time-series of wheel rotations per minute (B) Wavelet transform of the data in (A). (C) Time-averaged power from the wavelet transform.

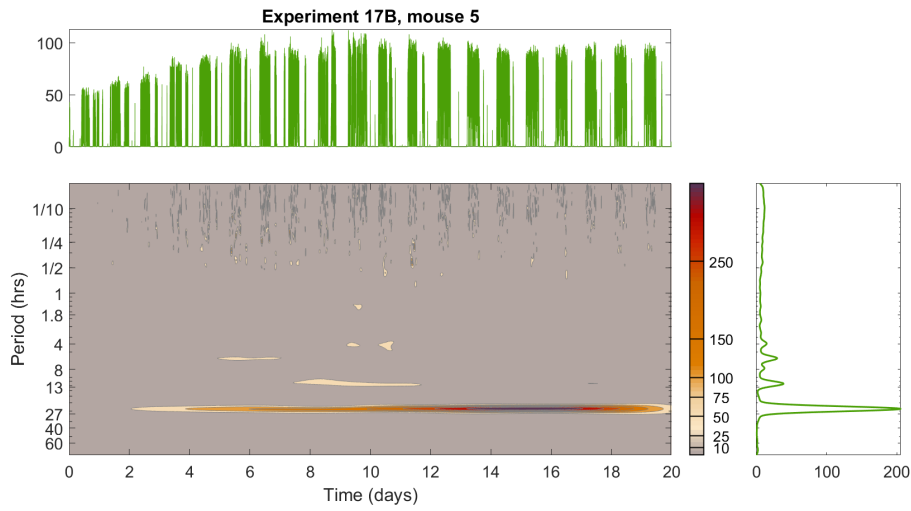


**Fig. S55.** Multiscale oscillatory activity in wild-type (20 day) mouse 5 from experiment 17B. (A) Time-series of wheel rotations per minute (B) Wavelet transform of the data in (A). (C) Time-averaged power from the wavelet transform.

91 **F. Wild-type 21 day.** Here we present the wavelet transforms for the wild-type mice in constant darkness for 21 days.

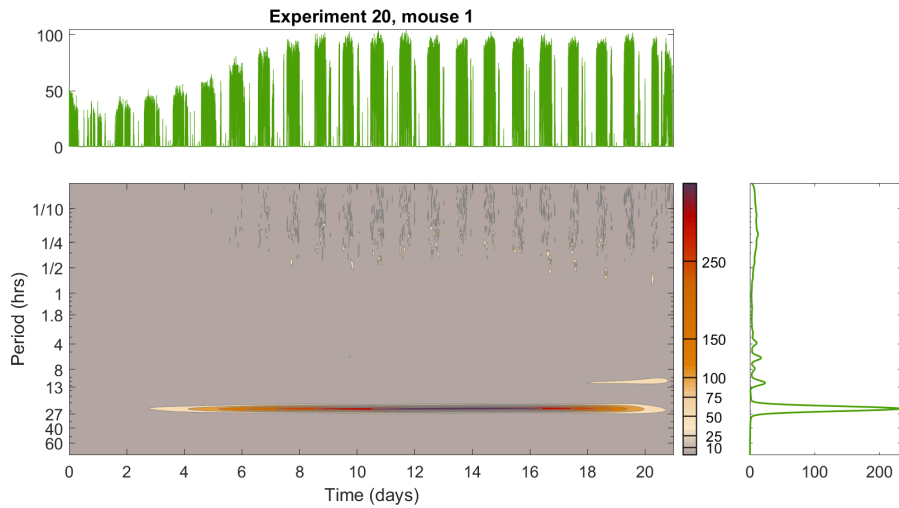


**Fig. S56.** Multiscale oscillatory activity in wild-type (21 day) mouse 1 from experiment 20. (A) Time-series of wheel rotations per minute (B) Wavelet transform of the data in (A). (C) Time-averaged power from the wavelet transform.

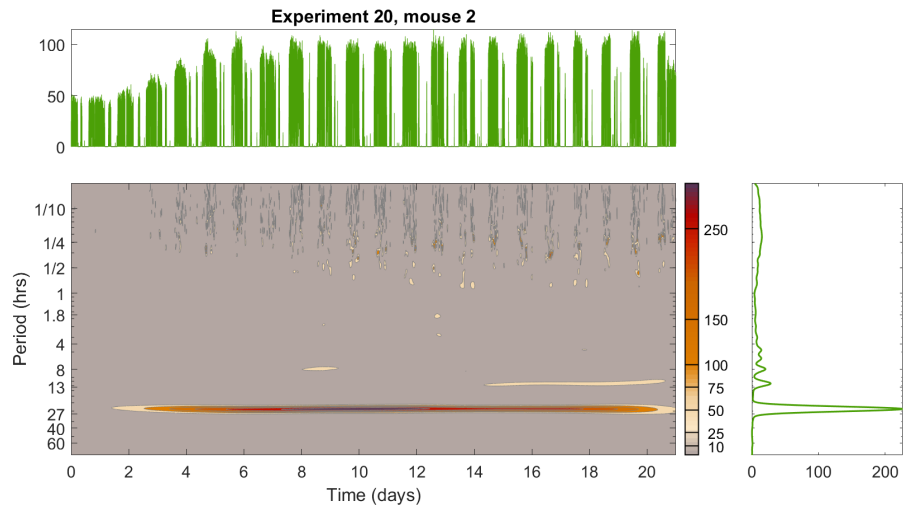


**Fig. S57.** Multiscale oscillatory activity in wild-type (21 day) mouse 2 from experiment 20. (A) Time-series of wheel rotations per minute (B) Wavelet transform of the data in (A). (C) Time-averaged power from the wavelet transform.

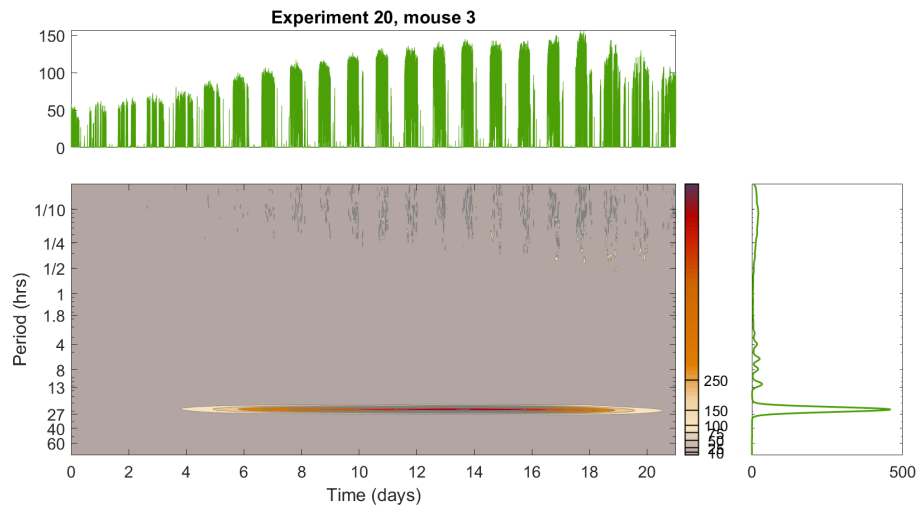


**Fig. S58.** Multiscale oscillatory activity in wild-type (21 day) mouse 3 from experiment 20. (A) Time-series of wheel rotations per minute (B) Wavelet transform of the data in (A). (C) Time-averaged power from the wavelet transform.

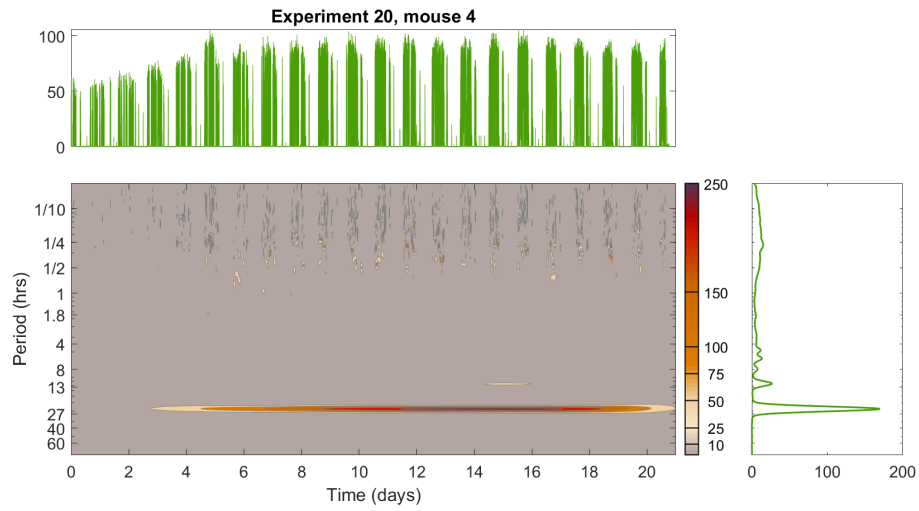


**Fig. S59.** Multiscale oscillatory activity in wild-type (21 day) mouse 4 from experiment 20. (A) Time-series of wheel rotations per minute (B) Wavelet transform of the data in (A). (C) Time-averaged power from the wavelet transform.

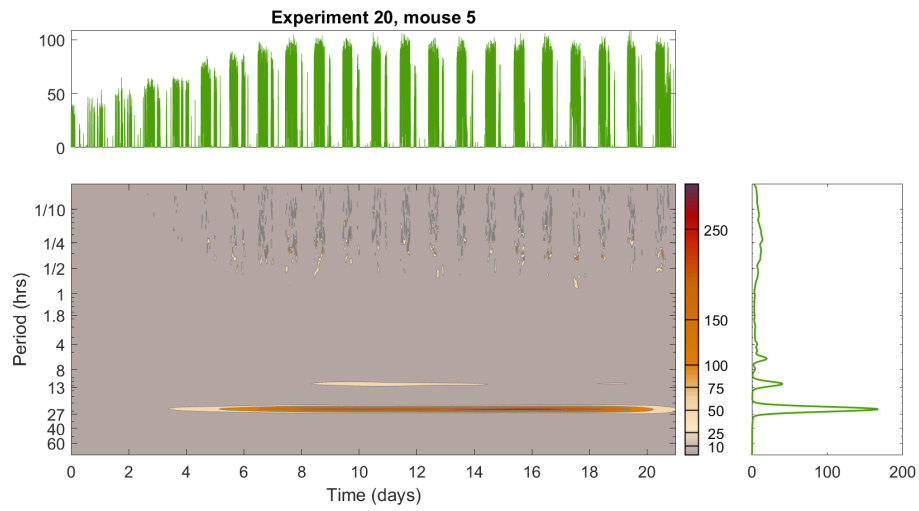


**Fig. S60.** Multiscale oscillatory activity in wild-type (21 day) mouse 5 from experiment 20. (A) Time-series of wheel rotations per minute (B) Wavelet transform of the data in (A). (C) Time-averaged power from the wavelet transform.



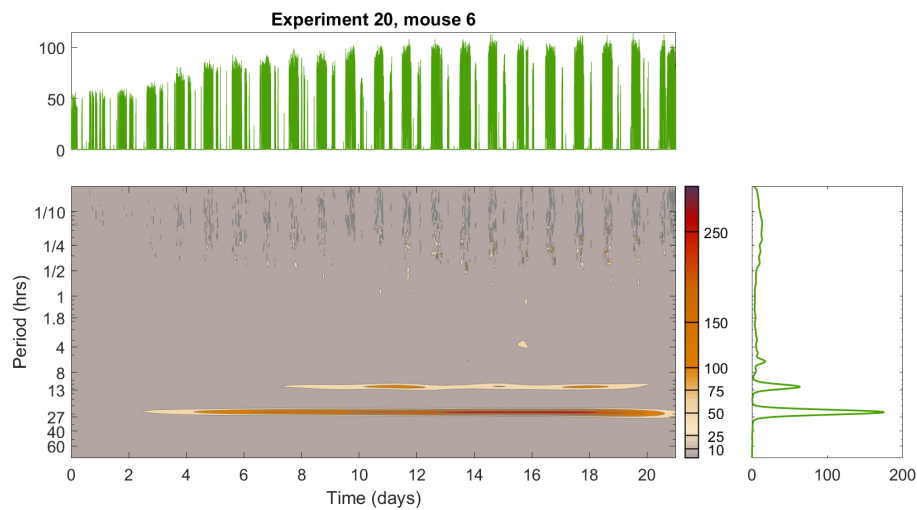


**Fig. S61.** Multiscale oscillatory activity in wild-type (21 day) mouse 6 from experiment 20. (A) Time-series of wheel rotations per minute (B) Wavelet transform of the data in (A). (C) Time-averaged power from the wavelet transform.

#### 4. Ridge extraction

To determine the time-localised frequencies within each band, ridge extraction was performed. The mean of the resultant frequencies were then calculated. The standard deviations across time were also calculated. Tabs. S2-S6 indicate the value of each mean frequency of the mode over time, and their variability.

**A. Heterozygous PER2::LUC knockin and wild-type littermate group, 30 day.** For the heterozygous PER2::LUC knockin and wild-type littermate 30 day group, the group median circadian period was  $23.9 \pm 0.1$  hours, the group median low frequency ultradian period was  $6.5 \pm 0.7$  hours and the group median high frequency ultradian period was  $0.35 \pm 0.26$  hours.

Mouse	Circadian (27-11hrs)	Low frequency ultradian(11-4hrs)	High frequency ultradian (4-0.04hrs)
1	$23.8 \pm 0.2$	$5.7 \pm 0.7$	$0.35 \pm 0.20$
2	$23.9 \pm 0.1$	$5.4 \pm 0.6$	$0.25 \pm 0.16$
3	$23.8 \pm 0.1$	$7.3 \pm 0.8$	$0.26 \pm 0.16$
4	$24.0 \pm 0.1$	$6.6 \pm 0.8$	$0.35 \pm 0.26$
5	$23.8 \pm 0.1$	$7.9 \pm 0.1$	$0.37 \pm 0.31$
6	$23.9 \pm 0.2$	$6.6 \pm 0.9$	$0.36 \pm 0.33$
7	$24.0 \pm 0.1$	$6.5 \pm 0.8$	$0.36 \pm 0.27$
8	$23.8 \pm 0.1$	$6.0 \pm 0.4$	$0.31 \pm 0.25$

**Table S2.** Ridges extracted for each mouse in the heterozygous PER2::LUC knockin and wild-type littermate 30 day group. The reported value is the mean  $\pm$  the standard deviation.

**B. Per1/2/3 KO DD.** For *Per1/2/3* knockout mice, the median circadian period was  $18.6 \pm 2.2$  hours, the median low frequency ultradian period was  $7.2 \pm 0.9$  hours and the median high frequency ultradian period was  $0.71 \pm 0.14$  hours.

Mouse	Circadian (27-13hrs)	Low frequency ultradian(11-4hrs)	High frequency ultradian (4-0.04hrs)
1	$18.6 \pm 2.1$	$6.9 \pm 0.8$	$0.76 \pm 0.15$
2	$18.7 \pm 1.9$	$7.4 \pm 1.0$	$0.67 \pm 0.16$
3	$18.3 \pm 2.4$	$6.4 \pm 0.8$	$0.56 \pm 0.11$
4	$20.7 \pm 2.3$	$6.9 \pm 0.9$	$0.55 \pm 0.09$
5	$19.1 \pm 2.3$	$8.8 \pm 0.8$	$0.81 \pm 0.17$
6	$18.8 \pm 2.1$	$7.6 \pm 1.0$	$0.87 \pm 0.12$

**Table S3.** Ridges extracted for each mouse in the *Per1/2/3* KO DD group. The reported value is the mean  $\pm$  the standard deviation.

**C. *Per1/2/3* KO DD MA.** For *Per1/2/3* knockout mice exposed to methamphetamine, the median circadian period was  $21.6 \pm 2.5$  hours, the median low frequency ultradian period was  $8.8 \pm 1.3$  hours and the median high frequency ultradian period was  $0.78 \pm 0.16$  hours. Fig. 1 in the main text contains violin plots of each of the measured frequencies.

Mouse	Circadian (27-11hrs)	Low frequency ultradian(11-4hrs)	High frequency ultradian (4-0.04hrs)
1	$21.6 \pm 1.7$	$7.9 \pm 1.1$	$0.83 \pm 0.17$
2	$19.2 \pm 2.5$	$8.8 \pm 1.4$	$0.67 \pm 0.16$
3	$20.8 \pm 3.5$	$8.8 \pm 1.0$	$0.89 \pm 0.16$
4	$22.2 \pm 3.3$	$8.5 \pm 1.3$	$0.59 \pm 0.15$
5	$22.4 \pm 1.8$	$8.8 \pm 1.3$	$0.78 \pm 0.18$

**Table S4. Ridges extracted for each mouse in the per KO DD MA group. The reported value is the mean  $\pm$  the standard deviation.**

**D. Wild-type 20 day.** For the 20 day WT DD mice, the median circadian period was  $23.4 \pm 0.2$  hours, the median low frequency ultradian period was  $6.9 \pm 1.0$  hours and the median high frequency ultradian period was  $0.32 \pm 0.21$  hours.

Mouse	Circadian (27-13hrs)	Low frequency ultradian(13-4hrs)	High frequency ultradian (1.8-0.04hrs)
1	$23.5 \pm 0.1$	$6.2 \pm 0.8$	$0.32 \pm 0.25$
2	$23.2 \pm 0.4$	$6.9 \pm 1.1$	$0.25 \pm 0.19$
3	$23.4 \pm 0.2$	$8.0 \pm 1.1$	$0.37 \pm 0.20$
4	$23.4 \pm 0.3$	$7.3 \pm 1.0$	$0.37 \pm 0.23$
5	$23.6 \pm 0.2$	$6.3 \pm 0.9$	$0.26 \pm 0.21$

**Table S5. Ridges extracted for the wild-type mice recorded in constant darkness for 20 days. The reported value is the mean  $\pm$  the standard deviation.**

**E. Wild-type 21 day.** For the 21 day WT DD mice, the median circadian period was  $23.6 \pm 0.2$  hours, the median low frequency ultradian period was  $6.7 \pm 0.8$  hours and the median high frequency ultradian period was  $0.31 \pm 0.19$  hours.

Mouse	Circadian (27-11hrs)	Low frequency ultradian(11-4hrs)	High frequency ultradian (4-0.04hrs)
1	$23.5 \pm 0.2$	$6.1 \pm 0.8$	$0.28 \pm 0.19$
2	$23.6 \pm 0.2$	$7.4 \pm 0.8$	$0.31 \pm 0.20$
3	$23.7 \pm 0.5$	$6.2 \pm 0.5$	$0.22 \pm 0.16$
4	$23.6 \pm 0.2$	$6.2 \pm 0.7$	$0.36 \pm 0.18$
5	$23.5 \pm 0.3$	$7.1 \pm 1.5$	$0.35 \pm 0.19$
6	$23.7 \pm 0.3$	$8.0 \pm 0.9$	$0.31 \pm 0.20$

**Table S6. Ridges extracted for the wild-type mice recorded in constant darkness for 21 days. The reported value is the mean  $\pm$  the standard deviation.**

108 **5. Harmonic analysis**

109 Here we present the harmonic analysis from each mouse analysed. due to the shortness of recordings, harmonic and coupling  
110 analyses were not attempted in the multiple condition, or wild-type 20 and 21 day datasets. As opposed to the other plots in  
111 this supporting information, we have represented the additional harmonic plots in continuous, rather than contour, format.  
112 This is to retain signatures of smaller harmonics that may be difficult to discern following the application of contour lines.

113 **A. Heterozygous PER2::LUC knockin and wild-type littermate group, 30 day.** Here we present the harmonic analysis for each of  
114 the mice in the heterozygous PER2::LUC knockin and wild-type littermate group. There is clear evidence of a harmonic relation  
115 from the circadian rhythm. Therefore the activity at 12, 8 and 6 hours is unlikely to be a wholly independent oscillation.

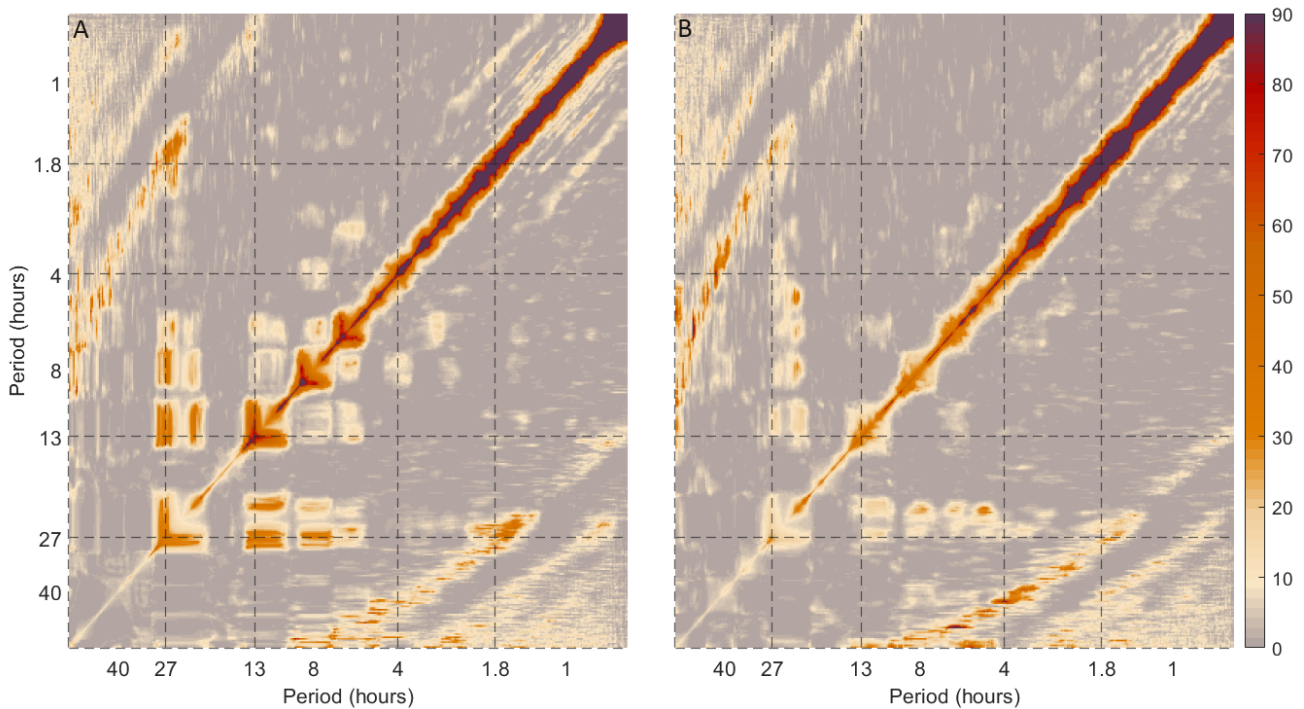


**Fig. S62.** Harmonic analysis for mouse 1 (A) and mouse 2 (B) in the heterozygous PER2::LUC knockin and wild-type littermate 30 day group.

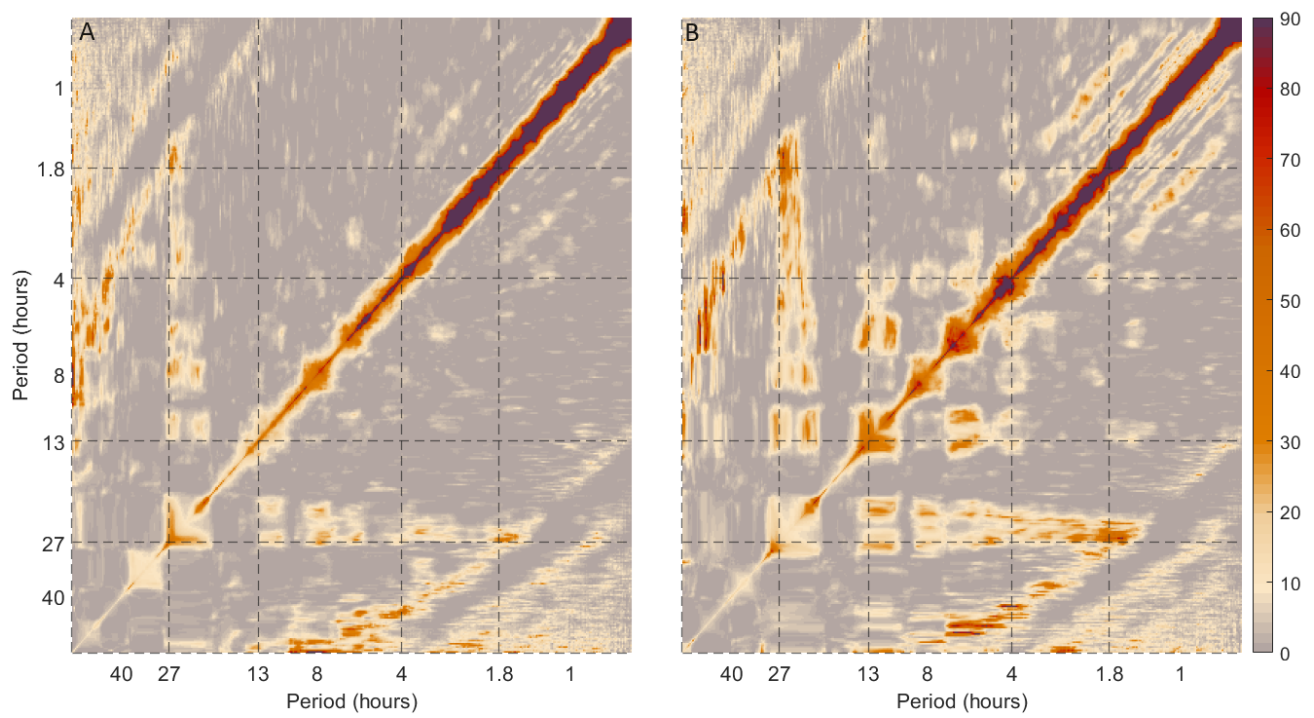


**Fig. S63.** Harmonic analysis for mouse 3 (A) and mouse 4 (B) in the heterozygous PER2::LUC knockin and wild-type littermate 30 day group.

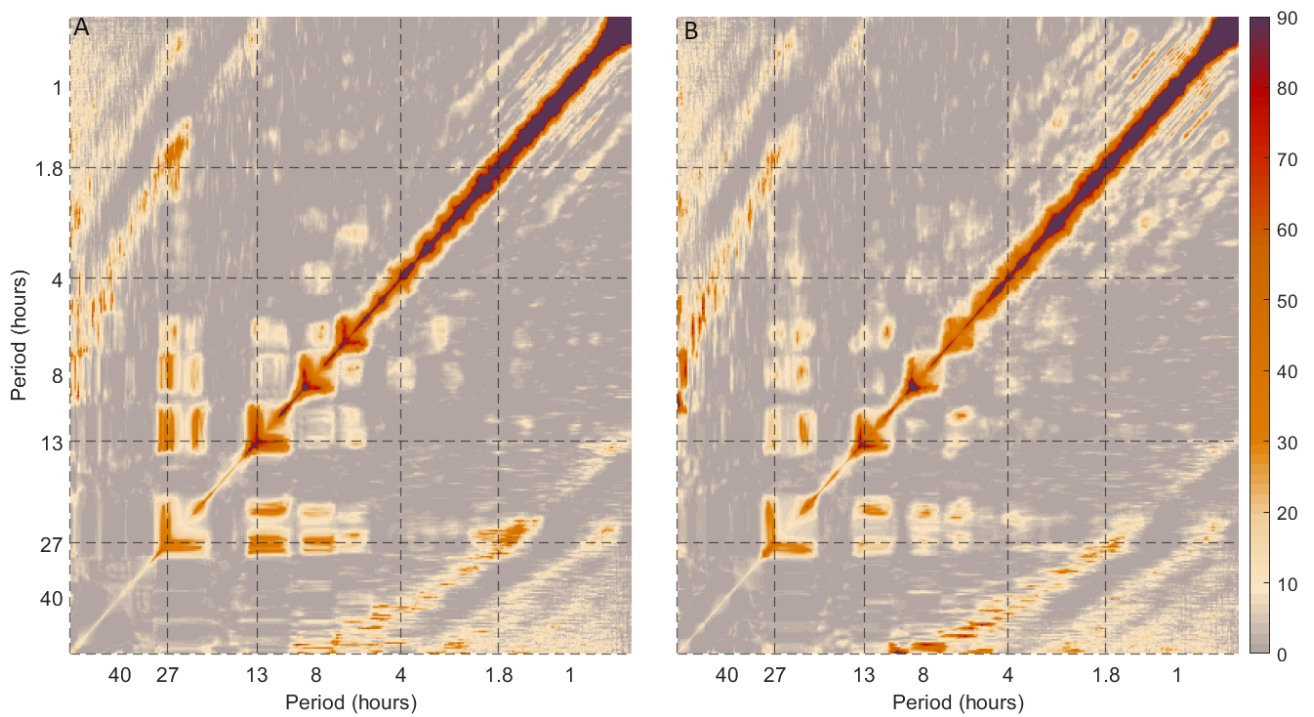


**Fig. S64.** Harmonic analysis for mouse 5 (A) and mouse 6 (B) in the heterozygous PER2::LUC knockin and wild-type littermate 30 day group.



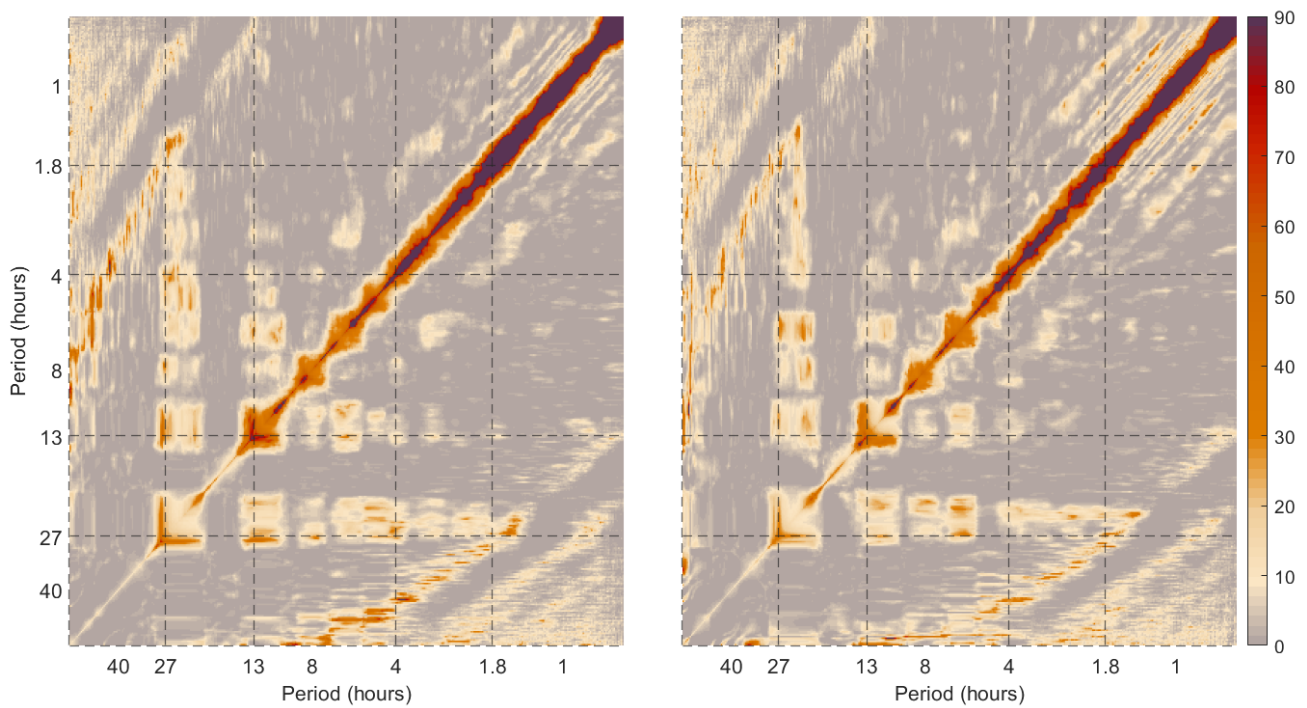


**Fig. S65.** Harmonic analysis for mouse 7 (A) and mouse 8 (B) in the heterozygous PER2::LUC knockin and wild-type littermate 30 day group.

116 **B. *Per1/2/3* KO DD.** Here we present the harmonic analysis for each of the mice in the 65 day *Per1/2/3* KO DD group. There is  
 117 some evidence of a harmonic between 7 and 3.5 hours.

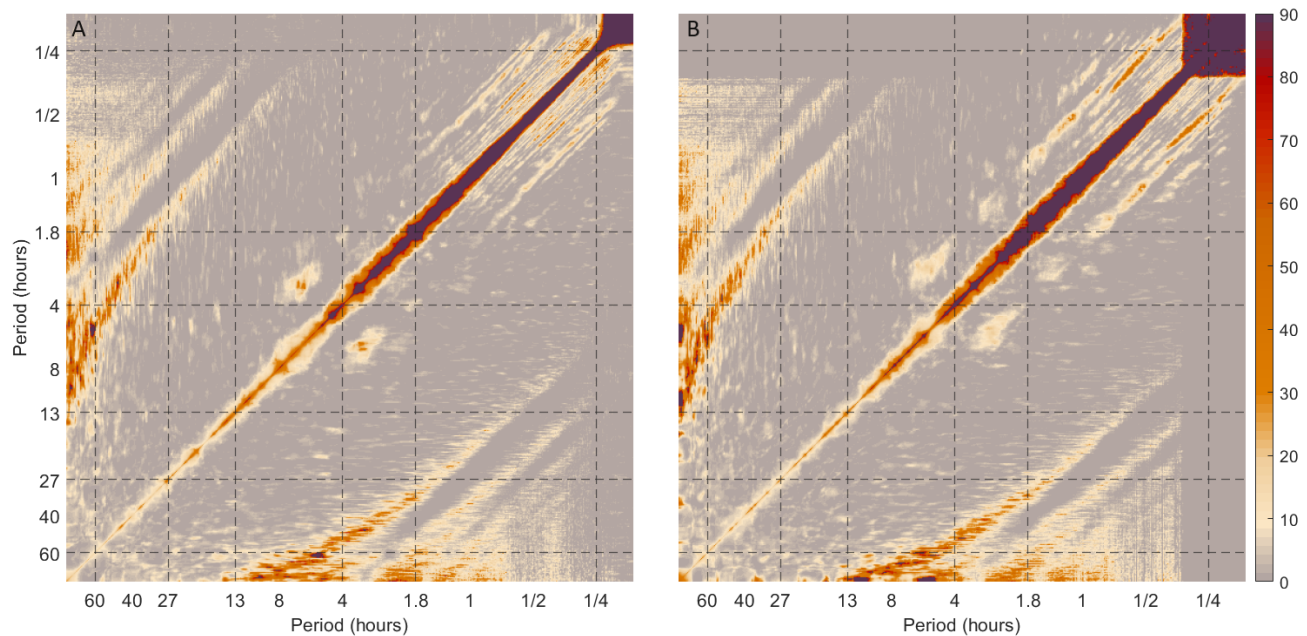


**Fig. S66.** Harmonic analysis for mouse 1 (A) and mouse 2 (B) in the *Per1/2/3* KO DD group.

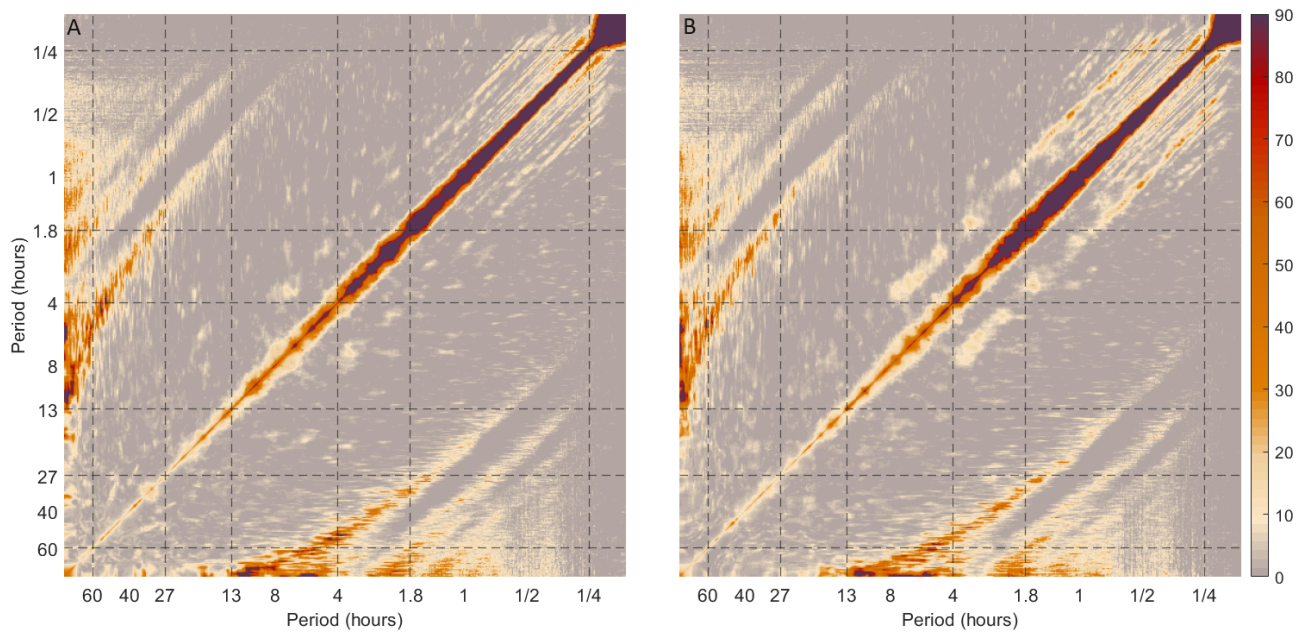


**Fig. S67.** Harmonic analysis for mouse 3 (A) and mouse 4 (B) in the *Per1/2/3* KO DD group.

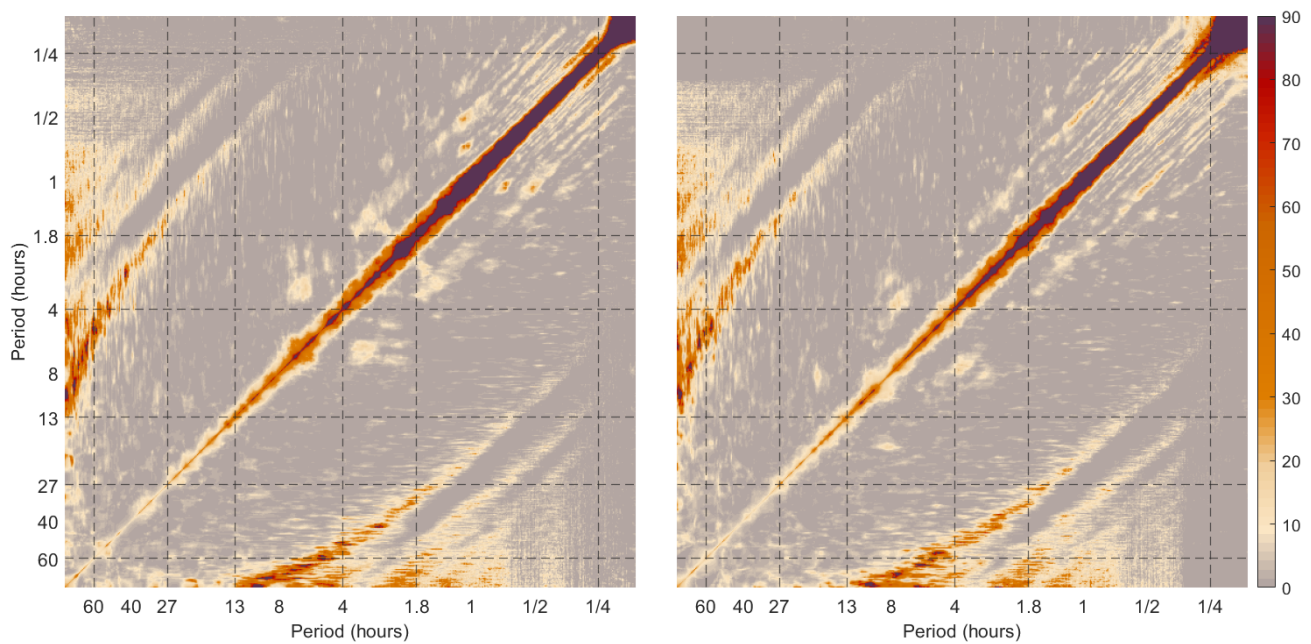


**Fig. S68.** Harmonic analysis for mouse 5 (A) and mouse 6 (B) in the *Per1/2/3* KO DD group.



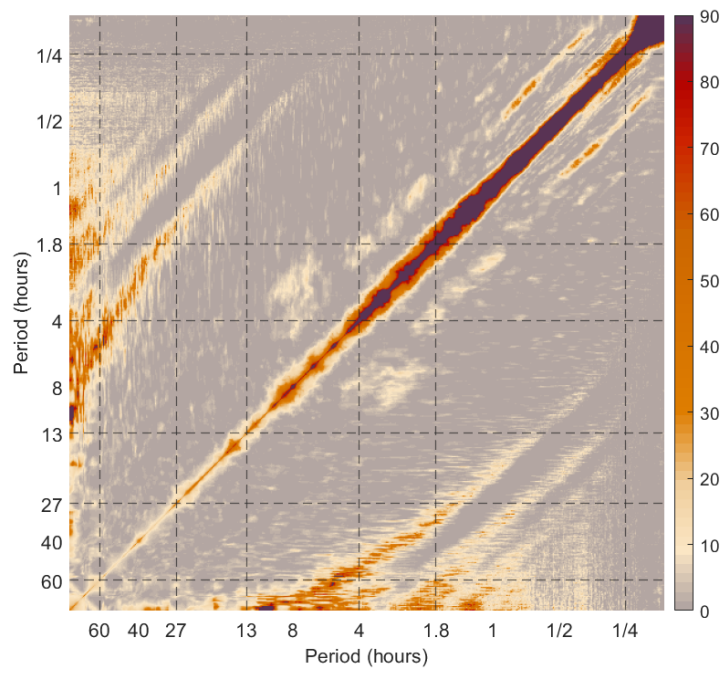


**Fig. S69.** Harmonic analysis for mouse 7 in the *Per1/2/3* KO DD group.

118 **C. *Per1/2/3* KO DD MA.** Here we present the harmonic analysis for each of the mice in the 65 day *Per1/2/3* KO DD MA mice.  
 119 There was no consistent evidence of harmonic relations between the oscillatory modes.

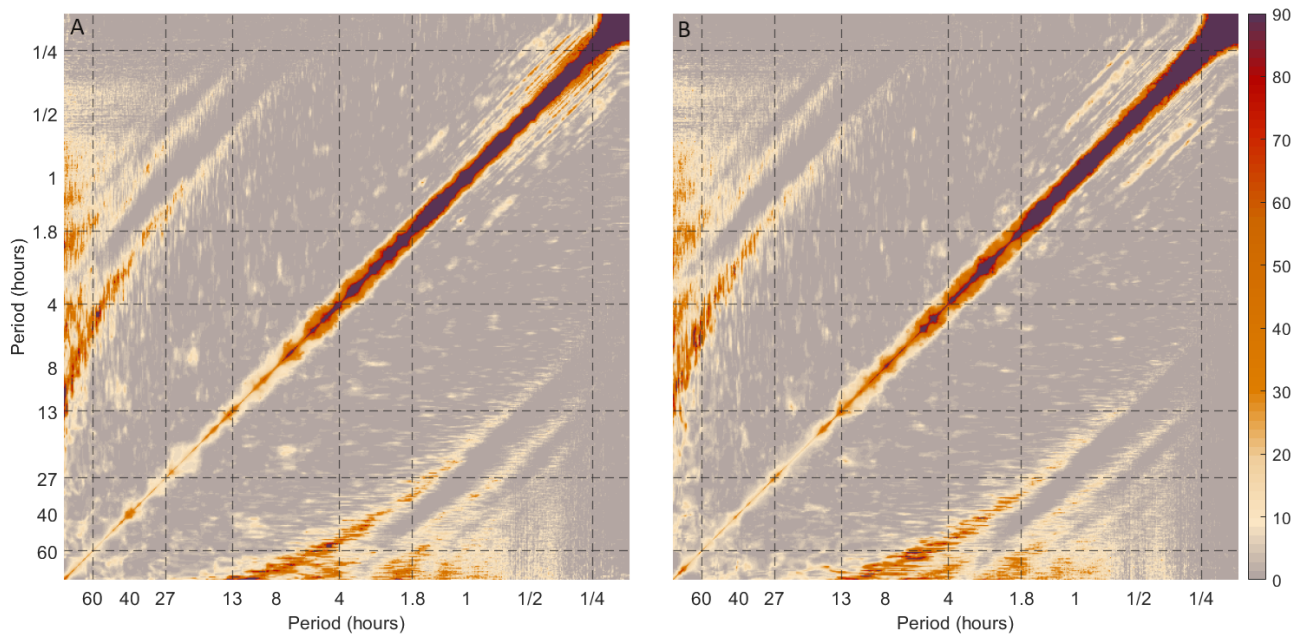


**Fig. S70.** Harmonic analysis for mouse 1 (A) and mouse 2 (B) in the *Per1/2/3* KO DD MA group.



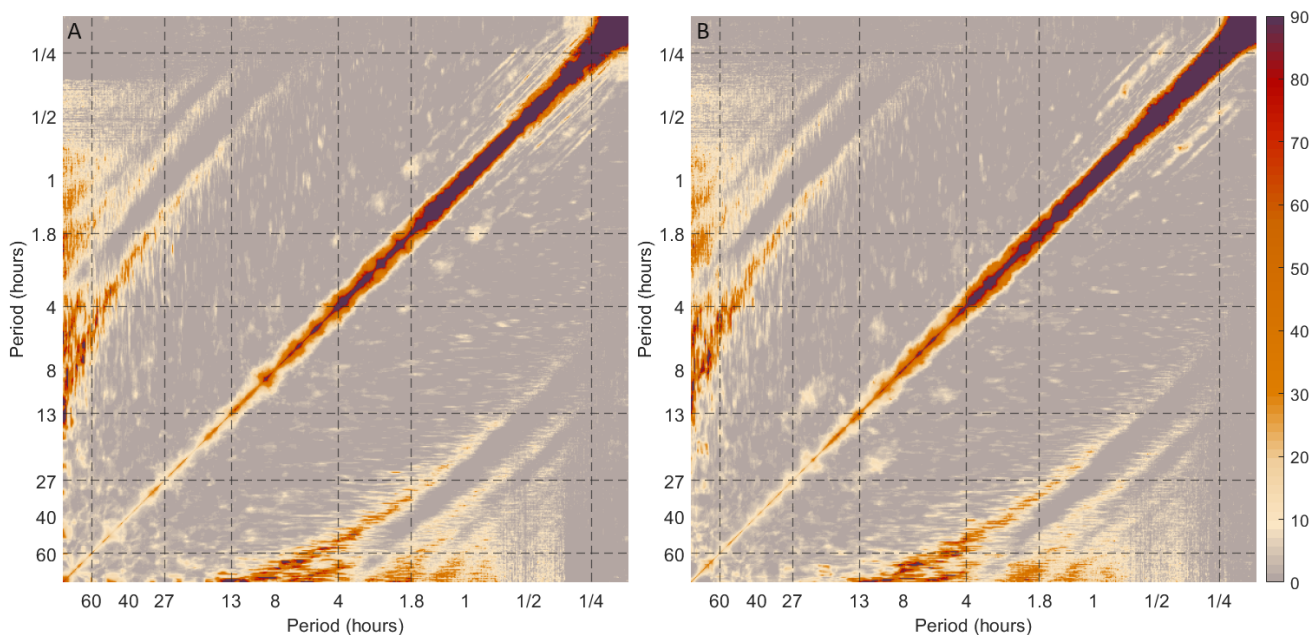


**Fig. S71.** Harmonic analysis for mouse 3 (A) and mouse 4 (B) in the *Per1/2/3* KO DD MA group.

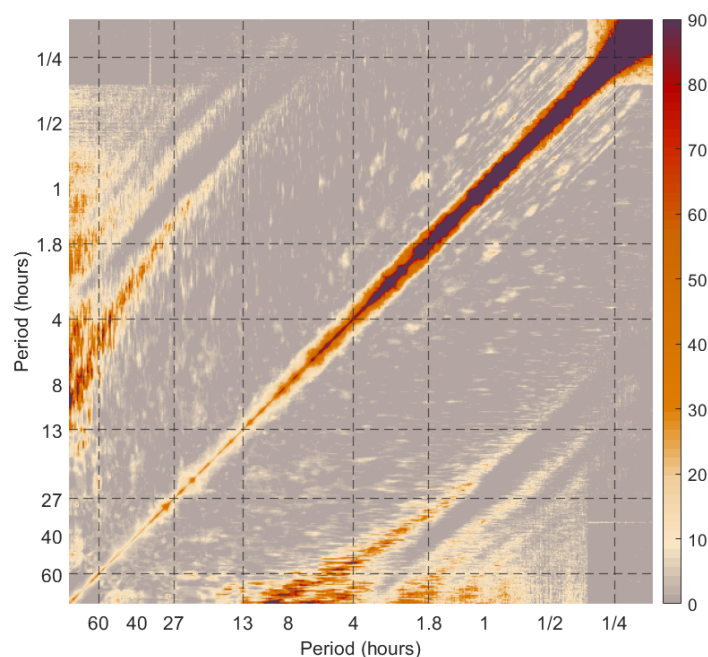


**Fig. S72.** Harmonic analysis for mouse 5 in the *Per1/2/3* KO DD MA group.

## 6. Bispectral analysis

Bispectral analysis was applied to the 30 day wild-type, *Per1/2/3* KO DD and *Per1/2/3* KO DD MA groups to uncover the presence of phase couplings between modes.

**A. Heterozygous *PER2::LUC* knockin and wild-type littermate 30 day group, 30 day.** As the Heterozygous *PER2::LUC* knockin and wild-type littermate 30 day group mice were only recorded for 30 days, there was insufficient information to observe couplings to the entire high frequency band. Although some evidence of coupling was found in the other frequency bands, this was not consistent throughout mice.

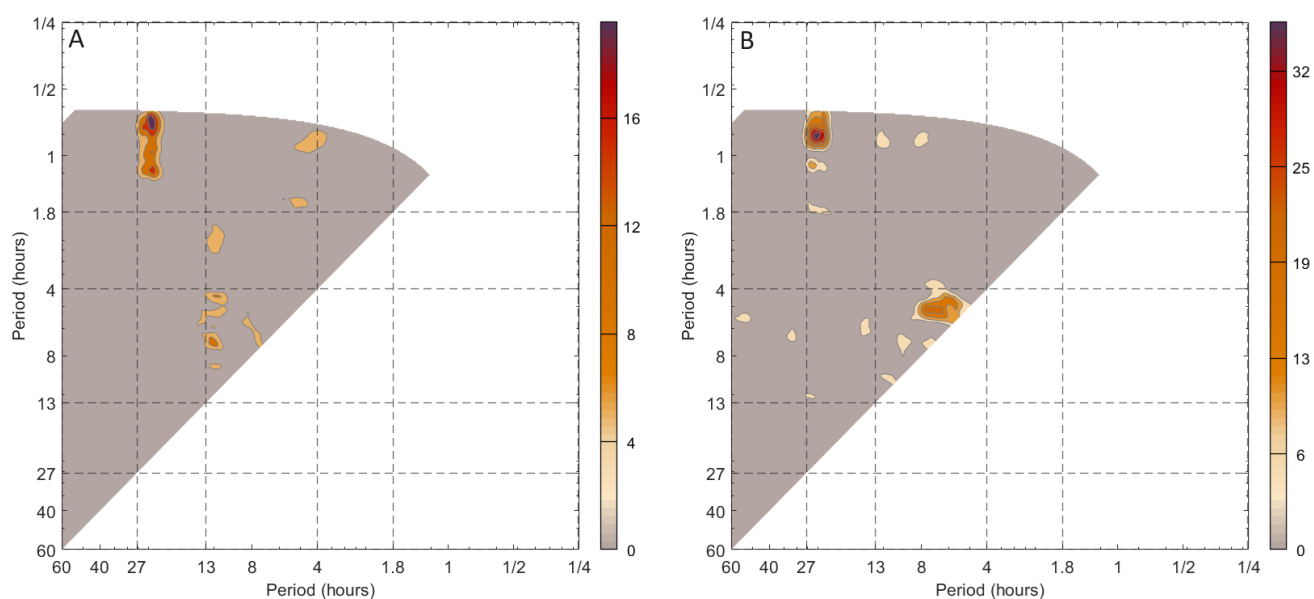


**Fig. S73.** Bispectral analysis for mouse 1 (A) and 2 (B) in the 30 day heterozygous PER2::LUC knockin and wild-type littermate 30 day group.

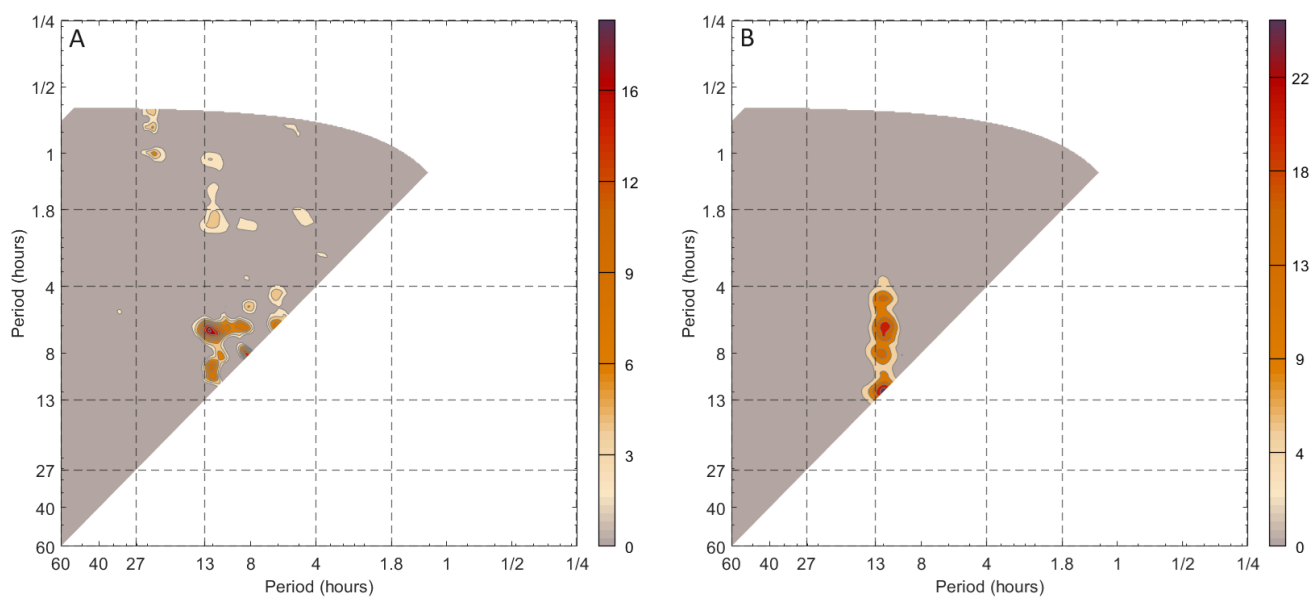


**Fig. S74.** Bispectral analysis for mouse 3 (A) and 4 (B) in the 30 day heterozygous PER2::LUC knockin and wild-type littermate 30 day group.

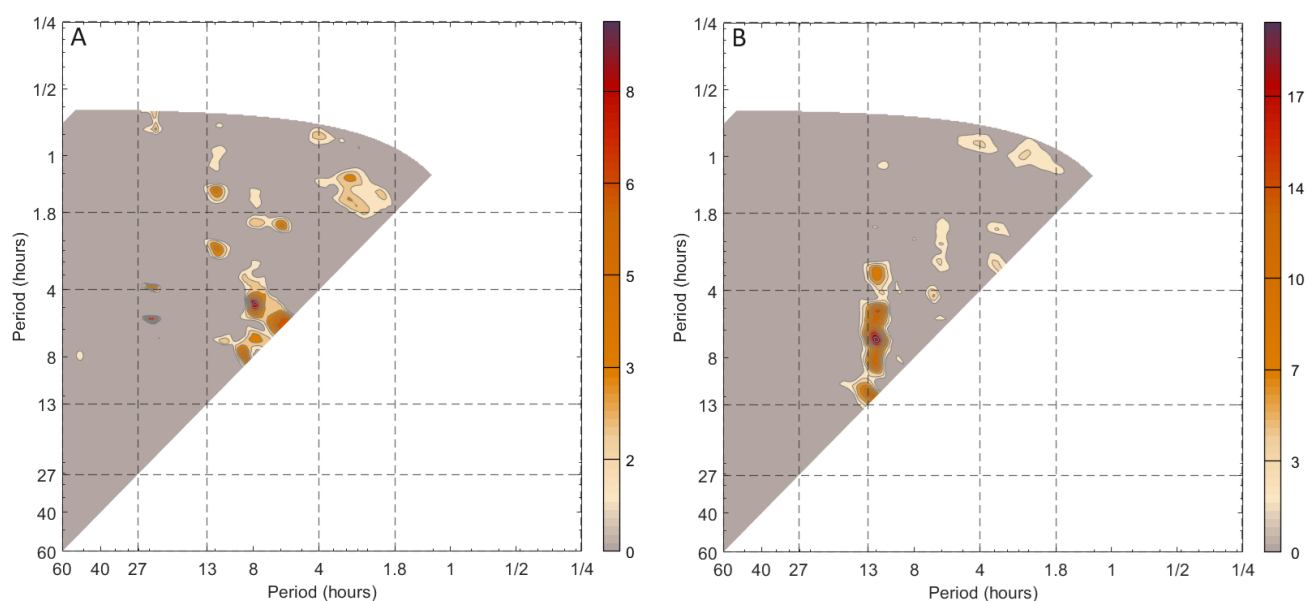


**Fig. S75.** Bispectral analysis for mouse 5 (A) and 6 (B) in the 30 day heterozygous PER2::LUC knockin and wild-type littermate 30 day group.

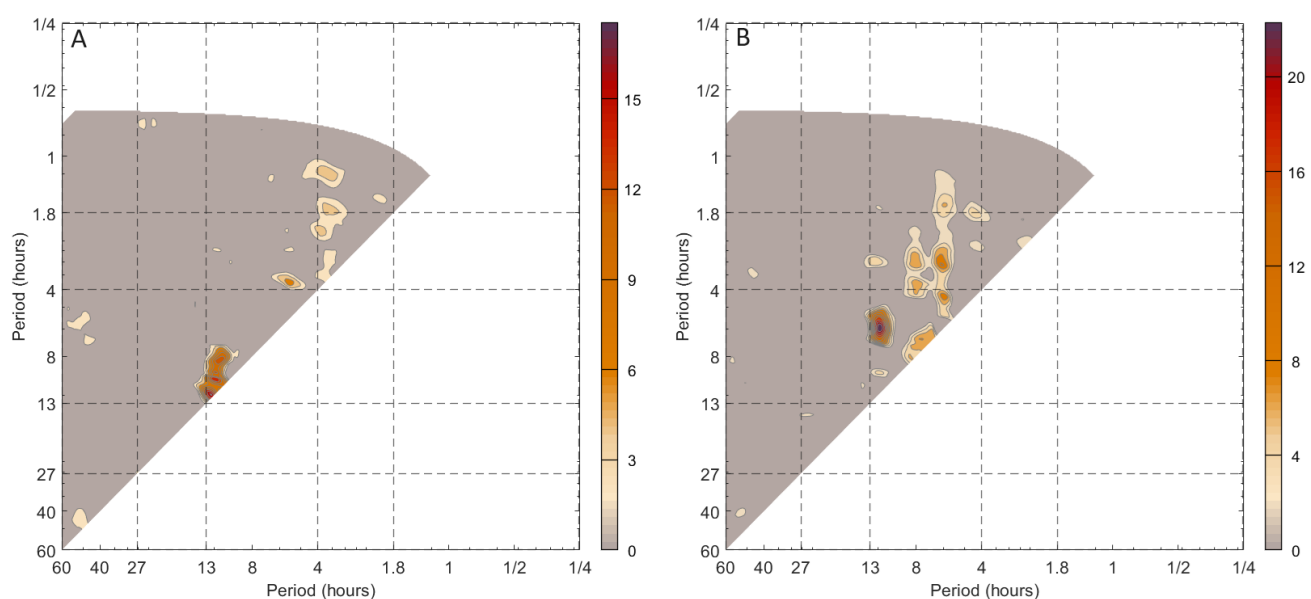


**Fig. S76.** Bispectral analysis for mouse 7 (A) and 8 (B) in the 30 day heterozygous PER2::LUC knockin and wild-type littermate 30 day group.

127 **B. *Per1/2/3* KO DD.** In the *Per1/2/3* KO DD group there was clear evidence of a coupling between high frequency activity and  
 128 the around 7 hour oscillation in all of the mice. Some circadian to high frequency coupling was also seemingly present, but did  
 129 not constitute the dominant coupling and was not consistent throughout all mice. Mouse 2 was not evaluated as it did not  
 130 complete the full recording length.

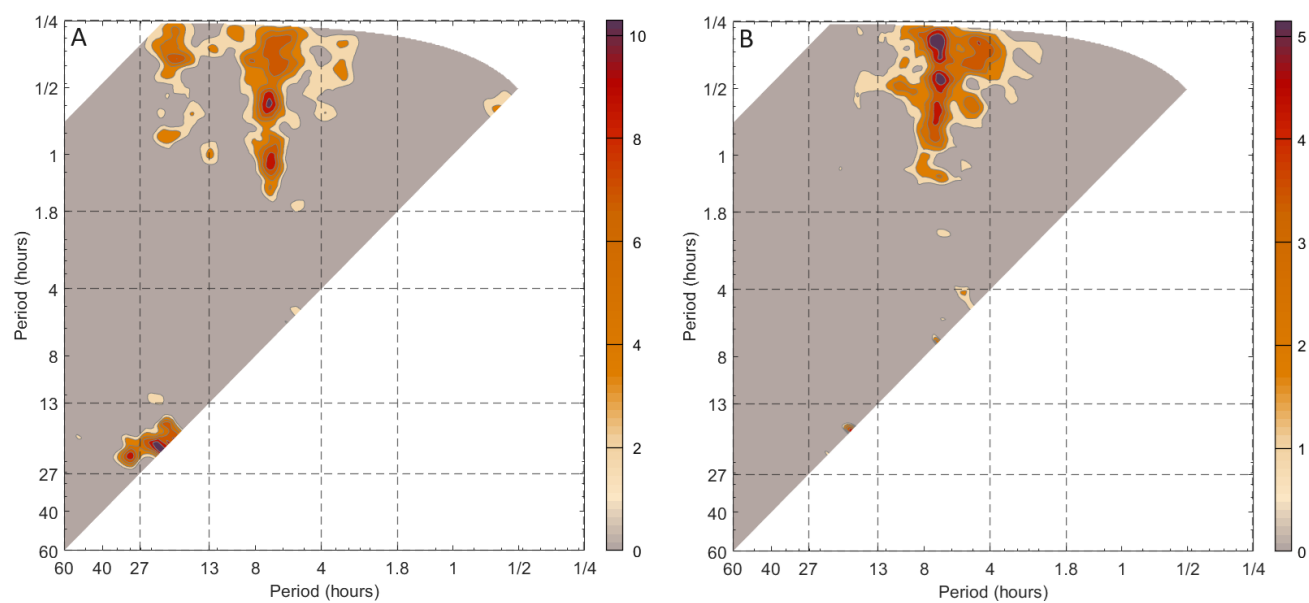


**Fig. S77.** Bispectral analysis for mouse 1 (A) and mouse 3 (B) in the *Per1/2/3* KO DD group.

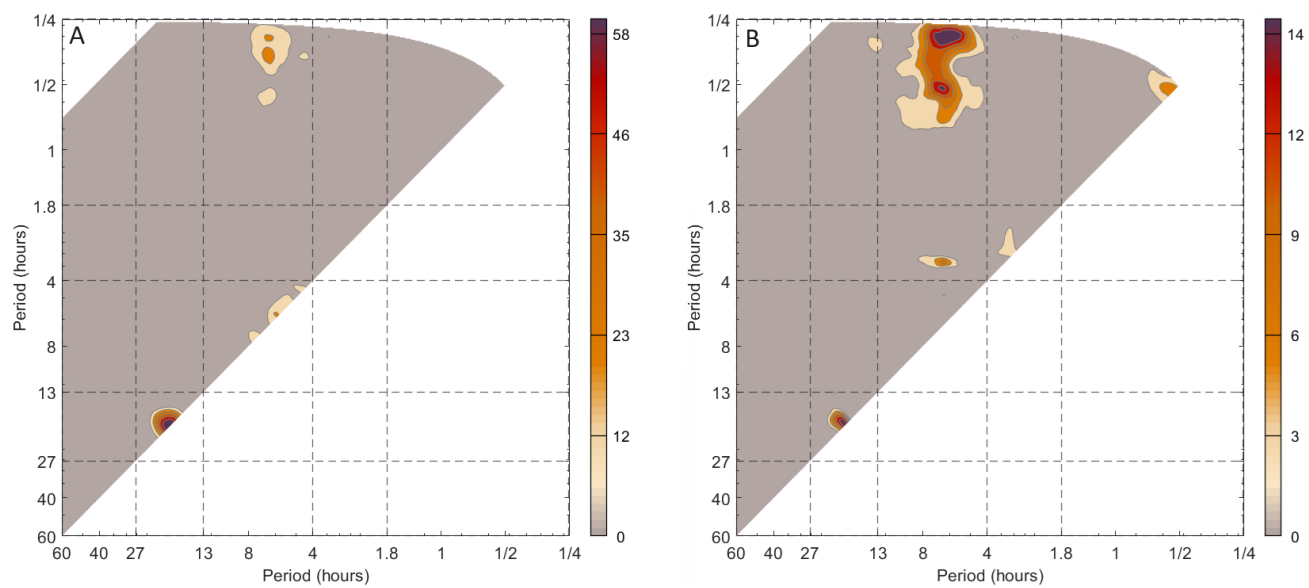


**Fig. S78.** Bispectral analysis for mouse 4 (A) and mouse 5 (B) in the *Per1/2/3* KO DD group.

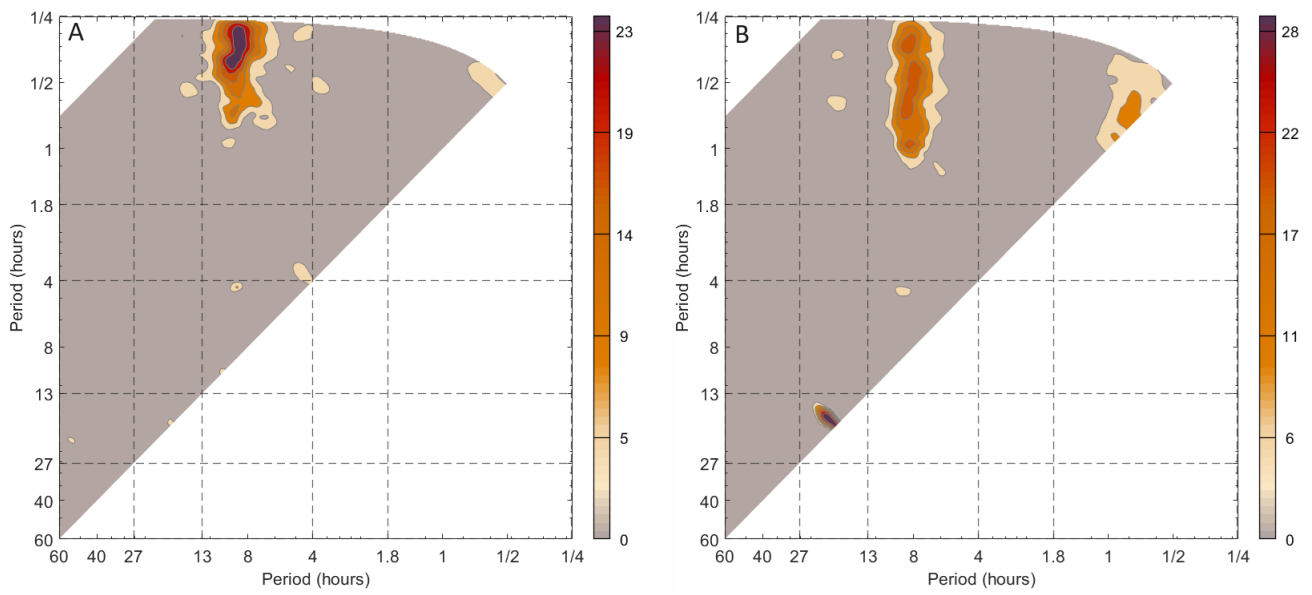


**Fig. S79.** Bispectral analysis for mouse 6 (A) and 7 (B) in the *Per1/2/3* KO DD group.

**C. *Per1/2/3* KO DD MA.** For the *Per1/2/3* KO DD MA group a strong coupling between the MASCO and high frequency activity was present across all the mice. Some mice also had traces of a coupling from around 7 hours to the higher frequencies, but the MASCO coupling was dominant and reflected a switch in the behavioural mode driving the high frequencies.

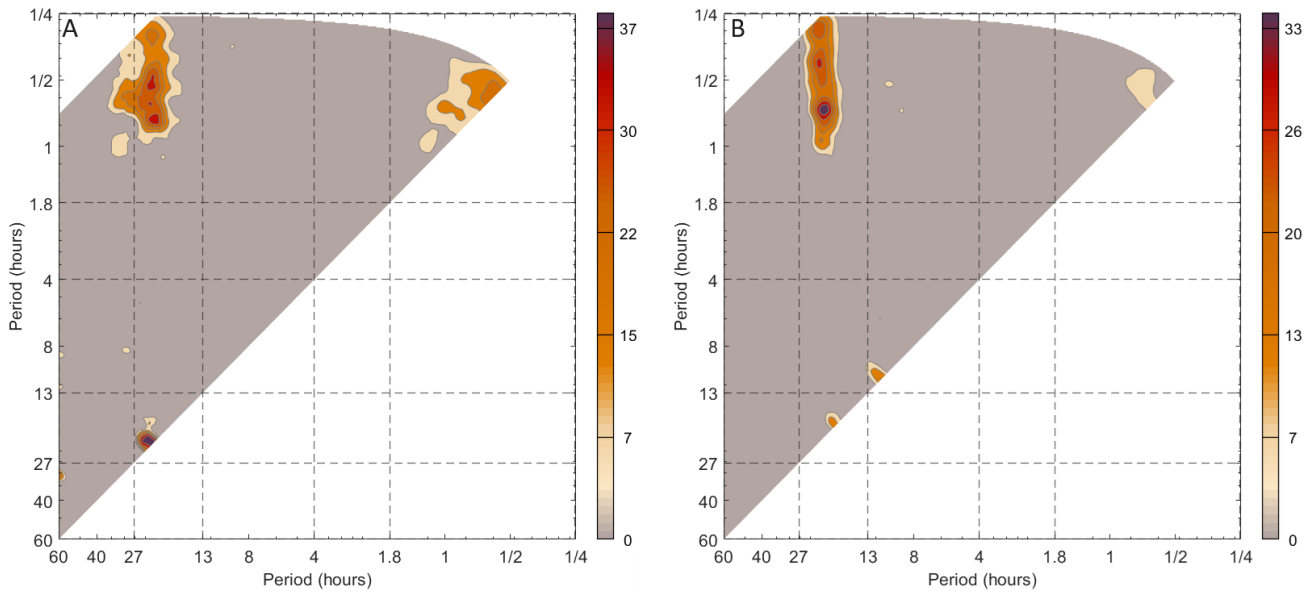


**Fig. S80.** Bispectral analysis for mouse 1 (A) and 2 (B) in the *Per1/2/3* KO DD MA group.

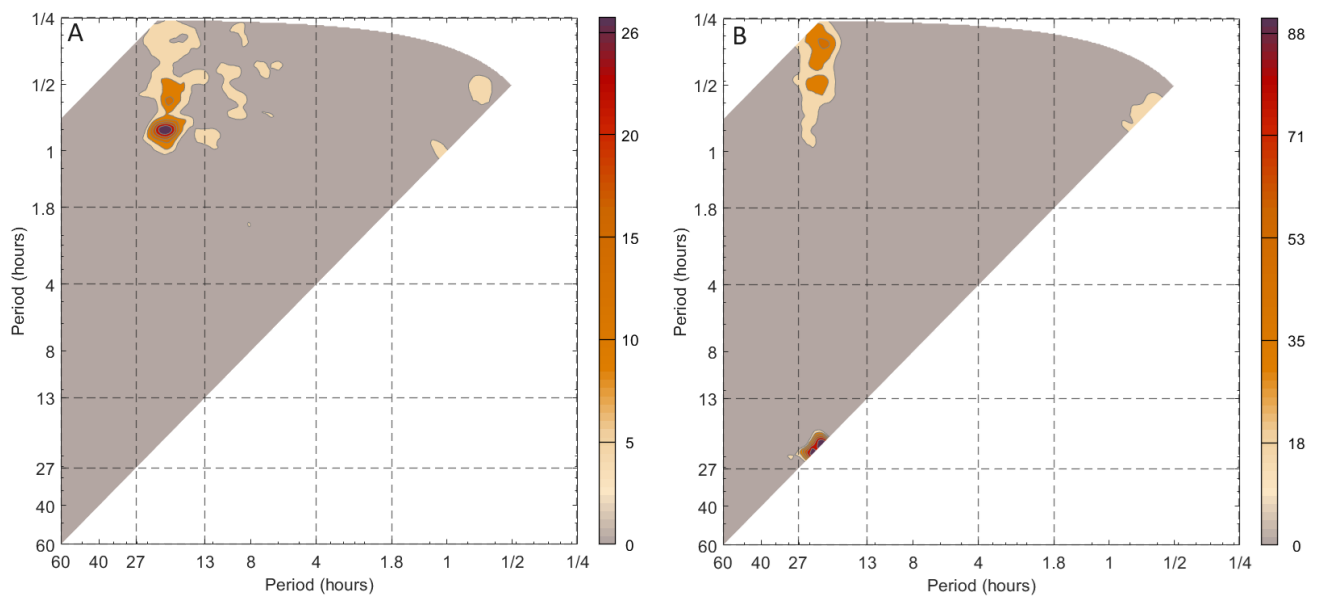


**Fig. S81.** Bispectral analysis for mouse 3 (A) and 4 (B) in the *Per1/2/3* KO DD MA group.

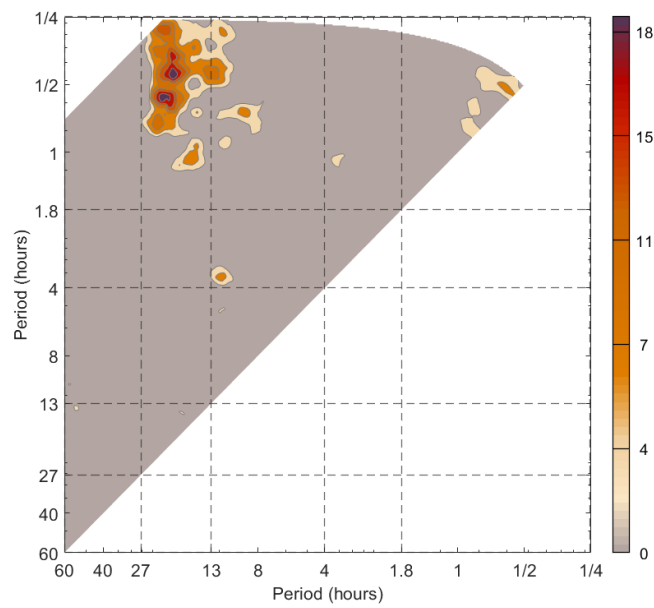


**Fig. S82.** Bispectral analysis for mouse 5 in the *Per1/2/3* KO DD MA group.

## 7. The model

Coupled phase oscillators were used to model the oscillatory modes and couplings found in the behavioural data. In this way, a ground truth with known parameters can be established to compare the results of the experimental investigation against.

**A. *Per1/2/3* KO mice.** The general structure of the model for the *Per1/2/3* KO DD mice with and without methamphetamine administration consisted of three main oscillators, one high frequency, one at around seven hours and a roughly circadian oscillator. As in the real data, the time step was set to 1 minute and time series length was 65 days. The coupling parameters were chosen to reflect the observed dynamics. The coupled phase equations for *Per1/2/3* KO DD mice are as follows

$$\begin{aligned}\dot{\phi}_1 &= \omega_1 \\ \dot{\phi}_2 &= \omega_2, \\ \dot{\phi}_3 &= \omega_3 + E_1 \cos(\phi_1 + \pi/2.5) + E_2 \cos(\phi_2 + \pi/2.5),\end{aligned}\tag{1}$$

Where  $E$  represents the coupling strength and  $\phi_i$  are the phases of each oscillator, which are subsequently added together following Runge-Kutta 4-step numerical integration to produce a time-series,

$$X(t) = A_1 \cos(\phi_1(t)) + A_2 \cos(\phi_2(t)) + A_3 \cos(\phi_3(t)).\tag{2}$$

The amplitudes,  $A$ , were selected to be the best recreation of the observed power spectra. The natural frequencies changed over time to allow us to represent the time-variability witnessed in the experimental results,

$$\omega_i(t) = \omega_{i0} + Amp_i sq(\omega_{ivar} * t),\tag{3}$$

where  $\omega_{i0}$  is the natural frequency,  $sq$  represents a square wave, and  $Amp_i$  is the amplitude of the frequency variation.

**B. Wild-type mice.** For the wild-type mice, there seemed to be several coupled modes present, with the circadian clearly the most dominant. As such, multiple phase oscillators were used

$$\begin{aligned}\dot{\phi}_1 &= \omega_1 + E_1 \cos(\phi_6 + \pi/2.5), \\ \dot{\phi}_2 &= \omega_2, \\ \dot{\phi}_3 &= \omega_3 + E_2 \cos(\phi_2 + \pi/2.5), \\ \dot{\phi}_4 &= \omega_4 + E_3 \cos(\phi_3 + \pi/2.5), \\ \dot{\phi}_5 &= \omega_5 + E_4 \cos(\phi_4 + \pi/2.5), \\ \dot{\phi}_6 &= \omega_6 + E_5 \cos(\phi_4 + \pi/2.5) + E_6 \cos(\phi_1 + \pi/2.5),\end{aligned}\tag{4}$$

The parameters for each of these configurations are as follows

Parameters	Wild-type	<i>Per1/2/3</i> KO DD	<i>Per1/2/3</i> KO DD MA
$\omega_{10}$ (Hz)	24	20	22
$\omega_{20}$ (Hz)	7.2	7.5	8
$\omega_{30}$ (Hz)	6	0.5	0.5
$\omega_{40}$ (Hz)	3	NA	NA
$\omega_{50}$ (Hz)	1.25	NA	NA
$\omega_{60}$ (Hz)	0.75	NA	NA
$\epsilon_1$	0.1	0.05	0.2
$\epsilon_2$	0.1	0.2	0.05
$\epsilon_3$	0.1	NA	NA
$\epsilon_4$	0.1	NA	NA
$\epsilon_5$	0.1	NA	NA
$\epsilon_6$	0.1	NA	NA
$A_1$	1.5	0.8	0.85
$A_2$	0.25	0.3	0.3
$A_3$	0.25	0.85	0.8
$A_4$	0.5	NA	NA
$A_5$	0.65	NA	NA
$A_6$	0.3	NA	NA



Parameters	Wild-type	<i>Per1/2/3</i> KO DD	<i>Per1/2/3</i> KO DD MA
$\omega_{1var}$ (Hz)	0.0000025	0.00025	0.00025
$\omega_{2var}$ (Hz)	0.0005	0.0003	0.0003
$\omega_{3var}$ (Hz)	0.001	0.1	0.1
$\omega_{4var}$ (Hz)	0.0025	NA	NA
$\omega_{5var}$ (Hz)	0.05	NA	NA
$\omega_{6var}$ (Hz)	0.015	NA	NA
$Amp_1$	0.000000000001	0.0005	0.0005
$Amp_2$	0.00001	0.0015	0.0015
$Amp_3$	0.0005	0.125	0.125
$Amp_4$	0.000001	NA	NA
$Amp_5$	0.0001	NA	NA
$Amp_6$	15	NA	NA

**C. Recreating Fig.1.** To demonstrate the feasibility of the model, here we recreate the figures from the main paper, using the simulated data. Despite being a phase based model, the powers are able to be reproduced.

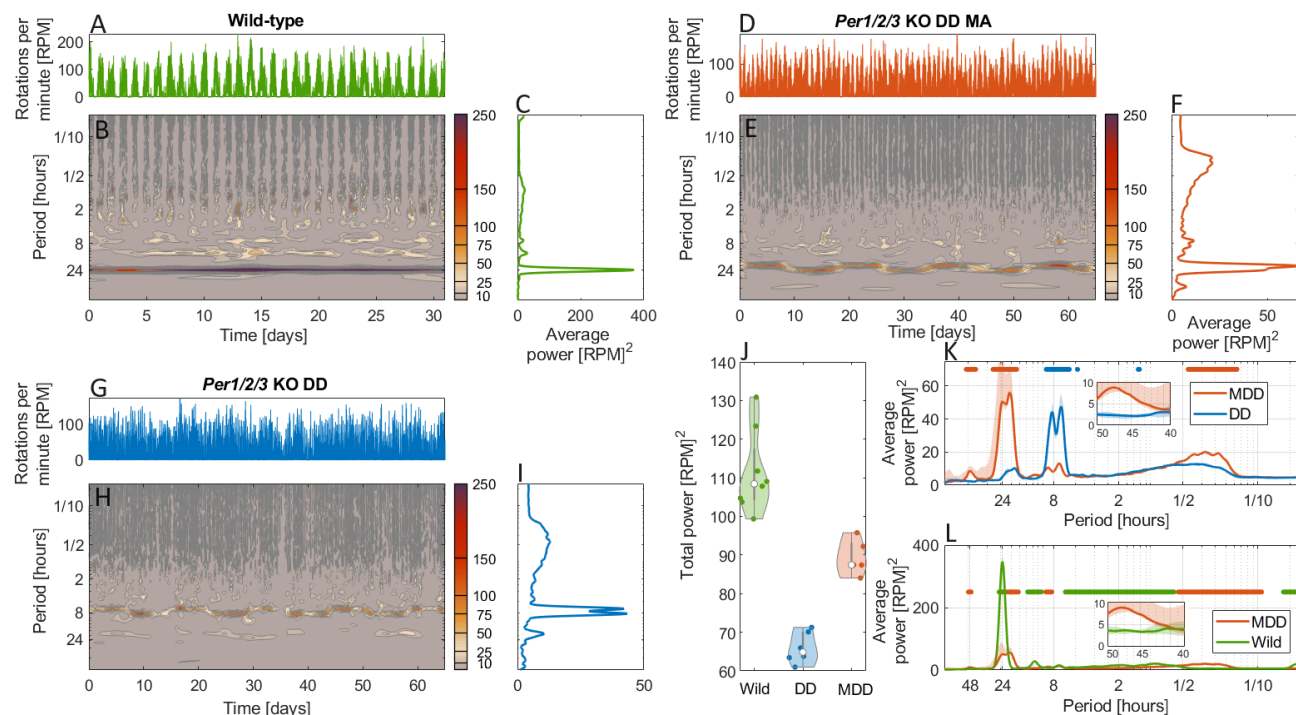


**Fig. S83.** A model simulated to recreate the multiscale oscillatory activity in wild-type and *Per1/2/3* KO mice with and without methamphetamine administration. (A, D, G) Time-series of wheel rotations per minute the wild-type, *Per1/2/3* KO DD MA, and *Per1/2/3* KO DD mice. (B, E, H) Time/frequency representations of the wild-type, *Per1/2/3* KO DD MA and *Per1/2/3* KO DD data. (C, F, I) Time-averaged power for each group, respectively. (J) Total power evaluated between periods of 84 hours and 4 minutes in each condition. (K,L) Group median time-averaged power plots. (K) Compares the *Per1/2/3* KO mice with and without methamphetamine, while (L) compares the *Per1/2/3* KO DD MA and wild-type mice. The shading represents the 25th and 75th percentile while the circles indicate frequencies where there were significant differences between groups, with the colour of the circle indicating the group with the greater power (Wilcoxon rank-sum test  $p < 0.01$ ).

Using coupled phase oscillators we are able to reproduce the time-localised power behaviour in a manor reminiscent to that in the real results. The use of square waves for the varying oscillator frequencies enabled the accurate representation of the experimental data.

160 **D. Recreating Fig.3.** Fig. S84 Demonstrates a switch in the primary coupling from 7 hours driving the high frequency activity  
 161 to a circadian oscillation being the dominant coupled oscillator. This was achieved by simply changing the degree of phase  
 162 coupling in the model. The purpose of this illustrative example is to show that the system may be described as coupled phase  
 163 oscillators, and that the results in the main body are due to a changing in the coupling strength between components.

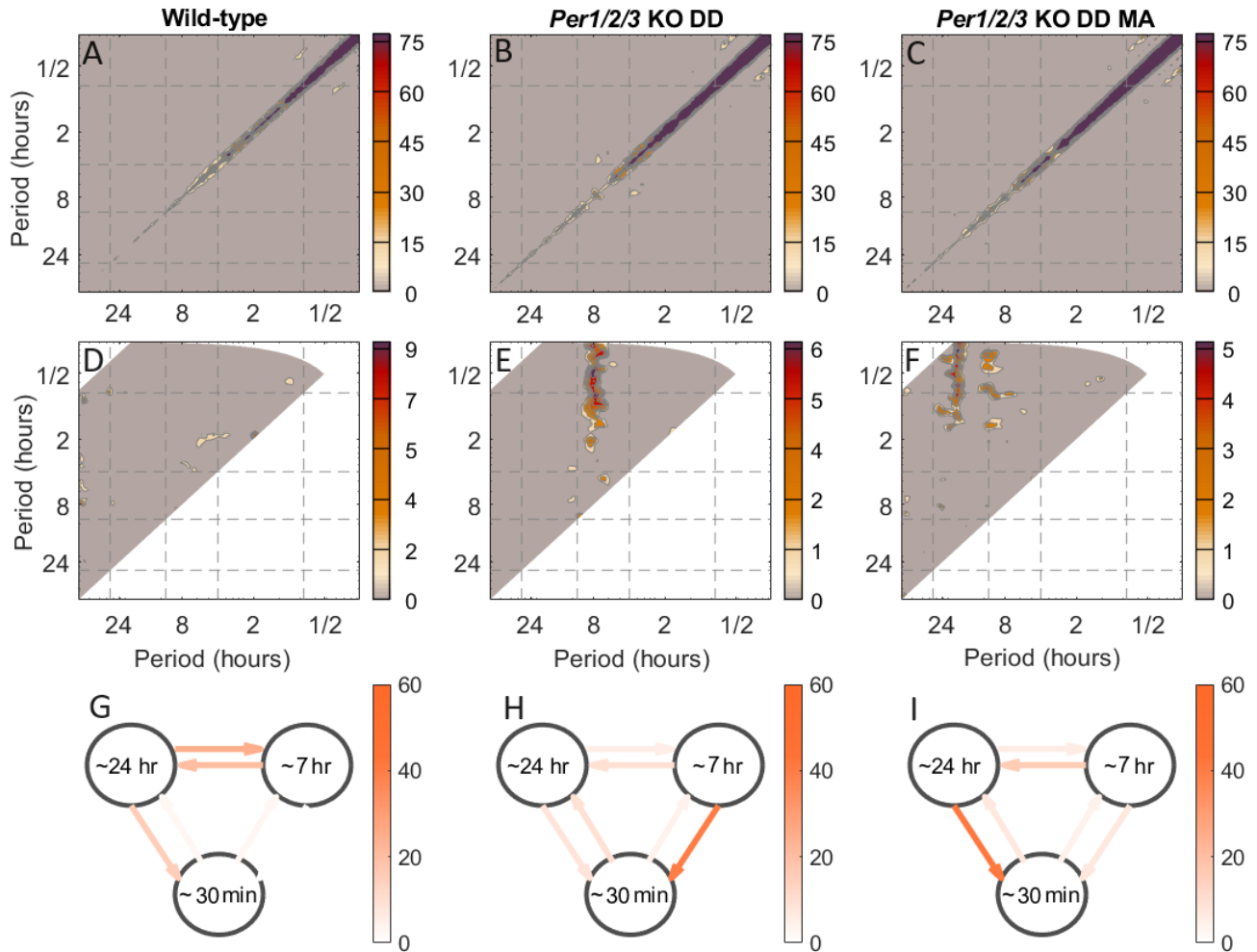


**Fig. S84.** Model replication of Fig. 3 from the main text. Harmonic and coupling analysis between wild-type (first column), *Per1/2/3* KO DD mice (second column), and *Per1/2/3* KO DD MA (third column). (A - C) Harmonic analysis. Bispectral analysis (D - F) demonstrates couplings between modes at different oscillatory frequencies. Dynamical Bayesian inference (G - I) reveals the percentage time over which oscillatory modes were coupled throughout the time-series.

164 This simple change was sufficient to replicate the dynamics. By use of coupled phase oscillators we are able to recreate the  
 165 observed experimental behaviour. Thus providing evidence that the analysis framework used here, which assumes that the  
 166 system is composed of a number of time-varying oscillatory components, was appropriate.

# Bibliography

- [1] Dorota Ali et al. “‘The key to this is not so much the technology. It’s the individual who is using the technology’: Perspectives on telehealth delivery for autistic adults during the COVID-19 pandemic”. In: *Autism* 27.2 (2023), pp. 552–564.
- [2] Anne Masi et al. “An overview of autism spectrum disorder, heterogeneity and treatment options”. In: *Neuroscience Bulletin* 33 (2017), pp. 183–193.
- [3] American Psychiatric Association. *Diagnostic and Statistical Manual of Mental Disorders*. 5th. American Psychiatric Association, 2013.
- [4] Holly Hodges, Casey Fealko, and Neelkamal Soares. “Autism spectrum disorder: definition, epidemiology, causes, and clinical evaluation”. In: *Translational Pediatrics* 9 (2020), S55.
- [5] Ginny Russell et al. “Time trends in autism diagnosis over 20 years: a UK population-based cohort study”. In: *Journal of Child Psychology and Psychiatry* 63.6 (2022), pp. 674–682.
- [6] Marcus E Raichle and Debra A Gusnard. “Appraising the brain’s energy budget”. In: *Proceedings of the National Academy of Sciences* 99.16 (2002), pp. 10237–10239.
- [7] Alexandre Vallée and Jean-Noël Vallée. “Warburg effect hypothesis in autism Spectrum disorders”. In: *Molecular Brain* 11 (2018), pp. 1–7.
- [8] Alexandre Vallée, Yves Lecarpentier, and Jean-Noël Vallée. “The key role of the WNT/ $\beta$ -catenin pathway in metabolic reprogramming in cancers under normoxic conditions”. In: *Cancers* 13.21 (2021), p. 5557.

- [9] Luigi Palmieri and Antonio M Persico. "Mitochondrial dysfunction in autism spectrum disorders: cause or effect?" In: *Biochimica et Biophysica Acta (BBA)-Bioenergetics* 1797.6-7 (2010), pp. 1130–1137.
- [10] Miae Oh, Soon Ae Kim, and Hee Jeong Yoo. "Higher lactate level and lactate-to-pyruvate ratio in autism spectrum disorder". In: *Experimental Neurobiology* 29.4 (2020), p. 314.
- [11] Simon Maier et al. "Increased cerebral lactate levels in adults with autism spectrum disorders compared to non-autistic controls: a magnetic resonance spectroscopy study". In: *Molecular Autism* 14.1 (2023), p. 44.
- [12] Hideo Hagihara, Tomoyuki Murano, and Tsuyoshi Miyakawa. "The gene expression patterns as surrogate indices of pH in the brain". In: *Frontiers in Psychiatry* 14 (2023), p. 1151480.
- [13] Elena Martinez-Cayuelas et al. "Sleep problems, circadian rhythms, and their relation to behavioral difficulties in children and adolescents with autism spectrum disorder". In: *Journal of Autism and Developmental Disorders* 54.5 (2024), pp. 1712–1726.
- [14] Alexandre Vallée et al. "The influence of circadian rhythms and aerobic glycolysis in autism spectrum disorder". In: *Translational Psychiatry* 10.1 (2020), p. 400.
- [15] Simonne Cohen et al. "The relationship between sleep and behavior in autism spectrum disorder (ASD): a review". In: *Journal of Neurodevelopmental Disorders* 6 (2014), pp. 1–10.
- [16] SK Tahajjul Taufique et al. "Genetics and functional significance of the understudied methamphetamine sensitive circadian oscillator (MASCO)". In: *F1000Research* 11 (2022).
- [17] Olivia J Veatch, Angela C Maxwell-Horn, and Beth A Malow. "Sleep in autism spectrum disorders". In: *Current Sleep Medicine Reports* 1 (2015), pp. 131–140.
- [18] Iman Mohammad-Rezazadeh et al. "Brain connectivity in autism spectrum disorder". In: *Current Opinion in Neurology* 29.2 (2016), p. 137.

- [19] Christian O'Reilly, John D Lewis, and Mayada Elsabbagh. "Is functional brain connectivity atypical in autism? A systematic review of EEG and MEG studies". In: *PloS One* 12.5 (2017), e0175870.
- [20] Eric Courchesne and Karen Pierce. "Why the frontal cortex in autism might be talking only to itself: local over-connectivity but long-distance disconnection". In: *Current Opinion in Neurobiology* 15.2 (2005), pp. 225–230.
- [21] Elena V Orekhova et al. "EEG hyper-connectivity in high-risk infants is associated with later autism". In: *Journal of Neurodevelopmental Disorders* 6 (2014), pp. 1–11.
- [22] Robert Coben et al. "EEG power and coherence in autistic spectrum disorder". In: *Clinical Neurophysiology* 119.5 (2008), pp. 1002–1009.
- [23] Abigail Dickinson et al. "Multivariate neural connectivity patterns in early infancy predict later autism symptoms". In: *Biological Psychiatry: Cognitive Neuroscience and Neuroimaging* 6.1 (2021), pp. 59–69.
- [24] Melody MY Chan et al. "Abnormal prefrontal functional connectivity is associated with inflexible information processing in patients with Autism Spectrum Disorder (ASD): an fNIRS study". In: *Biomedicine* 10.5 (2022), p. 1132.
- [25] Donato Liloia et al. "Atypical local brain connectivity in pediatric autism spectrum disorder? A coordinate-based meta-analysis of regional homogeneity studies". In: *European Archives of Psychiatry and Clinical Neuroscience* 274.1 (2024), pp. 3–18.
- [26] Joe Rowland Adams, Julian Newman, and Aneta Stefanovska. "Distinguishing between deterministic oscillations and noise". In: *The European Physical Journal Special Topics* 232.20 (2023), pp. 3435–3457.
- [27] Sophie Schwartz et al. "Electroencephalogram coherence patterns in autism: an updated review". In: *Pediatric Neurology* 67 (2017), pp. 7–22.
- [28] Samuel JK Barnes et al. "Phase coherence—A time-localized approach to studying interactions". In: *Chaos: An Interdisciplinary Journal of Nonlinear Science* 34.7 (2024).

- [29] Yasemin M Akay. "The Role of Neurons in Human Health and Disease". In: *International Journal of Molecular Sciences* 24.8 (2023), p. 7107.
- [30] Vidar Gundersen, Jon Storm-Mathisen, and Linda Hildegard Bergersen. "Neuroglial transmission". In: *Physiological Reviews* 95.3 (2015), pp. 695–726.
- [31] Shayne Mason. "Lactate shuttles in neuroenergetics—homeostasis, allostasis and beyond". In: *Frontiers in Neuroscience* 11 (2017), p. 43.
- [32] Pedro HM de Freitas et al. "EL, a modern-day Phineas Gage: Revisiting frontal lobe injury". In: *The Lancet Regional Health–Americas* 14 (2022).
- [33] CS Hoyt. "Visual function in the brain-damaged child". In: *Eye* 17.3 (2003), pp. 369–384.
- [34] Peter J Bayley, Ramona O Hopkins, and Larry R Squire. "The fate of old memories after medial temporal lobe damage". In: *Journal of Neuroscience* 26.51 (2006), pp. 13311–13317.
- [35] Hans-Joachim Freund. "Somatosensory and motor disturbances in patients with parietal lobe lesions." In: *Advances in Neurology* 93 (2003), pp. 179–193.
- [36] Sándor Beniczky and Donald Schomer. "Electroencephalography: basic biophysical and technological aspects important for clinical applications". In: *Epileptic Disorders* 6 (2020), pp. 697–715.
- [37] Paul L Nunez et al. "A theoretical and experimental study of high resolution EEG based on surface Laplacians and cortical imaging". In: *Electroencephalography and Clinical Neurophysiology* 90.1 (1994), pp. 40–57.
- [38] Jan Holsheimer and BWA Feenstra. "Volume conduction and EEG measurements within the brain: a quantitative approach to the influence of electrical spread on the linear relationship of activity measured at different locations". In: *Electroencephalography and Clinical Neurophysiology* 43.1 (1977), pp. 52–58.
- [39] Elysa J Marco et al. "Sensory processing in autism: a review of neurophysiologic findings". In: *Pediatric Research* 69.8 (2011), pp. 48–54.
- [40] Joachim Gross et al. "Good practice for conducting and reporting MEG research". In: *Neuroimage* 65 (2013), pp. 349–363.



- [41] Christopher Turner et al. "Developmental changes in individual alpha frequency: Recording EEG data during public engagement events". In: *Imaging Neuroscience* 1 (2023), pp. 1–14.
- [42] Dale Purves et al. "Stages of sleep". In: *Neuroscience* 2 (2001).
- [43] Thalía Harmony. "The functional significance of delta oscillations in cognitive processing". In: *Frontiers in Integrative Neuroscience* 7 (2013), p. 83.
- [44] Elizabeth Shephard et al. "Resting-state neurophysiological activity patterns in young people with ASD, ADHD, and ASD+ ADHD". In: *Journal of Autism and Developmental Disorders* 48 (2018), pp. 110–122.
- [45] Hans Berger. "Über das elektroencephalogramm des menschen". In: *Archiv für Psychiatrie und Nervenkrankheiten* 87.1 (1929), pp. 527–570.
- [46] Desmond J Oathes et al. "Worry, generalized anxiety disorder, and emotion: Evidence from the EEG gamma band". In: *Biological Psychology* 79.2 (2008), pp. 165–170.
- [47] Lucy Riglin et al. "Variable emergence of autism spectrum disorder symptoms from childhood to early adulthood". In: *American Journal of Psychiatry* 178.8 (2021), pp. 752–760.
- [48] L Kanner. "Autistic Disturbances of Affective Contact". In: *Nervous Child* 2 (1943).
- [49] Arnold M Cooper and Robert Michels. *Diagnostic and Statistical Manual of Mental Disorders, Revised (DSM-III-R)*. Washington, DC: American Psychiatric Association, 1988.
- [50] Waleed M Sweileh et al. "Bibliometric profile of the global scientific research on autism spectrum disorders". In: *Springerplus* 5 (2016), pp. 1–12.
- [51] Jakob Christensen et al. "Prenatal valproate exposure and risk of autism spectrum disorders and childhood autism". In: *JAMA* 309.16 (2013), pp. 1696–1703.
- [52] Marte-Helene Bjørk et al. "Association of prenatal exposure to antiseizure medication with risk of autism and intellectual disability". In: *JAMA Neurology* 79.7 (2022), pp. 672–681.

- [53] Selma Idring et al. "Parental age and the risk of autism spectrum disorders: findings from a Swedish population-based cohort". In: *International Journal of Epidemiology* 43.1 (2014), pp. 107–115.
- [54] Shunquan Wu et al. "Advanced parental age and autism risk in children: a systematic review and meta-analysis". In: *Acta Psychiatrica Scandinavica* 135.1 (2017), pp. 29–41.
- [55] Eva Kočovská et al. "Vitamin D and autism: clinical review". In: *Research in Developmental Disabilities* 33.5 (2012), pp. 1541–1550.
- [56] Zuqun Wang, Rui Ding, and Juan Wang. "The association between vitamin D status and autism spectrum disorder (ASD): a systematic review and meta-analysis". In: *Nutrients* 13.1 (2020), p. 86.
- [57] Lauren Rylaarsdam and Alicia Guemez-Gamboa. "Genetic causes and modifiers of autism spectrum disorder". In: *Frontiers in Cellular Neuroscience* 13 (2019), p. 385.
- [58] Amirhossein Modabbernia, Eva Velthorst, and Abraham Reichenberg. "Environmental risk factors for autism: an evidence-based review of systematic reviews and meta-analyses". In: *Molecular Autism* 8 (2017), pp. 1–16.
- [59] Pauline Chaste and Marion Leboyer. "Autism risk factors: genes, environment, and gene-environment interactions". In: *Dialogues in Clinical Neuroscience* 14.3 (2012), pp. 281–292.
- [60] Mark Galliver et al. "Cost of assessing a child for possible autism spectrum disorder? An observational study of current practice in child development centres in the UK". In: *BMJ Paediatrics Open* 1.1 (2017).
- [61] Opal Ousley and Tracy Cermak. "Autism spectrum disorder: defining dimensions and subgroups". In: *Current developmental disorders reports* 1 (2014), pp. 20–28.
- [62] Nicole Wolff et al. "Autism spectrum disorder and IQ—A complex interplay". In: *Frontiers in Psychiatry* 13 (2022), p. 856084.
- [63] Jacob I Feldman et al. "Relations between sensory responsiveness and features of autism in children". In: *Brain Sciences* 10.11 (2020), p. 775.

- [64] Amanda Brignell et al. "A systematic review and meta-analysis of the prognosis of language outcomes for individuals with autism spectrum disorder". In: *Autism & Developmental Language Impairments* 3 (2018), p. 2396941518767610.
- [65] Avital Hahamy, Marlene Behrmann, and Rafael Malach. "The idiosyncratic brain: distortion of spontaneous connectivity patterns in autism spectrum disorder". In: *Nature Neuroscience* 18.2 (2015), pp. 302–309.
- [66] Tomoya Hirota and Bryan H King. "Autism spectrum disorder: a review". In: *JAMA* 329.2 (2023), pp. 157–168.
- [67] Camille Hours, Christophe Recasens, and Jean-Marc Baleyte. "ASD and ADHD comorbidity: What are we talking about?" In: *Frontiers in Psychiatry* 13 (2022), p. 837424.
- [68] Roma A Vasa et al. "A scoping review of anxiety in young children with autism spectrum disorder". In: *Autism Research* 13.12 (2020), pp. 2038–2057.
- [69] Chloe C Hudson, Layla Hall, and Kate L Harkness. "Prevalence of depressive disorders in individuals with autism spectrum disorder: A meta-analysis". In: *Journal of Abnormal Child Psychology* 47 (2019), pp. 165–175.
- [70] Shafali Spurling Jeste and Roberto Tuchman. "Autism spectrum disorder and epilepsy: two sides of the same coin?" In: *Journal of Child Neurology* 30.14 (2015), pp. 1963–1971.
- [71] Hangwei Wang et al. "The power spectrum and functional connectivity characteristics of resting-state EEG in patients with generalized anxiety disorder". In: *Scientific Reports* 15.1 (2025), p. 5991.
- [72] Fernando Soares de Aguiar Neto and João Luís Garcia Rosa. "Depression biomarkers using non-invasive EEG: A review". In: *Neuroscience & Biobehavioral Reviews* 105 (2019), pp. 83–93.
- [73] Yogatheesan Varatharajah et al. "Characterizing the electrophysiological abnormalities in visually reviewed normal EEGs of drug-resistant focal epilepsy patients". In: *Brain Communications* 3.2 (2021), fcab102.
- [74] Christine Fountain et al. "Developmental trajectories of autism". In: *Pediatrics* 152.3 (2023), e2022058674.

- [75] Christine Fountain, Alix S Winter, and Peter S Bearman. "Six developmental trajectories characterize children with autism". In: *Pediatrics* 129.5 (2012), e1112–e1120.
- [76] Shafali S Jeste, Joel Frohlich, and Sandra K Loo. "Electrophysiological biomarkers of diagnosis and outcome in neurodevelopmental disorders". In: *Current Opinion in Neurology* 28.2 (2015), pp. 110–116.
- [77] Louise Bogéa Ribeiro and Manoel da Silva Filho. "Systematic review on EEG analysis to diagnose and treat autism by evaluating functional connectivity and spectral power". In: *Neuropsychiatric Disease and Treatment* (2023), pp. 415–424.
- [78] Michel JAM Van Putten, Sebastian Olbrich, and Martijn Arns. "Predicting sex from brain rhythms with deep learning". In: *Scientific Reports* 8.1 (2018), p. 3069.
- [79] Laurel J Gabard-Durnam et al. "Longitudinal EEG power in the first post-natal year differentiates autism outcomes". In: *Nature Communications* 10.1 (2019), p. 4188.
- [80] Ling Wang et al. "Autism spectrum disorder: neurodevelopmental risk factors, biological mechanism, and precision therapy". In: *International Journal of Molecular Sciences* 24.3 (2023), p. 1819.
- [81] Laura Hull, KV Petrides, and William Mandy. "The female autism phenotype and camouflaging: A narrative review". In: *Review Journal of Autism and Developmental Disorders* 7 (2020), pp. 306–317.
- [82] Rachel K Schuck, Ryan E Flores, and Lawrence K Fung. "Brief report: Sex/gender differences in symptomology and camouflaging in adults with autism spectrum disorder". In: *Journal of Autism and Developmental Disorders* 49 (2019), pp. 2597–2604.
- [83] Rachel Loomes, Laura Hull, and William Polmear Locke Mandy. "What is the male-to-female ratio in autism spectrum disorder? A systematic review and meta-analysis". In: *Journal of the American Academy of Child & Adolescent Psychiatry* 56.6 (2017), pp. 466–474.

- [84] Allison B Ratto et al. "What about the girls? Sex-based differences in autistic traits and adaptive skills". In: *Journal of Autism and Developmental Disorders* 48 (2018), pp. 1698–1711.
- [85] Aleksandra Miljevic et al. "Electroencephalographic connectivity: a fundamental guide and checklist for optimal study design and evaluation". In: *Biological Psychiatry: Cognitive Neuroscience and Neuroimaging* 7.6 (2022), pp. 546–554.
- [86] Robert J Barry and Frances M De Blasio. "EEG differences between eyes-closed and eyes-open resting remain in healthy ageing". In: *Biological Psychology* 129 (2017), pp. 293–304.
- [87] Ander Ramos-Murguialday and Niels Birbaumer. "Brain oscillatory signatures of motor tasks". In: *Journal of Neurophysiology* 113.10 (2015), pp. 3663–3682.
- [88] Giovanni Chiarion et al. "Connectivity analysis in EEG data: a tutorial review of the state of the art and emerging trends". In: *Bioengineering* 10.3 (2023), p. 372.
- [89] Francesco Precenzano et al. "Electroencephalographic abnormalities in autism spectrum disorder: characteristics and therapeutic implications". In: *Medicina* 56.9 (2020), p. 419.
- [90] Eric Van Diessen et al. "Increased power of resting-state gamma oscillations in autism spectrum disorder detected by routine electroencephalography". In: *European Archives of Psychiatry and Clinical Neuroscience* 265 (2015), pp. 537–540.
- [91] Emily Neuhaus et al. "Resting state EEG in youth with ASD: age, sex, and relation to phenotype". In: *Journal of Neurodevelopmental Disorders* 13 (2021), pp. 1–15.
- [92] Wei Siong Neo et al. "Resting-state EEG power differences in autism spectrum disorder: a systematic review and meta-analysis". In: *Translational Psychiatry* 13.1 (2023), p. 389.

- [93] Jun Wang et al. "Resting state EEG abnormalities in autism spectrum disorders". In: *Journal of Neurodevelopmental Disorders* 5 (2013), pp. 1–14.
- [94] Audrey M Carson et al. "Electroencephalogram coherence in children with and without autism spectrum disorders: decreased interhemispheric connectivity in autism". In: *Autism Research* 7.3 (2014), pp. 334–343.
- [95] Karen J Mathewson et al. "Regional EEG alpha power, coherence, and behavioral symptomatology in autism spectrum disorder". In: *Clinical Neurophysiology* 123.9 (2012), pp. 1798–1809.
- [96] Tianyi Zhou et al. "Early childhood developmental functional connectivity of autistic brains with non-negative matrix factorization". In: *NeuroImage: Clinical* 26 (2020), p. 102251.
- [97] Xinling Geng et al. "Abnormalities of EEG functional connectivity and effective connectivity in children with autism spectrum disorder". In: *Brain Sciences* 13.1 (2023), p. 130.
- [98] Mitsuru Kikuchi et al. "Reduced long-range functional connectivity in young children with autism spectrum disorder". In: *Social Cognitive and Affective Neuroscience* 10.2 (2015), pp. 248–254.
- [99] Abigail Dickinson et al. "Interhemispheric alpha-band hypoconnectivity in children with autism spectrum disorder". In: *Behavioural Brain Research* 348 (2018), pp. 227–234.
- [100] Jia Wang et al. "Increased EEG coherence in long-distance and short-distance connectivity in children with autism spectrum disorders". In: *Brain and Behavior* 10.10 (2020), e01796.
- [101] Dardo Tomasi and Nora D Volkow. "Reduced local and increased long-range functional connectivity of the thalamus in autism spectrum disorder". In: *Cerebral Cortex* 29.2 (2019), pp. 573–585.
- [102] Oana Gurau, William J Bosl, and Charles R Newton. "How useful is electroencephalography in the diagnosis of autism spectrum disorders and the delineation of subtypes: a systematic review". In: *Frontiers in Psychiatry* 8 (2017), p. 121.

- [103] Susanna Törnroth-Horsefield and Richard Neutze. "Opening and closing the metabolite gate". In: *Proceedings of the National Academy of Sciences* 105.50 (2008), pp. 19565–19566.
- [104] Reika Shiratori et al. "Glycolytic suppression dramatically changes the intracellular metabolic profile of multiple cancer cell lines in a mitochondrial metabolism-dependent manner". In: *Scientific Reports* 9.1 (2019), p. 18699.
- [105] Thomas Pfeiffer, Stefan Schuster, and Sebastian Bonhoeffer. "Cooperation and competition in the evolution of ATP-producing pathways". In: *Science* 292.5516 (2001), pp. 504–507.
- [106] Elidie Beard et al. "Astrocytes as key regulators of brain energy metabolism: new therapeutic perspectives". In: *Frontiers in Physiology* 12 (2022), p. 825816.
- [107] Suzana Herculano-Houzel. "Scaling of brain metabolism with a fixed energy budget per neuron: implications for neuronal activity, plasticity and evolution". In: *PloS One* 6.3 (2011), e17514.
- [108] ZiMian Wang et al. "Specific metabolic rates of major organs and tissues across adulthood: evaluation by mechanistic model of resting energy expenditure". In: *The American Journal of Clinical Nutrition* 92.6 (2010), pp. 1369–1377.
- [109] Ana C Andreazza et al. "Oxidative stress markers in bipolar disorder: a meta-analysis". In: *Journal of Affective Disorders* 111.2-3 (2008), pp. 135–144.
- [110] Charilaos Chourpiliadis et al. "Metabolic Profile and Long-Term Risk of Depression, Anxiety, and Stress-Related Disorders". In: *JAMA Network Open* 7.4 (2024), e244525–e244525.
- [111] Xinyi Gu et al. "Energy metabolism in major depressive disorder: Recent advances from omics technologies and imaging". In: *Biomedicine & Pharmacotherapy* 141 (2021), p. 111869.
- [112] G Delvecchio et al. "Metabolic alterations in generalised anxiety disorder: a review of proton magnetic resonance spectroscopic studies". In: *Epidemiology and psychiatric sciences* 26.6 (2017), pp. 587–595.



- [113] Otto Warburg and Seigo Minami. "Versuche an überlebendem carcinom-gewebe". In: *Klinische Wochenschrift* 2.17 (1923), pp. 776–777.
- [114] Maria V Liberti and Jason W Locasale. "The Warburg effect: how does it benefit cancer cells?" In: *Trends in Biochemical Sciences* 41.3 (2016), pp. 211–218.
- [115] Aranka László et al. "Serum serotonin, lactate and pyruvate levels in infantile autistic children". In: *Clinica Chimica Acta* 229.1-2 (1994), pp. 205–207.
- [116] Mary Coleman and John P Blass. "Autism and lactic acidosis". In: *Journal of Autism and Developmental Disorders* 15.1 (1985), pp. 1–8.
- [117] Brenda WJH Penninx and Sjors MM Lange. "Metabolic syndrome in psychiatric patients: overview, mechanisms, and implications". In: *Dialogues in Clinical Neuroscience* 20.1 (2018), pp. 63–73.
- [118] Tamara Žigman et al. "Inborn errors of metabolism associated with autism spectrum disorders: approaches to intervention". In: *Frontiers in Neuroscience* 15 (2021), p. 673600.
- [119] Liliana Rojas-Charry et al. "Abnormalities of synaptic mitochondria in autism spectrum disorder and related neurodevelopmental disorders". In: *Journal of Molecular Medicine* 99.2 (2021), pp. 161–178.
- [120] Diane C Chugani et al. "Evidence of altered energy metabolism in autistic children." In: *Progress in Neuro-psychopharmacology & Biological Psychiatry* 23.4 (1999), pp. 635–641.
- [121] Ya Wen and Martha R Herbert. "Connecting the dots: Overlaps between autism and cancer suggest possible common mechanisms regarding signaling pathways related to metabolic alterations". In: *Medical Hypotheses* 103 (2017), pp. 118–123.
- [122] Jacqueline R Weissman et al. "Mitochondrial disease in autism spectrum disorder patients: a cohort analysis". In: *PloS One* 3.11 (2008), e3815.
- [123] DA Rossignol and Richard E Frye. "Mitochondrial dysfunction in autism spectrum disorders: a systematic review and meta-analysis". In: *Molecular Psychiatry* 17.3 (2012), pp. 290–314.

- [124] Maheen F Siddiqui, Clare Elwell, and Mark H Johnson. "Mitochondrial dysfunction in autism spectrum disorders". In: *Autism* 6.5 (2016).
- [125] Richard E Frye and Daniel A Rossignol. "Mitochondrial dysfunction can connect the diverse medical symptoms associated with autism spectrum disorders". In: *Pediatric Research* 69.8 (2011), pp. 41–47.
- [126] Ning Cheng, Jong M Rho, and Susan A Masino. "Metabolic dysfunction underlying autism spectrum disorder and potential treatment approaches". In: *Frontiers in Molecular Neuroscience* 10 (2017), p. 34.
- [127] Jiaqi Liu et al. "Wnt/ $\beta$ -catenin signalling: function, biological mechanisms, and therapeutic opportunities". In: *Signal Transduction and Targeted Therapy* 7.1 (2022), p. 3.
- [128] Nathan D Okerlund and Benjamin NR Cheyette. "Synaptic Wnt signaling—a contributor to major psychiatric disorders?" In: *Journal of Neurodevelopmental Disorders* 3 (2011), pp. 162–174.
- [129] Hans Otto Kalkman. "A review of the evidence for the canonical Wnt pathway in autism spectrum disorders". In: *Molecular Autism* 3 (2012), pp. 1–12.
- [130] Pu-Hyeon Cha et al. "APC loss induces Warburg effect via increased PKM2 transcription in colorectal cancer". In: *British Journal of Cancer* 124.3 (2021), pp. 634–644.
- [131] Thomas H Wassink et al. "Evidence supporting WNT2 as an autism susceptibility gene". In: *American Journal of Medical Genetics* 105.5 (2001), pp. 406–413.
- [132] Vickie Kwan, Brianna K Unda, and Karun K Singh. "Wnt signaling networks in autism spectrum disorder and intellectual disability". In: *Journal of Neurodevelopmental Disorders* 8 (2016), pp. 1–10.
- [133] Matías A Medina et al. "Wnt/ $\beta$ -catenin signaling stimulates the expression and synaptic clustering of the autism-associated Neuroligin 3 gene". In: *Translational Psychiatry* 8.1 (2018), p. 45.

- [134] Li Wang et al. "Wnt signaling pathway participates in valproic acid-induced neuronal differentiation of neural stem cells". In: *International Journal of Clinical and Experimental Pathology* 8.1 (2015), p. 578.
- [135] Yongyi Li et al. "A novel mutation in intron 1 of Wnt1 causes developmental loss of dopaminergic neurons in midbrain and ASD-like behaviors in rats". In: *Molecular Psychiatry* 28.9 (2023), pp. 3795–3805.
- [136] Gaeun Park et al. "Dysregulation of the Wnt/ $\beta$ -catenin signaling pathway via Rnf146 upregulation in a VPA-induced mouse model of autism spectrum disorder". In: *Experimental & Molecular Medicine* 55.8 (2023), pp. 1783–1794.
- [137] Liyan Qin, Xufang Dai, and Yunhou Yin. "Valproic acid exposure sequentially activates Wnt and mTOR pathways in rats". In: *Molecular and Cellular Neuroscience* 75 (2016), pp. 27–35.
- [138] Mario O Caracci et al. "Wnt/ $\beta$ -catenin-dependent transcription in autism spectrum disorders". In: *Frontiers in Molecular Neuroscience* 14 (2021), p. 764756.
- [139] Robert Dallmann, Steven A Brown, and Frédéric Gachon. "Chronopharmacology: new insights and therapeutic implications". In: *Annual Review of Pharmacology and Toxicology* 54.1 (2014), pp. 339–361.
- [140] Alina Patke, Michael W Young, and Sofia Axelrod. "Molecular mechanisms and physiological importance of circadian rhythms". In: *Nature Reviews Molecular Cell Biology* 21.2 (2020), pp. 67–84.
- [141] Carolina Escobar et al. "Circadian disruption leads to loss of homeostasis and disease". In: *Sleep Disorders* 2011.1 (2011), p. 964510.
- [142] Filipa Rijo-Ferreira and Joseph S Takahashi. "Genomics of circadian rhythms in health and disease". In: *Genome Medicine* 11.1 (2019), p. 82.
- [143] Isabelle Niedhammer et al. "Shift and night work and all-cause and cause-specific mortality: Prospective results from the STRESSJEM study". In: *Journal of Biological Rhythms* 37.3 (2022), pp. 249–259.
- [144] Imre Janszky and Rickard Ljung. "Shifts to and from daylight saving time and incidence of myocardial infarction". In: *New England Journal of Medicine* 359.18 (2008), pp. 1966–1968.

- [145] Michael H Hastings, Elizabeth S Maywood, and Marco Brancaccio. "Generation of circadian rhythms in the suprachiasmatic nucleus". In: *Nature Reviews Neuroscience* 19.8 (2018), pp. 453–469.
- [146] Johanna H Meijer et al. "Light responsiveness of the suprachiasmatic nucleus: long-term multiunit and single-unit recordings in freely moving rats". In: *Journal of Neuroscience* 18.21 (1998), pp. 9078–9087.
- [147] Sato Honma. "The mammalian circadian system: a hierarchical multi-oscillator structure for generating circadian rhythm". In: *The Journal of Physiological Sciences* 68.3 (2018), pp. 207–219.
- [148] Jackelyn Melissa Kembro et al. "Dietary restriction modulates ultradian rhythms and autocorrelation properties in mice behavior". In: *Communications Biology* 7.1 (2024), p. 303.
- [149] Ken-ichi Honma and Sato Honma. "The SCN-independent clocks, methamphetamine and food restriction". In: *European Journal of Neuroscience* 30.9 (2009), pp. 1707–1717.
- [150] Yue Leng et al. "Association between circadian rhythms and neurodegenerative diseases". In: *The Lancet Neurology* 18.3 (2019), pp. 307–318.
- [151] Stephen P Becker. "ADHD and sleep: recent advances and future directions". In: *Current Opinion in Psychology* 34 (2020), pp. 50–56.
- [152] Anna Ashton and Aarti Jagannath. "Disrupted sleep and circadian rhythms in schizophrenia and their interaction with dopamine signaling". In: *Frontiers in Neuroscience* 14 (2020), p. 636.
- [153] Ryan W Logan and Colleen A McClung. "Rhythms of life: circadian disruption and brain disorders across the lifespan". In: *Nature Reviews Neuroscience* 20.1 (2019), pp. 49–65.
- [154] Alison L Baird et al. "Adult attention-deficit hyperactivity disorder is associated with alterations in circadian rhythms at the behavioural, endocrine and molecular levels". In: *Molecular Psychiatry* 17.10 (2012), pp. 988–995.
- [155] Ian D Blum et al. "A highly tunable dopaminergic oscillator generates ultradian rhythms of behavioral arousal". In: *Elife* 3 (2014), e05105.

- [156] Sylvie Tordjman et al. "Autism as a disorder of biological and behavioral rhythms: toward new therapeutic perspectives". In: *Frontiers in Pediatrics* 3 (2015), p. 1.
- [157] Ekin Yurdakul, Yaman Barlas, and Kutlu O Ulgen. "Circadian clock crosstalks with autism". In: *Brain and Behavior* 13.12 (2023), e3273.
- [158] Margaret C Souders et al. "Sleep in children with autism spectrum disorder". In: *Current Psychiatry Reports* 19 (2017), pp. 1–17.
- [159] Edward R Ritvo et al. "Elevated daytime melatonin concentrations in autism: a pilot study". In: *European Child & Adolescent Psychiatry* 2 (1993), pp. 75–78.
- [160] Isaac Nir et al. "Brief report: circadian melatonin, thyroid-stimulating hormone, prolactin, and cortisol levels in serum of young adults with autism". In: *Journal of Autism and Developmental Disorders* 25.6 (1995), pp. 641–654.
- [161] Blythe A Corbett et al. "Variable cortisol circadian rhythms in children with autism and anticipatory stress". In: *Journal of Psychiatry and Neuroscience* 33.3 (2008), pp. 227–234.
- [162] Andrew J Tomarken, Gloria T Han, and Blythe A Corbett. "Temporal patterns, heterogeneity, and stability of diurnal cortisol rhythms in children with autism spectrum disorder". In: *Psychoneuroendocrinology* 62 (2015), pp. 217–226.
- [163] Susan K Putnam et al. "Salivary cortisol levels and diurnal patterns in children with autism spectrum disorder". In: *Journal of Developmental and Physical Disabilities* 27 (2015), pp. 453–465.
- [164] Marion Leboyer et al. "Whole blood serotonin and plasma beta-endorphin in autistic probands and their first-degree relatives". In: *Biological Psychiatry* 45.2 (1999), pp. 158–163.
- [165] Chang-Jiang Yang et al. "The cortisol, serotonin and oxytocin are associated with repetitive behavior in autism spectrum disorder". In: *Research in Autism Spectrum Disorders* 18 (2015), pp. 12–20.
- [166] Anna B Fishbein, Kristen L Knutson, Phyllis C Zee, et al. "Circadian disruption and human health". In: *The Journal of Clinical Investigation* 131.19 (2021).

- [167] Ethan Lorsung, Ramanujam Karthikeyan, and Ruifeng Cao. “Biological timing and neurodevelopmental disorders: a role for circadian dysfunction in autism spectrum disorders”. In: *Frontiers in Neuroscience* 15 (2021), p. 642745.
- [168] Nanduri R Prabhakar and Ying-Jie Peng. “Peripheral chemoreceptors in health and disease”. In: *Journal of Applied Physiology* 96.1 (2004), pp. 359–366.
- [169] Santosh Manicka et al. “The nonlinearity of regulation in biological networks”. In: *NPJ Systems Biology and Applications* 9.1 (2023), p. 10.
- [170] Alan L Hodgkin and Andrew F Huxley. “Action potentials recorded from inside a nerve fibre”. In: *Nature* 144.3651 (1939), pp. 710–711.
- [171] M. G. Rosenblum, A. Pikovsky, and J. Kurths. *Synchronization – A universal concept in nonlinear sciences*. Cambridge: Cambridge University Press, 2001.
- [172] Rajendra Rajendra Acharya et al. “Heart rate variability: a review”. In: *Medical and Biological Engineering and Computing* 44 (2006), pp. 1031–1051.
- [173] Julian Newman et al. “Intermittent phase dynamics of non-autonomous oscillators through time-varying phase”. In: *Physica D: Nonlinear Phenomena* 461 (2024), p. 134108.
- [174] Steven H Strogatz et al. “Crowd synchrony on the Millennium Bridge”. In: *Nature* 438.7064 (2005), pp. 43–44.
- [175] Steven H Strogatz. *Nonlinear dynamics and chaos: with applications to physics, biology, chemistry, and engineering*. Chapman and Hall/CRC, 2024.
- [176] Peter Kloeden and Christian Pötzsche. *Nonautonomous Dynamical Systems in the Life Sciences Preface*. Vol. 2102. Nov. 2013.
- [177] Philip T Clemson and Aneta Stefanovska. “Discerning non-autonomous dynamics”. In: *Physics Reports* 542.4 (2014), pp. 297–368.
- [178] Maxime Lucas, Duccio Fanelli, and Aneta Stefanovska. “Nonautonomous driving induces stability in network of identical oscillators”. In: *Physical Review E* 99.1 (2019), p. 012309.
- [179] Lisa E Mash et al. “Transient states of network connectivity are atypical in autism: A dynamic functional connectivity study”. In: *Human Brain Mapping* 40.8 (2019), pp. 2377–2389.

- [180] Evie A Malaia, Sungwoo Ahn, and Leonid L Rubchinsky. "Dysregulation of temporal dynamics of synchronous neural activity in adolescents on autism spectrum". In: *Autism Research* 13.1 (2020), pp. 24–31.
- [181] Edmund T Rolls, Wei Cheng, and Jianfeng Feng. "Brain dynamics: the temporal variability of connectivity, and differences in schizophrenia and ADHD". In: *Translational Psychiatry* 11.1 (2021), p. 70.
- [182] Aneta Stefanovska. "Coupled oscillators: complex but not complicated cardiovascular and brain interactions". In: *IEEE Engineering in Medicine and Biology Magazine* 26.6 (2007), pp. 25–29.
- [183] Joe Rowland Adams and Aneta Stefanovska. "Modeling cell energy metabolism as weighted networks of non-autonomous oscillators". In: *Frontiers in Physiology* 11 (2021), p. 613183.
- [184] Elham Farshadi, Gijsbertus TJ van Der Horst, and Inês Chaves. "Molecular links between the circadian clock and the cell cycle". In: *Journal of Molecular Biology* 432.12 (2020), pp. 3515–3524.
- [185] Henri Poincaré. "Mémoire sur les courbes définies par une équation différentielle". In: *Journal de Mathématiques Pures et Appliquées* 8 (1882), pp. 251–296.
- [186] Yevhen F Suprunenko, Philip T Clemson, and Aneta Stefanovska. "Chronotaxic systems: a new class of self-sustained nonautonomous oscillators". In: *Physical Review Letters* 111.2 (2013), p. 024101.
- [187] Ljupco Kocarev and Ulrich Parlitz. "Generalized synchronization, predictability, and equivalence of unidirectionally coupled dynamical systems". In: *Physical Review Letters* 76.11 (1996), p. 1816.
- [188] Yevhen F Suprunenko and Aneta Stefanovska. "Generalized chronotaxic systems: Time-dependent oscillatory dynamics stable under continuous perturbation". In: *Physical Review E* 90.3 (2014), p. 032921.
- [189] Lingyun Xiong and Alan Garfinkel. "Are physiological oscillations physiological?" In: *The Journal of Physiology* (2023).
- [190] Samuel JK Barnes and Aneta Stefanovska. "Physics of cellular energy metabolism". In: *Contemporary Physics* 62.3 (2021), pp. 125–143.



- [191] Yoshiki Kuramoto. "Self-entrainment of a population of coupled non-linear oscillators". In: *International Symposium on Mathematical Problems in Theoretical Physics: January 23–29, 1975, Kyoto University, Kyoto/Japan*. Springer. 1975, pp. 420–422.
- [192] Yoshiki Kuramoto. *Chemical turbulence*. Springer, 1984.
- [193] Peter J Uhlhaas and Wolf Singer. "Neural synchrony in brain disorders: relevance for cognitive dysfunctions and pathophysiology". In: *Neuron* 52.1 (2006), pp. 155–168.
- [194] André Weber, Werner Zuschratter, and Marcus JB Hauser. "Partial synchronisation of glycolytic oscillations in yeast cell populations". In: *Scientific Reports* 10.1 (2020), p. 19714.
- [195] Thomas E Dick et al. "Cardiorespiratory coupling: common rhythms in cardiac, sympathetic, and respiratory activities". In: *Progress in Brain Research* 209 (2014), pp. 191–205.
- [196] Marcus JB Hauser. "Synchronisation of glycolytic activity in yeast cells". In: *Current Genetics* 68.1 (2022), pp. 69–81.
- [197] Donald C Michaels, Edward P Matyas, and Jose Jalife. "Dynamic interactions and mutual synchronization of sinoatrial node pacemaker cells. A mathematical model." In: *Circulation Research* 58.5 (1986), pp. 706–720.
- [198] Annette F Taylor et al. "Dynamical quorum sensing and synchronization in large populations of chemical oscillators". In: *Science* 323.5914 (2009), pp. 614–617.
- [199] Raphaël Sarfati, Julie C Hayes, and Orit Peleg. "Self-organization in natural swarms of *Photinus carolinus* synchronous fireflies". In: *Science Advances* 7.28 (2021).
- [200] Igor Belykh et al. "Emergence of the London Millennium Bridge instability without synchronisation". In: *Nature Communications* 12.1 (2021), p. 7223.
- [201] Steven H Strogatz. *Sync: How Order Emerges From Chaos In the Universe, Nature, and Daily Life*. Hyperion, 2012.

- [202] Brian W Johnston et al. "Heart rate variability: Measurement and emerging use in critical care medicine". In: *Journal of the Intensive Care Society* 21.2 (2020), pp. 148–157.
- [203] Maxime Lucas, Julian Newman, and Aneta Stefanovska. "Synchronisation and non-autonicity". In: *Physics of Biological Oscillators: New Insights into Non-Equilibrium and Non-Autonomous Systems*. Ed. by Peter VE McClintock Aneta Stefanovska. Springer, 2021, pp. 85–110.
- [204] Juan A Acebrón et al. "The Kuramoto model: A simple paradigm for synchronization phenomena". In: *Reviews of Modern Physics* 77.1 (2005), pp. 137–185.
- [205] Philip Clemson, Gemma Lancaster, and Aneta Stefanovska. "Reconstructing time-dependent dynamics". In: *Proceedings of the IEEE* 104.2 (2016), pp. 223–241.
- [206] Hideaki Oike, Yukino Ogawa, and Katsutaka Oishi. "Simple and quick visualization of periodical data using microsoft excel". In: *Methods and Protocols* 2.4 (2019), p. 81.
- [207] YW Lee. *Statistical Theory of Communication*. 1960.
- [208] Dennis Gabor. "Theory of communication. Part 3: Frequency compression and expansion". In: *Journal of the Institution of Electrical Engineers-Part III: Radio and Communication Engineering* 93.26 (1946), pp. 445–457.
- [209] G Kaiser. *A Friendly Guide to Wavelets*. 1994.
- [210] Akari Matsuki, Hiroshi Kori, and Ryota Kobayashi. "An extended Hilbert transform method for reconstructing the phase from an oscillatory signal". In: *Scientific Reports* 13.1 (2023), p. 3535.
- [211] Dmytro Iatsenko, Peter VE McClintock, and Aneta Stefanovska. "Extraction of instantaneous frequencies from ridges in time–frequency representations of signals". In: *Signal Processing* 125 (2016), pp. 290–303.
- [212] Lawrence W Sheppard, Aneta Stefanovska, and Peter VE McClintock. "Detecting the harmonics of oscillations with time-variable frequencies". In: *Physical Review E* 83.1 (2011), p. 016206.

- [213] Gemma Lancaster et al. "Surrogate data for hypothesis testing of physical systems". In: *Physics Reports* 748 (2018), pp. 1–60.
- [214] Claude E Shannon. "A mathematical theory of communication". In: *The Bell System Technical Journal* 27.3 (1948), pp. 379–423.
- [215] Karl J Friston. "Functional and effective connectivity: a review". In: *Brain Connectivity* 1.1 (2011), pp. 13–36.
- [216] Frederik Zernike. "The concept of degree of coherence and its application to optical problems". In: *Physica* 5.8 (1938), pp. 785–795.
- [217] Christopher Torrence and Peter J Webster. "Interdecadal changes in the ENSO–monsoon system". In: *Journal of Climate* 12.8 (1999), pp. 2679–2690.
- [218] Jean-Philippe Lachaux et al. "Studying single-trials of phase synchronous activity in the brain". In: *International Journal of Bifurcation and Chaos* 10.10 (2000), pp. 2429–2439.
- [219] Andriy Bandrivskyy et al. "Wavelet phase coherence analysis: application to skin temperature and blood flow". In: *Cardiovascular Engineering: an International Journal* 4 (2004), pp. 89–93.
- [220] Julian Newman, Aleksandra Pidde, and Aneta Stefanovska. "Defining the wavelet bispectrum". In: *Applied and Computational Harmonic Analysis* 51 (2021), pp. 171–224.
- [221] Janez Jamšek, Aneta Stefanovska, and Peter VE McClintock. "Wavelet bispectral analysis for the study of interactions among oscillators whose basic frequencies are significantly time variable". In: *Physical Review E* 76.4 (2007), p. 046221.
- [222] Tomislav Stankovski et al. "Coupling functions: Universal insights into dynamical interaction mechanisms". In: *Reviews of Modern Physics* 89.4 (2017), p. 045001.
- [223] Tomislav Stankovski et al. "A tutorial on time-evolving dynamical Bayesian inference". In: *European Physical Journal* 223 (2014), pp. 2685–2703.
- [224] Samuel JK Barnes et al. "Theta and alpha connectivity in children with autism spectrum disorder". In: *Brain Communications* (2025), fcaf084.

- [225] Samuel JK Barnes et al. "Methamphetamine alters the circadian oscillator and its couplings on multiple scales in *Per1/2/3* knockout mice". In: *Proceedings of the National Academy of Sciences Nexus* 4 (2025).
- [226] Hermann Koepsell. "Glucose transporters in brain in health and disease". In: *Pflügers Archiv-European Journal of Physiology* 472.9 (2020), pp. 1299–1343.
- [227] Shefteeq M Theparambil et al. "Adenosine signalling to astrocytes coordinates brain metabolism and function". In: *Nature* 632.8023 (2024), pp. 139–146.
- [228] Miguel A Aon, Sonia Cortassa, and Brian O'Rourke. "Mitochondrial oscillations in physiology and pathophysiology". In: *Advances in Experimental Medicine and Biology* 641 (2008), pp. 98–117.
- [229] Felix T Kurz et al. "Spatio-temporal oscillations of individual mitochondria in cardiac myocytes reveal modulation of synchronized mitochondrial clusters". In: *Proceedings of the National Academy of Sciences* 107.32 (2010), pp. 14315–14320.
- [230] Avraham Mayevsky and Gennady G Rogatsky. "Mitochondrial function in vivo evaluated by NADH fluorescence: from animal models to human studies". In: *American Journal of Physiology-Cell Physiology* 292.2 (2007), pp. C615–C640.
- [231] Akos A Gerencser et al. "Quantitative measurement of mitochondrial membrane potential in cultured cells: calcium-induced de- and hyperpolarization of neuronal mitochondria". In: *The Journal of Physiology* 590.12 (2012), pp. 2845–2871.
- [232] Lars F Olsen et al. "Regulation of glycolytic oscillations by mitochondrial and plasma membrane H<sup>+</sup>-ATPases". In: *Biophysical Journal* 96.9 (2009), pp. 3850–3861.
- [233] Louis NM Duysens and Jan Ames. "Fluorescence spectrophotometry of reduced phosphopyridine nucleotide in intact cells in the near-ultraviolet and visible region". In: *Biochimica et Biophysica Acta* 24 (1957), pp. 19–26.
- [234] Daniil P Aksenov et al. "Brain tissue oxygen regulation in awake and anesthetized neonates". In: *Neuropharmacology* 135 (2018), pp. 368–375.

- [235] Evan D Doubovnikov and Daniil P Aksenov. "Oscillations and concentration dynamics of brain tissue oxygen in neonates and adults". In: *Journal of Computational Neuroscience* 48.1 (2020), pp. 21–26.
- [236] Gemma Lancaster et al. "Modelling chronotoxicity of cellular energy metabolism to facilitate the identification of altered metabolic states". In: *Scientific Reports* 6.1 (2016), p. 29584.
- [237] Richard Bertram et al. "Interaction of glycolysis and mitochondrial respiration in metabolic oscillations of pancreatic islets". In: *Biophysical Journal* 92.5 (2007), pp. 1544–1555.
- [238] Allan K Poulsen and Lars F Petersen Mai Øand Olsen. "Single cell studies and simulation of cell–cell interactions using oscillating glycolysis in yeast cells". In: *Biophysical Chemistry* 125.2-3 (2007), pp. 275–280.
- [239] Silvia De Monte et al. "Dynamical quorum sensing: Population density encoded in cellular dynamics". In: *Proceedings of the National Academy of Sciences* 104.47 (2007), pp. 18377–18381.
- [240] Paul Smolen. "A model for glycolytic oscillations based on skeletal muscle phosphofructokinase kinetics". In: *Journal of Theoretical Biology* 174.2 (1995), pp. 137–148.
- [241] Matthew J Merrins et al. "Phase analysis of metabolic oscillations and membrane potential in pancreatic islet  $\beta$ -cells". In: *Biophysical Journal* 110.3 (2016), pp. 691–699.
- [242] Olga Vergun and Ian J Reynolds. "Fluctuations in mitochondrial membrane potential in single isolated brain mitochondria: modulation by adenine nucleotides and  $\text{Ca}^{2+}$ ". In: *Biophysical Journal* 87.5 (2004), pp. 3585–3593.
- [243] Felix T Kurz et al. "Wavelet analysis reveals heterogeneous time-dependent oscillations of individual mitochondria". In: *American Journal of Physiology-Heart and Circulatory Physiology* 299.5 (2010), H1736–H1740.
- [244] Philipp Mergenthaler et al. "Sugar for the brain: the role of glucose in physiological and pathological brain function". In: *Trends in Neurosciences* 36.10 (2013), pp. 587–597.

- [245] Joachim W Deitmer et al. "Energy dynamics in the brain: contributions of astrocytes to metabolism and pH homeostasis". In: *Frontiers in Neuroscience* 13 (2019), p. 1301.
- [246] Carlos Manlio Díaz-García and Gary Yellen. "Neurons rely on glucose rather than astrocytic lactate during stimulation". In: *Journal of Neuroscience Research* 97.8 (2019), pp. 883–889.
- [247] Gilles Bonvento and Juan P Bolaños. "Astrocyte-neuron metabolic cooperation shapes brain activity". In: *Cell Metabolism* 33.8 (2021), pp. 1546–1564.
- [248] Gary Yellen. "Fueling thought: Management of glycolysis and oxidative phosphorylation in neuronal metabolism". In: *Journal of Cell Biology* 217.7 (2018), pp. 2235–2246.
- [249] Bruce Alberts et al. *Molecular biology of the cell*. Vol. 3. Garland New York, 1994.
- [250] Peter T Fox et al. "Nonoxidative glucose consumption during focal physiologic neural activity". In: *Science* 241.4864 (1988), pp. 462–464.
- [251] Jakob Korf and Jaep De Boer. "Lactography as an approach to monitor glucose metabolism on-line in brain and muscle". In: *International Journal of Biochemistry* 22.12 (1990), pp. 1371–1378.
- [252] Yibai Hu and George S Wilson. "A temporary local energy pool coupled to neuronal activity: fluctuations of extracellular lactate levels in rat brain monitored with rapid-response enzyme-based sensor". In: *Journal of Neurochemistry* 69.4 (1997), pp. 1484–1490.
- [253] Leslie Mazuel et al. "A neuronal MCT2 knockdown in the rat somatosensory cortex reduces both the NMR lactate signal and the BOLD response during whisker stimulation". In: *PLoS One* 12.4 (2017), e0174990.
- [254] Vellingiri Balachandar et al. "Mitochondrial dysfunction: A hidden trigger of autism?" In: *Genes & Diseases* 8.5 (2021), pp. 629–639.
- [255] Yuan-Mei Wang et al. "Critical role of dysfunctional mitochondria and defective mitophagy in autism spectrum disorders". In: *Brain Research Bulletin* 168 (2021), pp. 138–145.

- [256] Richard E Frye et al. "Prenatal air pollution influences neurodevelopment and behavior in autism spectrum disorder by modulating mitochondrial physiology". In: *Molecular Psychiatry* 26.5 (2021), pp. 1561–1577.
- [257] Masuma A Taniya et al. "Role of gut microbiome in autism spectrum disorder and its therapeutic regulation". In: *Frontiers in Cellular and Infection Microbiology* 12 (2022), p. 915701.
- [258] Soo Heon Kwak et al. "Mitochondrial metabolism and diabetes". In: *Journal of Diabetes Investigation* 1.5 (2010), pp. 161–169.
- [259] Alessia Carocci et al. "Mercury toxicity and neurodegenerative effects". In: *Reviews of Environmental Contamination and Toxicology* (2014), pp. 1–18.
- [260] Tingting Ku et al. "PM2. 5, SO2 and NO2 co-exposure impairs neurobehavior and induces mitochondrial injuries in the mouse brain". In: *Chemosphere* 163 (2016), pp. 27–34.
- [261] Michael Salsaa et al. "Valproate inhibits mitochondrial bioenergetics and increases glycolysis in *Saccharomyces cerevisiae*". In: *Scientific Reports* 10.1 (2020), p. 11785.
- [262] Richard E Frye et al. "Mitochondria may mediate prenatal environmental influences in autism spectrum disorder". In: *Journal of Personalized Medicine* 11.3 (2021), p. 218.
- [263] Kathrin Nickel et al. "Altered markers of mitochondrial function in adults with autism spectrum disorder". In: *Autism Research* 16.11 (2023), pp. 2125–2138.
- [264] Stephanie Sprowl-Tanio et al. "Lactate/pyruvate transporter MCT-1 is a direct Wnt target that confers sensitivity to 3-bromopyruvate in colon cancer". In: *Cancer & Metabolism* 4 (2016), pp. 1–18.
- [265] Jaswinder K Sethi and Antonio Vidal-Puig. "Wnt signalling and the control of cellular metabolism". In: *Biochemical Journal* 427.1 (2010), pp. 1–17.
- [266] Niken Puspa Kuspriyanti, Eko Fuji Ariyanto, and Mas Rizky AA Syamsunarno. "Role of Warburg effect in cardiovascular diseases: a potential treatment option". In: *The Open Cardiovascular Medicine Journal* 15.1 (2021).



- [267] Jorge S Burns and Gina Manda. "Metabolic pathways of the Warburg effect in health and disease: perspectives of choice, chain or chance". In: *International Journal of Molecular Sciences* 18.12 (2017), p. 2755.
- [268] Carlos Manlio Díaz-García et al. "Neuronal stimulation triggers neuronal glycolysis and not lactate uptake". In: *Cell Metabolism* 26.2 (2017), pp. 361–374.
- [269] Toru Matsu-Ura, Sean R Moore, and Christian I Hong. "WNT takes two to tango: molecular links between the circadian clock and the cell cycle in adult stem cells". In: *Journal of Biological Rhythms* 33.1 (2018), pp. 5–14.
- [270] Luciana Pinato et al. "Dysregulation of circadian rhythms in autism spectrum disorders". In: *Current Pharmaceutical Design* 25.41 (2019), pp. 4379–4393.
- [271] Amanda L Richdale and Kimberly A Schreck. "Sleep problems in autism spectrum disorders: prevalence, nature, & possible biopsychosocial aetiologies". In: *Sleep Medicine Reviews* 13.6 (2009), pp. 403–411.
- [272] Hyo Sang Go et al. "Prenatal exposure to valproic acid increases the neural progenitor cell pool and induces macrocephaly in rat brain via a mechanism involving the GSK-3 $\beta$ / $\beta$ -catenin pathway". In: *Neuropharmacology* 63.6 (2012), pp. 1028–1041.
- [273] Niklas Krumm et al. "A de novo convergence of autism genetics and molecular neuroscience". In: *Trends in Neurosciences* 37.2 (2014), pp. 95–105.
- [274] Amy E Morgan and Mark T McAuley. "Vascular dementia: From pathobiology to emerging perspectives". In: *Ageing Research Reviews* (2024), p. 102278.
- [275] Christina A Castellani et al. "Thinking outside the nucleus: Mitochondrial DNA copy number in health and disease". In: *Mitochondrion* 53 (2020), pp. 214–223.